



PROCEEDINGS OF THE U.S. ARMY COMBAT CAPABILITIES
DEVELOPMENT COMMAND CHEMICAL BIOLOGICAL CENTER

FY22 **IN-HOUSE LABORATORY INDEPENDENT RESEARCH**
AND CHEMICAL BIOLOGICAL ADVANCED MATERIALS
MANUFACTURING SCIENCES PROGRAMS



APPROVED FOR PUBLIC RELEASE; DISTRIBUTION UNLIMITED

Message from the In-house Laboratory Independent Research Program Director

I am pleased to present the fourteenth annual edition of the Proceedings of the U.S. Army Combat Capabilities Development Command Chemical Biological Center's (DEVCOM CBC) In-house Laboratory Independent Research (ILIR) and Chemical Biological Advanced Materials and Manufacturing Science (CBAMMS) Programs. As the Senior Research Scientist (ST) for Chemistry and Director of the ILIR and CBAMMS programs, I am proud to lead the Center's Army-funded basic research and innovation programs. These programs offer DEVCOM CBC one of the most significant funding sources to conduct in-house research towards meeting the needs of the Center.

FY22 represented a pivotal year for our Army-funded basic research line. While these programs have always been designed to fulfill future Army capabilities, we took a hard look at shaping the Center's research to meet the needs laid out in the Army Modernization Strategy.

Part of that realignment involved expanding our historical surface science initiative (SSI) research program to place a greater focus on the fundamental science related to novel material science and signal management through smoke and obscuration. The result was the renaming of the SSI program to the Chemical Biological Advanced Materials and Manufacturing Science (CBAMMS) program. Additionally, we slightly reduced the target funding limits for each project, enabling more new starts in our pipeline. Adopting this strategy has already realized benefits.

- We initiated multiple projects focused on obscuration-based design strategies, one of which is supporting a principal investigator's (PI) Ph.D. program.
- We funded more new starts in a single year than ever before; most of these were led by early career PIs.
- We continued to foster the development of PIs, training them in the skills required to manage a project and effectively communicate their results.

I am proud of all we have accomplished this year and am looking forward to continued investment to increase the knowledge base, improve scientific capabilities, and lead to the next generation of DEVCOM CBC scientists.



This year also returned us to a sense of normalcy in a post-COVID world. We held our first in-person Technical Advisory Board (TAB) in September 2022 since the start of the pandemic, allowing us to continue our tradition of obtaining an external assessment of the content and quality of our basic research portfolio. Hosting the event in person allowed our expert scientific panel to engage more fully with the researchers and provide valuable feedback on how to improve individual projects and enhance the future of both portfolios. This report provides a few of those highlights.

This report concludes with a technical manuscript from each of the FY22 ILIR, CBAMMS, as well their smaller, quick-turn counterpart Seedling projects. Together, these projects covered areas of interest across the chemical, biological, and physical sciences, including Aerosol Sciences, Chemical and Biological Sensing, Computational Design and Development, Emerging Threats, Panomics and Molecular Toxicology, Rational Molecular Synthesis and Nano-system Design, Synthetic Biology, Materials, and Smoke and Obscuration sciences.

If you have questions regarding the ILIR Program or this report, please contact the DEVCOM CBC Public Affairs Office at usarmy.apg.devcom-cbc.mbx.communications-office@army.mil

Patricia (Trish) McDaniel, Ph.D.
Senior Research Scientist (ST) for Chemistry

Strategic Mission and Vision

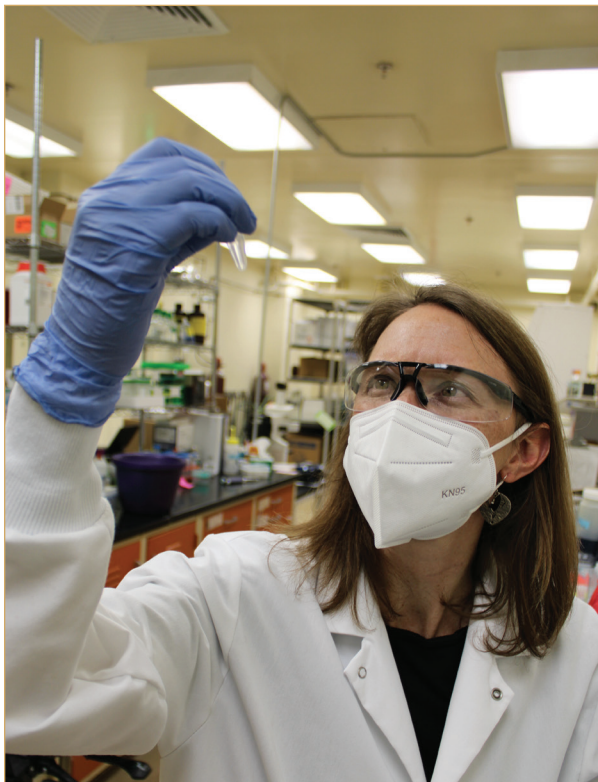
The U.S. Army Combat Capabilities Development Command Chemical Biological Center (DEVCOM CBC) is the Nation's principal research and development resource for non-medical chemical-biological (CB) defense. DEVCOM CBC has the unique ability to advance the mission of the Joint Warfighter and other stakeholders, while leveraging historical expertise, advanced equipment, and state-of-the-art facilities. The Center takes pride in its legacy of solutions born from more than a century of innovation.

Mission

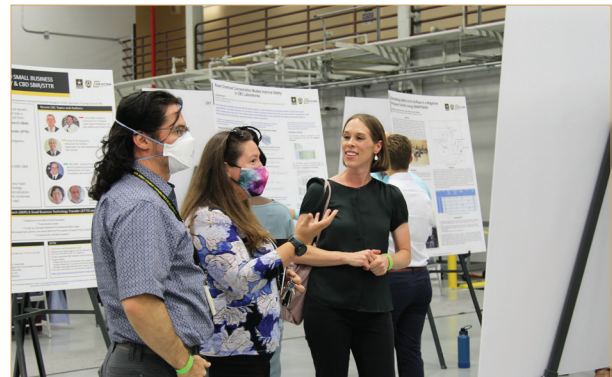
DEVCOM CBC's mission is to provide innovative chemical, biological, radiological, nuclear, and explosive (CBRNE) defense capabilities to enable the Joint Warfighters' dominance on the battlefield and interagency defense of the homeland. This mission recognizes that the Center's range of influence, while rooted in CB warfare defense, can be applied to all types of challenges in chemistry or biology. The Center's advanced capabilities in synthetic biology and materials science leverage existing core capabilities in biotechnology and decontamination sciences to develop next-generation capabilities that ensure our warfighters are always prepared to operate on the modern and future battlefield.

Vision

DEVCOM CBC's vision is to be the premier provider of innovative CBRNE solutions for the Army, DoD, the Nation, and our allies. For more than 100 years, the Center has been a distinct asset, providing innovative and economical CB defense technology solutions through scientific and engineering expertise, coupled with our unique facilities and collaboration with partners.



DEVCOM CBC scientists focus on the dangers that could face the warfighter. Above, Army biologist Alena Calm is one of many scientists working to develop the capability to detect, identify, and mitigate the harmful effects of waterborne organisms.



The ILIR, CBAMMS, and Seedling programs encourage participating scientists to communicate their results and ideas through poster presentations; data talks; or more formal lectures at regional, national, and international forums.



The basic research portfolios provide scientists the opportunity to establish collaborations both within the Center and with external scientists. These collaborations maximize efficiency and productivity while giving researchers the opportunity to work across disciplines and synergize current capabilities.

DEVCOM CBC Basic Research Project Selection and Evaluation Process

ILIR and CBAMMS Program Overview

The DoD defines basic research as a “systematic study directed toward greater knowledge or understanding of the fundamental aspects of phenomena and of observable facts without specific applications toward processes or products in mind.”¹ To foster and sustain basic research, the DoD created and supports an In-house Laboratory Independent Research (ILIR) program in each DEVCOM center. The Army’s Core 6.1 program, which adheres to the guidelines outlined in DoD Instruction 3201.04, dictates that “each DoD component that operates an R&D laboratory or center shall support an ILIR program” and that these laboratories “shall be given wide latitude in the use of ILIR funds...to enable performance of innovative, timely, and promising work without requiring formal and prior approval.”² Therefore, the purpose of the ILIR program is to identify and fund innovative basic research projects that are high-risk but have high potential payoff for fulfilling future Army capability needs.

The Department of the Army has also established a separate, directed basic research effort for DEVCOM Centers to fund basic research related to their missions. Historically, DEVCOM CBC dedicated this funding line as the Surface Science Initiative (SSI) program. In FY22, however, DEVCOM CBC expanded the scope of this program to align more closely to challenges outlined in the Army Modernization Strategy. As such, the Chemical Biological Advanced Materials and Manufacturing Science (CBAMMS) program was created to place a heavier focus on the fundamental science related to novel material science and signal management through smoke and obscuration.

The ILIR and CBAMMS programs are specifically designed to foster increased innovation within the Center. They are viewed as a critical part of the Center’s efforts to ensure a high level of quality in basic science; to innovate in the areas of chemistry and biology; mentor junior investigators in the art and practice of laboratory science; and to explore new technological innovations and phenomenology at the

boundaries of chemistry, biology, mathematics, or physics. These project must also focus on expanding the state-of-the-art technologies that support CBRNE defense missions. ILIR and CBAMMS projects are funded for up to three years and are expected to result in peer-reviewed publications, technical reports, patents, and presentations at local and national scientific gatherings.

ILIR and CBAMMS Project Selection

The ILIR and CBAMMS programs solicit the Center’s researchers for innovative proposals that correspond to topics highlighted in the DEVCOM CBC Research and Operations (R&O) Directorate’s Strategic Roadmap. The FY22 ILIR topics included Aerosol Sciences, Chemical and Biological Sensing, Computational Design and Development, Emerging Threats, Panomics and Molecular Toxicology, Rational Molecular Synthesis/Nano-system Design, and Synthetic Biology while the CBAMMS portfolio focused on Materials, Smoke, and Obscuration sciences. In FY22, twelve new ILIR and CBAMMS proposals were received, reviewed, and critiqued by a review panel comprised of scientists from the Department of Homeland Security, the United States Military Academy, DEVCOM Army Research Laboratory, United States Army Research Office, and DEVCOM CBC.

The review panel evaluates and scores each proposal on its scientific objective, the proposed methods, investigator qualifications, and the budget. Of these four categories, the scientific objective and methods are weighted as the most important criteria. The proposals are then ranked according to merit, and only proposals deemed as basic research by the panel are considered for funding. Reviewer comments are compiled and used, along with the numerical score, as a critical assessment of the proposal. This written feedback is shared with each PI and is used for the Center’s mentoring of researchers and justifying the elimination of research programs that are not competitive.

¹ DoD Financial Management Regulation, DoD 7000.14-R, Vol. 2B, Ch. 5

² In-House Laboratory Independent Research Program, DoDI 3201.04, October 15, 2018

In FY22, two new ILIR projects and eight new CBAMMS projects were funded. Of the CBAMMS projects, one received its funding from the Fabrication Advanced Materials/Manufacturing Sciences (FAMMS) campaign in FY22 with the goal of eventually transitioning to CBAMMS funding in year two or three of the project. These projects, along with two ILIR and three CBAMMS continuations, made up the basic science portfolios which received a total of \$3.2M in FY22.

ILIR and CBAMMS Project Evaluation

Projects selected for funding are reviewed quarterly; these reviews of project performance provide guidance to the program’s participants to ensure projects meet significant milestones, that substantive new knowledge is being produced, and that the knowledge is transferred to DEVCOM CBC and the broader scientific community. Each quarterly review features a different focus. Quarter one includes discussions on the project goals and proposed methods that will be executed throughout the year, quarter two focuses on the results and status of each program objective, and quarter three features the technical advancements made by each project.

DEVCOM CBC holds an external review in the fourth quarter, known as the Technical Advisory Board (TAB) Review, to assess year-to-date performance of the funded ILIR and CBAMMS projects. Comments and feedback from this review are used to justify continued funding, to course correct individual projects facing substantial roadblocks, and to pause or terminate the funding of individual ILIR or CBAMMS projects. The comments and insights provided by the expert panel are used to improve the quality and content of individual research projects, the scientific focus of the ILIR and CBAMMS portfolios, and to guide the overall mission of the programs into the future.

PROPOSAL SCORING CRITERIA

Exceptional ④ Comprehensive and complete in all areas; meets all significant objectives; offers a comprehensive project that exceeds the ILIR vision and is supportable by the proposed approach; has few weaknesses which are easily correctable.

Acceptable ③ Meets most of the significant objectives and is responsive to the ILIR vision; offers a feasible technical solution; weaknesses are readily correctable; proposal is complete to the extent that an award could be made in present terms.

Marginal ② Minimally meets ILIR vision and objectives (i.e., offers a project vision that is marginally supported by the proposed approach, and/or claims are not documented or substantiated); significant deficiencies exist.

Unacceptable ① Fails to meet significant characteristics of the ILIR vision and/or objectives stated in the Solicitation; has weaknesses and/or deficiencies that are significant and of such magnitude that they cannot be corrected without extensive discussion/major revision of the proposal.

	REVIEWERS							AVG
	1	2	3	4	5	6	7	
Scientific Objective	4	3	4	3	3	4	3	3.4
Methods and Approach	4	3	3	2	3	2	2	2.7
PI Qualifications	3	3	4	2	3	3	3	3.0
Budget	3	3	3	2	3	3	3	2.9
Overall Evaluation	3.5	3.0	3.5	2.3	3.0	3.0	2.8	3.0

FOUR REVIEWERS FROM DIFFERENT FEDERAL DEFENSE ORGANIZATIONS SERVED ON THE FY22 TAB PANEL, INCLUDING:

- **Edward Perkins, Ph.D.**, Senior Research Scientist for Environmental Networks and Genetic Toxicology, U.S. Army Engineer Research and Development Center
- **LTC Victor Jaffett, Ph.D.**, Assistant Director, Department of Chemistry and Life Science, United States Military Academy
- **LTC Barbara Cloutier, D.V.M., Ph.D., M.P.H.**, Medical Integrator, Defense Threat Reduction Agency – Joint Science and Technology Office
- **Calvin Chue, Ph.D.**, Biologist, United States Department of State



In FY22, the TAB was held in-person at the Center after being forced to take place virtually over the last two years due to the COVID-19 pandemic. The panel was tasked with producing an unbiased assessment of the content, quality, innovation, accomplishments, and relevance of the R&O basic science programs. Each project was evaluated based on seven areas: (1) scientific objectives, opportunity, and significance, (2) research methodology, (3) connections to the broader community, (4) overall capabilities and metrics, (5) use of PowerPoint, (6) use of time, and (7) overall presentation, with criteria 1–4 weighted as the most important. In FY22, the panel recommended all but one project receive continued funding and provided critical feedback to enhance the impact of several of the ongoing projects. Individual scores, portfolio reviews, and the key points from the TAB discussion were all used to generate a report for both project PIs and DEVCOM CBC leadership.

In FY22, the panel felt the funds invested in the portfolios resulted in excellent productivity and that the projects spanned a diverse set of topics important to the Army Modernization Strategy. The focus of many of the research projects excited the panel, with PIs engaged in emerging scientific disciplines including synthetic biology, metal organic frameworks (MOFs), and obscurant technology. With the bulk of the projects being led by first year PIs, the TAB was optimistic that the investments in new projects and PIs in each portfolio will pay off in the future with new capabilities, future deliverables, and an up-and-coming workforce that will power the Center for years to come. Further, the TAB reviewers were complimentary of the state-of-the-art technologies each project utilized, the quality of the presentations, the multiple, internal DEVCOM CBC collaborations, and the potential for projects to transition to external partners at the conclusion of their ILIR or CBAMMS funding.

While the two portfolios had many strengths, the TAB reviewers noted a need to balance the research areas in each portfolio beyond synthetic biology and metal-organic framework technology. The reviewers also stressed the need to pursue collaborations with experts outside of DEVCOM CBC to ensure PIs are staying up to date with the latest technologies and that each project includes a focused, testable hypothesis. Finally, it was noted that PIs should continue to hone their communication skills to ensure presentations can be understood by a learned audience that may not be experts in their given fields.

Seedling Program Overview

The Seedling program funds smaller, quick-turn (less than one year), “outside-the-box” exploratory basic research projects using funds obtained under the authority of 10 U.S.C § 2363 Funding Laboratory Enhancements Across-4 Categories (FLEX-4). Under FLEX-4, directors of DoD laboratories are directed to use funds to foster basic and applied research, transition novel technologies into operational use, further develop the workforce, and revitalize and recapitalize laboratory infrastructure and equipment. Seedling projects showing promise can then compete for additional funding under the ILIR or CBAMMS programs or external funding sources. Seedling projects also undergo a similar proposal review, selection, and evaluation process as ILIR projects; however, the Seedling review process is conducted internally at DEVCOM CBC and is more streamlined to fit the lower funding threshold. In FY22, 23 Seedling proposals were received, 11 of which were granted funding to focus on Operational Systems, Rational Molecular Synthesis and Nano-System Design, Chemical and Biological Sensing, Computer Science, and Emerging Threats.

FY22 Basic Research Program Highlights

FY22 Basic Research Program Productivity

11 

Presentations
and Posters

3 

Technical Reports
and Publications

2 

Filed
Patents

3 

Awards and
Recognition

Presentations and Posters

- DeCoste, J. Developing novel military materials from Biotechnology. *Presented at the Invited Colloquium, University of MD, Baltimore County, Baltimore, MD, 1 November 2021.*
- Polk, A.; Chintersingh, K.; Valdes, E.; Flickinger, M.; Weihs, T. Composite Microstructure and Ignition Properties of Aluminum-Zirconium Ball Milled Powders in Immiscible Liquid Process Control Agents. *Presented virtually at SERDP & ESTCP Symposium, November 2021.*
- DeCoste, J. Tuning the photocatalytic activity of metal-organic frameworks toward the oxidation of sulfur mustard in military relevant conditions. *Presented virtually at Pacifichem, 19 December 2021.*
- Lee, M.S. Cell-Free Bio-Functionality within Polymer Materials. *Presented virtually at the DoD Biotech Community of Interest STO Seminar, 5 April 2022.*
- Shearer, H.; Curtis, C.; Lee, T.; Houser, G.; Wright, H.; Lagasse, B.; Nguyen, C.; DeCoste, J. Metal Organic Framework Mediated Chemical Warfare Agent Degradation. *Presented at the USMA Projects Day, West Point, NY, 28 April 2022.*
- Bernhards, C.B.; Liem, A.T.; Berk, K.L.; Roth, P.A.; Gibbons, H.S.; Lux, M.W. Putative Phenotypically Neutral Genomic Insertions Points in Prokaryotes. *Presented at the Synthetic Biology: Engineering, Evolution & Design (SEED) Conference, Arlington, VA, 2–5 May 2022.*
- Parsons, N.; Kulisiewicz, A.; DeCoste, J. Effects on sulfur mustard degradation when lighting conditions are changed. *Presented at the Science and Math Academy Gallery Walk, Aberdeen, MD, May 2022.*
- Polk, A.; Chintersingh, K.; Valdes, E.; Flickinger, M.; Weihs, T. Composite Microstructure and Ignition Properties of Aluminum-Zirconium Ball Milled Powders in Immiscible Liquid Process Control Agents. *Presented at Gordon Research Conference-Energetics Materials, Manchester, NH, June 2022.*
- Antoshak, E.; McDonald, N.D. Engineering the Escherichia coli Lipopolysaccharide to mimic Yersinia pestis. *Poster Presented at Gordon Research Conference/Seminar: Bacterial Cell Surfaces, Mount Snow, VT, 24 June–1 July 2022.*
- Kulisiewicz, A.; Tovar, T.; Garibay, S.; Browe, M.; DeCoste, J. Controlling the heterogeneous catalysis of zirconium clusters bound to modified SBA-15, *Presented virtually at the 2022 ACS National Meeting, August 2022.*
- McDonald, N.D. Remodeling the Bacterial Outer Membrane for Synthetic Designer Microbes. *Presented Virtually at the 2022 DOD 6.1 Research Conference, 6–9 September 2022.*

3



Technical Reports and Publications

- Bernhards, C.B.; Liem, A.T.; Berk, K.L.; Roth, P.A.; Gibbons, H.S.; Lux, M.W. Putative Phenotypically Neutral Genomic Insertions Points in Prokaryotes. *ACS Synth. Biol.* **2022**, *11* (4), pp 1681–1685.
- Phillips, D.A.; Zacharoff, L.A.; Hampton, C.M.; Chong, G.W.; Malanoski, A.P.; Metskas, L.A.; Xu, S.; Bird, L.J.; Eddie, B.J.; Miklos, A.E.; Jensen, G.J.; Drummy, L.F.; El-Naggar, M.Y.; Glaven, S.M. A bacterial membrane sculpting protein with BAR domain-like activity. *eLife.* **2021**, *10*, pp e60049.
- Riley, P.C.; Deshpande, S.V.; Ince, B.S.; Wade, M.M.; O'Donnell, K.P.; Dereje, R.; Hauck, B.C. *Random Forest Permutation Feature Importance for Feature Selection in Ion Mobility Spectrometry*; DEVCOM CBC-TR-1768; U.S. Army Combat Capabilities Development Command Chemical Biological Center: Aberdeen Proving Ground, MD, **2022**; Unclassified Report.

2



Filed Patents

- Marilyn Lee, et. al. Processing active cell-free systems with organic solvents and encapsulation within polymer matrices. Application number 17/491,751. Filed **10/01/2021**.
- Shaun Debow, et. al. Apparatus and Method for Plasma coating Comminuted Material and Coated Comminuted Material Produced Using Same. Application number 17/665,795. Filed **02/07/2022**.

3



Awards and Recognition

Ms. Ameer Polk of the Obscuration & Nonlethal Engineering Branch was featured in the 2021 Materials Science in Extreme Environments Annual Newsletter published by Johns Hopkins University, where Ms. Polk is currently a doctoral candidate in the Whiting School of Engineering. The spotlight focused on the thermite formulation research Ms. Polk has been engaged in as a Research Chemical Engineer at DEVCOM CBC and the capabilities she envisions her work enabling in the future. The work detailed in the spotlight was leveraged in a successful CBAMMS project proposal in FY22. Ms. Polk anticipates defending her dissertation in 2023.



The Army Educational Outreach Program, National Science Teaching Association, and eCYBERMISSION combined forces to create a virtual reality experience that allows students to solve problems DoD scientists and engineers have already tackled. The project was led by **Dr. Jared DeCoste** and featured a script read by **Ms. Ann Kulisiewicz** that guides students in a laboratory as they design, create, and evaluate a MOF molecule that can adsorb water from the atmosphere. This outreach program is one of the first opportunities the Center has had to host K-12 students and has the potential to serve as a recruitment tool for years to come.



Dr. Patricia McDaniel was officially inducted as the Senior Research Scientist (ST) for Chemistry in May 2022. Dr. McDaniel had been serving in the position since May 2020, but the official ceremony was delayed due to the COVID-19 pandemic. As the ST for Chemistry, Dr. McDaniel directs two Army-funded basic research and innovation fundamental exploratory science programs including the ILIR and CBAMMS projects, and the Micro Sensors campaign. As she continues to oversee the basic research portfolio, Dr. McDaniel plans to emphasize training of junior researchers to grow as independent scientists and project managers.



Meet our FY22 Principal Investigators

In-house Laboratory Independent Research (ILIR) PIs



Nathan McDonald, Ph.D.
Research Biologist, BioTechnology
Branch, BioSciences Division

Dr. McDonald attended the University of Delaware, where he studied and conducted research in Biological Sciences. After earning his Ph.D. in 2018, Dr. McDonald continued his training as a Postdoctoral Fellow with the National Research Council until 2020 when he transitioned to his current Research Biologist position with DEVCOM CBC. Dr. McDonald has multiple publications that detail his research on modifying bacterial antigens for use in detection assay development, emerging threat assessment, and enhanced diagnostic and medical countermeasures. In 2021, Dr. McDonald was awarded a Federation of European Microbiological Societies Congress Attendance grant to attend and present at the American Society for Microbiology/Federation of European Microbiological Societies World Microbe Forum.



Danielle Kuhn, Ph.D.
Research Chemist, Smoke & Target
Defeat Branch, Protection Division

Dr. Kuhn earned a Ph.D. in Chemistry from Binghamton University in 2016. Immediately following her doctoral work, Dr. Kuhn began her career at DEVCOM CBC as an National Research Council Postdoctoral Fellow where she conducted research in semiconductor metal oxides and plasmonic particles. The goal of this research was to create novel materials that could enhance absorption of light and charge injection, increasing energy conversion and increasing efficacy of catalysis and enhancing obscuration. In 2018, Dr. Kuhn transitioned to her current role as a Research Chemist in the Smoke & Target Defeat Branch, working to create novel obscurants that function at multiple regions within the electromagnetic spectrum.



Casey Bernhards, Ph.D.
Research Biologist, BioChemistry Branch,
BioSciences Division

Dr. Bernhards earned her Ph.D. in Biological Sciences in 2014 from Virginia Polytechnic Institute and State University (Virginia Tech). Prior to joining DEVCOM CBC as a Research Biologist in 2021, Dr. Bernhards supported the Center's mission as a Postdoctoral Research Fellow sponsored by the Defense Threat Reduction Agency and National Research Council. Following her postdoctoral training, she continued to support DEVCOM CBC as a Senior Scientist with Excet, Inc. Dr. Bernhards research focuses on detection of engineered threats and understanding the off-target effects caused by CRISPR gene editing.



Brooke Ahern, Ph.D.
 Biologist, Molecular Toxicology
 Branch, Threat Agent
 Sciences Division

After completing a B.S. in Neuroscience at Brigham Young University in 2016, Dr. Ahern continued to study Physiology at the University of Kentucky, Lexington where she earned multiple awards and accolades, including the Department of Physiology Hardin Award and a New Investigator Travel Award for Basic Cardiovascular Sciences. While earning her Ph.D., Dr. Ahern worked as a Research Assistant/Electrophysiologist under the supervision of Dr. Jonathan Satin. After completing her doctorate, Dr. Ahern joined DEVCOM CBC as a Research Biologist where she specializes in electrophysiology and has been supported by a Defense Threat Reduction Agency Bio First Look award and a Defense Advanced Research Projects Agency Personal Protective Biosystems award.

Chemical Biological Advanced Materials Manufacturing Science (CBAMMS) PIs



Jared DeCoste, Ph.D.
 Research Chemist, CBR Filtration
 Branch, Protection Division

Dr. DeCoste earned a B.S. in Chemistry from the State University of New York before completing a Ph.D. in Materials Chemistry from Binghamton University in 2009. Dr. DeCoste worked as an Assistant Professor of Chemistry at Ball State University before joining DEVCOM CBC where he worked as a NRC Postdoctoral Associate, Principal Chemist with Leidos Inc., and, most recently, as a Research Chemist. His research interests range from the fundamentals of porous materials, especially for adsorption and catalysis, to engineering and scaling of functional nanomaterials. He has led many projects in this area and is regarded as an expert in designing MOFs for toxic chemical removal in the overarching scientific community. His work at the Center has led to more than 60 publications in top peer reviewed journals and has been recognized by his peers through multiple awards including the Leidos Publication Prize, Coffee with Colleagues Top Poster, DEVCOM CBC Rookie of the Year, and the 2018 Maryland American Chemical Society Chemist of the Year.



Marilyn Lee, Ph.D.
 Chemical Engineer, BioChemistry
 Branch, BioSciences Division

Dr. Lee attended Purdue University where she earned a B.S. in Chemical Engineering in 2012 before earning a Ph.D. in Chemical and Biomolecular Engineering from the University of California Berkeley in 2017. After graduation, she briefly worked as a Visiting Postdoctoral Scholar at Northwestern University before beginning her career at DEVCOM CBC as an Oak Ridge Institute for Science and Education (ORISE) and NRC post doctoral researcher from 2017 to 2020. After a successful postdoc, Dr. Lee transitioned to a civilian employee as a Chemical Engineer in 2020. Her area of research includes integrating cell-free protein synthesis with polymers to demonstrate broad implications on the design of sensors and devices harnessing biological activity.



Alex Miklos, Ph.D.
Research Biologist, BioChemistry
Branch, BioSciences Division

Prior to earning a Ph.D. in Biochemistry from Duke University in 2008, Dr. Miklos studied Chemistry at Kenyon College. Since completing his studies, Dr. Miklos continued his training as a Postdoctoral Fellow at the University of Texas at Austin where he led a project on protein engineering, then switched his focus to early-applied defense research projects that supported DEVCOM CBC as a Senior Scientist at Excet Inc. In 2012, Dr. Miklos began his career with DEVCOM CBC as a Research Biologist, and has led multiple chemical and biological detection projects, including his current work on biologically engineered metamaterials.



Thomas P. Pearl, Ph.D.
Research Chemist, Decontamination
Sciences Branch, Protection Division

Dr. Pearl began his academic career by earning a B.A. in Physics at Carleton College in 1994 and a Ph.D. in Chemistry at the University of Chicago in 2000. Dr. Pearl worked as an Assistant Professor in the Department of Physics at North Carolina State University, and as an industry scientist and contractor for various groups before formally joining DEVCOM CBC as a Research Chemist in 2020. As a DEVCOM CBC scientist, Dr. Pearl applies his expertise in the behavior of surfaces, interfaces, and thin films to the study of mass transport and reactivity arising from contaminant/decontaminant interactions with polymeric materials.



Mark Varady, Ph.D.
Research Engineer, Decontamination
Sciences Branch, CB Protection and
Decontamination Division

Dr. Varady received his Ph.D. in mechanical engineering from the Georgia Institute of Technology in 2010. He has been working with DEVCOM CBC since 2012, first as a contractor before transitioning to a civilian position in 2016. Dr. Varady focuses on understanding the applied and fundamental aspects of chemical transport in polymer-based materials. Dr. Varady has successfully published works on liquid spreading dynamics on rough surfaces in the context of military coating systems, has co-authored 5 technical reports, 20 peer-reviewed journal publications, and has been credited as an inventor on three U.S. patents.



Anne Walker, Ph.D.
Chemical Engineer, Respiratory
Protection Branch, Protection Division

Dr. Walker earned both a B.S. in Polymer Science Engineering in 2011 and a Ph.D. in Macromolecular Science and Engineering in 2019 from Case Western Reserve University. Prior to earning her degrees, Dr. Walker worked as an Engineering Aid and Engineering Technician for the United States Air Force Research Laboratory, and transitioned to a Researcher after completing her B.S. In 2019, Dr. Walker joined DEVCOM CBC as a Materials Researcher and, in 2020, to her current position as a Chemical Engineer. As a DEVCOM CBC researcher, Dr. Walker focuses her efforts on transitioning basic science developments into deployable devices and has worked to create an experimental additive manufacturing laboratory that seeks to streamline personal protective equipment research and development processes.



Eric Languirand, Ph.D.
 Research Chemist, Chemical Analysis &
 Physical Properties Branch, Threat Agent
 Sciences Division

Dr. Languirand attended Towson University where he earned a B.S. in Forensic Chemistry in 2012 and went on to study at the University of Maryland Baltimore County where he was awarded a Ph.D. in chemistry in 2017. Dr. Languirand then worked as a contracted scientist for Excet, Inc and then Leidos where he performed mathematical modeling for physical phenomena. After his time as a contractor, he transitioned to his current role as a Research Chemist for DEVCOM CBC in 2019. As a DEVCOM CBC scientist, Dr. Languirand has supported multiple spectroscopy and image-based projects and continues pioneering work by characterizing hyperspectral image data studies.



Ameer Polk
 Research Chemical Engineer,
 Obscuration & Nonlethal Engineering
 Branch, Protection Division

Ms. Polk earned a B.Ch.E. from the University of Delaware in 2004 and went on to earn a M.S. in Biotechnology from Johns Hopkins University in 2010. Prior to finishing her B.Ch.E., Ms. Polk spent a year as a Research Intern at Dupont Experimental Station. Immediately following her B.Ch.E., Ms. Polk joined the Pyrotechnics Team in 2004 of the Obscuration & Nonlethal Engineering Branch of DEVCOM CBC as a Chemical Engineer. As a Chemical Engineer, Ms. Polk has accrued multiple patents and has authored several technical reports relating to pyrotechnics, explosives, chemical warfare agent decontamination, dissemination, and detection. Ms. Polk is currently a doctoral student in the Department of Materials Science and Engineering at Johns Hopkins University Whiting School of Engineering and anticipates graduating with a D.Eng. in 2023.



Matthew Browe
 Chemical Engineer, CBR Filtration
 Branch, Protection Division

Mr. Browe was trained as a Chemical Engineer at the Pennsylvania State University where he earned a B.S. in 2011. After the completion of his degree, he began his career at DEVCOM CBC as a Chemical Engineer where he has successfully tested and evaluated novel materials for toxic chemical filtration and decontamination applications and has worked toward synthesizing polymer composite materials for toxic chemical mitigation and decontamination applications. Mr. Browe continued his education at the University of Delaware where he earned an M.S. in Chemical Engineering in 2022.



Ann Kulisiewicz
 Research Chemist, CBR Filtration
 Branch, Protection Division

Ms. Kulisiewicz attended Goucher College to study Chemistry, ultimately earning a B.A. in 2012 and continued to earn a M.S. in Chemistry at the University of Delaware in 2015. Immediately after completing her degree, Ms. Kulisiewicz joined Leidos as a Chemist while supporting various MOF-based projects in the CBR Filtration Branch. In 2018, Ms. Kulisiewicz joined DEVCOM CBC as a Research Chemist where she focuses on the synthesis, characterization, and testing of MOFs for filtration applications. As a researcher, Ms. Kulisiewicz has co-authored 11 peer-reviewed journal articles and has given multiple oral presentations at various American Chemical Society national meetings.

Seedling Pls

Justin Curtiss

Chemist, Chemical Analysis & Physical Properties Branch,
Threat Agent Sciences Division

Project keywords: Low volume deposition, printing,
piezoelectric

Shaun Debow

Chemical Engineer, Obscuration & Nonlethal Engineering
Branch, Protection Division

Project keywords: Nerve agent, chemical agent, VX,
organophosphorus, oxidation, degradation, electrocatalyst,
electrochemical

Kelley Evans, D.V.M.

Veterinary Medical Officer, BioChemistry Branch, BioSciences
Division

Project keywords: Canine, scent detection, detection dogs,
odor memory, odor discrimination, biological detector chemical
calibrant

Terry Henderson, Ph.D.

Research Chemist, Agent Chemistry Branch, Threat Agent
Sciences Division

Project keywords: Dipolar interaction, internuclear distance
measurement, metal-organic framework networks, molecular
structure, rotational-echo double resonance spectroscopy,
solid state nuclear magnetic resonance

Thomas Ingersoll, Ph.D.

Mathematician, Modeling, Simulation & Analysis Branch,
Physical Sciences Division

Project keywords: Monkeypox, network model, hierarchical
model, surveillance data, susceptible exposed infectious
resistant model, underreporting, disease dynamics, maximum
likelihood

Conor Jenkins

Research Biologist, BioDefense Branch, Biosciences Division

Project keywords: Post-transcriptional modifications, mass
spectrometry, exposomics, epitranscriptome, epigenome

Neal Kline, Ph.D.

Research Chemist, Spectroscopy Branch, Physical Sciences
Division

Project keywords: Infrared spectroscopy, Raman spectroscopy,
organophosphate nerve agent simulant, thioether rhodium
complex, diethyl chlorophosphate

Priscilla Lee

Biologist, Molecular Toxicology Branch, Threat Agent Sciences
Division

Project keywords: Bioprinting, in vitro model, liver,
Pluronic F-127, HepG2

Monica McEntee, Ph.D.

Research Chemist, CBR Filtration Branch, Protection Division

Project keywords: Active, aerosols, surfaces, simulants,
metal-organic frameworks

Jennifer Sekowski, Ph.D.

Research Molecular Toxicologist, BioDefense Branch,
BioSciences Division

Project keywords: Antimicrobial, tape, DNA, sample
preparation, trace collection, forensic collection

Nicole Vincelli

Research Biologist, Operational Toxicology Branch, Threat
Agent Sciences Division

Project keywords: Claramine, melittin, aminosterol, biotoxin
neutralization, biothreat

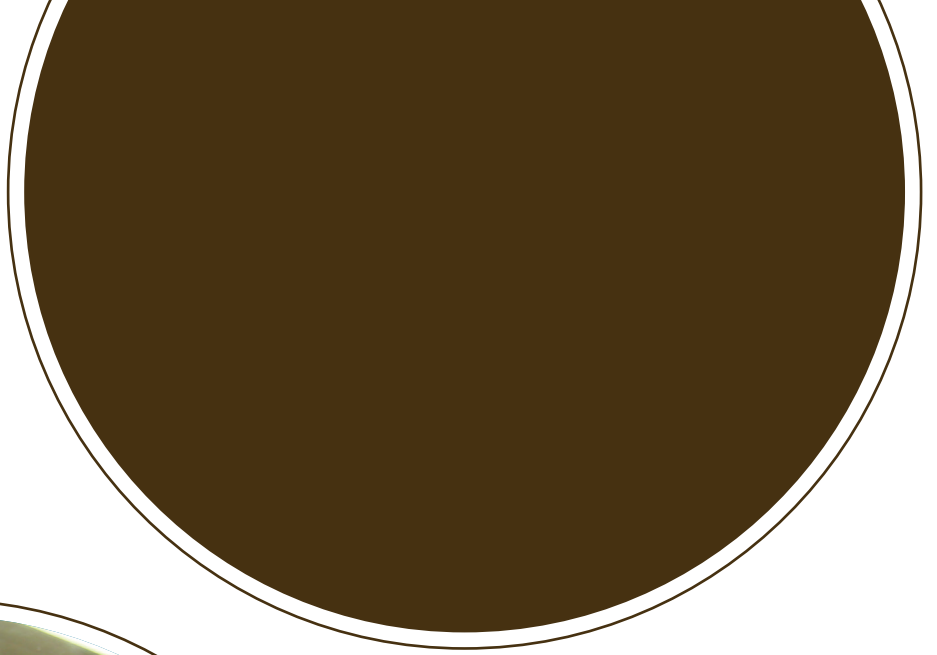


Table of Contents

In-house Laboratory Independent Research (ILIR) Projects

1 Remodeling the bacterial outer membrane for synthetic designer microbes *Erin E. Antoshak, Nathan D. McDonald**

Because of the danger associated with studying pathogenic organisms, novel ways to study individual virulence factors in non-pathogenic organisms are needed. Lipopolysaccharide, a virulence factor unique to each bacterial species, is a complex molecule that has not been extensively researched due to the challenges of working with highly pathogenic organisms. To remove the dangers associated with working with lipopolysaccharide, or any virulence factor in its native host, this project seeks to develop tools to transfer the necessary genes into non-pathogenic recipients for further analysis. Specifically, this study seeks to transfer the genes required for *Yersinia pestis* lipopolysaccharide synthesis into a non-pathogenic *Escherichia coli* recipient strain to create a hybrid outer membrane that can be used in the development of novel, targeted therapies, diagnostics, and combating antibiotic resistance.

11 Fundamental exploration into advanced plasmonic ceramic nitrides as multispectral obscurants *Danielle L. Kuhn*, Zachary B.S. Zander, Lena Vlahakis, Joshua Smith*

Obscurants are a class of materials that play a key role in protecting U.S. Warfighters by disrupting the line of sight between an object and trackers, sensors, or the human eye. Using a facile hydrothermal synthetic method, this study prepared doped-titanium nitride (d-TiN) nanofibers that were designed to exhibit broadband attenuation necessary for high-performing obscurants. The impact of various metal dopants, such as Ni, Cu, and Zn, on the attenuation capabilities of the TiN materials was also investigated.

21 Elucidating the prevalence of off-target effects of CRISPR-Cas editing in prokaryotes *Casey B. Bernhards*, Kimberly L. Berk, Alvin T. Liem, Pierce A. Roth, Mark A. Karavis, Matthew W. Lux*

CRISPR is a powerful gene editing tool that has the potential to be used to modify or create biological weapons. Despite this technology being the focus of multiple avenues of research, ongoing efforts have largely neglected to investigate how to determine if organisms, specifically prokaryotes, have been modified to increase virulence. This project seeks to determine if and how unintentional genetic scars can be identified in CRISPR-modified organisms using engineered *Escherichia coli* as a model organism.

31 Guided Linking Application to Decide Threat Interaction Effect Radius: A high throughput analysis for characterizing toxin and target interactions *Vishaka Santosh, Gabrielle M. Rizzo, Conor C. Jenkins, Andrew J. Walz, Brooke M. Ahern**

Neurotoxins, including α -conotoxins, represent a significant risk to the Warfighter but are technically challenging to characterize. This study proposes a novel analysis pipeline, called Guided Linking Application to Decide Threat Interaction Effect Radius (GLADTIER), to facilitate automated patch-clamping and cross-linking mass spectrometry (XL-MS) studies of the structural and functional changes that occurs in nicotinic acetylcholine receptors (nAChRs) after exposure to α -conotoxin EI. GLADTIER would streamline analysis of XL-MS data, allowing for the identification of important binding sites and the discovery of basic mechanisms of neurotoxin:ion channel interactions. Interestingly, the interactions between α -conotoxin EI and nAChRs did not recapitulate previously published findings, further highlighting the need for improved tools to study these toxins and their targets.

Chemical Biological Advanced Materials Manufacturing Science (CBAMMS) Projects

39 Toward understanding the generation and lifetime of singlet oxygen species in photosensitized rigid crystalline structures

*Ann M. Kulisiewicz, Sergio J. Garibay, Gabrielle Pozza, Matthew Browe, Ivan Jordanov, Owen Sparr, Sukh Singh, Lisa A. Kelly, Jared B. DeCoste**

The degradation of sulfur mustard is a complex process often complicated by slow reaction rates, toxic byproducts, or harsh reaction conditions. This study designed and characterized zirconium-based MOFs that serve as photocatalysts in the oxidation of sulfur mustard through the generation of a singlet oxygen species. After achieving rapid oxidation of a sulfur mustard simulant with UV and blue light, the underlying structure-property relationships responsible for this transform were investigated with spectroscopy and computational modelling.

49 Extending bio-functionality in materials via controlled polymer erosion

Marilyn S. Lee, Jennifer Lee, John R. Biondo, Jeffrey Lux, Danielle Kuhn, Matthew Browe, Maneesh K. Gupta, Matthew W. Lux*

Cell-free protein synthesis systems (CFPS) are synthetic biology tools for the expression of proteins and are particularly useful in situations that would not be conducive to living cells. CFPS reactions are capable of carrying out diverse functions, and components are able to be lyophilized and stored for long periods of time in ambient conditions. In this study, dried CFPS reactants were exposed to high temperatures and solvents to embed the reactions in polymers, after which they retained their expression activity. The ability to withstand these adverse environments while retaining their function unlocks the potential to use CFPS systems in a vast number of previously impossible applications.

61 Protein-sculpted membrane scaffolds as templates for conductive materials towards the development of biological metamaterials

*Daniel A. Phillips, John R. Biondo, Jennifer A. Lee, Patricia E. Buckley, Alexandr E. Miklos**

Biology has evolved to excel at building precise and complex structures at the nanometer scale, and patterned structures at this scale can produce interesting, metamaterial-like optical effects such as structural coloration. This project aims to understand and harness the phenomenon by which the curvature of bacterial membranes can be modified by proteins to reflect light and create camouflage or distinct coloration. If successful, this capability could build toward the development of tunable, biological metamaterials and lightweight, adaptive camouflage.

69 Determination of the influence of tunable chemical environment in metal-organic framework-polymer composites on the absorption of linear nonpolar toxic compounds

*Mark J. Varady, Gregory W. Peterson, Anne Y. Walker, Brent A. Mantooth, Adam R. Hinkle, Thomas P. Pearl**

Understanding the interaction of chemical warfare agents with material interfaces is a pivotal step in designing barrier materials with low chemical permeability. This study aims to understand the fundamental structure-property relationships of MOF-polymer composites that influence mass transport of chemical analytes. In the preliminary phase of this study, a Hansen-style solubility parameter analysis was performed for UiO-66-NH₂, to help predict compatibility with varying polymer backbone structures and mechanical properties of buried interfaces in UiO-66-NH₂-polymer composites were measured with atomic force microscopy and spectroscopy. Additionally, the potential for use of X-ray scattering and absorption-based measurements for characterization of MOF-polymer interfaces was investigated.

79 Nanofluids for removal of contaminants trapped in capillary features

Mark J. Varady, Brent A. Mantooth, Neil Hawbaker, Jill Ruth, Melissa S. Hulet, Melissa L. Sweat, Zhifeng Ren, Kent Kytken*

Liquid-phase chemical warfare agents can be entrained in capillary features on military assets, such as screw threads or mated surfaces on tanks or other military vehicles, making them difficult or impossible to completely decontaminate using current decontamination strategies. To achieve similar results in a related field, enhanced oil recovery techniques have been developed to displace oil trapped in underground rock formations using strong capillary and viscous forces. This project seeks to investigate if a reactive sodium-, silica-, or polyethylene glycol-based nanofluids could be used in a similar mechanism to better remove trapped or hidden chemical warfare agents.

89 Developing design rules for CBRN-relevant additive manufacturing systems by probing network structure and system free volume

*Kristian M. Van de Voorde, Cody C. Kendig, Bradley R. Ruprecht, James D. Severtsen, Melissa L. Sweat, Mark J. Varady, Anne Y. Walker**

3D printing, which can be used to produce highly modifiable and complex shapes, has the potential to be used to produce CBRN protective equipment; however, additional information is needed about network system structures in order to better understand how to fabricate polymers with specific properties. In this study, printing properties were modified to gain a better understanding of how processing parameters will impact the properties of printed structures. Specifically, the effects of printing direction, post-cure time, and layer thickness were investigated, resulting in increased knowledge of how polymer networks are formed during the printing process.

95 Janus metal-organic framework micromotors for the efficient removal of chemical agents

Matthew D. Collins, Eric R. Languirand, Angus Unruh, Ayusman Sen*

Leveraging molecular motion at the nano- or microscale may enable superior efficiency and precision for tasks such as transport or decontamination of chemical warfare agents. This project focuses on designing metal-organic framework-functionalized particles to act as micromotors that decontaminate chemical warfare agents at a faster rate compared to stationary particles. Results discussed in this work show the successful synthesis of particles and the effect of fuel, hydrogen peroxide, concentration, or bead material on micromotor motion.

105 Effect of composition and process control agent on the microstructure and ignition properties of ball-milled aluminum-zirconium powders

Amee Polk, Kerri-lee A. Chintersingh, Erica R. Valdes, Michael Flickinger, Timothy P. Weihs*

Historically, thermites have been used in welding, breaching, agent defeat, and enhanced energetics. Non-traditional thermites, however, are specialized reactions that generate minimal gas due to their unique oxidizer selections. To investigate additional functionality, microscale Al-Zr composite metal powders were created using planetary ball milling. These Al-Zr microscale powders are not pyrophoric, do not age during long-term storage, and have very low ignition temperatures with high reactivities. Three Al and Zr compositions were characterized using either hexane or immiscible liquid process control agents hexane/acetonitrile mixtures to limit cold welding. The 3Al:Zr composition had refined Zr particles with higher acetonitrile content having smaller Zr inclusions, smaller overall particle sizes, but, when combined with 100% HEX, failed to ignite altogether. The Al:3Zr 100% HEX sample's heat of reaction was lower than 3Al:Zr 100% HEX, yet featured a lower ignition temperature. The difference in ignition temperature was due to the decreased Zr inclusion size aiding Zr oxidation and nitration. The Al-rich composition also reached the preferential equilibrium state (Al₃Zr) upon heating to 1000 °C.

115 Molecular modeling of toxic industrial chemicals on metal-organic frameworks for next-generation filtration applications

*Matthew A. Browe**, Adam R. Hinkle, Ivan O. Jordanov, Wesley O. Gordon, John Landers, Shivam Parashar, Alex Neimark

Deployed military personnel are at risk of toxic chemical exposure through inhalation, causing acute distress and long-term damage. The overarching objective of this study is to enable sequestration of a wide range of chemical threats with a filtration media composed of MOF materials. Computational techniques, such as molecular dynamics and Monte Carlo methods, revealed key insights about the complex interactions between zirconium-based MOFs and small molecule analytes.

125 Controlling the heterogeneous catalysis of zirconium clusters within a porous SBA-15 scaffold

*Ann M. Kulisiewicz**, Sergio J. Garibay, Trenton B. Tovar, Matthew A. Browe

Catalytic degradation of chemical warfare agents may be achieved with porous Zr-based MOFs, which are known to have high surface areas, tunable pore channels, and opportunities for chemical functionalization. However, MOFs are difficult to synthesize and standardize. This work prepared the Zr_6 and Zr_{12} active clusters from the MOFs independent of the MOF structure, grafted the resulting Zr clusters onto silica supports, and studied the catalytic activity in the hydrolysis of an organophosphate nerve agent simulant. Transformation of the simulant to a nonreactive species was achieved in under 10 minutes with this novel zirconia cluster-modified silica material.

Seedling Projects

135 Effects of surface displacement on piezoelectric sample deposition

*Justin M. Curtiss**

In a process known as inkjet printing, where liquid materials are strategically deposited onto solid substrates, functional products can be manufactured with more design and material options than traditional methods. The printing process, however, is limited to flat surfaces in order to maintain the quality of the printed pattern. This study investigated the effect of printing with varying ethylene glycol concentrations and printhead displacements on the resulting pattern quality. The ideal concentration of ethylene glycol in the printing solution for large displacements (6–10 mm) was identified, which enables non-flat surfaces to be printed on with inkjet deposition methods.

139 MXene electrochemical degradation of chemical agent O-ethyl-S-[2-(diisopropylamino) ethyl]-methylphosphonothioate

*Shaun Debow**, Steven Harvey, Amanda Schenning, Michael Chesebrough, Zachary Zander, Jesse Brown, William Creasy, Brendan DeLacy, Yi Rao

Chemical agent detoxification often requires other agents that are hazardous to human health, often complicating or shifting the danger from one agent to another. A possible mechanism to detoxify chemical agents without the use of other dangerous chemical agents is to develop and deploy electrochemical catalysts into the field. In this study, a novel FeCo-MXene electrocatalyst was evaluated as a detoxification strategy against the VX nerve agent. Complete VX degradation was achieved, suggesting this novel strategy has the potential to be further refined and eventually used in the field as a safe method to decontaminate chemical agents.

145 Canine detection baseline training aid

Kelley L. Evans, Michele N. Maughan, Jenna D. Gadberry, Caitlin E. Sharpes, Patricia E. Buckley*

Military working dogs are an important asset to the Department of Defense, and canine detection dogs can outperform analytical machinery when detecting the sources of odor. However, there is not currently a universal canine detection baseline training aid, which would be a valuable tool for ensure that canines are detecting odors to a specific standard. Thirty chemicals were assessed for their suitability as a baseline training chemical, from which five promising chemicals were identified for further investigation.

151 Development of ^1H - ^{31}P rotational-echo double resonance techniques

Terry J. Henderson, Terry Gullion, Dennis D. Bevilacqua, Christopher J. Karwacki*

An NMR pulse program was written for executing ^1H -observe, ^1H - ^{31}P REDOR measurements and was tested against methylphosphonic acid and sodium phosphate, both without and with 97.5% perdeuteration. All results with fully protonated samples displayed a poor fit to theoretical predictions, however, those for perdeuterated samples were in very good agreement with theory, likely due to strong attenuation of ^1H - ^1H dipolar interactions via proton replacement with deuterons.

157 Generalized predictive disease networks

*Thomas E. Ingersoll**

Estimators for Disease Dynamics with Imperfect Surveillance (EDDIS) is a method of infectious disease dynamics modeling, initially developed for use during the 2020 SARS CoV-2 outbreak. This model has the potential to be used for other infectious diseases with heterogenous contact rates, underreported cases, and surveillance data that is not systematically sampled. To verify the utility of this model for other outbreaks and to improve the sophistication of the model itself, EDDIS was used to generate a predictive model for the 2022 outbreak of monkeypox in the United States, resulting in a model that correlates well to observed cases.

163 A modified nucleotide mass spectrometry library for epitranscriptome and epigenomic analysis

Conor C. Jenkins, Gabrielle Rizzo, Allison E. Melka, Daniel J. Angelini*

Environmental exposures and chemical warfare agents can cause detrimental changes to an individual's epigenome and epitranscriptome, which poses a risk for significant health issues in the Warfighter. Currently, next-generation sequencing is being used to understand these modifications; however, this is a time-consuming and expensive methodology, and has limited the speed at which this research can be conducted. Here, a more streamlined mass spectrometry-based technique is used to characterize 19 modified nucleotides, creating a library to be used for data analysis in future experiments.

169 Elucidating the mechanism of organophosphate nerve agent simulant reaction with thioester rhodium(II) complexes

Neal D. Kline, Desiree Moore, Eric Fussell, Ampofo Darko*

Developing novel technologies available for detecting chemical warfare agents, such as organophosphate nerve agents, is a crucial step in improving the safety and preparation of our Warfighters. This study investigated Rhodium(II) complexes with thioether ligands that are expected to selectively react with organophosphate nerve agents, thereby changing the color of the complex. Key changes to the vibrational band structure of the metal complexes after exposure to a nerve agent simulant, diethyl chlorophosphate, support the proposed mechanism for chromogenic detection.

175 Utilizing bioprinting technology to develop a 3D *in vitro* liver model

*Priscilla E. Lee**, Dylan H. Fudge, Bradley R. Ruprecht, James D. Severtsen

Bioprinting combines 3D printing technology with living cells to create customizable *in vitro* organ models, which could be used for downstream applications like predictive toxicology studies. Pluronic F-127 polymer was combined with the HepG2 liver cell line to create a scalable 3D liver model. The HepG2 cells remained viable after printing, and the 3D structure itself showed long-term stability in cell culture conditions. This proof-of-concept study marks the first successful bioprinting project at DEVCOM CBC.

181 Activated surfaces through aerosolized particle deposition

*Monica McEntee**, Gregory Peterson, Christopher Karwacki

The next generation of protective garments for warfighters will enable immediate protection against hazardous analytes by integrating advanced materials, such as metal-organic frameworks (MOFs) into textiles. In this study, MOF particles were deposited onto polyester/cellulose swatches with a spray nozzle from methanol suspensions. The ability of the MOF-activated textiles to capture and react with two CWA simulants was studied using gas-chromatography-mass spectrometry (GC-MS). Observations from this study highlight opportunities to develop garments integrated with advanced materials for sequestration and degradation of toxic species.

187 DNA extraction on a nano-organosilane coated polymer sheet: a novel low SWAP idea for field forward biological weapon agent sample prep

*Jennifer W. Sekowski** and Daniel Angelini

Nucleic acids obtained from pathogens and other microbes can be used for biodetection, but the need for complicated preparation limits the utility of this method in resource-limited environments. Organosilane nanoparticle-based printed surfaces, when applied to flexible polymer tape, could potentially facilitate DNA extraction from microbial samples by puncturing the cell walls and releasing nucleic acids. To test this hypothesis, a commercially available antimicrobial tape product was evaluated using an attenuated strain of *Bacillus anthracis* bacteria. Surprisingly, the coated tape was unable to bind or lyse the bacteria cells better than the uncoated control tape. Tests indicated that this particular product would not be effective for DNA isolation in the field; however, alternate polymer tape surfaces may yet prove suitable for this application.

195 Protective ratio of claramine against the toxic effects of melittin in mice

*Nicole M. Vincelli**, Ryan Limbocker, Michael S. Horsmon, Theodore S. Moran

Developing novel therapies against biological threat agents is a top concern of the CBRNE community. Previous work has shown that claramine, a chemical compound shown to suppress toxic effects in Alzheimer's and Parkinson's diseases, can also counteract melittin, a toxic polypeptide that affects neuroblastoma cells, *in vitro*. This study seeks to build our knowledge of claramine and to understand if its protective effects against melittin can be applied to an *in vivo* mouse model.



ILIR PROJECTS





Remodeling the bacterial outer membrane for synthetic designer microbes

Erin E. Antoshak^{a,b}, and Nathan D. McDonald^{1a*}

^aU.S. Army Combat Capabilities Development Command Chemical Biological Center, Research & Operations Directorate, 8198 Blackhawk Rd., Aberdeen Proving Ground, MD 21010

^bExcet Inc., 6225 Brandon Ave., Suite 360, Springfield, VA 22150

ABSTRACT

Synthetic biology and genomic engineering have facilitated the utilization of bacteria for applications ranging from medical treatments to biomanufacturing of complex molecules. The bacterial outer membrane, specifically the lipopolysaccharide within it, plays an integral role in physiology, pathogenesis, and as a target of existing detection assays. Despite its importance, the lipopolysaccharide has been under researched in genetic engineering studies due to challenges of working with the macromolecule. Advances in synthetic biology have enabled genomic mutations of the genes involved in lipopolysaccharide biosynthesis. Because bacteria all utilize roughly the same transcription and translation machinery, we hypothesize transferring the lipopolysaccharide biosynthesis system of one organism to another will result in the recipient producing the donor organism's lipopolysaccharide. To test this hypothesis, genes essential to *Yersinia pestis* lipopolysaccharide production will be inserted into an *Escherichia coli* recipient genome using Clustered Regularly Interspersed Palindromic Repeats/Cas recombineering, resulting in *E. coli* with an outer membrane mimicking that of *Y. pestis*. The work will evaluate if a bacterial outer membrane can be modified and demonstrate if outer membrane structures can be modified by synthetic biology. If successful, the ability to engineer lipopolysaccharide biosynthesis pathways can translate to targeted therapies, diagnostic detection enhancement, and combating antibiotic resistance.

Keywords: Lipopolysaccharide, *Yersinia pestis*, outer membrane, CRISPR/Cas9

1. INTRODUCTION

The advances in synthetic biology and genome engineering have allowed researchers to alter organisms, specifically bacteria, in ways never thought possible. The recently developed tools have resulted in bacteria which have been engineered for numerous purposes including drug delivery, biomanufacturing of economically valuable products, probiotics for disease treatment, biosensors, and diagnostics. The synthetic biology developments have paved the path for designer medicine, threat detection, and have stabilized supply chains among other groundbreaking developments. However, just as easily as these technologies can be used to benefit society, so too can they be used to create dangerous biological threats. The ease by which deadly pathogens can be enhanced, disguised, or created poses a serious threat to the DoD and the warfighter. Therefore, it is critical to understand the extent to which bacteria can be genetically engineered to grasp where potential threats may exist.

The hallmark feature of Gram-negative bacteria is the outer membrane component known as lipopolysaccharide (LPS). While the primary components are generally conserved, the LPS macromolecule is structurally diverse across bacteria. Because of this heterogeneity, the LPS has been rigorously characterized in hundreds of bacterial species, resulting in many highly defined structures. For the bacteria, the LPS is the primary component of the outer leaflet and contributes to the overall stability and permeability of the outer membrane and is essential for bacterial survival. Because it is embedded in the outer membrane of the bacteria and extends into the environment, LPS interacts with biotic and abiotic systems through bacterial adhesion, colonization, host immunomodulation, and acts as a virulence factor. Due to the conserved nature of LPS across all Gram-negative bacteria, higher ordered animals have evolved to recognize LPS and initiate an innate immune response. This robust, host immune response has led to LPS being considered an endotoxin. However, in a constant evolutionary arms race, many bacteria have developed mechanisms to alter various components of the LPS macromolecule to evade recognition and become resistant to antimicrobials.

The LPS molecule can generally be divided into three distinct domains: Lipid A, core oligosaccharide, and O-antigen, each of which possess unique characteristics and properties. While there are exceptions, one Lipid A unit is comprised of linked D-glucosamine disaccharide backbone, which is phosphorylated at positions 1' and 4' of the carbohydrates.¹ The backbone is acylated with branching fatty acid chains of varying lengths and substitutions depending on the species. The main unit of Lipid A can be further modified by various additions including phosphates, carbohydrates, and other small molecules which can alter the overall charge. Together, it is the Lipid A unit which is responsible for the endotoxic properties of LPS by activation of the innate immune system via recognition by Toll-like receptor 4 (TLR4).¹

Moving outward, linked to the Lipid A is the core oligosaccharide domain of the LPS. The function of the core oligosaccharide is to provide increased rigidity and structure to the outer leaflet of the Gram-negative bacteria through cationic interactions. All bacteria link the core oligosaccharide to the Lipid A via a common carbohydrate, KDO. Most Gram-negative bacteria possess a heptose-heptose-Kdo trisaccharide unit as the core composition, however exceptions to this have been identified.¹ The core oligosaccharide, much like the Lipid A, can also be further modified with substitutions. The most common substitutions to the core oligosaccharide include phosphates, additional carbohydrates and, in some cases, amino acids. The addition of these small molecules can dictate various interactions between the core oligosaccharide and the environment. Together, the Lipid A and the core oligosaccharide represent the minimal components necessary for bacterial survival. When bacteria only possess the core oligosaccharide and Lipid A, together known as the lipooligosaccharide (LOS) (Figure 1), they grow with and are defined by a rough colony morphology.

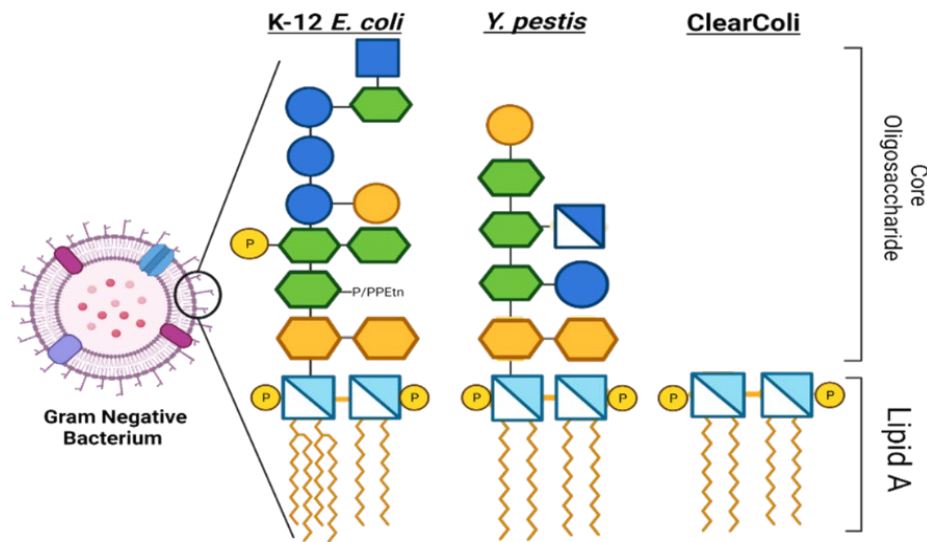


Figure 1. Representative depiction of the LOS structure from Gram-negative bacteria utilized in this study. The LOS is comprised of the inner Lipid A portion along with the outer core oligosaccharide. Shapes and colors indicate specific carbohydrates as indicated by the Symbol Nomenclature for Glycans. Circles: Hexoses; Squares: HexNAcs; Hexagons: Varies.

The final unit of LPS, the O-antigen, is the most genetically and structurally diverse component of the LPS. The O-antigen is comprised of monosaccharides assembled into units, which can be repeated anywhere between one to over one hundred times depending on the species and strain.¹ The structural diversity of O-antigens has allowed for researchers to classify strains within a species by serotyping, which, in the cases of *Escherichia coli* and *Vibrio cholerae*, results in the identification of hundreds of variants. The structural heterogeneity is a result of dramatic variations within the O-antigen biosynthesis gene clusters of these bacteria. In many cases, the bacteria can regulate the expression of O-antigen genes causing structural changes upon exposure to certain environments, such as during infection of a human host, known as phase variation. Alternatively, bacteria-specific viruses known as prophages can carry the genes for components of biosynthetic pathways and insert them within a bacterial genome, rapidly changing display structures.

The overall structure of the LPS in each organism can have profound effects. This macromolecule can itself serve as a virulence factor by a) masking a pathogen to evade the immune response, b) rendering the bacterial cell resistant to

antimicrobials both natural and synthetic, c) cause a dramatic immune response which can lead to rapid septic shock, and d) allow for bacteria identification and detection. Because of its role in bacteriology, the structure of LPS has been determined for numerous pathogens, including many select agents associated with biological warfare threats. In addition, because of the significance of the LPS, the genetics and biogenesis pathways for each of the domains has been defined across hundreds of species. The genomic age has provided researchers with the tools necessary to completely design and build organisms from the ground up. These tools have opened the door for advancing research with hazardous agents at lower biosafety levels and without threat to the scientist. To increase the detection and identification capabilities of U.S. Army Combat Capabilities Development Command – Chemical Biological Center we seek to develop a streamlined protocol to generate surrogate bacteria that retain the identifiable characteristics of potential bioweapons without the associated pathogenicity. To create these surrogates, we hypothesize that transferring an LPS biosynthesis system from one organism to another will result in the recipient organism producing the donor organism's LPS. In addition to enabling greater detection capabilities, these surrogates could also be used to further enhance diagnostic and medical countermeasures without the exposure risks normally associated with biological threat agents.

2. MATERIALS AND METHODS

2.1 Strains, plasmids, and constructs

ClearColi® BL21 (DE3) *E. coli* strain was received from Lucigen® and was used for Clustered Regularly Interspaced Short Palindromic Repeats (CRISPR) editing procedures. The modified CRISPR-Cas9 two plasmid system utilizes a pEcCas plasmid (Addgene #73227) for Cas9 expression and a pEcgRNA plasmid (Addgene #166581) including sgRNA directing it to the target region.² The ClearColi® strain was grown in Luria Bertani-(LB) Broth (Miller) (Sigma-Aldrich®; St. Louis, MO). The pEcgRNA plasmid was constructed to incorporate the targeting sgRNA by performing inverse polymerase chain reaction followed by Gibson Assembly using primers that contain the 20-base pair gRNA target sequence. Antibiotics were used as needed at the following concentrations: kanamycin (50 µg/mL), spectinomycin (50 µg/mL). Inducible expression constructs were developed as a control at each gene insertion step. The arabinose inducible vector pAJM.677 plasmid (Addgene #108530) was utilized as the expression plasmid.³ An IPTG-inducible pD451-MR (ATUM) vector was utilized for expression of the phosphoethanolamine transferase (EptA). Primers were developed to amplify the specific *Y. pestis* gene of interest from the donor DNA gBlock described in the following section in a polymerase chain reaction (PCR) amplification reaction. PCR was performed using primers specific to the pAJM.677 plasmid as well that amplify the surrounding area of the sequence where the gene will be inserted. The amplified plasmid and gene are then assembled using NEBuilder® HiFi DNA Assembly, New England Biolabs®. A list of primer sequences used in the construction of the pEcgRNA and pAJM.677 vectors are listed in Table 1. The *eptA* inducible vector was acquired commercially from ATUM.

2.2 Donor DNA amplification

The donor DNA was supplied as gBlocks™ (Integrated DNA Technologies™; Coralville, IA). The gBlock was constructed to include the specific *Y. pestis* A1122 gene of interest following the N20 sequence and PAM site indicated in the ClearColi® strain. Flanking the gene are 500 bp regions homologous to the target site in the ClearColi® genome. The gBlock™ was used as a template in a PCR amplification reaction. The reaction was performed with the Phusion® High Fidelity DNA Polymerase (New England Biolabs®; Ipswich, MA) following the provided NEB Phusion® protocol and utilizing the primers listed in Table 1. Gel electrophoresis was performed for conformation of the amplified gBlock™ at 120 V for 30 minutes on a 1 % agarose gel stained with EtBr. The amplified DNA was purified using a DNA Clean & Concentrator-100™ kit (Zymo Research®; Irvine, CA).

2.3 CRISPR-Cas editing

The pEcCas plasmid was first transformed into the ClearColi® electrocompetent cells using 50 ng of the pEcCas plasmid extracted using a ZymoPURE midiprep™ kit. These cells were then made electrocompetent by culturing in kanamycin supplemented LB broth grown at 37 °C with shaking at 225 rpm until the optical density at 600 nm (OD₆₀₀) reached 0.05. For induction of the λ-Red genes present in the pEcCas plasmid, 10 mM L-arabinose was added to the culture once the optical density at 600 nm (OD₆₀₀) reached 0.5–0.7. Following centrifugation, there were three washes performed using ice-cold 10 % glycerol. After resuspension, and a final OD₆₀₀ of between 220–250, the cells were stored at -80 °C. Next, 100 ng of the specific pEcgRNA plasmid and 400 ng of donor DNA were co-electroporated

into the ClearColi®+pEcCas cells. The electroporation was performed in 0.1 cm gap cuvettes at 1.8 kV and the cells recovered in a culture shaker at 37 °C for 1 hour at 225 rpm. Next, 50–150 µl of the cells were spread onto LB agar plates supplemented with kanamycin-spectinomycin and were incubated at 37 °C for 48 hours to select for transformants. Table 1 lists primers specific to the *Y. pestis* genes and areas of insertion that were used for confirming the CRISPR editing.

2.4 Reverse Transcription-Polymerase Chain Reaction

The Qiagen RNeasy Mini Kit was utilized to isolate RNA from each strain including *E. coli* BL21, *E. coli*+pAJM.677:*lpxM*, *E. coli*+pAJM.677:*lpxP*, and the edited ClearColi®:*lpxM:lpxP* strains. Overnight cultures were prepared of the previously listed strains and the following day 200 µl of each culture is added to new media and grown to approximately 1×10^7 cells and centrifuged at 5,000 x g for 5 minutes at 4 °C. RNA was isolated according following the manufacturer’s protocol and residual DNA was removed via DNA digest by combining 20 µl of isolated RNA with 2 µl of NEB DNaseI at 37 °C for 10 minutes. Following the DNA digest, 1 µl of 0.5 M EDTA was added and allowed to incubate at 75 °C for 10 minutes. The SuperScript™ IV Reverse Transcriptase kit was used to synthesize cDNA synthesis with 50 µM random hexamers following the recommended protocol. Finally, a PCR reaction with Phusion® High Fidelity DNA Polymerase was performed on the Reverse Transcription-Polymerase Chain Reaction (RT-PCR) samples using primers specific to the *Y. pestis* *lpxM* and *lpxP* genes (listed in Table 1) and confirmed using a 1 % agarose ETBr stained gel is run of the PCR samples at 120 V for 30 minutes.

Table 1. Primers used in this study.

Primer ID	Primer Type	Primer Sequence
5EClpxMctrl	Forward	ATT AAT TAA CAT CCA TTC GCA GCC G
3EClpxMctrl	Reverse	CCT ACA GTT CAA TGA TAG TTC AAC AGA TTT CG
Yp_LpxM.F	Forward	TCG GTT TCA CCC TCT TTC CG
Yp_LpxM.R	Reverse	ATT AGC TGG CAT AGG GCG TC
LpxM_Seq_F	Forward	GAA GCG GTT AAT CTG CTG CG
LpxM_Seq_R	Reverse	GGA TAA ACC AGC AGG CCG TA
LpxM_gblock_f	Forward	GTG CAC CGG CGT AAC GCC ACT CAAAAA AAG CAC CGA CTC G
LpxM_gblock_r	Reverse	TCA TGG TCG CAG CTA CAC CA
Ara_Marionette_lpxM_FWD	Forward	ATG TGC GCA AAG ATC TTT AGC TCG GTA CCA AAT TCC AGA A
Ara_Marionette_lpxM_REV	Reverse	TCA TTT TTT TCT TTG TGC ATC TAG TAT TTC CCC TCT TTC TCT
pTargetF-N20R	Reverse	ACT AGT ATT ATA CCT AGG ACT GAG
5EClpxPctrl	Forward	AGT AGC TGA AAG CAG TCA GC
3EClpxPctrl	Reverse	AGT AAC TTA CAA GTG TCT CAT ATC GG
Yp_LpxP.F	Forward	TAC AGC GAA GGT TCG CCA AT
Yp_LpxP.R	Reverse	ACG CGC ACA ACA AGG TAA AC
LpxP_Seq_F	Forward	TGC AAG ACT GTT GTG TAC GGA
LpxP_Seq_R	Reverse	GTA TTT TAC CGT GGG CAT CAC C
Pmarionette_LpxP_F	Forward	GCG AAC CTT CGC TGT AAC TCG GTA CCA AAT TCC AGA ATT
Pmarionette_LpxP_R	Reverse	AAT TTC TGC GGC TT ATC ATC TAG TAT TTCCCC TCT TTC TCT
Marionette_lpxP_F	Forward	AGA GAA AGA GGG GAA ATA CTA GAT GAT AAA GCC GCA GAA
Marionette_lpxP_R	Reverse	TTC TGG AAT TTG GTA CCG AGT TAA TAC AGC GAA GGT TCG C
EptA_Seq_F	Forward	AGG ATC AGT ACT GGC AGG GT
EptA_Seq_R	Reverse	GAT GGT CAT CAC CGC CAT GT
5EceptActrl	Forward	ATG TAT GCG CTG AAT TAC AAC C
3EceptActrl	Reverse	AAC CCT AAA TCC AGT ACC ACC

2.5 Matrix-assisted laser desorption/ionization-time-of-flight

Samples were prepared by using the SA method of Lipid Microextraction from cells as previously described.⁴ Briefly, overnight cultures of ClearColi®, ClearColi®+pEcCas *lpxm:lpxP*, or ClearColi® *eptA* were incubated in 5 mL LB-Miller broth with their respective selective antibiotic at 37 °C overnight. Next, 1 mL of an overnight culture was taken from each sample and was resuspended in 400 µl of 100 mM Sodium Acetate buffer (pH 4.0). After being resuspended, the samples were incubated at 100 °C for 30 minutes and briefly vortexed every 10 minutes. After cooling on ice, the samples were centrifuged at 8,000 x g for 5 minutes and the cell pellets were washed with 95% ethanol. 100 µl of 12:6:1 chloroform/methanol/water was added to each pellet, and the samples were centrifuged at 5,000 x g for 5 minutes. Monophosphoryl lipid A (MPLA) (#699800 Avanti Polar Lipids, Inc., Alabaster, AL, USA) control was spiked into the samples at a final concentration of 20 µg/mL and 10 mg/mL norharmane in 12:6:1 chloroform/methanol/water was prepared as the matrix and spotted on a matrix-assisted laser desorption/ionization-time-of-flight (MALDI-TOF) plate. The supernatant was placed on the pre-spotted areas on the MALDI-TOF stainless steel plate, and the mass spectra were collected under negative ion mode on the smartfleX MALDI-TOF MS System from Bruker Corporation.

3. RESULTS

3.1 Engineering of *Escherichia coli* with *Yersinia pestis* outer membrane biosynthesis pathways

We previously selected *Y. pestis* as the LPS biosynthesis pathways donor organism as the necessary genes have already been identified.⁵ To better facilitate the building of an engineered *E. coli* possessing a *Y. pestis* LOS, we specifically chose a strain of *E. coli*, known as ClearColi®, which was previously genetically modified to not produce endotoxin.⁶ The ClearColi® strain is a derivative of the commonly used BL21 lab strain of *E. coli* but with successive gene deletions resulting in minimal outer membrane structure known as Lipid IV_a (Figure 1 and 2).

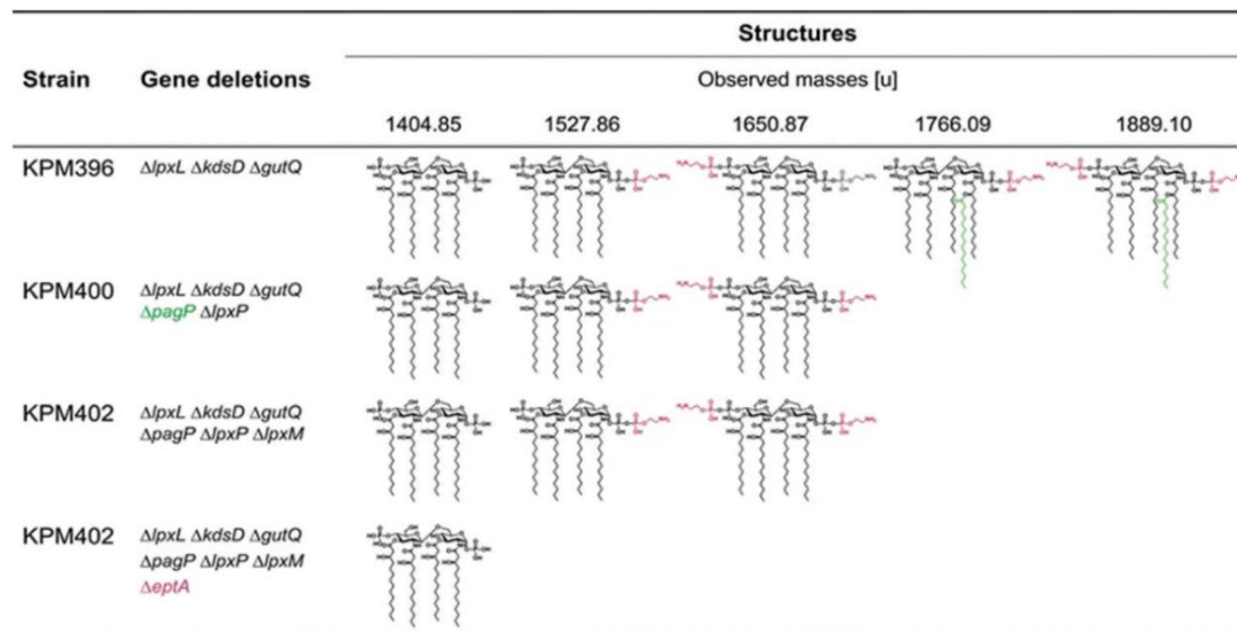


Figure 2. The outer membrane structure of the genetically engineered *E. coli* strain ClearColi®. Successive gene deletions in key LPS biosynthesis genes resulted in an *E. coli* strain with the minimal unit required for an outer membrane known as Lipid IV_a. This strain, known as ClearColi®, serves as the scaffold strain for engineering *Y. pestis* LPS in *E. coli*.

Having identified the donor organism (*Y. pestis*) and the associated outer membrane biosynthesis genes, along with our recipient ClearColi® strain, we set out to develop a method to conduct the genetic engineering. Traditional methods of gene insertions and recombineering in bacteria, while effective, can be time consuming requiring multiple cloning steps along with several iterations of recombination and plasmid curing. Recently, the implementation of CRISPR/Cas9 mediated genetic engineering has provided a rapid and effective tool to create site-specific insertions in bacterial chromosomes.⁶ We obtained a two-plasmid system consisting of an inducible Cas9 enzyme and

recombination proteins along with a guiding target plasmid (Figure 3). This system is advantageous because the donor insertion DNA can be co-transformed as a linear template, removing the need for additional cloning steps.^{2,7} In addition to utilizing CRISPR/Cas9 genome editing, each gene of interest will be inserted into an inducible expression vector. This expression vector approach will mitigate any risks associated with genes that are unable to be inserted in the genome or those that are not appropriately expressed (Figure 3).

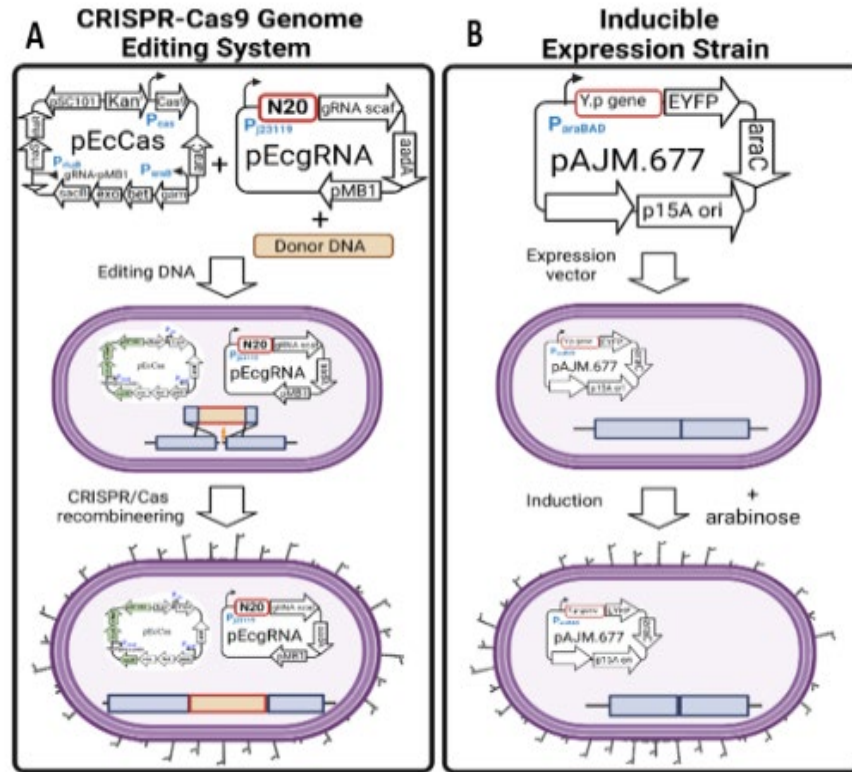


Figure 3. Genome editing design and approaches. A) The schematic depicts the process of the donor repair DNA, pEcCas9, and pEcgRNA plasmids in ClearColi® cells after induction. Together these three pieces facilitate the insertion of *Y. pestis* genes into designated genomic loci. **B)** The panel illustrates the construction and induction of the pAJM.677 expression plasmid containing the specific *Y. pestis* gene. These vectors place the gene of interest under the control of an arabinose inducible promoter.

The initial step in our cloning strategy was to insert the *lpxM* gene from *Y. pestis* into the cognate position of the ClearColi® genome. To ensure that the *lpxM* gene is correctly inserted, we first sequenced the ClearColi® genome to identify the flanking protospacer adjacent motif (PAM) sequences and any scar sequences remaining from the genetic engineering process. For *lpxM*, we verified the scar sequence and identified the PAM needed for the Cas9 enzyme recognition and the site of cleavage. Having confirmed the sequence on the recipient side, we next set out to design our *Y. pestis lpxM* donor DNA template. For efficient insertion of the *Y. pestis lpxM* gene, ~500 bp of flanking regions were added to either side of the gene homologous to the ClearColi® genome. These flanking regions enable the homologous recombination and insertion of the donor gene. The donor DNA was designed *in silico* and ordered as synthetic DNA from Integrated DNA Technologies as a gBlock™ which was subsequently amplified by high-fidelity PCR (Figure 4a). Together, the donor DNA and the targeting plasmid were co-transformed into the ClearColi® strain containing the pCas9 recombination vector. The resulting transformants were plated on selective media to identify unique colonies which were able to successfully incorporate the *Y. pestis lpxM* gene. Following selection, we screened 18 colonies as potential candidates for containing the new *lpxM*. To verify successful insertion of *lpxM*, a colony PCR reaction was run on the candidates with primers flanking the insertion site along with primers specific to the *Y. pestis lpxM* gene. From the colony PCR, a band corresponding to the successful insertion of *lpxM* was present for one of the 18 colonies screened (Figure 4b). Taken together, this data confirmed that we successfully inserted the *Y. pestis lpxM* gene into the cognate genomic loci in our ClearColi® strain, resulting in the strain ClearColi®:*lpxM*.

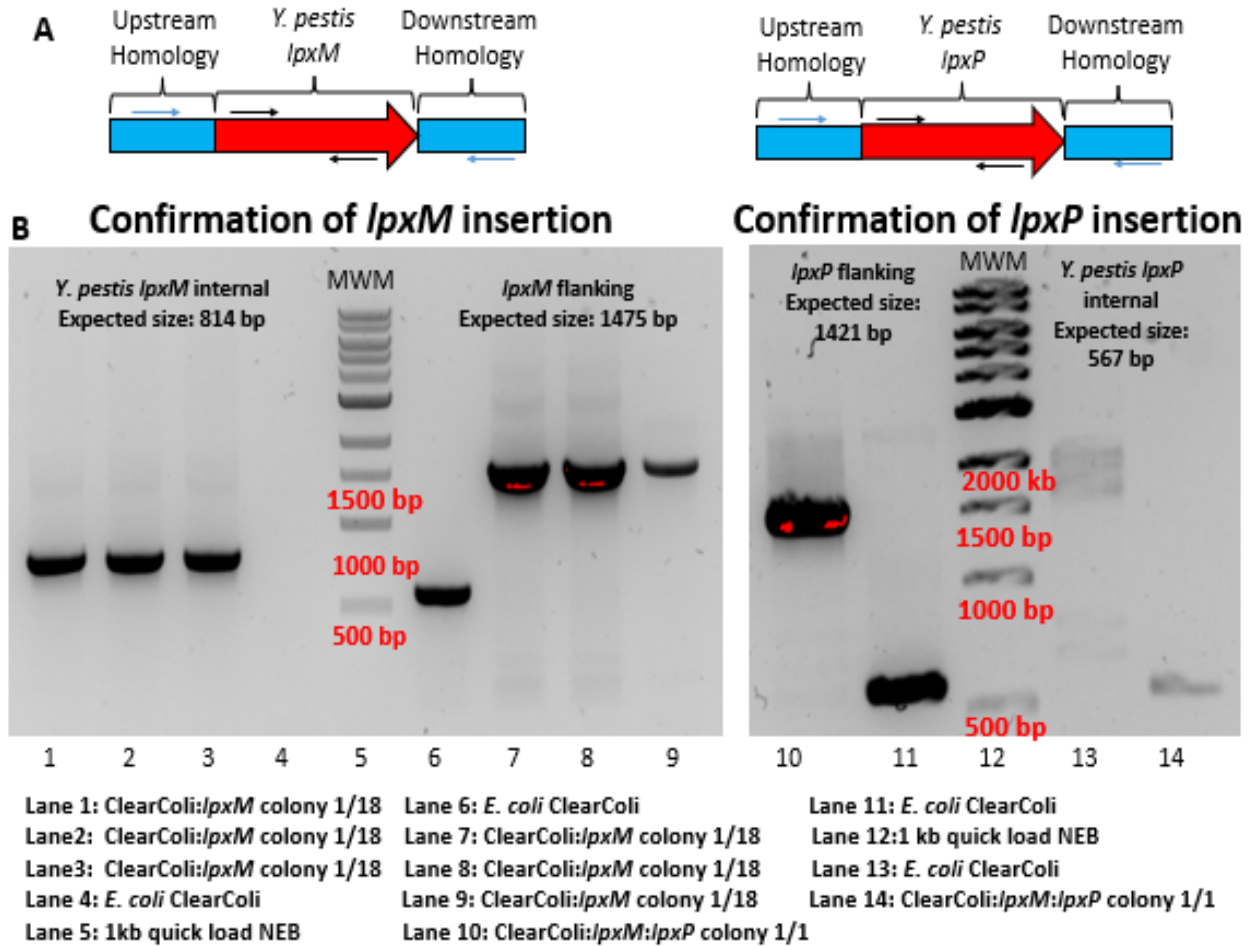


Figure 4. Colony PCR verification of *lpxM* insertion to ClearColi®. A colony PCR was conducted on the two transformants resulting from the engineering transformation with colonies flanking the insertion site. A) Representation of the DNA including the *lpxM* gene from *Y. pestis* and the homologous regions to ClearColi®. Arrows in blue represent flanking primers used for insertion confirmations via PCR. Arrows in black represent primers specific to the *Y. pestis* genome used for insertion confirmation via PCR. Representation of sequences for ClearColi® *lpxM*:*lpxP* genomic loci and the *Y. pestis lpxP* donor template. B) Gel confirmation of a single colony run in triplicate reactions. Colony PCR verification of *lpxP* insertion to ClearColi®. Arrows in red represent flanking primers used for insertion confirmations via PCR. Arrows in black represent primers specific to the *Y. pestis* genome used for insertion confirmation via PCR.

Having verified the successful construction of ClearColi®:*lpxM*, we targeted the late acyltransferase gene *lpxP* as the next target gene. Again, the donor DNA was designed *in silico* and ordered as a synthetic DNA template (Figure 4c). The donor repair *lpxP* DNA along with the guide editing plasmid were transformed into the ClearColi®:*lpxM* strain as previously described. After multiple transformation attempts, only a single colony was observed on the selective media. This colony was screened by both genomic flanking primers and *Y. pestis lpxP* specific primers to determine if the gene was successfully incorporated into the genome (Figure 4d). After confirming that we successfully inserted both *lpxM* and *lpxP* into the genome of *E. coli* ClearColi® generating the strain ClearColi®:*lpxM*:*lpxP*, we set out to generate expression vectors for each of these genes. The synthetic DNA for each gene was used as a template for a PCR amplification reaction targeting just the coding region of each gene. The amplified genes were cloned into an arabinose inducible vector via inverse PCR and Gibson assembly followed by transformation into the WT ClearColi® strain. The successful generation of the expression vector was confirmed via PCR for the *Y. pestis* specific genes (Figure 5).

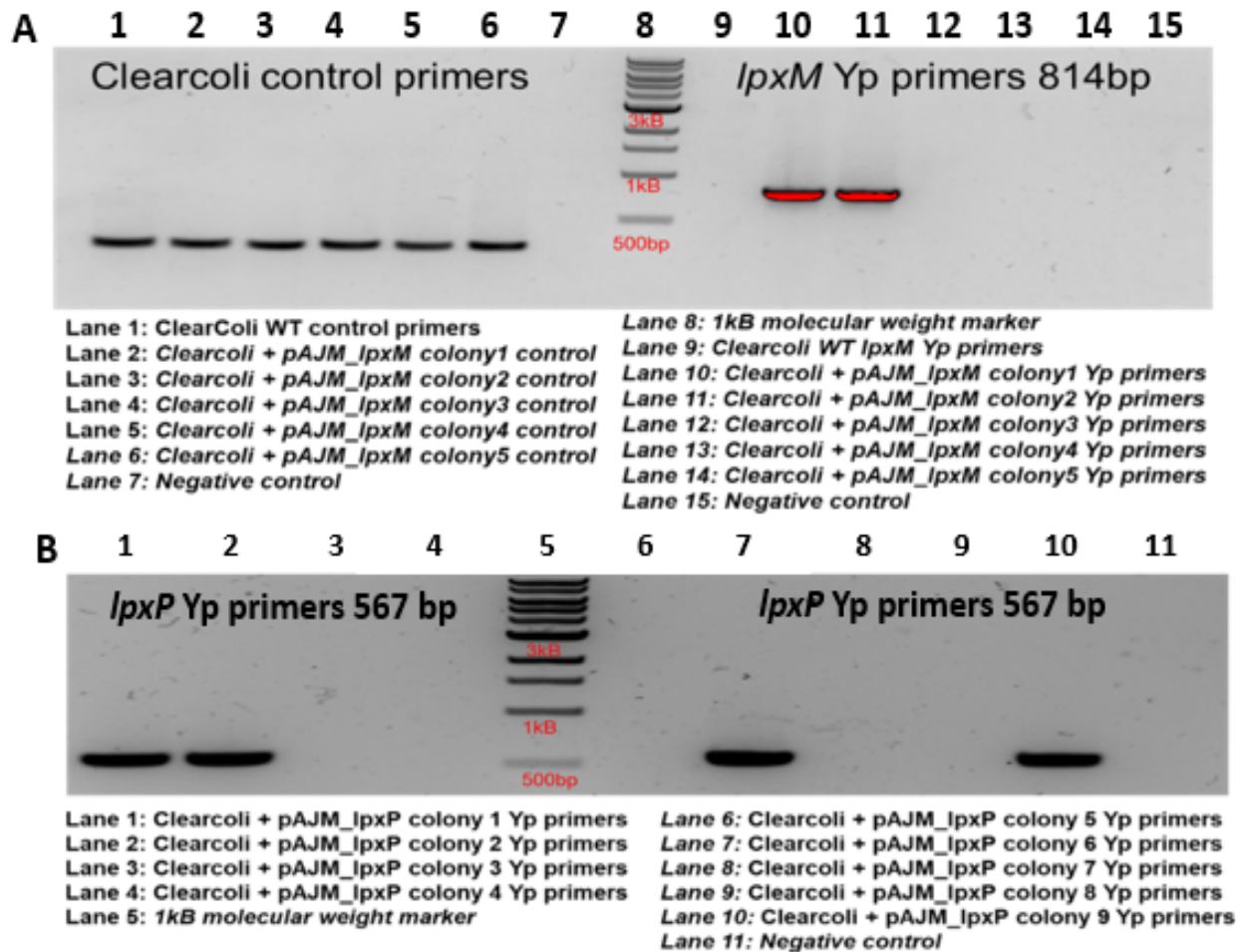


Figure 5. Colony PCR verification of *lpxM* and *lpxP* expression constructs. A) Colony PCR was conducted on transformants resulting from the transformation of the constructed *lpxM* expression vector. Primers specific to the *Y. pestis lpxM* were used for confirmation. B) Colony PCR was conducted on transformants resulting from the construction of the *lpxP* expression vector. Primers specific to the *Y. pestis lpxP* were used for confirmation.

Finally, having successfully created the genome edited ClearColi®:*lpxM:lpxP* strain along with the cognate expression vectors we set out to add the Lipid A modifying enzyme *eptA*. The *eptA* enzyme catalyzes the addition of phosphoethanolamine to the terminal phosphate groups of the Lipid A. We followed a similar strategy to incorporate *eptA* into the ClearColi® strain as described above, however, were unable to generate *eptA* inserted into the genome after screening ~100 transformants. As a mitigation we obtained an *eptA* expression vector that is IPTG inducible that can be transferred to our engineered strains of interest for evaluation.

3.2 Characterizing the engineered *E. coli* expressing the *Y. pestis* outer membrane

After the successful insertion of both *lpxM* and *lpxP* along with the generation of the expression vectors, we set out to characterize the functionality of the genes and any phenotypes associated with the genomic edits. First, we set out to confirm that the genes were being expressed from both native promoters used to drive expression as well as the inducible expression vectors. To do this we conducted RT-PCR on RNA isolated from engineered and induced strains. We found that expression was observed for *lpxM* and *lpxP* from both the engineered strain with the genomic inserts and the inducible vectors. This indicates that these genes are in fact being transcribed as expected (Figure 6).

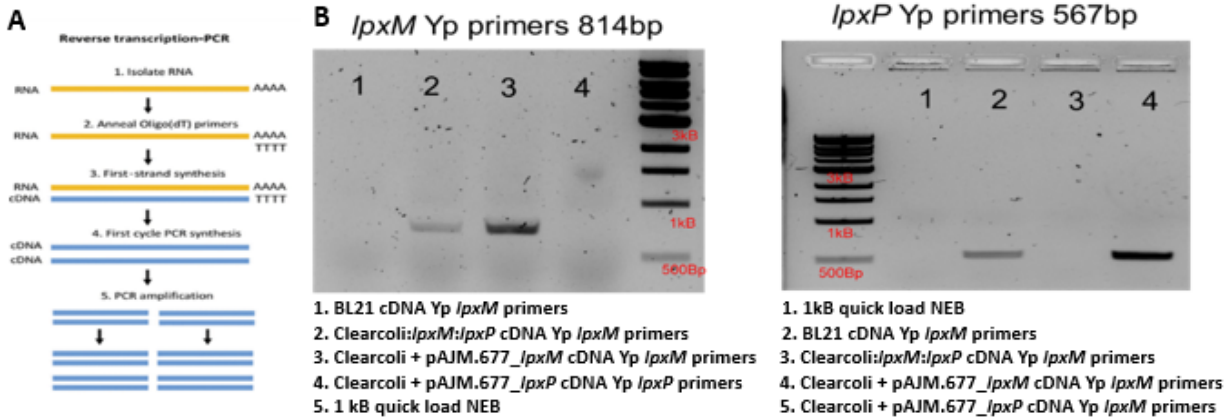


Figure 6. RT-PCR confirming expression of engineered genes. A) Schematic representing the process for RT-PCR. RNA was isolated from strains of interest and cDNA was generated. cDNA was used as a template for confirmatory PCR reactions. B) RT-PCR gel confirmation of *lpxM* expression from both the edited strain and the expression vector. Primers used are specific to *lpxM*. RT-PCR gel confirmation of *lpxP* expression from both the edited strain and the expression vector. Primers used are specific to *lpxP*.

Having confirmed that the genes of interest are expressed, we set out to determine if they are functionally active and involved in Lipid A biosynthesis. To do this, we utilized MALDI-TOF mass spectroscopy on isolated Lipid A fractions. The lipid fractions from WT ClearColi®, ClearColi®:*lpxM:lpxP*, and ClearColi®+pT7YpeptA were isolated and subjected to MALDI-TOF. As expected, we were able to correctly identify the main Lipid IV_a mass of 1404 m/z validating our process of lipid isolation from the WT ClearColi® (Figure 7). Next, we evaluate the effect of the *lpxM* and *lpxP* insertions to the Lipid A structure. We found that there was no difference in lipid structure between WT ClearColi® and ClearColi®:*lpxM:lpxP* (Figure 7). This result is not surprising as previous studies have indicated that lipid IV_a is not a substrate for these enzymes.⁶ We expect that as the Lipid A is continued to be constructed that we will observe the expected phenotypes associated with these enzymes. Finally, we evaluated the functionality of the inducible *eptA* expression vector. As expected, we observed a mass shift from 1404 m/z to 1528 m/z which corresponds to the addition of phosphoethanolamine to one terminal end of the Lipid A confirming that *eptA* is functional (Figure 7).

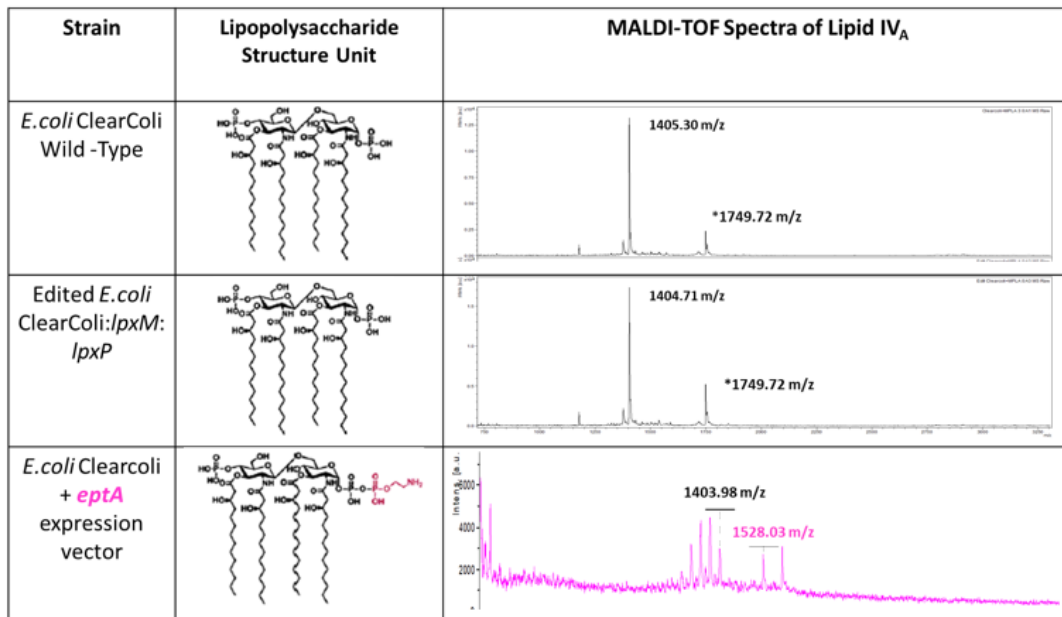


Figure 7. MALDI-TOF Mass Spectrometry of isolated Lipid A molecules. Lipids were isolated from WT ClearColi®, ClearColi®:*lpxM:lpxP*, and ClearColi®+pT7YpeptA with the respective Lipid IV_A structures. Insets on each figure represent the expected structure from previously described reports. *Spiked control indicates MPLA a lipid that was added to the sample as an internal reference.

4. CONCLUSION

Here, we describe our efforts to utilize rapid genome engineering to create a strain of *E. coli* that produces a bacterial outer membrane that includes *Y. pestis* LPS. We first identified the biosynthetic pathways for LPS biosynthesis in our donor organism *Y. pestis*. We hypothesized the enzyme associated in these pathways must be transferred and functional in our engineered recipient strain to obtain the novel outer membrane. We also identified and obtained our scaffold strain, *E. coli* ClearColi®, which only contains the LPS precursor lipid IV_A outer membrane, on which we would build out the pieces of LPS from *Y. pestis*. Finally, we demonstrated that we could successfully transfer *Y. pestis* LPS biosynthesis genes, *lpxM*, and *lpxP* into our recipient strain *E. coli* ClearColi®. In addition, we have expression vectors of each gene of interest including *eptA*. We demonstrated that these genes are expressed and that we can use MALDI-TOF to characterize the lipid fractions. Continuing work on this effort will add the biosynthesis genes in a processive manner. Along the engineering process, the outer membrane will be evaluated through biochemical and analytical methods verifying the functionality. Ultimately, this work informs the threats and benefits associated with the ability to modify and redesign bacterial membranes.

ACKNOWLEDGMENTS

Funding was provided by the U.S. Army via the In-house Laboratory Independent Research Program (PE 0601101A Project 91A) at the Combat Capabilities Development Command Chemical Biological Center.

REFERENCES

- [1] Knirel, Y. A.; Valvano, M. A. *Bacterial lipopolysaccharides: structure, chemical synthesis, biogenesis and interaction with host cells*; Springer Science & Business Media, 2011.
- [2] Li, Q.; Sun, B.; Chen, J.; Zhang, Y.; Jiang, Y.; Yang, S. A modified pCas/pTargetF system for CRISPR-Cas9-assisted genome editing in *Escherichia coli*. *Acta Biochim. et Biophys. Sin.* **2021**, *53* (5), pp 620–627.
- [3] Meyer, A.J.; Segall-Shapiro, T.H.; Glassey, E.; Zhang, J.; Voigt, C.A. *Escherichia coli* “Marionette” strains with 12 highly optimized small-molecule sensors. *Nat. Chem. Biol.* **2019**, *15* (2), pp 196–204.
- [4] Liang, T.; Leung, L.M.; Opene, B.; Fondrie, W.E.; Lee, Y.I.; Chandler, C.E.; Yoon, S.H.; Doi, Y.; Ernst, R.K.; Goodlett, D.R. Rapid Microbial Identification and Antibiotic Resistance Detection by Mass Spectrometric Analysis of Membrane Lipids. *Anal. Chem.* **2019**, *91* (2), pp 1286–1294.
- [5] Antoshak, E.; McDonald, N. Remodeling the bacterial outer membrane for synthetic designer microbes. FY21 Proceedings of the U.S. Army Combat Capabilities Development Command Chemical Biological Center In-House Laboratory Independent Research and Surface Science Initiative Programs ed.; U.S. Army Combat Capabilities Development Command Chemical Biological Center: Edgewood, MD, 2022; Vol. FY21, pp 11–18.
- [6] Mamat, U.; Wilke, K.; Bramhill, D.; Schromm, A.B.; Lindner, B.; Kohl, T.A.; Corchero, J.L.; Villaverde, A.; Schaffer, L.; Head, S.R. Detoxifying *Escherichia coli* for endotoxin-free production of recombinant proteins. *Microb. Cell Fact.* **2015**, *14* (1), pp 1–15.
- [7] Jiang, Y.; Chen, B.; Duan, C.; Sun, B.; Yang, J.; Yang, S. Multigene editing in the *Escherichia coli* genome via the CRISPR-Cas9 system. *Appl. Environ. Microbiol.* **2015**, *81* (7), pp 2506–2514.

Fundamental exploration into advanced plasmonic ceramic nitrides as multispectral obscurants

Danielle L. Kuhn^{a*}, Zachary B.S. Zander^a, Lena Vlahakis^b, Joshua Smith^b

^aU.S. Army Combat Capabilities Development Command Chemical Biological Center, Research & Operations Directorate, 8198 Blackhawk Rd., Aberdeen Proving Ground, MD 21010

^bLuna Labs USA, LLC, 706 Forest St. #A, Charlottesville, VA 22903

ABSTRACT

Obscurant materials play a crucial role in protecting the US warfighter. These materials will absorb, scatter, or emit radiation in the visible, infrared and millimeter wavelengths to interrupt the line of sight and infrared sensors between an objective and observer. However, current fielded visible/infrared obscuration technologies (i.e., broadband obscurants such as brass and graphite) are limited in obscuring modern devices due to low obscuring performance, incompatibilities with explosive dissemination, and poor deagglomeration of the materials upon dissemination in atmospheric conditions. By utilizing a facile hydrothermal synthetic strategy to prepare doped-titanium nitride nanofibers, we hypothesize the fabrication of both plasmonic ceramic nanofibers and their doped forms by hydrothermal synthesis resulting in enhanced optical and electrical properties designed for the broadband attenuation necessary for the next generation of high-performing obscurants. This work is expected to provide new obscuring materials and synthetic strategies to address the Army's need for broadband obscuration, and further the basic underlying phenomena relating metal-nitride ceramic doping, conductivity, and photonic absorption/scattering.

Keywords: Obscuration, plasmonic materials, broadband attenuation, synthetic chemistry

1. INTRODUCTION

Obscurants are materials that absorb, scatter, or emit radiation in the visible, infrared (IR), and millimeter wavelength range to interrupt the line of sight between an objective and observer. These materials play a crucial role in protecting the US warfighter by decreasing the electromagnetic energy available for the functioning of sensors, seekers, trackers, optical enhancement devices and the human eye. However, current visible/IR obscuration technologies (i.e., broadband obscurants such as brass and graphite) are limited in obscuring modern devices due to low obscuring performance, incompatibilities with explosive dissemination, and poor deagglomeration of the materials upon dissemination in atmospheric conditions.

From water distillation to cancer treatment, plasmonic nanoparticles (NPs) have found a variety of applications in the energy, defense, and medical sectors.¹⁻³ Plasmonic materials possess unique characteristics stemming from resonant oscillations of free electrons as a response to electromagnetic (EM) waves.¹ By controlling the size, shape, conductivity, dopants, and environment, the extinction efficiency and resonance position is readily tuned.^{2,3} This strong and tunable interaction with EM waves has attracted immense attention over the last few decades. While Au and Ag are the most well-known plasmonic materials and have had the most interest due to their superior performance in the visible region, these materials are less than ideal for broadband obscuration. Beside the large expense associated with manufacturing, these noble metals are limited to the visible and near infrared region of the EM spectrum, possess low melting points, and are easily compressed.⁴ In contrast, transition metal nitrides are known to exhibit plasmon resonances at longer wavelengths. Along with their unique plasmonic properties, metal nitrides are known for their refractory properties, meaning chemically stable at temperatures above 2000 °C, as well as high conductivity. The low cost, high stability, and high optical extinction of transition metal nitride NPs may be the ideal solution to solve the current problems existing in broadband obscurant systems. Until now, the shape-controlled synthesis of metal nitrides has been expensive, hazardous, and non-scalable.^{1,5} For instance, previous work done from Joshia et. al. used low temperature solid-state metathesis of titanium (III) chloride and sodium azide without the use of a solvent.⁵ This approach utilized chemicals which were highly corrosive and explosive, making it less than ideal to use as a method for scaled-up production. Thus, there is a critical need for facile and safe synthetic strategies to metal nitride NPs.

Recently, plasmonic nitrides such as titanium nitride (TiN) and zirconia nitride have received significant interest due to their low cost, scalability, and high durability. However, the synthetic methodologies to precisely control the size, shape, and composition of nitride NPs are significantly limited when compared to methods used to produce precious metal plasmonic NPs. Leveraging a facile hydrothermal method, Luna Labs worked with U.S. Army Combat Capabilities Development Command Chemical Biological Center to develop a versatile method to functionalize and/or dope TiN NPs with different metals. This new synthetic methodology unlocks new opportunities in designing TiN NPs with unique optoelectronic properties.

As alluded to above, the diversity of applications of plasmonic NPs arises from the ability to readily tune the localized surface plasmon resonances (LSPRs) of NPs.^{4,7} LSPRs occur in plasmonic materials (i.e., those that exhibit negative real permittivity) that have one or more dimensions smaller than the wavelength of incident light.^{4,7} A surface plasmon resonance is produced when the electron density of a material couples with incident EM radiation to create a coherent, collective oscillation of the conduction electrons.^{4,7} By confining a resonance to dimensions smaller than the wavelength of light, the electron density oscillates locally around the NP, and, thus, the plasmon's behavior is defined by the structural features of the NP.^{4,7} This localization means that the extinction (scattering and absorbance) spectra and electric field (EF) enhancements of plasmonic NPs can be modified for specific applications by changing their size, shape, composition, and environment.^{4,7}

For example, the wavelength (λ)-dependent extinction spectrum of a spherical metal NP can be calculated by equation (1),

$$E(\lambda) = \frac{24\pi^2 N \alpha^3 \epsilon_{out}^{3/2}}{\lambda \ln(10)} \left| \frac{\epsilon_i(\lambda)}{(\epsilon_i(\lambda) + \chi \epsilon_{out})^2 + \epsilon_i(\lambda)^2} \right|, \quad (1)$$

where size (α , radius), shape (χ , which equals 2 for a sphere), composition (ϵ_i and ϵ_r , the imaginary and real components of the metal dielectric function), and environment (ϵ_{out} , dielectric of surrounding media) all contribute to the scattering and absorption behavior. We refer readers to reviews by Willets *et al.* and Smith *et al.* for more expansive discussions.^{1,2}

In this work, we sought to develop a novel hydrothermal strategy to functionalize or dope the TiN NPs. Recall, functionalization is a broad term for adding metal to the TiN NPs. Doping refers to substitution of metal atoms into the crystal lattice.

2. EXPERIMENTAL

2.1 *In situ* doping

In situ metal-doped TiN NPs were synthesized by exposing TiN starting materials to various metal salts using Luna Labs's proprietary hydrothermal process. First, control experiments were conducted with each metal salt candidate alone under hydrothermal conditions. The purpose of this screening was to eliminate any metal candidate that undergoes a secondary reaction under hydrothermal conditions independent of TiN, since such secondary reactions would be difficult to discern. The solutions were analyzed for indications of a reaction between the metal and the solution. A reaction was identified by i) a color change in the solution or ii) the presence of colloids/solids.

From these results, $\text{Al}(\text{NO}_3)_3$, FeCl_3 , and $\text{Fe}(\text{NO}_3)_3$ were disqualified. CuCl_2 , NiCl_2 , $\text{Ni}(\text{NO}_3)_2$, ZnCl_2 , AgNO_3 , HAuCl_4 , and CeCl_3 did not show any side reactions during control experiments. Given that the metal salts did not have secondary reactions and the metal salts allowed the exploration of atomic size and binding energy, these metal salts were chosen for further investigation.

A later study was conducted with TiN synthesized with various mass loadings of each of the identified metal candidates. For each metal, the salt was added to the hydrothermal reactor at a range of mass ratios from 5–50 % with TiN, along with a 10 mM polyethylene glycol (PEG) solution. The reaction was processed at 160 °C overnight. The resulting material was isolated and washed by high-speed centrifugation, then oven dried. The dry powders were then characterized by ultraviolet-visible spectroscopy to measure optical transmittance and calculate the mass extinction coefficients (MECs), α , (in units of $\text{m}^2 \text{g}^{-1}$) from equation (2):

$$\alpha = \frac{-\ln(T)}{c \times l}, \quad (2)$$

where T represents transmission, c represents material concentration, and l represents path length.

2.2 Post-synthetic doping

Polyol synthesis metal doping on TiN NPs was preformed using TiN starting material synthesized by Luna Labs's propriety hydrothermal synthesis. Utilizing previous expertise of anisotropic plasmonic metal doping, the TiN was pre-treated with a 0.1M NaOH_(aq) solution.¹³ After the slurry stirred for 2 h, it was washed, rinsed, and oven dried. The base-treated TiN was used for the polyol synthesis which consisted of a reflux reaction with AgNO₃, polyvinyl pyrrolidone, and dimethyl formamide at 160 °C for 2 h. The reaction was washed and oven dried overnight. The dry powder was then characterized by Fourier-transform infrared spectroscopy (FTIR) to measure optical transmittance and calculate the MECS from equation (2).

3. RESULTS AND DISCUSSION

An initial set of experiments focused on three first-row D-metals, Ni, Cu, and Zn. Following the methods described above, chloride salts of each of these metals were added to the TiN hydrothermal reactions. This section describes the results of transmission electron microscopy (TEM), FTIR, and UV-vis characterization of the resulting TiN materials. Optical spectra and TEM images are presented in Figure 1, Figure 2, and Figure 3 for TiN synthesized in the presence of NiCl₂, CuCl₂, and ZnCl₂, respectively.

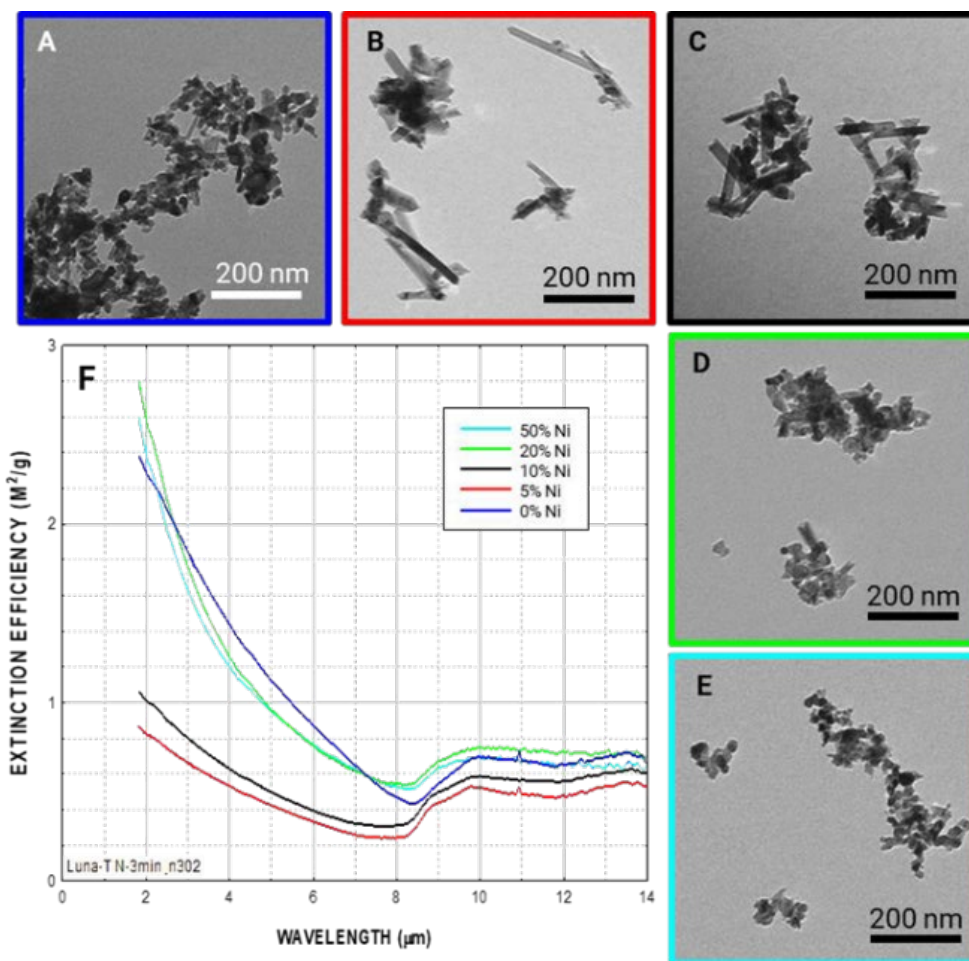


Figure 1. TEM images (A–E) and FTIR spectra (F) of hydrothermal TiN NPs prepared in the presence of NiCl₂ at 0 % (dark blue), 5 % (red), 10 % (black), 20 % (green), and 50 % (light blue) mass loading.

In the FTIR spectra in Figure 1F, the samples with lowest Ni concentration, 5 % and 10 %, show a smooth curve that slightly increases in MECs from the far-IR (FIR) towards the near-IR (NIR). In contrast, the higher Ni samples more closely match the control TiN, with a more defined slope upwards towards the NIR. These higher Ni samples also show the highest MECs through the FIR.

Visually, the solutions displayed colors from dark blue to black, with only small variation across the range of concentrations. The darkest material was the 50 % Ni, which most closely matched the black control TiN, then lightening to dark blue as the Ni concentration decreases. This dark color suggests a higher synthetic yield of titanium nitrides rather than conversion to oxynitrides, which tend towards a lighter blue color. Interestingly, the bluing of TiN is highly indicative of oxidation.

It is also notable that the supernatant of the 50 % Ni sample had a green tinge after centrifugation, indicating the presence of excess Ni salts in solution. This may account for some of the similarity between the 20 % and the 50 % samples, if the reaction of Ni with TiN reached a saturation point somewhere between 20 and 50 %.

TEM characterization of these samples (Figure 1A-E) also shows that the lower Ni concentration samples with flatter spectra displayed a nanowire morphology (lengths around 200 μm and diameters from 10–30 nm), while the higher Ni concentration samples had more rounded NPs mixed with some wires. Ultimately, the FTIR spectra and TEM indicate that the rounded NPs yielded higher MECs than the nanowires.

When considering the Drude model for IR extinction,⁹ this result is very interesting. Traditionally, nanowires are anticipated to have higher attenuation in the IR region due to their major dimension correlating to resonance modes, which correspond to wavelengths in the IR region. That is, the length of the material matches half the wavelength of the IR light. Furthermore, an increase in conductivity results in an increase in attenuation. Given this, it is hypothesized that samples prepared at 20 and 50 % mass loading of NiCl_2 display higher conductivities than those prepared at 5 and 10 % mass loading of NiCl_2 . If NiCl_2 oxidizes the TiN, then the nanowire morphologies may be an oxidation product. However, this hypothesis would need further investigation using energy dispersive X-ray spectroscopy in scanning transmission microscopy (STM-EDS), powder X-ray diffraction (PXRD), and X-ray photoelectron spectroscopy (XPS).

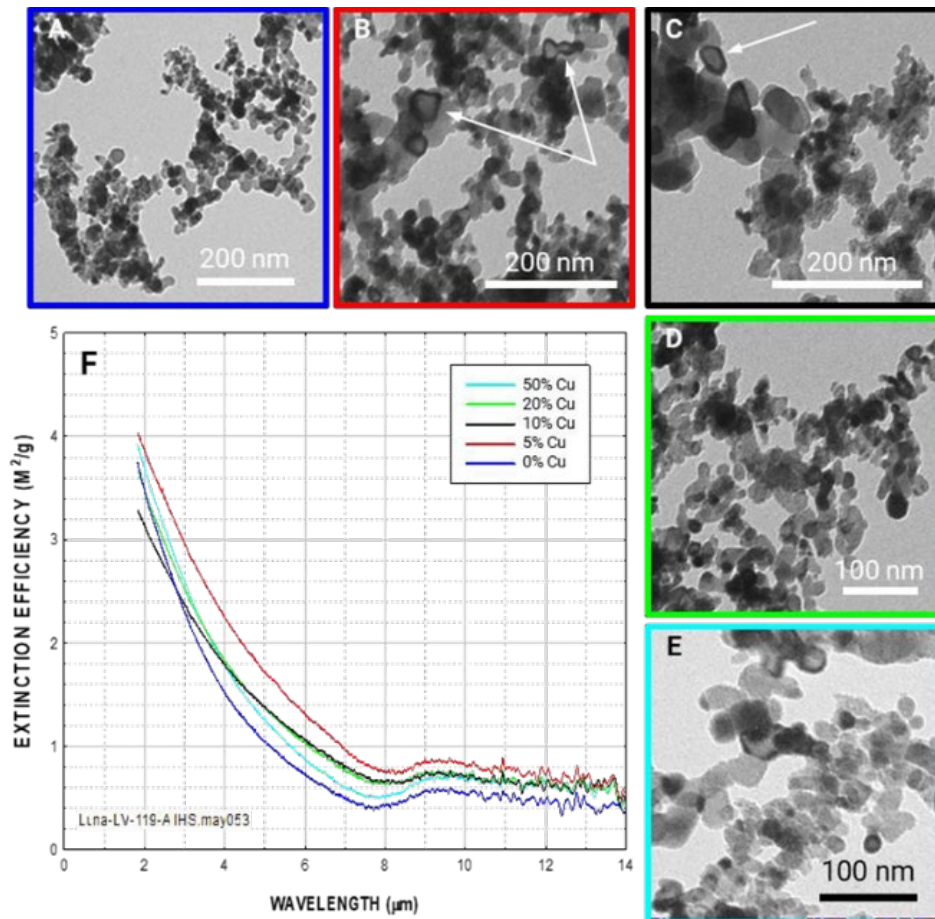


Figure 2. TEM images (A–E) and FTIR spectra (F) of hydrothermal TiN NPs prepared in the presence of CuCl_2 at 0 % (dark blue), 5 % (red), 10 % (black), 20 % (green), and 50 % (light blue) mass loading. White arrows indicate the presence of possible core-shell morphology in several NPs.

For the copper samples, the FTIR plot in Figure 2F shows little variation in spectral shape across all samples. Overall, there is a slight increase in MECs in all functionalized samples over the control TiN, and the lowest mass loading shows the highest MECs, which agrees with the UV-vis MECs previously found. Interestingly, optimal extinction is achieved at 5 % doping.

The TEM images in Figure 2A–E show mostly rounded NPs rather than nanowires, with an average diameter of approximately 20 nm. There is no significant change in particle shape across the range of copper loading. However, beginning with the 5- % sample, there is a notable appearance of particles with a high z-contrast (i.e., a darker line) outline surrounding a lighter particle. White arrows in Figure 2B–C identify several of these NPs. An increase in Z-contrast has been observed between heavier metals and more closed pack systems.¹⁰ Given that Cu was introduced into the system, it is proposed that Cu grew a conformal shell around the TiN NPs, resulting in the production of core@shell Cu-TiN NPs. The aggregation of particles in the images makes it difficult to determine if the presence of these particles decreases with increased doping. However, they appear to comprise only a small percentage of the total powder. This phenomenon is particularly interesting, as it is a morphology not previously seen in other functionalized or control TiN. Unlike the Ni samples, the material maintained similar IR efficiencies and spectral profile. Furthermore, the colors of the samples were similar, and no obvious oxidation was observed. Additional evaluation using elemental mapping is required to understand the architectures of these materials.

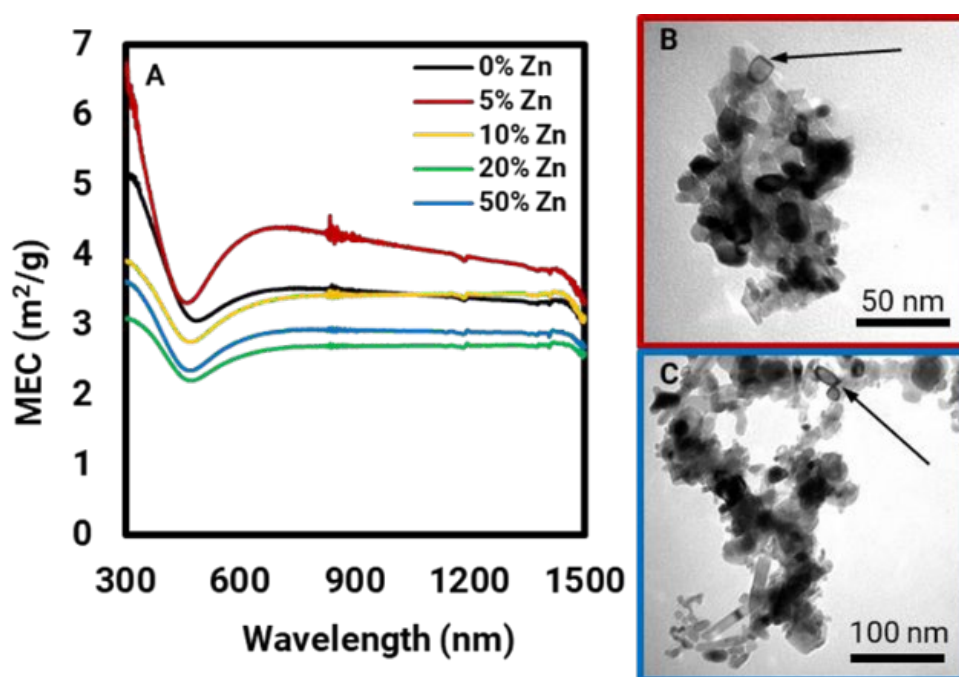


Figure 3. UV-vis spectra (A) and TEM images (B–C) of hydrothermal TiN NPs prepared in the presence of ZnCl₂ at 0 % (black), 5% (red), 10% (yellow), 20% (green), and 50% (blue) mass loading. Black arrows indicate the presence of possible core-shell morphology in several NPs.

The UV-vis spectra of Zn-functionalized TiN in Figure 3A show uniform spectral shapes like that of the control TiN, and average MECs around 3 m² g⁻¹ across the UV to NIR region. There also appears to be a slight blueshift of the Zn spectra when compared to the control TiN, most noticeable where the dip in the control TiN spectra at ~480 nm shifts to 460–470 nm for the higher Zn concentrations. The lowest Zn concentration, 5%, gave the highest MECs, followed by the control TiN. The particle color remained dark black across all samples, suggesting minimal oxidation of the TiN. This may also contribute to the slightly higher MECs noted here when compared to previous materials that yielded lighter blue particles.

The corresponding TEM images in Figure 3B–C show the overall morphology of these particles as a mixture of nanorods and rounded particles. They also show a similar phenomenon to the CuCl₂ samples, with the appearance of apparent core-shell Zn-TiN NPs indicated by a higher Z-contrast outline around several particles. Notably, this outline is present not only on rounded particles but also on higher aspect ratio particles as indicated by the arrow in Figure 3C. This result may be due to favorable deposition onto specific facets of TiN NPs; however, this claim needs to be confirmed with further analysis.

Given these results, it was of interest to explore the mechanisms of these reactions more thoroughly, and especially to examine the core-shell morphology found in the Cu and Zn particles. A set of follow-up experiments were conducted to examine any potential effects arising from the presence of different anionic components. For these experiments, $\text{Ni}(\text{NO}_3)_2$ was selected to compare results to the NiCl_2 presented above. These results are presented in Figure 4. AgNO_3 was also selected as an additional nitrate candidate, presented in Figure 5.

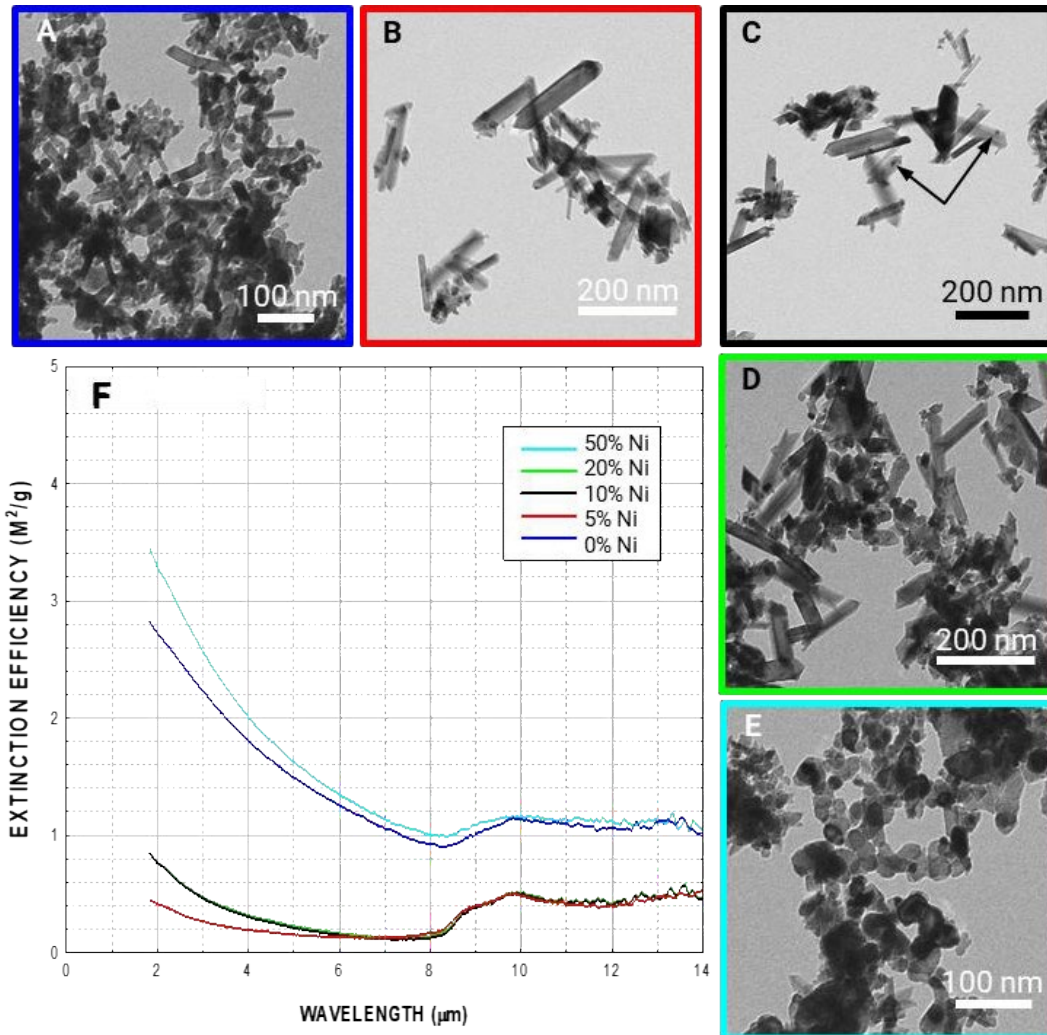


Figure 4. TEM images (A–E) and FTIR spectra (F) of hydrothermal TiN NPs prepared in the presence of $\text{Ni}(\text{NO}_3)_2$ at 0 % (dark blue), 5 % (red), 10 % (black), 20 % (green), and 50 % (light blue) mass loading. Black arrows indicate small dark spots which may be nickel NPs on the surface of the TiN fibers.

Across the range of Ni doping, there is a notable change in spectral shape in Figure 4F, with the 50 % sample most closely matching the control TiN, and at significantly higher MECs than the other three samples.

In the previous NiCl_2 experiment, the flatter spectral shape and more defined wires were found in the 5 % and 10 % samples, while the 20 % and 50 % samples matched the control TiN spectral shape. This most recent nitrate experiment is similar, apart from the 20 % sample, which switches from the control TiN shape to the flatter curve when switching from the chloride to nitrate. This result is interesting and may be due to i) the anion presents in solution, ii) the oxidation state of nickel cation, or iii) a combination of both.

The TEM images in Figure 4A–E show that this change in spectral shape is also matched by a change in particle morphology. The samples with lower loadings are composed primarily of nanorods or nanowires, with lengths around 200 nm and diameters ranging from 10–70 nm. Once the concentration exceeds 50 % mass loading, TiN NPs are formed, and the 50% sample was comprised of a mixture of mostly rounded particles with some nanorods. In this case, the larger and more defined nanowires give significantly lower MECs than the smaller rounded particles. The

decrease in oxidation at higher concentration may be due to a higher energy barrier to effectively oxidize the TiN NPs. Furthermore, Ni in solution may behave as an antioxidant.

Visual analysis of the colloidal solutions revealed that the solutions went from light blue to almost white until the doping level exceeded 50 %. In contrast, both the control TiN and 50 % sample were black in color. Coupling the solution color with the significantly lower MECs, it is expected that the lower concentration TiN NPs were significantly oxidized and transitioned from TiN NPs to oxynitride nanowires.

Closer inspection of the TEM image in Figure 4C reveals small high Z-contrast spheres located on the surface of oxynitride nanowires. While further investigation is required, it is anticipated that the small spheres are nickel NPs that grew on the surface of the oxynitride nanowires. This result is interesting, given that previous copper appeared to follow a layer-by-layer growth mechanism, whereas nickel appears to follow an island growth mechanism. Given that nitrate may be more significantly oxidizing the TiN, the difference in NP growth may be due to the Ni growing on an oxygen-rich surface.

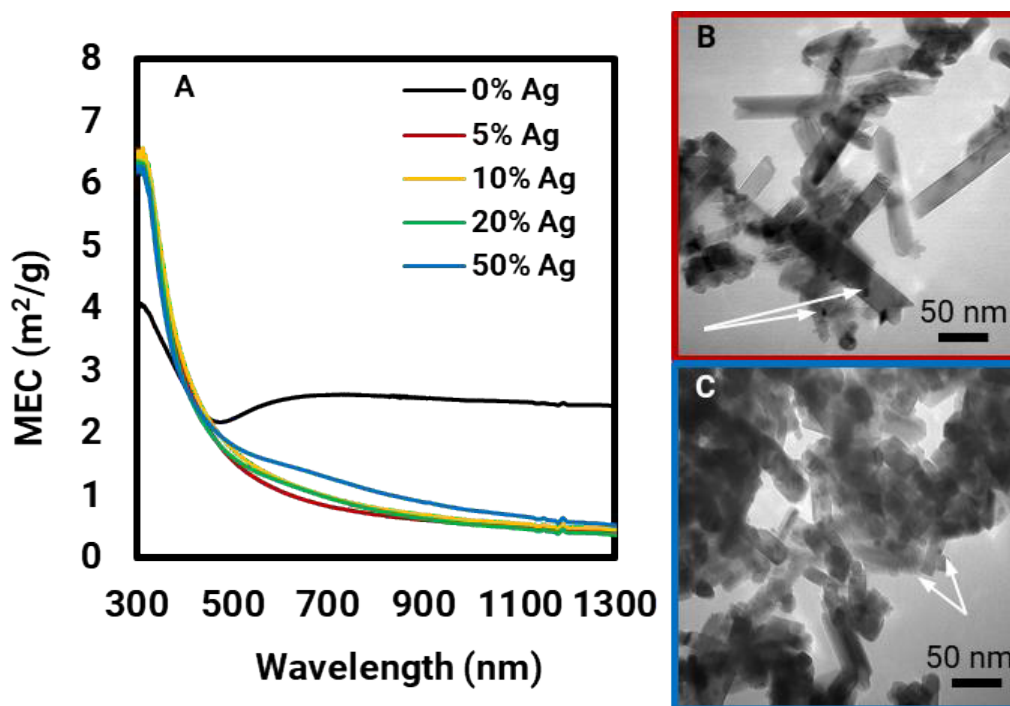


Figure 5. UV-vis spectra (A) and TEM images (B–C) of hydrothermal TiN NPs prepared in the presence of AgNO₃ at 0 % (black), 5 % (red), 10 % (yellow), 20 % (green), and 50 % (blue) mass loading. White arrows indicate the presence of possible core-shell morphology in several NPs.

Figure 5 shows the samples of various Ag mass loadings all very closely matching each other in UV-vis MECs, and a smooth spectral shape in contrast to the control TiN. The difference in spectral shape results in the Ag samples having significantly lower MECs in the NIR but rising to match and then exceed the control TiN towards the UV region. Notably, the powder particles displayed a range of light colors, from light blue to pale purples, when compared to the black control TiN. Generally, a pale color suggests a high degree of oxidation to oxynitrides within the TiN particles. The added purple tone of the higher Ag samples suggests the potential formation of additional materials such as Ag NPs.

TEM images of the 5 % and 50 % samples (Figure 5B–C) also show the presence of many small dark spots on the surfaces of the larger nanorods. These spots appear similar to the high Z-contrast spots noted on the Ni(NO₃)₂ samples, suggesting the formation of metal NPs on the surface of the TiN or oxynitride particles. These metal NPs in the Ag samples appear both more numerous and significantly smaller than those found in the Ni samples.

To further explore elements beyond the first row D-metals, Au and Ce were investigated by using HAuCl₄ and CeCl₃ salts in the hydrothermal reaction (Figure 6).

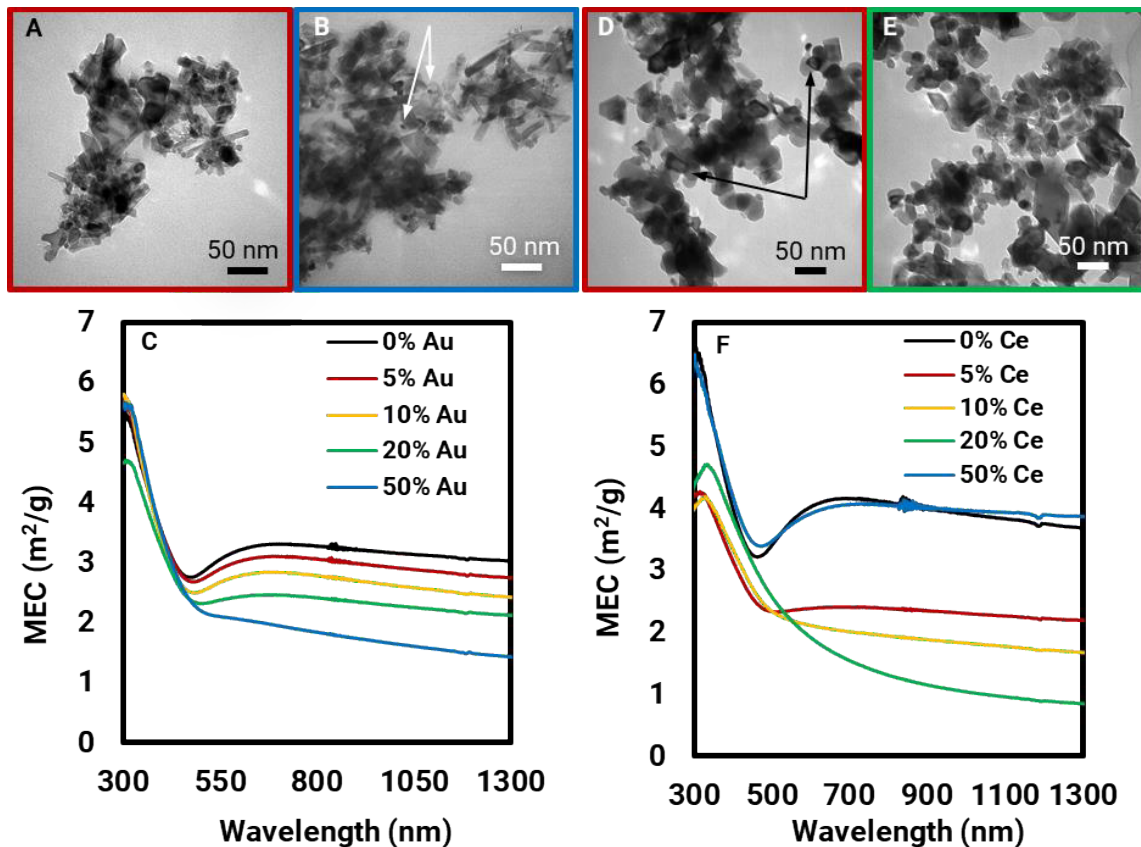


Figure 6. TEM images and UV-vis spectra of hydrothermal TiN NPs prepared in the presence of HAuCl_4 (A–C) and CeCl_3 (D–F) at 0 % (black), 5 % (red), 10 % (yellow), 20 % (green), and 50 % (blue) mass loading. White arrows in B indicate the presence of possible Au NPs on the surface of TiN, while black arrows in D indicate possible core-shell morphology in several NPs.

Figure 6C shows the UV-vis spectra for the Au experiments, with a spectral shape change from the control TiN with a defined dip near 480 nm to the higher concentration materials becoming a smooth curve increasing towards the UV. As the Au concentration increases, the spectral dip both redshifts and decreases in intensity to transition to the smooth curve. Across all functionalized samples, the average MEC in the visible range stays nearly constant around $3 \text{ m}^2 \text{ g}^{-1}$, while the average NIR MEC steadily decreases from the 0 % to the 50 % sample.

The TEM images in Figure 6A–B show mixtures of rounded particles and nanorods in aggregated clusters. A few high Z-contrast spots are identified in Figure 6B, like the spots found in the Ag samples. However, due to the aggregation of the particles, it is difficult to discern the quantity of metal NPs or any trend between the lower and higher concentration samples.

Also notable from these experiments is the precipitation of floating gold particles and two larger pieces of brown colored material, found inside the 20 % and 50 % reaction solutions before processing. The larger pieces of residue were removed, but the smaller flakes of floating particles were mixed into the material. It is likely that these gold particles were further broken down and dispersed into the material at very low concentrations during the washing process, as they could not be identified by eye. These may contribute to some of the high Z-contrast spots identified with TEM.

The UV-vis spectra of the Ce experiments in Figure 6F show a similar trend as the previous $\text{Ni}(\text{NO}_3)_2$, with the 50 % sample most closely matching the control TiN spectra and color. For the 5 %–20 % samples, the spectral shape change shows a similar trend as the Au, with the spectra transitioning from a more defined dip at 480 nm to a smooth curve. These spectra also show a more defined redshift, with a peak emerging near 300 nm not seen in previous experiments, which shifts towards the IR region as the Ce concentration increases.

Notable in the TEM images Figure 6D–E is the unique particle shapes in these samples, displaying a range of angular square and rhomboid shapes. Given the layered nature of the TEM images, it is possible that these particles have a

thin flake morphology. These shapes have not yet been previously seen in TiN samples. In addition, several of these particles appear to have a core-shell morphology, though difficult to positively identify due to the layering of the particles. Further investigation is underway.

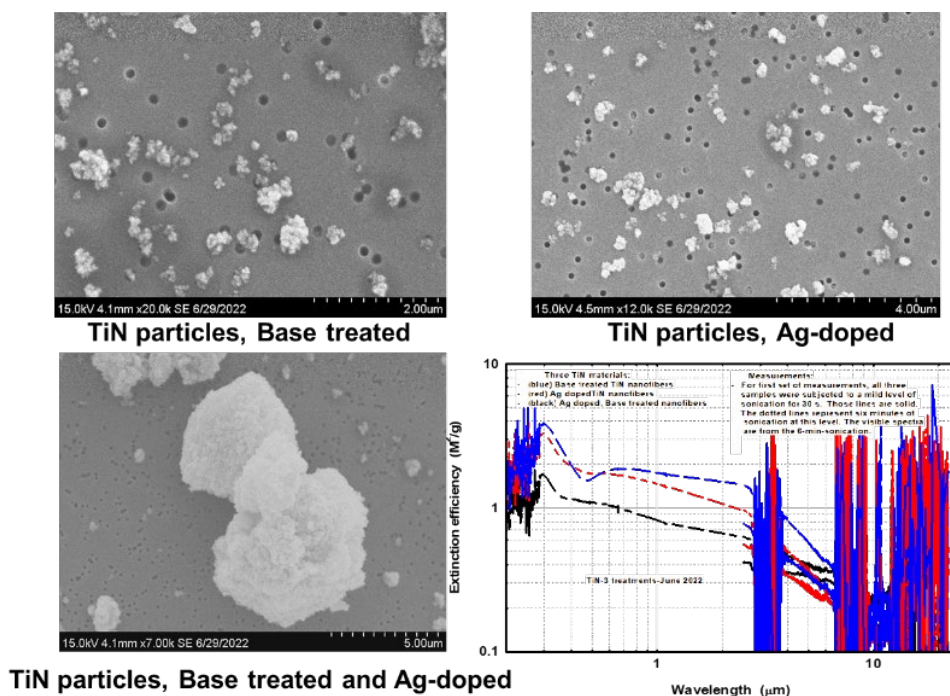


Figure 7. SEM images of Ag doping polyol synthesis on TiN and FTIR of associated MECs.

Figure 7 displays the results of the treatment of the TiN to promote the anisotropic growth of Ag on the surface via a polyol synthesis. After base treatment the TiN nanorods loses all rod shape. This also occurred when the TiN underwent the polyol synthesis without any prior treatment. The resulting material was still measured for MECs and the peak attenuation was apparent in the visible. This result is not surprising as the more spherical shape of the particles would attenuate in the visible due to Mie theory.

4. CONCLUSION

TiN NPs were successfully synthesized and functionalized with a variety of metals to tune the shape and composition of TiN NPs. By tuning the concentration of metal salts, TiN NPs synthesized in which the NPs were doped, core-shell, or island-functionalized. The visible and IR MECs were characterized at Luna Labs and New Mexico State University to understand the impact of metal functionalization on the TiN NPs obscuring properties. Overall, functionalizing TiN NPs with Cu or using high concentrations of metals appears to be a viable strategy to increase the overall attenuating properties of TiN NPs.

Future investigation will be needed to determine the specific reaction conditions and mechanisms for these unique structures. Further high-resolution imaging, X-ray photoelectron spectroscopy, and energy-dispersive X-ray spectroscopy is required to fully understand the growth mechanism and identify if the TiN NPs are indeed functionalized with metal shells or islands. Additionally, the advanced characterization will be required to write articles that can be submitted to public peer-reviewed journals such as Small, ACS Nano, or Nanoscale.

ACKNOWLEDGMENTS

Funding was provided by the U.S. Army via the In-house Laboratory Independent Research Program (PE 0601101A Project 91A) at the Combat Capabilities Development Command Chemical Biological Center.

REFERENCES

- [1] Smith, J.D.; Woessner, Z.J.; and Skrabalak, S.E. Branched Plasmonic Nanoparticles with High Symmetry. *J. Phys. Chem. C* **2019**, *123* (30), pp 18113–18123.
- [2] Willets, K.A.; Van Duyne, R.P. Localized Surface Plasmon Resonance Spectroscopy and Sensing. *Annu. Rev. Phys. Chem.* **2007**, *58*, pp 267–297.
- [3] Guler, U.; Naik, G.V.; Boltasseva, A. Performance analysis of nitride alternative plasmonic materials for localized surface plasmon applications. *Appl. Phys. B* **2012**, *107*, pp 285–291.
- [4] Progress in Solid State Chemistry. Volume 50, June 2018, Pages 1–15.
- [5] Joshia, U.A.; Chungb, S.H.; Leea, J.S. Low-temperature, solvent-free solid-state synthesis of single-crystalline titanium nitride nanorods with different aspect ratios. *J. Solid State Chem.* **2005**, *178*, pp 755–760.
- [6] Shin, H. Scaffold-Like Titanium Nitride Nanotubes with a Highly Conductive Porous Architecture as a Nanoparticle Catalyst Support for Oxygen Reduction. *ACS Catal.* **2016**, *6*, p39143920.
- [7] Hayashi, H.; Hakuta, Y. Hydrothermal Synthesis of Metal Oxide Nanoparticles in Supercritical Water. *Materials (Basel)*. **2010**, *3* (7), pp 37943817.
- [8] Metal Nanocrystals. (American Chemical Society, 2020). doi:10.1021/acs.infocus.7e4003.
- [9] Applied Catalysis A: General Volumes. Pp 413–414, 31 January 2012, pp 238–244.
- [10] Kumar, M.; Umezawa, N.; Ishii, S.; Nagao, T. Examining the Performance of Refractory Conductive Ceramics as Plasmonic Materials: A Theoretical Approach. *ACS Photonics*. **2016**, *3* (1), pp 43–50.
- [11] Patsalas, P. Optical Properties and Plasmonic Performance of Titanium Nitride. *Materials*. **2015**, *8*, pp 3128–3154.
- [12] Guler, U. Nanoparticle plasmonics: going practical with transition metal nitrides, *Materials Today* **2015**, *18* (4), pp 228–237.
- [13] Kuhn, D.; Zander, Z.; Kulisiewicz, A.M.; Debow, S.M.; Haffey, C.; Fang, H.; Kong, X.; Qian, Y.; Walek, S. D.; Govorov, A.O.; Rao, Y.; Dai, H.; Delacy, B.G. The Fabrication of Anisotropic Ag Nanoplatelets on the Surface of TiO₂ Fibers for Enhanced Photocatalysis of Chemical Warfare Agent Simulant, Methyl Paraoxon, *J. Phys. Chem. C* **2019**, *123* (32), pp 19579–19587.
- [14] Zhang, J.; Hu, H.; Liu, X.; Li, D. S. Development of the applications of titanium nitride in fuel cells. *Mater. Today Chem.* **2019**, *11*, pp 42–59.
- [15] Hu, Y.; Huo, K.; Ma, Y.; Lu, Y.; Xu, J.; Hu, Z.; Chen, Y. Synthesis and Field Emission Characterization of Titanium Nitride Nanowires. *J. Nanosci. Nanotechnol.* **2001**, *7*, pp 2922–2926.
- [16] Liu, J.; He, H.; Xiao, D.; Yin, S.; Ji, W.; Jiang, S.; Luo, D.; Wang, B.; Liu, Y. Recent Advances of Plasmonic Nanoparticles and Their Applications. *Materials*. **2018**, *11* (10), p 1833.
- [17] Albrecht, W.; Bladt, E.; Vanrompay, H.; Smith, J.D.; Skrabalak, S.E.; Bals, S. Thermal Stability of Gold/Palladium Octopods Studied in Situ in 3D: Understanding Design Rules for Thermally Stable Metal Nanoparticles. *ACS Nano*. **2019**, *13* (6), pp 6522–6530.
- [18] Feng, H.; Zhang, M.-H.; Yu, L.E. Hydrothermal synthesis and photocatalytic performance of metal-ions doped TiO₂. *Appl. Catal., A* **2012**, *413–414*, pp 238–244.
- [19] Kheirandish, A.; Sepehri Javan, N.; Mohammadzadeh, H. Modified Drude Model for Small Gold Nanoparticles Surface Plasmon Resonance Based on the Role of Classical Confinement. *Sci Rep.* **2020**, *10* (1), p 6517.
- [20] Pennycook, S.J. Z-Contrast Transmission Electron Microscopy: Direct Atomic Imaging of Materials. *Annu. Rev. Mater. Sci.* **1992**, *22* (1), pp 171–195.

Elucidating the prevalence of off-target effects of CRISPR-Cas editing in prokaryotes

Casey B. Bernhards^{a*}, Kimberly L. Berk^a, Alvin T. Liem^b, Pierce A. Roth^b, Mark A. Karavis^a,
Matthew W. Lux^a

^aU.S. Army Combat Capabilities Development Command Chemical Biological Center, Research & Operations Directorate, 8198 Blackhawk Rd., Aberdeen Proving Ground, MD 21010

^bDCS Corporation, 6909 Metro Park Dr., Suite 500, Alexandria, VA 22310

ABSTRACT

CRISPR-Cas has emerged as a powerful, dual-use gene editing tool that has been used to modify a variety of organisms, from bacteria to humans. Extensive work has gone into understanding off-target effects of CRISPR systems in higher level organisms due to the potential consequences of unintended mutations when used for medical applications, but this area of research has remained relatively unexplored in prokaryotes. Here, we describe similar work to understand the off-target effects of CRISPR editing in bacteria as a potential method to identify signatures of engineered threats. We describe a two-pronged approach based on an engineered selection system to quantify off-target rates *in vivo*, and a parallel *in vitro* approach that assesses off-target rates using purified molecular components. This report describes work completed in the third year of the project.

Keywords: gene editing, genome engineering, genetic signatures, synthetic biology, microbial forensics

1. INTRODUCTION

In recent years, the barriers to genetically engineer a wide range of prokaryotic organisms have been dramatically reduced, driven in large part by the application of CRISPR-Cas (Clustered Regularly Interspaced Short Palindromic Repeats and CRISPR-associated) gene editing systems.¹ CRISPR editing has already been demonstrated in eukaryotic organisms and at least 36 different prokaryotic species.² Compared to other techniques, CRISPR gene editing is relatively simple and requires only a few components: the Cas enzyme is required to create a double-strand break (DSB) in the DNA, a small guide RNA (gRNA), and short recognition motif known as a protospacer adjacent motif (PAM) sequence are needed for target a specific site in the DNA for Cas-mediated cleavage.³ In eukaryotic cells, the natural pathway for repair of CRISPR-induced DSBs is through non-homologous end joining (NHEJ), an error-prone pathway resulting in small insertions or deletions of DNA. However, an array of precise edits are possible through homology-directed repair (HDR) by providing a DNA repair template. As most bacteria lack a native NHEJ system, CRISPR editing in prokaryotes relies on the HDR pathway,⁴ which crucially leaves no additional markers (antibiotic resistance cassettes, extra bases, or scars) at the site of editing.

The characteristics that have made CRISPR-Cas a powerful genome editing tool, including its ease of use and broad applicability, are the same qualities that have prompted dual-use concerns. There is a need within the Department of Defense to be able to detect genetically engineered threats, particularly those arising from techniques like CRISPR, that lack traditional signatures. Despite being touted as a highly precise gene editing technique, CRISPR off-target effects (unintended modifications elsewhere in the genome) have been reported.⁵ Due to the potential ramifications of off-target effects for CRISPR applications like human gene therapy, there has been considerable interest and research in this area for eukaryotic organisms.⁶⁻¹⁰ Unfortunately, the pace of research into CRISPR off-target effects in prokaryotes has not kept up with its eukaryotic counterpart. Importantly, several factors suggest there may be differences observed between off-target effects in eukaryotic and prokaryotic organisms: (1) these groups have different routes of DNA repair (NHEJ versus HDR);⁴ (2) due to the lethal nature of unrepaired DSBs in prokaryotic cells, CRISPR editing may activate the cell's SOS response and increase the cell's mutation rate;¹¹ and (3) differences in off-target effects have been reported between *in vitro* and *in vivo* experiments in eukaryotic cells,^{7,8} which suggests the involvement of other cellular mechanisms. Characterization of off-target effects in prokaryotes may reveal signatures of editing and facilitate detection of CRISPR-modified organisms.

In this work, we genetically modify the model bacterium *Escherichia coli* using CRISPR-Cas9 and use engineered on- and off-target sites to assess CRISPR editing rates *in vivo*. In parallel, we apply *in vitro* editing and sequencing techniques specifically designed to identify off-target edits. We hypothesize that CRISPR editing in bacteria creates off-target effects that are detectable through these methods.

2. METHODOLOGIES

2.1 *In vivo* CRISPR experiments

2.1.1 CRISPR editing

CRISPR edits and insertions at sites in the chromosome of *E. coli* MG1655 (BEI Resources, #NR-2653) and derivative strains were performed based on a previously described method.¹² Using the pCas plasmid (a gift from Sheng Yang, Addgene plasmid #62225), which contains the genes for Cas9 and λ -Red recombinase, and derivatives of plasmid pTargetF (a gift from Sheng Yang, Addgene plasmid #62226) containing both gRNA and HDR template sequences. *E. coli* MG1655 cells containing pCas were made electrocompetent by culturing in Lysogeny Broth (LB) with kanamycin (50 $\mu\text{g}/\text{mL}$) at 30 °C with shaking at 250 rpm until reaching an OD₆₀₀ (optical density at 600 nm) of 0.4-0.6. L-arabinose was added to a final concentration of 10 mM during growth for induction of the λ -Red genes on the pCas plasmid. Cells were washed two times with ice-cold, sterile water followed by one wash with ice-cold, sterile 10 % glycerol. Cells were concentrated 100-fold, flash frozen in liquid nitrogen, and stored at -80 °C. Derivatives of plasmid pTargetF (100 ng) were added to 50 μL of electrocompetent cells and electroporated in 1 mm cuvettes at 1.8 kV. Transformed cells were recovered in 950 μL ice-cold Super Optimal Broth (SOB) for 2 hours at 30 °C with shaking before being spread onto LB agar plates containing kanamycin (50 $\mu\text{g}/\text{mL}$) and spectinomycin (50 $\mu\text{g}/\text{mL}$), unless otherwise indicated. Successful CRISPR editing was verified by colony PCR and DNA sequencing. For strains undergoing additional rounds of CRISPR editing, pTargetF-derivative plasmids were cured with 0.5 mM isopropyl- β -D-thiogalactopyranoside (IPTG), as previously described.¹²

2.1.2 Construction of on-target site

An on-target site consisting of a promoterless chloramphenicol resistance gene, 20-base *sacB* gRNA targeting site, and flanking bidirectional terminators was designed for insertion into Gap 2 of the *E. coli* MG1655 chromosome.¹³ The chloramphenicol resistance gene was PCR amplified from plasmid pACYC184 (Coli Genetic Stock Center, #12139), DT5 bidirectional terminator¹⁴ and *sacB* gRNA targeting site were obtained as a gBlock (Integrated DNA Technologies, IDT), and DT101 bidirectional terminator¹⁴ was obtained as a minigene (IDT) and PCR amplified. Isothermal DNA assembly (NEBuilder® HiFi DNA Assembly, New England Biolabs, NEB) was used to clone the DNA fragments into linearized plasmid pTarget-Gap2 containing a gRNA sequence and homologous DNA for CRISPR editing of Gap 2.¹³ The resulting plasmid, pOn-Target, was used to insert the on-target site into Gap 2 of the *E. coli* chromosome¹³ via CRISPR editing, as described above. Guide RNA sequences are provided in Table 1, and primer sequences are provided in Table 2.

Table 1. Guide RNA sequences.

Guide RNA	Sequence (5' to 3')
<i>sacB</i> gRNA/targeting site	TGCCAGCAGTGC GG TAGTAA
pTarget-Gap2 gRNA ¹³	CGGACGCTCGTTAATATTTA
pTarget-Gap5 gRNA ¹³	CCTCCATGCTTAATATAAGG
Non-targeting control gRNA (NC_162) ¹⁵	GATGTGTCACCTTCCACTGA

Table 2. Primer sequences.

Primer Name	Sequence (5' to 3')	Description/Use
Cm-F	ATGGAGAAAAAATCACTGGATAT ACC	PCR amplification of chloramphenicol resistance gene
Cm-R	GTTTAAGGGCACCAATAACTG	
CmR_DT101_pCBV54-F	AAGGCAGTTATTGGTGCC	PCR amplification of DT101 bidirectional terminator minigene
CmR_DT101_pCBV54-R	ATGTCTTAATCAATGAAGACCTTAA GTC	
pCBV54_linear-F	TTAAGGTCTTCATTGATTAAGACAT CC	Linearization and amplification of pTarget-Gap2
pCBV54_linear-R	ATATTAACGAGCGTCCGC	
sacB-F	GAGTCTAATAGAATGAGGTCCG	PCR amplification of <i>sacB</i> gene
sacB-R	TGCCAATAGGATATCGGC	
pCBV57_DT60_sacB-F	TTTTCAATCACCTTCCATCCAC	PCR amplification of DT60 bidirectional terminator minigene
pCBV57_DT60_sacB-R	TTTTCGACCTCATTCTATTAGACTCC	
sacB_DT54_pCBV57-F	AGAAAATGCCGATATCCTATTGG	PCR amplification of DT54 bidirectional terminator minigene
sacB_DT54_pCBV57-R	ACTGAAACCCTCCATGCT	
pCBV57_linear-F	TATATTAAGCATGGAGGGTTTCAG	Linearization and amplification of pTarget-Gap5
pCBV57_linear-R	AGGTGGATGGAAAGGTGATTG	
pCBV65_linear-F	ACGAGAGTCTAATAGAATGAGGTCCG	Linearization and amplification of pOff-Target1
pCBV65_linear-R2	TGTAGGTGGATGGAAAGG	
UpCm-F	TACCTGTGACGGAAGATC	PCR amplification of Pcat
PartCm_pCBV64-R	GCAGGTGCGACTCTAGAGAATGAAG AAGTTGTCCATATTGGC	
pTargetF_N20-R	ACTAGTATTATACCTAGGACTGAG	PCR amplification of pOn-Target for construction of pTarget-Pcat
pCBV64_linear-F	ATTCTCTAGAGTCGACCTG	
pTargetF_sacB_gRNA2-F	GTCCTAGGTATAAATACTAGTTGCCA GCAGTGCGGTAGTAAGTTTTAGAGC TAGAAATAGCAAG	PCR amplification of pOn-Target for construction of pTarget-Pcat
pCBV64_linear-R	GAAGTGATCTTCCGTCAC	
pTargetF_NC_162-F	GTCCTAGGTATAAATACTAGTGATGT GTCACCTTCCACTGAGTTTTAGAGC TAGAAATAGCAAG	Used with primer pTargetF_N20-R for PCR of pTarget-Pcat to construct pTarget-NC_162
Pcat_colony-F	ATCGGCACGTAAGAGGTTCC	Colony PCR for verification of Pcat insertion via CRISPR
Pcat_colony-R	CATTCTGCCGACATGGAAGC	
pCBV65_DT60_Up_sacB-F	CAATCACCTTCCATCCAC	PCR amplification of off-target sites for <i>in vitro</i> cleavage experiments
sacB_cleavage-R1	CTGTAGTTGCCTTCATCG	

2.1.3 Construction of off-target sites

An off-target site (Off-Target Site 1) containing the *sacB* gene and flanking bidirectional terminators was designed for insertion into Gap 5 of the *E. coli* MG1655 chromosome.¹³ The *sacB* gene and 219 bp upstream were PCR amplified from *Bacillus subtilis* 168 (Bacillus Genetic Stock Center, #1A1) genomic DNA, and the DT60 and DT54 bidirectional terminators¹⁴ were obtained as minigenes (IDT) and PCR amplified. Isothermal DNA assembly was used to clone the DNA fragments into linearized plasmid pTarget-Gap5 containing a gRNA sequence and homologous DNA for CRISPR editing of Gap 5 of the *E. coli* chromosome;¹³ the resulting plasmid was designated pOff-Target1.

A redesigned version of the *sacB* off-target site containing a second predicted native promoter upstream of *sacB* was also constructed (Off-Target Site 2). A gBlock (IDT) containing the DT60 bidirectional terminator¹⁴ and 463 bp of native DNA upstream of *sacB* was cloned into linearized pOff-Target1 via isothermal DNA assembly; the resulting plasmid was designated pOff-Target2.

Other variations of the off-target sites containing synonymous point mutations within the gRNA target region of *sacB* were constructed via site-directed mutagenesis (Q5[®] Site-Directed Mutagenesis Kit, NEB) of pOff-Target1 and pOff-Target2.

Plasmids pOff-Target1, pOff-Target2, and derivatives constructed by site-directed mutagenesis were used to insert the off-target sites into Gap 5 of the chromosomes of *E. coli* MG1655¹³ and derivative strain containing the on-target via CRISPR editing, as described above. Guide RNA sequences are provided in Table 1, and primer sequences are provided in Table 2.

2.1.4 Construction of editing and control plasmids for determining on- and off-target editing rates

The native promoter for the chloramphenicol resistance gene (Pcat) was PCR amplified from plasmid pACYC184, and portions of pOn-Target were PCR amplified using primers incorporating the *sacB* gRNA sequence. The DNA fragments were used to construct the editing plasmid, pTarget-Pcat, via isothermal DNA assembly. In addition to Pcat, plasmid pTarget-Pcat contains the *sacB* gRNA sequence and homologous DNA for CRISPR editing of the on-target site. A control plasmid, in which the *sacB* gRNA sequence of pTarget-Pcat was replaced with a non-targeting gRNA sequence (NC_162),¹⁵ was constructed using inverse PCR of pTarget-Pcat with primers containing the non-targeting gRNA sequence, followed by isothermal DNA assembly. The resulting non-targeting control plasmid was designated pTarget-NC_162. Guide RNA sequences are provided in Table 1, and primer sequences are provided in Table 2.

2.1.5 Determining on-target editing efficiency

Plasmid pTarget-Pcat was used to edit the chromosome of *E. coli* MG1655 containing the on-target site via CRISPR, as described above. Serial dilutions of transformed cells were spread onto LB agar plates containing kanamycin (50 µg/mL), kanamycin and spectinomycin (50 µg/mL), or kanamycin and chloramphenicol (25 µg/mL). Plates were incubated overnight at 30 °C and the resulting colonies counted to determine colony forming units (CFUs). Pcat insertion via CRISPR editing was confirmed with colony PCR. Primer sequences are provided in Table 2.

2.1.6 Testing *sacB* off-target sites

E. coli MG1655 strains containing the *sacB* off-target sites were tested for sucrose sensitivity by serially diluting either electrocompetent cells or cells grown overnight in liquid cultures in SOB medium and plating on LB agar plates containing kanamycin (50 µg/mL), or LB (minus NaCl) agar plates with kanamycin and 10 % sucrose. Plates were incubated overnight at 30 °C and the resulting colonies counted to determine CFUs.

Plasmids pTarget-Pcat and pTarget-NC_162 were used to test off-target site editing in the chromosome of *E. coli* containing Off-Target Site 2 via CRISPR, as described above. Serial dilutions of transformed cells were spread onto LB agar plates containing kanamycin (50 µg/mL), kanamycin and spectinomycin (50 µg/mL), or LB (minus NaCl) agar plates containing kanamycin and 10 % sucrose to select for sucrose-resistant cells. Plates were incubated overnight at 30 °C.

2.2 *In vitro* CRISPR experiments

2.2.1 *gRNA*

The *sacB* gRNA used for *in vitro* experiments was obtained commercially as an Alt-R® CRISPR-Cas9 sgRNA from IDT. Guide RNA sequence information is provided in Table 1.

2.2.2 *In vitro* cleavage of off-target site DNA

Approximately 1 kb regions of the off-target sites designed for *in vivo* experiments were PCR amplified from plasmid pOff-Target1 and derivatives constructed by site-directed mutagenesis. PCR products were purified using the QIAquick PCR Purification Kit (Qiagen). For *in vitro* cleavage tests, 0.1 μM Cas9 (NEB) and 0.1 μM gRNA (IDT) were first complexed in Buffer 3.1 (NEB) and nuclease-free water at room temperature for 10 min before adding 200 ng of purified PCR product. Negative control reactions omitted Cas9. Reactions were incubated for 1 hour at 37 °C, treated with Proteinase K (NEB) for 15 min at 37 °C, and analyzed by agarose gel electrophoresis. Primer sequences are provided in Table 2.

2.2.3 *CHANGE-seq*

CHANGE-seq methodology was performed based on the previously published method with modifications.¹⁶ Genomic DNA was isolated from the *E. coli* MG1655 derivative containing the on-target site (constructed above) using the DNeasy UltraClean Microbial Kit (Qiagen). Custom transposon oligonucleotides oCRL225 and oCRL226¹⁶ (IDT) were prepared as 100 μM stocks in 1X Tris-EDTA (TE) Buffer pH 8.0, and equal volumes were combined and annealed in a thermocycler with the following program: 95 °C for 5 min, cool to 65 °C at -0.1 °C/sec, 65 °C for 5 min, cool to 4 °C at -0.1 °C/sec. Equal volumes (10 μl each) of annealed oligonucleotides and Tn5 transposase (unloaded, Diagenode) were assembled at 23 °C for 30 min, followed by addition of 10 μl glycerol. The assembled Tn5-transposome (5 vol%) was incubated with 500 ng of purified genomic DNA in TAPS-DMF Buffer (final concentrations: 10 mM TAPS-NaOH pH 8.5, 5 mM MgCl₂, 10 % dimethylformamide) at 50 °C for 7 min for tagmentation of the DNA to an average size of 400 bp. The tagmentation reaction was stopped by incubation at 55 °C for 7 min with 2 vol% Proteinase K (NEB), and the DNA was purified using the DNA Clean & Concentrator kit (Zymo Research). Remaining steps were performed essentially as previously described,¹⁶ except that DNA purification steps were performed with the DNA Clean & Concentrator kit (Zymo Research) unless otherwise indicated. Briefly, gap repair of the tagmented DNA was performed using KAPA HiFi HotStart Uracil+ Ready Mix (Roche) and Taq DNA Ligase (NEB), followed by treatment with Proteinase K. Gap-repaired DNA was purified and treated with USER Enzyme (NEB) and T4 Polynucleotide Kinase (NEB). Resulting DNA was purified and circularized with T4 DNA Ligase (NEB). Circularized DNA was purified and treated with Plasmid-Safe ATP-dependent DNase (Lucigen), Lambda Exonuclease (NEB), and Exonuclease I (NEB) to degrade remaining linear DNA. At various points throughout the procedure, DNA was analyzed by Qubit fluorometer (dsDNA HS Assay Kit, Thermo Fisher Scientific) and TapeStation automated electrophoresis (D5000 ScreenTape, Agilent). Cas9 (NEB) and gRNA (IDT) were complexed at room temperature for 10 min and incubated with purified circularized DNA, followed by treatment with Proteinase K. A negative control DNA sample was also prepared by omitting Cas9 and gRNA. Digested DNA was purified using magnetic beads, A-tailed (KAPA LTP Library Preparation Kit, PCR-free, Roche), ligated with NEBNext® adapter for Illumina (NEB), and treated with USER enzyme. Next, DNA will be PCR amplified using KAPA HiFi HotStart Ready Mix (Roche) for adding dual-index barcodes (NEBNext® Multiplex Oligos for Illumina, Dual Index Primers Set 1, NEB). Completed libraries will be quantified using KAPA Library Quantification Kit (Roche) and sequenced with 150-bp paired-end reads on an Illumina MiSeq. CHANGE-seq data will be analyzed using code available on GitHub (<https://github.com/tsailabSJ/changeseq>).

3. RESULTS

3.1 Measuring CRISPR on- and off-target effects *in vivo*

Because CRISPR off-target effects are likely to be rare events in bacteria, we devised a counterselection system to isolate instances of off-target DSB formation in bacteria, as shown in Figure 1. *E. coli* strains were constructed in which two of the neutral insertion points (Gap 2 and Gap 5) identified by the targetFinder algorithm¹³ in previous years of this project were used for insertion of engineered “on-target” and “off-target” sites. The on-target site consists

of a promoterless chloramphenicol antibiotic resistance gene, and the off-target site contains the *sacB* gene, which makes growth in the presence of sucrose toxic to cells. Strong bidirectional terminators¹⁴ flank both sites to insulate the engineered sites from local genetic context. Both sites also contain a *sacB* gRNA target sequence that can be made less similar through synonymous point mutations in the gRNA region of *sacB*. Successful edits at the on-target site via homology-directed repair result in expression of the chloramphenicol resistance gene (via incorporation of the promoter on the DNA repair template), enabling selection by growth on the antibiotic. Cells surviving cleavage at the off-target site through error-prone DNA repair (resulting in a frameshift mutation in *sacB*), are selected by growth on sucrose. Colony counts from these different scenarios are then used to assess the CRISPR editing rates at the engineered sites.

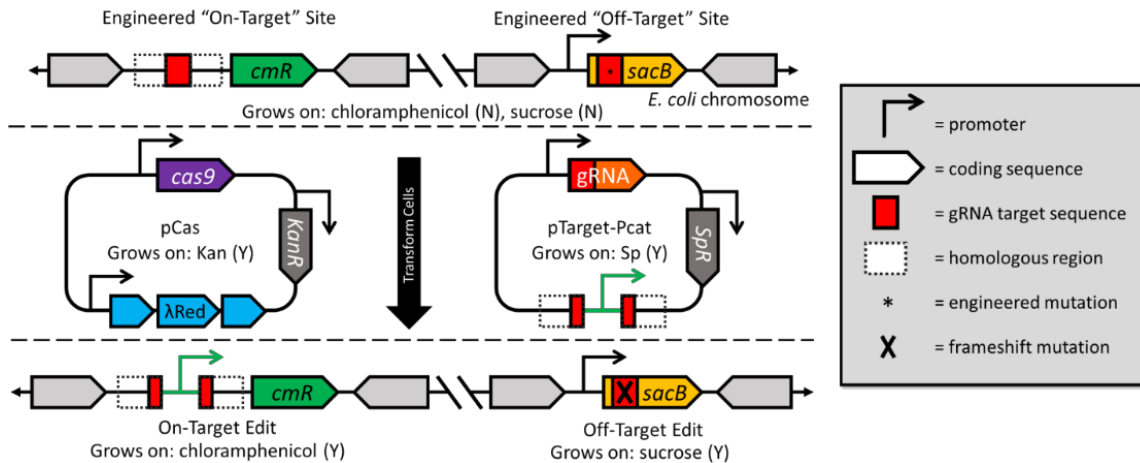


Figure 1. Strategy to measure CRISPR on- and off-target events *in vivo*. Two engineered sites, an “on-target” and an “off-target” site, were inserted into neutral sites in the *E. coli* genome. Following CRISPR editing, growth on plates containing chloramphenicol or sucrose is used to determine if an edit has occurred at the on-target or off-target site.

Using this strategy, the mean on-target site editing efficiency was 40.4 % with the editing plasmid expressing the *sacB* gRNA and containing the DNA repair template with the promoter for the chloramphenicol resistance gene (Figure 2A). In addition to selection of on-target editing events by plating on media containing chloramphenicol, colony PCR from a sample of transformants confirmed that 100 % of the chloramphenicol-resistant colonies had the promoter incorporated at the on-target site via CRISPR editing (Figure 2B).

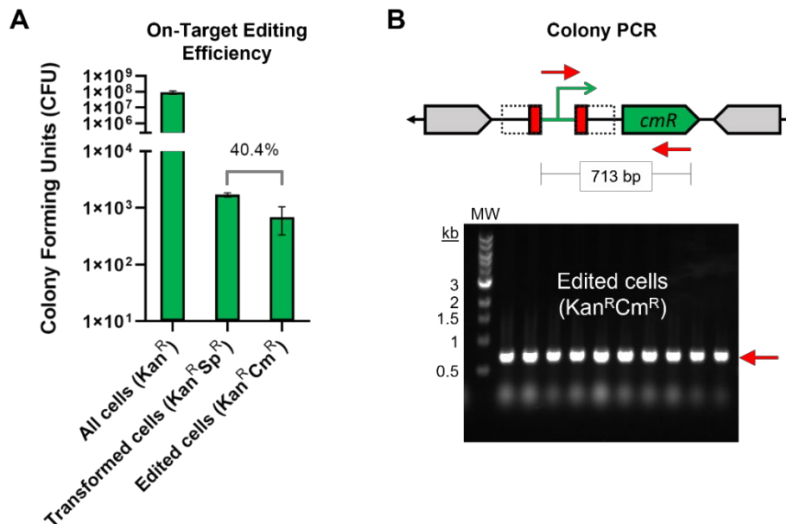


Figure 2. CRISPR editing of engineered on-target site *in vivo*. (A) On-target site editing efficiency. CFU values shown are the mean of five biological replicates; error bars represent the standard deviation. (B) Colony PCR and gel electrophoresis to verify chloramphenicol-resistant cells have the native promoter (green arrow) incorporated via CRISPR editing. Red arrows indicate PCR product that is only produced if the native promoter is present. Kan^R, kanamycin resistant; Sp^R, spectinomycin resistant; Cm^R, chloramphenicol resistant; molecular weight (MW) marker.

Initially, the *sacB* off-target site (Off-Target Site 1) included 219 bp of native DNA upstream of the *sacB* gene. Despite resulting in efficient sucrose-mediated killing of *E. coli* when Off-Target Site 1 was on a multi-copy plasmid during cloning (data not shown), *E. coli* cells with Off-Target Site 1 inserted at a neutral site in the chromosome showed no sucrose sensitivity (Figure 3A). Off-Target Site 2 was then constructed, which contains 463 bp native DNA upstream of *sacB* to include a second predicted promoter site. Insertion of Off-Target Site 2 in the *E. coli* chromosome resulted in significant sucrose-mediated killing and a three- to four-log reduction in CFUs; however, many sucrose-resistant cells still remained (Figure 3A). The impact of this background level of sucrose-resistant cells on the utility of this *sacB* counterselection system to capture rare off-target edits was apparent when CRISPR editing experiments were performed. No difference was observed between cells transformed with the editing plasmid versus a non-targeting control plasmid (Figure 3B). In both instances, plating on media with sucrose resulted in substantial background growth, preventing the differentiation of surviving cells arising from an off-target edit within *sacB* from the background sucrose-resistant population.

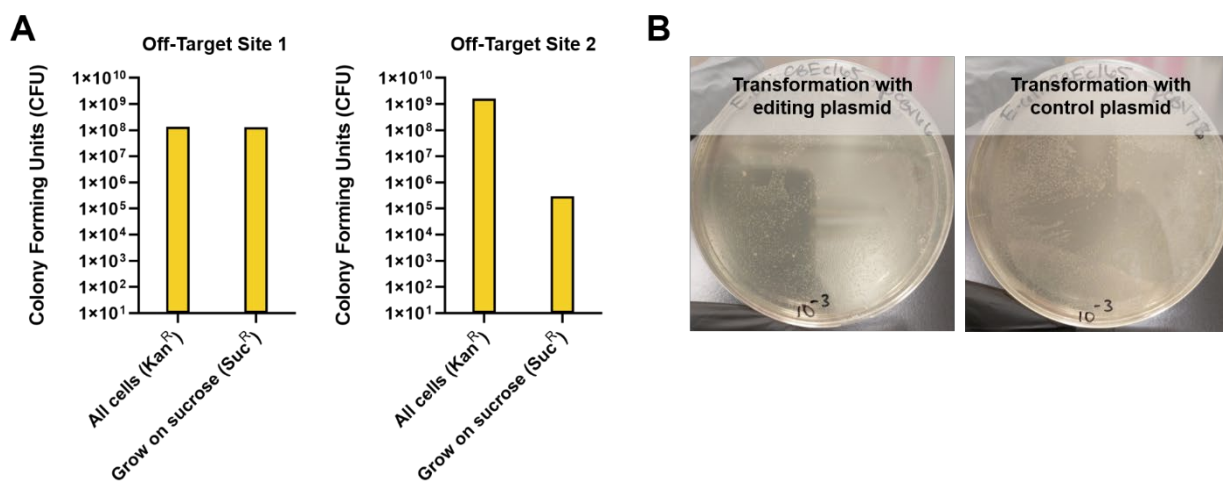


Figure 3. Assessment of *sacB* off-target sites *in vivo*. (A) Sucrose sensitivities of *E. coli* strains with engineered *sacB* Off-Target Site 1 (left) and Off-Target Site 2 (right). Kan^R, kanamycin resistant; Suc^R, sucrose resistant. (B) *E. coli* cells with Off-Target Site 2 transformed with editing plasmid (pTarget-Pcat, left) or non-targeting control plasmid (pTarget-NC_162, right) and plated on media containing kanamycin and sucrose.

3.2 *In vitro* screening of CRISPR off-target effects

As a complementary approach to the *in vivo* counterselection strategy to investigate CRISPR off-target effects, we identified a recently developed *in vitro* sequencing approach, called CHANGE-seq (circularization for high-throughput analysis of nuclease genome-wide effects by sequencing),¹⁶ which has been successfully used for off-target site discovery in eukaryotic organisms. In this procedure, purified genomic DNA is fragmented by a custom Tn5-transposome (a process referred to as tagmentation), and DNA fragments are enzymatically circularized and added to purified CRISPR components (i.e., Cas9 and gRNA). Circular genomic DNA fragments that contain CRISPR on- or off-target sites become linear following cleavage, enabling sequence adapter ligation, PCR amplification, and DNA sequencing for site identification. Cleavage sites determined *in vitro* also have the potential to be utilized for targeted sequencing of off-target sites *in vivo*.

As a part of testing the CHANGE-seq methodology, we assessed *in vitro* cleavage of PCR products containing the *sacB* off-target sites constructed for the *in vivo* experiments (Figure 4). In addition to an off-target site containing the wild-type *sacB* sequence (with 100 percent complementarity to the *sacB* gRNA), *sacB* variants with synonymous point mutations at one of seven positions (each resulting in a 1-bp mismatch with the gRNA sequence) were also tested. Despite these mismatches, each off-target site was able to be cleaved to various degrees by Cas9 and the *sacB* gRNA *in vitro*.

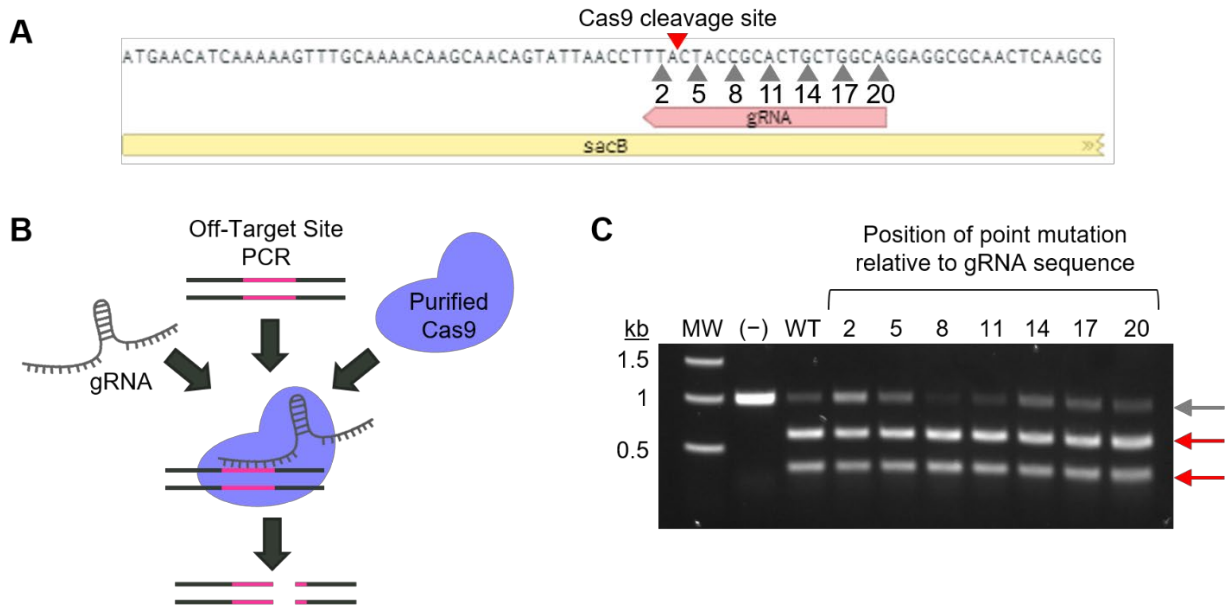


Figure 4. CRISPR cleavage of off-target site DNA *in vitro*. (A) Region of the *sacB* off-target site showing the 20-bp region of complementarity with the gRNA sequence, the location of the Cas9 cleavage site (red triangle), and the locations of the seven base pairs for creating synonymous point mutations in the DNA (gray triangles). (B) Diagram of the *in vitro* cleavage experiment. (C) Gel electrophoresis of resulting DNA fragments. Gray arrow indicates bands corresponding to uncut DNA, and red arrows indicate bands corresponding to DNA cleaved by CRISPR components. MW, molecular weight marker; (-), negative control; WT, wild-type.

We used CHANGE-seq to identify on- and off-target sites of the Cas9/*sacB* gRNA complex using purified genomic DNA from the engineered *E. coli* strain containing the on-target site. Initially, we attempted to express and purify the Tn5 transposon used for DNA fragmentation in house; however, this was unsuccessful (data not shown). We then obtained Tn5 commercially and performed further optimization steps from the published protocol¹⁶ to generate *E. coli* DNA fragments with an average size of approximately 400 bp (Figure 5A). Successful circularization of the DNA fragments was indicated by a shift in DNA mobility, consistent with circular DNA moving more slowly through a gel matrix than linear DNA (Figure 5B). *In vitro* cleavage of the circularized genomic fragments and DNA sequencing is in progress.

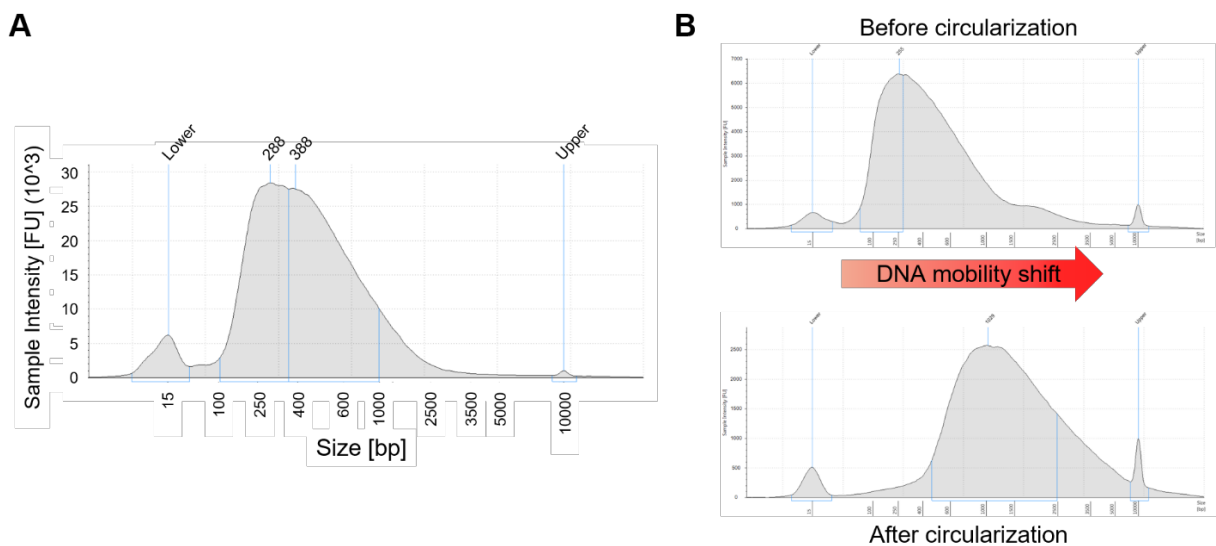


Figure 5. Automated electrophoresis of DNA during CHANGE-seq procedure. (A) DNA fragment size analysis following fragmentation of *E. coli* genomic DNA with custom Tn5-transposome. (B) DNA size analysis before (top) and after (bottom) circularization of DNA fragments.

4. CONCLUSIONS

This report describes progress toward determining the extent and identity of CRISPR off-target effects in bacteria. Using neutral *E. coli* genomic insertion points identified and experimentally validated in previous years of this effort, novel strains were constructed with on- and off-target sites to aid in the quantification of CRISPR editing rates. We demonstrated successful use of the engineered strains to determine CRISPR on-target editing efficiency; however, we were unsuccessful in assessing off-target editing rates using this approach, highlighting the difficulty of detecting CRISPR off-target effects *in vivo*. We also demonstrated that identification and screening of CRISPR off-target effects in bacteria can be accomplished *in vitro*, which may facilitate future work to study these sites *in vivo*. Knowledge of CRISPR off-target effects in bacteria will inform tools to identify signatures of genetic engineering in emerging threats.

ACKNOWLEDGMENTS

We thank Dr. Henry Gibbons from the U.S. Army Combat Capabilities Development Command Chemical Biological Center and Dr. Shengdar Tsai of St. Jude Children's Research Hospital for helpful discussions in support of this work. Funding was provided by the U.S. Army via the In-house Laboratory Independent Research Program (PE 0601101A Project 91A) at the Combat Capabilities Development Command Chemical Biological Center.

REFERENCES

- [1] Wang, H.; La Russa, M.; Qi, L.S.; CRISPR/Cas9 in Genome Editing and Beyond. *Annu. Rev. Biochem.* **2016**, *85*, pp 227–264.
- [2] Vento, J.M.; Crook, N.; Beisel, C.L.; Barriers to genome editing with CRISPR in bacteria. *J. Ind. Microbiol. Biotechnol.* **2019**, *46* (9–10), pp 1327–1341.
- [3] Jinek, M.; East, A.; Cheng, A.; Lin, S.; Ma, E.; Doudna, J. RNA-programmed genome editing in human cells. *eLife.* **2013**, *2*, e00471.
- [4] Cui, L.; Bikard, D. Consequences of Cas9 cleavage in the chromosome of Escherichia coli. *Nucleic Acid Res.* **2016**, *44* (9), pp 4243–4251.
- [5] Fu, Y.; Foden, J.A.; Khayter, C.; Maeder, M.L.; Reyon, D.; Joung, J.K.; Sander, J.D. High-frequency off-target mutagenesis induced by CRISPR-Cas nucleases in human cells. *Nat. Biotechnol.* **2013**, *31* (9), pp 822–826.
- [6] Hsu, P.D.; Scott, D.A.; Weinstein, J.A.; Ran, F.A.; Konermann, S.; Agarwala, V.; Li, Y.; Fine, E.J.; Wu, X.; Shalem, O.; Cradick, T.J.; Marraffini, L.A.; Bao, G.; Zhang, F. DNA targeting specificity of RNA-guided Cas9 nucleases. *Nat. Biotechnol.* **2013**, *31* (9), pp 827–832.
- [7] Cho, S.W.; Kim, S.; Kim, Y.; Kweon, J.; Kim, H.S.; Bae, S.; Kim, J.S. Analysis of off-target effects of CRISPR/Cas-derived RNA-guided endonucleases and nickases. *Genome Res.* **2014**, *24* (1), pp 132–141.
- [8] Pattanayak, V.; Lin, S.; Guilinger, J.P.; Ma, E.; Doudna, J.A.; Liu, D.R. High-throughput profiling of off-target DNA cleavage reveals RNA-programmed Cas9 nuclease specificity. *Nat. Biotechnol.* **2013**, *31* (9), pp 839–843.
- [9] Kim, D.; Bae, S.; Park, J.; Kim, E.; Kim, S.; Yu, H.R.; Hwang, J.; Kim, J.I.; Kim, J.S. Digenome-seq: genome-wide profiling of CRISPR-Cas9 off-target effects in human cells. *Nat. Methods.* **2015**, *12* (3), pp 237–243.
- [10] Veres, A.; Gosis, B.S.; Ding, Q.; Collins, R.; Ragavendran, A.; Brand, H.; Erdin, S.; Cowan, C.A.; Talkowski, M.E.; Musunuru, K. Low incidence of off-target mutations in individual CRISPR-Cas9 and TALEN targeted human stem cell clones detected by whole-genome sequencing. *Cell Stem Cell.* **2014**, *15* (1), pp 27–30.
- [11] Simmons, L.A.; Goranov, A.I.; Kobayashi, H.; Davies, B.W.; Yuan, D.S.; Grossman, A.D.; Walker, G.C. Comparison of responses to double-strand breaks between Escherichia coli and Bacillus subtilis reveals different requirements for SOS induction. *J. Bacteriol.* **2009**, *191* (4), pp 1152–1161.
- [12] Jiang, Y.; Chen, B.; Duan, C.; Sun, B.; Yang, J.; Yang, S. Multigene Editing in the Escherichia coli Genome via the CRISPR-Cas9 System. *Appl. Environ. Microbiol.* **2015**, *81* (7), pp 2506–2514.
- [13] Bernhards, C.B.; Liem, A.T.; Berk, K.L.; Roth, P.A.; Gibbons, H.S.; Lux, M.W. Putative Phenotypically Neutral Genomic Insertions Points in Prokaryotes. *ACS Synth. Biol.* **2022**, *11* (4), pp 1681–1685.
- [14] Park, Y.; Espah Borujeni, A.; Goroehowski, T.E.; Shin, J.; Voigt, C.A. Precision design of stable genetic circuits carried in highly-insulated *E. coli* genomic landing pads. *Mol. Syst. Biol.* **2020**, *16* (8), e9584.

- [15] Guo, J.; Wang, T.; Guan, C.; Liu, B.; Luo, C.; Xie, Z.; Zhang, C.; Xing, X.H. Improved sgRNA design in bacteria via genome-wide activity profiling. *Nucleic Acids Res.* **2018**, *46* (14), pp 7052–7069.
- [16] Lazzarotto, C.R.; Malinin, N.L.; Li, Y.; Zhang, R.; Yang, Y.; Lee, G.; Cowley, E.; He, Y.; Lan, X.; Jividen, K.; Katta, V.; Kolmakova, N.G.; Petersen, C.T.; Qi, Q.; Strelcov, E.; Maragh, S.; Krenčiute, G.; Ma, J.; Cheng, Y.; Tsai, S.Q. CHANGE-seq reveals genetic and epigenetic effects on CRISPR–Cas9 genome-wide activity. *Nat. Biotechnol.* **2020**, *38*, pp 1317–1327.

Guided Linking Application to Decide Threat Interaction Effect Radius: A high throughput analysis for characterizing toxin and target interactions

Vishaka Santosh^{a,b}, Gabrielle M. Rizzo^a, Conor C. Jenkins^a, Andrew J. Walz^a,
Brooke M. Ahern^{a*}

^aU.S. Army Combat Capabilities Development Command Chemical Biological Center, Research & Operations Directorate, 8198 Blackhawk Rd., Aberdeen Proving Ground, MD 21010

^bExcet Inc., 6225 Brandon Ave., Suite 360, Springfield, VA 22150

ABSTRACT

Neurotoxins, including α -conotoxins, represent a significant risk to the Warfighter but are technically challenging to characterize. This study proposes a novel analysis pipeline, called Guided Linking Application to Decide Threat Interaction Effect Radius, to facilitate automated patch-clamping and cross-linking mass spectrometry studies of the structural and functional changes that occurs in nicotinic acetylcholine receptors after exposure to α -conotoxin EI. Guided Linking Application to Decide Threat Interaction Effect Radius would streamline analysis of cross-linking mass spectrometry data, allowing for the identification of important binding sites and the discovery of basic mechanisms of neurotoxin:ion channel interactions. Interestingly, the interactions between α -conotoxin EI and nicotinic acetylcholine receptors did not recapitulate previously published findings, namely in that the same degree of inhibition on nicotinic acetylcholine receptor function was not seen compared to other works. This could be due to the source of the toxin, or due to potential inconsistencies in the expression of the nicotinic acetylcholine receptors on the cells. Future directions would include testing toxin synthesized from multiple sources and testing the toxin against cells that naturally express nicotinic acetylcholine receptors, such as isolated primary myocytes or stem cells driven into myocytes. The inconsistencies in this work compared to published articles further highlights the need for improved tools to study these toxins and their targets that is reproducible.

1. INTRODUCTION

Conotoxins are short, 10–30 amino acid residue-long neurotoxic peptides that can be isolated from the venom of cone snails;¹ these peptides affect numerous neurotransmitter receptors and ion channels, particularly those within the neuromuscular junction.²⁻⁷ In response to an action potential, voltage-gated calcium channels open to allow the flow of calcium into the nerve terminal. This promotes presynaptic vesicles to release their contents of acetylcholine (ACh) into the synaptic cleft to trigger action potential transmission to the muscle via nicotinic acetylcholine receptor (nAChR).^{8,9} Inhibition of nAChRs results in muscle paralysis and therefore potential death.^{8,9} Because of the inhibitory function of conotoxins, there are concerns within the biodefense community that conotoxins could be aerosolized and used as biological weapons.^{1,2} The heterogeneity in structure and the large spectrum of mechanisms/targets that these toxins affect creates barriers for making an effective antidote, leaving only respiratory support and intubation as treatment; however, this can still result in death within one to five hours.¹⁰

Conotoxins that selectively inhibit nAChRs are α -conotoxins.¹¹⁻¹⁴ α -conotoxins are the largest family of conotoxins, and are classified by their amino acid pattern of cysteines (CC-C-C) with a disulfide bond between Cys1-Cys3 and Cys2-Cys4.¹⁵ Within this family, there are further sub-classifications based on the number of residues in their inter-cysteine loops: α 3/5-conotoxins (3 residues in the first loop, and 5 in the second) that selectively target the muscle nAChR; α 4/7, α 4/4 and α 4/3 subfamilies generally target neuronal nAChRs.¹⁵ One unique α -conotoxin is α -conotoxin EI (α CTX-EI); it is a member of the α 3/5 subfamily which mainly blocks muscle nAChR, though it can inhibit some neuronal nAChRs as well.¹⁵ This is because α CTX-EI has high affinity for the α / δ and α / γ interfaces of the nAChR, contrary to most α 3/5 conotoxins that preferentially bind only to the α / γ interface.¹⁵ Because of the higher affinity for two interfaces of the receptor, α CTX-EI serves as an ideal candidate to use for understanding the complexity of the structural changes that occur between toxin/target, and how those changes yield physiological perturbations.

The techniques typically used to investigate the structure and function of ion channels are both monumental and extremely time-consuming. However, recent advancements in mass spectrometry and patch-clamping now make data collection and analysis more practical. The ideal method for investigating ion channel activity is the patch-clamp technique.¹⁶ For years, conventional manual patch-clamping has allowed for the study of alterations in ion channel activity in response to toxins in real time^{16,17}; however, manual patch-clamping requires highly trained individuals and large amounts of time that make high-throughput analysis difficult and extremely daunting.^{16,17} New improvements in technology have provided platforms for automated patch clamping, such as Sophion QPatch, which allows for a higher throughput and the ability to test a library of toxins, as well as various concentrations of said toxins, on a specific ion channel.^{16,17} The QPatch therefore provides an efficient primary method for assessing biophysical changes on ion channels in response to toxins. Cross-linking mass spectrometry (XL-MS) has also experienced a technological renaissance with the advent of ultra-high-resolution acquisition and novel chemical cross linker development. Deep inter- and intra-molecular interactions of numerous samples can be investigated rapidly at a targeted or global level within a week of preparation time; this vast amount of information found from a preliminary XL-MS can be used to guide the toxin/target analysis by supporting previously described molecular interactions and potentially identifying novel molecular interaction sites.^{18,19}

In this report, we present Guided Linking Application to Decide Threat Interaction Effect Radius, an analysis pipeline that combines recent advancements in patch-clamping and cross-linking mass spectrometry to characterize the structural and functional changes that can occur within the nAChR due to exposure to α -conotoxin EI; this emphasis will also serve as the foundation for expanding the understanding of other toxins that target nAChR, muscle or neuronal, as well as other ion channels. Our objective is to identify critical binding sites for α -conotoxin EI and nAChR to disrupt inhibition of the nAChR; we hypothesize that by preventing these specific interactions, normal nAChR function will be preserved. The combination of recently published data and our own data collection aim to provide a validated path towards high throughput investigation and analysis of nAChR, with the end goal of this method being applied to a library of other toxins and their specific ion channels targets. This outcome will lead to the discovery of basic mechanisms that could be exploited for future therapeutic development.

2. METHODOLOGY

2.1 Cell culture

Human embryonic kidney (HEK) cells expressing the nAChR $\alpha_1\beta_1\delta\epsilon$ (Eurofins) were cultured according to the protocol provided by Eurofins. Briefly, cells were grown in media containing Dulbecco's Modified Eagle Medium (DMEM), 10 % fetal bovine serum, 1 % non-essential amino acids, geneticin and hygromycin. Cells were incubated at 37 °C in a humidified atmosphere with 5 % CO₂.

2.2 Electrophysiology

Current was measured from the HEK cells using the Sophion qPatch (Sophion, Denmark). Cells were held in suspension in their media and placed in the machine. Through automation of the machine, cells were washed in extracellular solution (2 mM CaCl₂, 1 mM MgCl₂, 10 mM HEPES, 75 mM KCl, 75 mM NaCl), and plated onto the electrode plate. Once a gigaseal was reached, and the whole-cell mode of the patch clamp was reached, cells were exposed to Intracellular Solution (5.374 mM CaCl₂, 1.75 mM MgCl₂, 10 mM HEPES, 31.25 mM KOH, 10 mM EGTA, 120 mM KCl, 4 mM Na₂-ATP). The experiment was then initiated first by introducing 10 μ M acetylcholine (ACh, solution base was extracellular solution) to the cells and measuring the resulting current. Cells were then exposed to multiple concentrations of α -conotoxin EI (0.001–10 μ M; all mixed with 10 μ M ACh, based in extracellular solution), with resulting current measured for each concentration to produce a dose response curve. Current was measured at room temperature. Pipette resistance, cell capacitance, and series resistance were compensated by the machine before each sweep. Holding potential was set at -90 mV.

2.3 Sample preparation for mass spectrometry

Once the cells reached ~70 % confluency, they were harvested and resuspended in cross-linking buffer (20 mM HEPES, 150 mM NaCl, 1.5 mM MgCl₂, 0.5 mM DTT pH 7.8) at a density of 3.0x10⁶ cells/mL. After resuspension, 10 mM DSSO was added to the resuspended cells and allowed to incubate at room temperature for one

hour to induce protein-protein cross-linking. The cross-linking reaction was quenched with 20 mM Tris pH 8.0 and the cells were lysed via sonication for twenty minutes at 60 kHz and stored at -80 °C.

After thawing the cells, they were vortexed and then 100 μ L of each cell lysate was removed and mixed with 100 μ L concentrated lysis buffer (20 % sodium dodecyl sulfate, 100 mM triethylammonium bicarbonate pH 8.5). The lysate was then heated at 95 °C for 5 min at 500 rpm, then cooled to room temperature. After lysis, the cells were reduced by adding 20 mM dithiothreitol, then incubating at 95 °C for 10 min at 500 rpm. Then after cooling the lysate to room-temperature, the cells were alkylated by adding 0.1 M iodoacetamide and incubating in the dark at room temperature for 30 minutes with no shaking. Following alkylation, the cells were acidified with 1.5 % formic acid and mixed with six times their total reaction volume with S-Trap buffer (90 % methanol, 100 mM triethylammonium bicarbonate pH 8.5). Each lysed sample was loaded, 150 μ L at a time, into S-Trap Micro columns (Protifi). After each loading step, the columns were spun at 4,000 x g for 30 s, with flow-through discarded after each spin. The process was repeated until all the sample was loaded into its respective column. Each column was then washed four times by adding 150 μ L S-Trap buffer to the column and spinning at 4,000 x g for 30 s. After the final wash, 10 μ g Trypsin/Lys-C Mix in 20 μ L of 50 mM triethylammonium bicarbonate pH 8.5 was added to each column, wrapped in parafilm to prevent evaporation, and placed in a stationary incubator at 37 °C overnight to digest. Following digestion, samples were removed from the incubator and cooled to room temperature. Then, 40 μ L of 50 mM triethylammonium bicarbonate was added to each column and spun for 60 s at 4,000 x g. Prior to a final spin, 40 μ L of 0.2 % formic acid in water was then added to each column. Finally, 35 μ L of elution buffer (50 % acetonitrile, 0.2 % formic acid) was added to each column and spun a final time. The combine eluents were then dried in a speed-vac and peptide quantitation was performed by using a Pierce Quantitative Colorimetric Peptide Assay (ThermoFisher Scientific), according to the manufacturer's instructions. The peptides are then resuspended to a final concentration of 0.5 μ g/ μ L and transferred to liquid chromatography vials.

2.4 Spectral analysis for mass spectrometry

Samples were analyzed on the Orbitrap Eclipse Tribrid mass spectrometer (ThermoFisher Scientific) with FAIMS interface, paired with an Ultimate 3000 HPLC (ThermoFisher Scientific). Injections of 6 μ L of sample were loaded onto a PepMap 100, 75 μ m id \times 2 cm C18 trap column (ThermoFisher Scientific) at 3 μ L/min for 10 min with 2 % acetonitrile and 0.05 % formic acid followed by separation on an Easy-Spray 75 μ m id \times 75 cm length, 2 μ m, 100 Å C18 column (ThermoFisher Scientific) at 55 °C. Flow rate was kept at 0.3 μ L/min throughout the gradient. LC gradient was identical across all methods used: 5 % buffer B (80 % acetonitrile + 0.1 % formic acid in water) at 0–10 min; 10 % B for 10–150 min; 70 % B for 150–158 min; 80 % B for 158–161 min; 90 % B for 161–171 min; hold at 90 % B until 172 min; 5 % B for 172–182 min; hold at 5 % B until 200 min. Each sample was analyzed with two positive data-dependent acquisition methods: a stepped higher collisional energy HCD MS2 method and an MS2/MS3 method. Both methods utilized a topN, 2 s cycle time, with a dynamic exclusion of 60 s with 10 ppm error. FAIMS CVs for both methods were set to -50 V, -60 V, and -75 V, with the 2 s cycle time split between each CV.

The stepped higher collisional energy method used MS1 Orbitrap resolution of 60,000 with a mass range of 380–1400 m/z, with normalized automatic gain control target set to standard and RF lens set to 30 %. Monoisotopic peak determination was used, specifying peptides and intensity threshold of 2×10^4 for precursor selection. Data-dependent MS2 fragmentation was performed using higher-energy collisional dissociation at collision energies of 25 % and 30 % with quadrupole isolation at 1.6 m/z width.

The MS2/MS3 method used MS1 Orbitrap resolution of 60,000 with a mass range of 375–1600 m/z, with normalized AGC target set to standard and RF lens set to 30 %. Monoisotopic peak determination was used, specifying peptides and intensity threshold of 1×10^4 for precursor selection. Data-dependent MS2 fragmentation was performed using collision-induced dissociation (CID) at a collision energy of 25 % with quadrupole isolation at 1.6 m/z width. Targeted mass difference properties were selected to further downselect ions for MS3 analysis: mass list included one compound, DSSO, with Delta M1 of 31.9721, with two precursors in the targeted group. Partner intensity range relative to the most intense precursor was set to 10–100 %, with subsequent scans performed on the most intense ion in the pair. MS3 fragmentation was performed using CID at a collision energy of 35 % and CID activation time of 10 ms and activation Q of 0.25, and with MS isolation window of 2.15 m/z and MS2 isolation window of 2 m/z.

2.5 Data analysis

For electrophysiology data, raw data was downloaded from the qPatch and analyzed using Prism 9.4.1 (GraphPad, San Diego, CA). Raw current from each cell was normalized to its respective 10 μ M ACh induced current.

Crosslinking mass spectrometry data analysis was performed in Thermo Proteome Discoverer²⁰ version 2.5.0.400. Spectra were searched utilizing Sequest HT²¹ with Trypsin digest allowing for 2 missed cleavages at a 10 ppm MS1 tolerance and 0.02 Da MS2 tolerance for the sce-MS2 method and 10ppm MS1 tolerance with 0.6 Da MS2 tolerance for the MS2/MS3 method. Dynamic modifications include oxidation on methionine, disuccinimidyl sulfoxide (hydrolyzed) on lysine and disuccinimidyl sulfoxide (Tris) on lysine. A static modification of carbamidomethylation on cysteine was also included. A spectrum confidence filter post identification was applied to send the crosslinked spectra to the XlinkX²² node operating under sce-MS2 or MS2/MS3 searches depended on acquisition method utilized. The XlinkX search was performed with trypsin digestion allowing for two missed cleavages, a 10 ppm MS1 tolerance, a 40 ppm MS2 tolerance for orbitrap detection and 0.8 Da for ion trap detection. An FDR threshold of 0.01 was used as the confidence filter for the identifications.

3. RESULTS

α -conotoxin EI targets the muscle subtype of the nAChR, with an IC_{50} of 187 nM.²³ In order to functionally validate our cells and the α -conotoxin EI, we measured current from nAChR induced by ACh through whole cell patch clamping (Figure 1). Figure 1A displays current from a representative cell. When exposed only to ACh, nAChRs display large inward current, serving as a control and normalization for comparison to exposure to toxin (Figure 1A, black line). When cells were exposed to multiple concentrations of α -conotoxin EI (Figure 1A, colored lines), a decrease in inward current represents inhibition of nAChR activity. However, note that inward current is not completely inhibited in any of the concentrations. This is further displayed in the dose response curve (Figure 1B), showing ~40% inhibition across all concentrations of α -conotoxin EI. This is inconsistent with published literature since our higher concentrations of 1 μ M and 10 μ M should have inhibited nAChR activity by at least 50%.²³

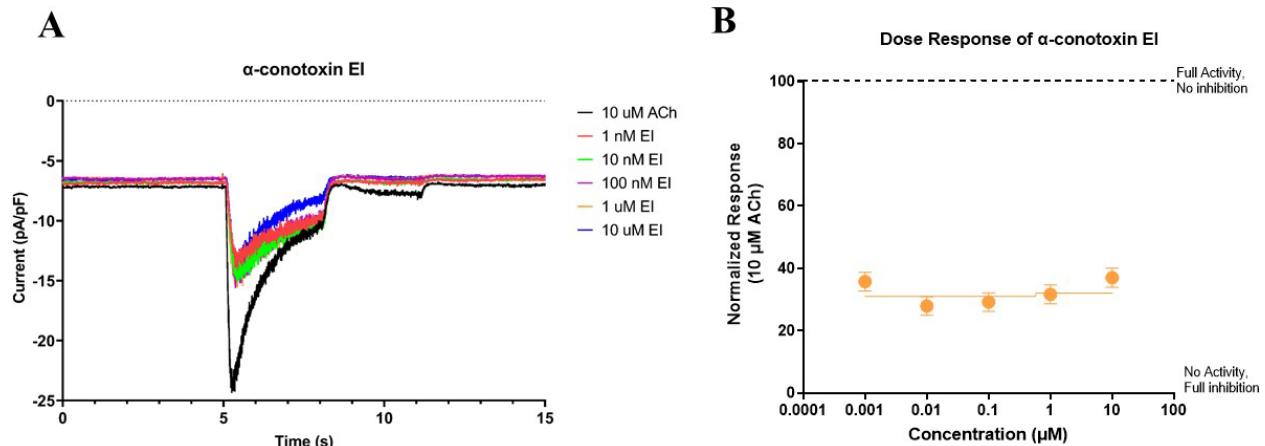


Figure 1. α -conotoxin EI does not completely inhibit acetylcholine-induced current. A) Representative current measured after exposure to 10 μ M acetylcholine (black line) and α -conotoxin EI (concentrations in specified colors). B) Dose response curve of exposure to α -conotoxin EI, normalized to 10 μ M acetylcholine. N=12 cells. Data in B fit with [inhibitor] vs. response, variable slope (four parameters) analysis in Prism.

Because of this inconsistency, we processed cells for cross-linking mass spectrometry to validate that the cells were expressing the correct nAChR, specifically the $\alpha_1\beta_1\delta\epsilon$ nAChR (Eurofins). Eleven technical replicates were compared to determine the consistency of expression of the different subunits of the nAChR in this cell line (Figure 2). Figure 2A demonstrates that three proteins critical for basic cell function, and common to many cell lines, were present in all eleven samples. Figure 2B illustrates the different types of α subunits that were detected in the cells; all eleven samples contained α_1 , the α subunit that designates the receptor as a muscle subtype. The other α subunits found (α_2 , α_4 , and α_9) are neuronal subtypes of the nAChR. Figure 2C displays that a majority of the samples contained the δ subunit and the γ subunit; however, the β_1 and ϵ subunits were not detected.

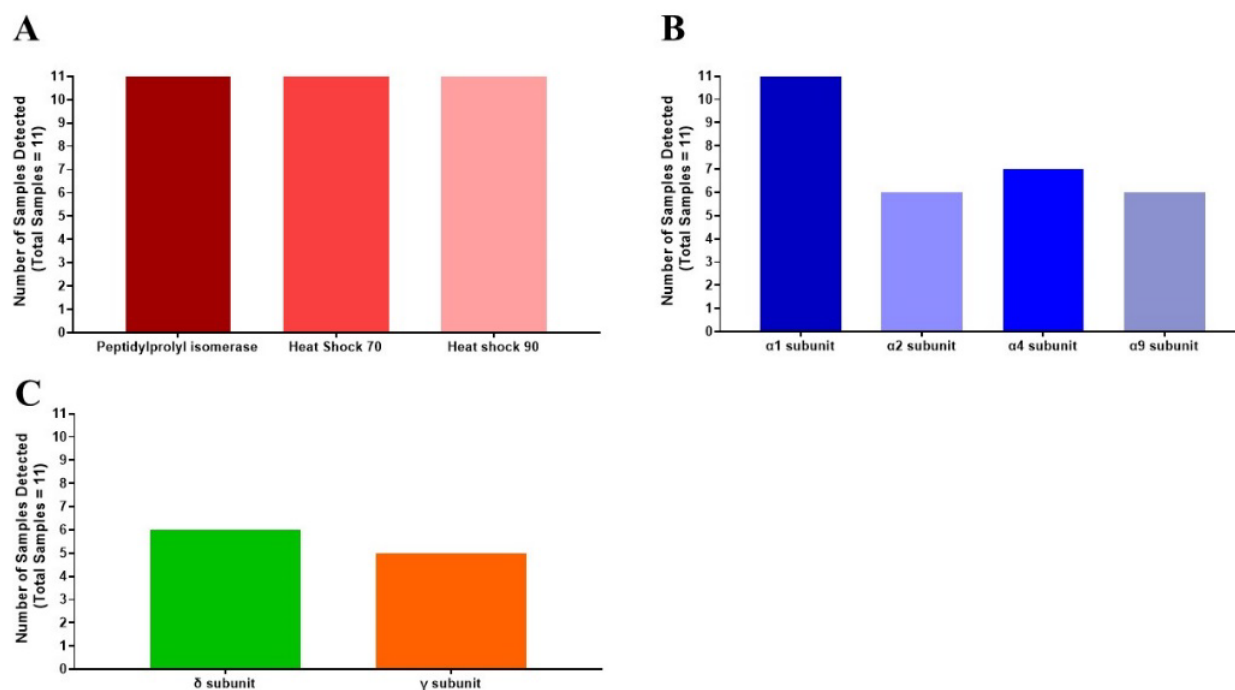


Figure 2. nAChRs cell line expresses multiple α subunits, and not all auxiliary subunits. A) Proteins expressed in cell line that are needed for basic cell function. B) α subunits identified in samples. C) Auxiliary subunits identified in samples. N= 11 samples.

4. CONCLUSIONS

The objective of this work was to establish a high throughput analysis pipeline to identify critical binding sites between α -conotoxin EI and the muscle subtype of the nAChR. The results of developing this pipeline uncovered two major discrepancies that require further validation and investigation for this work to move forward: 1) current measured from the nAChR overexpression cell line used was not completely inhibited and 2) the subunits expressed in the cell line do not align with expected expression. These two major points raise important questions which will be further discussed below.

α -conotoxin EI has been thoroughly investigated due to its unique nature of blocking muscle subtype nAChRs, though its structure would dictate that it favored neuronal subtypes.^{15,24} Studies have shown that concentrations of 10 μ M of α -conotoxin EI yielded almost complete inhibition of nAChR current.^{23,24} However, in our hands, our cells yielded about ~40 % inhibition (Figure 1). It is possible that the difference we see in our cells versus the published work could stem from the use of nicotine as the ligand rather than acetylcholine.²³ Nicotine and α -conotoxin EI could compete for the same binding sites while acetylcholine has an alternative binding mode, thereby producing a more significant inhibition of nAChR compared to our results. Furthermore, in previous studies, mouse nAChR was used to investigate the effects of α -conotoxin EI²⁴, so it is possible that the sequences of mouse nAChR and human nAChR differ enough that potency of α -conotoxin EI is less in human compared to mouse. Further investigations will utilize nicotine and acetylcholine as ligands, as well as utilize higher doses of α -conotoxin EI.

The structure of nAChR contains five transmembrane subunits: α (1-10), β (1-4), δ , γ , and ϵ .²⁵ While most are expressed in neurons, the muscle subtype is composed of α_1 , β_1 , δ , and γ (fetal), or ϵ (adult).²⁵ α -conotoxin EI interacts with both the α/δ interface and the α/γ interface.¹⁵ Initially, we concluded that the lack of inhibition in the electrophysiology data stemmed from the fact that the cell line expressed the ϵ subunit rather than the γ subunit, so full inhibition would not be seen. However, results from mass spectrometry displayed variability in what the cells were expressing (Figure 2), and presented a few confounding findings. One, a significant amount of samples were expressing not only α_1 , but were also expressing some neuronal subtypes (α_2 , α_4 , and α_9). While α -conotoxin EI mainly

inhibits muscle nAChRs, it can also inhibit certain neuronal subtypes.^{15,23} Second, neither β_1 nor ϵ were detected in any of the samples. Third, some samples expressed δ , but not all. Lastly, the γ subunit was also detected in some of the samples. The variability in subunits that are found in these cells leads to multiple questions: is the lack of complete inhibition of current by α -conotoxin EI due to variability in nAChR being muscle or neuronal subtype, not just the muscle subtype? Is there only partial inhibition due to certain samples not containing the δ subunit, which is critical for α -conotoxin EI binding? Do we see some inhibition solely because some samples expressed the γ subunit? Future directions of this project will aim to address these questions by purifying the nAChR expressed in the cells and analyzing these samples through mass spectrometry. These results will also be discussed with the vendor to verify that cells are correct and are being cared for properly.

In conclusion, the analysis pipeline we have attempted to establish has uncovered more questions than answers. However, the data presented in this report exemplifies the need for such a pipeline. Discrepancies in published literature versus experimental data highlight potential differences in mechanism of toxin in different tissue subtypes, different species, and different expression systems. All of these need to be understood in order to build the best, most informed and up-to-date library of toxin/target, which is the main goal of this project. Future work will aim to address these discrepancies, and better understand the structure and function of nAChR so that this knowledge can be applied to other toxins, their respective targets, and potential therapeutics.

ACKNOWLEDGMENTS

We, the authors, would like to thank Dr. Morgan Minyard, Branch Chief of Molecular Toxicology and Dr. Kelly Nobels, Branch Chief of Biodefense, for general supervision of research, as well as the administrative staff of both branches for general management and proper distribution of funds between branches. We would also like to thank Dr. Patricia McDaniel for indirect technical assistance via intellectual discussion, as well as guidance in management of the project. We also wish to extend our gratitude to Dr. McDaniel's staff (Jessica Parker, Rebecca Braun, Laurie VanDyke, and Dr. Patrick Gellings) for their assistance in program management.

Funding for this project was provided by the U.S Army via the In-house Laboratory Independent Research Program (PE 0601101A Project 91A) at the Combat Capabilities Development Command Chemical Biological Center.

REFERENCES

- [1] Anderson P.D.; Bokor, G. Conotoxins: Potential Weapons from the Sea. *J. Bioterrorism Biodef.* **2012**, *3* (3), pp 1–4.
- [2] Anderson, P.D. Bioterrorism: toxins as weapons. *J. Pharm. Practice.* **2012**, *25* (2), pp 121–129.
- [3] Bjørn-Yoshimoto, W.E.; Ramiro, I.B.R.; Yandell, M.; McIntosh, J.M.; Olivera, B.M.; Ellgaard, L.; Safavi-Hemami, H. Curses or Cures: A Review of the Numerous Benefits Versus the Biosecurity Concerns of Conotoxin Research. *Biomedicines.* **2020**, *8* (8), pp 235.
- [4] Abraham, N.; Healy, M.; Ragnarsson, L.; Brust, A.; Alewood, P.F.; Lewis, R.J. Structural mechanisms for α -conotoxin activity at the human $\alpha_3\beta_4$ nicotinic acetylcholine receptor. *Sci. Rep.* **2017**, *7* (1), pp 1–12.
- [5] Sameera; Shah, F.A.; Rashid, S. Conformational ensembles of non-peptide ω -conotoxin mimetics and Ca^{+2} ion binding to human voltage-gated N-type calcium channel $\text{Ca}_v2.2$. *Comput. Struct. Biotechnol. J.* **2020**, *18*, pp 2357–2372.
- [6] Ning, J.; Ren, J.; Xiong, Y.; Wu, Y.; Zhangsun, M.; Zhangsun, D.; Zhu, X.; Luo, S. 2019. Identification of Crucial Residues in α -Conotoxin EI Inhibiting Muscle Nicotinic Acetylcholine Receptor. *Toxins.* **2019**, *11* (10), pp 603.
- [7] Chen, R.; Chung, S.H. Complex Structures Between the N-Type Calcium Channel ($\text{Ca}_v2.2$) and ω -Conotoxin GVIA Predicted via Molecular Dynamics. *Biochemistry.* **2013**, *52* (21), pp 3765–3772.
- [8] Hirsch, N.P. Neuromuscular junction in health and disease. *Br. J. Anaesth.* **2007**, *99* (1), pp 132–138.
- [9] Cruz, P.M.R.; Cossins, J.; Beeson, D.; Vincent, A. The Neuromuscular Junction in Health and Disease: Molecular Mechanisms Governing Synaptic Formation and Homeostasis. *Front. Mol. Neurosci.* **2020**, *13*, pp 610964.
- [10] Fernandez, I.; Valladolid, G.; Varon, J.; Sternbach, G. Encounters with venomous sea-life. *J. Emerg. Med.* **2011**, *40* (1), pp 103–112.
- [11] Cruz, L.J.; Gray, W.R.; Olivera, B.M. Purification and properties of a myotoxin from *Conus geographus* venom. *Arch. Biochem. Biophys.* **1978**, *190* (2), pp 539–548.

- [12] Olivera, B.M.; McIntosh, J.M.; Cruz, L.J.; Luque, F.A.; Gray, W.R. Purification and sequence of a presynaptic peptide toxin from *Conus geographus* venom. *Biochemistry*. **1984**, *23* (22), pp 5087–5090.
- [13] Cruz, L.J.; Gray, W.R.; Olivera, B.M.; Zeikus, R.D.; Kerr, L.; Yoshikami, D.; Moczydlowski, E. *Conus geographus* toxins that discriminate between neuronal and muscle sodium channels. *J. Biol. Chem.* **1985**, *260* (160), pp 9280–9288.
- [14] Shon, K.-J.; Grilley, M.M.; Marsh, M.; Yoshikami, D.; Hall, A.R.; Kurz, B.; Gray, W.R.; Imperial, J.S.; Hillyard, D.R.; Olivera, B.M. Purification, Characterization, Synthesis, and Cloning of the Lockjaw Peptide from *Conus Purpurascens* Venom. *Biochemistry*. **1995**, *34* (15), pp 4913–4918.
- [15] Azam, L.; McIntosh, J.M. Alpha-conotoxins as pharmacological probes of nicotinic acetylcholine receptors. *Acta Pharmacol. Sin.* **2009**, *30* (6), pp 771–783.
- [16] Gao, J.; Zhang, H.; Xiong, P.; Yan, X.; Liao, C.; Jiang, G. Application of electrophysiological technique in toxicological study: From manual to automated patch-clamp recording. *TrAC, Trends Anal. Chem.* **2020**, *133*, pp 116082.
- [17] Yajuan, X.; Xin, L.; Zhiyuan, L. A comparison of the performance and application differences between manual and automated patch-clamp techniques. *Curr. Chem. Genomics*. **2012**, *6*, pp 87–92.
- [18] Matzinger, M.; Mechtler, K. Cleavable Cross-Linkers and Mass Spectrometry for the Ultimate Task of Profiling Protein-Protein Interaction Networks in Vivo. *J. Proteome Res.* **2021**, *20* (1), pp 78–93.
- [19] Orbán-Németh, Z.; Beveridge, R.; Hollenstein, D.M.; Rampler, E.; Stranzl, T.; Hudecz, O.; Doblmann, J.; Schlögelhofer, P.; Mechtler, K. Structural prediction of protein models using distance restraints derived from cross-linking mass spectrometry data. *Nat. Protoc.* **2018**, *13*, pp 478–494.
- [20] Orsburn, B.C. Proteome Discoverer—A Community Enhanced Data Processing Suite for Protein Informatics. *Proteomes*. **2021**, *9* (1), p 15.
- [21] Yates III, J.R.; Eng, J.K.; Clauser, K.R.; Burlingame, A.L. Search of sequence databases with uninterpreted high-energy collision-induced dissociation spectra of peptides. *J. Am. Soc. Mass Spectrom.* **1996**, *7* (11), pp 1089–1098.
- [22] Klykov, O.; Steigenberger, B.; Pektaş, S.; Fasci, D.; Heck, A.J.R.; Scheltema, R.A. Efficient and robust proteome-wide approaches for cross-linking mass spectrometry. *Nature Protoc.* **2018**, *13* (12), pp 2964–2990.
- [23] López-Vera, E.; Aguilar, M.B.; Schiavon, E.; Marinzi, C.; Ortiz, E.; Restano Cassulini, R.; Batista, C.V.F.; Possani, L.D.; Heimer de la Cotera, E.P.; Peri, F.; Becerril, B.; Wanke, E. Novel α -conotoxins from *Conus spurius* and the α -conotoxin EI share high-affinity potentiation and low-affinity inhibition of nicotinic acetylcholine receptors. *FEBS J.* **2007**, *274* (15), pp 3972–3985.
- [24] Ning, J.; Ren, J.; Xiong, Y.; Wu, Y.; Zhangsun, M.; Zhangsun, D.; Zhu, X.; Luo, S. Identification of Crucial Residues in α -Conotoxin EI Inhibiting Muscle Nicotinic Acetylcholine Receptor. *Toxins*. **2019**, *11* (10), p 603.
- [25] Ho, T.N.; Abraham, N.; Lewis, R.J. Structure-Function of Neuronal Nicotinic Acetylcholine Receptor Inhibitors Derived from Natural Toxins. *Front. Neurosci.* **2020**, *14*, p 609005.

This page intentionally left blank

CBAMMS **PROJECTS**





Toward understanding the generation and lifetime of singlet oxygen species in photosensitized rigid crystalline structures

Ann M. Kulisiewicz^a, Sergio J. Garibay^b, Gabrielle Pozza^c, Matthew Browe^a, Ivan Iordanov^a,
Owen Sparr^c, Sukh Singh^c, Lisa A. Kelly^c, Jared B. DeCoste^{a*}

^aU.S. Army Combat Capabilities Development Command Chemical Biological Center, Research & Operations Directorate, 8198 Blackhawk Rd, Aberdeen Proving Ground, MD 21010

^bLeidos, Inc., P.O. Box 68, Edgewood Chemical Biological Center, Aberdeen Proving Ground, MD 21010

^cDepartment of Chemistry and Biochemistry, University of Maryland Baltimore County, Baltimore, MD 21250

ABSTRACT

Metal-organic frameworks are highly versatile materials that have shown great promise in chemical warfare agent adsorption and decontamination. Sulfur mustard is one of the most prominently used chemical warfare agents over the last century; therefore, the development of effective detoxification strategies is of utmost importance. However, typical routes of detoxification are slow and may result in the production of harmful by-products. A zirconium-based metal-organic framework, NU-1000, has previously shown promise as a “soft” oxidizer that can readily detoxify sulfur mustard and its simulant 2-chloroethyl ethyl sulfide through the generation of singlet oxygen in the presence of either UV (396 nm) or blue (465 nm) light. Several variants of NU-1000 were synthesized (MOF-R, R = -Cl, -NO₂, -CH₃) with functional groups positioned either ortho or meta to the carboxylic acid on the linker. NU-1000-*o*-Cl and NU-1000-*m*-Cl showed significant enhancement of photooxidation of 2-chloroethyl ethyl sulfide due to spin-orbit coupling enhancing the intersystem crossing into the MOF triplet state. Furthermore, substitution of metal-organic framework linkers led to pyrene-phenyl rotation. Linkers with substituents in the ortho position were shown to have smaller pyrene-phenyl torsion angles leading to enhanced conjugation between the rings and a subsequent red shift in the absorption spectra. This red shift leads to enhanced reactivity of NU-1000-*o*-Cl under blue light conditions and gives perspective on making materials with enhanced reactivity utilizing visible light.

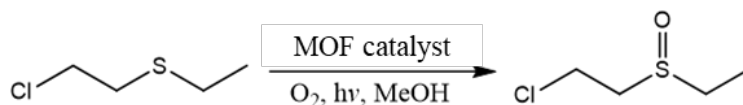
Keywords: metal-organic framework, photocatalysis, singlet oxygen, sulfur mustard, 2-chloroethyl ethyl sulfide

1. INTRODUCTION

Sulfur mustard has been the most predominantly used chemical warfare agents (CWAs) in modern warfare since its initial use during World War I.¹ Detoxification of sulfur mustard still poses a challenge as the three major routes (hydrolysis, dehydrohalogenation, and oxidation) each pose issues.² Hydrolysis and dehydrohalogenation pathways are both very slow, especially due to the insolubility of sulfur mustard in water. Conversely, traditional oxidation pathways are overly harsh and tend to produce a mixture of both the sulfoxide and sulfone products, the latter of which has a toxicity analogous to that of sulfur mustard. Soft oxidation pathways, such as those seen from singlet oxygen, are much more desirable as singlet oxygen can be generated quickly, catalytically, and does not produce the hazardous sulfone byproduct.

Metal-organic frameworks (MOFs) are highly porous crystalline structures that offer a wide array of physical adsorption and chemical reactivity capabilities. While some structures have been shown to stoichiometrically react with sulfur mustard simulants or catalytically react with nerve agents, there is a great need to design a MOF that can photocatalytically generate singlet oxygen efficiently with ambient light.³⁻⁹ Photocatalytic oxidation is a newly emerging application for MOFs in recent years that offers an opportunity for a “soft” oxidation pathway that can selectively oxidize sulfur mustard, and its simulant 2-chloroethyl ethyl sulfide (2-CEES), to the sulfoxide without the formation of the toxic sulfone byproduct (Scheme 1).¹⁰

MOFs have three components that can be tuned for photocatalysis—the metal nodes, the organic linkers, and molecules encapsulated in the crystalline structure. The metal nodes can either be directly excited by light or by the excitement of adjacent linker molecules that can then transfer that energy to the metal node in an antenna-like fashion.^{11,12} The linkers can be readily tuned by developing molecules that have adsorption profiles for specific wavelengths of interest (i.e. solar light, red light).^{13,14} Chromophores that can modulate the wavelength of excitement or enhance singlet oxygen generation can also be incorporated into the MOF structure through post-synthetic modification (PSM) of the linker or metal node.⁸



Scheme 1. Photocatalytic reaction of a sulfur mustard simulant, 2-CEES, with MOF catalyst to form nontoxic sulfoxide product.

Zirconium-based MOFs have been of particular interest for CWA degradation as they are highly stable to ambient conditions.¹⁹⁻²¹ Several zirconium-based MOFs have shown promise in recent years as photocatalysts for the degradation of sulfur mustard and its simulant 2-CEES.²²⁻²⁴ NU-1000 has been of particular interest as a photocatalyst due to its highly conjugated pyrene linker (1,3,6,8-tetrakis-(*p*-benzoic acid)pyrene [H₄TBAPy]) as well as its undercoordinated secondary building units (SBUs) that can accommodate the incorporation of additional photosensitizers to further modulate the photocatalytic activity of the MOF.²⁵ The pyrene linker of the MOF can be excited by UV (396 nm) or blue (495 nm) light to an excited singlet state that can then undergo intersystem crossing to an excited triplet state. This triplet state can interact with the ground-state triplet oxygen species to generate the reactive singlet oxygen species (Figure 1). As this generation pathway has been studied extensively for NU-1000 and PCN-222, which contain pyrene and porphyrin linkers, respectively, little work has been done to explore the effect that functionalizing these linkers can have on the generation of reactive oxygen species.

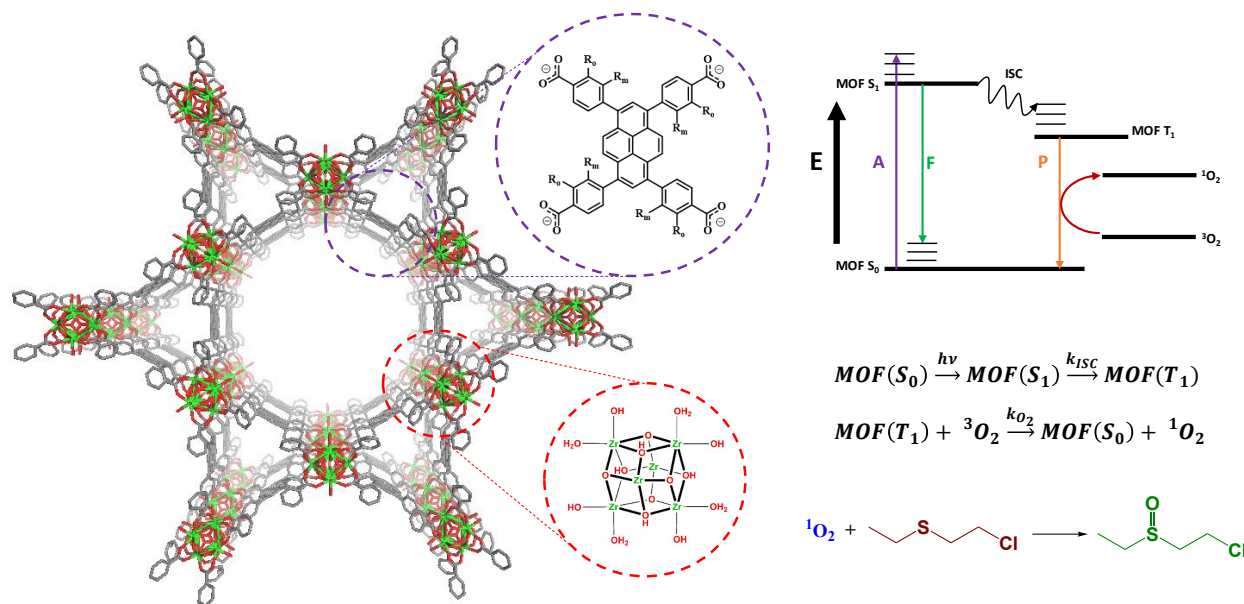


Figure 1. Photocatalytic formation of singlet oxygen from an excited state MOF ($R_0, R_m = -\text{H}, -\text{CH}_3, -\text{Cl}, -\text{NO}_2$).

The highly conjugated pyrene linker of NU-1000 is the key component in the generation of reactive oxygen species. While direct functionalization of the fused pyrene ring is troublesome, we show here that functionalization on the neighboring benzene ring can have substantial effects on the ability of the linker to absorb both UV and visible light. We compare previously reported NU-1000 with these novel NU-1000 derivatives. These newly reported MOFs constitute ways to functionalize a MOF to absorb lower energy light, and to more efficiently generate reactive oxygen species, which is used here to degrade the chemical warfare agent simulant 2-CEES. While solution studies on

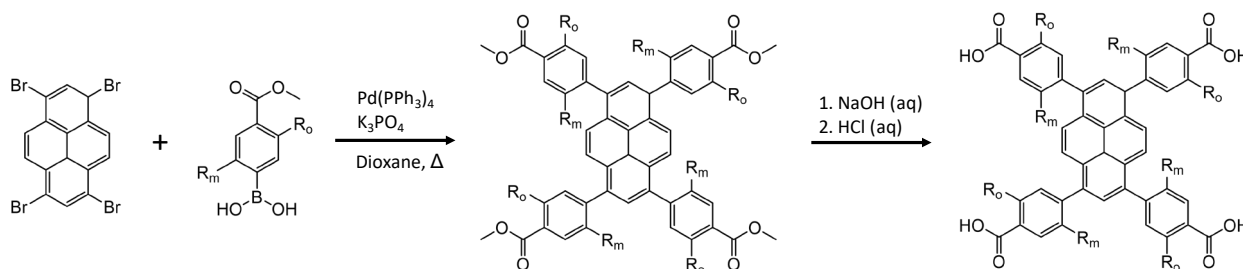
tetraphenylporphyrin-based photosensitizers have shown that heavy halogen groups substituted on phenyl rings neighboring a porphyrin by facilitating the intersystem crossing necessary to reach the spin-forbidden excited state, this phenomenon has yet to be realized in the solid state as we show here.²⁶

2. EXPERIMENTAL METHODS

2.1 Synthesis

2.1.1 Linker synthesis

All reagents were purchased from commercial sources and used without further purification. H₄TBAPy and functionalized (-CH₃, -NO₂, -Cl) derivatives were synthesized following published procedures as shown in Scheme 2.²⁸ To a 250 mL Schlenk flask reactor, 1,4-dioxane (150 mL) was added and purged with N₂ for 1.5 h using a syringe needle. While still purging, tetrabromopyrene (0.5 g, 0.96 mmol), 4-ethoxycarbonyl-3-chlorophenylboronic acid (0.97 g, 4.25 mmol), tripotassium phosphate (1.65 g, 7.77 mmol), and Pd(PPh₃)₄ (0.08 g, 0.07 mmol) were added into the reactor. The system was sealed and purged N₂ before heating to 90 °C for 72 h. The reaction was quenched with 100 mL of water and filtered. The resulting solid was washed with 100 mL water twice and with 200 mL of methanol. The crude product on the filter was purified by recrystallization. The crude product was dissolved in hot chloroform (300 mL) on the frit. The volume of the solution was reduced to 25 mL by evaporating the chloroform and the product was precipitated with 300 mL of methanol. The solid product was collected via filtration and dried in vacuum oven at 70 °C for 12 h (0.59 g, 69% yield). The ester precursors were hydrolyzed with KOH in a 1,4-dioxane aqueous solution and precipitated with concentrated HCl.



Scheme 2. Synthesis of H₄TBAPy derivatives (R₀, R_m = -H, -CH₃, -Cl, -NO₂).

2.1.2 Synthesis of functionalized Zr-H₄TBAPy MOFs.

ZrOCl₂•8H₂O (98 mg, 0.3 mmol) and benzoic acid (2 g, 16.4 mmol) were mixed in 8 mL of DMF in an 8-dram vial and ultrasonically dissolved. The clear solution was incubated in an oven at 100 °C for 1 h. After cooling down to room temperature, H₄-TBAPy (40 mg, 0.06 mmol) and trifluoroacetic acid (50 μL, 0.65 mmol) were added and ultrasonically mixed. The solution was incubated in an oven at 100 °C for 18 h. The MOF was isolated by centrifuge (5 min, 7500 rpm) and solvent exchanged with fresh DMF three times (10 mL each) followed by methanol or acetone three times (10 mL). The material was dried in a vacuum oven at 80 °C for 1 h, and then activated at 120 °C for 18 h.

2.2 Characterization

2.2.1 Powder X-ray diffraction

Powder x-ray diffraction (PXRD) patterns were measured on a Rigaku MiniFlex 600 diffractometer equipped with a D/teX Ultra detector with Cu-K_α radiation ($\lambda = 1.5418 \text{ \AA}$) over a range of $2\theta = 3\text{--}50^\circ$ at a scan rate of 5 deg min^{-1} .

2.2.2 ATR-FTIR

Attenuated total reflectance-Fourier-transform infrared (ATR-FTIR) spectra were measured on a Bruker Tensor 27 spectrometer from $4000\text{--}400 \text{ cm}^{-1}$ at a resolution of 2 cm^{-1} .

2.2.3 *N₂ physisorption*

N₂ isotherms were measured using a Micromeritics ASAP 2420 analyzer at 77 kelvin (K). Samples were off-gassed at 120 °C under vacuum for ~16 h. The Brunauer-Emmett-Teller (BET) method was used to calculate specific surface area in m² g⁻¹.

2.2.4 *UV-vis spectroscopy*

Solid state UV-vis measurements of MOF samples from 200–800 nm were collected on a JASCO V-650 UV-vis spectrophotometer equipped with a 150 mm integrating sphere.

2.3 Photocatalysis experiments

For CEES oxidation experiments, 2.2 mg of the MOF was dispersed in 1 mL anhydrous methanol and sealed in a 17 x 83 mm glass microwave vial. After purging with O₂ for 20 min, 23 μL (0.2 mmol) 2-CEES and 5 μL (0.04 mmol) internal standard (1-bromo-3,5-difluorobenzene) were added to the microwave vial with a 25 μL glass syringe. The vial was then exposed to either UV (396 nm) or blue (465 nm) LED irradiation using an LED setup constructed from solderless LEDs purchased from RapidLED that were then mounted onto a U-shaped aluminum sheet. Aliquots of 25 μL from the reaction vial were withdrawn using a syringe at 5 min intervals, filtered, and diluted with 1 mL of methanol into a GC vial. The samples were then subjected to GC-FID to monitor the reaction progress.

2.4 Excitation/emission spectral measurements

MOF suspensions were prepared in a standard 1 cm x 1 cm quartz cuvette using a ratio of 0.5 mg of MOF to 3.5 mL of solvent. Excitation spectra were initially acquired for MOFs of interest in methanol or acetonitrile using the excitation scan function on the fluorimeter. Various single emission wavelengths, ranging from 440–520 nm, were selected corresponding to the emission spectral maxima of the MOF. The spectra were found to be noisy due to scattering from the MOF. The quality of the excitation spectra was improved for NU-1000 MOF suspended in methanol without using the scan function. In this mode, excitation spectra were calculated by acquiring emission spectrum of the MOF suspensions at different excitation wavelengths (2 nm increments). The process was then automated by acquiring 3D emission scans from the Cary Eclipse fluorimeter. In triplicate, emission spectra were measured using excitation wavelengths between 290–690 nm, in 10 nm steps. The excitation spectra were corrected for the wavelength dependency of the excitation source. The area under the emission spectrum was obtained by integration of the spectra from 300–700 nm. The use of a 385-nm filter, placed between the sample and emission monochromator, was used to remove the 2nd order peak ($= 2 \times \lambda_{exc}$), which altered the integrated area. This integration was initially computed manually, and then automated using a Python program. The program fit each emission spectrum to a single or double Gaussian function in the range of 300–700 nm, allowing the exclusion of the 2nd order artifacts. Excitation spectra were obtained by plotting the calculated area under each emission spectrum as a function of excitation wavelength. The computational approach was validated by comparing the spectra with those generated manually. They were, within error, found to be identical.

2.5 Computational band gap measurements

The Highest Occupied Molecular Orbital-Lowest Unoccupied Molecular Orbit (HOMO-LUMO) gap calculations for H₄TBAPy and Tris(chloropropyl) phosphate derivatives were performed using the Gaussian 16 electronic structure package.⁹ Calculations were performed at the B3LYP/3-21G level of theory using default optimization criteria. Initial molecular specifications were constructed by building the molecules in the Avogadro molecular editor and performing a preliminary single-point energy minimization procedure using the Universal force field and steepest descent algorithm. The value for the HOMO-LUMO gap was calculated by simply subtracting the reported HOMO and LUMO energies.

3. RESULTS

3.1 Synthesis of functionalized Zr-H₄TBAPy MOFs

Functionalized H₄TBAPy linkers were synthesized using a palladium cross-coupling reaction between 1,3,6,8-tetrabromopyrene and the functionalized 4-methylcarbonylphenylboronic acid derivative, followed by a

deprotection of the resulting ester (Scheme 2).²⁸ NU-1000-R derivatives were synthesized using the resulting functionalized H₄TBAPy linkers. Under similar reaction conditions, the majority of functionalized H₄TBAPy linkers generated MOFs with csq topology that were analogous to NU-1000. However, H₄TBAPy-*o*-NO₂ generated a MOF of the scu topology characteristically, like NU-901, and H₄TBAPy-*m*-NO₂ generated a MOF of the ftw topology, like PCN-224. Each MOF structure was confirmed through PXRD and BET analysis.

3.2 Fluorescence excitation/emission spectra of MOF suspensions and soluble linkers

Photocatalytic efficiency is a direct function of the efficiency of light absorption by the MOF. Given the heterogeneity of the samples, conventional transmittance absorption spectra were not obtainable. However, acquisition of the fluorescence excitation spectrum is an equivalent way to obtain the absorption profiles of the suspensions.

Comparisons of the normalized absorption and fluorescence emission spectra of the esterified TBAPy linkers (dissolved in acetonitrile), with the fluorescence excitation and emission spectra of the MOF suspensions are shown in Figure 2. The excitation profiles of the MOF suspensions are significantly red-shifted relative to the soluble linker (Table 1). This observation is unlikely due to solvatochromic effects as spectra of the NU-1000 MOF is unchanged when measured in acetonitrile. The MOFs containing the ortho-substituted linkers (NU-1000-*o*-Cl₄ (Figure 2c) and NU-1000-*o*-(CH₃)₄ (Figure 2b)) show the largest red shift, with the onset of excitation starting at ca. 500 nm. A comparison of the absorption and fluorescence emission spectra of the TBAPy linkers (black lines) also show that ortho-substitution induces a larger red shift than substitution at the meta position.

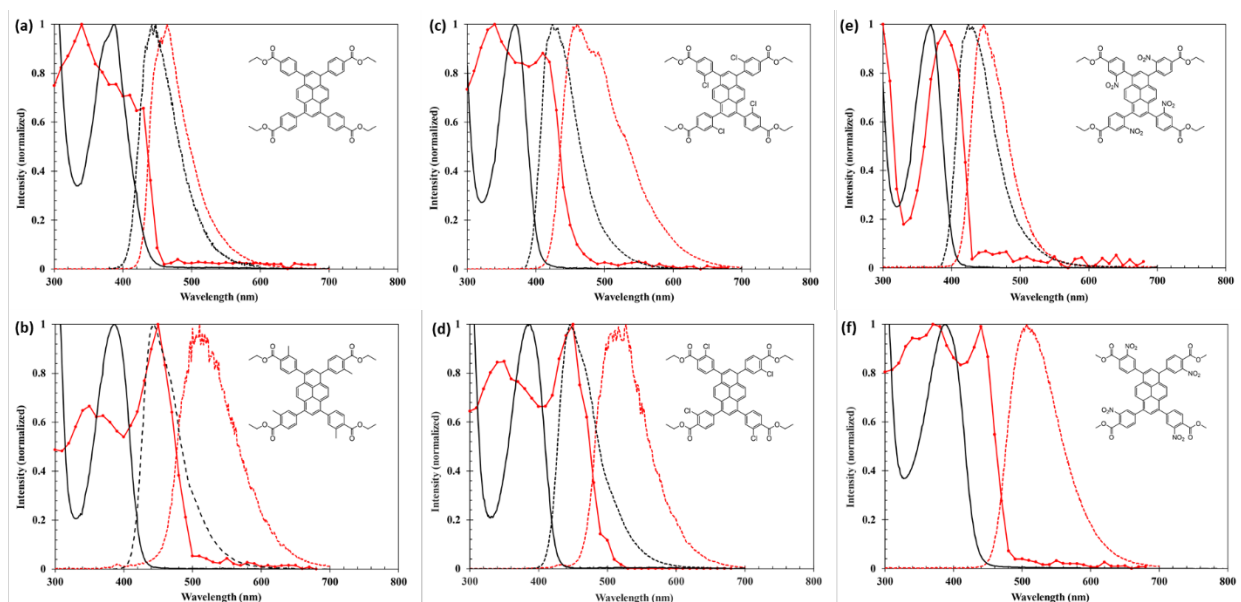


Figure 2. Comparison of the absorption (black, solid) and emission (black, dashed) spectra of TBAPy linkers in acetonitrile solution with the fluorescence excitation (red, solid) and emission (red, dashed) spectra of a methanol suspension of the MOFs (red). (a) NU-1000 (red) and (OEt)₄-TBAPy (black); (b) NU-1000-*o*-(CH₃)₄ (red) and (OEt)₄-TBAPy-*o*-(CH₃)₄ (black); (c) NU-1000-*m*-Cl₄ (red) and (OEt)₄-TBAPy-*m*-Cl₄ (black); (d) NU-1000-*o*-Cl₄ (red) and (OEt)₄-TBAPy-*o*-Cl₄ (black); (e) NU-901-*m*-(NO₂)₄ (red) and (OEt)₄-TBAPy-*m*-(NO₂)₄ (black); and (f) PCN-224-*o*-(NO₂)₄ (red) and (OMe)₄-TBAPy-*o*-(NO₂)₄ (black).

The effect of substitution pattern for the nitrated TBAPy linkers and their subsequent MOFs is consistent with the NU-1000 MOFs shown. Ortho-substitution induces a larger shift in the excitation and emission spectra than in the meta-substituted isomer. In both cases, the excitation profile of the MOF is substantially red-shifted relative to solutions of the linker. Interestingly, (OEt)₄-TBAPy-*o*-(NO₂)₄, does not exhibit fluorescence like the other linkers studied. A summary of the absorption and fluorescent emission properties of the TBAPy linkers and MOF suspensions is given in Table 1. When comparing the excitation intensities for the MOFs at the maximum intensities for the blue (465 nm) and UV light (396 nm) used in the photocatalysis experiments (I_{465}/I_{396}) it becomes apparent the effect the red shift seen in the ortho substituted constituents has on the photocatalytic results. Of particular note is the fact that the intensity for NU-1000-*o*-Cl₄ is equivalent at 465 and 396 nm. Another observation of significant note is the blue shift of the absorbance and emission wavelengths of free linkers upon meta substitution, which was observed with

both -Cl and -NO₂ derivatives in the fluorescent emission maxima relative to the unsubstituted or ortho-substituted analogues. Interestingly, when using NU-1000 and OEt₄-TBAPy as baselines, there is an observed red shift in the excitation wavelengths for ortho-substituted MOFs; however, this phenomenon exhibits itself as a blue shift for meta substitution in the free linker.

Table 1. Excitation and emission spectral properties of MOF suspensions and respective linkers.

MOF	I_{465}/I_{396} ^(a)	$\lambda_{\text{ex}}(50\%)/$ (nm) ^(b)	$\lambda_{\text{em}}(\text{max})/$ (nm) ^(c)	Free Linker	$\lambda_{\text{Abs}}(\text{max})/$ (nm) ^(d)	$\lambda_{\text{em}}(\text{max})/$ (nm) ^(c)
NU-1000	0.030	438	464	OEt ₄ -TBAPy	387	448
NU-1000- <i>o</i> -Cl ₄	1.0	475	527	OEt ₄ -TBAPy- <i>o</i> -Cl ₄	386	445
NU-1000- <i>m</i> -Cl ₄	0.097	436	460	OEt ₄ -TBAPy- <i>m</i> -Cl ₄	370	423
NU-1000- <i>o</i> -(CH ₃) ₄	1.3	478	510	OEt ₄ -TBAPy- <i>o</i> -(CH ₃) ₄	392	449
PCN-224- <i>o</i> -(NO ₂) ₄	0.45	462	507	OMe ₄ -TBAPy- <i>o</i> -(NO ₂) ₄	387	---
NU-901- <i>m</i> -(NO ₂) ₄	0.062	420	447	OEt ₄ -TBAPy- <i>m</i> -(NO ₂) ₄	370	424

^(a)Ratio of excitation spectra intensities at 465 and 396 nm. ^(b)Approximate wavelength at half-maximum observed in excitation spectra. ^(c)Maximum of the fluorescence emission spectrum. ^(d)Maximum emission of the excitation spectrum.

3.3 Photooxidation of 2-CEES

Each functionalized MOF reacted with 2-CEES in the presence of either UV (396 nm) or blue (465 nm) LED light. The reactions were conducted such that there was a catalytic amount of MOF present relative to the amount of 2-CEES present in the reaction solution (approximately 100:1, 2-CEES:H₄TBAPy). As previously reported, NU-1000 generates singlet oxygen rapidly and subsequently reacts with 2-CEES under both UV and blue light conditions, with much stronger activation under UV light.¹⁰ In our experiments NU-1000 degraded 50 % of the CEES in 3.0 and 40 min under UV and blue light conditions, respectively. This is consistent with the I_{465}/I_{396} for excitation of 0.03 reported in Table 1. PCN-224-*o*-(NO₂)₄, and NU-901-*m*-(NO₂)₄, showed very little to no reaction under both UV and blue light conditions as compared to the baseline material (Table 2), meaning that even though these materials were excited at these wavelengths, there was no phosphorescence observed, likely due to the inability of these materials to perform an intersystem crossing into the MOF triplet state. NU-1000-*o*-(CH₃)₄ showed reactivity in both light conditions; however, the reactivity (rate of singlet oxygen generation) was diminished under UV conditions when compared to NU-1000. Interestingly, the reactivity with the blue LED was similar to NU-1000, and only 4 times slower than the UV light, compared to ~13 times slower for NU-1000. This is consistent with higher excitation intensity at 465 nm than 396 nm for NU-1000-*o*-CH₃.

Interestingly, the two chlorinated NU-1000 derivatives showed enhancement of reactivity under different light conditions. NU-1000-*o*-Cl₄ exhibited a slightly slower reactivity than NU-1000 when irradiated with the UV LED; however, a 5-fold enhancement in reactivity was observed under blue light conditions, consistent with the I_{465}/I_{396} for NU-1000-*o*-Cl₄ being ~1, compared to ~0.03 for NU-1000. Conversely, NU-1000-*m*-Cl₄ showed 3-fold enhancement in CEES reactivity compared to NU-1000 when irradiated with UV light, but a large decrease in reactivity is observed under the blue light conditions (still faster than NU-1000). This is consistent with the I_{465}/I_{396} being ~0.1.

Table 2. Calculated half-lives for the oxidation of 2-CEES by the synthesized NU-1000 derivatives.

MOF	UV LED ($t_{1/2}$, min)	Blue LED ($t_{1/2}$, min)
NU-1000	3.0	40
NU-1000- <i>o</i> -(Cl) ₄	5.5	7.5
NU-1000- <i>m</i> -(Cl) ₄	1.0	25
NU-1000- <i>o</i> -(CH ₃) ₄	11	40
PCN-224- <i>o</i> -(NO ₂) ₄	>60	>60
NU-901- <i>m</i> -(NO ₂) ₄	>60	>60

3.4 Quantum yield of MOF linkers

The variation of photocatalytic efficiency among the MOFs shown in Table 2 depends on two key factors: (i) the amount of light absorbed at the LED excitation wavelength and (ii) the fraction of excited states that proceed to for singlet molecular oxygen. Direct measurements of these properties in the solid state proves incredibly difficult due to sample inhomogeneity and scattering of light. However, the excitation spectra shown in Figure 2, and summarized in Table 1, provide insight into the relative excitation intensities at 396 nm (UV) vs. 465 nm (blue) excitation wavelengths.

Additional insight into efficiency of singlet oxygen generation can be gained through the understanding of how each linker absorbs light and its efficiency for transition into the triplet state (Table 3). Each linker was studied at the wavelength of maximum absorbance (λ_{abs}), which was higher in energy than the UV LED (396 nm) used in the CEES oxidation studied. At the most fundamental level, the ability of the chromophore to absorb light efficiently is important; but the efficiency of the chromophore to induce an intersystem crossing into the triplet state. The only linker that exhibited a comparable quantum yield was the meta-chlorinated substituent. This comparable quantum yield is consistent with the enhanced reactivity of NU-1000-*m*-Cl₄ under UV conditions. Conversely, both OEt₄-TBAPy-*m*-(NO₂)₄ and OMe₄-TBAPy-*o*-(NO₂)₄ are weakly fluorescent ($\phi_{\text{F}} < 0.001$) and, relative to the other linkers, show very weak near phosphorescence ($\Phi_{\Delta} < 0.06$). These observations suggest that there are efficient non-radiative deactivation pathways that compete with fluorescence or intersystem crossing from the S₁ excited state of the nitrated linkers. The long half-lives for oxidation of 2- CEES observed for NU-901-*m*-(NO₂)₄ and PCN-224-*o*-(NO₂)₄ MOFs (Table 2) are consistent with a very low quantum yield of the reactive oxygen intermediate responsible for the photosensitized conversion of 2-CEES.

Table 3. Quantum yield of MOF linkers in acetonitrile

Free Linker	λ_{max} (nm)	Φ_{F}	Φ_{Δ}
OEt ₄ -TBAPy	386	-	-
OEt ₄ -TBAPy- <i>o</i> -(Cl) ₄	386	0.58	0.34
OEt ₄ -TBAPy- <i>m</i> -(Cl) ₄	370	0.33	0.68
OEt ₄ -TBAPy- <i>o</i> -(CH ₃) ₄	384	0.14	0.34
OMe ₄ -TBAPy- <i>o</i> -(NO ₂) ₄	388	<0.001	0.054
OEt ₄ -TBAPy- <i>m</i> -(NO ₂) ₄	370	<0.001	<0.001

4. DISCUSSION

The excitation profile of the MOFs each show a significant red shift as compared to the free linker (Figure 2 and Table 2). As previously reported, the baseline NU-1000 and NU-901 exhibits this bathochromic shift due to the interaction of neighboring chromophores in the crystalline MOF structure.²⁹ The pyrene-pyrene torsion angle for NU-901 and NU-1000 has been calculated to be 20° and 60°, respectively. Not only is the relationship from neighboring pyrenes important, but the torsion angle and resulting orbital overlap from the phenyl group play a pivotal role.

Figure 3 compares each free linker and MOF derivative studied herein. Interestingly, in all cases, the ortho-substituted linkers exhibit longer excitation wavelengths than the meta-substituted linkers. In the meta position, a larger pyrene-phenyl torsion angle would be expected due to steric hinderance between the substituted moiety on the phenyl group and the neighboring pyrene group. Conversely, substitution in the ortho position does not have the same effect and the pyrene-phenyl torsion angle is like that of the baseline OEt₄-TBAPy linker. DFT calculations (B3LYP/6-31g(d)) of the S₀→S₁ absorption the geometry optimized baseline and chlorinated linkers were conducted, which support these hypotheses. The trend for absorption bands for each of these MOF linkers was found to be consistent with experimental data, with a blue shift of OEt₄-TBAPy-*m*-Cl₄ when compared to OEt₄-TBAPy-*o*-Cl₄ and OEt₄-TBAPy, as summarized in Table 4. The increased torsion angle(s) for OEt₄-TBAPy-*m*-Cl₄ result in a less conjugated LUMO as the pyrene and phenyl are significantly out of phase. Also, of interest is that the two meta positions on the phenyl ring are not

equivalent, when the chloro group is nearest the fused rings, the torsion angle is greater (77°) than when it is on the other side, away from the fused rings (68°).

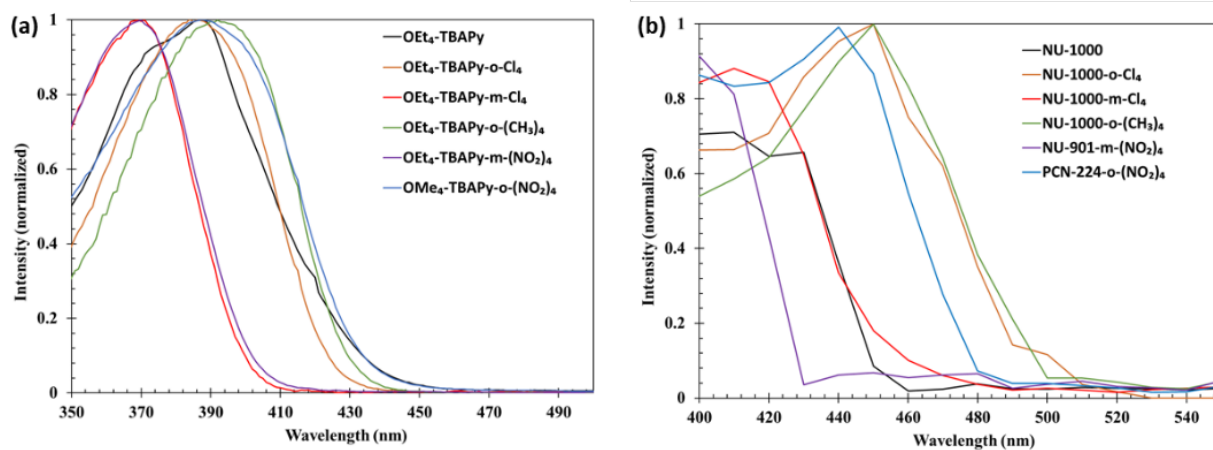


Figure 3. Comparison of (a) the absorption spectra for each of the MOF linkers, and (b) the excitation spectra for each of the MOFs.

While the increased pyrene-phenyl torsion angle in $\text{OEt}_4\text{-TBAPy-}m\text{-}(\text{Cl})_4$ exhibits a decreased conjugation and therefore an inability to absorb longer wavelengths of light, the rotation also places the chloro group in close proximity to the pyrene π cloud. In Figure 4, the overlap of the LUMO with the chloro group can be observed. This interaction has the ability to induce spin-orbit coupling and in turn enhance the $S_1 \rightarrow T_1$ transition. This is supported by the enhanced Φ_Δ observed for the meta chlorinated linker compared to the other substituted linkers (Table 3). This also offers strong evidence for the enhanced rate of reactivity of $\text{NU-1000-}m\text{-}(\text{Cl})_4$ with the UV LED.

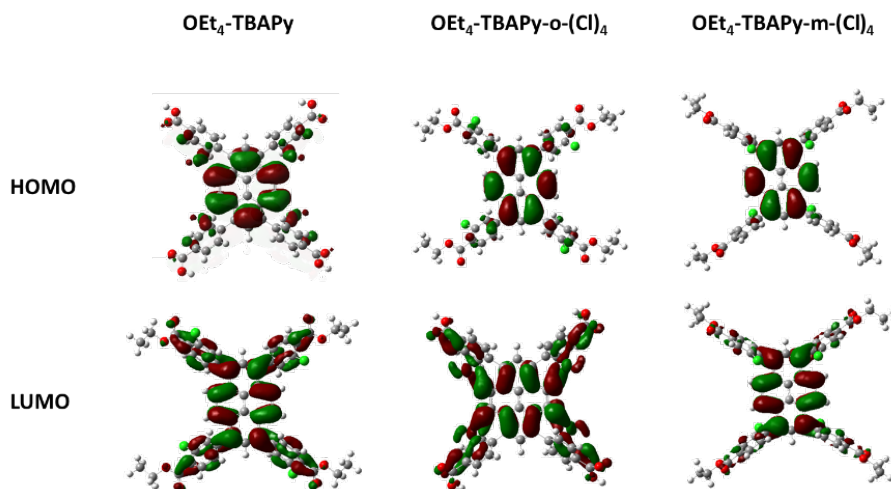


Figure 4. Calculated HOMO and LUMO for $\text{OEt}_4\text{-TBAPy}$, $\text{OEt}_4\text{-TBAPy-}o\text{-}(\text{Cl})_4$, and $\text{OEt}_4\text{-TBAPy-}m\text{-}(\text{Cl})_4$.

Figure 3b shows the opposite effect for the MOFs as compared to the linkers, as all the excitation wavelengths of the ortho-substituted MOFs are red shifted compared to NU-1000. While the geometry optimized calculations of the full MOF structure are beyond the scope of this manuscript, we offer fundamental observations on this phenomenon. The pyrene-pyrene torsion angle of NU-1000 is based on the topology of the MOF and is dictated by the crystal, therefore cannot deviate from 60° (the angle of an equilateral triangle).²⁹ However, the pyrene-phenyl rotation is still very important, as that torsion angle approaches 90° , functional groups in the ortho position get closer to one another, while substituents in the meta positions are far away from their nearest neighbor and do not have an effect. To alleviate steric and electronic effects from ortho substituents, the phenyl ring may rotate to a smaller torsion angle, therefore better aligning the pyrene and phenyl rings. This effectively increases the conjugation when compared to the baseline MOF and lowers the energy of the LUMO. The lower energy for the $S_0 \rightarrow S_1$ transition explains the enhanced absorption of blue light for each of the ortho substituted NU-1000 MOFs.

5. CONCLUSIONS/FUTURE WORK

Several novel MOF variants were successfully synthesized with functional groups (-Cl, -NO₂, -CH₃) positioned either ortho or meta to the carboxylic acid on the linker. Photocatalytic experiments showed that chlorine atoms significantly improve the photocatalytic reactivity of the material consistent with the trend shown previously in a tetraphenylporphyrin-based MOF that corresponds to an enhancement in the intersystem crossing to the triplet state of the MOF.³⁰ Interestingly, it was found that PCN-224-*o*-(NO₂)₄, and NU-901-*m*-(NO₂)₄, absorb light comparable to the other MOF derivatives, but do exhibit significant photocatalytic reactivity. This indicates a self-quenching mechanism in the case of PCN-224-*o*-(NO₂)₄ and NU-901-*m*-(NO₂)₄.

The blue shift of absorbance wavelengths observed for meta-substituted free linkers and the red shift of excitation wavelengths observed for ortho-substituted MOFs is a direct result of the pyrene-phenyl torsion angle, with the torsion angle and the degree of conjugation being inversely related. Further control of the geometric control via functionalization could lead to an even higher degree of conjugation over the linker leading to a further red shift and enhanced reactivity with lower energy visible light.

These results not only enhance the general knowledge of these materials but also contribute toward design principles for future MOF-based photocatalysts for the mitigation of toxic chemicals susceptible to oxidation including sulfur mustard, hydrogen sulfide, and other organic pollutants, particularly for a dynamic flow-through system which has already shown promise in this work.

ACKNOWLEDGEMENTS

Funding was provided by the U.S. Army via the Chemical Biological Advanced Materials and Manufacturing Science Program (PE 0601102A Project VR9) at the Combat Capabilities Development Command Chemical Biological Center.

REFERENCES

- [1] Ghabili, K.; Agutter, P.S.; Ghanei, M.; Ansarin, K.; Panahi, Y.; Shoja, M.M. Sulfur mustard toxicity: History, chemistry, pharmacokinetics, and pharmacodynamics. *Crit. Rev. Toxicol.* **2011**, *41* (5), 384-403.
- [2] Wang, Q.-Q.; Begum, R.A.; Day, V.W.; Bowman-James, K. Sulfur, oxygen, and nitrogen mustards: stability and reactivity. *Org. Biomol. Chem.* **2012**, *10* (44), pp 8786–8793.
- [3] Ploskonka, A.M.; DeCoste, J.B. Tailoring the Adsorption and Reaction Chemistry of the Metal–Organic Frameworks UiO-66, UiO-66-NH₂, and HKUST-1 via the Incorporation of Molecular Guests. *ACS Appl. Mater. Interfaces.* **2017**, *9* (25), pp 21579–21585.
- [4] Mondloch, J.E.; Katz, M.J.; Isley Iii, W.C.; Ghosh, P.; Liao, P.; Bury, W.; Wagner, G.W.; Hall, M.G.; DeCoste, J.B.; Peterson, G.W.; Snurr, R.Q.; Cramer, C.J.; Hupp, J.T.; Farha, O.K. Destruction of chemical warfare agents using metal–organic frameworks. *Nat Mater.* **2015**, *14* (5), pp 512–516.
- [5] Katz, M.J.; Mondloch, J.E.; Totten, R.K.; Park, J.K.; Nguyen, S.T.; Farha, O.K.; Hupp, J.T. Simple and compelling biomimetic metal-organic framework catalyst for the degradation of nerve agent simulants. *Angew Chem Int Ed Engl.* **2014**, *53* (2), pp 497–501.
- [6] Peterson, G.W.; Moon, S.-Y.; Wagner, G.W.; Hall, M.G.; DeCoste, J.B.; Hupp, J.T.; Farha, O.K. Tailoring the Pore Size and Functionality of UiO-Type Metal–Organic Frameworks for Optimal Nerve Agent Destruction. *Inorg. Chem.* **2015**, *54* (20), pp 9684–9686.
- [7] Liu, Y.; Howarth, A.J.; Vermeulen, N.A.; Moon, S.-Y.; Hupp, J.T.; Farha, O.K. Catalytic degradation of chemical warfare agents and their simulants by metal-organic frameworks. *Coord. Chem. Rev.* **2017**, *346*, pp 101–111.
- [8] Bobbitt, N.S.; Mendonca, M.L.; Howarth, A.J.; Islamoglu, T.; Hupp, J.T.; Farha, O.K.; Snurr, R.Q. Metal-organic frameworks for the removal of toxic industrial chemicals and chemical warfare agents. *Chem. Soc. Rev.* **2017**, *46* (11), pp 3357–3385.
- [9] DeCoste, J.B.; Peterson, G.W. Metal-organic frameworks for air purification of toxic chemicals. *Chem Rev.* **2014**, *114* (11), pp 5695–5727.
- [10] Dhakshinamoorthy, A.; Li, Z.; Garcia, H. Catalysis and photocatalysis by metal organic frameworks. *Chem. Soc. Rev.* **2018**, *47* (22), pp 8134–8172.

- [11] Bordiga, S.; Lamberti, C.; Ricchiardi, G.; Regli, L.; Bonino, F.; Damin, A.; Lillerud, K.-P.; Bjorgen, M.; Zecchina, A. Electronic and vibrational properties of a MOF-5 metal–organic framework: ZnO quantum dot behaviour. *Chem. Commun.* **2004**, *20*, pp 2300–2301.
- [12] Wang, C.; Xie, Z.; deKrafft, K.E.; Lin, W. Doping Metal–Organic Frameworks for Water Oxidation, Carbon Dioxide Reduction, and Organic Photocatalysis. *J. Am. Chem. Soc.* **2011**, *133* (34), pp 13445–13454.
- [13] Goh, T.W.; Xiao, C.; Maligal-Ganesh, R.V.; Li, X.; Huang, W. Utilizing mixed-linker zirconium-based metal–organic frameworks to enhance the visible light photocatalytic oxidation of alcohol. *Chem. Eng. Sci.* **2015**, *124*, pp 45–51.
- [14] Sun, D.; Gao, Y.; Fu, J.; Zeng, X.; Chen, Z.; Li, Z. Construction of a supported Ru complex on bifunctional MOF-253 for photocatalytic CO₂ reduction under visible light. *Chem. Commun.* **2015**, *51* (13), pp 2645–2648.
- [15] He, J.; Wang, J.; Chen, Y.; Zhang, J.; Duan, D.; Wang, Y.; Yan, Z. A dye-sensitized Pt@UiO-66(Zr) metal–organic framework for visible-light photocatalytic hydrogen production. *Chem. Commun.* **2014**, *50* (53), pp 7063–7066.
- [16] Zhang, H.; Wei, J.; Dong, J.; Liu, G.; Shi, L.; An, P.; Zhao, G.; Kong, J.; Wang, X.; Meng, X.; Zhang, J.; Ye, J. Efficient Visible-Light-Driven Carbon Dioxide Reduction by a Single-Atom Implanted Metal–Organic Framework. *Angew. Chem., Int. Ed.* **2016**, *55* (46), pp 14310–14314.
- [17] Zhou, T.; Du, Y.; Borgna, A.; Hong, J.; Wang, Y.; Han, J.; Zhang, W.; Xu, R. Post-synthesis modification of a metal–organic framework to construct a bifunctional photocatalyst for hydrogen production. *Energy Environ. Sci.* **2013**, *6* (11), pp 3229–3234.
- [18] Maza, W.A.; Morris, A.J. Photophysical Characterization of a Ruthenium(II) Tris(2,2'-bipyridine)-Doped Zirconium UiO-67 Metal–Organic Framework. *J. Phys. Chem. C.* **2014**, *118* (17), pp 8803–8817.
- [19] DeCoste, J.B.; Peterson, G.W.; Jasuja, H.; Glover, T.G.; Huang, Y.-g.; Walton, K.S. Stability and degradation mechanisms of metal-organic frameworks containing the Zr₆O₄(OH)₄ secondary building unit. *J. Mater. Chem. A.* **2013**, *1* (18), pp 5642–5650.
- [20] Kandiah, M.; Nilsen, M.H.; Usseglio, S.; Jakobsen, S.; Olsbye, U.; Tilset, M.; Larabi, C.; Quadrelli, E.A.; Bonino, F.; Lillerud, K.P. Synthesis and Stability of Tagged UiO-66 Zr-MOFs. *Chem. Mater.* **2010**, *22* (24), pp 6632–6640.
- [21] Cavka, J.H.; Jakobsen, S.; Olsbye, U.; Guillou, N.; Lamberti, C.; Bordiga, S.; Lillerud, K.P. A New Zirconium Inorganic Building Brick Forming Metal Organic Frameworks with Exceptional Stability. *J. Am. Chem. Soc.* **2008**, *130* (42), pp 13850–13851.
- [22] Howarth, A.J.; Buru, C.T.; Liu, Y.; Ploskonka, A.M.; Hartlieb, K.J.; McEntee, M.; Mahle, J.J.; Buchanan, J.H.; Durke, E.M.; Al-Juaid, S.S.; Stoddart, J.F.; DeCoste, J.B.; Hupp, J.T.; Farha, O.K. Postsynthetic Incorporation of a Singlet Oxygen Photosensitizer in a Metal–Organic Framework for Fast and Selective Oxidative Detoxification of Sulfur Mustard. *Chem. Eur. J.* **2016**, *23* (1), pp 214–218.
- [23] Liu, Y.; Howarth, A.J.; Hupp, J.T.; Farha, O.K. Selective Photooxidation of a Mustard-Gas Simulant Catalyzed by a Porphyrinic Metal–Organic Framework. *Angew. Chem., Int. Ed.* **2015**, *54* (31), pp 9001–9005.
- [24] Liu, Y.; Buru, C.T.; Howarth, A.J.; Mahle, J.J.; Buchanan, J.H.; DeCoste, J.B.; Hupp, J.T.; Farha, O.K. Efficient and selective oxidation of sulfur mustard using singlet oxygen generated by a pyrene-based metal–organic framework. *J. Mater. Chem. A.* **2016**, *4* (36), pp 13809–13813.
- [25] Lee, M.S.; Garibay, S.J.; Ploskonka, A.M.; DeCoste, J.B. Bioderived protoporphyrin IX incorporation into a metal-organic framework for enhanced photocatalytic degradation of chemical warfare agents. *MRS Commun.* **2019**, *9* (2), pp 464–473.
- [26] Marin, D.M.; Payerpaj, S.; Collier, G.S.; Ortiz, A.L.; Singh, G.; Jones, M.; Walter, M.G. Efficient intersystem crossing using singly halogenated carbomethoxyphenyl porphyrins measured using delayed fluorescence, chemical quenching, and singlet oxygen emission. *Phys. Chem. Chem. Phys.* **2015**, *17* (43), pp 29090–29096.
- [27] Walton, K.S.; Snurr, R.Q. Applicability of the BET Method for Determining Surface Areas of Microporous Metal–Organic Frameworks. *J. Am. Chem. Soc.* **2007**, *129* (27), pp 8552–8556.
- [28] Islamoglu, T.; Ortuño, M.A.; Prousaloglou, E.; Howarth, A.J.; Vermeulen, N.A.; Atilgan, A.; Asiri, A.M.; Cramer, C.J.; Farha, O.K. Presence versus proximity: the role of pendant amines in the catalytic hydrolysis of a nerve agent simulant. *Angew. Chem.* **2018**, *130* (7), pp 1967–1971.
- [29] Deria, P.; Yu, J.; Smith, T.; Balaraman, R.P. Ground-State versus Excited-State Interchromophoric Interaction: Topology Dependent Excimer Contribution in Metal–Organic Framework Photophysics. *J. Am. Chem. Soc.* **2017**, *139* (16), pp 5973–5983.
- [30] Kirchon, A.; Feng, L.; Drake, H.F.; Joseph, E.A.; Zhou, H.-C. From fundamentals to applications: a toolbox for robust and multifunctional MOF materials. *Chem. Soc. Rev.* **2018**, *47* (23), pp 8611–8638.

Extending bio-functionality in materials via controlled polymer erosion

Marilyn S. Lee^{a*}, Jennifer Lee^b, John R. Biondo^c, Jeffrey Lux^{d,e}, Danielle Kuhn^a,
Matthew Browe^a, Maneesh K. Gupta^d, Matthew W. Lux^a

^aU.S. Army Combat Capabilities Development Command Chemical Biological Center, Research & Operations Directorate, 8198 Blackhawk Rd., Aberdeen Proving Ground, MD 21010

^bDefense Threat Reduction Agency, 2800 Bush River Rd., Gunpowder, MD 21010

^cExcet Inc., 6225 Brandon Ave., Suite 360, Springfield, VA 22150

^dU.S. Air Force Research Laboratory, 2179 12th St., B652/R122 Wright-Patterson Air Force Base, OH 45433

^eUES, Inc., 4401 Dayton-Xenia Rd., Dayton, OH 45432

ABSTRACT

While synthetic biology has advanced complex capabilities like sensing and molecule synthesis in aqueous solutions, important applications may also be pursued for biological systems in solid materials. Technical challenges have hindered the use of biology in synthetic materials, including maintaining cell viability or protein activity during harsh processing steps and experienced over long-term use of the material. One technology that shows promise in circumventing these issues are cell-free protein synthesis systems. Cell-free protein synthesis reactions may be dried and stored for months to a year and maintain activity upon rehydration. Extending these observations, we find that dried CFPS reactions have remarkable stability to both heat and organic solvents, lending them to applications in synthetic materials. In this study, cell-free expression activity is successfully demonstrated in solvent and heat cast polymers, unlocking the potential for enabling new bio-reaction form factors, controlling water-induced activation, and delivering DNA-programmable bio-functionality in materials.

Keywords: Cell-free protein synthesis, polymers, synthetic biology, protein stability, sensing, biosynthesis

1. INTRODUCTION

Nature abounds with materials capable of complex dynamic functions that conventional material science cannot match. By applying rapidly developing tools to engineer biological systems, synthetic biology enables the design of similarly capable materials.¹ Sensing materials could detect damage or threats and provide outputs like color change, fluorescence, or electrical signal. Metabolic activity could be used to make useful molecules like therapeutics or antimicrobials *in situ*. Further, self-cleaning, self-repair, or self-degradation could be mediated by enzymes. A critical aspect of engineering living materials is ensuring the viability of the organisms. As a result, studies have focused on environments that are friendly to microbes, such as hydrogels² or biofilms on surfaces,³ or use organisms naturally adapted to target environments like architectural materials, soil, seawater, or the human gut.⁴ Spores are sometimes used to enable cells to withstand processing conditions or to extend the duration of function.⁵ Often, it is not clear how to make nutrients available to cells residing inside a material. Most approaches described by recent works involve soaking the object in a nutrient bath, which may not be appropriate for all applications and could limit the lifetime of the programmed functionality to feeding events.⁶ As a result, materials that are unfavorable to biological systems, whether in their processing or final form, remain off limits for engineered living materials.

Plastics represent an important class of synthetic materials for which the processing is generally inhospitable to biological systems. Many categories of polymeric materials exist with a wide range of synthesis methods, most of which involve conditions that damage biological systems due to high temperatures, exposure to solvents, radical generation, or UV radiation. Some studies have shown the possibility of proteins surviving these conditions, whether by protecting the protein with additives, encapsulation,⁷ or engineering the enzyme to be more robust.^{8,9} While promising, this approach limits the function to a single enzyme or set of enzymes without dynamic response capability and requires re-engineering the formulation or protein sequence variant for each new application.

One avenue that bypasses the drawbacks of both living cells and isolated enzymes to deliver programmable biological function to materials is cell-free protein synthesis systems (CFPS). CFPS systems are an alternative to living cells that can avoid problems like strain instability and concerns over environmental release of genetically modified organisms.¹⁰ CFPS reactions are complex mixtures of cellular components and excipient resources that are capable of transcription and translation of DNA instructions to enact genetic circuits like sensors and produce proteins like enzyme catalysts or therapeutics.¹¹ A CFPS reaction uses lysates or purified cellular machinery without a cell membrane or the need to maintain cell viability and replication. Other resources in the reaction include nucleosides, amino acids, phosphorylated or sugar energy source, buffer, and cofactors. When CFPS components are lyophilized, remarkable stability has been observed.¹² Several commonly used formulations based on either *E. coli* lysates or pure proteins can tolerate exposure to a variety of organic solvents when dried, although stability following solvent exposure can vary greatly depending on the individual components. While there are many considerations when developing and optimizing CFPS systems to embed in synthetic materials, these reactions are open systems that allow unfettered access to the reaction environment, breaking the limitations of living systems.

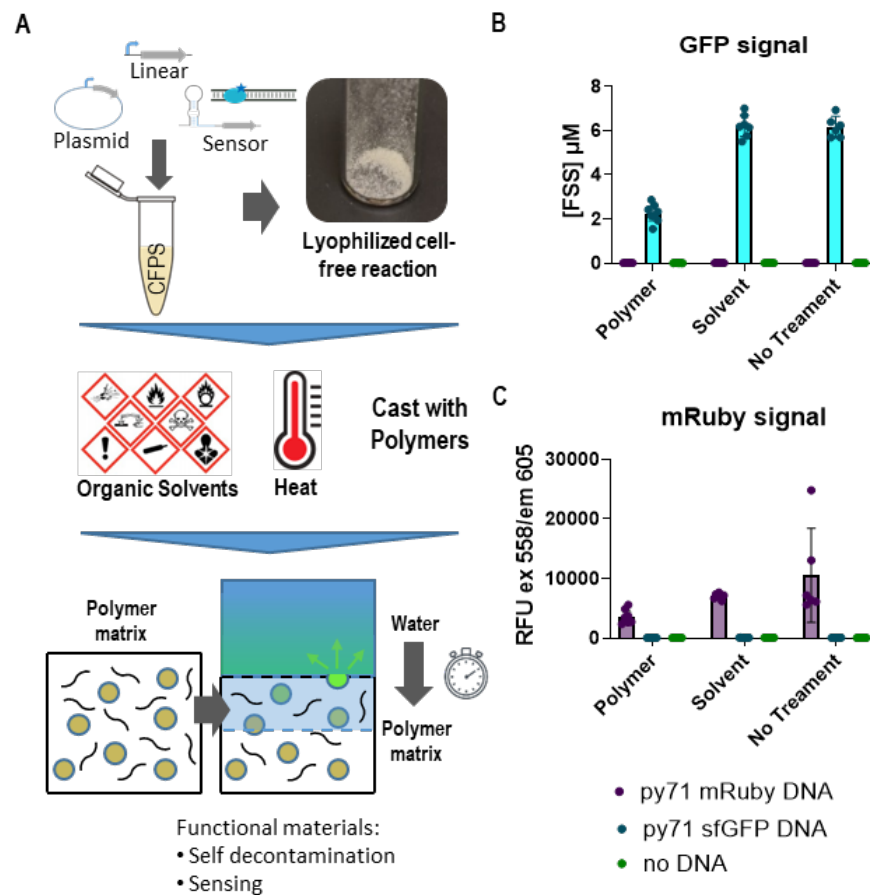


Figure 1. CFPS powder is cast into polymers. (A) Graphic for the incorporation of CFPS reactions in a polymer matrix: reaction assembly with DNA dictating function, formation of dry CFPS powder, polymer casting via harsh solvent and heat treatments to embed CFPS powder within a non-aqueous polymer matrix, and reactivation via water permeation into the CF-polymer composite and/or hydrolysis of the polymer. (B) Endpoint sfGFP fluorescence signal in concentration of equivalent Fluorescein [FSS] for samples containing mRuby DNA, sfGFP DNA, or no DNA. CFPS powder samples were mixed with PLGA solution, solvent alone, or untreated. The mean and individual 8-hr endpoints are shown, $n \geq 6$, error bars are the 95 % confidence interval. (C) mRuby fluorescence in relative fluorescence units (RFU) for the same samples described in (B).

Porous materials like fabrics, paper, and hydrogels have been functionalized with CFPS.^{13,14} In this study, we seek to establish a proof-of-concept for embedding CFPS reactions in solvent and heat cast polymer materials (Figure 1A). In previous years, we showed heat tolerance of dried reactions at temperatures up to 90 °C for up to 30 minutes and heat casting in poly caprolactone (PCL).¹⁵ Here we describe testing solvent casting of poly lactic-co-glycolic acid (PLGA) with embedded dried CFPS powder. Protein synthesis activity was recovered from films. Several functions

are demonstrated in solvent-cast CFPS-PLGA: constitutive production of a single fluorescent protein, patterned localized production of two fluorescent proteins in the same material, production of an antimicrobial Colicin to inhibit *E. coli* growth, and a toehold switch sensor responding to an RNA trigger. We conclude that polymer embedded CFPS reactions are a promising new way to deliver complex biological activity in materials. We also discuss the needs for further developments and the new directions that polymers could take CFPS-driven synthetic biology.

2. RESULTS

2.1 Solvent cast CFPS-PLGA and localized function

Dried CFPS powder is stable to organic solvent exposure.¹² This ability was harnessed to test encapsulation within solvent-cast polymer. PLGA was the first polymer chosen to test because it is biocompatible, it can readily absorb water, and it undergoes gradual hydrolysis of the polymer chains to release encapsulated cargo, all of which might give favorable conditions to reactivate the CFPS activity upon hydration. As a first test, the recovery of protein synthesis activity was measured after exposure to a solution of polymer in acetone. Acetone is both suitable to dissolve PLGA and is compatible with CFPS activity. The production of fluorescence was monitored in CFPS reactions containing plasmid DNA encoding either sfGFP (green fluorescent protein) or mRuby (red fluorescent protein). Samples were exposed to acetone alone, PLGA dissolved in acetone, or left untreated, and reactions were rehydrated after evaporation of acetone (Figure 1B, C). The results for mRuby and sfGFP products bore similar trends. Acetone exposure did not show any decrease in productivity as expected. The addition of polymer caused endpoint productivity to drop to 75 % and 37 % of untreated levels for mRuby and sfGFP, respectively. Though the drop in productivity is significant, this result verified that CFPS can work when processed with solvent-cast polymers and encouraged further exploration of polymer casting techniques.

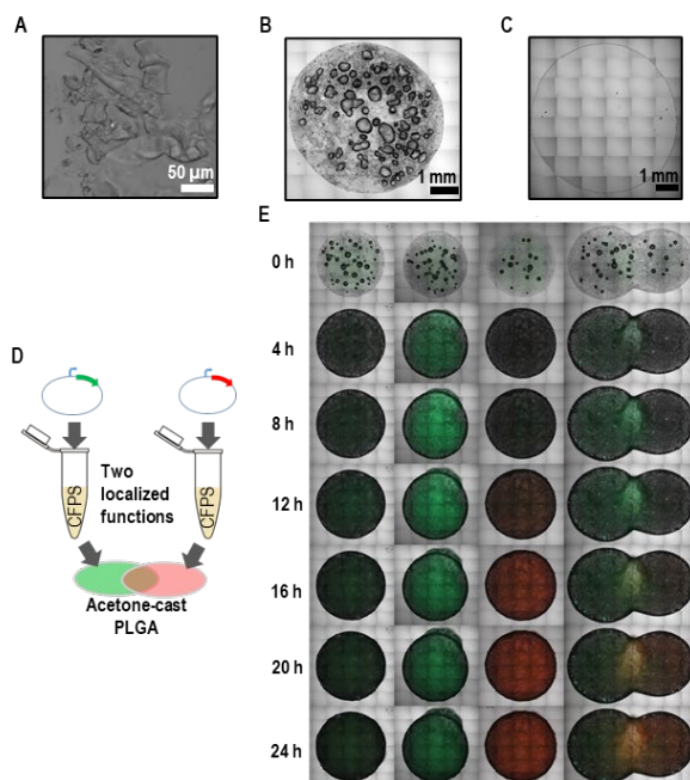


Figure 2. Microscopy of localized functions in CFPS-PLGA films (A) Differential interface contrast microscopy image depicting morphology of dried CFPS reaction powder embedded in PLGA solvent cast film. (B) Tiled DIC images depicting an entire CFPS-PLGA film. (C) Tiled DIC images depicting a PLGA film with no CFPS powder. (D) Diagram of two CFPS-PLGA “inks” functionalized with different DNA cast into adjacent and overlapping films. (E) Tiled microscopy images of whole CFPS-PLGA films. DIC, sfGFP (green), and mRuby (red) fluorescence channels are merged.

Next, CFPS-PLGA was solvent cast with acetone into films on a glass substrate. Films were made containing plasmid DNA encoding sfGFP or mRuby fluorescent proteins or without any DNA added. An inverted microscope was used to image rehydrated films. Differential interference contrast (DIC) was used to capture the morphology of the CFPS-PLGA film compared to PLGA alone (Figure 2A-C). The embedded CFPS powder particles are irregular and vary greatly from 1 to >100 μm . PLGA film is initially transparent, then addition of water causes an increase of opacity due to hydrolysis of the PLGA (Figure 2E). The appearance of green and red fluorescence is observed for each film, using time course and image stitching features to capture activity over the area of an entire film (Figure 2E). As expected, the films without DNA do not show increasing levels of fluorescence over time, while sfGFP and mRuby films produce green and red fluorescence, respectively. mRuby signal typically takes much longer to mature compared to sfGFP signal in CFPS reactions, and this trend is apparent for CFPS-films as well.

The ability to embed CFPS biological activity within polymers offers myriad opportunities to craft new reaction formats towards applications. One advantage could be spatial localization of functionalities within a material. Patterning of multiple functions within the same contiguous material offers interesting properties like controlled diffusion that can influence the interplay and behaviors of reactions in the material.¹⁶⁻¹⁸ Towards this concept, a simple example of a polymer film with dual localized functions was tested by preparing two different PLGA-CFPS “inks” suspended in acetone solvent. One ink contained DNA encoding mRuby, the other sfGFP; they were applied in adjacent areas, resulting in a continuous PLGA film with two differently functionalized regions (Figure 2D). Green and red fluorescence was monitored via microscopy to assess localization, which was observed in the expected distribution across the film (Figure 2E).

2.2 Production of colicin in CFPS-PLGA

Moving towards more practical applications, we sought to produce and test the activity of an antimicrobial protein, colicin E1, in CFPS reactions mixed with acetone or acetone-cast PLGA. There are demonstrated advantages to producing proteins like colicins using CFPS because of their toxicity to live bacterial hosts.^{19,20} Embedding the production of colicin in a polymer could yield self-decontaminating materials that may be useful to prevent colonization of harmful bacteria in devices like medical implants, ventilators, food processing equipment, or personal protective equipment. Antimicrobial proteins like colicins can have highly specific microbial activity, but they are typically sensitive to proteases and other modes of degradation. Each type of antimicrobial protein has differing degrees of heat or shelf stability.²¹ Thus, the ability to synthesize these molecules *in situ* is likely to improve their delivery in materials agnostic of protein type, reducing the effort required to tailor the process to each individual protein.

Linear PCR product encoding colicin under the control of a T7 promoter was added to the CFPS solution. Using linear DNA eliminates the need to construct plasmid DNA in a live host, avoiding toxicity issues caused by leaky expression of the potent antimicrobial protein. GamS nuclease inhibitor was also added to protect the linear template from degradation. After lyophilization, the CFPS reaction material with or without colicin DNA was rehydrated in an incubator after no treatment, treatment with pure acetone, or treatment with PLGA dissolved in acetone. Samples of the CFPS or CFPS-polymer supernatant solutions were then added to *E. coli* K12 subcultures to assess growth inhibition activity by colicin. All CFPS reactions containing the colicin DNA exerted significant growth inhibition on the *E. coli* cultures relative to no DNA controls (Figure 3A, B). Growth inhibition suggests active colicin was produced in solution even after exposure to solvent and polymer casting conditions. This promising result indicates polymer embedded CFPS could be used to produce useful proteins *in situ* simply by adding the necessary DNA to the system.

2.3 Sensor functionality in CFPS-PLGA

Finally, sensor-based regulation of protein expression in a polymer was demonstrated by embedding a toehold switch sensor in acetone-cast CFPS-PLGA. Lyophilized CFPS powder samples were prepared that contained combinations of two plasmids: one encoding LacZ under the translational control of a toehold switch, and another encoding the cognate trigger (Figure 3C). Some samples contained both switch and trigger, other samples only contained the switch to measure background activity. Positive control CFPS reactions contained a plasmid for constitutive LacZ expression, and negative controls contained no DNA. Lyophilized powder was mixed with PLGA solution and cast as films on glass. These films were rehydrated and incubated with a solution of Chlorophenol Red- β -D-Galactopyranoside (CPRG) indicator dye. LacZ cleaves galactose from the CPRG dye to change its color from yellow to magenta. The CPRG color change over time shows that constitutive production of LacZ was robust in PLGA. The toehold switch-controlled reactions embedded in PLGA also performed as expected. Samples with only switch plasmid had partial color change due to background activity. Samples with both trigger and switch

present had visibly stronger levels of color change by 8 hrs. The variability in switch performance compared to constitutive reactions could be due to reduced LacZ productivity from the switch construct or increased diffusion barriers, combined with variable CFPS powder loading across multiple films. Future efforts to improve dispersion and uniformity and to understand diffusion factors in solvent cast CFPS-PLGA could improve overall performance.

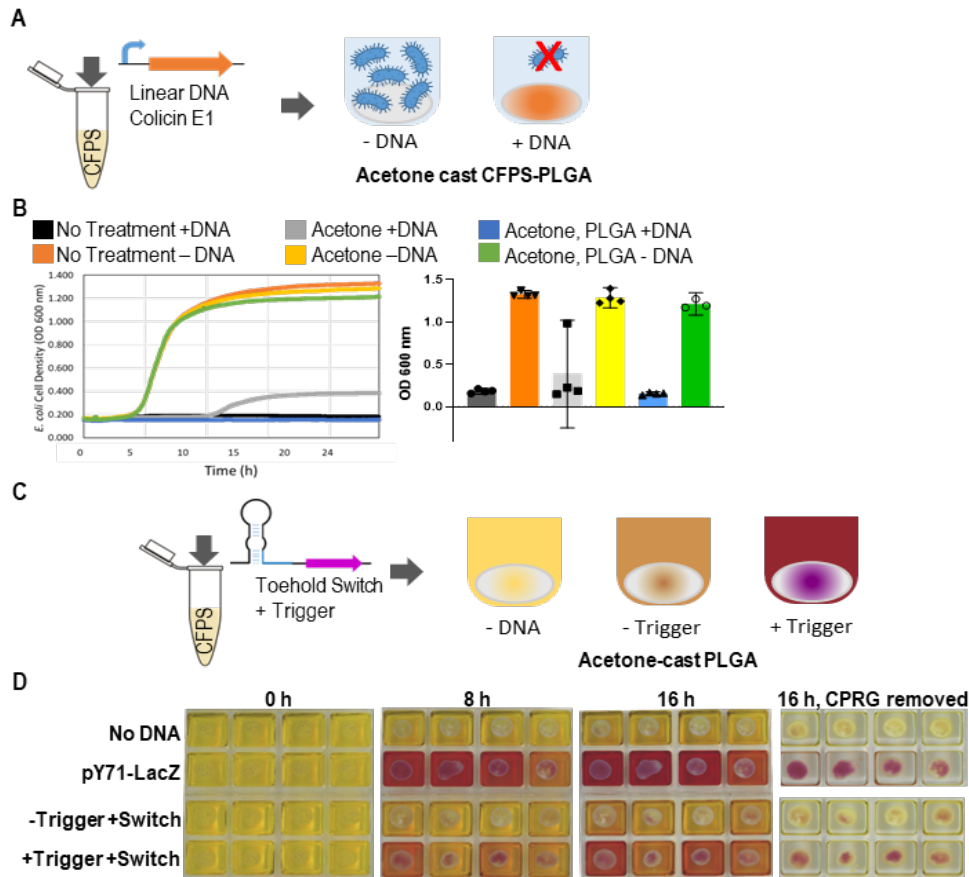


Figure 3. CFPS-Polymer applications. A) Antimicrobial polymer film formed by embedding CFPS functionalized with linear DNA encoding Colicin E1 in acetone-cast CFPS-PLGA. B) Optical density growth curve (left) and endpoint (right) data are shown for *E. coli* K12 cultures exposed to CFPS reaction solutions with or without colicin DNA after no treatment, treatment with pure acetone, or treatment with PLGA-acetone solution. Error bars are the 95 % confidence interval, $n \geq 3$. C) A CFPS-PLGA sensor includes DNA encoding colorimetric reporter under control of an RNA toehold switch as well as DNA encoding the cognate trigger RNA. D) Images of color change in CFPS-PLGA reactions containing the indicated DNA. Three time points are shown with films submerged in CPRG solution, the final timepoint is also depicted with supernatant solution removed.

2.4 Electrospun CFPS-polymer

Electrospinning is a technique for the fabrication of sub-micron diameter fibers that possess large surface to volume ratios and robust mechanical properties.²² In this process, a high voltage power supply is used to electrically charge a polymer solution, which is then drawn out by a syringe, yielding a web of interconnected nanofibers as the solvent evaporates. It has been demonstrated that biological materials can be mixed into a polymer solution prior to electrospinning and carried through to be dispersed throughout the polymer fibers.²³ Future functionalized fibers could offer threat detection or dynamic actuation of fabric properties such as breathability. Here, several polymer and solvent combinations were screened for their ability to carry CFPS powder into a spun fiber format (Table 1). Several conditions produced fibers that seemed to carry CFPS powder components (Figure 4A), but only one condition showed activity via production of GFP: polystyrene spun with dichloromethane (Figure 4B).

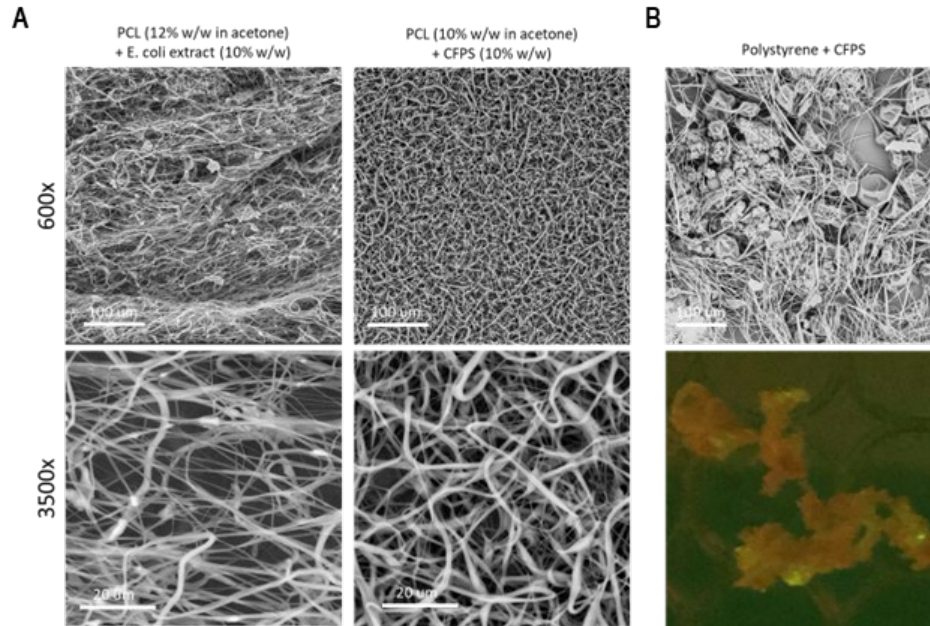


Figure 4. Electrospun fibers with and without CFPS powder. A) Example SEM images of PCL fibers with and without CFPS included. B) SEM image of polystyrene fibers electrospun with CFPS (top) and camera image of rehydrated polystyrene-CFPS fiber mat using blue light to show some production of sfGFP (bottom).

Table 1. Screen of electrospinning conditions with CFPS.

Polymer	Solvent	Qualitative Success in Fiber Production	Activity?
Polyethylene oxide	Water	*****	No
Polyethylene oxide	Dichloromethane	*****	No
Polycaprolactone	Dichloromethane	**	No
Polycaprolactone	Acetone	****	No
Polystyrene	Dichloromethane	**	Yes, slight
Cellulose acetate	Acetone	****	No
Polymethyl methacrylate	Chloroform + DMF	***	No
Polymethyl methacrylate	Acetone	**	No

2.5 COMSOL Multiphysics model of water diffusion and activity in CFPS polymers

Our testing with PLGA and PCL indicate that the polymer properties and morphology can impact the system's ability to be rehydrated with water for CFPS activation. PLGA readily absorbs water, while PCL is much more water repellant. We initially hypothesized that a polymer formulation might exist whereby water gradually infiltrates through the thickness of a polymer material to reactivate more and more of the dry and dormant CFPS powder, giving the overall material an extended period of biological activity. However, neither PLGA nor PCL exhibited this feature in the conditions we tested. Further, through perusal of potential polymer and morphology candidates to achieve this goal, it quickly became apparent it would be very difficult to test enough options to find the optimal formulation. We turned to building a computational reaction-diffusion model to understand how activity dynamics might depend on polymer properties and dimensions. Such a model might be used find optimal conditions more quickly, which then would lead the experimentalist to select polymers and casting methods more likely to yield the desired extended activity.

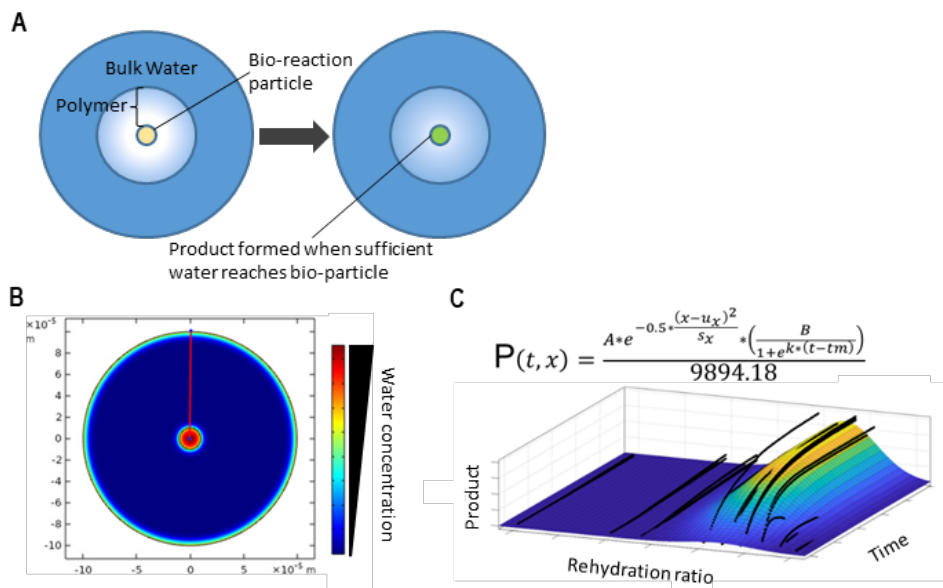


Figure 5. COMSOL Multiphysics model.

COMSOL Multiphysics software was used to build a model. Figure 5A illustrates the simplified geometry initially used. A particle at the center represents the area containing dry CFPS powder. This is surrounded by a polymer layer of specified thickness. Bulk water contacts the outside of the polymer layer. The model comprises a collection of additional parameters. Some, like density, are fixed estimates. Other parameters like polymer thickness, particle diameter, or water diffusivity can be screened for their effect on the productivity function, $P(t, x)$. Productivity, $P(t, x)$, is an equation for CFPS activity that is based on data collected for GFP production and its dependence on the amount of water present relative to CFPS powder mass (x). The dependence of productivity on time, t , was estimated based on observations of CFPS deactivation over time in the presence of water coupled to the normal dynamics of protein production. Figure 5B shows some preliminary outputs from the model demonstrating that the profile of water concentration behaves as expected. The current model productivity equation, $P(t, x)$ is shown in Figure 5C and is graphed as a surface in relation to experimental data (black lines). In potential future work, more advanced material geometries can be modeled, and parameters can be screened for optimal CFPS activity.

3. METHODOLOGY

3.1 Reagents and DNA

Unless otherwise noted, all reagents were purchased from Millipore Sigma, St. Louis, MO. The plasmid encoding sfGFP is PY71sfGFP (GenBank accession MT346027).²⁴ mRuby or LacZ sequences were inserted in place of sfGFP on the same plasmid backbone (PY71mRuby, PY71 LacZ) for production of red fluorescence or LacZ enzyme, respectively.¹⁴ The toehold switch sensor was Switch H selected from a publication by Pardee et. al.²⁵ and consisted of two plasmids pUCGA-swH-lacZ (switch) and pUCGA-trH (trigger) constructed as described by Blum et al.¹⁴ Plasmid DNA was purified from transformed *E. coli* using commercial midiprep or gigaprep kits.

Linear DNA encoding T7 polymerase-driven expression of Colicin E1 with a 6xHis tag was amplified by PCR from plasmid pKSJ331. pKSJ331 was a gift from Alan Finkelstein & Karen Jakes (Addgene plasmid # 103063; <http://n2t.net/addgene:103063>; RRID: Addgene_103063). The final amplicon solution was treated with a purification kit (Nucleospin, Takara Bio Inc., San Jose, CA).

3.2 CFPS reaction preparation and lyophilization

E. coli lysates were prepared from *E. coli* BL21 Star (DE3) flask cultures as described previously.²⁶ T7 RNA polymerase was added exogenously after lysate preparation. Lysis was performed either by sonication as described previously¹² or by homogenization using a Microfluidizer (Microfluidics M-110P). For homogenization, the cell

suspension was processed in one pass followed by centrifugation and flash freezing at $-80\text{ }^{\circ}\text{C}$. CFPS reactions contained 30 % v/v lysate and additional reagents following the PANOx-sp recipe.¹² After mixing on ice, CFPS reactions are frozen in liquid nitrogen, then lyophilized in plates, tubes, or vials as described for specific experiments. Small volumes were deposited in polypropylene microplate wells or 1.5 mL snap cap tubes. Larger volumes greater than 100 μL were distributed in glass vials so that the height of the liquid did not exceed 2 cm. CFPS lyophilized using a shelf-type lyophilizer (SP Scientific, VirTis Wizard 2.0) with a four-hour primary drying step at shelf temperature $20\text{ }^{\circ}\text{C}$, and an overnight ($\sim 17\text{ hr}$) or longer (up to 48 hr) secondary step with shelf temperature at $15\text{ }^{\circ}\text{C}$. After removal from the lyophilizer, CFPS powders were stored for minimal time in a desiccator at room temperature if needed prior to treatment or rehydration. Untreated CFPS powder was rehydrated immediately after lyophilization and simultaneously with experiments to check activity for quality control.

3.3 Acetone and acetone-PLGA treatments and films

CFPS reaction solutions were distributed 15 μL per well into a 96-well, v-bottom, polypropylene microplate (Costar 3357). The plates were lyophilized, then subjected to 15 μL acetone or a solution of 0.35 g/mL PLGA 75:25 L:G, 4–15K MW, acid terminated (Millipore Sigma 719919-5G) in acetone. The plate was uncovered to allow acetone to evaporate for one hour prior to rehydration with 15 μL water and measurement of protein production via fluorescence (GFP) or *E. coli* growth inhibition (colicin E1) via plate reader as described below.

CFPS reactions were prepared with plasmids encoding the reporters sfGFP (10 ng/ μL), mRuby (10 ng/ μL), or water (no DNA control). Reactions were frozen and lyophilized overnight in 1.5 mL snap-cap tubes. 0.35 g/mL PLGA in acetone was added to lyophilized CFPS at a 1:1 volumetric ratio relative to the volume of CFPS reaction pre-drying. A pestle (F19923-0000, Bel-Art, South Wayne, NJ) was used to crush the CFPS powder into a uniform suspension in the presence of PLGA solution. 10 μL of each CFPS-PLGA mixture was cast into films in an 8 well chamber slide (80821, Ibidi, Gräfelfing, Germany). For dual-function films, 10 μL of sfGFP CFPS-PLGA and 10 μL of mRuby CFPS-PLGA were cast side-by-side. The PLGA was allowed to cure uncovered for 4 h at room temperature, then 200 μL of nuclease free water was added to each well and slides were imaged on a Zeiss LSM 800 microscope with a Plan-Apochromat 10x/0.45 M27 objective at $37\text{ }^{\circ}\text{C}$. Tiled images of each film were taken with DIC, sfGFP, and mRuby channels. Images were taken each hour over the course of 24 hours.

3.4 Microplate reader fluorescence measurements and scanner imaging of LacZ reporter

Immediately after rehydration, plates were sealed with a polypropylene mat, transferred to a BioTek Synergy H1 microplate reader, and incubated at $37\text{ }^{\circ}\text{C}$ for 8 hours. Formation of sfGFP fluorescence was monitored with ex/em: 485/528 nm with a gain of 100. sfGFP readings in RFU were converted to μM sfGFP using fluorescence measurements of purified sfGFP standards.

For LacZ experiments, CFPS reactions were made with lysate prepared from ΔlacZ BL21 *E. coli*. 5 μg switch DNA, and either 10 μg trigger DNA (+Switch +Trigger) or equal volume PCR-grade water (+Switch -Trigger) were added to each 40 μL reaction volume. A positive control contained 500 ng plasmid that constitutively expressed lacZ (PY71 LacZ). A negative control did not contain DNA. Aliquots of 40 μL of thoroughly mixed reaction (CFPS+DNA) was added to 1.5 mL tubes, flash frozen, and lyophilized with shelf lyophilizer overnight as described above. The following day, lyophilized samples were ground into a powder using a plastic pestle. Separately, PLGA (75:25) was completely dissolved in acetone (33 % w/v) within a small glass bottle. 30 μL of dissolved polymer was then added to each tube containing the crushed CFPS reactions and gently mixed by pipetting. 25 μL of each mixture was then pipetted into individual wells of an 8-well chamber slide (Ibidi). The PLGA was allowed to cure uncovered for 2 hours at room temperature. Following evaporation, each reaction was rehydrated with 250 μL of 2 mM CPRG in water and incubated at $37\text{ }^{\circ}\text{C}$ for 16 hours. Images were taken every 30 minutes using a scanner placed inside of the incubator.

3.5 Colicin expression and growth inhibition assay

E. coli MG1655 cultures were prepared to assay colicin antimicrobial activity. On day 1 of the experiment, the strain was streaked from freezer stock onto Luria-Bertani (LB) agar. Then on day two, colonies were used to inoculate three biological replicates in 5 mL LB media with 1 % glucose in 50 mL conical tubes. These starter cultures were grown overnight at $37\text{ }^{\circ}\text{C}$, and 250 rpm orbital shaking. On day 3, *E. coli* starter cultures were diluted 1:100 in LB + 1 % glucose and grown until an OD600 of 0.05 or 4×10^8 cells/mL. Then the *E. coli* subcultures were diluted to $\sim 10^4$ cells/mL and are distributed at 200 μL per well in a sterile Costar 96-well flat bottom plate (#3370). All unused wells were filled with 200 μL blank media. On day 2, linear colicin DNA was added at 40 nM final concentration to

15 μL CFPS reactions in a 96-well microplate prior to lyophilization. When lyophilization was complete on day 3, dried reactions with and without DNA were exposed to acetone, a solution of PLGA in acetone, or left untreated. After solvent evaporation, reactions were rehydrated with 15 μL water and incubated for two hours at 37 $^{\circ}\text{C}$ to stimulate production of colicin. A total of 10 μL aliquots of CFPS reactions were added to each well of the prepared microplate of diluted *E. coli* cultures. The *E. coli* culture plate was sealed with a Breathe-Easy oxygen permeable plate sealer (Sigma Z380059). The plate was incubated at 30 $^{\circ}\text{C}$ in a BioTek Synergy Neo2 microplate reader for 24 hrs with linear shaking at 567 cpm, a 1 $^{\circ}\text{C}$ temperature gradient to prevent condensation and evaporation and reading optical density every 2 minutes.

4. DISCUSSION

This work demonstrates that complex CFPS reactions can tolerate both organic solvent and high temperature polymer processing conditions in the lyophilized state. Further, the reactions embedded within polymers PLGA or PCL can be hydrated to carry out a variety of DNA-encoded functions. Formulating bioactivity into polymer composites has far-reaching connotations for both engineering new material functions and modulating the characteristics of the embedded biological systems.

Casting CFPS into polymer materials is a significant step beyond embedding of individual enzymes. Several functionalities can be encoded in materials through gene regulation. Further, optimizing a single formulation for a polymer embedded CFPS system could greatly expand the ability to embed diverse proteins in polymer materials by simply adding different DNA to the system and avoiding exposure of the sensitive protein to the harsh polymer processing steps.

Differences in the hydrophobicity of PCL and PLGA polymers yielded different reactivation behaviors for CFPS. This highlights the potential for polymers to control hydration of the CFPS reaction in a material. One could envision using principles similar to controlled release to control hydration and therefore activate more and more of the CFPS reagents in the material over time. This might be used to extend the overall lifetime of CFPS-driven function in a polymer-CFPS system. Polymer barriers to water infiltration might also be used to extend shelf life. Thirdly, as the heat-cast PCL demonstrates, CFPS could be used to sense and/or repair damage to a material.

Aside from control over water transport, other small molecule transport could be slowed by the surrounding polymer matrix. Controlled transport could be used multiple ways. A material might allow the passage of an analyte of interest for sensing, while preventing infiltration of inhibitory contaminants. Substrates or intermediates might be concentrated locally to enhance the function of an enzyme cascade. Signaling between different bioparticles in a manner similar to quorum sensing could lead to long range or patterned responses to stimuli within a material.

We anticipate future development may include more classes of polymer materials with different properties, advanced formulations of dry cell-free material or casting techniques like fiber spinning briefly explored or layered deposition, and improved studies on the effects of hydration and polymer properties on biomolecule function and transport. Computational modeling will expedite these studies by identifying useful regions of the parameter space.

ACKNOWLEDGMENTS

We gratefully acknowledge experimental assistance with electrospinning from Anne Walker, Kristian Van De Voorde, and Greg Peterson. Funding was provided by the U.S. Army via the Chemical Biological Advanced Materials and Manufacturing Science Program (PE 0601102A Project VR9) at the Combat Capabilities Development Command Chemical Biological Center.

REFERENCES

- [1] Liu, A.P.; Appel, E.A.; Ashby, P.D.; Baker, B.M.; Franco, E.; Gu, L.; Haynes, K.; Joshi, N.S.; Kloxin, A.M.; Kouwer, P.H.J.; Mittal, J.; Morsut, L.; Noireaux, V.; Parekh, S.; Schulman, R.; Tang, S.K.Y.; Valentine, M.T.; Vega, S.L.; Weber, W.; Stephanopoulos, N.; Chaudhuri, O. The living interface between synthetic biology and biomaterial design. *Nat. Mater.* **2022**, *21* (4), pp 390–397.

- [2] Johnston, T.G.; Yuan, S.F.; Wagner, J.M.; Yi, X.; Saha, A.; Smith, P.; Nelson, A.; Alper, H.S. Compartmentalized microbes and co-cultures in hydrogels for on-demand bioproduction and preservation. *Nat. Commun.* **2020**, *11* (1), p 563.
- [3] Li, Z.; Wang, X.; Wang, J.; Yuan, X.; Jiang, X.; Wang, Y.; Zhong, C.; Xu, D.; Gu, T.; Wang, F. Bacterial biofilms as platforms engineered for diverse applications. *Biotechnol. Adv.* **2022**, *57*, p 107932.
- [4] Meng, D.; Mukhitov, N.; Neitzey, D.; Lucht, M.; Schaak, D.D.; Voigt, C.A. Rapid and simultaneous screening of pathway designs and chassis organisms, applied to engineered living materials. *Metab. Eng.* **2021**, *66*, pp 308–318.
- [5] Gonzalez, L.M.; Mukhitov, N.; Voigt, C.A. Resilient living materials built by printing bacterial spores. *Nat. Chem. Biol.* **2020**, *16* (2), pp 126–133.
- [6] Heveran, C.M.; Williams, S.L.; Qiu, J.; Artier, J.; Hubler, M.H.; Cook, S.M.; Cameron, J.C.; Srubar, W.V. Biomineralization and Successive Regeneration of Engineered Living Building Materials. *Matter.* **2020**, *2* (2), pp 481–494.
- [7] Panganiban, B.; Qiao, B.; Jiang, T.; DelRe, C.; Obadia, M.M.; Nguyen, T.D.; Smith, A.A.A.; Hall, A.; Sit I.; Crosby, M.G.; Dennis, P.B.; Drockenmuller, E.; Olvera de la Cruz, M.; Xu, T. Random heteropolymer preserve protein function in foreign environments. *Science.* **2018**, *359* (6381), pp 1239–1243
- [8] Chapman, R.; Stenzel, M.H. All Wrapped up: Stabilization of Enzymes within Single Enzyme Nanoparticles. *J. Am. Chem. Soc.* **2019**, *141* (7), pp 2754–2769.
- [9] Slocik, J.M.; Dennis, P.B.; Kuang, Z.; Pelton, A.; Naik, R.R. Creation of stable water-free antibody based protein liquids. *Commun. Mater.* **2021**, *2* (1).
- [10] Yamada, R.; Higo, T.; Yoshikawa, C.; China, H.; Yasuda, M.; Ogino, H. Random mutagenesis and selection of organic solvent-stable haloperoxidase from *Streptomyces aureofaciens*. *Biotechnol. Prog.* **2015**, *31* (4), pp 917–924.
- [11] Brookwell, A.; Oza, J.P.; Caschera, F., *Biotechnology Applications of Cell-Free Expression Systems. Life (Basel).* **2021**, *11* (12).
- [12] Silverman, A.D.; Karim, A.S.; Jewett, M.C., Cell-free gene expression: an expanded repertoire of applications. *Nat. Rev. Genet.* **2020**, *21* (3), pp 151–170.
- [13] Lee, M.S.; Raig, R.M.; Gupta, M.K.; Lux, M.W. Lyophilized Cell-Free Systems Display Tolerance to Organic Solvent Exposure. *ACS Synth. Biol.* **2020**, *9* (8), pp 1951–1957.
- [14] Nguyen, P.Q.; Soenksen, L.R.; Donghia, N.M.; Angenent-Mari, N.M.; de Puig, H.; Huang, A.; Lee, R.; Slomovic, S.; Galbersanini, T.; Lansberry, G.; Sallum, H.M.; Zhao, E.M.; Niemi, J.B.; Collins, J.J. Wearable materials with embedded synthetic biology sensors for biomolecule detection. *Nat. Biotechnol.* **2021**, *39* (11), pp 1366–1374.
- [15] Blum, S.M.; Lee, M.S.; Mgboji, G.E.; Funk, V.L.; Beabout, K.; Harbaugh, S.V.; Roth, P.A.; Liem, A.T.; Miklos, A.E.; Emanuel, P.A.; Walper, S.A.; Chavez, J.L.; Lux, M.W. Impact of Porous Matrices and Concentration by Lyophilization on Cell-Free Expression. *ACS Synth. Biol.* **2021**, *10* (5), pp 1116–1131.
- [16] Lee, M.S.; Kuhn, D.L.; Blum, S.M.; Gupta, M.K.; Lux, M.W. Extending bio-functionality in materials via controlled polymer erosion. FY20 Proceedings of the U.S. Army Combat Capabilities Development Command Chemical Biological Center In-House Laboratory Independent Research and Surface Science Initiative Programs. **2021**, pp 57–70.
- [17] Niederholtmeyer, H.; Chaggan, C.; Devaraj, N.K. Communication and quorum sensing in non-living mimics of eukaryotic cells. *Nat. Commun.* **2018**, *9* (1), p 5027.
- [18] Levy, M.; Falkovich, R.; Vonshak, O.; Bracha, D.; Tayar, A.M.; Shimizu, Y.; Daube, S.S.; Bar-Ziv, R.H. Boundary-Free Ribosome Compartmentalization by Gene Expression on a Surface. *ACS Synth. Biol.* **2021**, *10* (3), pp 609–619.
- [19] Primo, G.A.; Mata, A. 3D Patterning within Hydrogels for the Recreation of Functional Biological Environments. *Adv. Funct. Mater.* **2021**, *31* (16).
- [20] Ouyang, X.; Zhou, X.; Lai, S.N.; Liu, Q.; Zheng, B. Immobilization of Proteins of Cell Extract to Hydrogel Networks Enhances the Longevity of Cell-Free Protein Synthesis and Supports Gene Networks. *ACS Synth. Biol.* **2021**, *10* (4), pp 749–755.
- [21] Jin, X.; Kightlinger, W.; Hong, S.H. Optimizing Cell-Free Protein Synthesis for Increased Yield and Activity of Colicins. *Methods Protoc.* **2019**, *2* (2).
- [22] Tan, P.; Fu, H.; Ma, X. Design, optimization, and nanotechnology of antimicrobial peptides: From exploration to applications. *Nano Today.* **2021**, *39*.
- [23] Huang, Z.-M.; Zhang, Y.Z.; Kotaki, M.; Ramakrishna, S. A review on polymer nanofibers by electrospinning and their applications in nanocomposites. *Compos. Sci. Technol.* **2003**, *63* (15), pp 2223–2253.

- [24] Zussman, E. Encapsulation of cells within electrospun fibers. *Polym. Adv. Technol.* **2011**, *22* (3), pp 366–371.
- [25] Bundy, B.C.; Swartz, J.R. Site-specific incorporation of p-propargyloxyphenylalanine in a cell-free environment for direct protein-protein click conjugation. *Bioconjug Chem.* **2010**, *21* (2), pp 255–263.
- [26] Pardee, K.; Green, A.A.; Ferrante, T.; Cameron, D.E.; DaleyKeyser, A.; Yin, P.; Collins, J.J. Paper-Based Synthetic Gene Networks. *Cell.* **2014**, *159* (4), pp 940–954.
- [27] Kwon, Y.C.; Jewett, M.C. High-throughput preparation methods of crude extract for robust cell-free protein synthesis. *Sci Rep.* **2015**, *5*, p 8663.

This page intentionally left blank

Protein-sculpted membrane scaffolds as templates for conductive materials towards the development of biological metamaterials

Daniel A. Phillips^a, John R. Biondo^b, Jennifer A. Lee^{a,c}, Patricia E. Buckley^a, Aleksandr E. Miklos^{a*}

^aU.S. Army Combat Capabilities Development Command Chemical Biological Center, Research & Operations Directorate, 8198 Blackhawk Rd., Aberdeen Proving Ground, MD 21010

^bExcet Inc., 6225 Brandon Ave., Suite 360, Springfield, VA 22150

^cDefense Threat Reduction Agency, 8725 John J Kingman Rd. #6201, Fort Belvoir, VA 22060

ABSTRACT

Biology naturally excels at building precise structures at nanometer scales using a variety of biopolymers. Utilizing proteins to control the formation of these nanoscale structures can enable development of biomaterials with metamaterial properties like those found in nature, such as structural coloration. Membrane curvature formation mediated by proteins possessing Bin/Amphiphysin/Rvs (BAR) domains can generate high aspect ratio tubule particles with dimensions that could serve as templates for conductive materials. Incident electromagnetic waves interacting with these materials could behave in metamaterial-like ways. Here, we build on previous work investigating the BAR domain-like protein BdpA by demonstrating membrane binding and remodeling activity *in vitro*. Engineered BdpA truncation mutants were generated to produce a range of membrane sculpting proteins towards the goal of varying tubule sizes in downstream assays. Membranes sculpted with engineered BdpA constructs were incubated with gold nanoparticles to form plasmonic aggregates, and the protein:nanoparticle interaction resulted in a blue-shift of the absorbance spectra. This early research into tunable template scaffolds using membrane sculpting proteins and lipids builds toward the possibility of lightweight, adaptable biological metamaterials.

Keywords: Metamaterials, synthetic biology, membrane sculpting, BAR domain, cell-free, tunable, obscurants

1. INTRODUCTION

A negative index of refraction allows electromagnetic fields to bend in unconventional directions, as demonstrated by optical metamaterials (OMMs).^{1,2} This feature can be harnessed to bend light around an object for optical cloaking technology. OMMs require patterning conductive structures into ordered, three-dimensional arrays on a surface such that the operational electromagnetic wavelength is larger than the spatial interval between the conductive materials.³ A 3D structure must be within 10 to 100 nm in diameter for such materials to alter the way visible light reflects off a surface,³ making synthesis of flexible OMMs that are functional within this range costly and difficult. Surface plasmons are created from the array of conductive materials, causing the incident electromagnetic waves to travel along the surface of an object, rather than reflected back towards the source. Inorganic OMMs are bulky, cumbersome, and are seldom adaptable or responsive. These design constraints pose a significant challenge towards developing an OMM surface coating for the Warfighter at larger scales.

By contrast, examples of OMMs can be found in nature where biology excels at producing micro- and nanoscale ordered structures. Famous examples of these natural OMMs include the blue morpho butterfly wing's brilliant blue color⁷ or the iridescent blue marble berry^{8,9}, both of which are formed through structural coloration. Structural color occurs when non-pigmented but conductive biopolymers are ordered in the same 3D manner as man-made metamaterials. Visible light encounters the surface, but the precise ordering of the structures create a plasmonic effect, selectively reflecting a specific wavelength of light and producing color.^{4,5} Examples of biological structures resulting in metamaterial-like properties (iridescence) can even be found in bacterial colonies.⁶ Biofilms, or clusters of bacterial cells growing on a surface held together by an extracellular polymeric substances composed of DNA, proteins, and sugars, can naturally form a self-healing coating on a surface. Through synthetic biology and engineering, bacterial synthesis of ordered structures could be harnessed to produce cost-effective and scalable methods for producing OMMs.

An in-depth understanding of the individual biological parts is required to make biological OMMs a reality. The brilliant blue color observed in the marble berry is formed through microscale lipid membrane features that give rise to the macroscale structural coloration.^{7,8} Lipids comprise structures and scaffolds throughout all living cells but forming lipids into these precise structures requires the assistance of membrane sculpting proteins or other scaffolding polymers. Membrane sculpting mechanisms are ubiquitous in eukaryotic cells due to the necessity of membrane trafficking, organelle biogenesis, vesicle transport, and protein-lipid scaffolding.^{9,10,11} Among the various membrane sculpting mechanisms, the Bin/Amphiphysin/Rvs (BAR) domain family achieves membrane sculpting activity through electrostatic interactions between positively charged residues on the protein and negatively charged lipids. The intrinsic curvature of the banana-shaped dimers of certain members of the BAR domain family promotes tubule formation through this protein-lipid association.¹¹ Recent attempts at optogenetic control of membrane sculpting utilized light-actuated BAR domain protein activity, resulting in controlled membrane deformation capabilities.¹² We identified a bacterial membrane shaping BAR domain-like protein (BdpA) localized within the conductive outer membrane extensions and vesicles produced naturally by *Shewanella oneidensis*.¹⁴ When expression of this protein is induced in cells, long-distance (>10 μm) outer membrane structures with a diameter less than 100 nm can be generated. These high aspect ratio tubules could be harnessed through synthetic biology with a greater understanding of the biochemical and biophysical activity of their formation.

Here, we show progress towards characterization of the membrane sculpting capabilities of BdpA. Through targeted mutagenesis of this protein, we have purified engineered variants of BdpA towards the goal of altering the physical parameters of the resultant membrane sculpting phenotypes generated through protein-lipid interaction. We show that BdpA binds to membranes through electrostatic interactions. The membrane:protein structures formed through incubation of BdpA variants with purified lipids *in vitro* are then used as templates for plasmonic nanoparticles. Basic research into the ability of BdpA to alter dimensions and aspect ratios of membrane structures could enable the production of tunable biological metamaterials from these membrane scaffolds capable of performing over a range of electromagnetic wavelengths.

2. RESULTS

2.1 Expression and purification of engineered BdpA proteins

2.1.1 Using predictive models to inform BdpA mutagenesis

The predicted model obtained through trRosetta was used to determine sites for initial mutagenesis constructs (Figure 1a). Here, truncation mutants of the 502 amino acid residue protein BdpA were designed to isolate the predicted galactose-binding domain-like (GBD) region and the BAR domain-containing region into individual protein constructs. The GBD-only region consisted of the amino acid residues from positions 23–160, while the BAR-only region spanned amino acid residues 161–502. Predicted models of the individual GBD-only domain (Figure 1b) and BAR-only domain (Figure 1c) domain fragments maintain the similar predicted domain structures comprising the structure model of the full length BdpA protein.

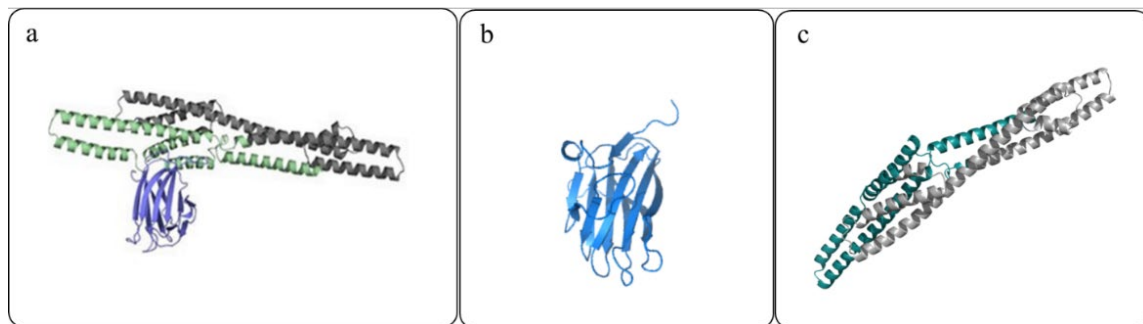


Figure 1. Predicted models of BdpA truncation mutagenesis constructs. a) Full length BdpA with colors corresponding to the predicted domains (blue = GBD, green = BAR). b) GBD-only predicted model showing the characteristic jellyroll fold of a putative galactose-binding domain-like domain. c) BAR-only predicted model with the putative BAR domain region highlighted in green. The green region corresponds to the section of the protein that had homology to other BAR domains found in eukaryotes, while the grey region indicates amino acids that could be included in an updated bacterial BAR domain family.

2.1.2 Immobilized metal affinity chromatography purification and size exclusion chromatography of BAR-only and GBD-only constructs

Poly-histidine tagged expression plasmids with codon-optimized open reading frames corresponding to the amino acid regions detailed above were obtained for both the GBD-only and BAR-only protein constructs and were transformed into *E. coli* Rosetta2 (DE3) cells for expression and protein purification. GBD-only was highly expressed and soluble, and the immobilized metal ion chromatography chromatograms showed a large peak from the protein elution fractions (Figure 2a). SDS-PAGE of the elution fractions showed a highly pure sample, even without downstream polishing chromatography steps (Figure 2b). Expression and purification of the BAR-only construct proceeded in a similar manner. Elution fractions from the BAR-only construct did not demonstrate the same degree of purity following Immobilized Metal Affinity Chromatography (IMAC) purification (Figure 3a) as the GBD-only construct (Figure 2b), so size exclusion chromatography (SEC) was needed. The SEC chromatogram of the BAR-only construct contained seven unique peaks (Figure 3b) that were each analyzed for the presence and purity of the BAR-only protein by SDS-PAGE (Figure 3c). Fraction 2 contained the BAR-only fragment, and the fractions corresponding to that peak were pooled and concentrated for downstream membrane sculpting assays.

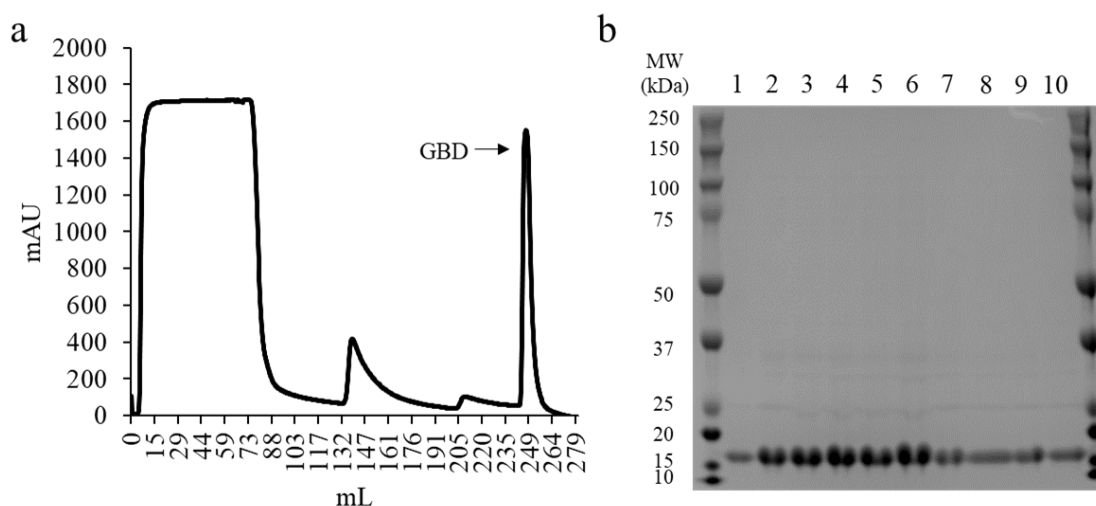


Figure 2. IMAC purification of GBD-only protein construct. a) Chromatogram of absorbance at 280 nm from IMAC purification of GBD-only. The arrow indicates the elution peak. b) SDS-PAGE of the ten 1 mL fractions corresponding to the indicated GBD peak from the chromatogram.

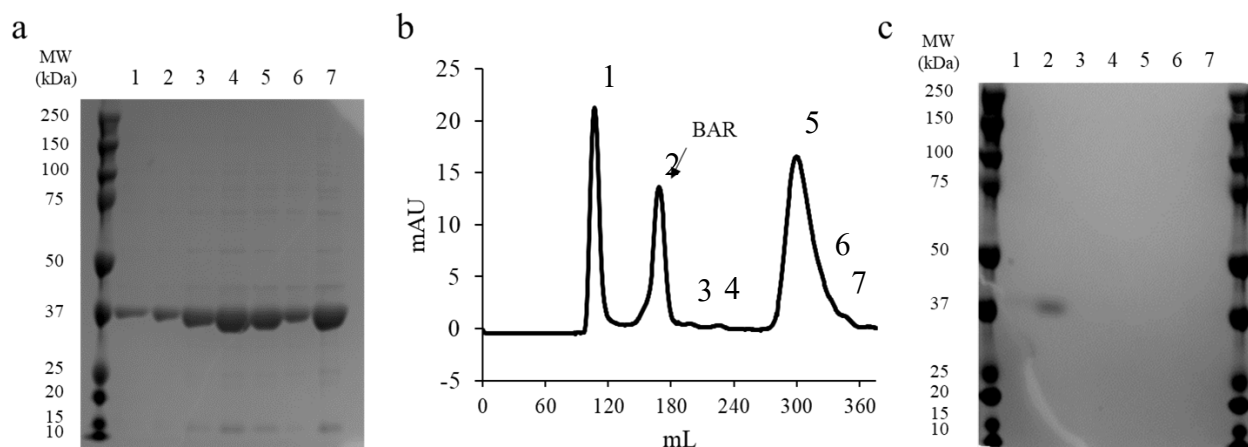


Figure 3. Purification of BAR-only protein construct. a) SDS-PAGE gel of the seven elution fractions from IMAC purification of the BAR-only construct. b) Chromatogram of absorbance at 280 nm from size exclusion chromatography of the pooled elution fractions from the BAR-only IMAC purification. c) SDS-PAGE of the individual peaks from the size exclusion chromatography fractions. Fraction 2 corresponds to the second chromatogram peak indicated with the arrow.

2.2 *In vitro* membrane binding and sculpting activity of BdpA

2.2.1 Liposome cosedimentation

BAR domain-containing proteins bind to lipids through electrostatic interactions. Liposome cosedimentation experiments were performed to demonstrate that BdpA binds to the lipopolysaccharide (LPS) outer membrane of *S. oneidensis* through electrostatic interaction as well, demonstrating BAR domain-like activity of BdpA *in vitro*. Here, liposomes were made using the LPS of *S. oneidensis* and were incubated with purified BdpA protein in buffers containing increasing concentrations of salt. The protein:lipid mixture was centrifuged at high speed to pellet the LPS liposomes. BdpA was detected in the pelleted fraction when co-incubated with the liposomes, and that interaction dissipated with increased concentrations of salt, indicating electrostatic interaction between BdpA and the LPS liposomes (Figure 4).

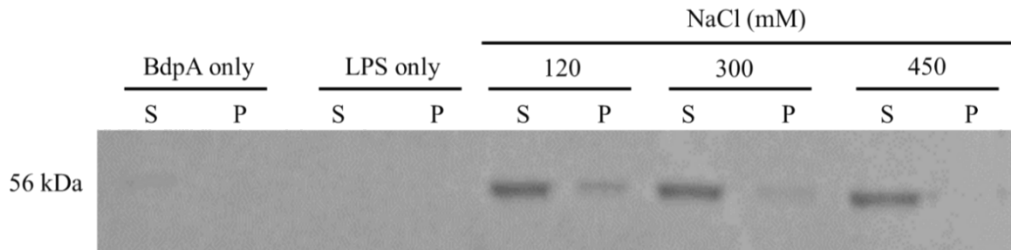


Figure 4. BdpA binds to membranes through electrostatic interactions. In this SDS-PAGE gel of samples following coincubation of BdpA and LPS liposomes, BdpA is detected in both the supernatant (S) and the pellet (P) at lower concentrations of NaCl. At higher salt concentrations, the presence of BdpA in the pellet fraction decreases.

2.2.2 Dynamic light scattering

Through liposome co-sedimentation, we demonstrated that BdpA binds to *S. oneidensis* LPS. Next, we used dynamic light scattering (DLS) to detect changes in the hydrodynamic radius of the LPS liposomes as a result of BdpA binding. This assay facilitates rapid screening of mutagenesis constructs for membrane sculpting activity through the presence of a shift in the diameter of the LPS liposomes following the addition of BdpA. BdpA alone has a predicted monomeric length of 8 nm, or 14.5 nm when measured as a dimer (not shown), which is consistent with the observed diameter measured through DLS (Figure 5). LPS liposomes ranged in diameter from 170–300 nm, but when incubated with BdpA, the observed diameter shifted into three distinct populations: within the range of BdpA alone, at the upper end of the LPS liposome range, or a new population centered around 10 μm . While this technique did not show structural phenotypes, e.g., tubules, it was able to detect a change in diameter when the purified protein and liposomes were incubated together.

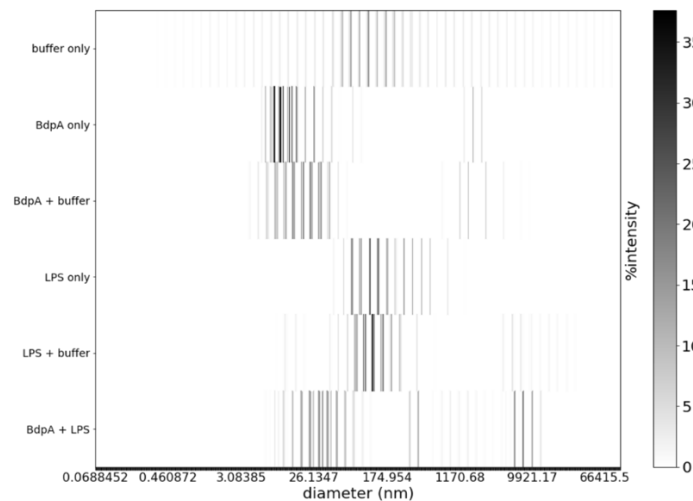


Figure 5. Co-incubation of BdpA with LPS liposomes alters the hydrodynamic radius of the particles. The hydrodynamic radii of BdpA and LPS liposomes were measured by DLS. Bands for each sample ran in triplicate show the diameter of the observed particles in solution, with the darker bands indicating higher intensity of particles at that diameter.

2.2.3 Using sculpted membranes as templates for plasmonic materials

Preliminary tests were performed to determine if membranes sculpted by BdpA could elicit an optical phenotype if used to template gold nanoparticles into ordered structures. Aggregation of gold nanoparticles can alter their plasmonic properties, leading to a shift in absorbance spectra.¹⁴ Gold nanoparticles with a diameter of 15 nm were co-incubated with purified BdpA and BAR-only construct proteins, LPS liposomes, or protein:liposome mixtures, and absorbance spectra were measured. The 15 nm nanoparticles diluted in buffer or incubated in the presence of LPS liposomes alone had a prominent absorbance peak between 700–730 nm, well within the range of red visible light. Addition of purified BdpA, BAR-only, bovine serum albumin (BSA) control, or the protein:lipid mixtures resulted in a blue-shift towards a peak at 530 nm, within the range of green visible light. The appearance of this new peak that was present but less prominent in the gold nanoparticle-only and gold:liposome only samples suggests that aggregation of the nanoparticles through protein interaction caused the shift.

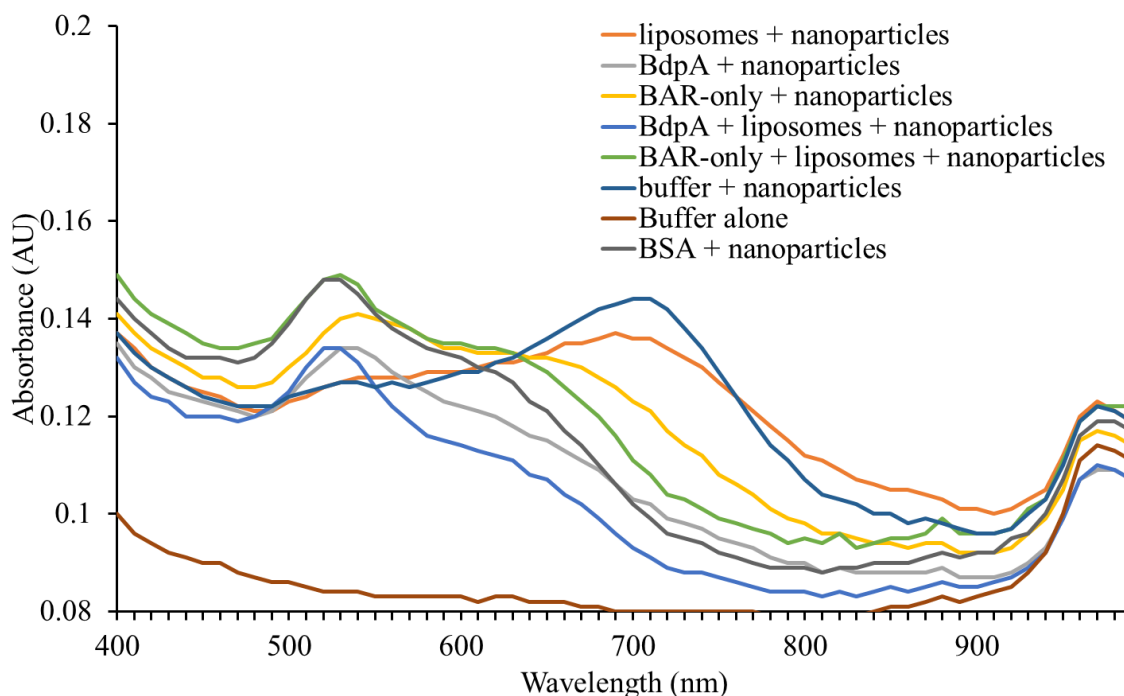


Figure 6. Aggregation of gold nanoparticles in the presence of proteins shifts absorbance spectra. Absorbance spectra was measured for gold nanoparticles in the presence of BAR domain-containing proteins (BdpA and BAR-only), liposomes, protein:lipid mixtures, or BSA and buffer only controls. Protein incubated with the nanoparticles blue-shifts the absorbance spectra towards a prominent peak centered at 530 nm.

3. DISCUSSION

The results shown here hint at the possibility that membrane sculpting could be a viable method towards the production of structural coloration. Preliminary work was performed to demonstrate the feasibility of controlling membrane shapes with proteins to serve as templates for plasmonic materials. BdpA demonstrated *in vitro* membrane sculpting activity by DLS, and the coinubation of protein and liposomes led to downstream work using gold nanoparticles. These assays did not show the morphology of the resultant membrane sculpting phenotypes that could potentially be formed, such as tubules, stacked sheets, or lamellae. Techniques such as cryogenic transmission electron microscopy (cryo-TEM) would provide the most accurate depiction of membrane tubule phenotypes arising from interactions between BdpA and liposomes, which will in turn inform subsequent templating experiments. The present attempts to alter the absorbance spectra of the gold nanoparticles through aggregation could be improved. It is possible that the addition of the nanoparticles results in a loss of tertiary structure of the purified protein, obscuring any potential effect from ordered templating on the protein-sculpted membranes. A buffer with higher protein stability could unmask an ordered phenotype from a purely aggregative one, and ultimately improve the tunability of the resultant structures.

Future attempts will also include de novo formation of nanoparticles from metal salts. Coordination of metal ions through 6x-histidine tags could provide an additive benefit for nucleation of the nascent metal nanoparticles.

4. METHODS

4.1 Protein purification

The codon-optimized BdpA constructs were ordered and cloned into the pET-28(a) expression vector using Gibson assembly with an N-terminal 6x-His tag, GSSGSS linker, and a thrombin cleavage site by Twist Bioscience. Plasmid constructs were transformed into chemically competent *E. coli* Rosetta2(DE3) cells for protein expression. For protein expression, transformed cells were grown as overnight cultures in 30 mL Hyper broth (Athena ES) supplemented with 50 μ M kanamycin and 25 μ M chloramphenicol at 30 °C with 250 rpm shaking. Cultures of 1 L Hyper broth with 50 μ M kanamycin and 25 μ M chloramphenicol were inoculated with 10 mL of the overnight culture and incubated at 37 °C with 250 rpm shaking until an OD₆₀₀ of 1.0 was reached. Cultures were then cooled for 15 minutes in an ice bath, induced with 500 μ M IPTG, and incubated overnight at 16 °C for 16 hours. Cultures were centrifuged, and the cell pellet was resuspended in 100 mL of lysis buffer (50 mM Tris, 500 mM NaCl, 40 mM imidazole, 1% Triton X-100, 1 mM DTT, two tablets of EDTA-free cOmplete protease inhibitor (Millipore Sigma), pH 8.0). Resuspended cells were lysed by microfluidization, centrifuged, and the clarified lysate was filtered through 0.45 μ m filters before loading onto a 5 mL HisTrap Ni-NTA resin column on an AKTExpress (Cytiva) FPLC machine. After loading, the column was washed with Buffer A (50 mM Tris, 500 mM NaCl, 40mM imidazole, 1% Triton X-100, 1 mM DTT, pH 8.0) until the A280 signal stabilized back to baseline. The imidazole gradient was increased to 80 mM until the A280 signal returned to baseline again. Finally, the imidazole concentration was ramped up to 500 mM, and fractions were collected of the purified protein. Fractions containing purified protein were concentrated using Amicon Ultra spin concentrators, molecular weight cut off 10 kDa (Sigma). Secondary purification size exclusion chromatography was performed by injecting 6 mL of the concentrated elution fractions onto a HiLoad Superdex S200 26/60 gel filtration column and collecting fractions. Fractions containing BAR-only and GBD-only were determined by SDS-PAGE. These fractions were pooled, concentrated again using a 10k molecular weight cut off spin concentrator, and the remaining Triton X-100 was desalted out using a HiTrap 5 mL Desalting column. Protein was concentrated to 1 mg/mL aliquots and either used immediately or stored at 4 °C.

4.2 Liposome preparation

For co-sedimentation, DLS, and nanoparticle templating experiments, LPS liposomes were prepared by rehydrating 2 mg of purified *S. oneidensis* LPS with 1 mL of 50 mM Tris, 250 mM NaCl, pH 8.0 buffer. Lipid suspensions were sonicated at 30 °C for 10 minutes while incubating at 30 °C in a water bath sonicator.

4.3 Liposome co-sedimentation

Purified BdpA protein was diluted to 1 mg/mL in the indicated salt concentration buffer, then incubated with 1 mg/mL LPS liposomes at room temperature for 20 minutes. Protein:liposome mixtures were pelleted by centrifugation at 20k x g for 30 minutes. After centrifugation, the supernatant fraction was transferred to a new microcentrifuge tube, and the remaining pellet was resuspended in an equal volume of the dilution buffer. Pellet and supernatant fractions for each sample were assessed for the presence of BdpA by SDS-PAGE.

4.4 Dynamic light scattering

Samples were prepared similar to methods outlined above for liposome co-sedimentation, but the salt concentration of 150 mM NaCl in the buffer was kept constant throughout the experiment. Particles were measured with Wyatt Technology's Möbiuž DLS instrument and DYNAMICS software for data collection and analysis. Custom software was written in Python to visualize the data through Matplotlib.

4.5 Nanoparticle templating and absorbance measurements

As before, samples for nanoparticle templating of protein-sculpted membrane structures were prepared similar to the method described above for liposome cosedimentation. Samples were incubated at a final concentration of 1 mg/mL for both liposomes (5 μ L) and purified proteins (5 μ L) after dilution in 50 mM Tris, 150 mM NaCl, pH 8.0 buffer.

Gold nanoparticles (5 μL) were added each sample where indicated, for a final reaction volume of 15 μL . Absorbance spectra was measured in clear bottom 384 well plates in the Biotek H1 plate reader.

ACKNOWLEDGMENTS

We would like to thank Robert Ernst at the University of Maryland, Baltimore for preparing the purified LPS used in this study. Daniel Phillips and Aleksandr Miklos wrote the proposal, acquired funding, planned, and supervised research, generated predicted structure models, and wrote the report. Daniel Phillips, Jennifer Lee, and John Biondo purified proteins. Daniel Phillips, John Biondo, Jennifer Lee, and Aleksandr Miklos interpreted data. Funding was provided by the U.S. Army via the Chemical Biological Advanced Materials Manufacturing Science program (PE 0601102A Project VR9) at the Combat Capabilities Development Command Chemical Biological Center.

REFERENCES

- [1] Pendry, J.B.; Smith, D.R. Reversing Light With Negative Refraction. *Physics Today*. **2004**, *57* (6), pp 37–43.
- [2] Pendry, J.B.; Schurig, D.; Smith, D.R. Controlling Electromagnetic Fields. *Science*. **2006**, *312* (5781), pp 1780–1782.
- [3] DuFort, C.C.; Dragnea, B. Bio-enabled synthesis of metamaterials. *Annu. Rev. Phys. Chem.* **2010**, *61*, pp 323–344.
- [4] Ruiz-Clavijo, A.; Tsurimaki, Y.; Caballero-Calero, O.; Ni, G.; Chen, G.; Boriskina, S.V.; Martín-González, M. Engineering a Full Gamut of Structural Colors in All-Dielectric Mesoporous Network Metamaterials. *ACS Photonics*. **2018**, *5* (6), pp 2120–2128.
- [5] Yang, W.; Xiao, S.; Song, Q.; Liu, Y.; Wu, Y.; Wang, S.; Yu, J.; Han, J.; Tsai, D-P. All-dielectric metasurface for high performance structural color. *Nat. Commun.* **2020**, *11*, pp 1–8.
- [6] Johansen, V.E.; Catón, L.; Hamidjaja, R.; Oosterink, E.; Wilts, B.D.; Rasmussen, T.S.; Sherlock, M.M.; Ingham, C.J.; Vignolini, S. Genetic manipulation of living bacterial color. *Proc. Natl. Acad. Sci.* **2018**, *115* (11), pp 2652–2657.
- [7] Vignolini, S.; Rudall, P.J.; Rowland, A.V.; Reed, A.; Moyroud, E.; Faden, R.B.; Baumberg, J.J.; Glover, B.J.; Steiner, U. Pointillist structural color in Pollia fruit. *Proc. Natl. Acad. Sci.* **2012**, *109* (39), pp 15712–15715.
- [8] Middleton, R.; Sinnott-Armstrong, M.; Ogawa, Y.; Jacucci, G.; Moyroud, E.; Rudall, P.J.; Prychid, C.; Conejero, M.; Glover, B.J.; Donoghue, M.J.; Vignolini, S. Viburnum tinus Fruits Use Lipids to Produce Metallic Blue Structural Color. *Curr. Biol.* **2020**, *19* (30), pp 3804–3810.
- [9] Daum, B.; Auerswald, A.; Gruber, T.; Hause, G.; Balbach, J.; Kühlbrandt, W.; Meister, A. Supramolecular organization of the human N-BAR domain in shaping the sarcolemma membrane. *J. Struc. Bio.* **2016**, *194* (3), pp 375–382.
- [10] Daumke, O.; Roux, A.; Haucke, V. BAR domain scaffolds in dynamin-mediated membrane fission. *Cell*. **2014**, *156* (5), pp 882–892.
- [11] Frost, A.; Perera, R.; Roux, A.; Spasov, K.; Destaing, O.; Egelman, E.H.; De Camilli, P.; Unger, V.M. Structural basis of membrane invagination by F-BAR domains. *Cell*. **2008**, *132* (5), pp 807–817.
- [12] Jones IV, T.; Liu, A.; Cui, B. Light-Inducible Generation of Membrane Curvature in Live Cells with Engineered BAR Domain Proteins. *ACS Syn. Bio.* **2020**, *9* (4), pp 893–901.
- [13] Simunovic, M.; Evergren, E.; Callan-Jones, A.; Bassereau, P. Curving Cells Inside and Out: Roles of BAR Domain Proteins in Membrane Shaping and Its Cellular Implications. *Annu. Rev. Cell Dev. Bio.* **2019**, *35* (1), pp 111–129.
- [14] Bird, L.J.; Wang, Z.; Malanoski, A.P.; Onderko, E.L.; Johnson, B.J.; Moore, M.H.; Phillips, D.A.; Chu, B.J.; Doyle, J.F.; Eddie, B.J.; Glaven, S.M. Development of a Genetic System for *Marinobacter atlanticus* CP1 (*sp. nov.*), a Wax Ester Producing Strain Isolated from an Autotrophic Biocathode. *Front Microbiol.* **2018**, (9), p 3176.
- [15] Norman, T.J.; Grant, C.D.; Magana, D.; Zhang, J.Z.; Liu, J.; Cao, D.; Bridges, F.; Van Buuren, A. Near Infrared Optical Absorption of Gold Nanoparticle Aggregates. *J. Phys. Chem. B.* **2002**, *106* (28), pp 7005–7012.
- [16] Phillips, D.A.; Zacharoff, L.A.; Hampton, C.M.; Chong, G.W.; Malanoski, A.P.; Metskas, L.A.; Xu, S.; Bird, L.J.; Eddie, B.J.; Miklos, A.E.; Jensen, G.J.; Drummy, L.F.; El-Naggar, M.Y.; Glaven, S.M. A bacterial membrane sculpting protein with BAR domain-like activity. *eLife*. **2021**, *10*, e60049.

This page intentionally left blank

Determination of the influence of tunable chemical environment in metal-organic framework-polymer composites on the absorption of linear nonpolar toxic compounds

Mark J. Varady^a, Gregory W. Peterson^a, Anne Y. Walker^a, Brent A. Mantooth^a,
Adam R. Hinkle^b, Thomas P. Pearl^{a*}

^aU.S. Army Combat Capabilities Development Command Chemical Biological Center, Research & Operations Directorate, 8198 Blackhawk Rd., Aberdeen Proving Ground, MD 21010

^bDCS Corporation, 4696 Millennium Dr., Suite 450, Belcamp, MD 21017

ABSTRACT

This proof-of-concept study addresses the chemical environment at the interfaces present in metal-organic framework-polymer composites and their role in mass transport behavior for permeating molecular contaminants using UiO-66-NH₂ as a prototypical metal-organic framework. While the ultimate focus is on determining the role of interfaces in transport behavior for molecules like sulfur mustard, a systematic understanding of chemical interactions and polymer chain behavior at metal-organic framework-polymer interfaces is crucial. Mass uptake screening measurements were performed for a range of UiO-66-NH₂-polymer combinations including polyvinyl alcohol, polyvinylidene fluoride, polystyrene, polyethylene oxide, and polymethyl methacrylate. Work was done to assess UiO-66-NH₂ Hansen solubility-style parameters, to determine the degree compatibility of the metal-organic framework with different polymers. Atomic force microscopy-based measurements of thin film cross sections were executed to address spatial variations in mechanical properties for UiO-66-NH₂-polymer composites, specifically in the vicinity of UiO-66-NH₂-polymer interfaces. Lastly, the viability of X-ray characterization techniques was investigated (e.g., ultrasmall angle X-ray scattering and X-ray absorption fine structure spectroscopy) to determine structural and chemical bonding variations at the interfaces as a function of polymer type.

Keywords: metal-organic frameworks, polymer composites, interfaces, chemical permeability

1. INTRODUCTION

The development of materials for hazard mitigation and protection applications associated with chemical warfare agents (CWAs) fundamentally relies on understanding chemical-material interactions. For protective coatings, barrier materials, and permeable membranes, which are often composed of polymers or polymer composites, there is a need to better understand how to control (i.e., to suppress or enhance) mass transport. Previous studies looked at the interaction of CWAs and respective simulants with polymeric materials in order to develop more efficacious decontamination processes as well as to contribute to the design of coatings materials (e.g., low gloss paints) to enhance chemical resistance.¹ These composite materials involve the dispersal of solids in polymer matrices to impart specific material properties. Consistently, there has been great difficulty in increasing chemical agent resistance or decreasing retention for linear nonpolar chemicals, such as sulfur mustard. Concurrently, metal-organic frameworks (MOFs) and MOF-polymer composites have been developed and characterized to establish new materials with customizable functionalities and structures, including the ability to specifically address CWA hazards (e.g., barrier materials).^{2,3} Understanding the role of polymer-particle interfaces in chemical transport is of particular importance in the development of coatings or filtration materials. MOFs offer a synthetic handle to modify the polymer-particle interface through controlled functionalization of the MOF crystal surfaces.

There is a need to craft materials systems that present a stronger barrier to chemical absorption including protective paint coatings (as much as 50 μm thick) and conformal thin films (less than 1 μm thick). The underlying structure-property relationships of polymer composites influence transport of incoming analytes, which are informed by the properties of the penetrant chemical and the nature of dispersal of solids in the composite. A systematic study of these interactions is necessary to design and optimize novel polymer composites. Nonpolar molecular species are readily soluble in certain polymer matrices and exhibit entrainment within surface and bulk layer textures. These challenges

exist for a broad class of polymer composites where the solids dispersed in host polymer matrices introduce spatially localized variations in the density and voids in the binder system that can facilitate transport. Molecular size, shape, and functionality of the penetrant chemical are major factors that impact transport and solubility in bulk polymers.⁴ The dispersion of solids or particles and the chemical and physical environments associated with polymer-particle interfaces have been shown to significantly influence the overall chemical transport properties of a composite,^{5,6} including specific MOF examples.⁷

The interface of MOF-polymer composites presents a key challenge since defects often form due to the general incompatibility between nanoparticles and polymers.^{8,9} Within films, and especially thin films (1 μm or less), these defects can dictate permeation through the substrate. Several approaches are available for enhancing the compatibility between MOFs and polymers, thereby reducing interfacial defects. Growing polymers from the MOF (i.e., polymer@MOF) is an excellent technique for achieving low-defect composites. In this approach, the MOF typically is modified with a polymerizable monomer (e.g., an acrylate) and then subsequently polymerized in solution. While effective, this approach has drawbacks associated with larger scale production and has not yet led to high molecular weight polymers that are required for effective films. A more facile approach is to modify the external crystal of MOFs with functional groups that are compatible with the polymer of interest.

The overall objective of this project is to develop a systematic understanding of how physicochemical environment in polymer-based composites facilitates absorption and transport of specific types of penetrants/agents. Figure 1 shows the relevant aspects of the systems under study in a schematic cross-sectional view, including presence of polymer, MOF crystals, resultant MOF-polymer interfaces, and a penetrant permeating the bulk of the film. To engender a root-level understanding of what characteristics of composite thin films would promote enhanced transport for linear nonpolar molecules, we have proposed to use functionalized MOFs incorporated into various polymer films to control the chemical environment at the interfaces between MOF crystals and the polymer. Through this work, we will develop an understanding of how to tune MOF-polymer interfaces to control transport in other polymer composite materials. The chemical interactions that dictate the transport behavior for specific chemical species will be interrogated with a combination of experimental tools and modeling methods, which should reveal structure-property relationships that will enable the design of superior barrier materials. Polymer chain interactions with the MOF particle periphery, including pore blockage and penetration, produce interfaces in MOF-polymer composites that can determine chemical permeability of sulfur mustard (HD) in thin films (i.e., greater/lesser disruption of bulk polymer mechanical properties at interfaces will result in less/more chemical resistance). *The objective of the work is not to optimize a single MOF-polymer system but to understand what factors are most influential in driving transport behavior for a specific class of penetrant.*

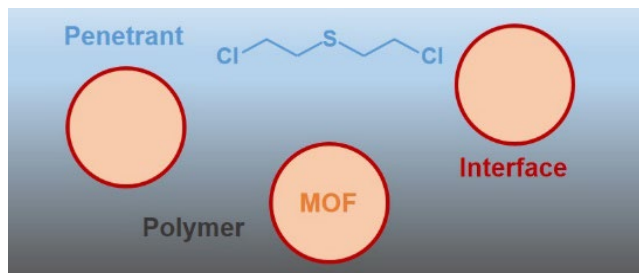


Figure 1. Illustration of the material cross section to specify main components in a MOF-polymer composite as well as the principal penetrant type of interest.

For this proof-of-concept study, a single MOF and a set of polymers with backbone functionalities that we predict will interact in a range of fashions with the MOF have been chosen. UiO-66-NH₂ was prioritized as the principal MOF since it is well-studied and employed in the relevant application areas,^{2,3,10} can be synthesized with controlled crystal shapes and sizes less than 200 nm (which is important for thin films such that crystals do not transverse the film), and is one of the most stable MOFs known.¹¹ The thickness of the interfacial region between the MOF and polymer where defects may occur can be on the order of 1–100 nm from the particle surfaces. A suite of experiments and techniques were explored to provide indirect indications of the presence of the defects at the interface to inform physical properties of, and transport within, composite films. We have identified polymers that have a variety of functionalities to explicitly tune MOF-polymer interactions and bulk film properties (e.g., density, absorption properties, surface energy, etc.). The different functional groups and polymer backbones of the chosen polymers will change the inherent solubility parameters (i.e., dispersion, polarity, and hydrogen bonding), which should translate to a variety of thermodynamic and kinetic effects for diffusion of probe molecules. In order to study which factors drive transport

behavior, a stepwise characterization of these materials is necessary and is aligned to the objective of this work. Figure 2 highlights what factors need to be considered in building an understanding of interfacial effects on mass transport and chemical concentration distributions.

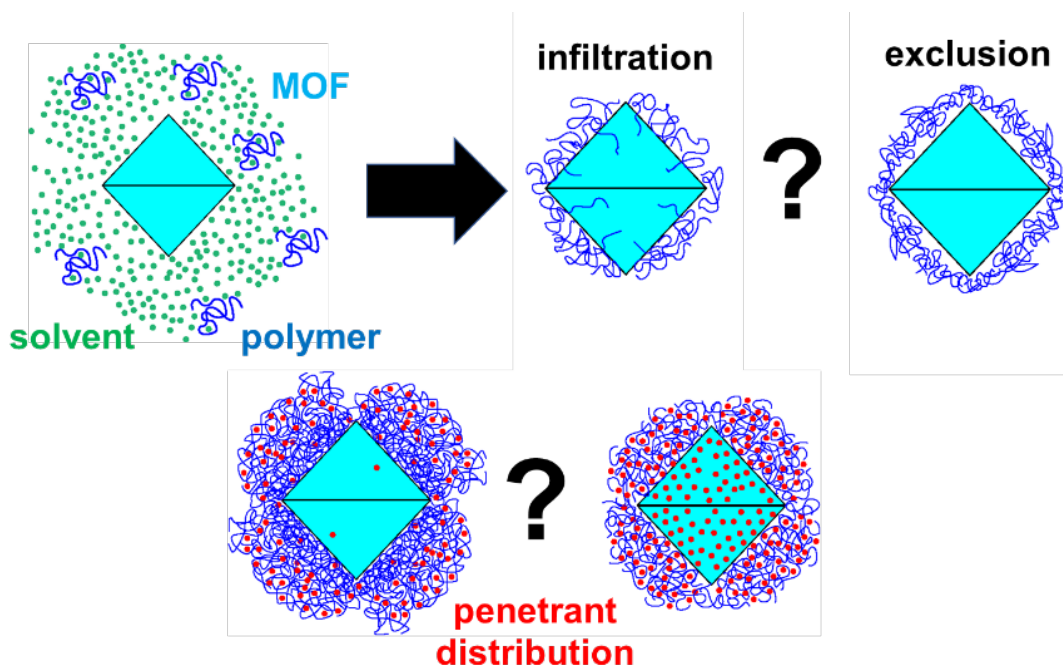


Figure 2. Key relationships to determine for chemical penetrants in MOF-polymer systems. Top: Given a polymer (blue) dispersed in a solvent (green) in the vicinity of a MOF crystal (aqua), polymer chains can infiltrate the MOF pores or collapse on the periphery of the MOF. **Bottom:** For a chemical penetrant (red) permeating through the MOF-polymer composite, the penetrant concentration can remain localized in the polymer or redistribute between MOF and polymer.

2. MATERIALS AND METHODS

2.1 MOF-polymer composite films preparation

Materials involved the use of UiO-66-NH₂ MOF crystals (two different nominal crystal sizes or diameters, 200 nm (NuMat Technologies) and 2 μm (TDA Research, Inc.)) incorporated into polymers to generate cast thin films at variable loading levels (5 and 10 wt%), see Figure 3. All films involved dispersing MOF crystal in polymers of interest (dilute solutions using polymer-specific solvents), including polyvinyl alcohol, polyvinylidene fluoride (PVDF), polystyrene (PS), polyethylene oxide (PEO), and polymethyl methacrylate (PMMA), then these solutions were drawn down on dewetting surfaces (e.g., Teflon®) to a wet film thicknesses of approximately 250 μm resulting in films that were less than 100 μm thick when cured (thicker films were also produced selectively). Details of similar sample preparations have been published elsewhere.^{2,12} Attenuated total reflectance-Fourier transform infrared (ATR-FTIR) spectroscopy, scanning electron microscopy (SEM), and optical microscopy were used to confirm film composition and distribution of MOF crystals in the polymers. These films were either used as received without further conditioning in mass uptake screening evaluations or cross sectioned for atomic force microscopy (AFM) measurements. To directly measure MOF-polymer interfaces, films were cross sectioned using a Leica EM UC7 ultramicrotome. Composite films were rough-cut to expose the cross section, then cooled (e.g., -80 °C) and cut with a glass knife before performing a finishing cut using thin (150 nm) slices with a diamond knife (45 deg, Diatome). Cross sectioned samples were temperature equilibrated for at least 24 h prior to AFM imaging to relieve any stress induced by the cutting process.

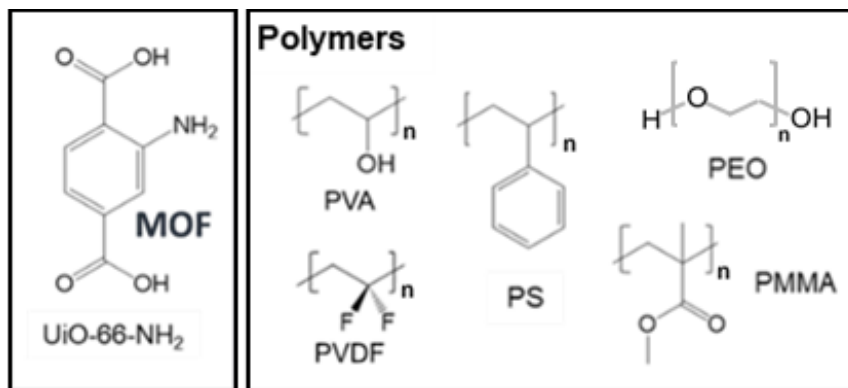


Figure 4. Organic linker associated with UiO-66-NH₂ MOF and polymers involved in study.

2.2 Analytical chromatography for probe molecule mass uptake

We utilized a relatively facile means of quantifying mass uptake for materials under study, useful for the purpose of screening and relative comparisons, to assess whether the spectrum of materials configurations would respond differently with respect to absorbed chemical mass. The experimental set-up involved long duration exposure (~18 h) of composite films to vapor emanating from a proximal evaporating droplet in a closed cell. This approach is similar to the measurement of water absorption in hygroscopic materials,¹³ but instead of tracking droplet evaporation, the mass transfer to the material is measured by analysis of extraction solutions. Briefly, liquid contaminant (100 μ L) was placed in an aluminum foil well at the center of ground glass container (with a matching glass lid to seal the volume) large enough to hold the well and as many as 10 pieces of composite material (each piece approximately 1 cm², nominal mass 5 mg). To assess the contaminant mass uptake from vapor after exposure, the films were removed and immersed in contaminant-specific solvents to extract chemical mass from the films. Liquid-phase extraction solutions were analyzed by chromatography to evaluate material retention of chemical species. Extraction solution samples were diluted, and the analytes were quantified using gas chromatography (GC) for all probe molecules, including, dichlorohexane (DCH), methyl salicylate (MeS), diethylmalonate (DEM), and bis(2-chloroethyl) sulfide (distilled mustard, HD) (typical instrument, model 6890/7890 GC system equipped with a model 5975 mass selective detector [Agilent Technologies; Santa Clara, CA]). Details on the use of the chromatography platforms are published elsewhere.¹⁴ A variety of verification steps, including gravimetric measurements, were taken to ensure that the measurement of absorbed chemical mass per mass of composite film was not unduly influenced by trapping of chemical in MOF crystal pores or insufficient extraction.

2.3 Turbidity measurements

In order to perform a Hansen solubility parameter-style assessment of UiO-66-NH₂, turbidity (i.e., suspension opacity) as a function of time on suspensions was employed using a set of solvents appropriate for determination of Hansen solubility parameters.¹⁵ The basic procedure involved preparation of 10 mL of 10 mg mL⁻¹ suspensions of UiO-66-NH₂ in each probe solvent, then mixing with Scilogex homogenizer (setting 1.5) for 2 mins. Suspensions were transferred to measurement cuvettes and placed in a turbidimeter measurement chamber (Hanna Instruments HI-88713 ISO turbidity meter) to record turbidity values over the course of multiple days. The subsequent analysis involved plotting normalized (to $t = 0$ measurement) turbidity versus time curves for all solvents then rank ordering and assigning values of 1 to 6, where 1 corresponds to a long time constant, i.e., MOF wants to stay in suspension, and six corresponds to a short time constant, i.e., MOF crashes out quickly. A time frame was established over which there was significant variation associated with different groups of solvents and these values were used in Hansen solubility parameter software (Hansen Solubility Parameters in Practice (HSPiP)) to ultimately determine MOF solubility parameters.

2.4 Atomic force microscopy and spectroscopy

AFM-based imaging of composite cross sections was performed with amplitude modulation (AM) – frequency modulation (FM)^{16,17} and measurement of loss tangent^{18,19} (Molecular Force Probe (MFP)-3D, Asylum Research). Typical cantilevers were either Oxford Instruments AC200TS ($k \sim 9$ N/m, $f_1 \sim 115$ kHz, $f_2 \sim 690$ kHz) or Applied NanoStructures ACLA ($k \sim 36$ Nm⁻¹, $f_1 \sim 190$ kHz, $f_2 \sim 1.14$ MHz). In each case, the cross sectioned composite sample was placed on a temperature control stage and allowed to equilibrate. After thermal equilibration of the sample, the

AFM tip was brought into contact with the sample then retracted slightly before tuning the operating frequencies to ensure that the cantilever was driven at resonance during the imaging scans. Analysis of all images was performed in MATLAB™ (R2019b). Typical data acquisition involved collecting overview images over a $\sim 20 \times 20 \mu\text{m}^2$ area to identify particles that had been cleanly cross sectioned, then smaller areas at $\sim 5 \times 5 \mu\text{m}^2$ and $\sim 1.5 \times 1.5 \mu\text{m}^2$ to better spatially resolve the interfacial regions around the sectioned particles. Analyzed images were either 512×512 or 1024×1024 pixels. Topography (Z) and phase (ϕ_1) are the standard outputs from AM-AFM, commonly known as tapping mode, in which the tip-sample distance is adjusted to maintain a constant cantilever oscillation amplitude. Variation in ϕ_1 over the sample is indicative of material property variations, although this information is also convolved with tip-sample interaction, which can be influenced by factors like adhesion and capillary forces. AM-FM AFM involves an additional higher frequency resonance (typically the first harmonic) at a much lower oscillation amplitude and maintains this at resonance (90 deg phase) by adjusting the drive frequency while also maintaining the oscillation amplitude by adjusting the drive voltage. The difference between the free resonance and modulated frequency (Δf_2) provides information on the sample stiffness (stiffer samples cause higher frequency shift) while the variation in drive voltage (dissipation, A_2) provides information on vibrational energy loss in the sample (higher dissipation means greater loss). Additionally, nanoindentation measurements using AFM were performed along line profiles or in 2D grids as a means of resolving local mechanical properties.

3. RESULTS AND DISCUSSION

3.1 Screening of materials

From the drawdown films produced, a set of screening experiments were performed to assess the degree of measurable mass uptake when the MOF-polymer films were exposed to chemical probe vapor. This measurement, along with a survey of the drawdown films using ATR-FTIR, SEM, and optical microscopy provided an overview of the degree of variation that would be expected in transport response as a function of different polymers chosen. An illustration of this measurement is shown in Figure 4, which involved 2 mm diameter UiO-66-NH₂ MOF crystals. As illustrated in the variability gauge chart, there are cases where the inclusion of MOF in the polymer film caused an increase (red), decrease (green), or no change (yellow) in mass uptake. Both the magnitude of the mass uptake as well as the variation in mass uptake response as a function of polymer type serve as useful indicators for upcoming experiments that utilize higher time resolution tools, e.g., ATR-FTIR and quartz crystal microbalance (QCM),^{20,21} for tracking absorption and desorption profiles. Based in part on the results of these screening measurements as well as discussions on challenges associated with using PEO for this MOF-centric study, PEO was ultimately removed from the set of polymers to be considered.

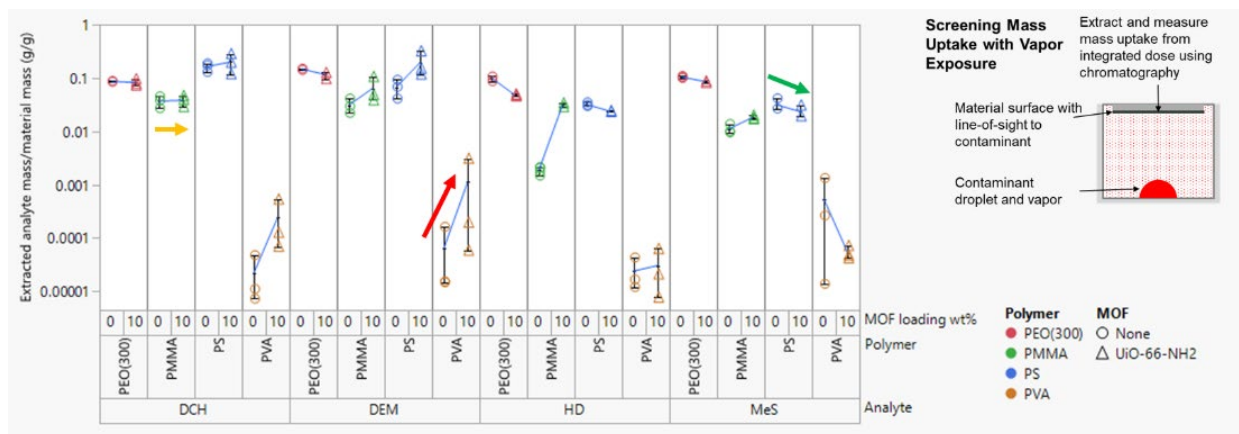


Figure 5. Relative mass uptake as quantified by mass of analyte per mass of polymer film for polymers with and without dispersed UiO-66-NH₂ crystals.

Hansen solubility-style parameters were acquired for 200 nm diameter UiO-66-NH₂ crystals based on time-dependent turbidity measurements involving MOF crystals dispersed in a specific set of probe chemicals designed to predict chemical interaction types. Figure 5 shows the data collected and the rank ordering that was assigned to the different groups of solvents that resulted in more (1) to less (4) affinity of the MOF for the solvent.

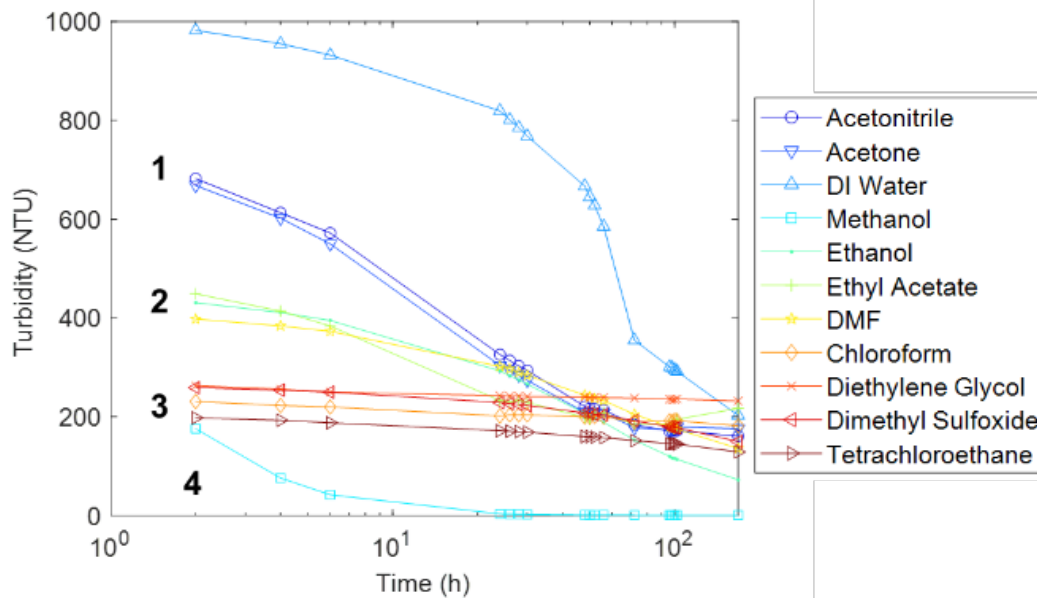


Figure 6. Turbidity measurements for UiO-66-NH₂ in probe chemicals. Rank ordering specifies more to less relative affinity of the MOF to the solvent based on tendency of the MOF to stay in suspension rather than precipitate out.

Based on these turbidity measurements, the position and size of the solubility sphere for UiO-66-NH₂ in Hansen solubility parameter space (δ_D , δ_P , δ_H) was determined through HSPiP to be $\delta_D=13.9$, $\delta_P=11.7$, $\delta_H=11.8$, with $\delta_{Total}=21.6$ and $R=9.0$. The Hansen solubility parameters describe the dependence of molecular, polymer, and nanoparticle properties like solubility and diffusion on dispersion (δ_D , van der Waals), polarity (δ_P , related to dipole moment), and hydrogen bonding (δ_H) type chemical interactions. Given Hansen solubility parameters for polymers of interest (available in HSPiP software databases) and UiO-66-NH₂, it is possible to calculate the relative energy difference (RED) values between UiO-66-NH₂ and different polymers using Equation (1). The RED in Hansen solubility parameter space estimates relative compatibility and the variation in RED values shown in Table 1 suggests a range of possible interactions between UiO-66-NH₂ and the set of polymers chosen that is anticipated to result in different interface types.

$$RED = \frac{1}{R^{MOF}} \sqrt{(\delta_D^{MOF} - \delta_D^{pol})^2 + (\delta_P^{MOF} - \delta_P^{pol})^2 + (\delta_H^{MOF} - \delta_H^{pol})^2} \quad (1)$$

Table 1. List of Hansen Solubility Parameters for polymers of interest and computation of relative energy difference (RED) between UiO-66-NH₂ and polymers.

Polymer	δ_D (MPa ^{0.5})	δ_P (MPa ^{0.5})	δ_H (MPa ^{0.5})	MOF-Polymer RED
PVDF	17	12.1	10.2	0.39
PEO	17	11	5.2	0.81
PMMA	18.1	10.5	5.1	0.89
PVOH	15	17.2	17.8	0.91
PVC	17.6	7.8	3.4	1.11
PS	18	5	5	1.15

3.2 Characterization of interfaces

AFM was used to probe interfaces between MOF crystals and the host polymer, including measurements of local variations in mechanical properties. An example is shown in Figure 6 and Figure 7 for UiO-66-NH₂ dispersed in polystyrene. As part of these measurements, spatially resolved stiffness/elasticity and dissipation as well as topography and loss tangent were recorded as illustrated in Figure 6. The modulus difference between polystyrene and UiO-66-NH₂ is readily apparent as shown by the nanoindentation measurements along the light blue profile in Figure 7 highlighted in the topography image, which crosses the MOF-polymer boundary. However, the interface has proven to be more difficult to resolve and may be very narrow spatially. Likewise, there are probing considerations that need to be addressed to permit proper deconvolution of response of force-based sensors in regions with greater disparities in local mechanical properties. Work is on-going to develop sample preparation protocols that will permit cross sectional interfaces to be more amenable to local measurements based on force microscopy and spectroscopy.

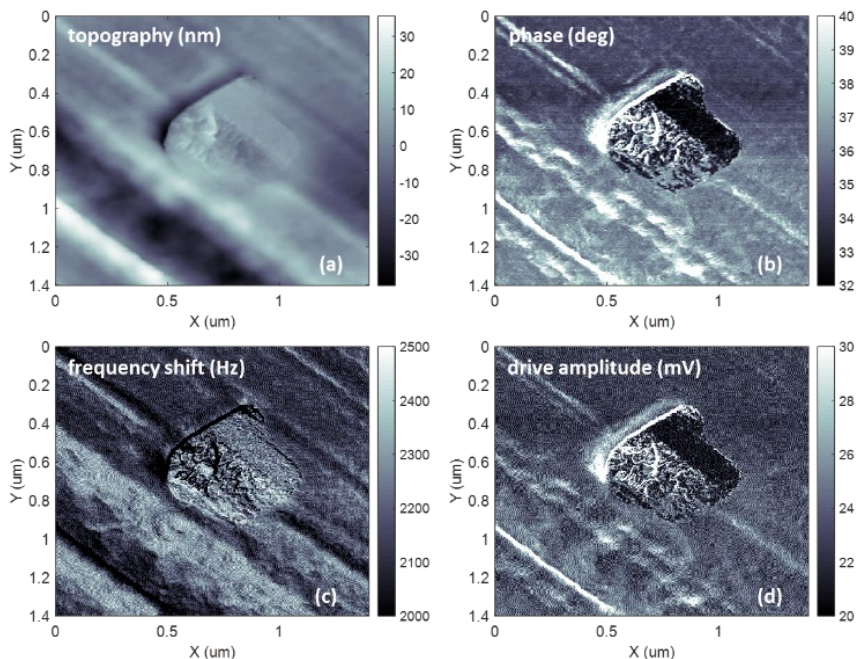


Figure 7. AM-FM AFM measurements to assess variations in mechanical properties in a MOF-polymer cross section. Each data channel can be associated with different materials properties including morphology in topography (a), loss tangent derived from phase (b), stiffness from frequency shift (c), and dissipation in drive amplitude (d).

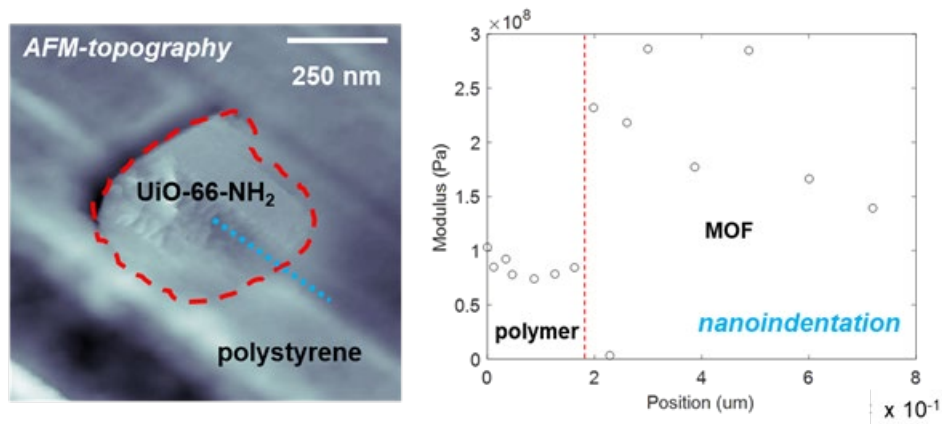


Figure 8. Viscoelastic AFM measurements to resolve interfaces MOF-polymer interfaces revealed in the thin film cross section for UiO-66-NH₂ dispersed in polystyrene. Left: AFM topography image with red outline highlighting the boundary between MOF and polymer regions. Right: modulus measurements performed by local nanoindentation measurements along the light blue profile shown in the topography image.

Work was done on assessing the challenges associated with using AFM-based methods for addressing interfaces in composites. Recent experimental and computational research on polyurethane-silica composites has shown there are numerous technical considerations with regards to quantifying the degree of integration of solids in polymer matrices as evidenced by spatially resolved transitions at interfaces. These efforts follow from recent advances in the use of local probes to resolve materials properties, especially for conjoined, dissimilar constituents.^{22,23}

As part of pursuing complementary means of quantifying the structure of buried interfaces in composites, X-ray scattering and absorption measurements have been pursued and are an active area of work. Collaboration with the National Institute of Standards and Technology (NIST) and Argonne National Laboratory (ANL) Advanced Photon Source (APS) has been developed in this work for the purpose of determining the utility of different X-ray-based measurements for resolving interfacial characteristics in MOF-polymer composites as a function of thin film processing conditions. Specifically, NIST received MOF and polymer materials from U.S. Army Combat Capabilities Development Command Chemical Biological Center (DEVCOM CBC) to conduct ultrasmall angle X-ray scattering measurements aimed at resolving shape and structure driven by MOF dispersal in polymers^{24,25} and DEVCOM CBC scientists participated in X-ray absorption fine structure measurements at the ANL APS to assess chemical bonding or interactions by measure of radial distribution functions.²⁶ These experiments are in-progress and will directly inform the work that has been conducted; both efforts are the direct result of leveraging on-going efforts in current externally funded DEVCOM CBC research programs.

4. CONCLUSIONS AND FUTURE WORK

Work is in-progress on the characterization of buried interfaces for a range of UiO-66-NH₂-polymer composites using a set of complementary experimental tools. Two main objectives have been pursued: (1) identification and confirmation of a set of UiO-66-NH₂-polymer combinations that will exhibit a range of chemical mass uptake responses and (2) measurement of variable interface characteristics for that set of UiO-66-NH₂-polymer combinations due to the interaction between polymer chains and the MOF crystals.

Future work will focus on continuation of work on interface characterization that will be paired with mass transport measurements. To address the influence of molecular structure in the limit of nonpolar, linear species, retention and transport will be measured for a range of penetrant chemicals related to HD. Recent efforts have illustrated that simulants and agents absorb into the topcoat layers of military relevant coatings (composites),¹ via molecular diffusion.^{27,28} Previously, QCM and ATR-FTIR spectroscopy were used to characterize sorption of a penetrant chemical into different bulk polymers to probe penetrant-polymer interactions.^{20,21,29,30} QCM measures the rate and extent of sorption into the polymer as the concentration of a penetrant vapor is exposed to the polymer, while ATR-FTIR enables the characterization penetrant-polymer molecular interactions.²¹ The penetrant chemicals will be used to explore the transport properties through defective and defect-free composites. Recent work has illustrated that there can be strong correlations between the transport characteristics and mechanical characteristics (e.g., T_g , molecular weight between crosslinks (M_c), etc.) of nanocomposites. We will crosswalk the QCM results with dynamic mechanical analysis to investigate these correlations.^{9,31}

Additionally on the horizon, computational modeling will be used to complement the experimental efforts by examining of transport properties at the molecular scale in MOF-polymer composites using atomistic simulations. We will study diffusive transport primarily through molecular dynamics calculations where special attention is given to the MOF-polymer interface and surface morphology of the MOF. Recent work has revealed a strong dependence of the composite's structure on the interfacial connectivity,²¹ which in turn can greatly affect permeability and selectivity in the presence of diffusive penetrants.^{6,32} The first stage of modeling will focus on understanding the compatibility of UiO-66-NH₂ and select polymers as characterized by the mass density at the interface, polymer rigidity, porosity, and percolation of voids and other defects. Quantitative comparisons of these properties will be made to those of the bulk polymer, and these results will inform subsequent calculations of transport of gaseous species. Both equilibrium and non-equilibrium methods will be used to directly probe transport behavior. This includes the possibility of performing concentration gradient-driven molecular dynamics, which is a novel method of simulating transport separation of fluids through membranes that has been shown to be more accurate than the traditional technique of equilibrium molecular dynamics combined with grand canonical Monte Carlo.³²⁻³⁴

ACKNOWLEDGMENTS

The authors thank colleagues in Decontamination Sciences, CBR Filtration, and Respiratory Protection Branches at DEVCOM CBC who supported this effort. Funding was provided by the U.S. Army via the Chemical Biological Advanced Materials and Manufacturing Science Program (PE 0601102A Project VR9) at DEVCOM CBC.

REFERENCES

- [1] Cooley, K.A.; Pearl, T.P.; Varady, M.J.; Mantooth, B.A.; Willis, M.P. Direct Measurement of Chemical Distributions in Heterogeneous Coatings. *ACS Appl. Mater. Interfaces*. **2014**, *6* (18), pp 16289–16296.
- [2] Peterson, G.W.; Browe, M.A.; Durke, E.M.; Epps, T.H. Flexible SIS/HKUST-1 Mixed Matrix Composites as Protective Barriers against Chemical Warfare Agent Simulants. *ACS Appl. Mater. Interfaces*. **2018**, *10* (49), pp 43080–43087.
- [3] Peterson, G.W.; Wang, H.; Au, K.; Epps, T.H. Metal-Organic Framework Polymer Composite Enhancement via Acyl-Chloride Modification. *Polym. Int.* **2021**, *70* (6), pp 783–789.
- [4] Kwan, K.S.; Subramaniam, C.N.P.; Ward, T.C. Effect of penetrant size and shape on its transport through a thermoset adhesive: I. n-alkanes. *Polymer*. **2003**, *44* (10), pp 3061–3069.
- [5] Jancar, J.; Douglas, J.F.; Starr, F.W.; Kumar, S.K.; Cassagnau, P.; Lesser, A.J.; Sternstein, S.S.; Buehler, M.J. Current issues in research on structure-property relationships in polymer nanocomposites. *Polymer*. **2010**, *51* (15), pp 3321–3343.
- [6] Keskin, S.; Altinkaya, S.A. Review on Computational Modeling Tools for MOF-Based Mixed Matrix Membranes. *Computation*. **2019**, *7* (3), p 36.
- [7] DeCoste, J.B.; Denny, M.S.; Peterson, G.W.; Mahle, J.J.; Cohen, S.M. Enhanced aging properties of HKUST-1 in hydrophobic mixed-matrix membranes for ammonia adsorption. *Chem. Sci.* **2016**, *7* (4), pp 2711–2716.
- [8] Denny, M.S.; Moreton, J.C.; Benz, L.; Cohen, S.M. Metal-organic frameworks for membrane-based separations. *Nat. Rev. Mater.* **2016**, *1* (12), p 16078.
- [9] Semino, R.; Moreton, J.C.; Ramsahye, N.A.; Cohen, S.M.; Maurin, G. Understanding the origins of metal-organic framework/polymer compatibility. *Chem. Sci.* **2018**, *9* (2), pp 315–324.
- [10] Palomba, J.M.; Wirth, D.M.; Kim, J.Y.; Kalaj, M.; Clarke, E.M.; Peterson, G.W.; Pokorski, J.K.; Cohen, S.M. Strong, Ductile MOF-Poly(urethane urea) Composites. *Chem. Mater.* **2021**, *33* (9), pp 3164–3171.
- [11] DeCoste, J.B.; Peterson, G.W.; Jasuja, H.; Glover, T.G.; Huang, Y.G.; Walton, K.S. Stability and degradation mechanisms of metal-organic frameworks containing the $Zr_6O_4(OH)_4$ secondary building unit. *J. Mater. Chem. A*. **2013**, *1* (18), pp 5642–5650.
- [12] Peterson, G.W.; Lu, A.X.; Hall, M.G.; Browe, M.A.; Tovar, T.; Epps, T.H. MOFwich: Sandwiched Metal-Organic Framework-Containing Mixed Matrix Composites for Chemical Warfare Agent Removal. *ACS Appl. Mater. Interfaces* **2018**, *10*, pp 6820–6824.
- [13] Shukla, P.; Jagdhari, T.; Fugaro, A.P.; Boreyko, J.B. Characterizing Hygroscopic Materials via Droplet Evaporation. *Langmuir*. **2020**, *36*, pp 1871–1877.
- [14] Shue, M.; Lalain, T.; Mantooth, B.; Humphreys, P.; Hall, M.; Smith, P.; Sheahy, M. *Low-Level Analytical Methodology Updates to Support Decontaminant Performance Evaluations*; ECBC-TR-883; U.S. Army Edgewood Chemical Biological Center: Aberdeen Proving Ground, MD, 2011. UNCLASSIFIED Report, Public Release (ADA546021).
- [15] Elangovan, D.; Nidoni, U.; Yuzzay, I.E.; Selke, S.E.M.; Auras, R. Poly(l-lactic acid) Metal Organic Framework Composites. Mass Transport Properties. *Ind. Eng. Chem. Res.* **2011**, *50* (19), pp 11136–11142.
- [16] Kocun, M.; Labuda, A.; Meinhold, W.; Revenko, I.; Proksch, R. Fast, High Resolution, and Wide Modulus Range Nanomechanical Mapping with Bimodal Tapping Mode. *ACS Nano*. **2017**, *11* (10), pp 10097–10105.
- [17] Labuda, A.; Kocun, M.; Meinhold, W.; Walters, D.; Proksch, R. Generalized Hertz model for bimodal nanomechanical mapping. *Beilstein J. Nanotechnol.* **2016**, *7*, pp 970–982.
- [18] Proksch, R.; Kocun, M.; Hurley, D.; Viani, M.; Labuda, A.; Meinhold, W.; Bemis, J. Practical loss tangent imaging with amplitude-modulated atomic force microscopy. *J. Appl. Phys.* **2016**, *119* (13), p 134901.
- [19] Proksch, R.; Yablon, D.G. Loss tangent imaging: Theory and simulations of repulsive-mode tapping atomic force microscopy. *Appl. Phys. Lett.* **2012**, *100* (7), p 073106.

- [20] Boyne, D.A.; Varady, M.J.; Lambeth, R.H.; Eikenberg, J.H.; Bringuier, S.A.; Pearl, T.P.; Mantooh, B.A. Solvent-Assisted Desorption of 2,5-Lutidine from Polyurethane Films. *J. Phys. Chem. B.* **2018**, *122* (7), pp 2155–2164.
- [21] Varady, M.J.; Boyne, D.A.; Pearl, T.P.; Lambeth, R.H.; Mantooh, B.A. Composition-dependent Multicomponent Diffusivity of 2,5-Lutidine with Acetonitrile in Polyurethane. *Polymer.* **2019**, *180*, p 121697.
- [22] Collinson, D.W.; Eaton, M.D.; Shull, K.R.; Brinson, L.C. Deconvolution of Stress Interaction Effects from Atomic Force Spectroscopy Data across Polymer-Particle Interfaces. *Macromolecules.* **2019**, *52* (22), pp 8940–8955.
- [23] Collinson, D.W.; Sheridan, R.J.; Palmeri, M.J.; Brinson, L.C. Best practices and recommendations for accurate nanomechanical characterization of heterogeneous polymer systems with atomic force microscopy. *Prog. Polym. Sci.* **2021**, *119*, p 101420.
- [24] Zhang, F.; Ilavsky, J. Ultra-Small-Angle X-ray Scattering of Polymers. *J. Macromol. Sci., Polym. Rev.* **2010**, *50*, pp 59–90.
- [25] Danielsen, S.P.O.; Beech, H.K.; Wang, S.; El-Zaatari, B.M.; Wang, X.; Sapir, L.; Ouchi, T.; Wang, Z.; Johnson, P.N.; Hu, Y.; Lundberg, D.J.; Stoychev, G.; Craig, S.L.; Johnson, J.A.; Kalow, J.A.; Olsen, B.D.; Rubinstein, M. Molecular Characterization of Polymer Networks. *Chem. Rev.* **2021**, *121*, pp 5042–5092.
- [26] Chantler, C.T. Development and applications of accurate measurement of X-ray absorption. *Eur. Phys. J.: Spec. Top.* **2009**, *169*, pp 147–153.
- [27] Jonquieres, A.; Clement, R.; Lochon, P. Permeability of block copolymers to vapors and liquids. *Prog. Polym. Sci.* **2002**, *27* (9), pp 1803–1877.
- [28] Koros, W.J.; Burgess, S.K.; Chen, Z. Polymer Transport Properties. In *Encyclopedia of Polymer Science and Technology*, 4th ed.; Mark, H.F., Ed. Wiley: **2015**.
- [29] Varady, M.J.; Knox, C.K.; Cabalo, J.B.; Bringuier, S.A.; Pearl, T.P.; Lambeth, R.H.; Mantooh, B.A. Molecular dynamics study of competing hydrogen bonding interactions in multicomponent diffusion in polyurethanes. *Polymer.* **2018**, *140*, pp 140–149.
- [30] Bringuier, S.A.; Varady, M.J.; Pearl, T.P.; Mantooh, B.A. Characterization of Composition-Dependent Maxwell-Stefan Diffusivities in Mixtures of Polydimethylsiloxane, Nerve Agent VX, and Methanol. *Ind. Eng. Chem. Res.* **2017**, *56* (13), pp 3713–3725.
- [31] Kalaj, M.; Bentz, K.C.; Ayala, S.; Palomba, J.M.; Barcus, K.S.; Katayama, Y.; Cohen, S.M. MOF-Polymer Hybrid Materials: From Simple Composites to Tailored Architectures. *Chem. Rev.* **2020**, *120* (16), pp 8267–8302.
- [32] Ozcan, A.; Semino, R.; Maurin, G.; Yazaydin, A.O. Modeling of Gas Transport through Polymer/MOF Interfaces: A Microsecond-Scale Concentration Gradient-Driven Molecular Dynamics Study. *Chem. Mater.* **2020**, *32* (3), pp 1288–1296.
- [33] Namsani, S.; Ozcan, A.; Yazaydin, A. Direct Simulation of Ternary Mixture Separation in a ZIF-8 Membrane at Molecular Scale. *Adv. Theory Simul.* **2019**, *2* (11), p 7.
- [34] Velioglu, S.; Keskin, S. Simulation of H₂/CH₄ mixture permeation through MOF membranes using non-equilibrium molecular dynamics. *J. Mater. Chem. A.* **2019**, *7* (5), pp 2301–2314.

Nanofluids for removal of contaminants trapped in capillary features

Mark J. Varady^{a*}, Brent A. Mantooth^a, Neil Hawbaker^a, Jill Ruth^b, Melissa S. Hulet^b,
Melissa L. Sweat^a, Zhifeng Ren^c, Kent Hytken^d

^aU.S. Army Combat Capabilities Development Command Chemical Biological Center, Research & Operations Directorate, 8198 Blackhawk Rd., Aberdeen Proving Ground, MD 21010

^bLeidos, 1750 Presidents St., Reston, VA 20190

^cDepartment of Physics, University of Houston, 3507 Cullen Blvd., Room 617, Houston, TX 77204

^dFutureEnergy/NaNoEOR, LLC, 12651 Briar Forest Dr., Suite 165, Houston, TX 77077

ABSTRACT

Liquid-phase chemical warfare agent (or contaminants in general) can become entrained in constrained geometries (capillary features) on military assets (e.g., screw threads or between mated surfaces). If the liquid contaminant wets the solid, capillary forces stabilize the contaminant in these features, making decontamination by conventional means difficult. This work seeks solutions to this problem by leveraging research in the field of enhanced oil recovery, which has used nanofluids to displace oil trapped in underground rock formations by strong capillary and viscous forces. Two types of nanofluids are studied here: (1) a reactive sodium-based nanofluid and (2) silica and polyethylene glycol-based nanofluids that promote contaminant dewetting. It is found that the sodium nanofluid is effective at displacing contaminant by gas bubble formation and expansion, providing a force that pushes against the contaminant. The silica and polyethylene glycol-based nanofluids are effective at dewetting contaminant from capillary walls relative to aqueous surfactant-based controls, but do not provide a force to remove the contaminant from the capillary. However, it was found that the silica nanofluids form a pore network upon water evaporation and contaminant trapped in an adjacent capillary can be passively pulled into this pore network and out of the capillary feature. Further study of the mechanism by which the silica nanofluid decontaminates chemical agents and how it can be coupled with the dewetting capability of silica nanofluids could lead to other decontamination strategies in the future.

Keywords: capillary displacement, complex features, nanofluids, enhanced oil recovery, dewetting, visualization

1. INTRODUCTION

Much of the research on decontamination of materials exposed to chemical warfare agents (CWAs) has focused on the ideal case of a flat, horizontally-oriented material surface. However, real military assets are complex with small gaps resulting from mated surfaces, discontinuities, and screw threads, for example. When liquid-phase CWA interacts with a military asset as shown in Figure 1a, it can be pulled into these small gaps by capillary forces as shown schematically in Figure 1b. Once the CWA is stabilized in such a capillary feature, it is difficult to remove and interaction with a decontaminant is limited by the exposed surface area, which can be extremely small. Figure 1c shows a schematic of liquid agent entrained in a simple capillary feature with height, H , and how the capillary and viscous forces as well as the exposed surface area scale with the size of the capillary. It is seen that both the capillary force determined from the Laplace pressure, $P_c \sim \frac{\gamma}{H}$, and viscous force, determined from the shear stress given by Newton's law of viscosity $\tau_v \sim \frac{\mu}{H}$ become greater as the size of the capillary decreases and the liquid becomes more difficult to remove. In addition, as the available interaction area decreases the rates of evaporation, dissolution, or reaction taking place at the capillary entrance is similarly minimized.

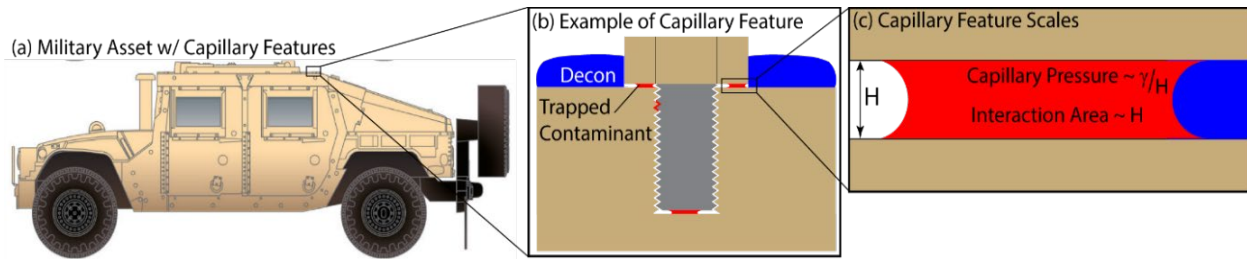


Figure 1. Schematic of (a) military asset with (b) magnified view of example capillary feature formed by mating of a screw with a surface and (c) depiction of how capillary pressure and interaction scales with capillary size. The contaminant is denoted in red while the decontaminant is shown in blue.

Recent research has been able to quantify the amount of contaminant remaining after various decontamination processes including a water rinse, $Zr(OH)_4$ -based slurry, and exposure to hot, humid air.¹ These results definitively show that these treatment processes are ineffective at removing contaminant from capillaries less than $\sim 100 \mu\text{m}$ in diameter. Therefore, it is important to develop decontaminants aimed specifically at removing and/or neutralizing contaminants trapped in these small capillary features. Fortunately, there is a large body of research on the physically similar problem of enhanced oil recovery (EOR). Leveraging that large body of knowledge to develop decontaminants could save time and resources in the development process.

After the primary (drilling and pumping) and secondary (water flooding) oil recovery processes, up to 50 % of the original oil in place remains trapped in the underground rock formations and held by strong capillary and viscous forces.² EOR processes attempt to displace and recover this oil with a wide array of techniques including high pressure CO_2 and high temperature water/steam. Of interest for decontaminant development are the less energy intensive chemical EOR (cEOR) methods, which use various additives such as polymers, surfactants, and nanoparticles in aqueous solution to typically alter the oil-water interfacial tension or the wetting characteristics of the rock surface. Nanofluids (or suspensions of nanosized inclusions in water) have been increasingly studied over the past 10 years as a potential cEOR technique to enhance the displacement of oil. There are myriad possible nanofluid formulations using 0D nanoparticles, 1D nanorods or tubes, and 2D nanosheets with various surface functionalities or charges.^{3,4} For example, the dewetting rate of hexane from a calcite surface has been significantly improved by tuning the surface charge of silica nanoparticles in aqueous suspension with a surfactant.⁵ Another example uses Janus graphene oxide nanosheets functionalized with a polar group on one side and a nonpolar group on the opposite side such that the sheets aggregate at the oil-water interface and lower interfacial tension.⁶

In this work, two types of nanofluid were investigated for use as decontaminants: (1) a reactive sodium-based nanofluid and (2) silica and polyethylene glycol (PEG)-based nanofluids aimed at improving dewetting efficacy. The reactive nanofluid developed at the University of Houston is a suspension of Na metal nanoparticles ($\sim 100 \text{ nm}$) suspended in a silicone oil (viscosity $\sim 10 \text{ cP}$). This works in a two-step process where water is first injected into the oil reservoir followed by the sodium nanofluid. Na nanoparticles react with the water at the silicone oil water interface where H_2 bubbles provide pressure inside the capillary that pushes the contaminant. At the same time the production of heat and NaOH serve to lower viscosity and interfacial tension, all of which work together to effect contaminant removal (Figure 2a).^{7,8} The silica and PEG-based nanofluids operate by promoting dewetting of oil (or a contaminant) from the capillary wall as described in a series of articles published at Illinois Institute of Technology.^{9,10} As a wedge film forms between the contaminant and the capillary wall, nanoparticles (or polymer coils in solution) form layered ordered structures in this region, and increase the structural disjoining pressure.¹¹

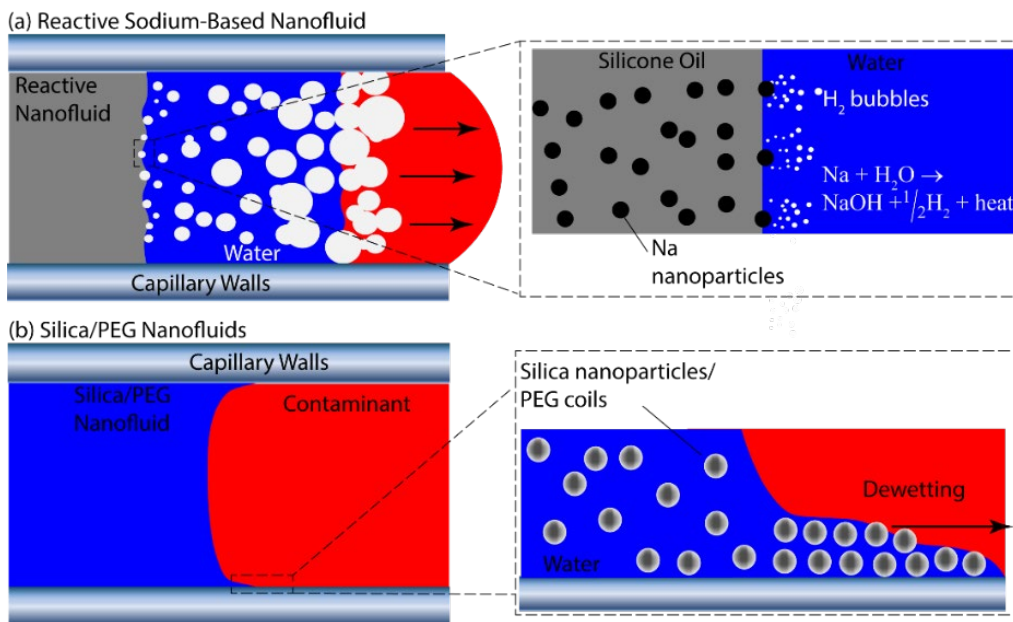


Figure 2. Schematics depicting mechanisms of action for (a) reactive sodium-based nanofluid showing H₂ gas bubble formation at the silicone oil-water interface due to reaction of the sodium nanoparticles and (b) silica/PEG-based nanofluids showing layering of the nanoparticles in the wedge film region as the contaminant dewets from the capillary wall.

2. MATERIALS AND METHODS

2.1 Materials

Suspensions of sodium nanoparticles in silicone oil were provided by the University of Houston and prepared according to the procedure previously published in the literature.^{7,8} Surfactants sodium dodecyl sulfate (SDS), dodecyl trimethyl ammonium chloride (DTAC), and Tergitol 15-S-7 were procured from Sigma Aldrich. Aqueous surfactant solutions were prepared by mixing the appropriate amount of the surfactant with deionized water. Colloidal silica was purchased from Sigma Aldrich (Ludox® SM, Sigma P/N 420794). Two types of PEG, both with average molecular weight = 8000 g/mol, were purchased from Sigma Aldrich (Sigma P/Ns PHR2894, 89510). Simulants used to mimic sulfur mustard (HD) were 1-chlorooctane and 1,8-dichlorooctane. Silicone oil was used to mimic the critical properties of nerve agent VX. Fluorescent dyes were used to enhance contrast in visualization experiments. Green/yellow dye (Fluorosol GR7200, Koch Color) was used for 1,8-dichlorooctane, red dye (Fluorosol Red 7348) was used for 1-chlorooctane, and green BoDIPY 505/515 was used for silicone oil.

2.2 Methods

Two capillary geometries were used to assess the performance of the different nanofluids under investigation, a rectangular capillary and radial capillary. A rectangular capillary with cross sectional dimensions 0.05 mm × 1.0 mm (Electron Microscopy Science, Fisher Scientific P/N 50-335-61) or 0.1 × 2 mm (Electron Microscopy Science, Fisher Scientific P/N 50-335-63) was connected to fluid reservoirs at each end, sealed and placed on a microscope stage for observation (Leica DVM6). Dyed simulant was placed in one reservoir and the simulant filled the capillary as shown in Figure 3a. The test fluid (e.g., nanofluid) was then deposited in the opposite reservoir and displacement of the simulant was observed and recorded by the microscope. The radial capillary consisted of two 25-mm diameter glass cover slides (Fisher Scientific, P/N 12-545-102P) with their centers offset and separated with a 50- μm washer (McMaster P/N 98126A161) and held together with a UV cure glue (Loctite AA349) as shown in Figure 3b. The radial capillary was placed on the microscope stage for observation, 1–5 μL of contaminant was deposited at the entrance to the capillary, followed by deposition of 10–50 μL of the test fluid.

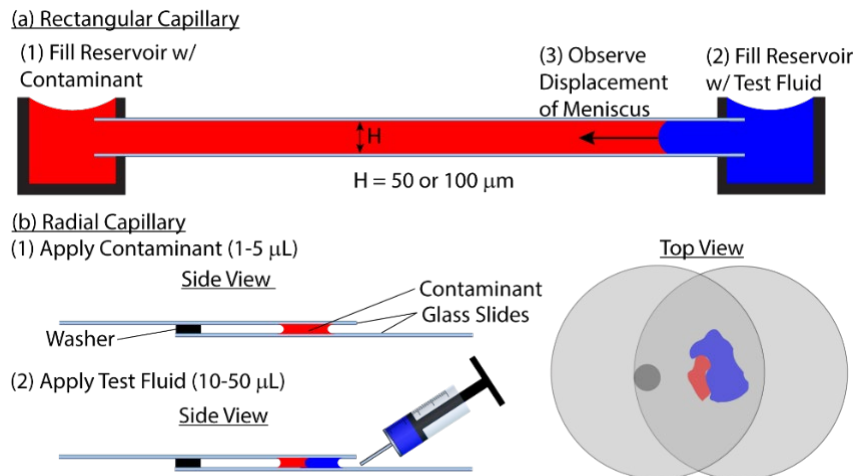


Figure 3. Schematics of capillary geometries used in visualization experiments. (a) Rectangular capillary in which one end sits in a reservoir that is filled with contaminant and the other end sits in a reservoir that is filled with the test fluid after the capillary has been filled with contaminant. (b) Radial capillary formed by two circular glass slides and separated by a washer in which contaminant is deposited followed by deposition of a test fluid to observe displacement.

Nanofluids were tested for removal efficacy of sulfur mustard (HD) and nerve agent VX from 50 μm radial capillaries developed in a separate Defense Threat Reduction Agency-funded program.¹ These capillaries were formed from bare or polyurethane paint coated stainless steel washers separated by a 50 μm washer and held together with a screw/nut assembly. The general procedure is to (1) deposit 1 μL of agent in the capillary, (2) wait 60 min, (3) apply the treatment (e.g., sodium and PEG nanofluids), (4) wait 30 min, and (5) rinse three times with 20 μL aliquots of water to remove any accessible agent that was extracted during the treatment process. For the sodium nanofluid, 100 μL of water was first deposited followed immediately with 50 μL of the nanofluid. For the aqueous-based PEG nanofluid, 50 μL of the nanofluid only was deposited. Two control cases were also run: (1) no treatment, (2) no treatment or rinse. After the contamination and treatment/rinse processes, the capillary (shim panel) was immersed in 40 mL of isopropyl alcohol to extract and dissolve any remaining agent trapped within the capillary. All extractions were performed for 1 h and solution samples were diluted, and the analytes were quantified using gas chromatography (GC) for HD (Agilent 6890/7890 GC equipped with a 5975 mass selective detector [Agilent Technologies; Santa Clara, CA]) or liquid chromatography (LC) with a mass spectrometer for VX (Agilent 1200/1290 series LC and Applied Biosystems [Carlsbad, CA] API5000/5500 triple-quadrupole mass spectrometer equipped with a TurboV ion source). Details on use of the chromatography platforms have been published elsewhere.¹²

3. RESULTS AND ANALYSIS

3.1 Aqueous surfactant controls

Two concentrations of each of the aqueous surfactant solutions was prepared, one below and one above the corresponding critical micelle concentration (CMC). Each of these solutions was used as the test fluid in both the rectangular and radial capillary geometries with each of the simulants. As summarized in Table 1, no displacement was observed for any of the aqueous surfactant solutions with any of the simulants. The simulant did not fill the entire volume of the radial capillary, and as a result, some of the aqueous surfactant solution entered the capillary. This resulted in deformation and movement of the liquid simulant within the capillary, but it did not exit the capillary.

Table 1. Summary of visualization experiments run using the aqueous surfactant controls.

Simulants	Test Fluids	Capillaries	Results
1-chlorooctane 1,8-dichlorooctane Silicone oil	Deionized Water Sodium dodecyl sulfate (0.008 M and 0.02 M) Dodecyl Trimethyl Ammonium Chloride 0.02 M and 0.08 M Tergitol 39 ppm and 155 ppm	Rectangular, 50 μm Radial, 50 μm	No displacement observed for any of the listed combinations

3.2 Sodium nanofluid

The sodium nanofluid uses a two-step process where first an aqueous phase is deposited, followed by the sodium nanofluid to induce reaction of the sodium nanoparticles with water at the silicone oil-water interface. The sodium nanofluid was evaluated using all of the surfactant solutions as the aqueous component in both the rectangular and radial capillaries.

In the rectangular capillary, once the simulant was deposited in one reservoir and the capillary was filled, the aqueous surfactant was deposited in the opposite reservoir followed by deposition of the sodium nanofluid on top of the aqueous solution. Displacement was only observed using the SDS solutions with the nanofluid for 1-chlorooctane in 50 μm capillaries (Figure 4a). Gas generation after deposition of the sodium nanofluid is observed on the left side of the image series. Possible mechanisms of action include lowering of interfacial tension and viscosity by heat generation and gas bubble-induced pressure overcoming contact line pinning of the simulant at the entrance to the capillary.

In the radial capillary, the sodium nanofluid effectively displaced the simulant when used in combination with any of the aqueous surfactant solutions, including pure water. Because the entrance to the capillary (extending along the perimeter of the top glass slide) is much larger than that of the rectangular capillary, there are multiple pathways for generated gas bubbles to enter and exit the capillary, providing direct pressure on the trapped simulant. As Figure 4b shows, as time passes, the amount of dyed simulant in the capillary decreases.

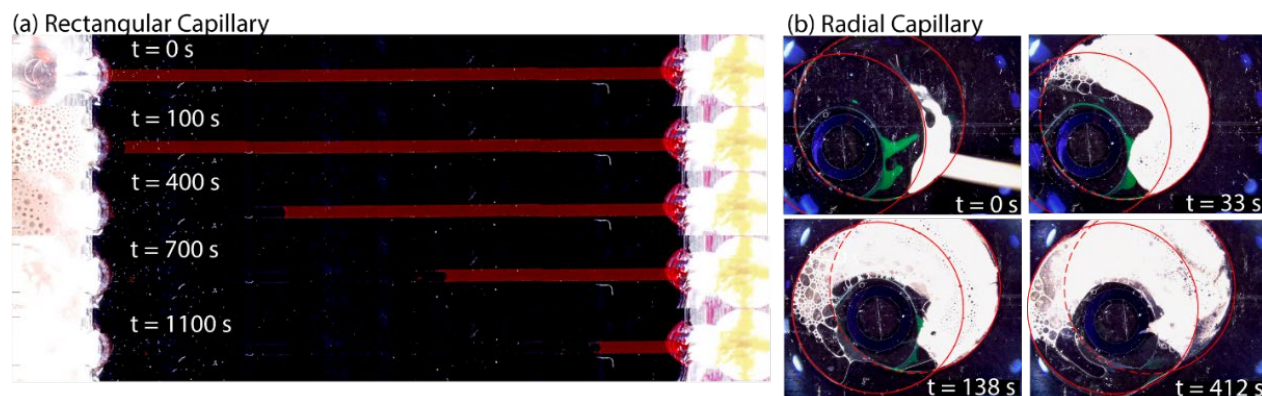


Figure 4. (a) Displacement of red-dyed 1-chlorooctane from 50 μm rectangular capillary using sodium nanofluid with aqueous solution of 0.08 M SDS. At $t = 0$, the SDS solution was in the reservoir on the right side of the image and the sodium nanofluid was deposited over the SDS solution before $t = 100$ s. (b) Displacement of green-dyed 1,8-dichlorooctane from a 50 μm radial capillary using sodium nanofluid with aqueous solution of 0.08 M SDS. At $t = 0$ the SDS solution had already been deposited and entered the capillary before deposition of the sodium nanofluid. Red lines have been added to the images to highlight the periphery of the glass slides forming the radial capillary.

3.3 PEG and silica nanofluids

Basic formulation rules for nanofluids operating on the basis of enhanced structural disjoining pressure have been established in the series of papers published by the Illinois Institute of Technology.^{9-11,13,14} They specifically found that (1) the water-contaminant-solid contact angle should be as small as possible to promote wedge film formation, (2) nanoparticles should be smaller than 20 nm and monodisperse to effectively layer within the wedge film region, and (3) the osmotic pressure in the nanofluid should be as large as possible.¹³ In accordance with point (1), attention was confined to using SDS as a surfactant based on the results of separate experiments (not presented here) showing that SDS produces the smallest contact angle on glass of the surfactants studied here. Dynamic light scattering experiments performed on dilute aqueous PEG solutions and silica nanoparticle suspensions showed that for the PEG coils the hydrodynamic diameter was $D_h \sim 6$ nm and for the silica nanoparticles $D_h \sim 17$ nm with both showing low polydispersity. The volume fraction of the nanofluids (PEG coils or silica nanoparticles) ranged from 0.05–0.30, which aligned with studies of similar nanofluids in the literature.¹⁴ Increasing volume fraction further can result in deleterious effects, especially particle-particle interactions and increased viscosity. Table 2 presents the compositions of the PEG and silica nanofluids studied in this work.

Table 2. Compositions of aqueous PEG and silica nanofluids.

Nanofluid	Volume Fractions	Concentrations (mg/mL)	Surfactant
PEG-8000	0.1, 0.2, 0.3	11.8, 23.5, 35.3	SDS 0.004 M, 0.02 M
Silica	0.05, 0.1, 0.17	110, 220, 374	SDS 0.004 M, 0.02 M

Similar behavior is observed for both the PEG and silica nanofluids displacing contaminant from a rectangular capillary as shown in Figure 5 for 1,8-dichlorooctane in a 50 μm capillary. In both cases, the nanofluid initially dewets the contaminant on the sides of the capillary faster than in the middle. This occurs because the cross section of the rectangular capillary is rounded at the sides, in effect creating a smaller capillary size at the sides and thus a higher capillary pressure driving force for displacement. This effect was not observed for the pure SDS solutions, highlighting the efficacy of both the PEG and silica nanofluids for dewetting the contaminant from the capillary walls. However, this efficacy results in the undesirable effect of contaminant slugs being pinched off and remaining in the rectangular capillary. The displacement process was observed to be slower for the silica nanofluid due to the higher viscosity compared to that of the PEG nanofluid.

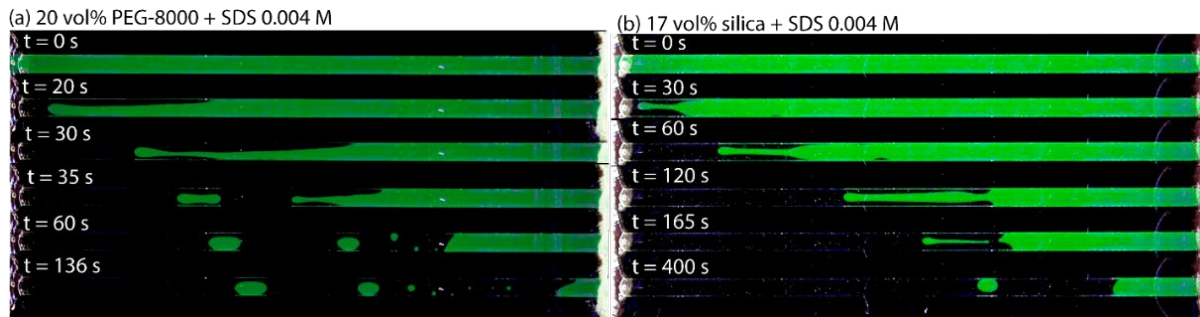


Figure 5. Displacement of green dyed 1,8-dichlorooctane from 50 μm rectangular capillary using (a) aqueous solution of PEG-8000 (20 vol%) and SDS (0.004 M), (b) aqueous suspension of silica nanoparticles (17 vol%) and SDS (0.004 M).

Figure 6 shows the displacement of 1,8-dichlorooctane from a radial capillary using both PEG and silica nanofluids. In both cases, the nanofluid enters the capillary, shifts and distorts the contaminant slug very quickly (< 10 s), but it does not exit the capillary. In the case of the PEG nanofluid, some of the contaminant is broken up into small droplets as shown in the magnified view of Figure 6c.

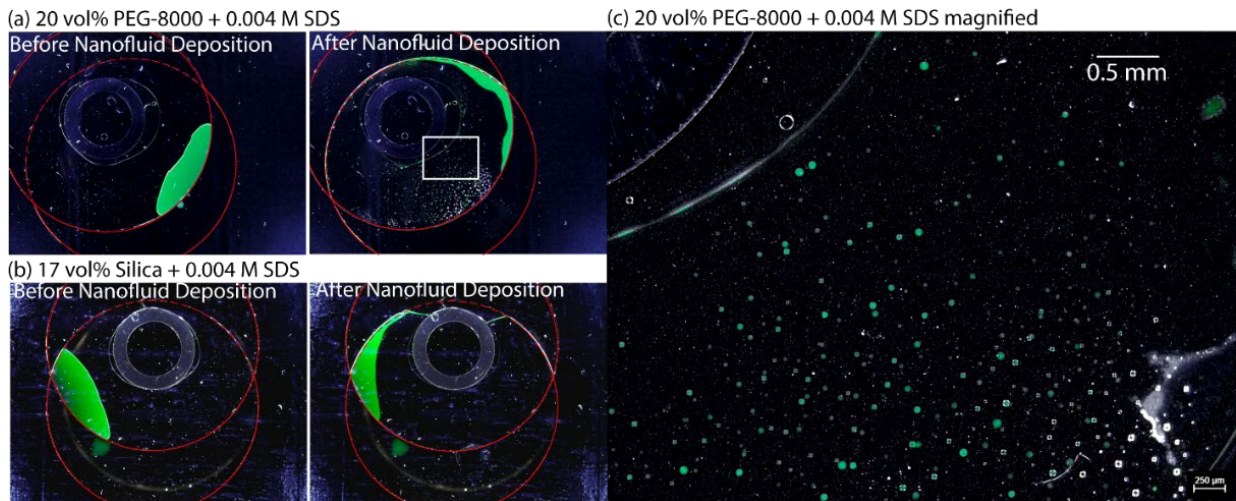


Figure 6. Displacement of green dyed 1,8-dichlorooctane from 50- μm radial capillary using (a) aqueous solution of PEG- 8000 (20 vol%) and SDS (0.004 M), (b) aqueous suspension of silica nanoparticles (17 vol%) and SDS (0.004 M). Red lines have been added to the images to highlight the periphery of the glass slides forming the radial capillary. Area enclosed by white rectangle in (a) is magnified in panel (c).

3.4 CWA testing

The efficacy of the sodium and PEG-based nanofluids was quantified for removing sulfur mustard (HD) and nerve agent VX from 50 μm radial capillaries formed from stainless steel and polyurethane coated substrates (termed shim panels in a DTRA-funded program) as described in the Methods section. Figure 7 shows the mass of agent remaining in the capillaries after treatment with the nanofluids in comparison to two control cases, (1) with no treatment and (2) with no treatment and no rinse. The sodium nanofluid effectively removes all HD from both the bare stainless steel and PU coated capillaries while it demonstrates less efficacy for VX relative to the control cases. The PEG nanofluid is not effective at removing either HD or VX from either type of capillary. These results align with the visualization observations, namely that the gas pressure generation of the sodium nanofluid is effective at pushing contaminant from the capillary, and that although the PEG nanofluid is effective at dewetting contaminant from the capillary walls, there is no force causing contaminant removal from the capillary.

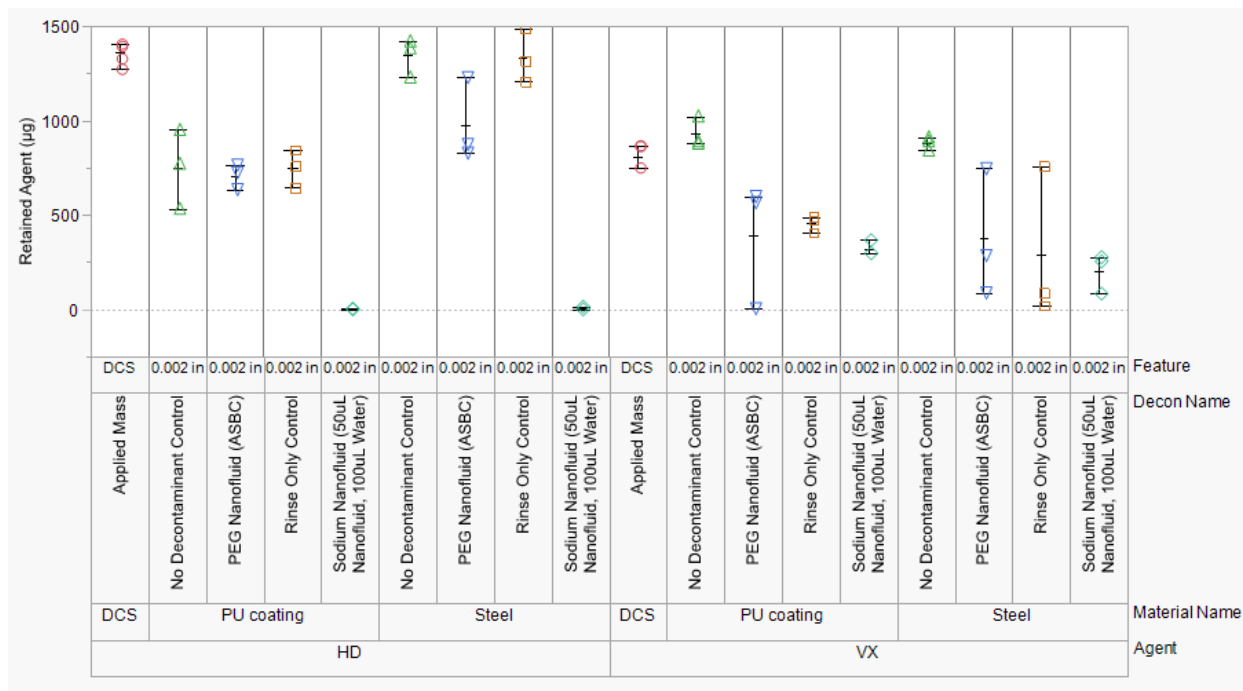


Figure 7. Mass of agent (HD or VX) remaining in 50 μm radial capillary composed of bare stainless steel or coated with a polyurethane-based paint and treated with sodium nanofluid or PEG nanofluid followed by a water rinse to remove any accessible agent that was displaced from the capillary. Additional control cases were also run, one in which no treatment was applied, but the water rinse was performed and another in which no treatment was applied and no water rinse was performed.

3.5 Silica nanofluid – gel formation and capillary extraction

Experiments performed with the silica nanofluids resulted in an unexpected behavior that could be useful for extracting contaminant from a capillary. Figure 8 shows the treatment of 1,8-dichlorooctane in a 50 μm radial capillary with a 17 vol% silica (aq) nanofluid. The nanofluid fills the remaining volume of the radial capillary and additional silica nanofluid sits at the entrance to the capillary as denoted by the blue outlined regions in Figure 8. As the water evaporates from the nanofluid, the silica nanoparticles aggregate to form a gel and the pore network with a morphology dependent on how the nanoparticles pack together as shown in Figure 9. Because the 1,8-dichlorooctane partially wets the surface of the silica nanoparticles and the capillary pressure is greater in the pore network than in the radial capillary, the 1,8-dichlorooctane in contact with the silica gel is drawn into the pore network within 20–30 min. This is clearly seen in Figure 8 as the green dyed area within the radial capillary decreases and the silica gel takes on a green hue.

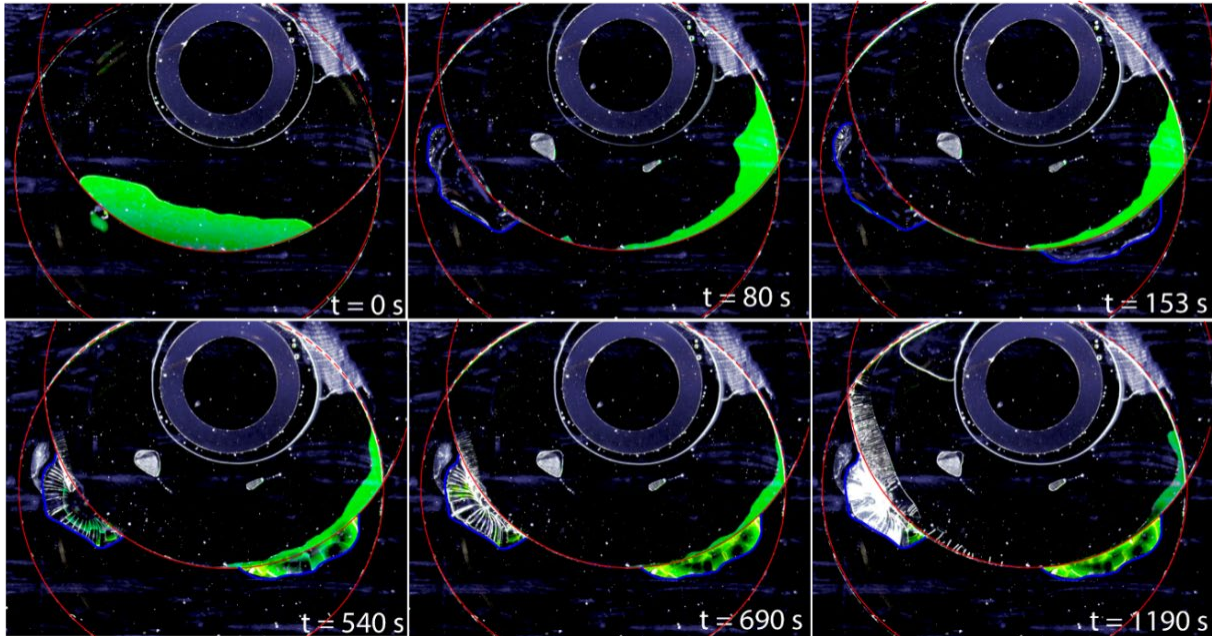


Figure 8. Treatment of green dyed 1,8-dichlorooctane in a 50 µm radial capillary using 17 vol% silica (aq) nanofluid. Image at $t = 0$ s is before deposition of the nanofluid. At $t = 80$ and 153 s, the silica nanofluid has filled the capillary and shifted the 1,8-dichlorooctane. Silica nanofluid outside of the capillary is outlined in blue. From $t = 540$ –1190 s, water from the silica nanofluid outside of the capillary evaporates, causing aggregation/gelation of the silica nanoparticles and formation of a pore network. Most of the 1,8-dichlorooctane within the radial capillary is drawn into the silica pore network.

The visualization And CWA results for the PEG and silica nanofluids showed that dewetting/emulsification of the contaminant is not sufficient; there must be a driving force to remove the contaminant from the capillary. The extraction of contaminant into an adjacent pore network driven by a capillary pressure gradient may be a viable passive mechanism for accomplishing this in practice. Further work is needed to optimize the pore morphology and wetting characteristics as well as the dynamics of the pore formation process. This would involve tuning the size and surface functionalization of the silica nanoparticles in addition to exploring faster gel formation mechanisms such as altering the pH or ionic strength of the liquid medium.

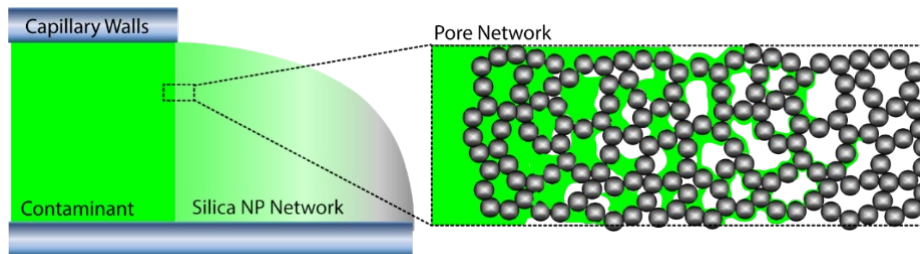


Figure 9. Schematic depiction of contaminant extraction from capillary into pore network formed by aggregation of silica nanoparticles.

4. CONCLUSIONS AND NEXT STEPS

Two types of nanofluids were investigated for removing contaminants in small capillary features, (1) a reactive sodium nanofluid and (2) PEG and silica based nanofluids that promote dewetting. Visualization results showed that the sodium nanofluid effectively pushed contaminant out by formation and expansion of gas bubbles created by reaction with water. However, there are significant safety concerns with ignitability of the sodium nanofluid that would prevent its use in the field. Alternative safer reactive schemes may prove effective, but more work would have to be done to identify viable candidates. The PEG and silica nanofluids demonstrated efficacy at dewetting the contaminant from

the capillary walls, but do not provide a driving force to remove the contaminant in open capillary geometries like the radial capillary studied in this work.

Experiments with the silica nanofluids showed that evaporation of water and resulting formation of a pore network by gelation of the silica nanoparticles leads to extraction of contaminant from the capillary into the pore network. This passive mechanism relies on a gradient of capillary pressure between the capillary feature and the pore network due to the small size of the pores (capillary pressure is inversely proportional to pore size). Further work is needed to optimize the morphology and wettability of the pore network in addition to the dynamics of its formation for its use as an effective decontaminant. Studies should examine the effect of nanoparticle size, concentration, surface functionalization, and the pH and ionic strength of the carrier liquid on the morphology and formation dynamics of the pore network as well as the dynamics of imbibition of contaminant into the pore network.

ACKNOWLEDGMENTS

The authors thank colleagues in the Decontamination Sciences Branch at DEVCOM CBC who supported this effort and Dr. Bernadette Higgins, Dr. James Noah, and Dr. Charles Bass at the Defense Threat Reduction Agency for their interest and conversations about this work. Funding was provided by the U.S. Army via the Chemical Biological Advanced Materials and Manufacturing Science Program (PE 0601102A Project VR9) at the Combat Capabilities Development Command Chemical Biological Center.

REFERENCES

- [1] Hawbaker, N. H.; Mantooth, B. A.; Pearl, T. P. Effect of complex features, surfaces, and interfaces on post-decontamination vapor emission from contaminated materials; TR-1734; U.S. Army DEVCOM Chemical Biological Center: **2021**, UNCLASSIFIED Report.
- [2] Druetta, P.; Raffa, P.; Picchioni, F. Chemical enhanced oil recovery and the role of chemical product design. *Appl. Energy*. **2019**, *252* (1), p. 43.
- [3] Li, K.; Wang, D.; Jiang, S. Review on enhanced oil recovery by nanofluids. *Oil & Gas Sci. Tech.* **2018**, *73* (37), pp 37–63.
- [4] Sun, Y.; Yang, D.; Shi, L.; Wu, H.; Cao, Y.; He, Y.; Xie, T. Properties of Nanofluids and Their Applications in Enhanced Oil Recovery: A Comprehensive Review. *Energy Fuels*. **2020**, *34* (2), pp 1202–1218.
- [5] Alzobaidi, S.; Wu, P.K.; Da, C.; Zhang, X.; Hackbarth, J.; Angeles, T.; Rabat-Torki, N.J.; MacAuliffe, S.; Panja, S.; Johnston, K.P. Effect of surface chemistry of silica nanoparticles on contact angle of oil on calcite surfaces in concentrated brine with divalent ions. *J. Colloid Interface Sci.* **2021**, *581*, pp 656–668.
- [6] Zhang, B.; Mohamed, A.I.A.; Goual, L.; Piri, M. Pore-scale experimental investigation of oil recovery enhancement in oil-wet carbonates using carbonaceous nanofluids. *Sci. Rep.* **2020**, *10*:17539.
- [7] Luo, D.; Ren, Z. Synthesis of sodium nanoparticles for promising extraction of heavy oil. *Mater. Today Phys.* **2021**, *16*, 100276.
- [8] Zareei, D.; Luo, D.; Kostarelos, K.; Ren, Z., Sodium nanofluid for efficient oil recovery in heavy oil and oil sand reservoirs. *Soft Sci.*, **2021**, *1* (8), pp 1–11.
- [9] Kondiparty, K.; Nikolov, A.D.; Wasan, D.; Liu, K.L. Dynamic Spreading of Nanofluids on Solids. Part I: Experimental. *Langmuir*. **2012**, *28* (41), pp 14618–14623.
- [10] Zhang, H.; Ramakrishnan, T.S.; Nikolov, A.; Wasan, D. Enhanced oil displacement by nanofluid's structural disjoining pressure in model fractured porous media. *J. Colloid Interface Sci.* **2018**, *1* (511), pp 48–56.
- [11] Nikolov, A.; Zhang, H. The dynamics of capillary-driven two-phase flow: The role of nanofluid structural forces. *J. Colloid Interface Sci.* **2015**, *449*, pp 92–101.
- [12] Shue, M.; Lalain, T.; Mantooth, B.; Humphreys, P.; Hall, M.; Smith, P.; Sheahy, M. Low-Level Analytical Methodology Updates to Support Decontaminant Performance Evaluations; ECBC-TR-883; U.S. Army Edgewood Chemical Biological Center: Aberdeen Proving Ground, MD, **2011**. UNCLASSIFIED Report, Public Release (ADA546021).
- [13] Zhang, H.; Nikolov, A.; Wasan, D. Enhanced Oil Recovery (EOR) Using Nanoparticle Dispersions: Underlying Mechanism and Imbibition Experiments. *Energy Fuels*. **2014**, *28* (5), pp 3002–3009.
- [14] Zhang, H.; Nikolov, A.; Wasan, D. Dewetting Film Dynamics Inside a Capillary Using a Micellar Nanofluid. *Langmuir*. **2014**, *30* (31), pp 9430–9435.

This page intentionally left blank

Developing design rules for CBRN-relevant additive manufacturing systems by probing network structure and system free volume

Kristian M. Van de Voorde, Cody C. Kendig, Bradley R. Ruprecht, James D. Severtsen,
Melissa L. Sweat, Mark J. Varady, Anne Y. Walker*

U.S. Army Combat Capabilities Development Command Chemical Biological Center, Research
& Operations Directorate, 8198 Blackhawk Rd., Aberdeen Proving Ground, MD 21010

ABSTRACT

At their heart, 3D printed parts created through vat polymerization are complex polymer networks. Probing these systems using established polymer network theory and analysis techniques should lead to a deeper understanding of the additive manufacturing process, allowing these systems to exist as less of a “black box” and more as truly characterized polymer systems. Current additive manufacturing resin development generally identifies a desired property and uses a guess-and-check method to develop a resin that maximizes that property. This investigation seeks instead to probe three primary printing parameters: polymer chemistry, particle geometry, and light interactions, to assess their influence on resultant network structure. Our overall hypothesis is that changes to the parameters outlined above directly affects polymer chain mobility, and that characterizing system free volume is the most direct route to understanding how to control network behavior by manipulating those properties. We will investigate additively manufactured systems via multiple classical polymer analysis techniques to develop a complete picture of polymer networks created through vat polymerization techniques. This knowledge can be used to develop a set of design rules that will allow for focused development of additive manufacturing resins to exhibit specific properties, enabling more rapid development of resins and eliminating tedious guesswork.

Keywords: additive manufacturing, 3D printing, advanced manufacturing, vat polymerization, digital light processing, polymer networks

1. INTRODUCTION

The utility of additive manufacturing (AM) technology, also known as 3D printing, is attenuated by a number of problems, including low print volume, poor scalability, and variable mechanical properties.^{1,2} Though there are some examples of successful implementation of AM for commercial products, the technology still does not see widespread production use.³ A majority of the 3D printed (3DP) parts that see commercial use neither require particularly robust mechanical properties, nor possess especially high chemical resistance, nor well-defined transport characteristics.^{3,4} This makes AM almost a non-starter when considering the materials requirements for CBRN protective equipment. On the other hand, the tunability of AM parts and the ability to produce complex shapes makes it enormously appealing for personal protective equipment, given the variable and intricate shapes required.¹

With this in mind, we embarked on a focused study on vat polymerization-based additive manufacturing methods that considers structure-property relationships that arise from tuning different aspects of the printing process. The first focus of this study revolved around the influence of print properties, e.g., layer thickness, cure time, etc., on resultant mechanical properties to facilitate future explorations of how those properties are affected by network structure. Much of the research done on vat polymerization AM focuses on a specific target property (e.g., enhancing tensile strength), but stops short of characterizing the polymer network, searching instead for “whatever works”.^{5,6} Our primary focus for the fundamental part of this study will be on how different variables affect network formation and polymer chain mobility/free volume, and correlating these changes to changes in overall system properties. This investigation seeks to characterize why the system behaves the way it does, rather than chasing after properties and settling on “good enough.”

Vat polymerization utilizes liquid polymer resins that are crosslinked using radiation, UV, or visible light to produce solid parts. Likely the most familiar and accessible vat polymerization AM method is stereolithography (SLA), popularized by such familiar names as Formlabs and Anycubic. The process utilizes UV light to initiate spatially-specific crosslinking reactions in a photoactive polymer resin bath.⁷ Such crosslinked polymer systems are

not found just in the AM world. Numerous commercial applications utilize crosslinked polymer networks due to the potential to achieve robust properties, and corresponding research can be leveraged to better design vat polymerization systems to achieve similar results. Moreover, most of the techniques used to design and characterize these systems can be directly translated to parts produced via AM, enabling us to probe the relationship between network structure and manufacturing parameters. This relationship will, in turn, provide deeper insight into resulting material properties of our 3D printed parts, extract important information, and enable the development of a rational design scheme for Center-relevant AM methods.

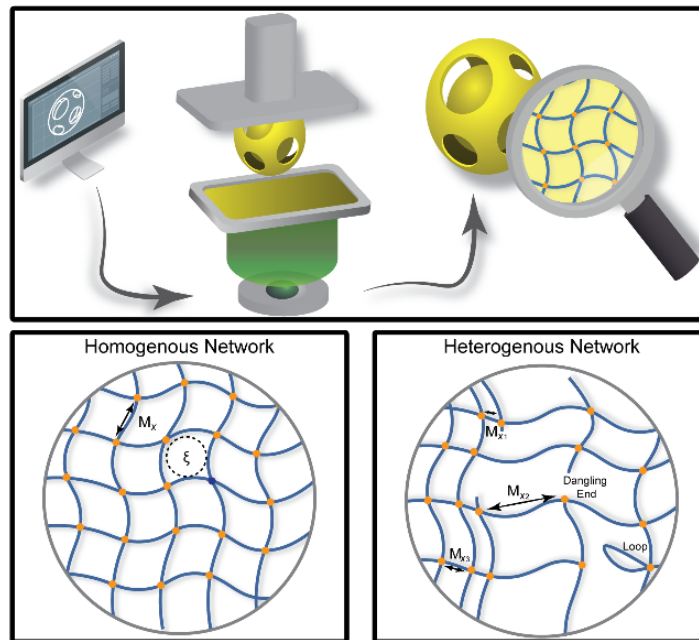


Figure 1. During vat printing, a laser is utilized to initiate a crosslinking reaction in a resin. A resin typically consists of a linear polymer, multifunctional crosslinker, photoinitiator, and a dye. Key features of the printed form factor are a direct consequence of the resin formulation and printing parameters: molecular weight between crosslinks (M_c), crosslink density (x), and mesh size (ξ). These parameters dictate important bulk properties of the printed material such as mechanical and diffusion.

Previous work in polymer networks has quantitatively described the relationships between network features and bulk properties. These relationships, however, assume an ideal, homogenous network architecture. Several considerations, such as the reaction mechanism and processing considerations, can result in the formation of a heterogeneous network architecture (Figure 1). Heterogeneous networks have significantly depressed bulk properties, and so each aspect of the manufacturing processes that contributes to the network formation is important to fundamentally understand. There are numerous avenues by which network inhomogeneity can be introduced in AM process. Typical resin formulations rely on the high reactivity of acrylated, linear polymers but, due to the lack of selectivity associated with their reaction mechanism, heterogeneous networks are produced. Additionally, a dye is often utilized in the formulation of a 3D printable resin. The purpose of the dye is to scatter light from the laser to prevent initiation of crosslinking reactions within the bulk of the resin to manufacture materials with a higher accuracy. However, the scattering is dependent on the geometry of the dye particles. Consequently, the regularity of the polymer network is connected to their geometry. Another aspect of the printing process that can influence the network architecture is the intensity of the laser. Recent works in vat manufacturing, however, have challenged the assumption that different laser intensities produced parts with different mechanical properties.⁷

The bottom line for investigating 3D printed parts, and perhaps one of the reasons they often are treated as somewhat of a black box, is that this is a complex, multivariate system. We propose that the major operating variables described above can be grouped into three categories: polymer chemistry, particle geometry and interaction, and light source considerations. These categories can be broken down further but serve to group experiments and guide modeling efforts, allowing us to approach structure-property determination in a rational way. We hypothesize that each of the variables outlined above has a direct influence on the chain mobility in the system and that the key to truly understanding these systems is a focused study of the influence of various parameters on system free volume. It is

critical to relate any changes in mechanical or transport properties back to the network's structure, and to understand the genesis of that structural change. We expect that, when probed directly, we will find that parts created from vat polymerization will be highly heterogeneous, and that each variable will affect the network in different ways. Focused study on the formation of these inhomogeneities should allow design of better AM resin systems with specific properties by understanding and balancing the different changes in the network. We may not be able to perfectly control each variable, but we hope to understand their contributions and find saddle points that balance each variable to achieve desired results. In short, we hope to develop a deeper fundamental understanding of vat polymerization and establish a set of rules that will guide resin system formulation. This knowledge will enable us to "demystify" additive manufacturing in a way, allowing us to use the powerful tool represented by this technology to create better personal protective solutions for the warfighter and further add to our materials development capabilities at U.S. Army Combat Capabilities Development Command Chemical Biological Center.

The first year of the project focused on more traditional polymer characterization techniques, primarily dynamic mechanical analysis (DMA), using simplified systems to acquire a baseline understanding of material behavior. This information will be used to inform second-year studies using more advanced techniques.

2. MATERIALS AND METHODS

2.1 3D printed dogbones

A single commercially available resin (Green, Anycubic) was used to print dog bones per American Society for Testing and Materials standards on the Anycubic Photon-S SLA 3D printer. This investigation focused on three printing parameters: exposure time, printing orientation, and post-cure time. As a baseline, a 6-second exposure, vertical orientation, and 10-minute post cure was established as our benchmark print. Prints were oriented either vertically or horizontally. Layer thickness was varied from 10 μm to 100 μm . Post-cure time varied from 1 minute to 5 minutes at an intensity of 13 mW/cm².

Sample nomenclature for this study was set to H/V#-##. The 'H' refers to horizontally printed parts, and the 'V' refers to vertically printed parts. The first number after the letter refers to the post processing cure time (1/5, minutes). The secondary number in the sample name refers to the layer thickness (10/50/100, μm).

2.2 Material characterization

Mechanical characteristics were assessed by applying tension to printed dogbones via tensile testing on a ZwickRoell ZwickiLine equipped with a 0.5 kN load cell. Samples were strained at 50 % min⁻¹ and tests were performed in replicate sets of five samples per set. Tests were conducted at room temperature and ambient humidity. Stress and strain at yield point were determined via analysis of the resulting stress-strain curve. The elastic modulus was determined using a linear fit at 2 % strain, and toughness was calculated as an integral of the tensile curve. OriginLab graphing software was used to plot the stress/strain curves as well as the modulus and toughness bar graphs. Each representative bar graph marked the average value calculated, and error bars were included used to illustrate the standard deviation.

3. RESULTS AND DISCUSSION

Mechanical characteristics were assessed by applying tension to printed dogbones via tensile testing on a ZwickRoell ZwickiLine equipped with a 0.5 kN load cell. Samples were strained at 50 % min⁻¹ and tests were performed in replicate sets of five samples per set. Tests were conducted at room temperature and ambient humidity. Stress and strain at yield point were determined via analysis of the resulting stress strain curve. The elastic modulus were determined using a linear fit at 2 % strain, and toughness was calculated as an integral of the tensile curve. OriginLab graphing software was used to plot the stress/strain curves as well as the modulus and toughness bar graphs. Each representative bar graph marked the average value calculated, and error bars were used to illustrate the standard deviation.

In an effort to decouple the effects of printing parameters on the properties of printed parts, dogbones manufactured on an Anycubic Digital Light Processing printed with their commercially available resin (transparent green, 405 nm) were examined. Specifically, the effect of the printing direction, post-cure time, and layer thickness were

systematically analyzed during tensile testing because these printing parameters were highlighted as key variables during the Digital Light Processing AM process.

Initially, the print direction effects were examined. Horizontal prints contained layers perpendicular to the applied force, and vertical prints were made up of layers normal to the applied force. The tensile curves for samples printed horizontal (Figure 2A) appeared to be similar to the tensile curves recorded for the vertical prints (Figure 2B). For most samples, the toughness did not change when print direction changed (Figure 2C), and the elastic modulus was slightly higher for the horizontal prints (Figure 2D).

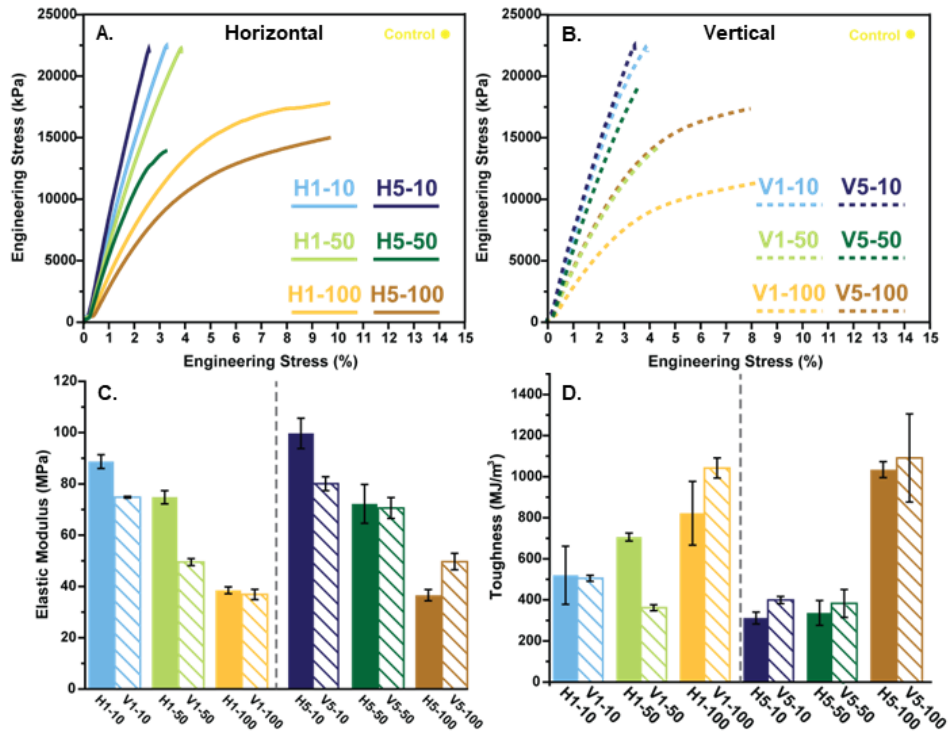


Figure 2. Tensile data for effect of print direction. A. Tensile curves for horizontal prints B. Tensile curves for vertical prints C. Elastic Modulus D. Toughness.

This variation in property does highlight that the manufacturing process does, in fact, manipulate the overall bulk properties. The horizontal prints were anticipated to have a strength because the interface between the cured could not act as a failure mechanism. However, the relationship between print direction and mechanical properties cannot be applied globally. A material printed vertically was found to be stronger than its horizontal counterpart when: 1) the layer thickness was 100 μm, and 2) a 5-minute post cure time was utilized. This relationship implies that a stronger interface between layers can be achieved when 2 conditions are met: larger layer thickness and longer cure time.

Similarly, the relationship between mechanical properties and the post-cure time was dependent on the layer thickness (Figure 3A, 3B). In systems with smaller layers (10 μm), a higher strength and toughness was calculated for systems that were cured for 5 minutes instead of 1 minute (Figure 3 C, D). This relationship indicates a higher conversion was achieved when samples were cured longer. Additionally, this also indicates that samples with smaller layers did not form robust networks during the cure. Comparatively, mechanical properties across systems with larger layers (100 μm) was relatively consistent, independent from the post-cure time. This relationship indicates more uniform materials were printed when a larger layer thickness was utilized during the additive manufacturing process.

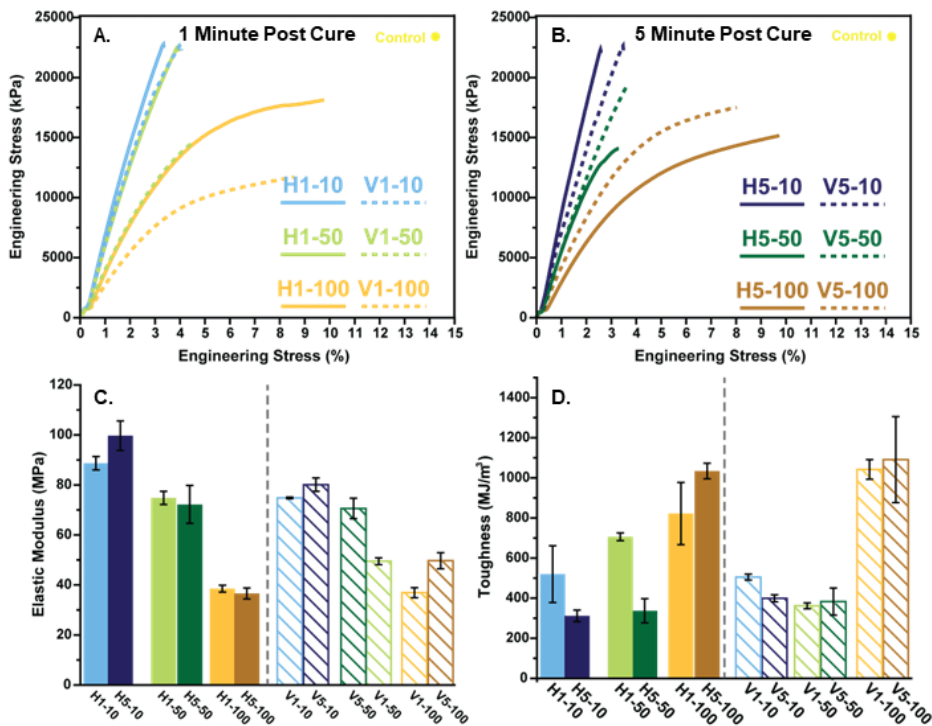


Figure 3. Tensile data for effect of post cure time. A. Tensile curves for 1-minute post cure B. Tensile curves for 5-minute post cure C. Elastic Modulus D. Toughness.

Notably, both the print direction effects, and the post cure time effects were dictated by the layer thickness. Satisfyingly, the shape of the tensile curves for the 10 μm (Figure 4A), 50 μm (Figure 4B), and 100 μm (Figure 4C) layer thickness systems described transition from a brittle material to ductile-like material as the layer thickness increased.

Overall, the strength of the material decreased as the layer thickness increased (Figure 4D). Additionally, the toughness of the material increased as the layer thickness increased (Figure 4E). The effect of the layer thickness on the material properties was found to be the most influential. The key reason for the heavy influence is because the change in layer thickness fundamentally changed how the network formed during the manufacturing process.

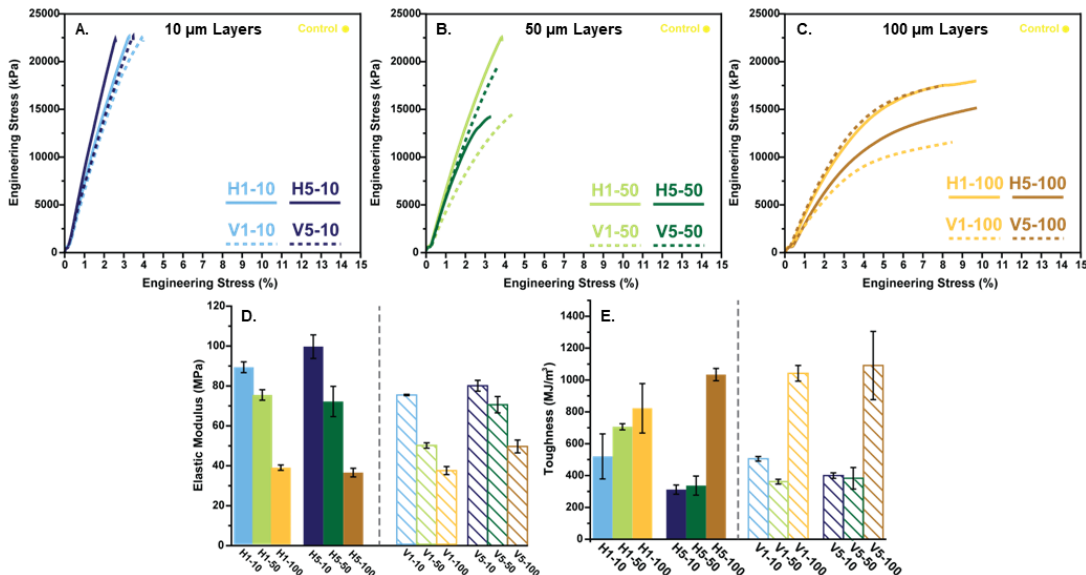


Figure 3. Tensile data for effect of layer thickness. A. Tensile curves for 10 μm layer thickness B. Tensile curves for 50 μm layer thickness C. Tensile curves for 100 μm layer thickness D. Elastic Modulus E. Toughness.

4. CONCLUSIONS

This study was able to manipulate the mechanical properties of a singular resin formulation by changing the printing parameters, revealing additional information about both the network formation and the relationship between the mechanical properties of the printed parts and variations during the manufacturing process. These property variations are a consequence of the nature of resin printing, which rely on a sequential crosslinking reaction. As established by thermoset knowledge, the properties of a polymer network are dictated by the overall network structure. When defects are present within a network, such as dangling ends or loops, lower mechanical properties are anticipated. Additionally, the crosslinking density also shifts the mechanical properties. Applying this knowledge to the results of this study, it can be inferred that alterations in the layer thickness yielded changes to the bulk network structure. In a printing process with smaller layers, the network conversion within a single layer is higher (Figure 5). Due to the high conversion, few covalent bonds are able to form across the interface between the stacked layers. Conversely, a gradient in the degree of conversion is likely when a printing process utilizes larger layers, and this is favorable as it enables higher crosslinking reactions across the interface, which leads to stronger layer adhesion. In future studies, the network architecture will be more directly probed to gain a more complete understanding through scattering methods such as small angle x-ray scattering, wide angle x-ray scattering, and small angle neutron scattering.

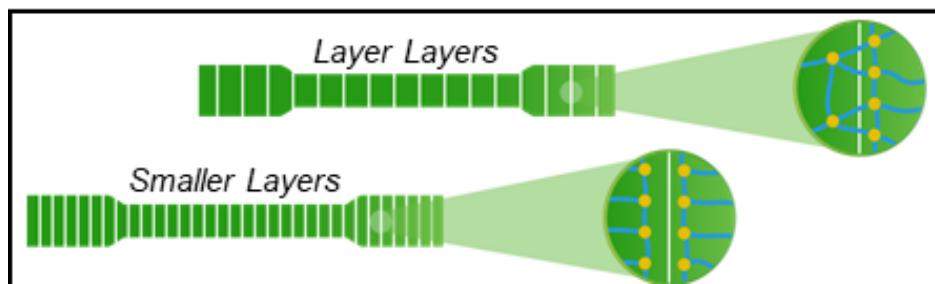


Figure 4. Proposed network formation at the interface of two layers.

ACKNOWLEDGMENTS

Funding was provided by the Director, Combat Capabilities Development Command Chemical Biological Center under the authorities and provisions of Section 2363 of the FY 2022 NDAA to develop new technologies, engineer innovations, and introduce game-changing capabilities.

REFERENCES

- [1] Abdulhameed, O.; Al-Ahmari, A.; Ameen, W.; Mian, S.H. Additive manufacturing: Challenges, trends, and applications. *Adv. Mech. Eng.* **2019**, *11* (2), pp 1–27.
- [2] Wang, A.; Vargas-Lara, F.; Younker, J.M.; Iyer, K.A.; Shull, K.R.; Keten, S. Quantifying Chemical Composition and Cross-link Effects on EPDM Elastomer Viscoelasticity with Molecular Dynamics. *Macromolecules*. **2021**, *54* (14), pp 6780–6789.
- [3] Singh, S.; Ramikrishana, S.; Singh, R. Material issues in additive manufacturing: A review. *J. Manuf. Process.* **2017**, *25*, pp 185–200.
- [4] Bikas, H.; Stavropoulos, P.; Chryssolouris, G. Additive manufacturing methods and modelling: a critical review. *J. Adv. Manuf. Technol.* **2016**, *83*, pp 389–405.
- [5] Weng, Z.; Zhoua, Y.; Lin, W.; Senthila, T.; Wu, L. Structure-property relationship of nano enhanced stereolithography resin for desktop SLA 3D printer. *Composites, Part A*. **2016**, *88*, pp 234–242.
- [6] van Bochove, B.; Hannink, G.; Buma, P.; Grijpma, D.W. Preparation of Designed Poly(trimethylene carbonate) Meniscus Implants by Stereolithography: Challenges in Stereolithography. *Macromol. Biosci.* **2016**, *16* (12), pp 1853–1863.
- [7] Gibson, I.; Rosen, D.; Stucker, B. *Additive Manufacturing Technologies: 3D printing, Rapid Prototyping, and direct digital manufacturing*; Springer Verlag, **2016**.

Janus metal-organic framework micromotors for the efficient removal of chemical agents

Matthew D. Collins^a, Eric R. Languirand^{b*}, Angus Unruh^c, Ayusman Sen^c

^aLeidos, 1750 Presidents St., Reston, VA 20190

^bU.S. Army Combat Capabilities Development Command Chemical Biological Center, Research & Operations Directorate, 8198 Blackhawk Rd., Aberdeen Proving Ground, MD 21010

^cDepartment of Chemistry, The Pennsylvania State University, University Park, PA 16802

ABSTRACT

Chemically powered micromotors are an active matter system that developed for potential applications in chemical warfare agent decontamination. Specifically, micromotors can increase the rate of chemical warfare agent decontamination through active movement compared to stationary decontamination particles limited by passive diffusion without mechanical stirring. In this work, we functionalized platinum Janus micromotors with UiO66 metal-organic frameworks that have been previously shown to be effective at decontaminating chemical warfare agents because of its high porosity/surface area compared to other commonly used materials for decontamination. Here, we share the current progress of synthesizing and characterizing the motion of standard micromotors as well as Pt/UiO66@SiO₂ micromotors. Future work of this project will include comparing the decontamination efficiency of simulants and chemical warfare agents with Pt/UiO66@SiO₂ Janus micromotors to stationary UiO66 metal organic frameworks with the goal that the Pt/UiO66@SiO₂ Janus micromotors will show chemical warfare agent decontamination at a magnitude faster compared to stationary UiO66 metal organic frameworks without mechanical stirring. Through this work, we aim to find the optimal micromotor design for rapid and efficient chemical warfare agent decontamination.

Keywords: micromotors, active matter, Janus particles, metal-organic frameworks, chemical warfare agent, decontamination

1. INTRODUCTION

The objective of this work is to design self-powered autonomous systems for the rapid and efficient removal of chemical agents. Most currently available systems for chemical agent neutralization are passive in that the chemical agents must reach the neutralization center by simple Brownian diffusion. In principle, the process can be sped up if the neutralization center can move autonomously and actively “seek out” the chemical agent molecules. This feature may prove particularly useful in accelerating decontamination against chemical agent molecules found embedded within surface micro cracks, strongly adsorbed on target surfaces, or migrated within the matrix of items to be cleaned. By using self-powered autonomous motion, these particles may move against fluid flows or may be more likely to move into harder to reach smaller interspecies, thereby interacting with the target analyte more rapidly compared to passive diffusion alone.

Achieving this potentially significant increase in decontamination efficiency will require an “active” system that can self-propel by harvesting energy locally. Synthetic nano/micromotors constitute one class of active systems, which developed over the last decade with potential applications in self-assembly, chemical sensing, and targeted drug delivery.¹⁻⁴ Additionally, these active motors are beginning to be investigated for possible Department of Defense-related applications, such as chemical warfare agent detection and/or decontamination.⁵⁻⁷ Typically, these motors are asymmetrical particles that catalyze a chemical reaction, converting the released chemical energy into directed mechanical motion.³ The most well-known example are platinum/gold microrods that move by a generated proton gradient upon addition of hydrogen peroxide fuel.^{3,8} There are other types of catalytic motors including metal/polymer Janus particles (e.g., one hemisphere of the particle is metal, while the other hemisphere is polymer), metal/oxide photocatalytic motors, and enzyme-powered motors that utilize other propulsion mechanisms. Additionally, micromotors incorporating metal-organic frameworks (MOFs) are recently being explored as micromotors for water purification/nuclear waste removal.⁹⁻¹² Previously, MOFs have also shown great potential for

rapid chemical agent decontamination, in part because of highly porous surfaces.^{13,14} These results suggest the MOF-based micromotors as particularly attractive systems for the rapid and efficient decontamination of a broad spectrum of chemical agents.

Specifically, this work is developing a micromotor for organophosphate-based CWA decontamination by capping platinum onto UiO66@SiO₂ Janus particles. The resulting Pt/UiO66@SiO₂ Janus micromotors will have two faces: one side with Pt to achieve motion by catalytically decomposing hydrogen peroxide fuel and the other side with UiO66 MOF with active sites to decontaminate CWA. We hypothesize that the Pt/UiO66@SiO₂ Janus micromotors will decontaminate CWA at a timescale that is a magnitude faster compared to stationary UiO66 MOFs without any mechanical stirring. If successful, the technique is agnostic to the type of MOF and may be expanded to incorporate other MOF structures for decontamination. This report summarizes the progress of our results, which comprises three main components: 1) control experiments characterizing the motion of standard self-electrophoretic micromotors, 2) characterization of the synthesized UiO66@SiO₂ Janus particles, and 3) characterization of the motion of the Pt/UiO66@SiO₂ Janus micromotors.

2. METHODOLOGY

2.1 Chemicals and materials

The base substrate particles used to synthesize standard Pt/PS micromotors include 3- μm sulfate functionalized polystyrene beads (Fisher Scientific, S37223A) and 1- μm sulfate functionalized polystyrene beads (Fisher Scientific, S37498). For Pt/SiO₂ micromotors, 3- μm silica beads (Bangs Laboratories, SS05001) or 40–60 μm aminosilica beads (Fisher Scientific, AC360180100) were used as the base substrate particles. Platinum metal targets (Ted Pella, 91114) were used to coat the base substrate particles with platinum to yield Pt/PS or Pt/SiO₂ micromotors. Other chemicals used include methanol (Sigma Aldrich, 322415), deionized (DI) water (Neu-Ion), 30 % hydrogen peroxide (Sigma Aldrich, H1009), 20% Sodium Dodecyl Sulfate Solution (Fisher Scientific, BP1311-1), and Sodium Cholate (Sigma Aldrich, 229101). All chemicals were used as received.

2.2 Pt/UiO66@SiO₂ micromotor synthesis

A schematic showing the synthetic steps to make Pt/UiO66@SiO₂ micromotors can be seen in Figure 1. As seen in the top portion, a shell of UiO66 MOFs were synthesized on amino functionalized SiO₂ micro beads to form UiO66@SiO₂ particles according to previously published procedures.¹⁵ These UiO66@SiO₂ particles were then suspended in methanol as a fast-evaporating solvent and dropcasted on clean glass microscope slides to form an approximately monolayer of UiO66@SiO₂ particles on the glass microscope slide when dried. Afterwards, as shown in the bottom portion, about 10 nm of Pt was sputtered onto the UiO66@SiO₂ particles with a Cressington 208 HR sputter coater (80 mA current). Microscope brushes are used to suspend the Pt/UiO66@SiO₂ micromotors into DI water. The micromotor sample is centrifuged and washed twice to result in the micromotor sample used in the following experiments. Additionally, Pt/PS and Pt/SiO₂ micromotors were synthesized according to the same procedure without any UiO66 for control micromotor motion characterization experiments.

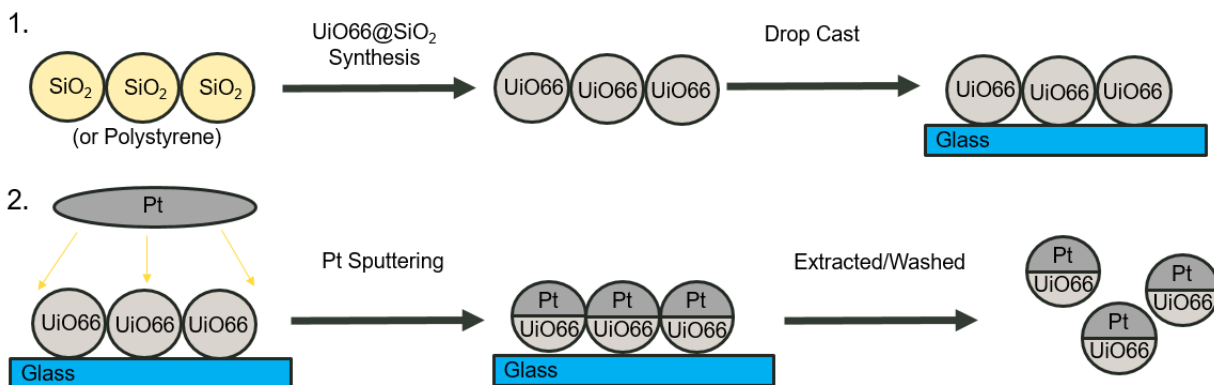


Figure 1. Schematic showing the synthesis steps to make Pt/UiO66@SiO₂ micromotors. Step 1 synthesizes UiO66@SiO₂ particles. Step 2 coats the UiO66@SiO₂ particles with platinum to result in Pt/UiO66@SiO₂ micromotors.

2.3 Micromotor motion characterization

The motion of the micromotors was characterized in aqueous solution with a Keyence optical microscope. The micromotor sample of interest, hydrogen peroxide fuel, and any surfactant (only for bubble-propelled motors) were pipetted into a 1.5 mL Eppendorf tube. The solutions were mixed with vortexing and/or sonication and 20 μL were placed on a clean glass microscope slide. Videos of the micromotors' motion were recorded at 15 fps. Self-electrophoretic motors were recorded with 1000x magnification at the solution/glass interface to prevent any observed fluid flows. The bubble-propelled motors were recorded at the air/solution interface for optimized viewing with 200x magnification. All videos were tracked with custom MATLAB code to record the position of each particle's center of mass between frames. The tracked data of the micromotors was used to calculate the trajectory of each particle as well as the average speed of each micromotor sample of interest.

3. RESULTS AND DISCUSSION

This section summarizes results of the control movement behavior of self-electrophoretic Pt/PS and Pt/SiO₂ micromotors in hydrogen peroxide fuel without any UiO66 MOFs.

3.1 Effect of H₂O₂ fuel concentration

When the 3 μm Pt/PS micromotors are in DI water without hydrogen peroxide fuel, the particles exhibit minimal Brownian motion that is not directional. In contrast, the 3- μm Pt/PS micromotors exhibit directional movement when hydrogen peroxide fuel is added to the system, which can be seen in Figure 2. The micromotors move independently of each other in different directions (Figure 2, left, red arrows) within the same viewing window. The average speed of the 3- μm Pt/PS micromotors increases when the concentration of hydrogen peroxide is increased from a speed of about 2.0 $\mu\text{m s}^{-1}$ at 0 % (w/w) H₂O₂ to a speed of about 6.0 $\mu\text{m s}^{-1}$ at 18 % (w/w) H₂O₂ (Figure 3). This observed increase of micromotor speed upon increasing the hydrogen peroxide fuel concentration matches previously reported observations.¹⁷ Note that this potentially 3D movement was measured in a 2D plane, which may lead to an apparent velocity that is lower than the true velocity.

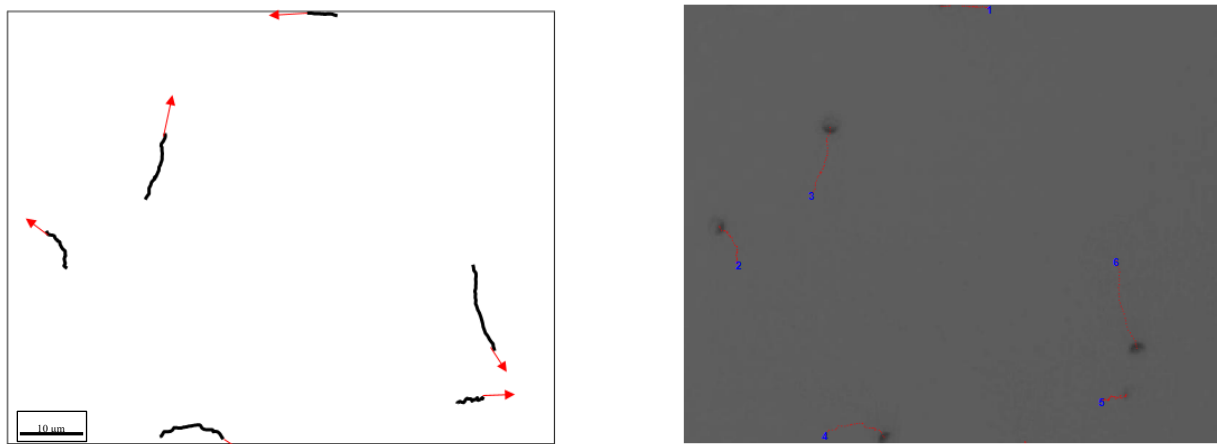


Figure 2. The 3- μm Pt/PS micromotors move directionally and independent of each other in hydrogen peroxide fuel. The left side shows the micromotor trajectories without the background image and the right side shows the same micromotor trajectories with the background image.

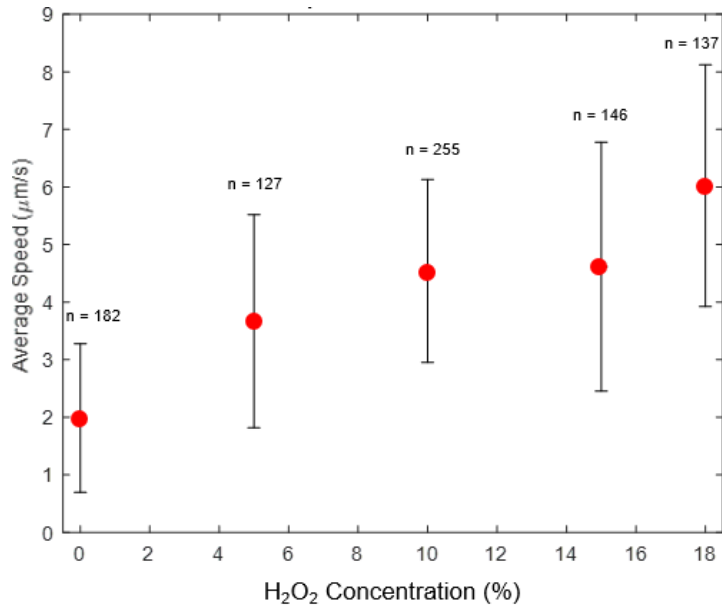


Figure 3. Scatter plot of the average speed of micromotors as a function of the hydrogen peroxide fuel concentration w/w. Every five frames were analyzed, with n representing the number of measurements, and the error bars represent standard deviation.

3.2 Effect of varying particle size

The effects of varying the particle size between 1 μm and 3 μm Pt/PS micromotors at similar concentrations of hydrogen peroxide fuel can be seen in Figure 4. Generally, the lighter and smaller 1-μm Pt/PS micromotors exhibit faster average speeds compared to the larger 3-μm Pt/PS micromotors, which is like previously reported observations.¹⁸ Additionally, the particle speeds exhibit a bimodal behavior suggesting two subsets of the population move at different speeds as the concentration of hydrogen peroxide increases, which can be seen in Figure 5. As the hydrogen peroxide concentration increases, the speeds of the faster peak increases while the slower peak remains constant, which results in greater peak separation. While this slower peak may be due to surface/particle interactions as reflected in the bimodal distribution, the average speed of the particles in the system are increased.

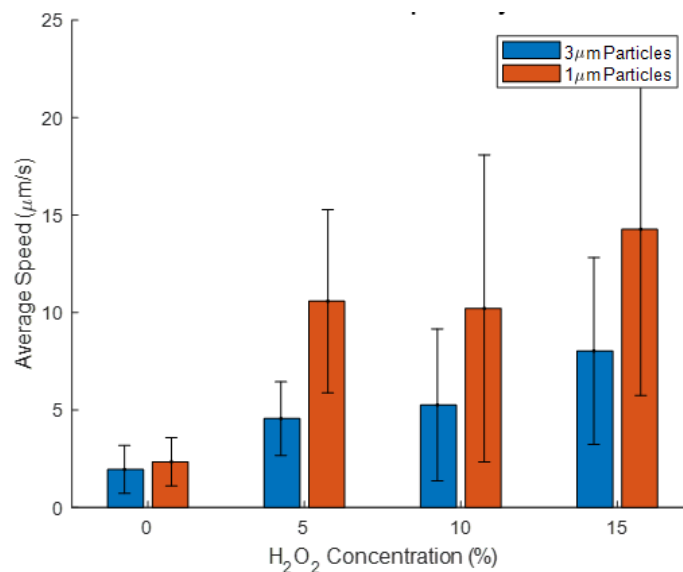


Figure 4. The average speed of the Pt/PS micromotors is faster when the particle size is smaller. Every five frames were analyzed, and the error bars represent standard deviation.

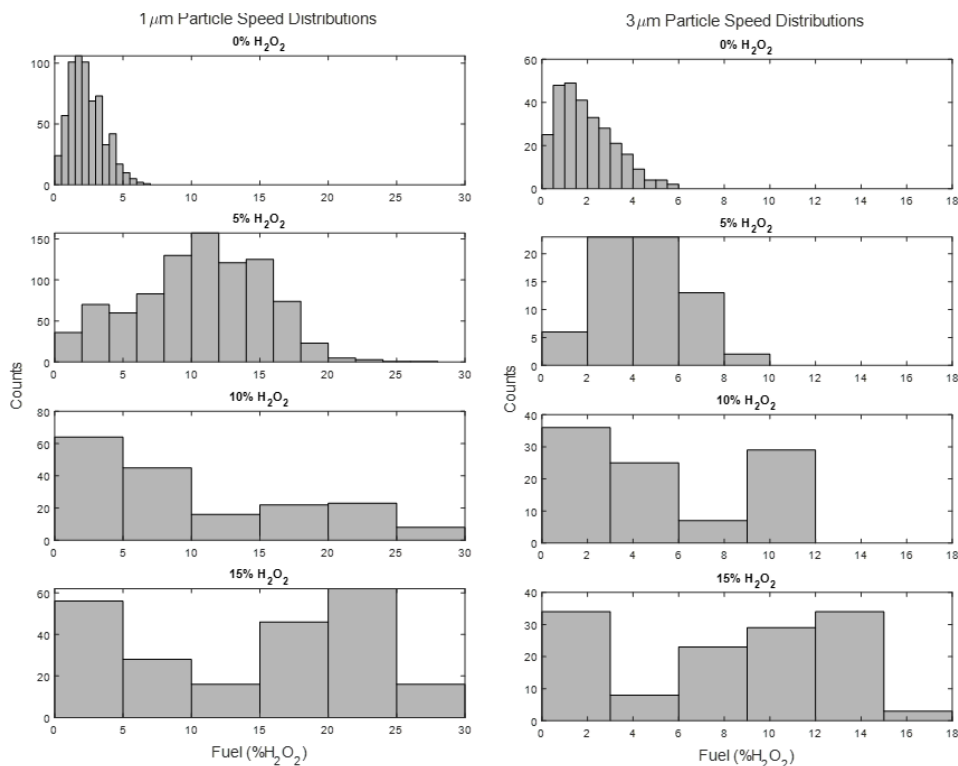


Figure 5. As the concentration of hydrogen peroxide fuel increases, the particle speeds exhibit a bimodal behavior with faster and slower peaks.

3.3 Effect of base substrate particle material

The effects of varying the base substrate particle material of the micromotors between polystyrene (Pt/PS) or silica (Pt/SiO₂) at a size of 3-μm can be seen in Figure 6. In general, the average speed of the Pt/SiO₂ micromotors is slower but comparable to Pt/PS micromotors of the same size. The similar speeds of the Pt/SiO₂ and Pt/PS micromotors indicates that the base substrate particle used in the design of the UiO66 micromotors has a less pronounced effect than particle size on particle speed. Additionally, the distribution of observed particle speeds of the Pt/SiO₂ and Pt/PS micromotors can be seen in Figure 7. As the hydrogen peroxide concentration increases, the Pt/PS exhibit a greater difference in bimodal distribution that was similarly observed in Figure 5. In contrast, the Pt/SiO₂ micromotors exhibit a broader speed distribution due to the heavier particles. This result is expected considering the same propulsion mechanism for both particles, and that Si has more mass per unit volume than PS.

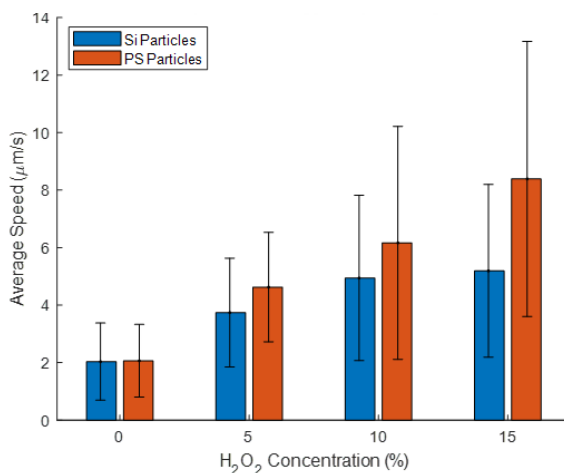


Figure 6. The average speed of the Pt/SiO₂ micromotors is slower but comparable to Pt/PS micromotors of the same size (3 μm). Every five frames were analyzed, and the error bars represent standard deviation.

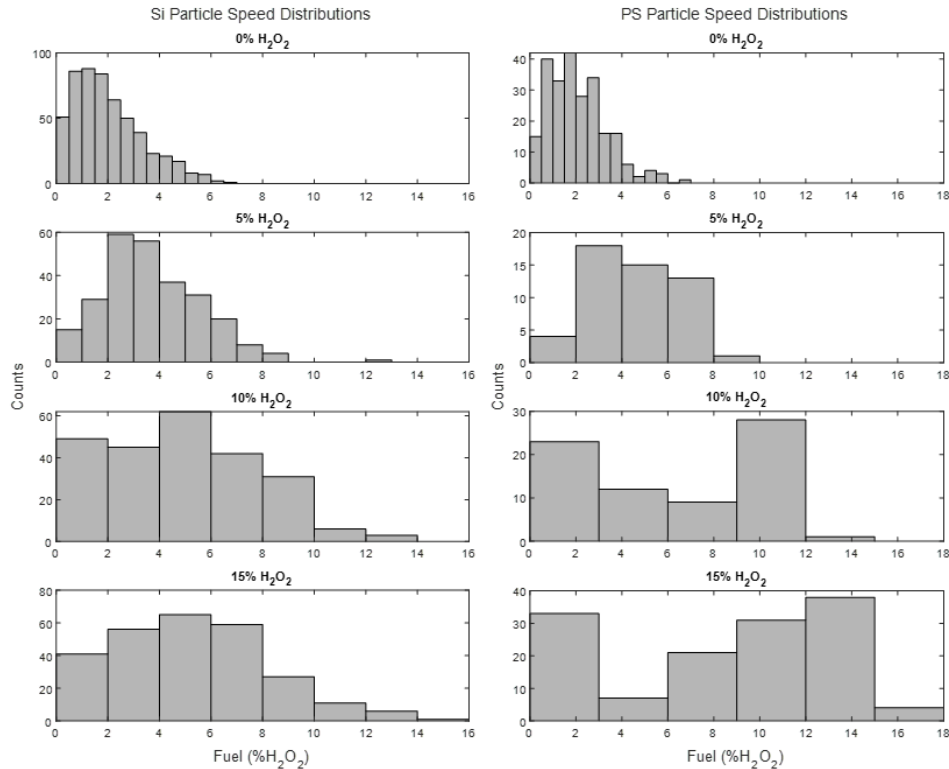


Figure 7. The speed distribution of the $3\mu\text{m}$ Pt/ SiO_2 and Pt/PS micromotors. The Pt/ SiO_2 micromotors exhibit a broader speed distribution due to the heavier particles while the Pt/PS micromotors exhibit a bimodal distribution as previously observed.

3.4 UiO66@ SiO_2 Janus particle characterization

UiO66@ SiO_2 Janus particles were designed to be explored as micromotors. Figure 8 shows characterization of the UiO66 MOFs that were first synthesized without any polystyrene or silica particles according to previous procedures.¹⁶ The left image of Figure 8 shows an SEM image of the UiO66 MOFs showing that the particles are on the nano scale in size. The right image of Figure 8 shows a powder X-ray diffraction (PXRD) spectrum showing the comparison between the synthesized UiO66 MOFs (black) and literature spectrum (blue).¹⁹ The spectrum of the synthesized UiO66 MOFs and the literature spectrum both show a similar pattern of the peak locations (degrees) and peak heights (intensity) indicating that the UiO66 MOF was properly synthesized. Additionally, previously reported procedures to grow a UiO66 shell on SiO_2 core particles to yield UiO66@ SiO_2 Janus particles were used (Figure 9).¹⁵ As there was a backorder of reagents, a first attempt with similar reagents that were on hand was attempted, which resulted in SiO_2 particles with partial UiO66 coverage as seen in the left SEM image of Figure 9. When proper reagents were received and used, the SiO_2 particles had complete coverage, which can be seen in the right SEM image of Figure 9. Note that the SiO_2 particles used for this synthesis were 40–60 μm in size and varied in morphology (Figure 9). Furthermore, energy dispersive spectroscopy (EDS) elemental analysis was completed on the UiO66@ SiO_2 Janus particles, which can be seen in Figure 10 showing that the presence of Si, Zr, and N are approximately observed in the same location. The co-localization of these elements indicates that the Zr as UiO66 was successfully grown on the SiO_2 core. The presence of Zr and N in similar locations indicates that the Zr from the UiO66 is associating with N from the amino functionalized silica as shown from previous research.¹⁵

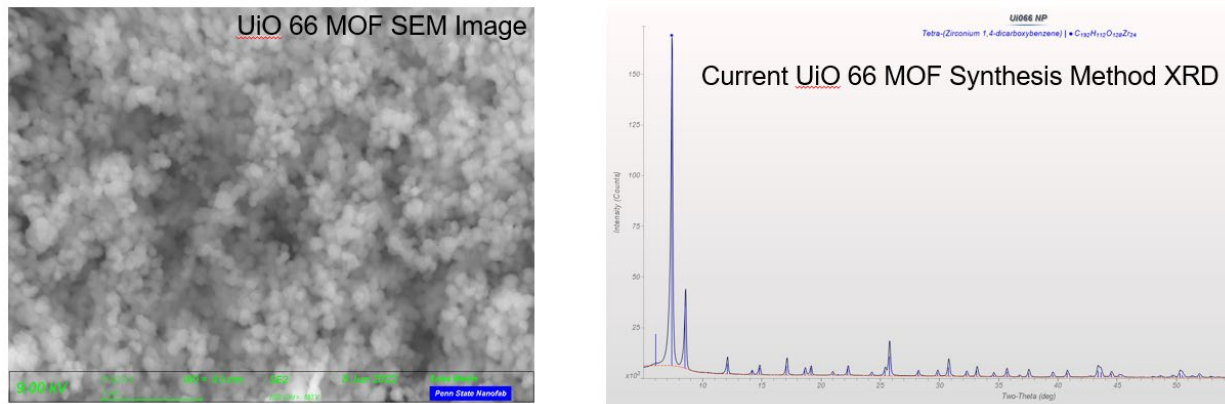


Figure 8. SEM image (left) and XRD (right) of UiO66 MOFs. XRD traces shown for material synthesized here (black) and a previously reported UiO66 MOF material (blue).

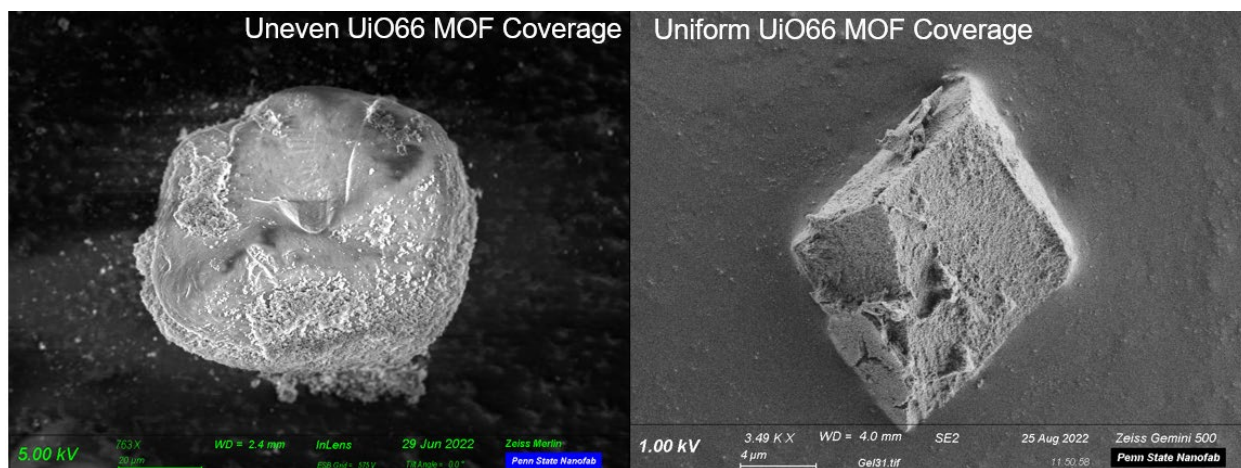


Figure 9. SEM images of UiO66@SiO₂ Janus particles. The left image shows partial UiO66 coverage from Pennsylvania State University’s first attempt without the proper reagents in stock. The right image shows complete UiO66 coverage from Pennsylvania State University’s second attempt with the proper reagents in stock.

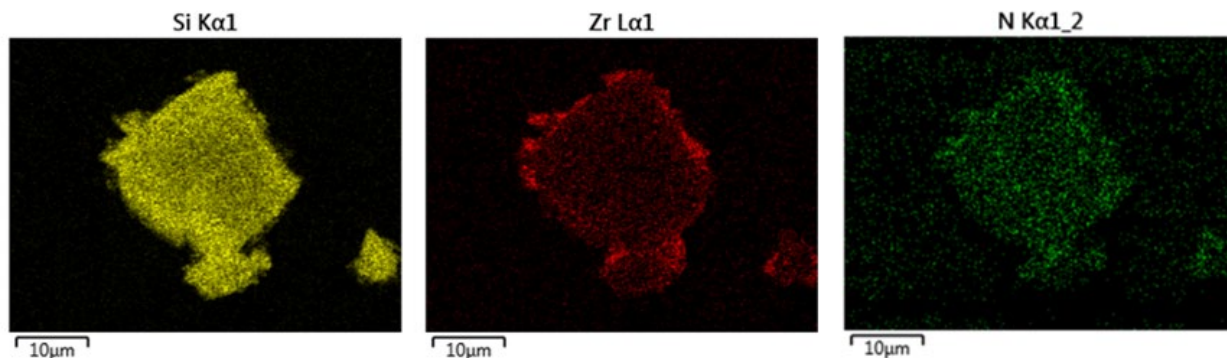


Figure 10. EDS elemental analysis of a UiO66@SiO₂ Janus particle showing that the presence of Si, Zr, and N are approximately observed in the same location. These elements found in similar locations indicates that the Zr as UiO66 was successfully grown on the SiO₂ core. The presence of Zr and N in similar locations indicates that the Zr from the UiO66 is associating with N from the amino-functionalized silica as shown from previous work.

3.5 Pt/U_iO₆₆@SiO₂ Janus micromotor movement characterization

The trajectory of a typical Pt/U_iO₆₆@SiO₂ Janus micromotor over a 3 s period with the motor starting at the right side of the viewing window with hydrogen peroxide fuel and 1 % (w/w) SDS surfactant to promote oxygen bubble nucleation (Figure 11). The red line of Figure 11 traces out the observed trajectory with the Pt/U_iO₆₆@SiO₂ Janus micromotor moving at a speed of $\sim 12.4 \mu\text{m s}^{-1}$. The bubble propulsion will likely result in greater mixing and more rapid decontamination as well. Current efforts are looking at how to track bubble-propelled particles appropriately for comparison to electrophoretic micromotors.

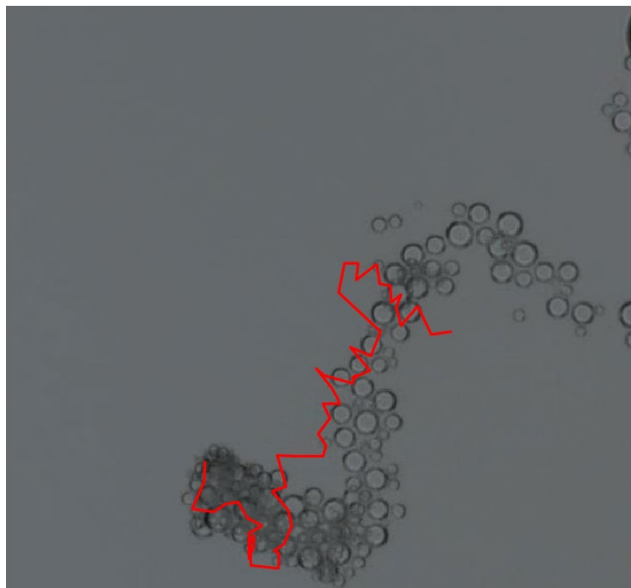


Figure 11. Trajectory of a typical Pt/U_iO₆₆@SiO₂ Janus micromotor over a 3 s period with the motor starting at the right side of the viewing window with hydrogen peroxide fuel and 1% (w/w) SDS surfactant to promote oxygen bubble nucleation. The red line shows the trajectory of the Pt/U_iO₆₆@SiO₂ Janus micromotor moving at a speed of $\sim 12.4 \mu\text{m s}^{-1}$.

4. CONCLUSIONS

Here, we reported the synthesis of standard Pt/PS and Pt/SiO₂ micromotors and characterized the motion of the micromotors in different conditions. These characterization data were further verified with comparison to previously published observations. We showed that Pt/PS motors move faster in higher concentrations of hydrogen peroxide, smaller micromotors generally move faster compared to larger micromotors, and micromotors made with silica beads move marginally slower to micromotors made with polystyrene beads. Moreover, we successfully synthesized U_iO₆₆@SiO₂ Janus particles and coated the resulting particles with platinum to create Pt/U_iO₆₆@SiO₂ Janus micromotors that move with hydrogen peroxide fuel and SDS surfactant to nucleate oxygen bubbles.

Future work for this project will focus on motion characterization of the Pt/U_iO₆₆@SiO₂ Janus micromotors under different conditions. Other future work will include comparing the decontamination efficiency of CWA simulants with Pt/U_iO₆₆@SiO₂ Janus micromotors to stationary U_iO₆₆ MOFs with the goal that the Pt/U_iO₆₆@SiO₂ Janus micromotors will show CWA decontamination at a magnitude faster compared to stationary U_iO₆₆ MOFs without mechanical stirring. Beyond this project, we would like to explore developing a micromotor that uses CWA as a fuel instead of hydrogen peroxide for the combined application of simultaneous sensing and decontamination.

ACKNOWLEDGMENTS

We would like to thank Erik Emmons and Ashish Tripathi from U.S. Army Combat Capabilities Development Chemical Biological Center for allowing us to use their Cressington 208 HR sputter coater in this work. Additionally, we would like to acknowledge the fruitful comments and discussions born from the CBC reviewers of our work. Funding was provided by the U.S. Army via the Chemical Biological Advanced Materials and Manufacturing Science

Program (PE 0601102A Project VR9) at the U.S. Army Combat Capabilities Development Command Chemical Biological Center.

REFERENCES

- [1] Altemose, A.; Harris, A.J.; Sen, A., Autonomous Formation and Annealing of Colloidal Crystals Induced by Light-Powered Oscillations of Active Particles. *Chem Systems Chem.* **2020**, *2* (1), p e1900021.
- [2] Jurado-Sánchez, B.; Wang, J., Micromotors for environmental applications: a review. *Environ. Sci.: Nano.* **2018**, *5* (7), pp 1530–1544.
- [3] Sengupta, S.; Ibele, M.E.; Sen, A. Fantastic Voyage: Designing Self-Powered Nanorobots. *Angew. Chem. Int. Ed.* **2012**, *51* (34), pp 8434–8445.
- [4] Wang, W.; Li, S.; Mair, L.; Ahmed, S.; Huang, T.J.; Mallouk, T.E. Acoustic Propulsion of Nanorod Motors Inside Living Cells. *Angew. Chem. Int. Ed.* **2014**, *53* (12), pp 3201–3204.
- [5] Li, J.; Singh, V.V.; Sattayasamitsathit, S.; Orozco, J.; Kaufmann, K.; Dong, R.; Gao, W.; Jurado-Sanchez, B.; Fedorak, Y.; Wang, J. Water-Driven Micromotors for Rapid Photocatalytic Degradation of Biological and Chemical Warfare Agents. *ACS Nano.* **2014**, *8* (11), pp 11118–11125.
- [6] Singh, V.V.; Martin, A.; Kaufmann, K.; D.S. de Oliveira, S.; Wang, J., Zirconia/Graphene Oxide Hybrid Micromotors for Selective Capture of Nerve Agents. *Chem. of Mater.* **2015**, *27* (23), pp 8162–8169.
- [7] Singh, V.V.; Wang, J. Nano/micromotors for security/defense applications. A review. *Nanoscale.* **2015**, *7* (46), pp 19377–19389.
- [8] Dey, K.K.; Wong, F.; Altemose, A.; Sen, A. Catalytic Motors—Quo Vadimus? *Curr. Opin. Colloid Interfaces Sci.* **2016**, *21*, pp 4–13.
- [9] Li, J.; Yu, X.; Xu, M.; Liu, W.; Sandraz, E.; Lan, H.; Wang, J.; Cohen, S.M. Metal–Organic Frameworks as Micromotors with Tunable Engines and Brakes. *J. Am. Chem. Soc.* **2017**, *139* (2), pp 611–614.
- [10] Wang, R.; Guo, W.; Li, X.; Liu, Z.; Liu, H.; Ding, S. Highly efficient MOF-based self-propelled micromotors for water purification. *RSC Advances.* **2017**, *7* (67), pp 42462–42467.
- [11] Yang, Y.; Arqué, X.; Patiño, T.; Guillerm, V.; Blerch, P.-R.; Pérez-Carvajal, J.; Imaz, I.; Maspoch, D.; Sánchez, S. Enzyme-Powered Porous Micromotors Built from a Hierarchical Micro- and Mesoporous UiO-Type Metal–Organic Framework. *J. Am. Chem. Soc.* **2020**, *142* (50), pp 20962–20967.
- [12] Ying, Y.; Pourrahimi, A.M.; Sofer, Z.; Matějková, S.; Pumera, M. Radioactive Uranium Preconcentration via Self-Propelled Autonomous Microrobots Based on Metal–Organic Frameworks. *ACS Nano.* **2019**, *13* (10), pp 11477–11487.
- [13] Islamoglu, T.; Chen, Z.; Wasson, M.C.; Buru, C.T.; Kirlikovali, K.O.; Afrin, U.; Mian, M.R.; Farha, O.K. Metal–Organic Frameworks against Toxic Chemicals. *Chem. Rev.* **2020**, *120* (16), pp 8130–8160.
- [14] Liu, Y.; Howarth, A.J.; Vermeulen, N.A.; Moon, S.-Y.; Hupp, J.T.; Farha, O.K. Catalytic degradation of chemical warfare agents and their simulants by metal-organic frameworks. *Coord. Chem. Rev.* **2017**, *346*, pp 101–111.
- [15] Zhang, X.; Han, Q.; Ding, M. One-pot synthesis of UiO-66@SiO₂ shell–core microspheres as stationary phase for high performance liquid chromatography. *RSC Advances.* **2015**, *5* (2), pp 1043–1050.
- [16] Zhang, X.; Zhao, Y.; Mu, S.; Jiang, C.; Song, M.; Fang, Q.; Xue, M.; Qiu, S.; Chen, B. UiO-66-Coated Mesh Membrane with Underwater Superoleophobicity for High-Efficiency Oil–Water Separation. *ACS Appl. Mater. Interfaces.* **2018**, *10* (20), pp 17301–17308.
- [17] Paxton, W.F.; Kistler, K.C.; Olmeda, C.C.; Sen, A.; St. Angelo, S.K.; Cao, Y.; Mallouk, T.E.; Lammert, P.E.; Crespi, V.H. Catalytic Nanomotors: Autonomous Movement of Striped Nanorods. *J. Am. Chem. Soc.* **2004**, *126* (41), pp 13424–13431.
- [18] Meng, S.; Zhang, Y.; Liu, Y.; Zhang, Z.; Ma, K.; Chen, X.; Gao, Q.; Ma, X.; Wang, W.; Feng, H. The Effect of Particle Size on the Dynamics of Self-Electrophoretic Janus Micromotors, Sputtering, Distribution, and Rectifying Voltage. *JCIS Open.* **2022**, *5*, p 10046.
- [19] Xu, W.; Dong, M.; Di, L.; Zhang, X. A Facile Method for Preparing UiO-66 Encapsulated Ru Catalyst and its Application in Plasma-Assisted CO₂ Methanation. *Nanomaterials.* **2019**, *9*, p 1432.

This page intentionally left blank

Effect of composition and process control agent on the microstructure and ignition properties of ball-milled aluminum-zirconium powders

Amee Polk^{a,b*}, Kerri-lee A. Chintersingh^{b,c}, Erica R. Valdes^a, Michael Flickinger^b,
Timothy P. Weihs^b

^aU.S. Army Combat Capabilities Development Command Chemical Biological Center, Research & Operations Directorate, 8198 Blackhawk Rd., Aberdeen Proving Ground, MD 21010

^bDepartment of Materials Science and Engineering, Johns Hopkins University, 3400 North Charles Street, Baltimore, MD 21218

^cDepartment of Chemical and Materials Engineering, New Jersey Institute of Technology, University Heights, Newark, NJ 07102

ABSTRACT

Aluminum-zirconium (Al-Zr) composite powders with varying atomic ratios, 3Al:Zr, Al:Zr, and Al:3Zr, were prepared using arrested reactive ball milling in a planetary mill with hexanes as a process control agent. All prepared materials were characterized for particle morphology, microstructure, low-temperature inter-metallic reactions, and ignition temperatures in air. Since Al-rich powders had significant cold welding during preparation by milling, acetonitrile, a known solvent for reducing aluminum particle size, was introduced to replace hexane as a process control agent to minimize this effect. Data is presented for Al-rich composites milled with 0 vol%, 6.25 vol% and 12.5 vol% of acetonitrile with the balance as hexane.

Keywords: intermetallic, ignition, arrested reactive milling

1. INTRODUCTION

Micron-sized metal powders are potential fuel additives in explosives, pyrotechnics, and propellants due to their high energy densities,^{1,2} and aluminum (Al) is the traditional metal of choice for these applications.³ However, the ignition threshold for Al is heavily dependent on particle size, and the combustion efficiency of pure, commercial, micron-sized aluminum powder is low.⁴ To mitigate these challenges, some researchers have introduced metal additives such as zirconium (Zr) or magnesium (Mg) into Al powders through arrested reactive ball-milling (ARM)^{5,6} which lowers ignition temperatures, increases combustion rates and temperatures, and improves combustion efficiencies.^{7,8} The reduction of ignition thresholds is attributed to the exothermic mixing of Al and Zr, the more rapid, low-temperature oxidation of Zr, and the early release of Mg vapor on heating.⁹ The higher combustion efficiencies in closed-chamber blast tests are attributed to the alloyed powders combusting in both a vapor phase and a condensed phase, which is often referred to as dual-phase combustion.

Al powders are commonly used in reduction-oxidation or thermite reactions to join or heat other objects.¹⁰ However, in most cases, significant gas is generated during the thermite reaction which is an undesirable side effect in many applications. Therefore, this project aims to create a powder compact capable of a thermite reaction with low gas formation when coupled with the more reactive, Al composite powders. Initially, the microstructure and reactive properties of Al-Zr composite powders that were fabricated by ball milling and range in chemistry from Zr-rich (25 at% Al) to Al-rich (75 at% Al) were examined. Focus was placed on the binary Al-Zr system while the Al-Mg-Zr ternary system was largely ignored as Mg is known to generate vapor at relatively low reaction temperatures. For fabrication, ARM was utilized as it can generate composite powders with Zr inclusions in an Al matrix, and the refinement of the Zr inclusions can be tuned by varying milling parameters such as total time or the ball to powder ratio.^{9,11-15} Such composite structures are expected to have lower ignition thresholds compared to gas atomized powders where the Al and Zr are fully mixed. ARM processing also produces large powder volumes and can be used to generate large thermite powder compacts in subsequent efforts.

While ARM can generate significant volumes of composite powders with relatively uniform chemistries and sizes, Al-rich chemistries are prone to cold welding of the Al component due to its soft mechanical nature.^{8,13} In contrast, due to the brittle mechanical properties of Zr, the Zr rich and 50:50 chemistries are less prone to cold welding. To combat the cold-welding of the Al rich chemistry, two processing control agents (PCA): hexane and acetonitrile that are immiscible were used. Recent work found that these PCAs not only act as cooling agents during milling by absorbing the heat generated by collisions, they can also functionalize the milled material,^{11,16,17} tailor particle size and morphology, and inhibit cold welding.¹⁷ In this study we fabricate, characterize and compare Al:3Zr, Al:Zr, and 3Al:Zr composite powders using a single PCA (hexane). In addition, we assess how much acetonitrile must be added to hexane to prevent cold-welding during ARM of 3Al:Zr composite powders and thereby produce these powders with attractive size distributions and reaction properties.

2. MATERIALS AND METHODS

2.1 Material preparation

Aluminum (Alfa Aesar, 99.5 % pure, -325mesh, APS 7-15 μm) and zirconium (Atlantic Equipment Engineers, 99.5 % pure, -20 to +60 mesh) powders were purchased and milled in a Retsch PM400 planetary ball mill in air for one hour at 400 RPM. The milling cycle consisted of four 15-minute milling sessions separated by 30 minutes of rest and air cooling. Al-Zr composite powders with three atomic compositions: 75 at %Al (3Al:Zr), 50 at% Al (Al:Zr), and 25 at% Al (Al:3Zr) were prepared in 100 g or 60 g batches by loading the requisite mass of Al and Zr powders, specific volumes of hexane (Fisher Chemical 98.5 % pure) and/or acetonitrile (Fisher Chemical 99.95 % pure) as process control agents, and 3/8" stainless steel balls into 500 mL hardened steel milling vials. A ball to powder mass ratio of 3 was used for all milling, and the masses of powders and the volume of the two PCAs are listed in Table 1. Samples prepared with greater than 12.5 vol% acetonitrile were found to be pyrophoric upon exposure to air during recovery and therefore were not tested further. In addition, the mass of powders and the volume of PCA were reduced to minimize hazards after the sample with 100 % acetonitrile was found to be pyrophoric. Thus, the study presents and discusses results for 3Al:Zr samples milled with 0 vol% acetonitrile, 6.25 vol% acetonitrile and 12.5 vol% acetonitrile following earlier volume ratios.¹⁵ Preliminary studies showed that for these chemistries milling with 60 g vs. 100 g did not significantly affect the material microstructure or performance. Lastly, all samples milled with acetonitrile were allowed to passivate for 24 hours prior to handling and subsequent characterization.

Table 1. Summary of milling conditions for Al-Zr composites

Target Composition/ Sample ID	Mass of Al loaded (g)	Mass of Zr loaded (g)	Volume of hexane (mL)	Volume of acetonitrile (mL)	Reactivity upon recovery
Al:3Zr 100 % HEX	9.025	91.038	100	0	None
Al: Zr 100 % HEX	22.864	77.286	100	0	None
3Al:Zr 100 % HEX	47.144	52.888	100	0	None
3Al:Zr 6.25 % ACN	28.224	31.704	45	3	None
3Al:Zr 12.5 % ACN	28.215	31.215	42	6	None
3Al:Zr 30 % ACN	28.223	31.783	33.6	14.4	Pyrophoric
3Al:Zr 50 % ACN	28.205	31.941	24	24	Pyrophoric
3Al:Zr 100 % ACN	47.131	52.892	0	84	Pyrophoric

2.2 Material characterization

All milled samples were dry sieved using a Dual Manufacturing Co. Inc. D-4326 motorized shaker at 2000 vpm in a 3", 75 μm (200-mesh) brass sieve for a minimum of 30 minutes to eliminate larger, un-milled Zr fragments and agglomerates. A portion of each composite powder was also left un-sieved for comparison.

The sieved powders were examined using a JEOL 7001LV FESEM for particle morphology and elemental composition. Samples were mounted onto aluminum stubs using carbon tape to fix the loose particles in place. Secondary electron and backscatter electron images were recorded at varying magnifications. An Oxford Aztec EDS with X-Max 80 mm detector was used to collect compositional information for each of the loose powder samples.

Samples of each of the sieved powders were mounted in epoxy and polished using a Struers Tegramin-20 with silicon carbide polishing paper (sequentially finer grits, 320, 600, 800, 1000, and 1200) to prepare cross-sections for analysis of Zr inclusions. Large panoramic backscattered electron images of the cross-sectioned samples were generated by stitching together 10,000x high magnification images. These images were collected using the MAPS 3.0 software and a Thermo Scientific Helios G4 UC Focused Ion Dual Beam Instrument equipped with a monochromated electron beam for scanning electron imaging and Tomahawk ion column. The stitched images were analyzed for distribution of Zr inclusion area using a customized code for processing in ImageJ, a commercially available software. A script was written in Java[®] to process each image that first sets the scalebar and threshold value to determine the cumulative distribution of Zr inclusions within each sample.

Powder size distributions were determined using a Horiba LA-950 V2 particle size analyzer. The powders were dispersed in isopropanol and the particle size determined using low angle laser scattering with 60s ultrasonication to break agglomerates.

Densities of the sieved and as-milled (un-sieved) composite powders were measured via helium pycnometry using a Micromeritics AccuPyc II 1340 pycnometer and Mettler Toledo microbalance. The sample runs were completed in triplicates and the average and standard deviations of the measurements recorded.

Porosity and surface area measurements were determined using nitrogen isotherms with a Micromeritics ASAP 2040 analyzer at 77 K. Samples were de-gassed at 100 °C under vacuum for ~16 h. The Brunauer–Emmett–Teller (BET) method was used to calculate surface area.

Crystalline phases of each as-milled composite powder were determined using a Bruker D8 Focus Diffractometer with LynxEye detector at 45 kV and 40 mA with Cu-K α radiation. Samples were mounted onto a steel puck with an aluminum insert. A 1 mm source slit with anti-scatter was used, and scans were run from 10 ° to 80 ° 2 θ . XRD patterns were analyzed using Match! 3.0 software. The reaction products of samples heated to 600 °C and 1000 °C in an inert environment were also characterized by powder XRD analysis.

2.3 Low temperature reaction characterization

2.3.1 Thermogravimetric analysis

The atomic intermixing of Al and Zr and their formation of compounds were characterized under slow heating condition using a TA Instruments SDT Q600 Differential Thermal Analysis (DTA) system. Approximately 10 ± 0.058 mg of sample was heated twice from 50 °C to 1000 °C at a rate of 40 °C/min under high purity argon flowing at 200 mL/min. The first heating was used to determine the heat released by the intermixing and formation reactions, knowing they are irreversible. The second heating provides the baseline heat capacity of the reacted material and crucible and was subtracted from the first heating cycle to determine the net heat flow. The net heat flow was integrated from 120 °C to 660 °C to calculate the total heat released from the intermixing and formation reactions at low temperatures, a range that incorporates ignition temperatures measured on rapid heating. DTA analyses were completed for both sieved and un-sieved samples and repeated three times for each sample. Samples were also quenched from 600 °C and 1000 °C and characterized using a Bruker D8 Focus Diffractometer with a LynxEye detector to identify the intermetallic phases formed during different stages of heating.

2.3.2 Wire ignition

Ignition temperatures of the sieved samples were measured in air as a function of heating rate using a custom heated filament setup.^{8,18} Dilute suspensions of the powders were prepared in hexane; coated onto a 1 cm length of a 7 cm long, 28-gauge pretensioned nichrome wire; and then resistively heated using three 12 V car battery totaling 36 V DC (approximately 80 A). The temperature of the wire was recorded using a Luna Sense two-color, low-temperature infrared pyrometer calibrated for temperatures between 200 °C and 1000 °C. The moment of ignition, defined by the first instance of light seen by the camera, was captured using a Photron Limited Fastcam SA-Z high-speed camera set to record at 20,000 fps. A square wave 5 V pulse was generated through a LabView program to trigger simultaneous data collection by the high-speed video camera and pyrometer. The videos captured from the scene were analyzed using MATLAB to determine the moment of first light with an approximate 1 frame (0.5 ms) accuracy. This corresponds to a maximum uncertainty of 10 K in the temperature measurement.

Additionally, a NAC Memrecam HX-6 high-speed camera operating at 20,000 fps was used to capture color images of the burning particles.

3. RESULTS

3.1 Particle morphology and microstructure

Figure 1 provides representative secondary electron SEM images of ball-milled powders recorded at the same magnification (500 x) with secondary electrons (left column) and stitched backscattered electron SEM images of particle cross sections (right column). In the secondary electron images, all powders, regardless of composition, displayed similar morphology. All have rough, jagged surfaces, slightly elongated geometries, and a range of particle sizes. As the chemical composition becomes more Al-rich when milling in hexane, the particle size shifts larger Figure 1(a-c), and as the volume fraction of acetonitrile increases for the 3Al:Zr samples, Figure 1(c-e), the primary particle size decreases and agglomerates of smaller primary particles are more common (Figure 1(e)). Particle size distributions of the preparations are like the SEM measurements (data not shown).

Backscattered SEM particle cross-section images show the internal microstructure for each of the five samples in Figure 1, with Zr displaying as very light gray/bright white inclusions in a darker gray Al matrix. The higher atomic number of Zr leads to its lighter color. The black background of the samples is the epoxy used to fix the powders. Most of the inclusions are ellipsoids or elongated strands. The size of Zr inclusions appears to be largest in the 50 at% Al:Zr composition (Figure 2(g)). As the concentration of Al increases for samples milled in 100 % hexanes, the Zr morphology transitions from larger aspect ratio inclusions or strands to distinct equi-axed particles of Zr enveloped in the Al matrix. For the 3Al:Zr samples milled in hexane and acetonitrile, as the acetonitrile vol% increases, the particles appear less homogeneous, and transition to porous agglomerates with visible voids and cracks. Of note, in the 12.5 % ACN sample, there are several small Zr particles which are not incorporated in an Al matrix, which will impact the kinetics of Al-Zr intermixing and will provide more surface area for Zr oxidation in air.

To analyze the distribution of the size of Zr inclusions in samples, stitched images were imported into ImageJ, and thresholded based on pixel intensity so that the bright white regions representative of Zr were selected and separated from the black background and dark gray Al matrix upon conversion of the image to binary. This thresholding value was consistent for all images. A custom ImageJ code was then used to analyze the inclusion areas via the analyze particles feature. All inclusions contacting the edges of the images were ignored to prevent incomplete particle areas from being included in the analysis. Figure 2 shows an example of a raw input image and the processed image, where the black areas represent the Zr inclusions.

For each sample, three stitched images (each a 10 x 10 grid resulting in 100 images, giving a total of 300 images) were processed to determine the respective Zr inclusion area cumulative distribution function. The plots are shown in Figure 3. Samples milled in mixed PCAs have smaller inclusion areas; the smallest was for 6.25 vol% acetonitrile. The largest Zr inclusions are seen in the Al:Zr composition. The Zr-rich samples could not be analyzed, as the contrast of the images is the basis for thresholding.

The densities of the as milled and sieved samples differed by 0.01 to 0.03 g/cm³ for a given chemistry/PCA, indicating very little unrefined Zr exists after milling. The largest difference was recorded for the Al:Zr sample. A noticeable decrease in density is observed with increased acetonitrile fraction (data not shown). All samples were slightly lower than their predicted density, which may be a result of instrumentation drift, enclosed pores, or carbon incorporation during milling.

The surface area density of each chemistry was calculated via two methods: analysis of nitrogen isotherms using BET, and calculation of the diameter and volume fraction of particles in each size bin determined through particle size analysis (PSA). Both the BET and PSA calculated surface area densities show a small increase in surface area as the Zr at% increases and a substantial increase in surface area with rising acetonitrile fraction, as detailed in Table 2. These trends agree with decreases in mean particle sizes as the Zr at% increases and as the fraction of acetonitrile increases. However, the BET surface area densities are much higher than the calculated surface area densities for the Zr-rich powders milled in hexane and the Al-rich powder milled in acetonitrile. This difference correlates with observation of pores in the Al:3Zr powders in the cross-sectional images in Figure 1(j) and the observation of agglomeration of the 3Al:Zr 12.5 % ACN powders in Figure 1(e).

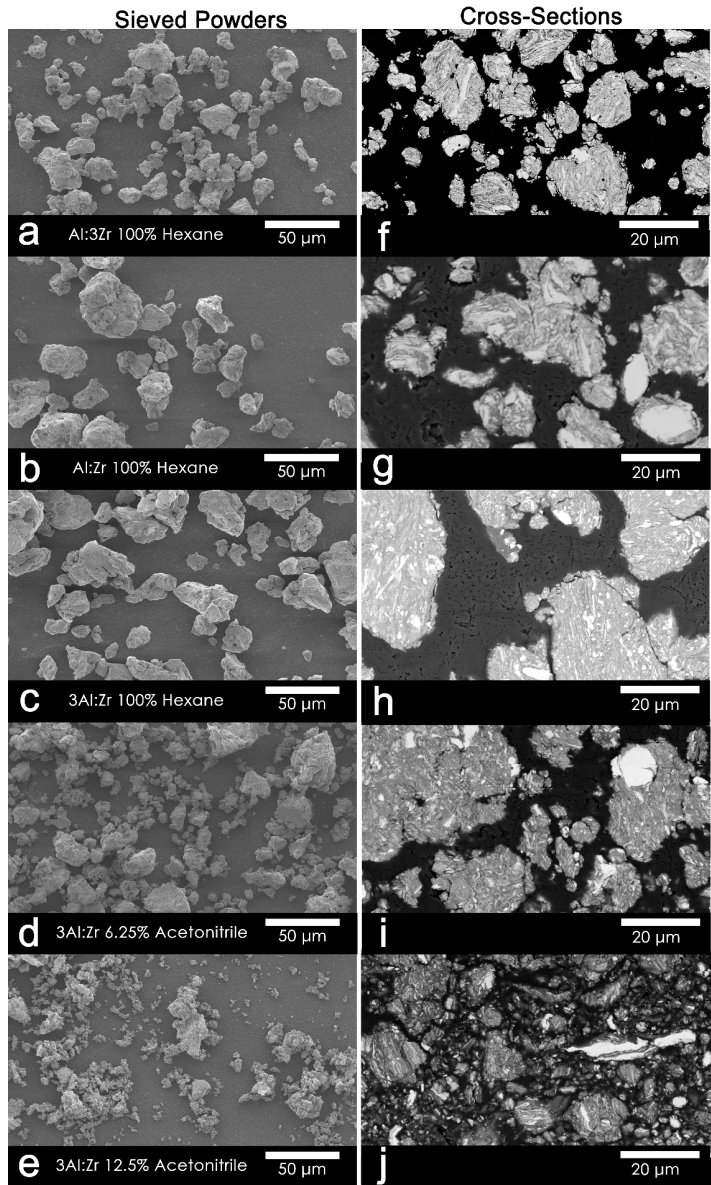


Figure 1 Left column: SEM images captured with secondary electrons for Al-Zr composites at 500 x magnification. Top images (a-c) show the effect of varying chemical compositions (Al:3Zr to 3Al:Zr) and images (c, d, and e) show the effect of varying vol% of acetonitrile (0, 6.25 % and 12.5 %). Right column: Stitched SEM images of cross-sections of Al-Zr powders milled in hexanes and mixed PCAs. Top images (f-h) show Al-Zr powders with increasing Al compositions milled in hexane, and images (h, i, and j) show 3Al:Zr powders milled with 0 %, 6.25 % and 12.5 % acetonitrile.

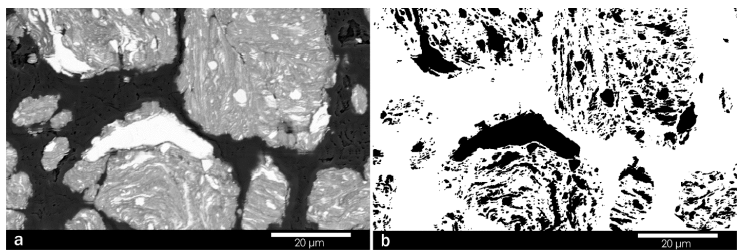


Figure 2. Example of raw and processed SEM backscatter electron images of a 3Al:Zr cross-section processed using ImageJ for Zr inclusion area analysis. Image (a) is raw input image and (b) is the image processed with black regions representing Zr inclusions.

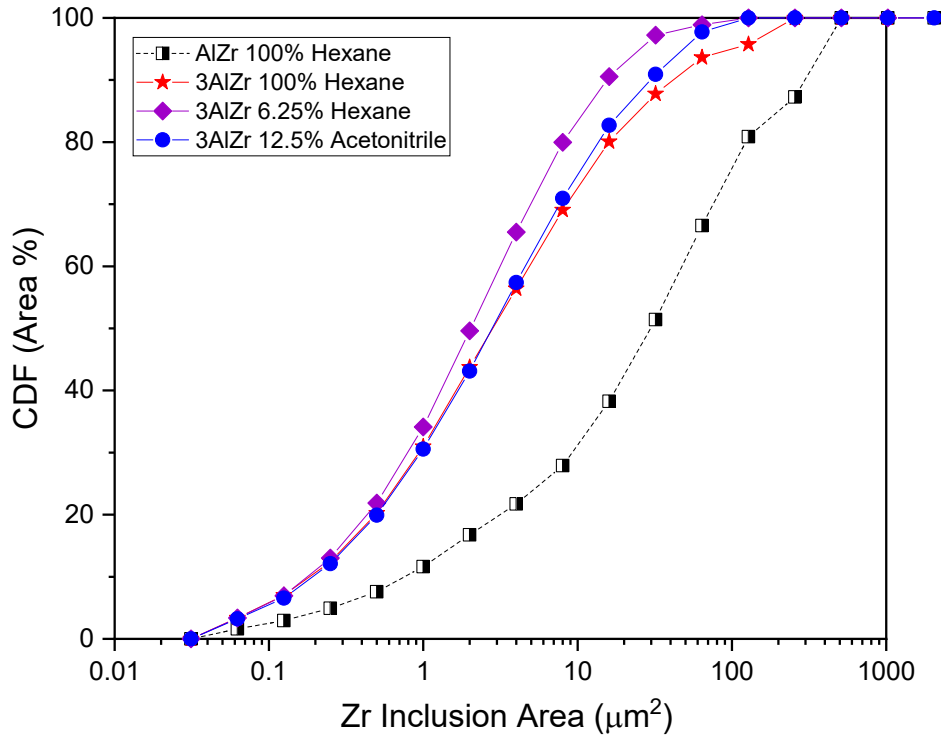


Figure 3. Cumulative distributions of Zr inclusion areas for ball milled Al-Zr powders with various chemistries and PCA ratios.

Table 2. Surface area (SA) as calculated via BET and PSA data

Sample	Al:3Zr 100 % HEX	Al:Zr 100 % HEX	3Al:Zr 100 % HEX	3Al:Zr 6.25 % ACN	3Al:Zr 12.5 % ACN
BET SA (m ² /g)	1.8	0.6	0.4	2	6.3
Calculated SA (m ² /g)	0.6	0.51	0.4	1	2.9

3.2 Thermal analysis

DTA scans of milled and sieved Al-Zr powders in all samples have a broad exotherm begins around 120 °C, peaks near 400 °C, and is attributed to the intermixing of Al-Zr and then the formation of the Al₃Zr intermetallic compound, as seen in earlier studies.^{15,20} This exotherm is smallest in the Zr-rich samples, large and sharp in the Al:Zr samples, and broadens and grows in magnitude for the 3Al:Zr samples as the percent of acetonitrile increases. More exotherms appear at higher temperature due to the formation of more Zr-rich compounds in the Al:Zr and Al:3Zr samples. The 3Al:Zr samples have an additional broad exotherm above 700 °C that appears to grow in magnitude with the acetonitrile concentration.

The heats of the intermetallic formation reaction were calculated for each of the sieved samples. These values were obtained by integrating the heat flow of the DTA signals from 120 °C to 660 °C, using a linear baseline. The heats calculated by Fischer et. al.²⁰ and Kematick et. al.²¹ are reported for comparison. Error bars represent the standard deviation between the three trials run for each composition. For the samples milled in pure hexane, the Al:Zr composition has the highest heat, with values for Zr-rich and Al-rich decreasing similar to the values seen in literature.^{20,21} Overall the highest heat is seen for the 3Al:Zr 12.5 % ACN sample, with the trend to higher heats with increasing ACN concentration.

3.3 Wire ignition in room air

The results of the hot-filament ignition test correspond to moderate heating rates, which are defined as 10³–10⁴ C/s. All ignition temperatures are well below the ignition temperature of Al, which is dependent on the particle size and

can vary from the melting point of pure Al (660 °C) for nanosized particles to the melting point of the native oxide (2050 °C) for micron sized particles. The 3Al:Zr 100 % HEX sample did not ignite. Both 3Al:Zr samples milled with acetonitrile did ignite, with the 3Al:Zr 6.25 % ACN sample having a lower ignition temperature and the lowest overall.

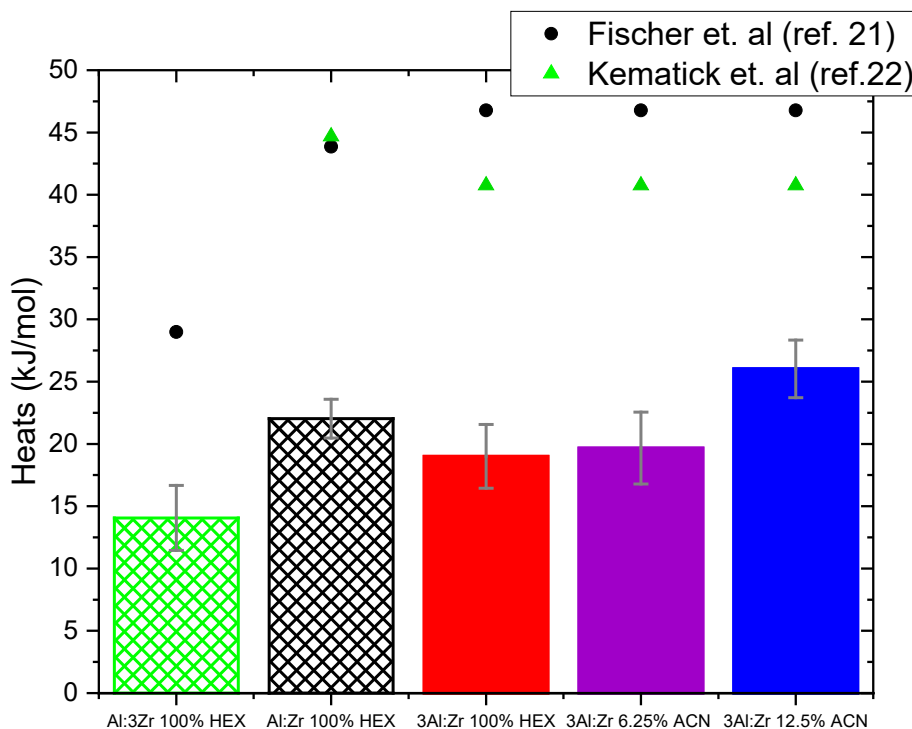


Figure 4. Heats of the intermetallic formation reaction obtained by integrating the heat flow from the DTA signals from 120 °C to 660 °C. Included are heats reported by Fischer et. al²⁰ and Kematick et. al²¹

Figure 5 (a, b) shows the progression of combustion in the Al:3Zr and Al:Zr 100 %HEX samples and (c-e) shows the progression for 3Al:Zr samples milled with 0 %, 6.25 % and 12.5 %ACN. In (a,b) ignition is visible for Al:3Zr and Al:Zr powders followed by combustion, Al vaporization, and microexplosions. In (c) the Al:3Zr 100 % HEX do not ignite and appear as dark spots on the wire as it warms and begins to flow. In Figure 5 (d, e) 3Al:Zr particles milled in 6.25 % and 12.5 % ACN can be seen microexploding, however, due to their finer size the Al vapor burning and Zr burning are not clearly visible.

4. DISCUSSION

4.1 Effect of Al to Zr ration on microstructure and reactive properties

Al and Zr have vastly different mechanical properties; Al is ductile while Zr is brittle, allowing for Al to deform and cold-weld, in contrast to Zr whose brittle nature leads to fracturing when ball milled.¹⁵ This difference in mechanical properties between the starting materials has been shown to impact the final microstructure and physical properties of the ball milled product.^{5,8,14,23} As the powders are milled, they are exposed to high impact energies via collisions with the milling balls and the milling jars themselves, causing fracture, plastic deformation, atomic intermixing, and reactions between the starting materials.¹² In the case of Al and Zr, these forces, coupled with the different mechanical properties of the starting materials, cause the Al to encompass the fractured Zr particles, as seen in the cross sections in Figure 1. This fracturing of Zr and envelopment by Al is clearly displayed by the particle size analysis distribution and cross sections. The chemistries having the higher composition of Zr have smaller average particle sizes, verifying the theory that Al is cushioning the impacts of the Zr with the milling media/jars.⁸ Less Al allows for more fracturing of the Zr, thus driving down the average inclusion size as shown in Figure 3. With less Al there is also less encapsulation of the Zr, resulting in smaller overall particle size.

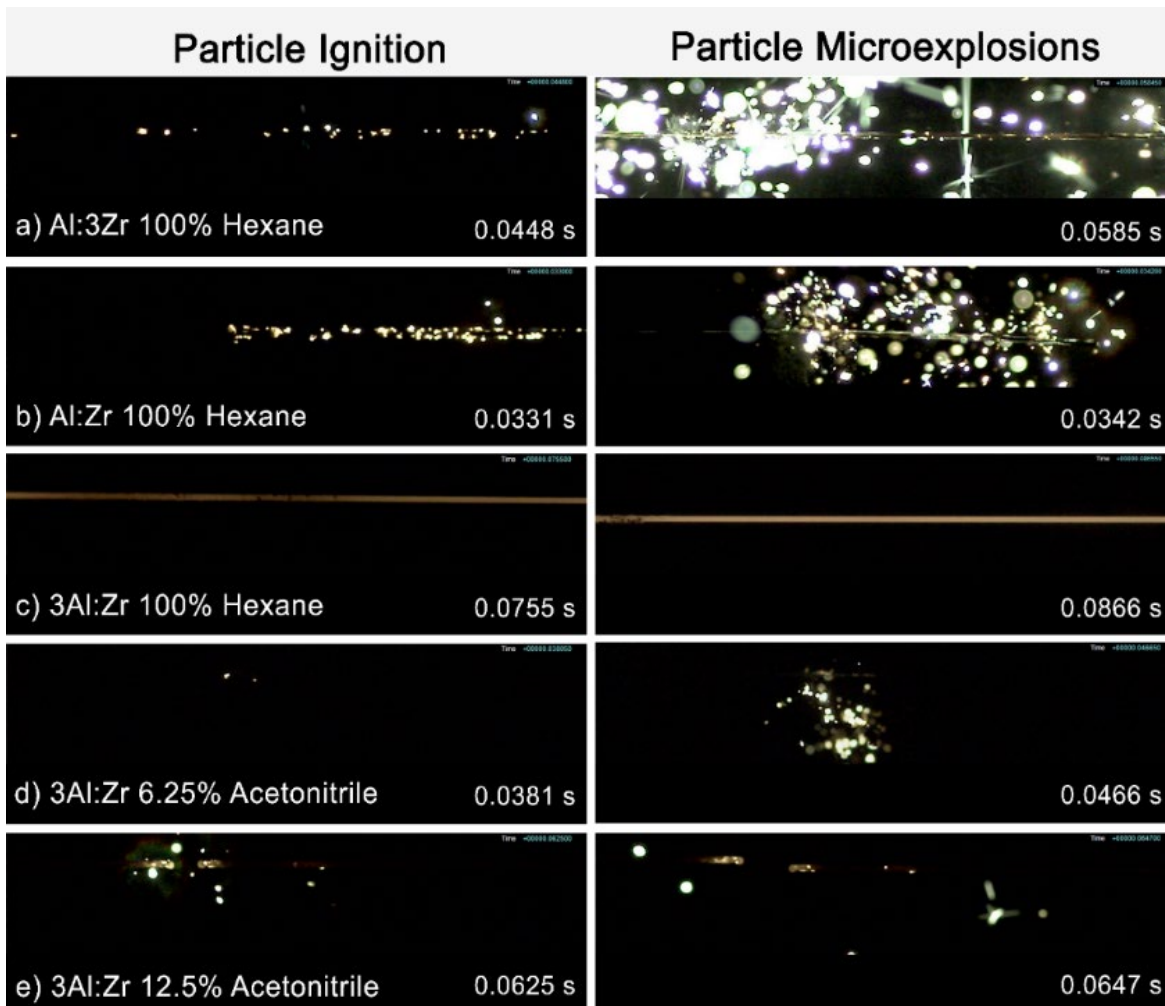


Figure 5. Progression from particle ignition to reaction for a) Al:3Zr 100 %HEX, b) Al:Zr 100%HEX, c) 3Al:Zr 100 %HEX, d) 3Al:Zr 6.25 %ACN, and e) 3Al:Zr 12.5 %ACN.

Al and Zr have vastly different mechanical properties; Al is ductile while Zr is brittle, allowing for Al to deform and cold-weld, in contrast to Zr whose brittle nature leads to fracturing when ball milled.²² This Al and Zr have vastly different mechanical properties; Al is ductile while Zr is brittle, allowing for Al to deform and cold-weld, in contrast to Zr whose brittle nature leads to fracturing when ball milled.²² This difference in mechanical properties between the starting materials has been shown to impact the final microstructure and physical properties of the ball milled product.^{5,8,14,23} As the powders are milled, they are exposed to high impact energies via collisions with the milling balls and the milling jars themselves, causing fracture, plastic deformation, atomic intermixing, and reactions between the starting materials.¹² In the case of Al and Zr, these forces, coupled with the different mechanical properties of the starting materials, cause the Al to encompass the fractured Zr particles, as seen in the cross sections in Figure 2. This fracturing of Zr and envelopment by Al is clearly displayed by the particle size analysis distribution and cross sections. The chemistries having the higher composition of Zr have smaller average particle sizes, verifying the theory that Al is cushioning the impacts of the Zr with the milling media/jars.⁸ Less Al allows for more fracturing of the Zr, thus driving down the average inclusion size as shown in Figure 3. With less Al there is also less encapsulation of the Zr, resulting in smaller overall particle size.

Previous works have demonstrated how intermetallic formation reactions can drive ignition of the particles.^{8,14,24} Here, given the phases identified on heating to 600°C, the formation of Al₃Zr is the dominant phase and is possibly the reaction driving the ignition. Although the Al rich forms the most Al₃Zr, it does not ignite while the AlZr and Al₃Zr do. One might expect the chemistries with the highest heats of formation as determined by DTA to have the lowest ignition temperature.⁸ This is true for the Al:Zr powders milled in hexane. However, when comparing the other two samples milled in hexane, the Al:3Zr sample has a lower measure heat than the 3Al:Zr sample, but it

ignites while the 3Al:Zr samples does not. As discussed below, the ZrC formation reaction could also assist ignition. However, the heat for the ZrC formation should appear in the integration of the DTA traces and thus cannot explain the difference. This suggests that reactions with the O and N in air may be assisting ignition as reported.⁸

5. CONCLUSIONS

In this work we have characterized the effect of planetary ball milling in hexane on three compositions of Al and Zr, as well as the impact of using immiscible liquid PCAs in planetary ball milling on an Al rich composition, by analyzing microstructure and reactive properties. Compositions having a Zr-rich chemistry resulted in finer Zr inclusions due to less cushioning of the Zr by the Al. Of the samples milled in pure hexane, we see the highest heat of reaction in the Al:Zr 100 %HEX system, corresponding with it having the lowest ignition temperature. The Al:3Zr 100 % HEX sample's heat of reaction was lower than 3Al:Zr 100 % HEX, however, the Al:3Zr 100 % HEX resulted in a lower ignition temperature (as opposed to 3Al:Zr 100 % HEX, which did not ignite) due to the aiding of Zr oxidation and nitration via the decreased Zr inclusion size. The Al rich composition did reach the preferential equilibrium state (Al₃Zr) upon heating to 1000 °C, as shown by XRD. Neither Al:Zr 100 % HEX or Al:3Zr 100 % HEX reached their equilibrium state upon heating to 1000 °C, suggesting incomplete reaction of the two materials.

The incorporation of immiscible liquid PCAs in the planetary ball milling of the 3Al:Zr composition resulted in refinement of the Zr particles, with higher acetonitrile content having smaller Zr inclusions and smaller overall particle sizes. The Al rich samples did not cold weld; the high surface free energy believed to be abated by the preferential adsorption of the nitrile group to the Al surface instead of the Al to itself. The increase in acetonitrile volume fraction also increased the heat of reaction and resulted in Al rich samples which were able to ignite on the hot nichrome wire. While all three of the Al rich samples milled in varying acetonitrile volume fractions reached the equilibrium reaction state upon heating to 1000 °C, increasing acetonitrile led to an increase in ZrC formation.

Additional studies should be conducted to assess the impact of oxidation and nitration on the ignition properties of these chemistries. The use of acetonitrile as a PCA does result in the production of a tunable system to control the ignition temperature, heat of reaction, and particle size of Al rich compositions.

ACKNOWLEDGMENTS

Funding was provided by the U.S. Army via the Chemical Biological Advanced Materials and Manufacturing Science Program at the Combat Capabilities Development Command Chemical Biological Center. The authors wish to thank Warren Gardner, Jesse Grant, Michael Kauzlarich, and Rayna Mehta for their technical support and editorial assistance.

REFERENCES

- [1] Yen, N.H.; Wang, L.Y. Reactive metals in explosives. *Propellants, Explos. Pyrotech.* **2012**, *37* (2), pp 143–155.
- [2] Dreizin, E.L. Metal-based reactive nanomaterials. *Prog. Energy Combust. Sci.* **2009**, *35* (2), pp 141–167.
- [3] Dreizin, E.L. Phase changes in metal combustion. *Prog. Energy Combust. Sci.* **2000**, *26* (1), pp 57–78.
- [4] Sundaram, D.S.; Puri, P.; Yang, V. A general theory of ignition and combustion of nano- and micron-sized aluminum particles. *Combust. Flame.* **2016**, *169*, pp 94–109.
- [5] Dreizin, E.L.; Schoentiz, M. Mechanochemically prepared reactive and energetic materials: a review. *J. Mater. Sci.* **2017**, *52*, pp 11789–11809.
- [6] Adams, D.P. Reactive multilayers fabricated by vapor deposition: A critical review. *Thin Solid Films.* **2015**, *576* pp 98–128.
- [7] Suryanarayana, C. Mechanical Alloying: A Novel Technique to Synthesize Advanced Materials. *Research.* **2019**, pp 1–17.
- [8] Lakshman, S.V.; Gibbins, J.D.; Wainwright, E.R.; Weihs, T.P. The effect of chemical composition and milling conditions on composite microstructure and ignition thresholds of Al-Zr ball milled powders. *Powder Technol.* **2019**, *343*, pp 87–94.

- [9] Stamatis, D.; Wainwright, E.R.; Lakshman, S.V.; Kessler, M.S.; Weihs, T.P. Combustion of explosively dispersed Al-Mg-Zr composite particles. *Combust. Flame*. **2020**, *217*, pp 93–102.
- [10] Grapes, M.D.; Reeves, R.V.; Fezzaa, K.; Sun, T.; Densmore, J.M.; Sullivan, K.T. In situ observations of reacting Al/Fe₂O₃ thermite: Relating dynamic particle size to macroscopic burn time. *Combust. Flame*. **2019**, *201*, pp 252–263.
- [11] Nguyen, Q.; Huang, C.; Schoenitz, M.; Sullivan, K.T.; Dreizin, E.L. Nanocomposite thermite powders with improved flowability prepared by mechanical milling. *Powder Technol.* **2018**, *327*, pp 368–380.
- [12] Suryanarayana, C. Mechanical alloying and milling. *Prog. Mater. Sci.* **2001**, *46*, pp 1–184.
- [13] Wainwright, E.R.; Inouye, M.; Niu, M.; Chintersingh, K.; Weihs, T.P. Comparing the ignition and combustion of ball-milled Al-based composites with Ti, Zr, and Mg additives. *J. Energ. Mater.* **2021**, *41*, pp 43–62.
- [14] Wainwright, E.R.; Weihs, T.P. Microstructure and ignition mechanisms of reactive aluminum-zirconium ball milled composite metal powders as a function of particle size. *J. Mater. Sci.* **2020**, *55* pp 14243–14263.
- [15] Mursalat, M.; Schoenitz, M.; Dreizin, E.L. Custom particle morphology in energetic nanocomposites prepared by arrested reactive milling in immiscible liquids. *Powder Technol.* **2020**, *359*, pp 238–246.
- [16] Lakshman, S.V.; Gibbins, J.D.; Weihs, T.P. Evaluating the effect of microstructural refinement on the ignition of Al-Mg-Zr ball-milled powders. *Powder Tech.* **2021**, *379*, pp 447–456.
- [17] Yu, J.; McMahan, B.W.; Boatz, J.A.; Anderson, S.L. Aluminum Nanoparticle Production by Acetonitrile Assisted Milling: Effects of Liquid- vs Vapor-Phase Milling and Milling Method on Particle Size and Surface Chemistry. *J. Phys. Chem. C*. **2016**, *120* (35), pp 19613–19629.
- [18] Ward, T.S.; Trunov, M.A.; Schoenitz, M.; Dreizin, E.L. Experimental methodology and heat transfer model for identification of ignition kinetics of powdered fuels. *Int. J. Heat Mass Transfer*. **2006**, *49*, pp 4943–4954.
- [19] Weihs, T.P.; Barbee, T.W.; Wall, M.A. Measuring Enthalpies of Formation Using Thick Multilayer Foils and Differential Scanning Calorimetry. *MRS Online Proc. Libr.* **1995**, *382*, pp 21–26.
- [20] Fischer, E.; Colinet, C. An Updated Thermodynamic Modeling of the Al-Zr System. *J. of Phase Equilib. Diffus.* **2015**, *36*, pp 404–413.
- [21] Kematick, R.J.; Franzen, H.F. Thermodynamic study of the zirconium-aluminum system. *J. Solid State Chem.* **1984**, *54* (2), pp 226–234.
- [22] Suryanarayana, C. Mechanical alloying and milling. *Prog. Mater. Sci.* **2001**, *46* (1), pp 1–184.
- [23] Santhanam, P.R.; Dreizin, E.L. Predicting conditions for scaled-up manufacturing of materials prepared by ball milling. *Powder Technol.* **2012**, *221*, pp 403–411.
- [24] Overdeep, K.R.; Joress, H.; Zhou, L.; Livi, K.J.T.; Barron, S.C.; Grapes, M.D.; Shanks, K.S.; Dale, D.S.; Tate, M.W.; Philipp, H.T.; Gruner, S.M.; Gufnagel, T.C.; Weihs, T.P. Mechanisms of oxide growth during the combustion of Al:Zr nanolaminate foils. *Combust. Flame*. **2018**, *191*, pp 442–452.

Molecular modeling of toxic industrial chemicals on metal-organic frameworks for next-generation filtration applications

Matthew A. Browe^{a*}, Adam R. Hinkle^{a,b}, Ivan O. Iordanov^a, Wesley O. Gordon^a,
John Landers^{a,c}, Shivam Parashar^d, Alex Neimark^d

^aU.S. Army Combat Capabilities Development Command Chemical Biological Center, Research & Operations Directorate, 8198 Blackhawk Rd., Aberdeen Proving Ground, MD 21010

^bDCS Corporation, 4696 Millennium Drive, Suite 450, Belcamp, MD 21017

^cLeidos, Inc., 1750 Presidents St., Reston, VA 20190

^dRutgers University, 57 U.S. Highway 1, New Brunswick, NJ 08901

ABSTRACT

Adsorption and chemical reactions of zirconium-based metal-organic frameworks (i.e., UiO-66, UiO-66-NH₂, and MOF-808) against guest molecules of interest are simulated using Monte Carlo and molecular dynamics methods. Utilizing chemically reactive force fields allowing for bond breaking and formation. Baseline effects of defects and residual solvent in UiO-66 and UiO-66-NH₂ on the nitrogen adsorption isotherms have been determined. Baseline effects of defects, residual solvent, and capping group in MOF-808 on the nitrogen adsorption isotherms were also determined. Suitable reactive force fields were determined for molecular dynamics simulation of toxic industrial chemical reaction on MOF-808 using water as a guest molecule. Introductory efforts of toxic chemical interaction studies with MOFs commenced and focused on CO₂ on the trifluoroacetic acid-modulated analogue of MOF-808.

Keywords: Monte Carlo, molecular dynamics, metal-organic frameworks, molecular simulation, adsorption, chemical reaction, ReaxFF

1. INTRODUCTION

Removal of toxic industrial chemicals (TICs) from the air is a prominent concern in military filtration applications. The high vapor pressure of TICs precludes removal via noncovalent interactions such as physical adsorption, mandating that a variety of reaction chemistries be incorporated into any filtration media for removal of a broad spectrum of threats. Currently fielded filtration media, such as metal-incorporated activated carbon, cannot adequately address the full spectrum of chemical threats. Metal-organic frameworks (MOFs) are a promising candidate for filtration media due to ¹high surface areas, high porosity, and tunable physical and chemical properties, which enables a range of reaction chemistries to be incorporated into the structure for chemical removal.¹ Additionally, zirconium-based MOFs are of high interest due to their wide stability under a range of environmental and synthetic conditions,² which is a drawback of other MOFs.²

Three zirconium-based MOFs, UiO-66, UiO-66-NH₂, and MOF-808, are the strongest candidates for filtration applications due to the pore sizes in the range of 10–15 angstroms.³ These MOFs can undergo post-synthetic modifications to enhance their abilities for removing guest molecules of interest. The UiO-66 and UiO-66-NH₂ MOFs can be physically modified through induced defects in the structure, in which a linker molecule is removed and the resulting site is terminated through either a formate group (in the traditional synthesis involving formic acid) or hydroxyl groups.⁴ The UiO-66 family of MOFs can vary chemically through functionalization of the linker, represented by UiO-66-NH₂ in which an amine moiety is incorporated onto the benzene dicarboxylic acid linker through synthesis variation, using aminoterephthalic acid instead of terephthalic acid.² The MOF-808 material can be chemically modified through modulator incorporation on the node, a feature not available on pristine UiO-66 due to all possible node sites bonded to linker molecules.⁵ All MOFs are subject to contamination of residual solvent, such as dimethylformamide (DMF) and water, from their traditional synthesis.²

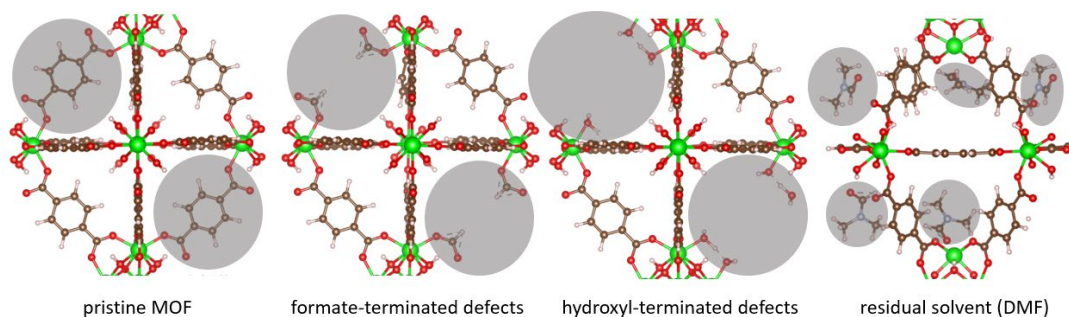


Figure 1. Modifications considered for UiO-66 and UiO-66-NH₂ MOFs. From left to right: pristine MOF, MOF with formate-terminated defects, MOF with hydroxyl-terminated defects, MOF with residual solvent (DMF or water).

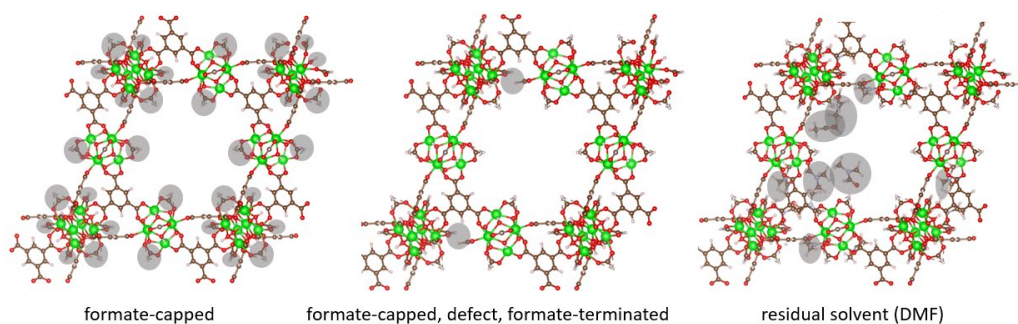


Figure 2. Modifications considered for MOF-808 MOFs. From left to right: capping group on MOF (formate capping highlighted here, hydroxyl capping also simulated), MOF with formate-terminated defects, MOF with residual solvent (DMF or water).

This study aims to determine the effect of various physical and chemical modifications of zirconium-based MOFs on adsorption and chemical reaction against guest molecules of interest using computational techniques. Adsorption properties are typically evaluated by simulating an adsorption isotherm, measuring uptake of an inert gas such as nitrogen as a function of applied pressure, using Monte Carlo methods. Chemical reactions can be evaluated using molecular dynamics simulations incorporating reactive force fields (ReaxFF⁶), which allow for explicit bond breaking and bond formation phenomena. Insights gleaned from modelling these complex interactions can be used to improve and optimize the filtration capabilities of MOFs through rational design.

2. METHODS

Crystallographic information files for UiO-66, UiO-66-NH₂, and MOF-808 were obtained from the Cambridge Structural Database website.⁷ Defects were introduced into the structure using the Avogadro molecular editor, and the resulting structure was subsequently geometry optimized with the Quantum Espresso code⁸ using the “relax” option of the pw.x executable of Quantum Espresso, which adjusts bond lengths and bond angles but not unit cell parameters. Simulation settings used a kinetic energy cutoff distance of 60 Ry for wavefunctions, a kinetic energy cutoff distance of 480 Ry for charge density, Gaussian smearing for metals with a degauss parameter of 0.002, the semiempirical Grimme’s DFT-D2 van der Waals dispersion correction, the Broyden-Fletcher-Goldfarb-Shanno quasi-newton algorithm for ion dynamics, and a mixing factor of 0.7 for self-consistency. Default settings for convergence were used. UiO-66 and UiO-66-NH₂ analogues with dehydroxylated nodes were also prepared and simulated in Monte Carlo methods but will be discussed in the future.

Nitrogen adsorption isotherms of all MOFs were simulated using the Monte Carlo code RASPA⁹ with assistance from Shivam Parashar and Dr. Alex Neimark of Rutgers University.⁹ In the simulations, a total of 20,000 Monte Carlo cycles and 5,000 initialization cycles were used, with a cutoff distance of 17 Å at 77 kelvin (K) with equal probabilities of translation, rotation, reinsertion, and swap. All simulations assumed a rigid framework structure; no framework flexibility was accounted for. Electrostatic effects were not accounted for when using nitrogen as the adsorbate. For water and DMF, electrostatic effects were accounted for using the Ewald charge method at 300 K, and partial charges were assigned to the framework atoms in the MOFs using the default charge equilibration method in RASPA. Water adsorption was simulated on all MOFs with the Tip4pEw force field, found to reproduce the experimental water adsorption isotherm best on UiO-66,¹⁰ and DMF was simulated using a force field developed for DMF adsorption on MOFs.^{10,11} A cutoff distance of 12 Å was used for both force fields. A representative configuration of water loading (1 wt% concentration) and representative DMF loadings (1 wt% and 5 wt% concentrations) in the MOF were saved from their Monte Carlo simulations and subsequently subjected to nitrogen adsorption in a follow-on Monte Carlo simulation; the preadsorbed molecules were treated as extra-framework species in the force field definitions in line with previous studies.¹² Simulations for UiO-66 and UiO-66-NH₂ used a 2 x 2 x 3 unit cell domain, and simulations for MOF-808 used a 2 x 2 x 2 unit cell domain. Adsorbate locations are output in xyz coordinates and compartmentalized by pore type in the UiO-66 and MOF-808 family MOFs, to provide an advanced insight on the adsorption phenomena in line with previous efforts (Figure 3).¹³

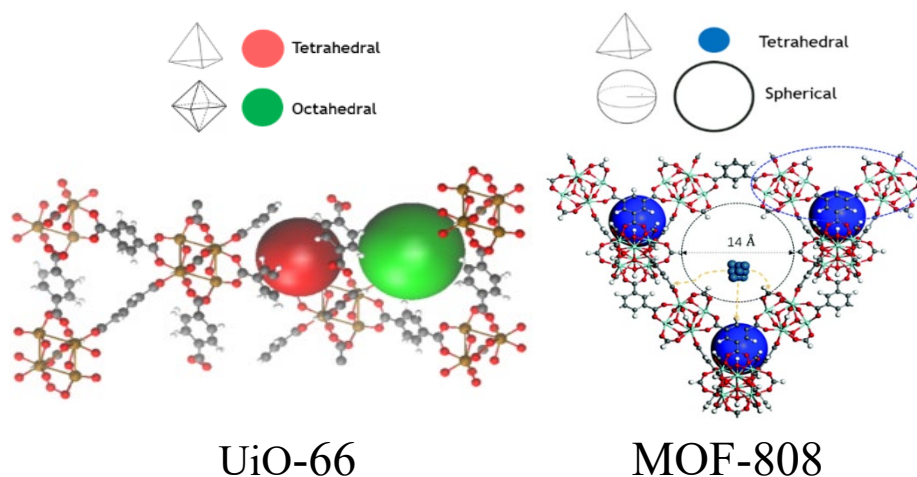


Figure 3. Pore types considered for (left) UiO-66 derivatives and (right) MOF-808 derivatives. In the UiO-66 MOFs, a tetrahedral pore is filled by a red sphere, and an octahedral pore is filled by a green sphere. In the MOF-808 MOFs, a tetrahedral pore is filled by a blue sphere, and a spherical pore is filled by an empty circle.

Molecular dynamics simulations were conducted by Dr. Adam Hinkle using the LAMMPS¹⁴ code.¹³ In the codes, a 2 x 2 x 2 unit cell of MOF-808 was utilized. ReaxFF⁶ reactive force fields jz0c02930,¹⁵ trained on the zirconium-based MOF MIL-140C, and jz501891,¹⁶ trained on yttria-stabilized zirconia, were considered for the zirconium-based MOFs, as they were parameterized and trained on structurally similar materials to the MOFs used in this study.^{6,14,15} The carbon and zirconium atoms of the MOF were held rigid and a time step of 0.1 fs was used in all simulations.

3. RESULTS AND DISCUSSION

Nitrogen isotherms of the baseline/unmodified UiO-66 structure and UiO-66 modified with defects or residual solvent can be compartmentalized by pore type (Figures 4-5). For the UiO-66 structure, introducing a greater number of defects in the structure reduces total adsorption at lower pressures and increases total adsorption at higher pressures. Adsorption at lower pressures involves guest molecule interaction on the surface sites of the MOF, and adsorption at higher pressures is a function of the total pore volume of the MOF. Results from the RASPA simulations show that at lower pressures, the linker molecules in the UiO-66 structure are favorable interaction sites for nitrogen molecules. Thus, it follows that adsorption would decrease at lower pressures when the linkers are removed from the structure. Removing the linkers is expected to increase total pore volume, which would increase total adsorption at higher

pressures. Both observations, reduced adsorption at lower pressures and increased adsorption at higher pressures, were more pronounced in the case of hydroxyl-terminated defects compared to formate-terminated defects.

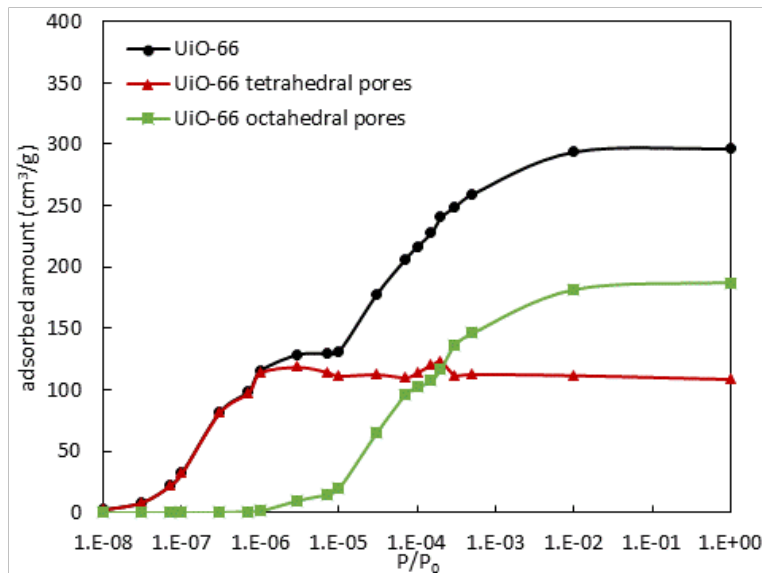


Figure 4. Simulated nitrogen isotherm and pore type decomposition for pristine UiO-66.

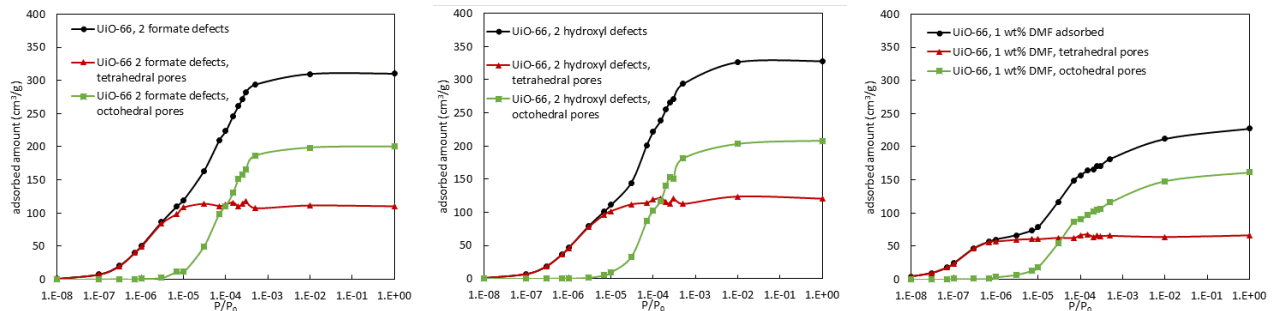


Figure 5. Simulated nitrogen isotherms and pore-type decompositions for UiO-66 with two formate-terminated defects per unit cell (left), two hydroxyl-terminated defects per unit cell (middle), and 1 wt% preadsorbed dimethylformamide (right).

Adsorption trends from the isotherms of the modelled UiO-66 structures can be compared to the experimental material (Figure 6, top row). One of the formate-terminated defect simulations involved a zirconium node removed from UiO-66 (referred to as a node defect) for comparison, which involved the unit cell being replicated twice in the x direction and four times in the y direction to avoid adjacent vacant node sites in the simulation. In addition to the defect trends discussed, the presence of residual solvent (water or DMF) reduces the adsorbed amount of nitrogen in the isotherm evenly at all pressures at 1 wt% but reduces the adsorption significantly at 5 wt%, with a greater fractional reduction at higher pressures than at lower pressures.

Considering the fraction of adsorbate atoms in octahedral pores as a function of total adsorbed atoms per unit cell further sheds light on these adsorption trends (Figure 6, bottom row). For the formate-terminated and hydroxyl-terminated defect-induced materials, the fraction of adsorbate atoms in octahedral pores (normalized by total number of atoms adsorbed) increased with increasing number of defects, with formate-terminated defects having a stronger influence than hydroxyl-terminated defects, but the fractional content of adsorbed atoms in octahedral pores at saturation remained the same as the pristine material. For the UiO-66 samples with preadsorbed DMF, both the fraction of adsorbate atoms in octahedral pores and the fractional content at saturation increased, due to DMF preferentially occupying tetrahedral pores and fully saturating tetrahedral pores at slightly above 5 wt%.

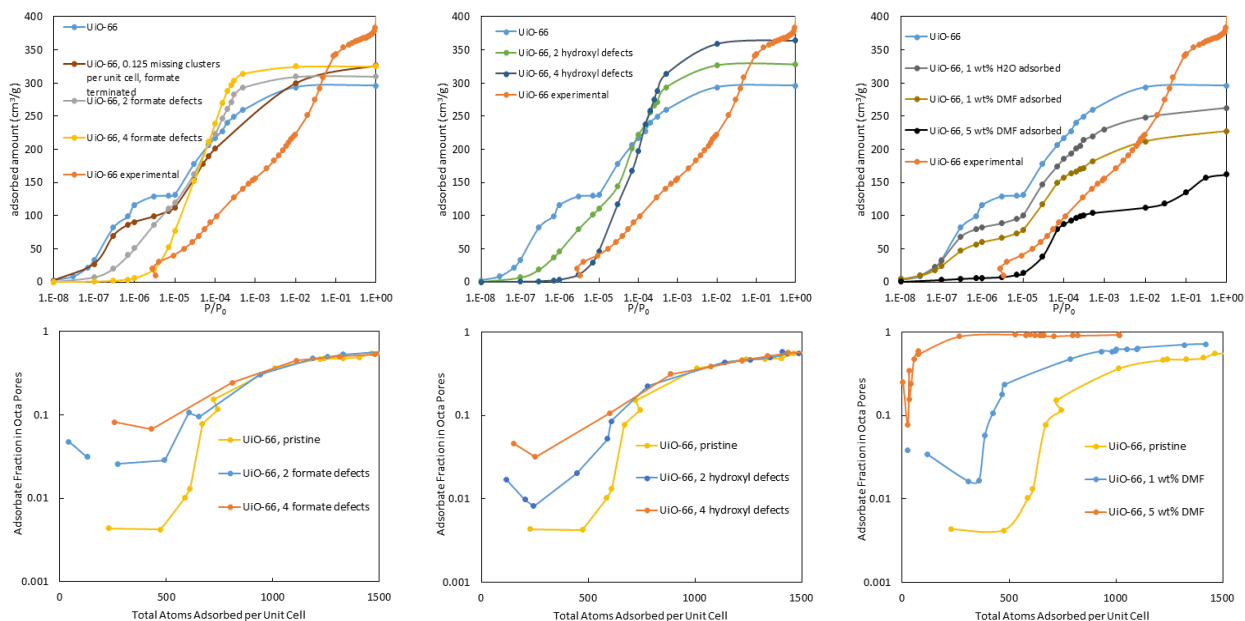


Figure 6. Top: UiO-66 nitrogen isotherms with varying formate-terminated defects, UiO-66 nitrogen isotherms with varying hydroxyl-terminated defects, and UiO-66 nitrogen isotherms with varying residual solvent content, all compared to the experimental UiO-66 isotherm. Bottom: Trends in nitrogen adsorption by pore type for UiO-66 with varying formate-terminated defects, UiO-66 with varying hydroxyl-terminated defects, and UiO-66 with varying content of DMF.

Nitrogen isotherms of the baseline UiO-66-NH₂ structure and UiO-66-NH₂ modified with defects or residual solvent can be compartmentalized by pore type (Figures 7-8). Similarly to the UiO-66 structure with induced defects, it is seen that a greater number of defects in the structure reduces total adsorption at lower pressures and increases total adsorption at higher pressures. Also, as with UiO-66, both observations (reduced adsorption at lower pressures and increased adsorption at higher pressures) were stronger in the case of hydroxyl-terminated defects compared to formate-terminated defects. When comparing all UiO-66 materials to the corresponding analogue of UiO-66-NH₂, it is seen in all cases that adsorption at lower pressures is increased in UiO-66-NH₂ due to guest molecule interaction with the amine moiety and adsorption at higher pressures is reduced in UiO-66-NH₂ due to lower total pore volume from occlusion by the amine moiety.

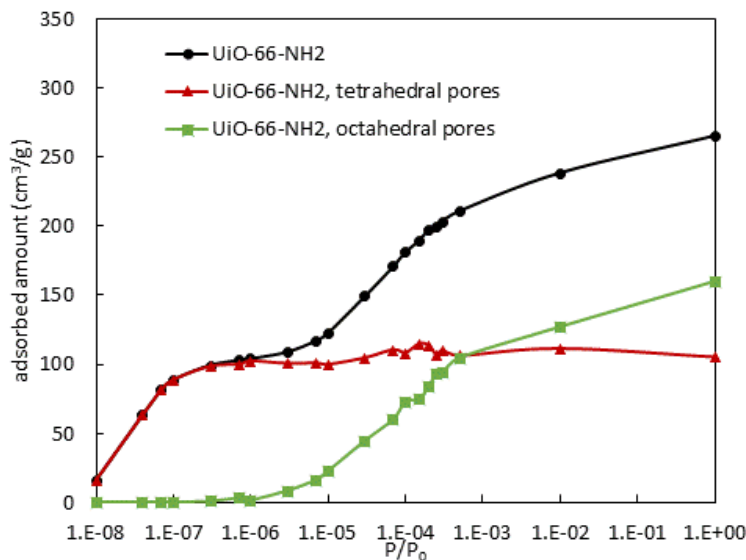


Figure 7. Simulated nitrogen isotherm and pore type decomposition for pristine UiO-66-NH₂.

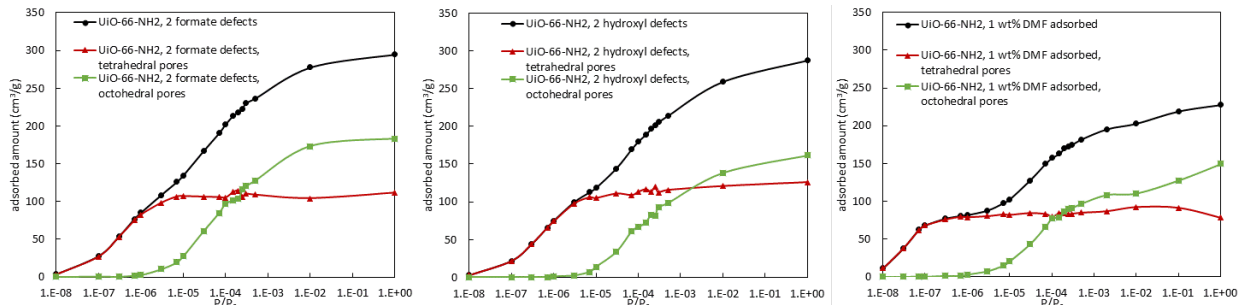


Figure 8. Simulated nitrogen isotherms and pore-type decompositions for UiO-66-NH₂ with two formate-terminated defects per unit cell (left), two hydroxyl-terminated defects per unit cell (middle), and one wt % preadsorbed dimethylformamide (right).

Adsorption trends from the isotherms of the modelled UiO-66-NH₂ structures can be compared to the experimental material (Figure 9). Results are also similar when comparing the trends in the bottom row to UiO-66, in terms of trends in adsorption by pore type upon induced defects and presence of residual solvent. Further simulations are needed to determine if there is a distinct difference in the adsorption behavior trends by pore type, normalized by total number of atoms adsorbed, between UiO-66 and UiO-66-NH₂, as results to date are inconclusive.

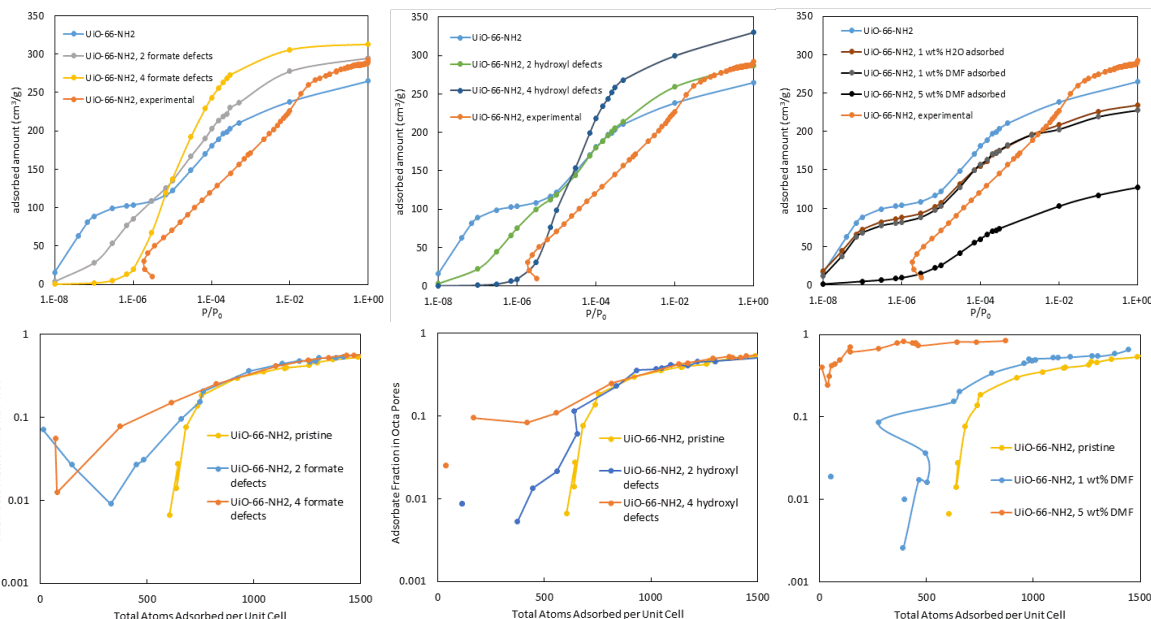


Figure 9. Top: UiO-66-NH₂ nitrogen isotherms with varying formate-terminated defects, UiO-66-NH₂ nitrogen isotherms with varying hydroxyl-terminated defects, and UiO-66-NH₂ nitrogen isotherms with varying residual solvent content, all compared to the experimental UiO-66-NH₂ isotherm. Bottom: Trends in nitrogen adsorption by pore type for UiO-66-NH₂ with varying formate-terminated defects, UiO-66-NH₂ with varying hydroxyl-terminated defects, and UiO-66-NH₂ with varying content of DMF.

Finally, adsorption trends from simulated isotherms of the MOF-808 structures with tetrahedral and spherical pores, were analyzed (Figures 10–12). Minimal nitrogen adsorption occurred in the tetrahedral pores of MOF-808, typically one nitrogen molecule per pore, and so the adsorption process is dominated in the large spherical pores of the MOF (Figure 10). Larger molecules, such as water and DMF, do not enter the smaller tetrahedral pores according to the Monte Carlo simulations. Formate capping of the node of MOF-808 matches the experimental isotherm much closer than hydroxyl capping, and preadsorbing 5 wt% DMF into the formate-capped MOF-808 structure matches the experimental isotherm best to date. However, in all cases, nitrogen uptake at lower pressures is underestimated compared to experiments. Improvements to consider involve inducing electrostatic effects for the nitrogen adsorption isotherms on MOF-808 and incorporation of flexibility to the MOF-808 structure, both phenomena of which could circumvent this discrepancy.^{17,18}

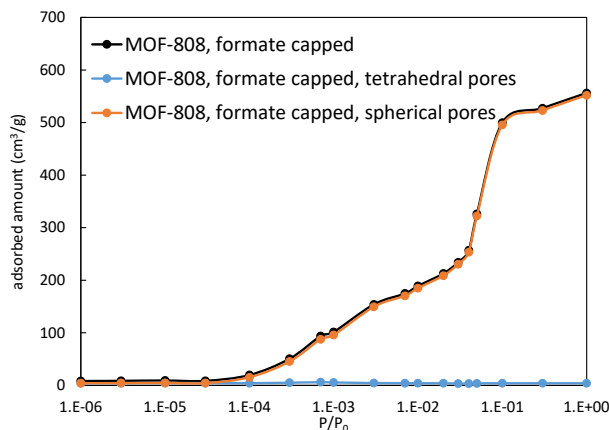


Figure 10. Simulated nitrogen isotherm and pore type decomposition for formate-capped MOF-808.

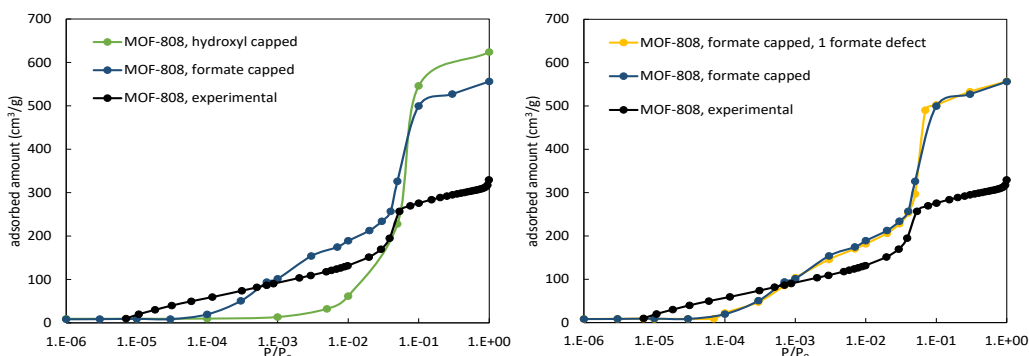


Figure 11. Simulated nitrogen isotherms for MOF-808 with formate or hydroxyl capping (left) and MOF-808 with formate capping and one formate-terminated defect per unit cell (right).

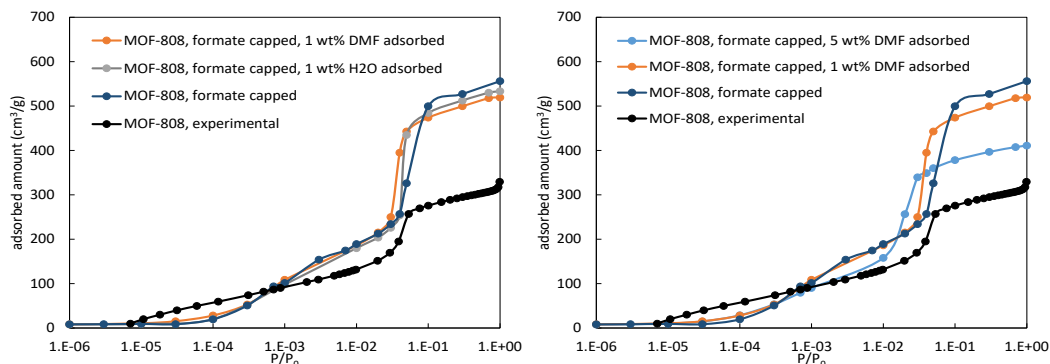


Figure 12. Simulated nitrogen isotherms for formate-capped MOF-808 with 1 wt% preadsorbed DMF or water (left) and formate-capped MOF-808 with 1 wt% and 5 wt% preadsorbed DMF (right).

The interaction of MOF-808 and water was modelled with molecular dynamics simulations (Figure 13). All molecular dynamics efforts utilized force fields from the ReaxFF family,⁶ which allow for explicit bond breaking and formation to occur, simulating chemical reaction phenomena.⁶ This effort expanded previous studies in which water transport in MOF-808 during the thermal activation process was studied,¹⁹ though a smaller cluster model of MOF-808 was used and picosecond time scale simulations were run.¹⁸ Here, simulation settings used a much larger $2 \times 2 \times 2$ unit cell domain of MOF-808 and nanosecond time scale simulation to capture a basic scenario of bond breaking and formation of a guest molecule on a MOF and achieve equilibrium statistics. The jz0c02930 force field,¹⁵ developed from a zirconium-based MOF, was used to start, and simulations were run for 6 ns to achieve steady state.¹⁴ In the simulations,

each atom is assigned a unique identifier number, with its bonding explicitly tracked roughly every 1 % of the total simulation time, including its total number of bonds and the identifier number of the atoms that it is bonded to. This information was then converted by a postprocessing code into time-dependent species population data. It is seen in this case that roughly two-thirds of the water molecules detach from the MOF-808 nodes and enter the pore space.

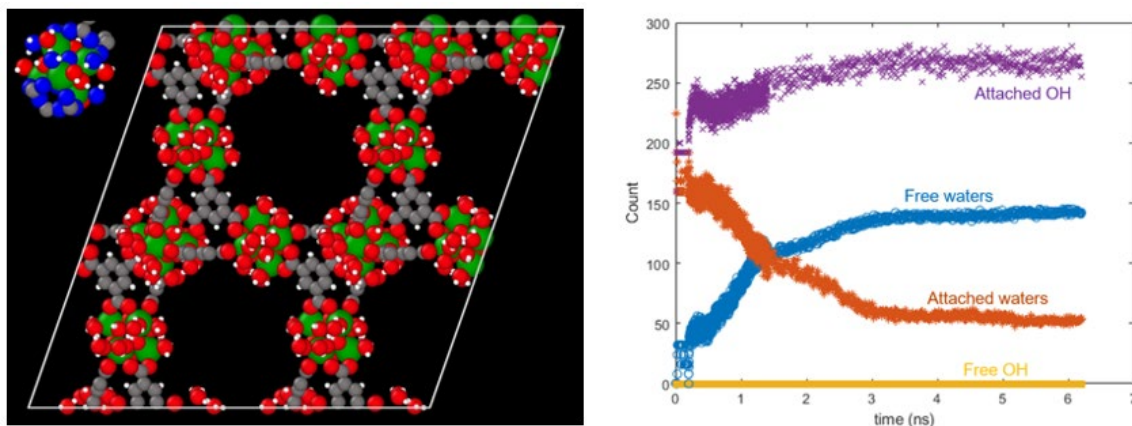


Figure 13. Molecular dynamics simulation of water desorption on MOF-808, with dynamic statistics of species formation and depletion shown (right).

A higher-fidelity assessment of the suitable force fields was performed (Figure 14). Here, the effect of temperature and the behavior of the water molecules was assessed, using two suitable force fields for these systems, jz0c02930¹⁵ and jz501891.¹⁴⁻¹⁶ From prior knowledge of these systems and adsorption thermodynamic fundamentals, it was expected that a lower amount of water would be adsorbed on the MOF at higher temperatures. This is clearly seen in the jz0c02930 force field (left) but is not as apparent with the jz501891 force field (right). Further, in the jz501891 force field, desorbed water clustered in the pores, which is considered an unlikely behavior. Therefore, the jz0c02930 force field was considered most suitable for proceeding with guest molecule studies involving water.

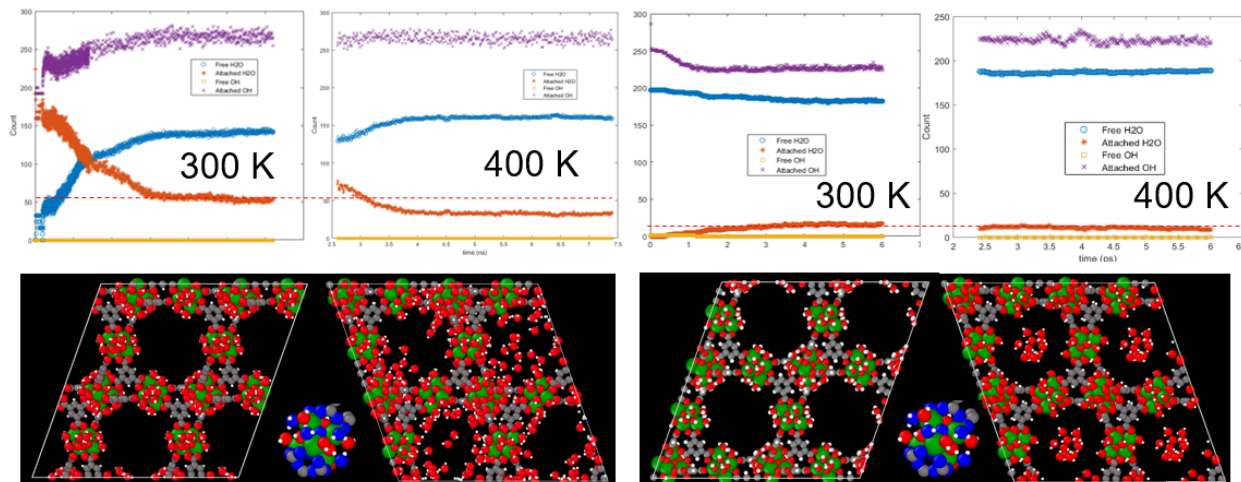


Figure 14. Molecular dynamics simulations of water desorption from MOF-808 with force fields jz0c02930 (left) and jz501891 (right). Top: Effect of temperature on dynamic statistics. Bottom: Depictions of starting and equilibrium configuration of water molecules in the pores of MOF-808.

Introduction of additional guest molecules to the system was then performed with carbon dioxide. Carbon dioxide removal is of high interest for rebreather applications, as exhaled air has roughly 100 times greater carbon dioxide concentration than atmospheric air.²⁰ Fluorinated species have shown high promise for carbon dioxide removal,²¹ and so the trifluoroacetic acid-modulated derivative of MOF-808⁵ was chosen for this purpose.^{5,19} Images of carbon dioxide introduction to formate-capped MOF-808 and trifluoroacetic acid-modulated MOF-808 are shown in Figure 15. Results have not been fully processed to date, but the desired outcome would involve evidence of substantially lower free CO₂ molecules in the trifluoroacetic acid-modulated MOF-808 relative to the formate-capped

MOF-808 as well as binding of the CO₂ molecules to the fluorine atoms of the trifluoroacetic acid-modulated MOF-808 as a baseline assessment for simulation fidelity.

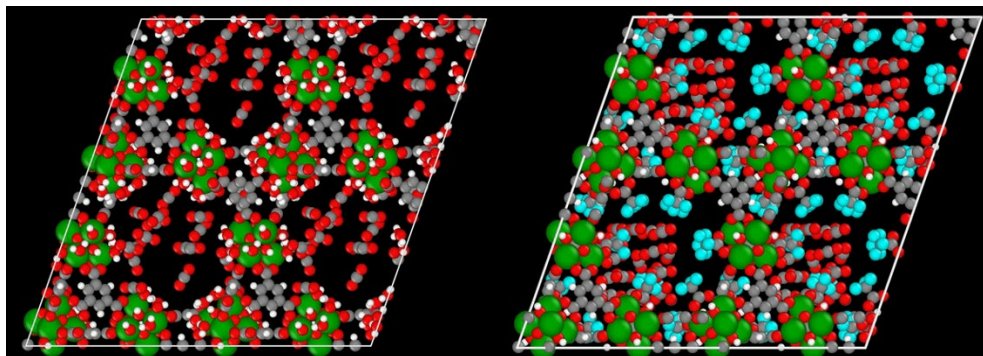


Figure 15. Molecular dynamics simulations of carbon dioxide reaction with formate-capped MOF-808 (left) and trifluoroacetic acid-modulated MOF-808 (right). The fluorine atoms of trifluoroacetic acid are colored light blue.

Follow-on efforts would involve further experimental investigation of studied MOFs to support data from the Monte Carlo and molecular dynamics simulations. More specifically, efforts such as thermogravimetric analysis coupled with mass spectrometry can shed light on the number of defects in the UiO-66 family MOFs, as well as the wt% of residual solvent, and differentiate DMF content from water content. Nuclear magnetic resonance spectroscopy data can be used to elucidate the termination chemistry of the defects. Finally, diffuse reflectance infrared fourier transform spectroscopy techniques can be used to evaluate dynamic interaction of toxic industrial chemicals with these MOFs, with ultrahigh vacuum capabilities and detector accessories capable of capturing nanosecond-level sampling times that enable experiments that closely mimic conditions being represented in the molecular simulations.

4. CONCLUSIONS

Monte Carlo and molecular dynamics simulations have been used to simulate adsorption and chemical reaction on zirconium-based MOFs UiO-66, UiO-66-NH₂, and MOF-808. Effects of individual modifications such as induced defects, type of defect termination, capping of open node sites, and various content of residual solvent (DMF or water) on the nitrogen adsorption isotherm have been simulated and compared to experiments. Further efforts in FY23 will involve incorporating combinations of these features and collecting supplemental experimental data to try to match the isotherms of experimental materials and support findings. Molecular dynamics simulations have been set up probing water behavior on MOF-808 and have progressed to evaluating carbon dioxide on the trifluoroacetic acid-modulated MOF-808 to gauge toxic chemical removal.

ACKNOWLEDGMENTS

Funding was provided by the U.S. Army via the Chemical Biological Advanced Materials and Manufacturing Science Program (PE 0601102A Project VR9) at the Combat Capabilities Development Command Chemical Biological Center.

REFERENCES

- [1] Bobbitt, N.S.; Mendonca, M.L.; Howarth, A.J.; Islamoglu, T.; Hupp, J.T.; Farha, O.K.; Snurr, R.Q. Metal-organic frameworks for the removal of toxic industrial chemicals and chemical warfare agents. *Chem. Soc. Rev.* **2017**, *46* (11), pp 3357–3385.
- [2] Kandiah, M.; Nilsen, M.H.; Usseglio, S.; Jakobsen, S.; Olsbye, U.; Tilset, M.; Larabi, C.; Quadrelli, E.A.; Bonino, F.; Lillerud, K.P. Synthesis and Stability of Tagged UiO-66 Zr-MOFs. *Chem. Mater.* **2010**, *22* (24), pp 6632–6640.

- [3] Winarta, J.; Shan, B.H.; McIntyre, S.M.; Ye, L.; Wang, C.; Liu, J.C.; Mu, B. A Decade of UiO-66 Research: A Historic Review of Dynamic Structure, Synthesis Mechanisms, and Characterization Techniques of an Archetypal Metal-Organic Framework. *Cryst. Growth Des.* **2020**, *20* (2), pp 1347–1362.
- [4] Liu, L.M.; Chen, Z.J.; Wang, J.J.; Zhang, D.L.; Zhu, Y.H.; Ling, S.L.; Huang, K.W.; Belmabkhout, Y.; Adil, K.; Zhang, Y.X.; Slater, B.; Eddaoudi, M. Imaging defects and their evolution in a metal-organic framework at sub-unit-cell resolution. *Nat. Chem.* **2019**, *11* (7), pp 622–628.
- [5] Thur, R.; Van Velthoven, N.; Lemmens, V.; Bastin, M.; Smolders, S.; De Vos, D.; Vankelcom, I.F.J. Modulator-Mediated Functionalization of MOF-808 as a Platform Tool to Create High-Performance Mixed-Matrix Membranes. *Acs Appl. Mater. Interfaces.* **2019**, *11* (47), pp 44792–44801.
- [6] Senftle, T.P.; Hong, S.; Islam, M.M.; Kylasa, S.B.; Zheng, Y.X.; Shin, Y.K.; Junkermeier, C.; Engel-Herbert, R.; Janik, M.J.; Aktulga, H.M.; Verstraelen, T.; Grama, A.; van Duin, A.C.T. The ReaxFF reactive force-field: development, applications and future directions. *npj Comput. Mater.* **2016**, *2*, pp 1–14.
- [7] Groom, C.R.; Bruno, I.J.; Lightfoot, M.P.; Ward, S.C. The Cambridge Structural Database. *Acta Crystallogr., Sect. B: Struct. Sci., Cryst. Eng. Mater.* **2016**, *B72*, pp 171–179.
- [8] Giannozzi, P.; Andreussi, O.; Brumme, T.; Bunau, O.; Nardelli, M.B.; Calandra, M.; Car, R.; Cavazzoni, C.; Ceresoli, D.; Cococcioni, M.; Colonna, N.; Carnimeo, I.; Dal Corso, A.; Gironcoli, S.; Delugas, P.; DiStasio, R.A.; Ferretti, A.; Floris, A.; Fratesi, G.; Fugallo, G.; Gebauer, R.; Gerstmann, U.; Giustino, F.; Gorni, T.; Jia, J.; Kawamura, M.; Ko, H.-Y.; Kokalj, A.; Küçükbenli, E.; Lazzeri, M.; Marsili, M.; Marzari, N.; Mauri, F.; Nguyen, N.L.; Nguyen, H.-V.; Otero-de-la-Roza, A.; Paulatto, L.; Poncé, S.; Rocca, D.; Sabatini, R.; Santra, B.; Schlipf, M.; Seitsonen, A.P.; Smogunov, A.; Timrov, I.; Thonhauser, T.; Umari, P.; Vast, N.; Wu, X.; Baroni, S. Advanced capabilities for materials modelling with QUANTUM ESPRESSO. *J. Phys.: Condens. Matter.* **2017**, *29* (46), pp 1–30.
- [9] Dubbeldam, D.; Calero, S.; Ellis, D.E.; Snurr, R. Q. RASPA: molecular simulation software for adsorption and diffusion in flexible nanoporous materials. *Mol. Simul.* **2016**, *42* (2), pp 81–101.
- [10] Jajko, G.; Gutierrez-Sevillano, J.J.; Slawek, A.; Szufla, M.; Kozyra, P.; Matoga, D.; Makowski, W.; Calero, S. Water adsorption in ideal and defective UiO-66 structures. *Microporous Mesoporous Mater.* **2022**, *330*, pp 1–9.
- [11] Evans, J.D.; Coudert, F.X. Microscopic Mechanism of Chiral Induction in a Metal-Organic Framework. *J. Am. Chem. Soc.* **2016**, *138* (19), pp 6131–6134.
- [12] Jajko, G.; Kozyra, P.; Gutierrez-Sevillano, J.J.; Makowski, W.; Calero, S. Carbon Dioxide Capture Enhanced by Pre-Adsorption of Water and Methanol in UiO-66. *Chem. - Eur. J.* **2021**, *27* (59), pp 14653–14659.
- [13] Parashar, S.; Zhu, Q.; Dantas, S.; Neimark, A.V. Monte Carlo Simulations of Nanopore Compartmentalization Yield Fingerprint Adsorption Isotherms as a Rationale for Advanced Structure Characterization of Metal-Organic Frameworks. *Acs Appl. Nano Mater.* **2021**, *4* (5), pp 5531–5540.
- [14] Thompson, A.P.; Aktulga, H.M.; Berger, R.; Bolintineanu, D.S.; Brown, W.M.; Crozier, P.S.; in 't Veld, P.J.I.; Kohlmeyer, A.; Moore, S.G.; Nguyen, T.D.; Shan, R.; Stevens, M.J.; Tranchida, J.; Trott, C.; Plimpton, S.J. LAMMPS—a flexible simulation tool for particle-based materials modeling at the atomic, meso, and continuum scales. *Comput. Phys. Commun.* **2022**, *271*, p 108171.
- [15] Dwivedi, S.; Kowalik, M.; Rosenbach, N.; Alqarni, D.S.; Shin, Y.K.; Yang, Y.J.; Mauro, J.C.; Tanksale, A.; Chaffee, A.L.; van Duin, A.C.T. Atomistic Mechanisms of Thermal Transformation in a Zr-Metal Organic Framework, MIL-140C. *J. Phys. Chem. Lett.* **2021**, *12* (1), pp 177–184.
- [16] van Duin, A.C.T.; Merinov, B.V.; Jang, S.S.; Goddard, W.A. ReaxFF Reactive Force Field for Solid Oxide Fuel Cell Systems with Application to Oxygen Ion Transport in Ytria-Stabilized Zirconia. *J. Phys. Chem. A.* **2008**, *112* (14), pp 3133–3140.
- [17] Agrawal, M.; Sholl, D.S. Effects of Intrinsic Flexibility on Adsorption Properties of Metal-Organic Frameworks at Dilute and Nondilute Loadings. *Acs Appl. Mater. Interfaces.* **2019**, *11* (34), pp 31060–31068.
- [18] Becker, T.M.; Heinen, J.; Dubbeldam, D.; Lin, L.C.; Vugt, T.J.H. Polarizable Force Fields for CO₂ and CH₄ Adsorption in M-MOF-74. *J. Phys. Chem. C.* **2017**, *121* (8), pp 4659–4673.
- [19] Ardila-Suarez, C.; Perez-Beltran, S.; Ramirez-Caballero, G.E.; Balbuena, P.B. Enhanced acidity of defective MOF-808: effects of the activation process and missing linker defects. *Catal. Sci. Technol.* **2018**, *8* (3), pp 847–857.
- [20] Affek, H.P.; Eiler, J.M. Abundance of mass 47 CO₂ in urban air, car exhaust, and human breath. *Geochim. Cosmochim. Acta.* **2006**, *70* (1), pp 1–12.
- [21] Chen, H.; Yang, Z.Z.; Do-Thanh, C.L.; Dai, S. What Fluorine Can Do in CO₂ Chemistry: Applications from Homogeneous to Heterogeneous Systems. *ChemSuschem.* **2020**, *13* (23), pp 6182–6200.

Controlling the heterogeneous catalysis of zirconium clusters within a porous SBA-15 scaffold

Ann M. Kulisiewicz^{a*}, Sergio J. Garibay^{a,b}, Trenton B. Tovar^a, Matthew A. Browe^a

^aU.S. Army Combat Capabilities Development Command Chemical Biological Center, Research & Operations Directorate, 8198 Blackhawk Rd., Aberdeen Proving Ground, MD 21010

^bLeidos, Inc., 3465 Box Hill Corporate Center Dr., Abingdon, MD 21009

ABSTRACT

Metal-organic frameworks with Zr-based secondary building units are promising materials for catalytic degradation of chemical agents. These Zr-based secondary building units have been shown to be the primary reactive component in these materials for catalytic hydrolysis reactions. However, the variables inherent to metal-organic framework structures (e.g., pore size, structure, connectivity, crystal size, etc.) complicate the understanding of the reactivity of the material, especially the role of the secondary building unit. We explored the reactivity of a system consisting of Zr₆ and Zr₁₂ clusters grafted onto silica to understand the reactivity of the secondary building units component of the metal-organic frameworks, independent of other variables inherent to metal-organic frameworks structures. Silica supports functionalized with sulfuric or phosphoric acid groups were used to tether individual Zr clusters to the surface. The final products were characterized by powder diffraction and Brunauer-Emmett-Teller analysis to confirm porosity of the material and crystallinity of the Zr cluster post-attachment. Hydrolysis reactivity of these materials was assessed through ³¹P-nuclear magnetic resonance experiments under buffered and non-buffered conditions in the presence of dimethyl nitrophosphate. Buffering moieties on either the monocarboxylic acid modulators or the silica supports were explored to enhance reactivity of the materials under neutral aqueous conditions.

Keywords: metal-organic framework, catalysis, acid-modified silica

1. INTRODUCTION

Metal-organic frameworks (MOFs) have shown immense promise in recent years for the catalytic degradation of chemical warfare agents (CWAs). MOFs are materials consisting of metal nodes, referred to as secondary building units (SBUs), bridged in a crystalline arrangement by organic linkers to create a porous framework. By varying the SBU and linker, a wide array of MOFs can be synthesized with different structural or chemical properties tailored to a specific application. MOFs containing Zr₆O₄(OH)₄¹²⁺ SBUs have recently shown promise as catalytically active materials for nerve agent hydrolysis, including UiO-66, UiO-67, NU-1000, NU-901, MOF-808, and many variants of these structural topologies with functionalized linkers. For each of these MOFs, the hydrolysis reaction mechanism of two organophosphate nerve agents, VX and GB, depends only on the SBU and not the linker.¹ Despite having the same reaction site and mechanism, the reaction rate varies greatly based on both the MOF and the agent. Currently, the reason why some Zr-MOFs perform better for agent hydrolysis is not understood.

The inability to quantify the number of active sites within a MOF significantly hinders studying the reactivity of these materials. Different Zr-MOFs can have connectivity of 6, 8, or 12 linkers per SBU, possibly revealing more active Zr sites. Due to pore size, it has been hypothesized that some agents cannot access the interior of some MOFs based on steric constraints, thus reactivity is limited only to sites on the surface causing crystal size to become the main determinant for reactivity. However, crystal sizes are determined by synthesis conditions and can vary greatly. The presence of defect sites in certain MOFs, which cannot be accurately quantified and depend on synthetic conditions, have been shown to greatly impact reactivity.

MOF linkers can further complicate the understanding of reactivity profiles. While linkers do not participate in the hydrolysis reaction, linker topology can create steric effects at the SBU which can affect the adsorption and subsequent reactivity of the MOF with CWAs. In addition, functionalized linkers could induce electronic effects on the SBU, thereby affecting reactivity. In this study, we explore hydrolysis reactions on Zr-MOF SBU clusters independent of the MOF structure to better understand the reactivity of the Zr cluster and the role of the local chemical environment on reactivity. To generate a suite of standardized materials for this study, Zr₆ and Zr₁₂ clusters with varying

monocarboxylic acid modulators (MCAMs) were synthesized. The MCAMs varied in pKa, steric, and electronic properties to mimic the effect of the MOF linker on the Zr cluster reactivity. The reactive material consists of an inert, mesoporous silica support functionalized with different acid groups to tether a quantifiable number of Zr clusters to the surface. This material was then assessed for hydrolysis activity when reacted with dimethyl nitrophosphate (DMNP), a nerve agent simulant, under buffered and non-buffered aqueous conditions.

2. EXPERIMENTAL METHODS

2.1 Synthesis

2.1.1 Zirconium cluster synthesis

All reagents were purchased from commercial sources and used without further purification. Zr₆-acetic acid, Zr₆-glycine, and Zr₁₂-SBUs was synthesized according to modified literature procedures as previously described.^{2,3,4}

[Zr₆(O)₄(OH)₄(H₂O)₈(Gly)₈]•12Cl•8H₂O cluster synthesis: In an 8-dram vial ZrOCl₂•8H₂O (0.403 g, 1.25 mmol) was dissolved with H₂O (12 mL). To this vial, glycine (0.375 g, 5 mmol) and 0.1 mL of an 8 mM HCl_(aq) solution were added. After briefly stirring the solution (5 min) the vial was heated at 98 °C for 4 days which slowly evaporated off the water. The gel was recrystallized with 4–6 mL of hot deionized water at 100 °C on a hot plate. Upon heating at 100 °C and evaporation ~ 3 mL of water remained. The vial was removed from the hot plate and allowed to cool. After 2 hours, the vial generated a white solid. The cluster was solvent exchanged with CHCl₃ (3 mL x 3).

[Zr₆(O)₄(OH)₄(AA)₈]•3Cl•2H₂O cluster synthesis: In a 50 mL round-bottom flask was added ZrCl₄ (2 g, 8.58 mmol) and a stir bar. Isopropanol (5 mL) was added to the flask then acetic acid (3 mL, 53 mmol). The flask was fitted with a reflux condenser and heated at 120 °C for 1 hour. After cooling to room temperature, the SBU was then filtered and washed with acetone.

[Zr₆(O)₄(OH)₄(BA-CH₂NH₂)₁₀]•5Cl cluster synthesis: Zr₆-AA-SBU (0.1 g, 0.07 mmol) was added to an 8-dram vial with a stir bar. BA-CH₂NH₂ (0.140 g, 0.927 mmol) was dissolved in 12 mL H₂O and added to vial. The vial was heated at 50 °C for 30 minutes with stirring on a hot plate then capped and heated at 80 °C for 18 hours in an oven. The solution was removed through rotary evaporation.

[Zr₆(O)₄(OH)₄(BA-CH₂Morph)₁₂]•5Cl cluster synthesis: Zr₆-AA-SBU (0.1 g, 0.07 mmol) was added to an 8-dram vial with a stir bar. BA-CH₂Morph (0.204 g, 0.924 mmol) was dissolved in 12 mL H₂O and added to vial. The vial was heated at 80 °C for 30 minutes with stirring on a hot plate then capped and heated at 80 °C for 18 hours in an oven. The solution was removed through rotary evaporation.

[Zr₆(O)₄(OH)₄(BA)₁₀]•2Cl•2H₂O cluster synthesis: In a 50 mL round-bottom flask, ZrCl₄ (2 g, 8.58 mmol) and a stir bar were added. Isopropanol (10 mL) was added to the flask then benzoic acid (6.39 g, 52.35 mmol). The flask was fitted with a reflux condenser and heated at 120 °C for 18 hours. After cooling to room temperature, the SBU was then filtered and washed with acetone.

Zr₁₂O₈(OH)₈(AA)₂₄ cluster synthesis: ZrOCl₂•8H₂O (1.16 g, 3.6 mmol) was dissolved with N,N-Dimethylformamide (DMF) (1.8 mL) in an 8-dram vial with magnetic stir bar. Acetic acid (7.95 mL, 139 mmol) was added to the vial and the solution was stirred for 5 minutes until solution became clear. The vial was capped and placed in a pre-heated oven at 110 °C for 24 hours. The white crystalline solid was filtered and washed with 50 mL of a 1:1 DMF:acetic acid solution. The solid was transferred to an 8-dram vial and solvent exchanged with CHCl₃ (3 mL x 3). Residual chloroform was evaporated with N₂ (g) at room temperature.

2.1.2 Synthesis of sulfuric acid treated SBA-15

Sulfuric acid treated SBA-15 was synthesized according to literature procedures from Crisci et al.⁵ Pluronic P-123 (0.67 g) was dissolved in 23 mL 1.6 M HCl at 35 °C. Then, 1.4 mL of tetraethyl orthosilicate (TEOS) and 140 mg NaCl were added, and the solution was stirred for 1 hour. The solution was then equally divided into three vials. In one vial, 12 μL of 3-mercaptopropyltrimethoxysilane (MPTMS) was added. In a second vial, 48 μL of MPTMS were added in 12 μL increments every 15 minutes. Then, H₂O₂ (1.4 mmol) was added to all three vials, and the solutions were stirred for 24 hours. The three samples were then put in Parr bombs and heated at 100 °C for 24 hours. The samples were filtered and washed with water. From each sample, the Pluronic[™] surfactant was extracted with ethanol under reflux.

The samples were washed with ethanol and the extraction was repeated. The two samples with MPTMS were washed with water and suspended in HCl for 3 hours. The HCl treated samples were filtered and washed with water, dried in air at 60 °C overnight, and then dried under vacuum at 150 °C.

2.1.3 Synthesis of phosphoric acid treated SBA-15

From section 2.1.2, the sample that did not contain MPTMS was suspended in a H₃PO₄/acetone solution. The sample was stirred at 60 °C until the acetone evaporated. The sample was dried in air at 60 °C overnight and then dried under vacuum at 150 °C.

2.1.4 Synthesis of zirconium cluster treated acid functionalized SBA-15

Phosphoric or sulfuric acid functionalized SBA-15 (70 mg) was added to an 8-dram vial. A solution of Zr-SBU cluster (70 mg) in 12 mL of DMF was added to the vial and capped. The vial sulfuric acid functionalized SBA-15 was placed in a 55 °C oven while the phosphoric acid functionalized SBA-15 was placed in a 100 °C pre-heated oven for 18 hours. The vials were solvent exchanged with fresh DMF and acetone (12 mL x 3).

2.1.5 Synthesis of acid-base functionalized SBA-15

A bifunctional acid-base SBA-15 support was synthesized according to Shao et. al.⁶ Pluronic P-123 (1.0 g) was dissolved in 40 mL of water and 5 mL of HCl at 40 °C. Then, 5 mL of TEOS, 200 µL of MPTMS, and 3-tert-butyloxycarbonylaminopropyltrimethoxysilane (NHBoc) were added, and the solution was stirred for 24 hours. The protecting group on the amine of NHBoc was necessary as post synthetic grafting of aminopropyltrimethoxysilane was unsuccessful for producing a bifunctional support. The solution was then put in a Parr bomb and heated at 100 °C for an additional 24 hours. The product was washed with water and then extracted with ethanol under reflux. The material was then treated with H₂O₂ to oxidize the mercapto groups to sulfonic acid sites. The sample was then heated at 185 °C under vacuum for 24 hours to remove the protecting group and leave basic amino sites.

2.1.6 Synthesis of zirconium cluster treated acid-base functionalized SBA-15

Propylamine-propylsulfuric acid-functionalized SBA-15 (70 mg) was added to an 8-dram vial. A solution of Zr₁₂-acetic acid-SBU cluster (70 mg) in 12 mL of DMF was added to the vial and capped. The vial was placed in a 55 °C oven for 18 hours. The vials were solvent exchanged with fresh DMF and acetone (12 mL x 3).

2.2 Characterization

2.2.1 Powder X-ray diffraction

Powder x-ray diffraction (PXRD) patterns were measured on a Rigaku MiniFlex 600 diffractometer equipped with a D/teX Ultra detector with Cu-K_α radiation ($\lambda = 1.5418 \text{ \AA}$) over a range of $2\theta = 3\text{--}50^\circ$ at a scan rate of 5 deg min⁻¹.

2.2.2 ATR-FTIR

Attenuated total reflectance-Fourier transform infrared (ATR-FTIR) spectra were measured on a Bruker Tensor 27 spectrometer from 4000–400 cm⁻¹ at a resolution of 2 cm⁻¹.

2.2.3 N₂ physisorption

N₂ isotherms were measured using a Micromeritics ASAP 2420 analyzer at 77 kelvin (K). Samples were off-gassed at 120 °C under vacuum for ~16 hours. The Brunauer-Emmett-Teller (BET) method was used to calculate specific surface area in m² g⁻¹.

2.2.4 Scanning electron microscopy (SEM)

SEM images were taken with a Phenom GSR desktop instrument. Samples were placed on double-sided carbon tape. Samples were imaged at an accelerating voltage of 15 kV and a working distance of ~10 mm. Energy dispersive X-ray spectroscopy (EDS) was used to map elemental dispersion throughout the materials.

2.3 Catalysis experiments

Cluster modified SBA-15 (12 mol%, ~8.6 to 8.7 mg) were added to a vial. A solution of 9:1 H₂O:D₂O (0.9/0.1 mL) was added to the vial and capped. The vial was briefly (1 min) sonicated, then transferred to a nuclear magnetic resonance (NMR) tube. N-ethylmorpholine (50 μ L) was added to the solution within the NMR tube. DMNP (4 μ L, 25 μ mol) was added to the top sidewalls of the NMR tube. The tube was capped and carefully inverted thrice to mix the components. The tube was inserted into the NMR instrument and conversion was monitored by ³¹P-NMR.

2.4 Computational modeling of zirconium clusters

A 28 x 28 x 14 Å slab of beta-cristobalite silica was prepared in the Materials Studio molecular editor. The slab was fed into the Large-scale Atomic/Molecular Massively Parallel Simulator molecular dynamics code and subjected to a melt-quench algorithm using a Tersoff interatomic potential for all atoms, a common procedure for preparing an amorphous silica surface.⁷ A representative “patch” of silica was cut out of the surface, approximately 100 atoms in total, to minimize computational intensiveness. The patch was modified so that all oxygen atoms contained two bonds and all silicon atoms contained four bonds, satisfying all oxygen bonding with hydrogen atoms, and satisfying all silicon bonding with hydroxyl (–OH) groups. The resulting structure was then geometrically optimized and energy minimized using the Gaussian 16 quantum chemistry software at the B3LYP/lanl2dz level of theory. All Zr₆-based clusters were based off a Zr₆O₈ core structure with 24 additional oxygen atoms bonded to the zirconium atoms and protruding to the outer edge of the cluster. These external oxygen atoms were then subjected to different capping chemistries. Previous literature on sulfate group binding to these clusters was used as a guide for modelling bound zirconium clusters to the silica surface. The net result involved removal of the capping group and bonding of oxygen atoms from the functional group to the zirconium atoms of the cluster.⁸ A few possible configurations were explored using polarizable continuum implicit solvation models (designating water as the solvent) in Gaussian 16 at the B3LYP/lanl2dz level of theory. In these calculations, the atoms native to the optimized silica patch were fixed to save on computational resources; only the functional groups and zirconium cluster atoms were allowed to move. The mapping of electrostatic potential at constant electron density was then generated in Vesta for bonded and non-bonded zirconium clusters. A value of 0.001 atomic units is commonly used for the contour of constant electron density and was utilized here.⁹ Electrostatic potential was mapped from a maximum of 0.05 atomic units (red) to a minimum of -0.05 atomic units (blue) and is loosely considered a metric for identifying regions of guest molecule affinity, with higher electrostatic potential (red) correlating to higher guest molecule affinity.

3. RESULTS

The zirconium clusters were synthesized following a modified literature procedure using a thermal synthesis of a zirconium source with excess MCAMs. The PXRD patterns of the synthesized clusters closely resembled that of their simulated patterns derived from their single crystal X-ray diffraction structures (Figure 1). With both Zr₆- and Zr₁₂-clusters in hand, we explored their catalytic properties in the hydrolysis of DMNP under aqueous conditions through ³¹P-NMR spectroscopy. Like many Zr-MOFs, hydrolysis of DMNP with the Zr clusters requires basic conditions or amine co-catalyst for effective reactivity. As expected, the Zr clusters which have monocarboxylic acids bound to zirconium sites do not facilitate DMNP hydrolysis under strictly aqueous (pH = 7) conditions (Table 1). However, the use of N-ethylmorpholine (NEM) engenders the Zr clusters to facilitate DMNP hydrolysis (Table 1). Presumably, the NEM facilitates the dissociation of MCAMs, which induces DMNP access to the resulting Zr-OH, -H₂O catalytic sites for hydrolysis. The Zr₆-(glycine) cluster fully facilitates the hydrolysis of DMNP after 18 hours with a half-life (*t*_{1/2}) of 69 minutes. Interestingly, the Zr₁₂-(acetic acid) cluster performs relatively faster with a DMNP *t*_{1/2} of 12 minutes. This may be attributable to the relatively larger number of available Zr-OH, -H₂O catalytic sites of the Zr₁₂-(acetic acid) cluster than the Zr₆-(glycine) cluster (2:1, respectively). To better facilitate DMNP hydrolysis with the Zr clusters, HCl-activation was performed to displace the monocarboxylic acids from the SBU. Both Zr clusters retain their crystallinity after HCl-activation (Figure 2). As expected, the HCl-activated Zr₁₂-(acetic acid) cluster facilitated faster DMNP hydrolysis (*t*_{1/2} = 7 min) than the inactivated Zr₁₂-(acetic acid) cluster under 0.45 M NEM aqueous conditions (*t*_{1/2} = 12 min) (Table 1).

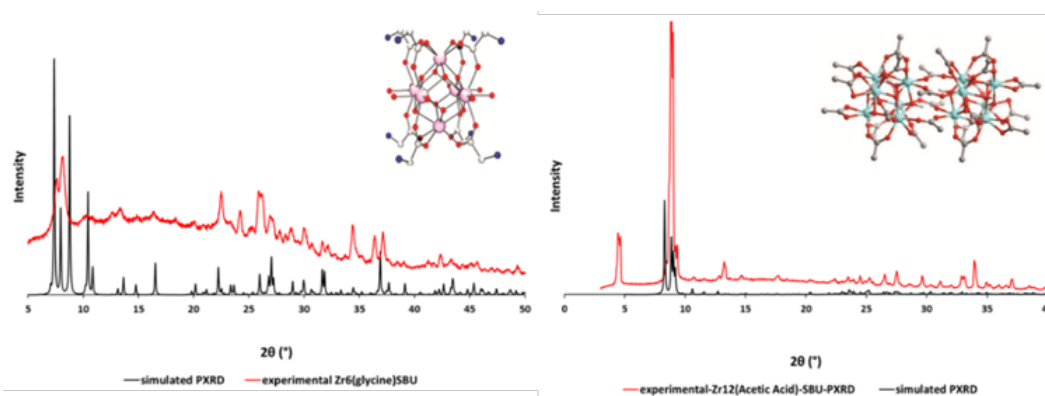


Figure 1. (Left) Simulated PXRD pattern of Zr_6 -(glycine) (bottom, black) and experimental PXRD pattern of Zr_6 (glycine) SBU (top, red) with the representation of the Zr_6 cluster derived from single X-ray diffraction data. (Right) Simulated PXRD pattern of Zr_{12} -(acetic acid) (bottom, black) and experimental PXRD pattern of Zr_{12} -(acetic acid) (top, red) note that simulated spectra begins at 5° with the representation of the Zr_{12} -(acetic acid) cluster derived from single X-ray diffraction data.

Table 1. DMNP hydrolysis by zirconium clusters in 0.45 M NEM buffer and aqueous conditions (missing entries correspond to experiments yet to be done).

Material	$t_{1/2}$ (min), DMNP, water	$t_{1/2}$ (min), DMNP, 0.45 M NEM buffer
Zr_{12} -(acetic acid)	N.R.	12
Zr_6 -(glycine)	N.R.	69
Zr_6 -(acetic acid)		17
Zr_6 -(benzoic acid)	N.R.	20
HCl activated Zr_{12} -(acetic acid)		7
Zr_6 -(BA- CH_2NH_2)	1000	69
Zr_6 -(BA- CH_2 -morpholine)	1000	<2

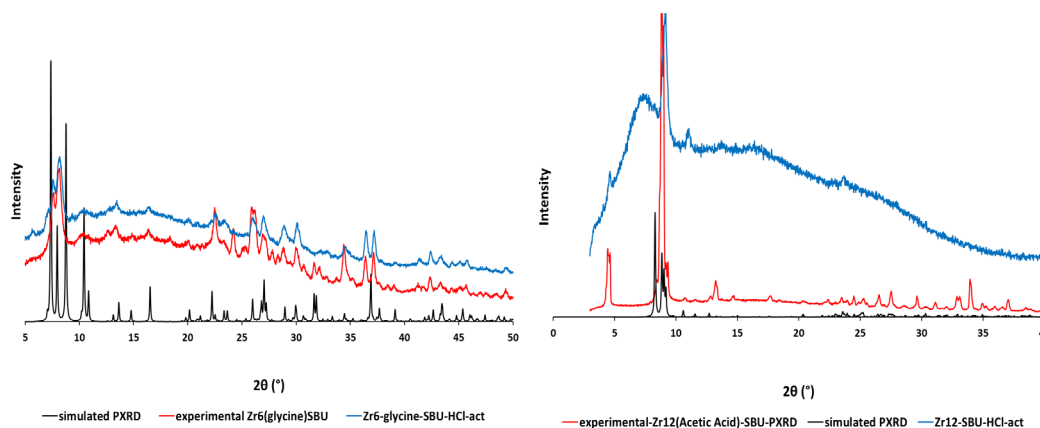


Figure 2. (Left) Simulated PXRD pattern of Zr_6 -(glycine) (bottom, black), experimental PXRD pattern of Zr_6 (glycine) (middle, red) and after HCl-activation (blue, top). (Right) Simulated PXRD pattern of Zr_{12} -(acetic acid) (bottom, black), experimental PXRD pattern of Zr_{12} -(acetic acid) (middle, red) and after HCl-activation (blue, top).

To tether the zirconium clusters to silica, silica particles (SBA-15) were modified with sulfuric acid and phosphoric acid. The synthesized particles were characterized by ATR-FTIR and BET analysis to determine crystallinity and porosity. The IR spectrum of phosphoric acid functionalized SBA-15 (P-SBA-15) contain peaks around 1323 cm^{-1} and 626 cm^{-1} corresponding to the P=O and P-OH stretches respectively (Figure 3). After phosphoric acid

functionalization, the N_2 adsorption significantly decreases, which corresponds to a decrease in porosity (Figure 3). The observed decrease in porosity might be due to the high degree of residual H_3PO_4 within the pores of P-SBA-15 or a high level of functionalization. Indeed, when P-SBA-15 was utilized for DMNP hydrolysis under 0.45 M NEM aqueous conditions, residual H_2PO_4 is observed in the ^{31}P -NMR spectrum at 2.5 ppm. Interestingly, P-SBA-15 is not selective towards DMNP, instead it primarily and slowly ($t_{1/2} \geq 220$ min) generates the undesired P–O–Me cleavage product methyl 4-nitrophenyl phosphate (M4NP). Due to the enhanced performance of the Zr_{12} -clusters as compared to the Zr_6 clusters, the modified SBA-15 materials were reacted with Zr_{12} -clusters to generate Zr_{12} -modified SBA-15. Dissolved Zr_{12} -(acetic acid) was introduced to P-SBA-15 through heating overnight. Residual clusters were removed through successive solvent exchange. The stretches associated with P=O and P–OH in P-SBA-15 shift or decrease after introduction of the Zr_{12} -(acetic acid) (Figure 3). More importantly, new C=O stretches corresponding to the acetic acid within the Zr_{12} -(acetic acid) appear. However, the stretches associated with the Zr–O–H stretches of the cluster at 3390 cm^{-1} completely disappear after introduction into P-SBA-15 presumably through the binding of Zr to the Si centers or phosphoric acid within P-SBA-15. The PXRD of Zr_{12} -SBU-P-SBA-15 contains broad peaks that indicate a low degree of crystallinity, possibly due to the relatively low amount of Zr retained in the SBA-15 as the EDS-SEM indicates the Si:P:Zr ratio is 1:0.5:0.09 respectively (Figure 4, Table 2). Remarkably, Zr_{12} -(acetic acid)-P-SBA-15 facilitates the fast ($t_{1/2} = 69$ min) and selective hydrolysis of DMNP to DMP under 0.45 M NEM aqueous conditions (Table 3). The stark contrast in DMNP hydrolysis reactivity and selectivity is clearly attributable to the introduction of the Zr_{12} -(acetic acid) clusters into SBA-15.

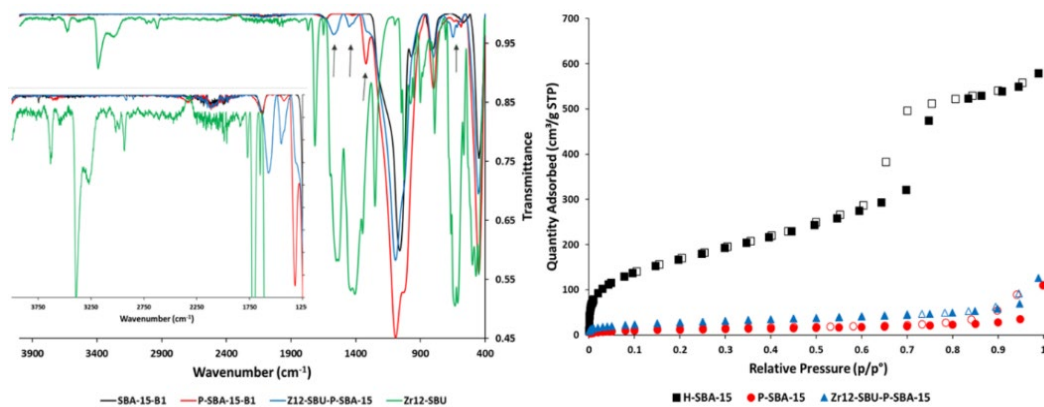


Figure 3. (Left) FTIR spectra of SBA-15 (black), P-SBA-15 (red), Zr_{12} -(acetic acid)-P-SBA-15 (blue), and Zr_{12} -(acetic acid) (green). Inset displays spectral region from 3900 to 1200 cm^{-1} . (Right) N_2 adsorption isotherms of SBA-15 (black squares), P-SBA-15 (red circles), and Zr_{12} -(acetic acid)-P-SBA-15 (blue triangles). Solid symbols represent adsorption, empty symbols represent desorption.

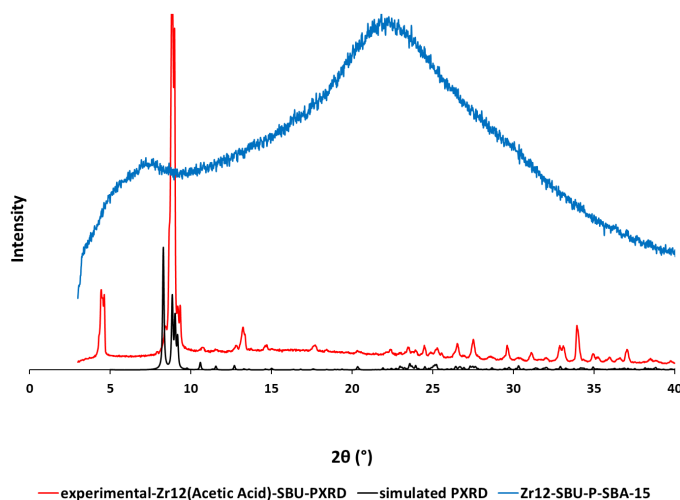
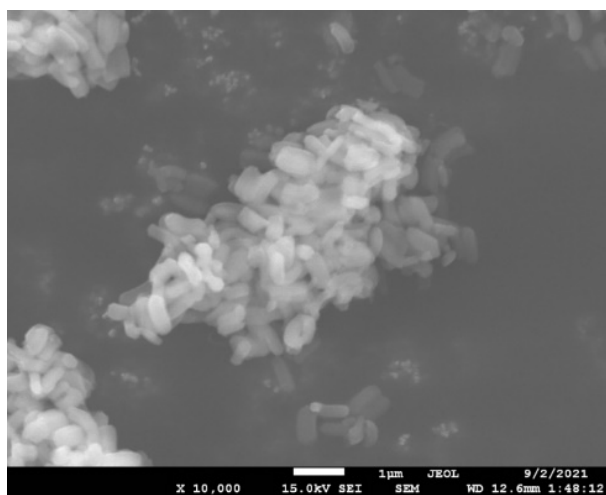


Figure 4. Simulated PXRD pattern of Zr_{12} -(acetic acid) (bottom, black), experimental PXRD pattern of Zr_{12} -(acetic acid) (middle, red), and experimental PXRD pattern of Zr_{12} -(AA)-SBU-P-SBA-15 (top, blue). Note that simulated PXRD spectra begins at 5° .

Table 2. EDS analysis of zirconium clusters bound to silica surfaces. Atomic percentage ratios of key elements are tabulated for each sample.

Sample	%Si	%O	%S	%P	%Zr
L-SO ₃ H-SBA-15	23.8	76	0.20	N/A	0
Zr ₁₂ -acetic acid-L-SO ₃ H-SBA-15	80	N/A	N/A	N/A	20
H-SO ₃ H-SBA-15	24	75.4	0.6	N/A	0
Zr ₁₂ -acetic acid-H-SO ₃ H-SBA-15	94	N/A	N/A	N/A	6
PO ₃ H-SBA-15	63	32	N/A	5	N/A
Zr ₁₂ -acetic acid- PO ₃ H-SBA-15	96	N/A	N/A	N/A	4

SBA-15 was modified with different amounts of SO₃H to generate H-SO₃H-SBA-15 and L-SO₃H-SBA-15 (H = high, L = low). EDS-SEM analysis indicates that H-SO₃H-SBA-15 has a 3.9-fold greater sulfide content than L-SO₃H-SBA-15 (Figure 5, Table 2). The IR spectrum of H-SO₃H-SBA-15 contains a peak at 688 cm⁻¹ corresponding to the S–OH stretch (Figure 6). Upon introduction of the Zr₁₂-(acetic acid), the S–OH stretch disappears and new stretches at 1586 cm⁻¹ and 1480 cm⁻¹ corresponding to the acetic acid within the Zr₁₂-(acetic acid). Similar to P-SBA-15, H-SO₃H-SBA-15 slowly and primarily generates M4NP when it was utilized in the hydrolysis of DMNP in 0.45 M NEM aqueous conditions. Modification of SBA-15 with SO₃H reduces the porosity. Similar to Zr₁₂-(acetic acid)-P-SBA-15, Zr₁₂-(acetic acid)-H-SO₃H-SBA-15 also does not exhibit crystallinity (Figure 7). The introduction of the Zr₁₂-(acetic acid) into H-SO₃H-SBA-15 changes the catalytic properties in the hydrolysis of DMNP (Table 3). Zr₁₂-(acetic acid)-H-SO₃H-SBA-15 facilitates the fast ($t_{1/2}$ = 15 min) and selective hydrolysis of DMNP to DMP under 0.45 M NEM aqueous conditions. Interestingly, there is a stark three-fold greater Zr content within Zr₁₂-(acetic acid)-L-SO₃H-SBA-15 than its analog Zr₁₂-(acetic acid)-H-SO₃H-SBA-15 (Si:Zr ratios 1:0.24 and 1:0.083, respectively). Based on the elemental analysis of their precursors (3.9:1 H- vs. L-respectively), it was expected that H-SO₃H-SBA-15 would have bound relatively more Zr₁₂-(acetic acid) clusters within the pores of SBA-15. This dramatic increase in the zirconium content appears to significantly affect hydrolysis as Zr₁₂-(acetic acid)-L-SO₃H-SBA-15 quickly and selectively converts DMNP into DMP ($t_{1/2}$ = 8 min). Both Zr₁₂-(acetic acid)-L-SO₃H-SBA-15 and Zr₁₂-(acetic acid)-H-SO₃H-SBA-15 samples show significantly enhanced reactivity over Zr₁₂-SBU-P-SBA-15. To better understand this trend, electrostatic potential maps of a Zr₆-(acetic acid) cluster bound to sulfate-functionalized and phosphate-functionalized amorphous silica patches were generated. It was found that the clusters on the sulfate modified materials had higher electrostatic potentials than the phosphate modified materials.¹⁰ These larger areas of electrostatic potential indicate a higher potential of non-covalent interaction between the guest molecule (DMNP) and zirconium catalyst and support the experimental observation of enhanced reactivity of Zr₁₂-(acetic acid)-L-SO₃H-SBA-15 and Zr₁₂-(acetic acid)-H-SO₃H-SBA-15 over Zr₁₂-SBU-P-SBA-15.

**Figure 5. SEM image of Zr₁₂-SBU-L-SO₃H-SBA-15.**

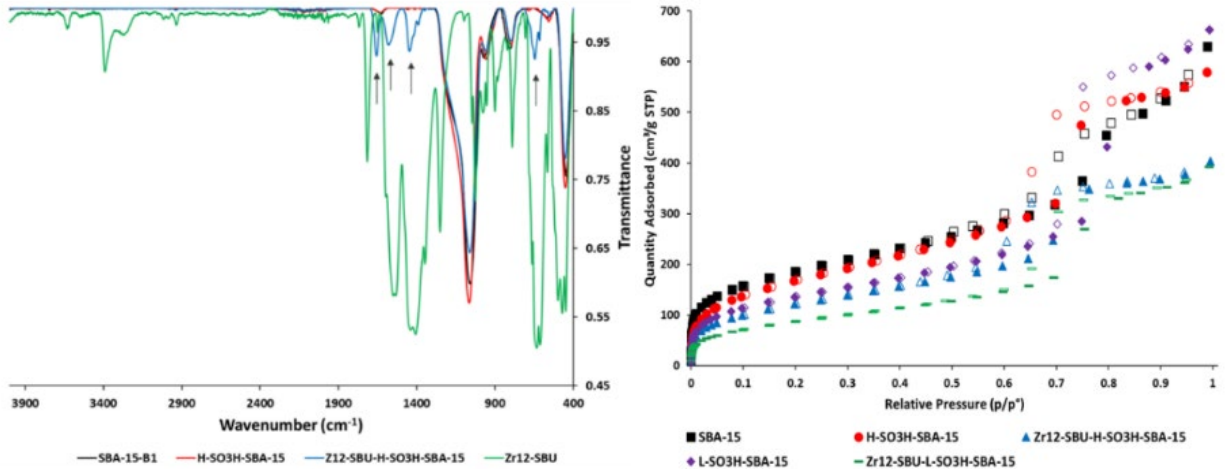


Figure 6. (Left) FTIR spectra of SBA-15 (black), H-SO₃H-SBA-15 (red), Zr₁₂-SBU-H-SO₃H-SBA-15 (blue), and Zr₁₂-(acetic acid) SBU (green). (Right) N₂ adsorption isotherms of SBA-15 (black squares), H-SO₃H-SBA-15 (red circles), Zr₁₂-SBU-H-SO₃H-SBA-15 (blue triangles), L-SO₃H-SBA-15 (purple diamonds), and Zr₁₂-SBU-L-SO₃H-SBA-15 (green line). Solid symbols represent adsorption, empty symbols represent desorption.

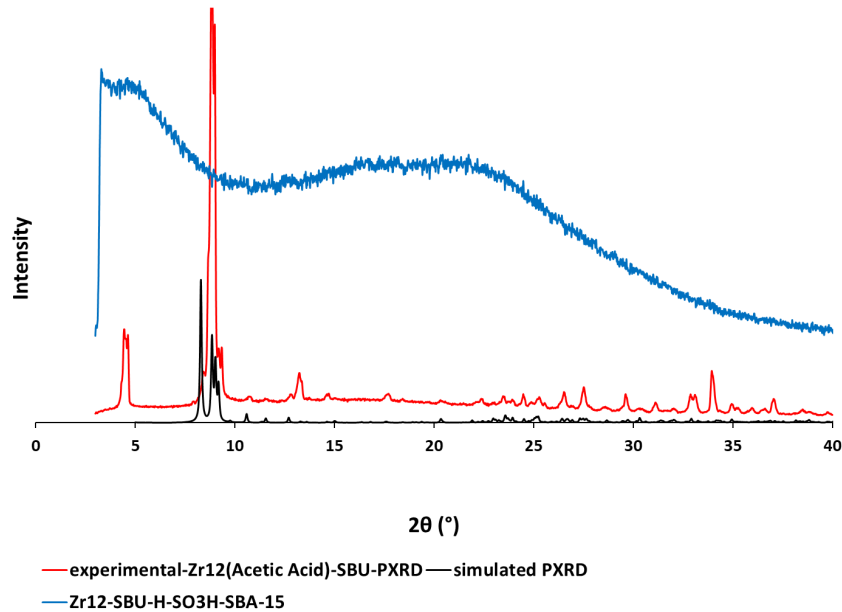


Figure 7. Simulated PXRD pattern of Zr₁₂-(acetic acid) SBU (bottom, black) and experimental PXRD pattern of Zr₁₂-(acetic acid) (middle, red) and experimental PXRD pattern of Zr₁₂-SBU-H-SO₃H-SBA-15 (top, blue).

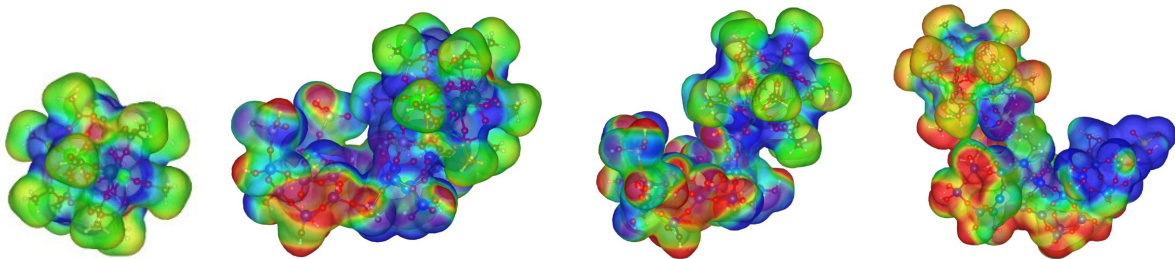


Figure 8. Electrostatic potential maps at constant electron density of 0.001 atomic units for (left to right): baseline Zr₆-acetate cluster, Zr₆-acetate bonded to one phosphate group on silica, Zr₆-acetate bonded to two phosphate groups on silica, and Zr₆-acetate bonded to two sulfate groups on silica.

Table 3. DMNP hydrolysis of bound Zr clusters in 0.45 M NEM buffer and aqueous conditions

Material	$t_{1/2}$ (min), DMNP, water	$t_{1/2}$ (min.), DMNP, 0.45 M NEM buffer
P-SBA-15		>220
H-SO ₃ H-SBA-15		1080
L-SO ₃ H-SBA-15-(CH ₂) ₃ NH ₂	~20 % (18 h)	550
SBA-15-(CH ₂) ₃ NH ₂	>1080	>550
Zr-SBA-15		>550
Zr ₁₂ -acetic acid-SBA-15-(CH ₂) ₃ NH ₂	>1080	>550
Zr ₁₂ -acetic acid-P-SBA-15		69
Zr ₁₂ -acetic acid-H-SO ₃ H-SBA-15		13
Zr ₆ -benzoic acid-L-SO ₃ H-SBA-15		24
Zr ₆ -acetic acid-L-SO ₃ H-SBA-15		18
Zr ₁₂ -acetic acid-L-SO ₃ H-SBA-15	~10% (18 h)	15 ± 2
Zr ₁₂ -acetic acid-L-SO ₃ H-SBA-15-PEI	~20% (18 h)	
Zr ₁₂ -acetic acid-L-SO ₃ H-SBA-15-(CH ₂) ₃ NH ₂	~50% (18 h)	

While the Zr cluster modified SBA-15 materials show fast, selective activity for DMNP hydrolysis, this activity is limited to buffered conditions. To extend the reactivity of these materials to non-buffered aqueous media, amine moieties were incorporated into the material in two ways: either the MCAM of the zirconium cluster or directly onto the silica strut. To introduce an amine moiety into the material through the MCAM, Zr₆-(BA-CH₂NH₂) and Zr₆-(BA-CH₂-morpholine) were synthesized and incorporated into SBA-15 and the hydrolysis reactivity of the resulting materials was measured under buffered and non-buffered conditions. Although Zr₆-(BA-CH₂-morpholine) showed enhanced reactivity under buffered conditions, neither material showed appreciable reactivity under non-buffered conditions (Table 2). Based on recent work incorporating polyethyleneimine into SBA-15, L-SO₃H-SBA-15-PEI was synthesized prior to reacting with the zirconium clusters to introduce an amine moiety that could facilitate reactivity under buffered conditions.¹¹ The resulting material showed improved reactivity in aqueous conditions with double the amount of DMNP degraded in the same amount of time.

To further enhance reactivity under neutral aqueous conditions, adjacent acid/base moieties were incorporated onto the silica support using a grafting method as previously reported in the literature.¹¹ The baseline silica material, L-SO₃H-SBA-15-(CH₂)₃NH₂, showed enhanced reactivity under aqueous conditions (Table 2). However, the baseline material also showed formation of the undesired M4NP product. When the material was modified to include Zr₁₂-(acetic acid) clusters, the material (Zr₁₂-acetic acid-L-SO₃H-SBA-15-(CH₂)₃NH₂) showed much faster and selective reactivity for DMNP hydrolysis under non-buffered conditions (50 % conversion after 18 hours).

4. CONCLUSIONS/FUTURE WORK

A novel modified silica material decorated with zirconia clusters was developed in this work and has been shown to selectively hydrolyze DMNP to the desired DMP product in less than 10 minutes under buffered conditions. The modified silica without the bound zirconia clusters, however, shows slow hydrolysis to the less desired product, M4NP. In addition, the bound zirconia clusters exhibit analogous reactivity as compared to the unbound zirconia clusters indicating that the silica support does not hinder reactivity. The sulfate-modified silica afforded enhanced reactivity on the zirconium cluster over the phosphate modified silica indicating that the binding method must also be considered as a factor in reactivity when designing these materials. Computational data supports the observed experimental trend by showing an enhanced electrostatic potential on the zirconium clusters bound to the sulfate

modified silica as opposed to the phosphate modified silica. In addition, it has been determined that incorporating acid/base moieties onto the silica strut could prove promising for synthesizing materials with appreciable catalytic capabilities under neutral aqueous conditions. These initial experiments demonstrate the potential use of this silica platform to study and optimize zirconia clusters for chemical warfare agent decontamination. In addition, these novel materials are scalable and can be readily transitioned into relevant form factors such as fibers and polymer coatings. Future work with these materials will include variation of the amount of SO₃:NH₂ on the silica strut to enhance reactivity of the material under neutral aqueous conditions, variations in the amount of zirconia clusters on the particles to determine optimal reactivity, incorporation of this porous materials into fibers and coatings, and studies to determine reactivity of these materials with agents.

ACKNOWLEDGEMENTS

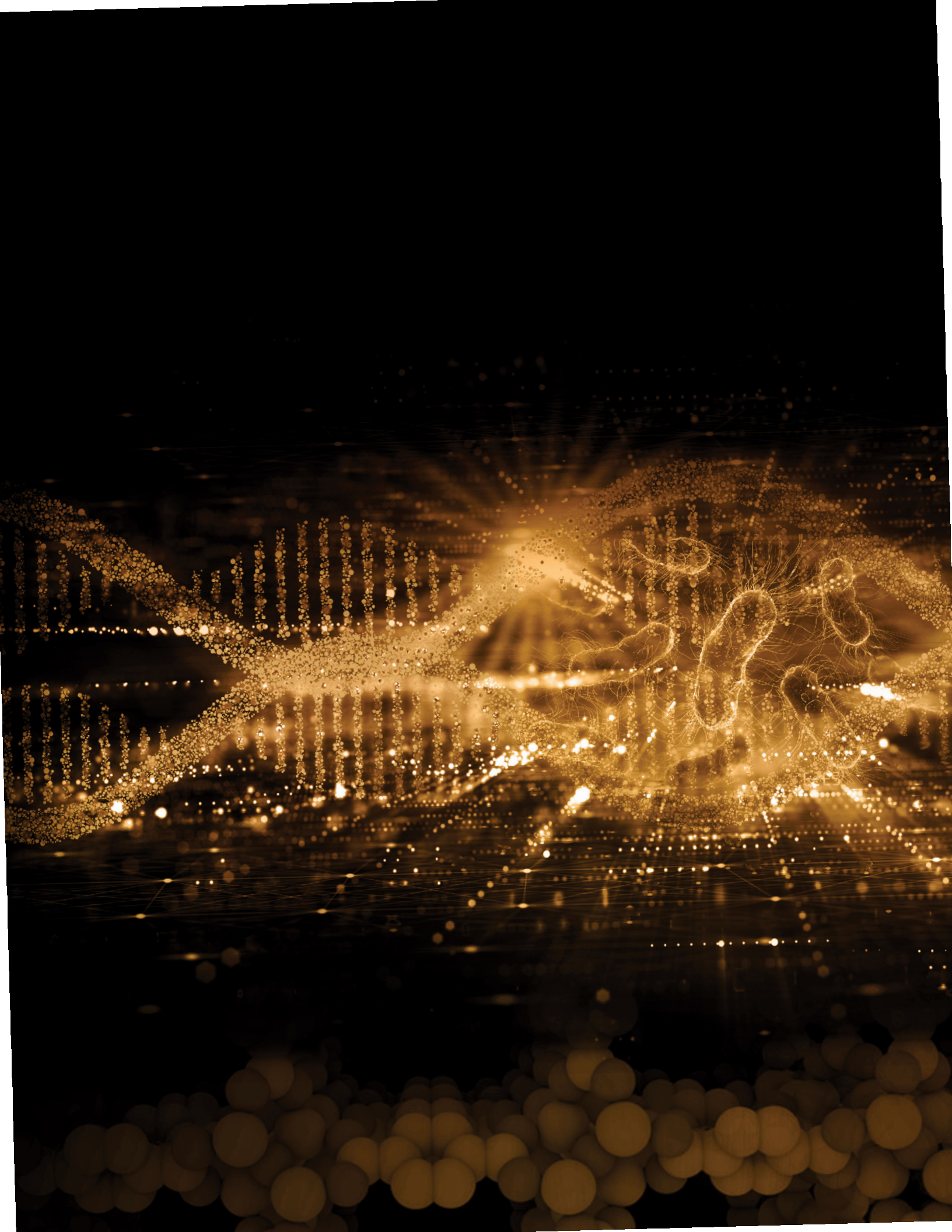
Funding was provided by the U.S. Army via the Chemical Biological Advanced Materials and Manufacturing Science Program (PE 0601102A Project VR9) at the Combat Capabilities Development Command Chemical Biological Center.

REFERENCES

- [1] Troya, D. Reaction Mechanism of Nerve-Agent Decomposition with Zr-Based Metal Organic Frameworks. *J. Phys. Chem. C*. **2016**, *120* (51), pp 29312–29323.
- [2] Dai, S.; Simms, C.; Dovgaliuk, I.; Patriarche, G.; Tissot, A.; Parac-Vogt, T.N.; Serre, C. Monodispersed MOF-808 Nanocrystals Synthesized via a Scalable Room-Temperature Approach for Efficient Heterogeneous Peptide Bond Hydrolysis. *Chem. Mater.* **2021**, *33*, pp 7057–7066.
- [3] Pappas, I.; Fitzgerald, M.; Huang, X.; Li, J.; Pan, L. Thermally Resolved in Situ Dynamic Light Scattering Studies of Zirconium(IV) complex formation. *Cryst. Growth Des.* **2009**, *9*, pp 5213–5219.
- [4] Bezrukov, A.A.; Tornroos, K.W.; Le Roux, E.; Dietzel, P.D.C. Incorporation of an intact dimeric Zr₁₂ oxo cluster from a molecular precursor in a new zirconium metal-organic framework. *Chem. Commun.* **2018**, *54*, pp 2735–2738.
- [5] Crisci, A.J.; Tucker, M.H.; Lee, M.Y.; Jang, S.G.; Dumesic, J.A.; Scott, S.L. Acid-Functionalized SBA-15-Type Silica Catalysts for Carbohydrate Dehydration. *ACS Catal.* **2011**, *1* (7), pp 719–728.
- [6] Shao, Y.; Liu, H.; Yu, X.; Guan, J.; Kan, Q. Synthesis, characterization and catalytic activity of acid-base bifunctional materials through protection of amino groups. *Mater. Res. Bull.* **2012**, *47*, pp 768–773.
- [7] Moreno, J.J.G.; Pan, K.; Wang, Y.; Li, W. Computational Study of APTES Surface Functionalization of Diatom-like Amorphous SiO₂ Surfaces for Heavy Metal Adsorption. *Langmuir*. **2020**, *36*, pp 5680–5689.
- [8] Feng, X.; Hajek, J.; Jena, H.S.; Wang, G.; Veerapandian, S.K.P.; Morent, R.; De Geyter, N.; Leyssens, K.; Hoffman, A.E.J.; Meynen, V.; Marquez, C.; De Vos, D.E.; Van Speybroeck, V.; Leus, K.; Van Der Voort, P. Engineering a Highly Defective Stable UiO-66 with Tunable Lewis-Bronsted Acidity: The Rose of the Hemilabile Linker. *J. Am. Chem. Soc.* **2020**, *142*, pp 3174–3183.
- [9] Bader, R.F.W.; Carroll, M.T.; Cheeseman, J.R.; Chang, C. Properties of atoms in molecules: atomic volumes. *J. Am. Chem. Soc.* **1987**, *109*, pp 7968–7979.
- [10] Murray, J.S.; P. Politzer. The electrostatic potential: an overview. *WIREs Comput. Mol. Sci.* **2011**, *1*, pp 153–163.
- [11] Gargiulo, N.; Peluso, A.; Aprea, P.; Pepe, F.; Caputo, D. CO₂ Adsorption on Polyethyleneimine-Functionalized SBA-15 Mesoporous Silica: Isotherms and Modeling. *J. Chem. Eng. Data.* **2014**, *593*, pp 896–902.

SEEDLING PROJECTS





Effects of surface displacement on piezoelectric sample depositions

Justin M. Curtiss

U.S. Army Combat Capabilities Development Command Chemical Biological Center, Research & Operations Directorate, 8198 Blackhawk Rd., Aberdeen Proving Ground, MD 21010

ABSTRACT

In this work, opportunities for the expansion of inkjet deposition technology for surface sample preparation was investigated by determining if the displacement between the surface and print head can be increased. The current technology is limited to smooth flat substrates as the print head must be within 1 mm of the substrate. These substrates do not represent realistic surfaces and thus limit the capability to prepare samples using the printing technique for testing purposes. Solutions of ethylene glycol and a high volatility solvent were printed onto a painted steel panel at increasing displacements between the print head and sample. High resolution images and depth compositions of the printed samples were captured and analyzed with optical microscopy. These images showed that as the displacement increased, the quality of the printed pattern decreased. Upon lowering the concentration of ethylene glycol in the printing solution, the image quality decreased less and overspray on the substrate surface decreased. A maximum displacement of 10 mm was demonstrated with minimal degradation of printing quality.

Keywords: low volume deposition, printing, piezoelectric

1. INTRODUCTION

Piezoelectric-based deposition is a common technology used in household and industrial inkjet printers using electrical potential to discharge a liquid from a small channel. These technologies are also currently used by various groups around the world, including U.S. Army Combat Capabilities Development Command Chemical Biological Center, for controlled sample preparation.¹ Currently, for these types of instruments, the sample is required to be flat or smooth. The piezoelectric print head moves at a specific optimal height, the zero-point displacement of approximately 1 mm, and deposits material onto the surface. If the sample is not flat or has protrusions, the print head may contact the sample surface causing damage to both the print head and sample. The objective of this work is to investigate and model the effects on sample deposition quality using this piezoelectric technology when the displacement from the sample surface is changed from its zero-point displacement in order to accommodate non-flat substrates, such as concrete or asphalt. This would expand sample preparation capabilities using available infrastructure and allow for more threat realistic substrates to be used for testing.

We hypothesize that as the print head displacement is increased from its zero-point height, the quality of the deposition onto the substrate will begin to decrease.^{2,3} As the displacement from the surface is further increased from the optimal distance the deposited material may begin to agglomerate in the air above the substrate surface and fall as droplets onto the surface, as opposed to a thin film. Increasing the displacement between the surface and print head could also incur aerosol generation due to the discharged material becoming airborne. Investigating this modification to the methodology will increase the overall capabilities of U.S. Army Combat Capabilities Development Command Chemical Biological Center and promote the development of a model of the phenomenology behind the technique.

As a baseline for comparison, samples will be generated by depositing a pattern onto smooth flat surfaces with liquids of various viscosities from the zero-point displacement. Additional samples will then be created with the print head at increasing displacement from the surface, increasing until the print head reaches its maximum height of 2 inches or no discernable pattern is deposited on sample surface. We expect to determine the relationship between the sample and print head displacement, which will allow the operational capabilities of the instrument to be increased to include threat-relevant surfaces that are not smooth or flat.

2. EXPERIMENTAL

Solutions of ethylene glycol (10, 25, and 50 % (v/v)) in a compatible solvent were prepared. Each of these solutions were loaded into individual printer cartridges that were used to prepare printed samples. For each solution, the cartridge was inserted into a single channel of the print head and three priming cycles were run to purge the print head of all air and cleaning solution. For each printed sample, a 25 mm square steel panel, painted red with a clear coat, was placed on the printer bed and the print head displacement was set. The zero-point displacement is adjusted automatically by the printer and for each increasing displacement, the distance was adjusted manually and measured using a laser displacement sensor (IL-100, Keyence Inc.). A 5 x 5 mm square was then printed on to the panel surface with a resolution of 720 x 720 dots-per-inch resolution. After printing, the sample was removed and imaged using a digital optical microscope (VHX-7000, Keyence Inc.). A still image with a calibration scale bar and depth composition was captured. The microscope software stacked 20 individual images in 450 μm increments to create a depth composition. The images were imported into ImageJ for processing where each image was converted into CIELAB color space stack.⁴ The lightness image from the LAB stack was then binarized using the Otsu method for thresholding and the resulting image was analyzed using the process tool in ImageJ.⁵ From that data, the droplet count, the average droplet size, and the percent area coverage for each sample was determined.

3. RESULTS AND DISCUSSION

Initial experiments focusing on printhead displacement showed that at a distance greater than 9 mm from the zero-point displacement, approximately 10 mm from the surface, the quality of the printed pattern degraded to the point where the square pattern was not recognizable. Therefore, a total displacement of 10 mm from the surface was chosen as the maximum distance to evaluate.

After printing with the 50 % (v/v) ethylene glycol solution, optical images of the printed area (5.2 x 5.2 mm) showed liquid droplets on the panel surface (Figure 1, top row). The images of the printed area were processed with ImageJ (Figure 1, middle row) The white portion represents the background of the surface while the black areas are the liquid, as identified by the software. Due to the observed overspray outside of the 5 x 5 mm printed area, caused by the side-to-side motion of the printhead, the images were reprocessed analyzing a 10 x 10 mm area to capture the over sprayed portion (Figure 1, bottom row).

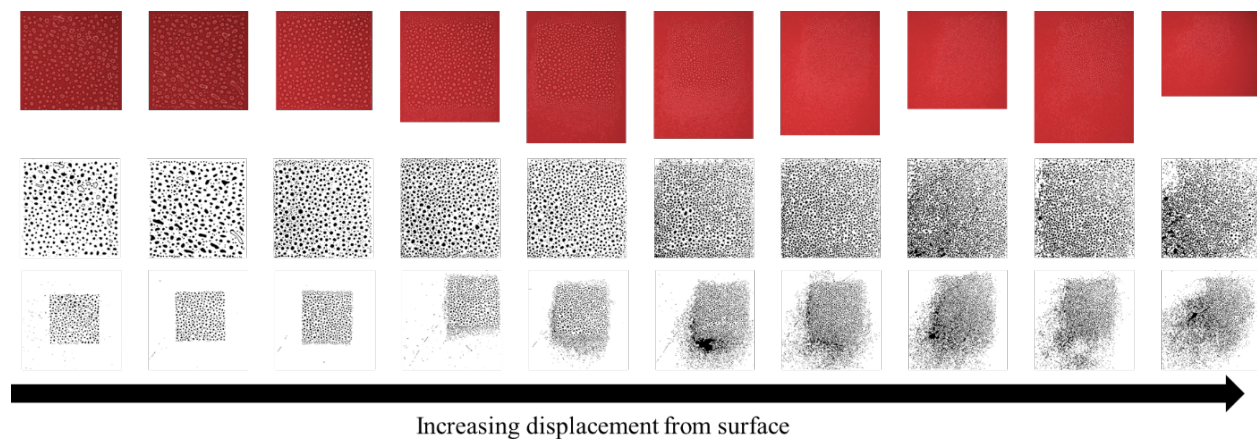


Figure 1. Surface printed with 50 % (v/v) ethylene glycol solution as print head displacement increases from 1-mm to 10-mm. Unprocessed images of liquid droplets on printed surface area (5.2 x 5.2 mm) (top row). Images processed with ImageJ (middle row). Black areas represent the liquid, and the white areas represent the background. Reprocessed images of larger printed area (10 x 10 mm), which show the over sprayed portion of the surface (bottom row).

As the displacement is increased, smaller droplets begin to form on the surface and the edges of the printed square pattern begin to blur. Both results were expected based on our hypothesis. When the displacement is small (< 5 mm), the solution is deposited on the surface as a thin film and the solvent rapidly evaporates leaving behind the ethylene glycol. Cohesion within the ethylene glycol forces the small droplets to agglomerate, rather than remaining as

individual droplets. As the displacement is increased, the solvent partially evaporates before the printing solution reaches the surface, which leaves smaller droplets of ethylene glycol than at lower displacements. The smaller droplets are physically separated and therefore cannot form larger droplets, as shown in images of the printed surfaces (Figure 1). When the displacement is further increased, more solvent can evaporate before reaching the surface, resulting in a larger fraction of small droplets and a smaller fraction of larger droplets (Figure 3 and 4).

Compared to the 50 % (v/v) ethylene glycol solution, the 10 % (v/v) solution produced smaller droplets at lower displacements (Figure 2 and 4). The agglomeration of ethylene glycol droplets was also observed in the 10 % (v/v) solution but yield fewer large droplets than the 50 % (v/v) solution. There appears to be less overspray when printing with the 10 % (v/v) ethylene glycol solution compared to the 50 % (v/v) solution (Figure 1 and 2). This may be due to ImageJ not capturing the smallest droplets from the lowest concentration solution. Also, the overspray has a lower density of droplets compared to the center of the printer area, thus less overspray was observed for the lower concentration solution because there is less ethylene glycol in the solution. Reducing the ethylene glycol concentration in the printing solution appears to improve the spray pattern quality by increasing the number of small droplets that cannot as easily agglomerate. This result is because the solvent decreases the surface tension and the viscosity of the solvent allowing it to be more easily discharged from the printhead. Overall, the square printed pattern is clearly visible at a displacement of 10 mm with the 10 % (v/v) solution, but with the 50 % (v/v) solution degradation becomes obvious at 6 mm of displacement.

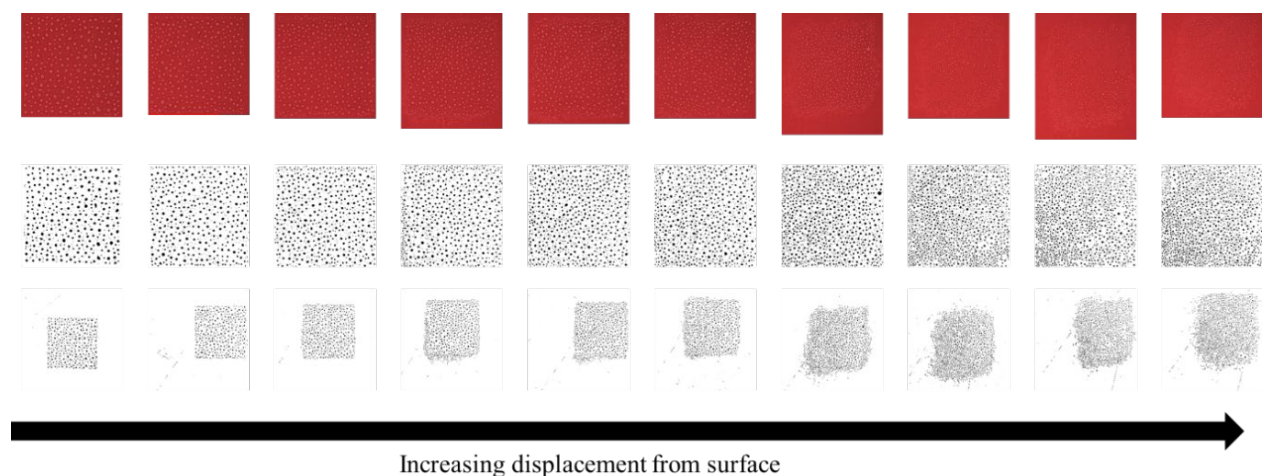


Figure 2. Images from 10 % ethylene glycol solution showing change in droplet size and distribution as the displacement is increased.

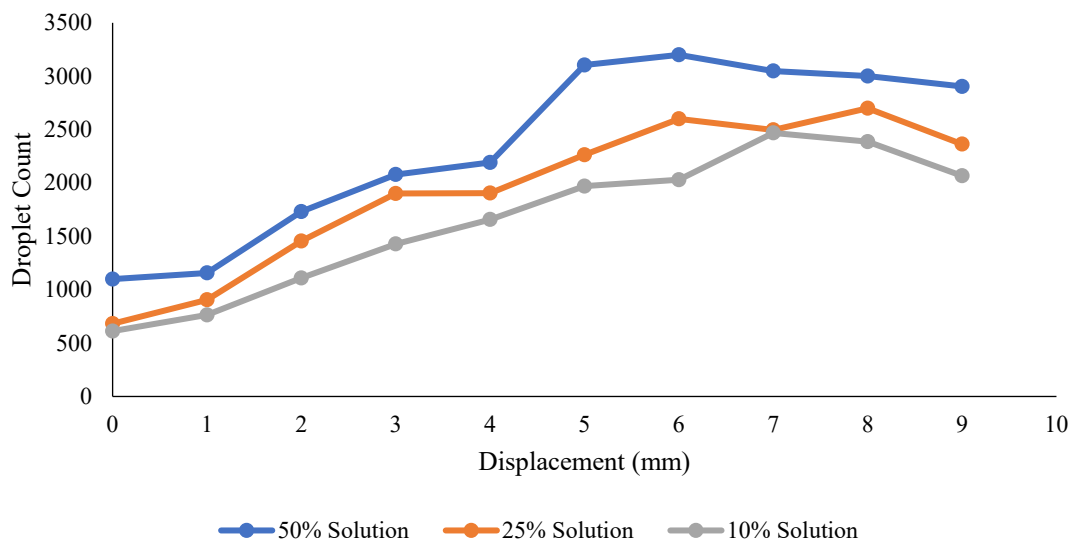


Figure 3. Averaged droplet size for each ethylene glycol solution with increasing displacement from the surface.

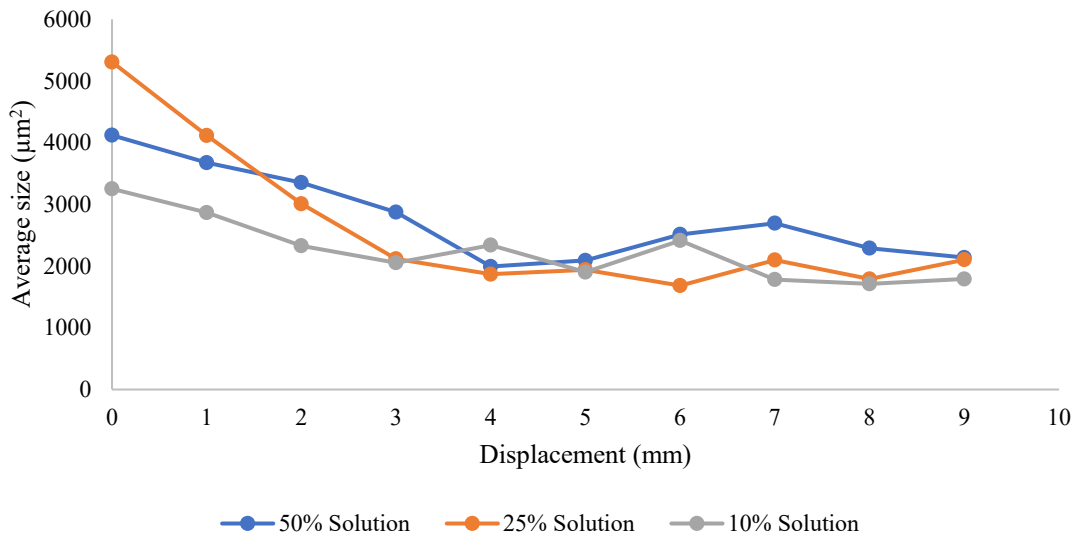


Figure 4. Average droplet size for each ethylene glycol solution over the total displacement range evaluated.

4. CONCLUSIONS

As the displacement from the surface increases from the zero-point distance, the quality of the printed pattern decreases and overspray outside of the designated printed pattern increases. At a distance greater than 6 mm the square pattern begins to become deformed with less defined edges. The lower concentration of ethylene glycol in the solution decreases the amount of overspray and allows the displacement to be greater while maintaining the shape of the printed pattern. Overall, these results show that using a 10 % solution of ethylene glycol, a surface displacement of 6–10 mm can be achieved. This allows for more threat relevant surfaces, such as concrete or asphalt, to be used with inkjet deposition technology to prepare samples for testing.

ACKNOWLEDGMENTS

Funding was provided by the Director, Combat Capabilities Development Command Chemical Biological Center under the authorities and provisions of Section 2363 of the FY 2022 NDAA to develop new technologies, engineer innovations, and introduce game-changing capabilities.

REFERENCES

- [1] Moon, R.; Guicheteau, J.; Christesen, S.; Fountain III, A.; Ginter, J.; Tokarz, J.; Green, N.; Tripathi, A.; Emmons, E.; Hung, K. *Preparation of chemical samples on relevant surfaces using inkjet technology*; ECBC-TR-1056, U.S. Army Edgewood Chemical Biological Center: Aberdeen Proving Ground, MD, **2013**; UNCLASSIFIED Report.
- [2] Derby, B. Inkjet Printing of Functional and Structural Materials: Fluid Property Requirements, Feature Stability, and Resolution. *Annu. Rev. Mater. Res.* **2010**, *40* (1), pp 395–414.
- [3] Chen, C. T. Inkjet Printing of Microcomponents: Theory, Design, Characteristics and Applications in *Features of Liquid Crystal Display Materials and Processes*. Intech Open: London, **2011**, pp 43–60.
- [4] *Colorimetry 3rd Edition*, International Commission on Illumination: France. **2004**.
- [5] Yousefi, J.; Image Binarization using Otsu Thresholding Algorithm. *University of Guelph*. **2011**.

MXene electrochemical degradation of chemical agent O-ethyl-S-[2-(diisopropylamino)ethyl]-methylphosphonothioate

Shaun Debow^{a*}, Steven Harvey^a, Amanda Schenning^a, Michael Chesebrough^a, Zachary Zander^a,
Jesse Brown^c, William Creasy^a, Brendan DeLacy^b, Yi Rao^c

^aU.S. Army Combat Capabilities Development Command Chemical Biological Center, Research
& Operations Directorate, 8198 Blackhawk Rd, Aberdeen Proving Ground, MD 21010

^bBallydel Technologies, Inc., 200 Powder Mill Rd., Wilmington, DE 19803

^cUtah State University, 0300 Old Mail Hill, Logan, UT 84322

ABSTRACT

Chemical agent detoxification often requires caustic solids and liquids having considerable storage, handling, and transportation restrictions. Developing electrochemical catalysts for chemical agent degradation can reduce collateral hazards, reduce the logistic burden, and increase on-site availability by generating reactive species in-situ anytime, anywhere decontamination is needed. In this work, a novel FeCo-MXene electrocatalyst was successfully demonstrated to detoxify O-ethyl-S-[2-(diisopropylamino)ethyl]-methylphosphonothioate nerve agent. Complete O-ethyl-S-[2-(diisopropylamino)ethyl]-methylphosphonothioate degradation was achieved after 720 minutes with an applied current of 650 μ A and without formation of the toxic EA-2192 byproduct.

Keywords: nerve agent, chemical agent, O-ethyl-S-[2-(diisopropylamino)ethyl]-methylphosphonothioate (VX), organophosphorus, oxidation, degradation, electrocatalyst, electrochemical

1. INTRODUCTION

1.1 Background

Chemical agent detoxification for decontamination or destruction often requires caustic solids and liquids with considerable storage, handling, and transportation restrictions¹. Hazardous chemicals required for agent destruction can pose a secondary hazard to operators and the environment beyond the primary chemical agent hazard. Developing safer methods to achieve chemical agent detoxification can reduce risks to both operators and the environment. In this study, we investigated a Ti₃C₂ MXene-based electrochemical catalyst for chemical agent detoxification that reduces collateral hazards, reduces the logistic burden, and increases availability by generating reactive species *in situ* anytime and anywhere chemical detoxification is needed.

1.2 O-ethyl-S-[2-(diisopropylamino)ethyl]-methylphosphonothioate (VX) chemical agent

VX chemical agent is a persistent, low vapor-pressure organophosphorus molecule that interferes with the enzyme acetylcholinesterase, prevents hydrolysis of the neurotransmitter acetylcholine, and results in its toxic accumulation at the neuron-muscle cell junction. Cutaneous exposure to VX in quantities as low as 5 mg can be lethal to humans. VX degradation typically follows several pathways, as shown by Smith in Figure 1.² These frequently include scission of the P-S bond and the P-O bond. When the latter occurs, it can result in a very toxic but stable byproduct, EA-2192, that retains nearly the same toxicity of the parent VX molecule and is difficult to degrade.^{1,2} Identifying methods to safely detoxify VX while preventing formation of other toxic degradation byproducts during chemical destruction are vitally important for successful detoxification.

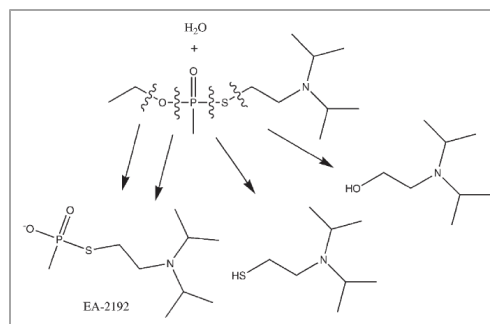


Figure 1. Common hydrolysis pathways of O-ethyl-S-[2-(diisopropylamino)ethyl]-methylphosphonothioate (VX) chemical agent.²

1.3 Ti₃C₂ MXene

MXenes are layered 2D carbides, carbonitrides or nitrides of early transition metals.^{3,4} MXenes are formed by selectively etching a sacrificial layer from a ceramic MAX phase, where M is an early transition metal, A is a sacrificial layer (such as Al, Si), and X is C, N, or CN. After etching the MAX phase, an accordion-like, multi-layer structure remains with a composition of $M_{n+1}X_nT_x$, where T is a variable surface termination (such as F, Cl, O, OH) and $n = 1, 2, \text{ or } 3$.^{5,6,7} Sonication or vigorous shaking can delaminate the multi-layer structure and results in few- or single-layer MXene. The resulting MXene is a layered 2D material having rich surface terminations (e.g., -OH, =O, -F, -Cl) and highly-conductive basal planes with adjustable electronic properties.⁴ These surface terminations are very polar and enable MXenes to form stable suspensions in aqueous systems and in other polar solvents.⁵ Surface terminations also serve as nucleation sites for attaching or growing a diverse range of ligands or guest particles on the MXene surface, while active Ti sites promote catalysis.^{4,8,9} These properties are ideal, and enable MXenes to be used as catalysts by forming and immobilizing metal particles on the MXene surface.

1.4 Electrocatalyst

Electrocatalysts have been reported to degrade recalcitrant chemicals, such as antibiotics and dyes.¹⁰⁻¹³ Their use represents a more environmentally sound way to treat pollutants before entering waste streams or their discharge to the environment.^{14,15} In previous, unpublished research, we fabricated a MXene-based electrocatalyst, and evaluated its durability and feasibility to degrade methyl orange dye. The electrocatalyst remained stable over a 20-hour evaluation period and rapidly bleached methyl orange dye. Inspired by our prior results, we fabricated an FeCo-MXene electrocatalyst and tested its ability to detoxify VX chemical agent.

2. METHODOLOGY

2.1 Generation of FeCo-MXene carbon paper electrodes

For this study, FeCo-MXene carbon-paper electrodes were generated for the purpose of electrochemical reactions with VX. Fabrication of the electrodes involved a multi-step process in which a FeCo-MXene ink was prepared, then drop cast onto carbon paper affixed to copper conductive tape. First, the FeCo-MXene catalyst was formed by nucleating and growing FeCo layered double hydroxides (LDH) on the surface of Ti₃C₂-MXene. Briefly, 0.125 g CoCl₂·6H₂O, 0.047 g FeCl₃·6H₂O, 1.72 g urea, 2.8 mL H₂O (18.2 MΩ), and 2.8 mL anhydrous ethanol were combined and stirred for 60 minutes at room temperature. Separately, 10 mg MXene was sonicated in 4.5 mL DMF for 90 minutes at room temperature. Once thoroughly mixed, the reagents and MXene substrate were combined, stirred for an additional 30 minutes, and then transferred to a 20 mL PTFE autoclave vessel. The autoclave vessel was heated to 120 °C and held for 16 hours. Next, 6.0 mg FeCo-MXene LDH catalyst, 1160 μL ethanol (anhydrous), 800 μL DI H₂O (18.2 MΩ), and 40 μL Nafion (5%) were combined to form the FeCo-MXene ink. Generation of the catalyst ink allows for maintaining a stable suspension of the FeCo-MXene catalyst, while promoting quick solvent evaporation for electrode fabrication. Finally, FeCo-MXene carbon-paper electrodes were fabricated by drop-casting 80 μL of the FeCo-MXene ink onto carbon paper fixed onto conductive copper tape. The carbon paper was allowed to air dry until no liquid was visible. The electrodes were transferred to a vacuum oven and held at 30 °C for 16 hours and reached a surface area of approximately 0.5 cm². Each electrode was fixed to folded copper-tape and the interface was sealed with Parafilm.

Electrochemical reactions were performed using a Gamry electrochemical workstation, model 1010E, in a Gamry Dr. Bob's electrochemical cell fitted with a Saturated Calomel Electrode (SCE) as the reference electrode, and a 5-mm diameter graphite rod as the counter electrode and FeCo-MXene catalyst electrode as the working electrode. The electrochemical workstation was operated in chronopotentiometry or chronoamperometry modes. The reaction liquid phase was formed by diluting VX to a concentration of 3 mM in 25 mL of a 0.1 M potassium phosphate buffer at pH 8. The liquid phase was continuously stirred inside the electrochemical cell by use of a polytetrafluoroethylene stir bar and a stir plate. All electrodes were positioned approximately 2 cm apart to prevent physical contact while stirring. FeCo-MXene electrodes were positioned so only the FeCo-MXene catalyst and carbon paper support contacted the liquid phase with the catalyst surface facing the counter electrode, care was taken to prevent the copper-tape conductor from contacting the liquid phase.

Aliquots (10 μ L) of the reaction mass were drawn from the reaction cell at specified times and immediately diluted into 990 μ L anhydrous isopropyl alcohol (IPA), resulting in a 100x dilution. Care was taken to ensure all analyte was transferred from the pipette tip by rinsing the pipette tip with the diluted IPA-analyte solution. Just prior to analysis, a second 100x serial dilution was made in IPA to bring the VX concentration into the calibration range of the analysis platform.

VX was quantified using an Applied Biosystems 5500 QTrap Triple-Quadrupole Mass Spectrometer, equipped with a TurboV Ion Source. Sample introduction and chromatography were performed with an Agilent 1200 series high-performance liquid chromatography (HPLC), which included an Agilent Binary Pump, Degasser, Thermal Column Compartment (TCC), High Performance Automatic Liquid Sampler (ALS), and an ALS Thermostat. Sample effluent was directed from the LC directly to the TurboV ion source of the API5500 mass spectrometer (MS). The instrument operation and data analysis were performed with the Applied Biosystems Analyst software package (v. 1.5.1.). Detailed HPLC-MS parameters are given in Table 1.

Table 1. HPLC-MS parameters.

LC Parameters		
Mobile Phase A: 0.1% Formic Acid and 5 mM Ammonium Acetate in 95 % Deionized Water / 5% Isopropanol		
Mobile Phase B: 0.1% Formic Acid and 5 mM Ammonium Acetate in 5 % Deionized Water / 95% Isopropanol		
Gradient:		
<u>Time (min):</u>	<u>%A</u>	<u>%B</u>
0.00	50.0	50.0
4.00	50.0	50.0
Flow Rate: 0.2 mL/min		
Analytical Column: Phenomenex Synergi Hydro-RP, 4 μ m, 2 x 150 mm		
Typical Column Pressure: 180 bar		
Analytical Column Temperature: 40 $^{\circ}$ C		
Injection Volume: 10 μ L		
Autosampler Temperature: 5 $^{\circ}$ C		
Post-injection Needle Wash: 10 seconds of Mobile Phase B		
Mass Spectrometer Parameters		
Scan Type: Multiple Reaction Monitoring (MRM)		
Polarity: Positive Mode		
Curtain Gas: 30		
CAD Gas: Medium		
Source Temperature: 300 $^{\circ}$ C		
GS1: 40		
GS2: 50		
Declustering Potential: 100		
Exit Potential: 10		
Collision Energy: 25 (for all analytes)		
MRM for VX: 268.1 > 128.0		
MRM for EA2192: 240.1 > 128.0		
MRM for VX Sulfonic Acid: 210.1 > 126.2		
MRM for EMPA: 125.1 > 97.1		
MRM for VX-d5 Internal Standard: 273.1 > 128.0		

3. DATA

Electrochemical reactions were performed according to the previously described methodology using FeCo-MXene catalyst with applied currents of 8.5 mA, 650 μ A, and 0 A. An additional baseline reaction, without catalyst, was acquired to determine adsorption of VX onto the carbon paper support. The reaction time for each condition was 60 minutes (Figure 2A). Feasibility for complete degradation was investigated using a 650 μ A applied current for 720 minutes (Figure 2B).

To explore current-dependent electrochemical degradation rates, higher electrode currents of +100 mA, -100 mA and +45 mA were evaluated. These applied currents were too high for the carbon-paper supports, resulting in rapid swelling to a sponge-like consistency and complete electrode failure prior to the end of each reaction. Results of these high-current reactions were inconclusive.

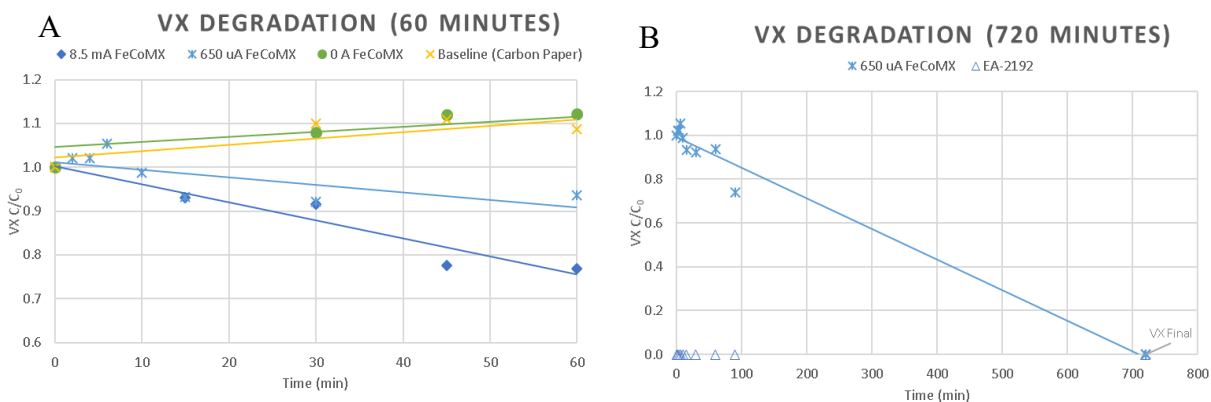


Figure 2: A) Change in VX concentrations as an effect of applied current for 60 minutes. B) Change in VX concentration over time at 650 μ A for 720 minutes.

4. RESULTS

VX decomposition by FeCo-MXene electrocatalyst was studied for applied currents of 8.5 mA and 650 μ A, no current, and contrasted under the same conditions with a pristine carbon-paper support without catalyst. Results in Figure 2A suggest that decomposition rates increased with increasing current, spontaneous decomposition on the FeCo-MXene with no applied current was negligible, and adsorption to the carbon paper alone was negligible. Results in Figure 2B show decomposition proceeded to completion by 720 minutes with no detectable VX remaining and with no toxic EA-2192 byproduct detected.

Reaction half-life rates were calculated for the 8.5 mA and 650 μ A currents, a decrease in half-life was observed for the higher current with $t_{1/2}$ of 147 minutes compared with $t_{1/2}$ of 234 minutes, respectively.

5. CONCLUSION

Electrochemical VX nerve agent detoxification was successfully demonstrated by a novel FeCo-MXene electrocatalyst in an electrochemical cell. Complete VX degradation was observed after 720 minutes at an applied current of +650 μ A; no toxic EA-2192 byproduct was detected. Reaction kinetics suggest a current-density rate dependence that increases with increasing current density at the working electrode. Evaluating kinetic dependence at higher current densities was not possible during this study due to swelling and complete failure of the carbon-paper support used for electrode fabrication.

Lessons learned from this research suggest that reaction kinetics may be increased by identifying and applying the FeCo-MXene catalyst to a different electrode support material that can withstand higher applied current densities. Additionally, understanding the kinetic dependence of FeCo-MXene catalyst loading on the working electrode will help to optimize reaction kinetics. Finally, investigating other transition metal, carbide, carbonitride and nitride MXenes will help to understand how the MXene substrate affects both performance and stability of the electrocatalyst.

ACKNOWLEDGMENTS

Funding was provided by the Director, Combat Capabilities Development Command Chemical Biological Center under the authorities and provisions of Section 2363 of the FY 2018 NDAA to develop new technologies, engineer innovations, and introduce game-changing capabilities.

REFERENCES

- [1] Yang, Y.-C.; Szafraniec, L.L.; Beaudry, W.T.; Rohrbaugh, D.K. Oxidative detoxification of phosphonothiolates. *J. Am. Chem. Soc.* **1990**, *112* (18), pp 6621–6627.
- [2] Smith, B.M. Catalytic methods for the destruction of chemical warfare agents under ambient conditions. *Chem. Soc. Rev.* **2008**, *37*, pp 470–478.
- [3] Naguib, M.; Kurtoglu, M.; Presser, V.; Lu, J.; Niu, J.; Heon, M.; Hultman, L.; Gogotsi, Y.; Barsoum, M.W. Two-Dimensional Nanocrystals Produced by Exfoliation of Ti_3AlC_2 . *Adv. Mater.* **2011**, *23* (37), pp 4248–4253.
- [4] Naguib, M.; Mashtalir, O.; Carle, J.; Presser, V.; Lu, J.; Hultman, L.; Gogotsi, Y.; Barsoum, M.W. Two-Dimensional Transition Metal Carbides. *ACS Nano*. **2012**, *6* (2), pp 1322–1331.
- [5] Naguib, M.; Mochalin, V.N.; Barsoum, M.W.; Gogotsi, Y. 25th Anniversary Article: MXenes: A New Family of Two-Dimensional Materials. *Adv. Mater.* **2014**, *26* (7), pp 992–1005.
- [6] Alhabej, M.; Maleski, K.; Anasori, B.; Lelyukh, P.; Clark, L.; Sin, S.; Gogotsi, Y. Guidelines for Synthesizing and Processing of Two-Dimensional Titanium Carbide ($\text{Ti}_3\text{C}_2\text{T}_x$ MXene). *Chem. Mater.* **2017**, *29* (18), pp 7633–7644.
- [7] Hope, M.A.; Forse, A.C.; Griffith, K.J.; Laukatskaya, M.R.; Ghidu, M.; Gogotsi, Y.; Grey, C.P. NMR reveals the surface functionalisation of Ti_3C_2 MXene. *Phys. Chem. Chem. Phys.* **2016**, *18*, pp 5099–5102.
- [8] Hantanasirisakul, K.; Gogotsi, Y. Electronic and Optical Properties of 2D Transition Metal Carbides and Nitrides (MXenes). *Adv. Mater.* **2018**, *30* (52), p 1804779.
- [9] Qian, X.; Wei, Y.; Sun, M.; Han, Y.; Zhang, X.; Tian, J.; Shao, M. Heterostructuring 2D TiO_2 nanosheets in situ grown on $\text{Ti}_3\text{C}_2\text{T}_x$ MXene to improve the electrocatalytic nitrogen reduction. *Chinese J. Catal.* **2022**, *43* (7), pp 1937–1944.
- [10] Qi, H.; Sun, X.; Sun, Z. Cu-doped Fe_2O_3 nanoparticles/etched graphite felt as bifunctional cathode for efficient degradation of sulfamethoxazole in the heterogeneous electro-Fenton process. *Chem. Eng. J.* **2022**, *427*, pp 131695.
- [11] Kulaksiz, E.; Kayan, B.; Gözmen, B.; Kalderis, D.; Oturan, N.; Oturan, M.A. Comparative degradation of 5-fluorouracil in aqueous solution by using H_2O_2 -modified subcritical water, photocatalytic oxidation and electro-Fenton process. *Environ. Res.* **2022**, *204* (38), p 111898.
- [12] Jiang, W.; Tang, P.; Lu, S.; Xue, Y.; Zhang, X.; Qiu, Z. Comparative studies of $\text{H}_2\text{O}_2/\text{Fe(II)}$ /formic acid, sodium percarbonate/ Fe(II) /formic acid and calcium peroxide/ Fe(II) /formic acid process for degradation performance of carbon tetrachloride. *Chem. Eng. J.* **2018**, *344*, pp 453–461.
- [13] Rivera, F.L.; Menendez, N.; Mazario, E.; Herrasti, P. ElectroFenton with Reticular Vitreous Carbon and Iron Oxide Nanoparticles for Dye Removal: A preliminary Study. *Appl. Sci.* **2022**, *12* (16), p 8293.
- [14] Zhang, M.-H.; Dong, H.; Zhao, L.; Wang, D.-X.; Meng, D. A review on Fenton process for organic wastewater treatment based on optimization perspective. *Sci. Total Environ.* **2019**, *670*, pp 110–131.
- [15] Xu, Z.P.; Zhang, J.; Adebajo, M.O.; Zhang, H.; Zhou, C. Catalytic applications of layered double hydroxides and derivatives. *Appl. Clay Sci.* **2011**, *53* (2), pp 139–150.

This page intentionally left blank

Canine detection baseline training aid

Kelley L. Evans^{a*}, Michele N. Maughan^b, Jenna D. Gadberry^c, Caitlin E. Sharpes^b,
Patricia E. Buckley^a

^aU.S. Army Combat Capabilities Development Command Chemical Biological Center, Research & Operations Directorate, 8198 Blackhawk Rd., Aberdeen Proving Ground, MD 21010

^bExcet Inc., 6225 Brandon Ave, Suite 360, Springfield, VA 22150

^cIntrinsic 24, LLC, 10739 N Government Way, Hayden, ID 83835

ABSTRACT

A standardized canine detection baseline training aid is not available for the Department of Defense to use to evaluate a military working dog's aptitude for detection before procurement nor to allow for positive reinforcement during initial or sustainment training for explosives or narcotics threats. Although canines routinely outperform analytical machinery in detecting sources of odor, canine teams, unlike laboratory instruments, have not had access to a method of calibration to ensure they are meeting certain detection standards. Eight mandatory and four desired criteria were developed for a canine detection baseline training aid, but this concept has not been widely adopted and very few chemicals have been explored to determine which chemical(s) would be optimal to use. Thirty chemicals from various chemical classes, as well as atypical chemicals such as artificial flavorings and artificial odors, were evaluated for suitability as a baseline training aid.

Keywords: canine, scent detection, detection dogs, odor memory, odor discrimination, biological detector chemical calibrant

1. INTRODUCTION

The idea behind having a standardized canine detection baseline training aid is to ensure that every day the canine detection team goes to work, the canine can accurately and consistently detect what it has been trained to detect. This concept is equivalent to calibrating equipment before use to ensure that it is functioning correctly and within specified limits. The canine's ability to correctly detect explosives, narcotics, or other odors has been questioned in courts in similar ways that laboratory equipment has, but unlike laboratory equipment, the canine detection community does not have a method to demonstrate that their canine was performing within standardized detection parameters at the time the odor was found. Standardizing the baseline detection chemical would also standardize the odor or volatile organic compounds (VOCs) profile that each detection canine is detecting to allow for comparisons between different canines' detection capabilities from day to day and at different chemical concentration thresholds.

A perfect example of where the canine detection baseline training aid would be very beneficial is in the development of canine physiological monitoring systems. The canine detection baseline training aid would standardize the chemical that detection canines are detecting and determine if their physiological parameters change with different concentrations of the chemical. Comparisons could also be made between detection canines allowing for more precise physiological performance standards to be developed.

This research was designed to identify and evaluate chemicals that could be developed into a standardized canine detection baseline training aid that is safe, easily reproducible, low cost, and commercially available. To prevent false alerts, the chemicals' odors should not overlap with any potential odor that the canine has been trained to detect during its career nor any odor that is commonly found in the environment. The chemical(s) chosen should meet the eight mandatory and four desired criteria as outlined in prior research to provide consistency in evaluations.¹

2. METHODOLOGY

A literature review was conducted to determine knowledge gaps in the field; no applicable research has occurred within the past seven years for the development of a canine detection baseline training aid. In 2013, research into the

development of universal detector calibrant for biological (canine) and instrument detectors outlined eight mandatory and four desirable criteria of the ideal chemical (Table 1).¹ The eight mandatory criteria served as the starting point to either include or exclude each chemical assessed. Further research is needed to determine if any of the chemicals evaluated in this study can be detected by detection canines. Once the mandatory criteria were met, the four desirable criteria were evaluated. Further research is needed to determine if the prototype odor delivery device will allow for consistent odor release of the selected chemical. Table 1 outlines the eight mandatory and four desirable criteria and describes the importance of each criterion.

Table 1. Canine detection baseline training aid criteria and description.

Training aid criteria	Criteria description
Mandatory	
Minimal health hazard	The chemical must present minimal health hazards since the canine detection baseline training aid is designed to be used daily by canines and handlers. Chemicals selected should be only classified as irritants with no special transportation, disposal, or special handling requirements determined by the chemical’s National Library of Medicine’s PubChem data.
Non-target odor	The chemical may be used for explosives, narcotics, human remains, search and rescue, electronics, invasive plants or animals, conservation of endangered plants and animals, human tracking, cancer, or infectious diseases detection canines. Because of this wide variety of potential odors, the chemical will not be part of a common odor that any of these detection canines may encounter over their career.
Stable	The chemical will be used in a wide variety of indoor and outdoor environmental conditions during storage and training. The developed criteria recommended that the chemical have one to 20 carbon atoms. ¹ The chemical should also have a long half-life to prevent the decaying of the compound and potentially change the volatile organic compound's profile.
Readily available	The chemical will be available from multiple suppliers. Alternatively, the training aid could be conveniently prepared to make it commercially available, such as by taking the primary chemical and adding a carrier compound such as cellulose. Chemicals with a complex manufacturing process will not be considered.
Rare in environment	The chemical will not be commonly available or used in a wide variety of products. This limits the possibility of a detection canine falsely alerting while training or on missions in diverse indoor and outdoor environmental conditions.
Volatile	The chemical will readily move into a gaseous state releasing volatile organic compounds for canine or instrument detection. The developed criteria recommended that the chemical have a vapor pressure of 10^{-7} mmHg and a boiling point of less than 325 °C. ¹
Detectable by detection canines	The chemical will be detectable by detection canines. Canines can be trained to detect a wide variety of volatile organic compounds; however, some volatile organic compounds do not produce enough odor or an odor profile that can be differentiated by detection canines.
Low chemical reactivity	The chemical will not react with any commonly used materials. This allows for fewer limitations on testing, storage, manufacturing, training, and odor delivery device configurations. For example, corrosive chemicals are not suitable as they present health and safety issues.
Desirable	
Low cost	The chemical should be affordable for the canine detection community, as funding is of concern for any canine detection program. The final cost will be determined by the chemical chosen, the chemical amount required to produce the training aids that can emit different volatile organic compound profiles, and the odor delivery device used.
Detectable by other animals including humans	The chemical should be detectable by humans. This allows the handler or other personnel to easily determine if the canine detection baseline training aid lacks odor or if the odor profile has changed signaling the need for a new canine detection baseline training aid.
Readily detected by instruments	The chemical should not require sample preparation, have a distinct mass spectral fragmentation pattern, be detectable by a wide variety of laboratory and handheld instruments, and be easily dissolved in commonly used solvents that pose a minimum health hazard to laboratory personnel. This potentially allows the canine baseline training aid to be used during training and exercises that include handheld detectors.
Consistent odor release	The chemical should give off odor at a constant rate by itself or through the configuration of the odor delivery device used to make the canine detection baseline training aid.

Perfluorooctyl bromide, 1-bromooctane, perfluoro-n-heptyl iodide, and perfluorotributylamine were excluded from evaluations based on previous research.¹ A group patented 1-bromooctane as a universal detection calibrant for canine and instrument detection.^{2,3} Previously, 1-bromooctane has been used successfully as a universal detection calibrant with detection canines; however, the patent owners have no plans to make this product commercially available in the foreseeable future. Due to the successful use of 1-bromooctane, chemicals with a similar chemical structure to 1-bromooctane were evaluated.

Chemical Abstracts Service SciFinder and the National Library of Medicine's PubChem databases were consulted to research chemicals that could be used to develop the canine baseline detection training aid. The Good Scents Company database was consulted if no odor was listed in the PubChem database. Safety data sheets were examined if the information was not available in these three databases. Thirty chemicals were selected for evaluation. After reviewing all the data collected, a "yes" was used to indicate if the chemical met each criterion description; a "no" was used if the chemical did not meet each criterion description.

3. RESULTS

Chemical Abstracts Service SciFinder identified over 205,000 chemicals that meet the vapor pressure and boiling point and were commercially available from at least ten vendors. 1-bromodecane; 1-bromododecane; 2-bromododecane; 1-bromohexadecane; 2-bromooctane; 1-bromotridecane; 1,9-dibromononane; and 1,12-dibromododecane were evaluated since their chemical structures are like 1-bromooctane. Artificial insect pheromones were assessed as a novel chemical group and included ipsdienol, ipsenol, 3-methyl-2-cyclohexenone, and 2-methyl-3-buten-2-ol. Flavoring agents were also assessed because most of these chemicals also have a VOC profile. The list of flavoring agents that were assessed included benzaldehyde, camphor, diphenyl ether, ethyl hexanoate, eugenol, hexyl butyrate, isoamyl acetate, isobutyl isobutyrate, isobutyl salicylate, 2-isobutyl-3-methoxypyrazine, 2-methyl-3-buten-2-ol, 3-methyl-2-cyclohexenone, 4-methylcyclohexanone, menthol, methyl anthranilate, octyl acetate, and pentyl acetate. This approach presented a wide variety of chemicals to evaluate from various chemical classes and uses.

Of the chemicals examined, 1-bromotridecane; camphor; 1,12-dibromododecane; 1,4-dichlorobenzene; ethyl hexanoate; isoamyl acetate; isobutyl isobutyrate; 4-methylcyclohexanone; naphthalene; and pentyl acetate were excluded due to not meeting the minimal health hazard criteria. Benzaldehyde; 1-bromodecane; 1-bromododecane; camphor; 1,4-dichlorobenzene; diphenyl ether; ethyl hexanoate; eugenol; hexyl butyrate; isoamyl acetate; isobutyl isobutyrate; 2-methyl-3-buten-2-ol; menthol; methyl anthranilate; naphthalene; octyl acetate; and pentyl acetate were excluded because of their prevalence in either nature or use in multiple common products. Benzaldehyde, cyclohexyl hexanoate, and methyl anthranilate were excluded of their sensitivity to the air. These chemicals would be exposed to canine's constantly during detection training. Two chemicals, 2-bromooctane and cyclohexyl hexanoate, were excluded since those chemicals are limited to research or experimental use only. Ipsdienol and ipsenol were eliminated because neither chemical was readily available commercially nor low cost. Two other chemicals, 1-bromohexadecane and 4-methylcyclohexanone, were excluded because they possessed a boiling point greater than 325 °C and an odor described as a musty animal, respectively. Table 2 represents the down selection to five out of the thirty chemicals assessed.

Table 2. Canine detection baseline training aid criteria and candidates.

Training aid criteria	Selected chemicals				
	2-Isobutyl-3-methoxypyrazine	3-Methyl-2-cyclohexenone	Isobutyl salicylate	2-bromododecane	1,9-Dibromononane
Mandatory					
Minimal health hazard	Yes	Yes	Yes	Yes	Yes
Non-target odor	Yes	Yes	Yes	Yes	Yes
Stable	Yes	Yes	Yes	Yes	Yes
Readily available	Yes	Yes	Yes	Yes	Yes
Rare in environment	Yes	Yes	Yes	Yes	Yes
Volatile	Yes	Yes	Yes	Yes	Yes
Detectable by detection canines	Requires future research	Requires future research	Requires future research	Requires future research	Requires future research
Low chemical reactivity	Yes	Yes	Yes	Yes	Yes
Desirable					
Low cost	Yes	Yes	Yes	Yes	Yes
Detectable by other animals including humans	Green bell pepper or green pea	Nutty	Somewhat harsh, floral, herbaceous odor or clover herbal orchid floral	No data available	No data available
Readily detected by instruments	Yes	Yes	Yes	Yes	Yes
Consistent odor release	Requires future research	Requires future research	Requires future research	Requires future research	Requires future research

Finally, 2-bromododecane and 1,9-dibromononane were included even though no data is currently available describing if either has an odor because both met the rest of the criteria. The “detectable by detection canines” and “consistent odor release” criteria require further research since these chemicals are not part of the detection canines’ normal VOC portfolio. This data serves as a starting point for further research to establish a canine detection baseline training aid using the five most promising chemicals.

4. CONCLUSION

Based on recent research, it is possible to train detection canines to discriminate between up to forty different odors.⁴ Thus, adding a new training aid odor to a detection canine’s portfolio is very plausible. Assessing chemicals from various chemical classes and uses provided the opportunity to take advantage of each group’s unique characteristics for developing the canine detection baseline training aid. The chemical down-selection data represents only a small fraction of all chemicals that could be assessed for this effort.

Continuing to advance this research would afford the Department of Defense and law enforcement agencies the ability to use the canine detection baseline training aid for their procurement evaluation process and as part of both initial and sustainment training programs. Determining an untrained canine’s natural capacity for odor detection without interfering with their intended learned class of odors would save valuable time, money, and manpower during the procurement process. The canine detection baseline training aid would allow canine detection teams to continue to train when normal training aids are not accessible due to specific storage or transportation requirements. Adoption of the canine detection baseline training aid will also advance U.S. Army Combat Capabilities Development Command Chemical Biological Center (DEVCOM CBC) Olfactory Science programs by providing a new mechanism to assess

military and federal working dogs for their detection capability before being used in research, development, test, and evaluation programs and to keep detection canines motivated during participation in future projects.

The canine detection baseline training aid could be used to assess any potential detection canine's aptitude for detection at any time in its career and for maintenance detection training, allow the canine to learn the basics of scent detection before introducing a novel odor. Other canine detection disciplines that could benefit from this work include human remains, search and rescue, electronics, invasive plants or animals, conservation of endangered plants and animals, human tracking, cancer, and infectious diseases detection canines. The canine detection baseline training aid could also be used to train other detection species such as rodents, butterflies, and elephants.

The next step for this work is to select one or more of these chemicals and perform a headspace analysis to determine the number of the VOCs available to the detection canines. Once the VOCs are determined and amounts can be assessed, the prototype canine detection baseline training aid could be developed. Future research is needed to explore and minimize variables that introduce inconsistencies between batches and optimize the carrier material for the chosen chemical. Research is also needed to evaluate if detection canines can detect the selected chemical(s) in a training aid prototype followed by determining the low and high concentration limits of the chemical that detection canines can identify. In addition, shelf-life and service life assessments of the canine detection baseline training aid are needed before commercialization. The end goal is to optimize the canine baseline detection training aid by making it a low-cost, commercially available, easily reproducible, standardized baseline training aid for the Department of Defense and other canine detection communities and a training aid that could potentially be used with handheld detection equipment during training and exercises.

ACKNOWLEDGMENTS

I would like to thank Dr. Nicole Rosenzweig for her support in acquiring funding for this research. I want to also thank my co-authors in the DEVCOM CBC Olfactory Sciences group for their research and writing assistance, technical editing, language editing, proofreading, direct technical assistance, and indirect technical assistance via intellectual discussions. We would also like to thank our collaborators at Indiana University–Purdue University Indianapolis, University of Colorado Boulder, and Texas Tech University for providing their expertise. Funding was provided by the Director, DEVCOM CBC under the authorities and provisions of Section 2363 of the FY 2022 NDAA to develop new technologies, engineer innovations, and introduce game-changing capabilities.

REFERENCES

- [1] Beltz, K. The Development of Calibrants Through Characterization of Volatile Organic Compounds from Peroxide Based Explosives and a Non-Target Chemical Calibration Compound. Ph.D. Dissertation, Florida International University, Miami, Florida, **2013**.
- [2] Furton, K.; Beltz, K. Universal Detector Calibrant. U.S. Patent US 9,250,222 B2. **2016**.
- [3] Furton, K.; Beltz, K. Universal Detector Calibrant. U.S. Patent US 9,575,038 B2. **2017**.
- [4] Waggoner, P.; Lazarowski, L.; Hutchings, B.; Angle, C.; Porritt, F. Effects of learning an increasing number of odors on olfactory learning, memory and generalization in detection dogs. *Appl. Anim. Behav. Sci.* **2022**, *247*, p 105568.

This page intentionally left blank

Development of ^1H - ^{31}P rotational-echo double resonance techniques

Terry J. Henderson^{a*}, Terry Gullion^b, Dennis D. Bevilacqua^{a,c}, Christopher J. Karwacki^a

^aU.S. Army Combat Capabilities Development Command Chemical Biological Center, Research & Operations Directorate, 8198 Blackhawk Rd., Aberdeen Proving Ground, MD 21010

^bC. Eugene Bennett Department of Chemistry, 217 Clark Hall, West Virginia University, Morgantown, WV 26506

^cLeidos, 11951 Freedom Dr., Reston, VA 20190

ABSTRACT

We have created a radiofrequency pulse program for executing ^1H -observe, rotational-echo double-resonance (REDOR) measurements for determining ^1H - ^{31}P internuclear distances in nerve agent complexes with metal-organic framework systems and other host molecules. This project was used to collect preliminary data with methylphosphonic acid, and for sodium phosphate both without and with perdeuteration to ~97.5 atom % D. Plots of percent dephasing as a function of dipolar evolution time displayed a poor fit to theoretical data in the case of fully protonated samples. The plot derived from the perdeuterated sample, however, displayed stronger dephasing at each dipolar evolution time and that additional dephasing could be measured at significantly longer evolution times. These enhancements, likely due to strong attenuation of ^1H - ^1H dipolar interactions via proton replacement with deuterons, allowed a very good fit to the theoretical data. The results demonstrate clearly that ^1H - ^1H dipolar interactions are substantially attenuated via perdeuteration and that multi-proton spin systems need to be incorporated into theoretical calculations for predicting results from fully protonated samples.

Keywords: dipolar interaction, internuclear distance measurement, metal-organic framework networks, molecular structure, rotational-echo double resonance spectroscopy, solid state nuclear magnetic resonance

1. INTRODUCTION

Metal-organic framework (MOF) compounds are crystalline, porous solids made of organic linker groups with interconnecting inorganic moieties referred to as secondary building units. Units generally include metal ions like ^{25}Mg , ^{27}Al , or ^{67}Zn aggregated into metal-oxygen-carbon clusters with multidentate linkers such as carboxylate. Interactions between organic and inorganic components are relatively strong, resulting in two- or three-dimensional (2D or 3D) network structures. On the other hand, these organic-inorganic interactions are relatively weak (~100 kJ/mol) compared to covalent or ionic bonds. MOF networks, therefore, exhibit a high degree of conformational flexibility in comparison with typical porous solids such as zeolites and activated carbons.¹ Accompanied by their crystalline structures, this flexibility gives rise to the collective and cooperative effect,¹ which is capable of initiating substantial changes in 2D or 3D structures.² These changes can open a previously “closed” structure to promote selective binding or adsorption of specific ligands.^{3,4} Exploiting these conformational changes to design MOF networks that selectively bind and catalytically hydrolyze chemical warfare agents into harmless products is the central tenant of MOF research today in chemical defense applications.

A mechanistic understanding of functional materials relies heavily on elucidating the molecular architectures and flexibilities at their active sites and is essential for rational design. The design and development of functional MOF compounds requires accurate characterization of their active site centers in terms of: (1) their native 3D structure (or conformation), (2) their inherent conformational flexibilities (fast interconversion between different conformations), and (3) their conformational changes induced by ligand binding that allow MOF function. Due to the complexity of these compounds, investigating the properties usually requires several different physical techniques. These techniques can include conventional powder X-ray diffraction and solid-state nuclear magnetic resonance (ssNMR) spectroscopy, used in conjunction with mathematical computation and numerical simulation methods⁵ for data interpretation and integration. While the resulting theoretical models can be informative, experimentally characterizing authentic MOF compounds for evaluating the fitness of such models in a “real world” sense remains challenging and formidable.

There is a genuine need, therefore, to develop new experimental techniques to determine the 2D and 3D structures of MOF active site centers, especially for efforts focused on incorporating unique functional activities at the sites.

ssNMR spectroscopy offers several experimental options for characterizing the physical properties of MOF compounds in their natural solid-state.⁶ Most rely on magic angle spinning (MAS, spinning the sample at kilohertz speeds and an angle of 54.7° relative to the applied magnetic field) for improving detection sensitivity and spectral resolution, but there is a need to move past conventional MAS techniques and develop an experimental means for directly measuring structural information for MOF active site centers. Recently, a new class of NMR experiments was developed that are now used routinely to examine the molecular structures for large and small molecules alike.⁷⁻⁹ Known as rotational-echo, double-resonance (REDOR) spectroscopy, the technique is used to accurately determine the distances between two heteronuclei (such as ¹³C and ³¹P) in solid samples under high-resolution MAS conditions by measuring the dipole-dipole interaction between them. We have been developing a REDOR technique for determining distances between ¹H-³¹P heteronuclear pairs in MOF-nerve agent complexes. According to our knowledge and a comprehensive literature search, a ¹H-³¹P REDOR technique has never been reported.

2. THEORETICAL BACKGROUND

A dipole-dipole (or dipolar) coupling between two heteronuclei in a magnetic field, i.e., the interaction between the magnetic moments of the two heteronuclear spins I and S in the applied magnetic field of a NMR spectrometer, is described by the truncated dipolar Hamiltonian \mathcal{H}_D :¹⁰

$$\mathcal{H}_D = \omega_D I_Z S_Z, \quad (1)$$

$$\omega_D = \left(\frac{3 \cos^2 \theta - 1}{2} \right) \cdot D, \quad (2)$$

$$D = \frac{\mu_0 \gamma_I \gamma_S \hbar}{8\pi^2 r^3}, \quad (3)$$

where I_Z and S_Z are the macroscopic longitudinal magnetizations for heteronuclei I and S , respectively, γ_I and γ_S are the gyromagnetic ratios of I and S , respectively, μ_0 is the permeability constant, and \hbar is the reduced Planck constant. The equation reveals that the dipolar coupling, D , contains geometric structural information in the form of θ , the angle between the internuclear vector connecting I and S and the direction of the spectrometer applied magnetic field, and distance information in the form of r , the distance between the two heteronuclei. The magnitude of D is measured directly by REDOR spectroscopy, which as seen in the equation, is proportional to the inverse third power of r , making it an extremely accurate indicator of the distance separating coupled spins.

3. EXPERIMENTAL

3.1 Methods

Sodium phosphate monobasic monohydrate [Na2HPO4 · H2O, 98%], methylphosphonic acid [CH3P(O)(OH)2, 98%], and deuterium oxide [D2O, 99.9 atom % D] were purchased from Sigma-Aldrich (St. Louis, MO). The sodium phosphate and deuterium oxide were used directly without further purification, and the methylphosphonic acid was either exchanged once in 1.6 x deuterium oxide (moles Na2HPO4/moles D2O),¹¹ or used directly without purification or sample preparation. Silica nitride ssNMR rotors (5 mm diameter) and Kel F short rotor caps (5 mm) for were purchased from Doty Scientific, Inc. (Columbia, SC).

3.2 Experimental methods

All ssNMR measurements were carried out on a narrow-bore 600 MHz DD2 spectrometer (Agilent Technologies, Santa Clara, CA) using a double-resonance 5-Fmm MAS probe built by Doty Scientific, Inc. (serial number DSI – 883). Samples were spun at 14.5 or 16 kHz at room temperature for all data acquisitions. Data sets of 2048

complex points and 12 kHz spectral windows were obtained from the accumulation of 256 or 512 free-induction decays using a ^1H observe REDOR radiofrequency pulse sequence (Figure 1) incorporating a 5-second relaxation delay. The REDOR data sets were recorded onto computer disk and Fourier transformed directly into spectra before final phase correction into pure absorption mode. ^1H chemical shifts were calculated from the ^2H lock frequency that was referenced to the downfield ^{13}C signal of external adamantane at 38.3 ppm. Values for dipolar couplings, D , between ^1H - ^{31}P heteronuclear pairs and the internuclear distances between them were calculated from the absorption mode REDOR spectra (see below) using the software program Mathematica 13.1¹² on a macOS Monterey 12.6 computer workstation (Apple Computer, Cupertino, CA).

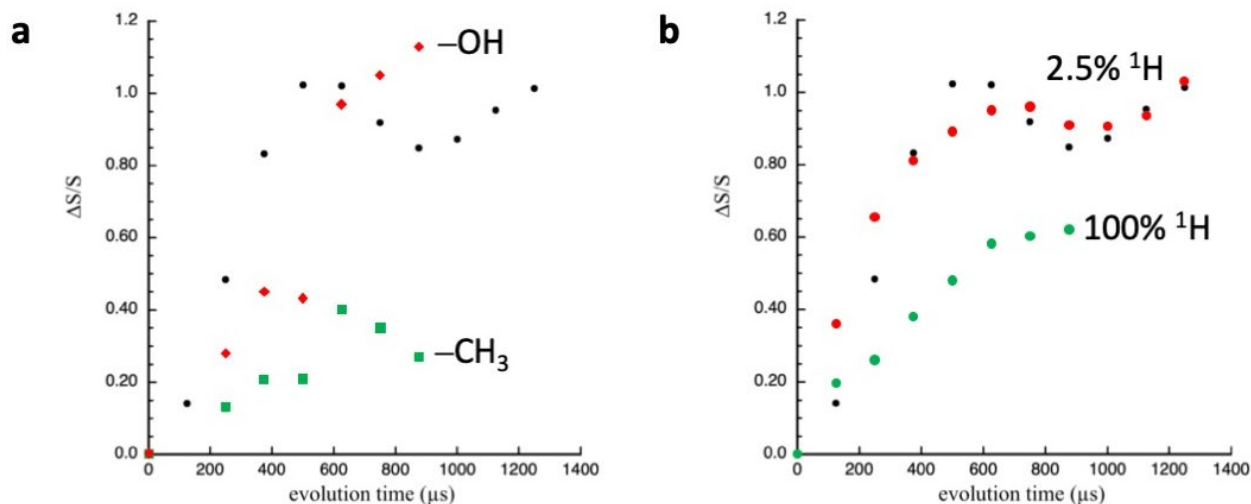


Figure 1. Percent dephasing ($\Delta S/S_0$) as a function of dipolar evolution time (evolution time) for ^1H - ^{31}P pairs for samples of methylphosphonic acid and sodium phosphate monobasic monohydrate. (a) Methylphosphonic acid data are dipolar couplings between its phosphorus nucleus and the protons of the hydroxyl groups (\blacklozenge) or methyl group (\blacksquare). (b) Data for sodium phosphate are from a 100% protonated (\bullet) as well as a 2.5% protonated (\bullet) sample. A theoretical curve calculated from equation (3) with $D = 3,000$ Hz (\bullet) is included in both plots.

4. RESULTS AND DISCUSSION

4.1 Design and implementation of the ^1H - ^{31}P REDOR radiofrequency pulse program

At the heart of any REDOR pulse sequence is a train of dipolar dephasing π -pulses synchronized with MAS rotation. As shown in Figure 2, we incorporate two of these pulse trains on the ^{31}P channel to create a ^1H -observe ^1H - ^{31}P REDOR pulse sequence. The pulse trains are synchronized so that that one π -pulse is executed for each half-revolution of the rotor to maintain dipolar dephasing.¹¹ The pulse trains symmetrically flank a ^1H π -pulse (180 in Figure 2) used to refocus isotropic chemical shifts and produce an echo at the start of data acquisition.

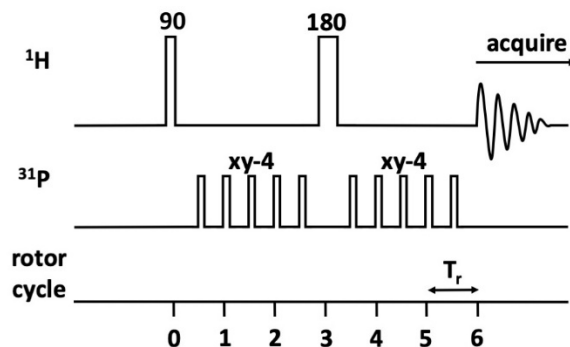


Figure 2. Six rotor periods of the ^1H -observe ^1H - ^{31}P REDOR radiofrequency pulse sequence. The ^1H and ^{31}P channels are shown together with MAS rotor cycles. 90 and 180 are $\pi/2$ - and π -pulses, respectively, and xy-4 are rotor-synchronized π -pulses with xy-4 phase cycling (xyxy). T_r is the time for one rotor revolution.

A program to execute the ^1H - ^{31}P REDOR pulse sequence for execution on NMR spectrometers controlled by VnmrJ software (Agilent Technologies) was written and summarily executed. The program executes the radiofrequency pulse sequence shown in Figure 1, except with dephasing π -pulse trains containing multiples of eight pulses using xy -8 supercycle schemes. The phase supercycles ($xyxy$ $yxyx$) effectively eliminate deleterious artifacts from pulse imperfections.^{13,14} The program calculates the delay times between successive π -pulses from the MAS speed and the ^1H and ^{31}P π -pulse widths specified by the user and sets them into the spectrometer operating instructions at compilation. The user can also change the time used for dipolar dephasing by changing a parameter value that specifies the number of π -pulses in all dephasing pulse trains. The parameter, for example, can be arrayed between 0–64 in steps of 8 to collect a series of nine data sets with increasing dipolar dephasing times. Another parameter permits the user to eliminate all dephasing π -pulse trains while preserving both observe channel pulses, allowing the acquisition of a REDOR control experiment without dephasing. The program can also be used as a ^{31}P -observe ^1H - ^{31}P REDOR pulse sequence, and for such applications, we are writing a second ^1H - ^{31}P REDOR pulse sequence that includes ^1H decoupling during data acquisition to increase detection sensitivity.

4.2 Dipolar dephasing in and distance determination from ^1H - ^{31}P REDOR measurements

REDOR measurements involve two data acquisitions, one without and one with rotor-synchronized dephasing pulses, to generate a full echo spectrum, S_0 , and a dephased or reduced spectrum, S , respectively. The data collection for the full echo spectrum is a control experiment (mentioned above) because it maintains full intensity rotational echoes at the end of each rotor period (T_r in Figure 2). In the second data acquisition, rotor-synchronized π -pulses are applied to the dephasing spin (the ^{31}P channel in Figure 2) to flip the sign of the dipolar coupling at each pulse, yielding an average precessional frequency, $\omega_D(\alpha, \beta; t)$, for each coupled spin in the powder.⁷ Each π -pulse coincident to the rotor periods adds to the dephasing of subsequent rotor periods. The total time that the dipolar coupling operates is the dipolar evolution time, $N_r T_r$. Each spin accumulates a net phase due to dipolar transitions during this time, defined as

$$\Delta\varphi = \overline{\omega_D}(\alpha, \beta; t_1) T_r N_r \quad , \quad (2)$$

where $\Delta\varphi$ is the accumulation of phase, N_r is the number of rotor cycles, ω_D is the average precessional frequency for each coupled spin (defined in equation (1)), α and β are the azimuthal and polar angles, respectively, in a coordinate system with the z -axis parallel to the rotor axis, and t_1 is the application time of the π -pulse from the start of the rotor period. ω_D is expressed in cycles per second, and, therefore, multiplication of ω_D by $T_r N_r$ gives a pure phase.

Thus, dipolar couplings generate signal attenuation at the end of every rotor period when dephasing π -pulses are applied, and, consequently, signals in the reduced spectrum are less intense than the corresponding signals in the full echo spectrum. As distance between a dipolar decoupled ^1H - ^{31}P pair decreases, so too does signal intensity in the reduced spectrum (equation 1). Subtracting the reduced spectrum from the full echo spectrum gives a difference spectrum, $\Delta S = S_0 - S$, which only contains signals from spins that are dipolar coupled to the dephasing spin (^{31}P in Figure 2). For each signal in the difference spectrum, its intensity is divided by that of the corresponding signal in the full echo spectrum to give $\Delta S/S_0$. Numerous $\Delta S/S_0$ values from data sets acquired with different dipolar evolution times are plotted against dephasing time (Figure 1). We have written curve-fitting programs to find the dipolar coupling, D , directly from these plots. The programs are based on a close approximation for $\Delta S/S_0$:

$$\frac{\Delta S}{S_0} = \frac{\sqrt{2}\pi}{4} J_{1/4}(\sqrt{2} T_r N_r D) J_{-1/4}(\sqrt{2} T_r N_r D) \quad , \quad (3)$$

where $J_k(x)$ is a Bessel function of the first kind and order k and dipolar decoupling is between two $\sin \frac{1}{2}$ nuclei,⁷ as for ^1H - ^{31}P pairs. The distance r between the two nuclei is then calculated from this value of D and its expression in equation (1) and is used directly in molecular modeling applications.

4.3 Preliminary ^1H - ^{31}P REDOR results

Preliminary observations from the ^1H - ^{31}P REDOR pulse sequence are shown in Figure 1 for samples of methylphosphonic acid and for sodium phosphate monobasic monohydrate, both fully protonated and perdeuterated to ~ 2.5 atom % H. Data are presented as plots of measured values for percent dephasing as a function of dipolar

evolution time,^{7,10} and include theoretical points calculated from equation 3, assuming a 3,000 Hz dipolar decoupling strength from a ^1H - ^{31}P distance of 2.5 Å.¹⁵ Casual observation of the methylphosphonic acid data display a poor fit to the theoretical points, as does the fully protonated sodium phosphate data. In contrast, data from the perdeuterated sodium phosphate agree reasonably well with the theoretical data, largely resulting from stronger dephasing measured at each evolution time in the perdeuterated sample. Perdeuteration also improved dephasing detection, allowing additional measurements at longer dipolar evolution times (up to ~33 % longer). These enhancements are an expected consequence of extensive attenuation of ^1H - ^1H dipolar interactions through a nearly complete replacement of protons with deuterons.^{16,17} Agreement between data measured on the fully protonated samples and the theoretical values are likely to significantly improve with the incorporation of multi-proton spin systems into the calculations.

5. CONCLUSIONS

A ^1H -observe REDOR pulse program was created for measuring ^1H - ^{31}P dipolar dephasing and determining the internuclear distances between ^1H - ^{31}P pairs. Preliminary results with methylphosphonic acid and sodium phosphate samples reveal poor agreement with theory from fully protonated samples, but very reasonable agreement after sample perdeuteration. The results strongly suggest that ^1H - ^1H dipolar interactions are substantially attenuated via perdeuteration, and that multi-proton spin systems need to be incorporated into theoretical calculations for predicting results from fully protonated samples. The latter is central to our current focus, along with developing a ^{31}P -observe REDOR pulse program with ^1H -decoupling as a complementary technique.

ACKNOWLEDGMENTS

Funding was provided by the Director, Combat Capabilities Development Command Chemical Biological Center, under the authorities and provisions of Section 2363 of the FY 2018 NDAA to develop new technologies, engineer innovations, and introduce game-changing capabilities.

REFERENCES

- [1] Férey, G.; Serre, C. Large Breathing Effects in Three-Dimensional Porous Hybrid Matter: Facts, Analyses, Rules and Consequences. *Chem. Soc. Rev.* **2008**, *38*, pp 1380–1399.
- [2] Serre, C.; Millange, F.; Thouvenot, C.; Nogués, M.; Marsolier, G.; Louër, D.; Férey, G. Very Large Breathing Effect in the First Nanoporous Chromium(III)-based Solids: MIL-53 or Cr(III)(OH) x [O(2)C–C(6)H(4)–Co(2)] x [HO(2)C–C(6)H(4)–CO(2)H] x H(2)O(y). *J. Am. Chem. Soc.* **2002**, *124*, pp 13519–13526.
- [3] Ripka, E.G.; Deschene, C.R.; Franck, J.M.; Bae, I.-T.; Maye, M.M. Understanding the Surface Properties of Halide Exchanged Cesium Lead Nanoparticles. *Langmuir.* **2018**, *34*, pp 11139–11146.
- [4] Shi, Y.-X.; Li, W.-X.; Zhang, W.-H.; Lang, J.-P. Guest-Induced Switchable Breathing Behavior in a Flexible Metal–Organic Framework with Pronounced Negative Gas Pressure. *Inorg. Chem.* **2018**, *57*, pp 8627–8633.
- [5] Martineau, C.; Cadiau, A.; Bouchevreau, B.; Senker, J.; Taulelle, F.; Adil, K. SMARTER Crystallography of the Fluorinated Inorganic–Organic Compound Zn₃Al₂F₁₂·[HAMTAZ]₆. *Dalton Trans.* **2012**, *41*, pp 6232–6241.
- [6] Hoffmann, H.C.; Debowski, M.; Müller, P.; Paasch, S.; Senkovska, I.; Kaskel, S.; Brunner, E. Solid-State NMR Spectroscopy of Metal–Organic Framework Compounds (MOFs). *Materials (Basel).* **2012**, *5*, pp 2537–2572.
- [7] Gullion, T.; Schaefer, J. Development of REDOR Rotational-Echo Double Resonance NMR. *J. Magn. Reson.* **1989**, *213*, pp 196–200.
- [8] Gullion, T.; Schaefer, J. Detection of Weak Heteronuclear Dipolar Coupling by Rotational-Echo Double-Resonance Nuclear Magnetic Resonance. In: *Adv. Magn. Reason.*; Warren, W.S., Ed.; Academic Press: San Diego, **1989**, Vol. 13, pp 57–84.
- [9] Gullion, T. Rotational-Echo, Double-Resonance NMR. In *Mod. Magn. Reason.*; Webb, G.A., Ed.; Springer: New York, **2008**, pp 713–718.
- [10] Toke, O.; Cegelski, L. REDOR Applications in Biology: An Overview. In *Solid-State NMR Studies of Biopolymers*; McDermott, A.E., Polenova, T., Eds.; John Wiley & Sons, Ltd.: Hoboken, **2010**; Ch. 28, pp 473–490.

- [11] Okazaki, N.; Okumura, A. A study of Dehydration and Hydration of Sodium Dihydrogen Phosphate and Racemic Acid by Means of the Deuterium Exchange Reaction. *Bull. Chem. Soc. Jpn.* **1961**, *34*, pp 985–989.
- [12] Wolfram Research, Inc., Mathematica, Version 13.1, Champaign, IL (2022).
- [13] Gullion, T.; Baker, D.B.; Conradi, M.S. New, Compensated Carr-Purcell Sequences. *J. Magn. Reson.* **1990**, *89*, pp 479–484.
- [14] Gullion, T.; Schaefer, J.J. Elimination of Resonance Offset Effects in Rotational-Echo, Double-Resonance NMR. *Magn. Reson.* **1991**, *92*, pp 439–442.
- [15] Gamoke, B.; Neff, D.; Simons, J. Nature of PO Bonds in Phosphates *J. Chem. Phys. A.* **2009**, *113*, pp 5677–5684.
- [16] Long, Z.; Park, S.H.; Opella, S.J. Effects of Deuteration on Solid-State NMR Spectra of Single Peptide Crystals and Oriented Protein Samples. *J. Magn. Reson.* **2019**, *309*, pp 106613–106625.
- [17] Reif, B. Deuteration for High-Resolution Detection of Protons in Protein Magic Angle Spinning (MAS) Solid State NMR. *Chem. Rev.* **2022**, *122*, pp 10019–10035.

Generalized predictive disease networks

Thomas E. Ingersoll

U.S. Army Combat Capabilities Development Command Chemical Biological Center, Research & Operations Directorate, 8198 Blackhawk Rd., Aberdeen Proving Ground, MD 21010

ABSTRACT

Estimators for Disease Dynamics with Imperfect Surveillance (EDDIS) is a method for estimating infective disease dynamics parameters when contact rates are heterogeneous, surveillance data are not systematically sampled, and cases are underreported. EDDIS was originally applied to a special case, data from early in the Coronavirus disease 2019 outbreak. This report extends EDDIS for work on a variety of emerging diseases, with monkeypox used as an example. The effective reproductive number determines the rate at which new infections occur, and responds to intervention strategies such as vaccination, quarantine, and social distancing. However, accurate estimation of R_e is complicated by shortcomings in surveillance data collection. Instead, the basic reproductive number R_0 may be used along with contact parameters derived from network characteristics within the host population. Network characteristics are typically derived from detailed contact tracing data, especially for sexually transmitted diseases. EDDIS includes a method of extracting network characteristics from surveillance data using hierarchical models, which was extended for work on the 2022 monkeypox outbreak. Implicit estimators in EDDIS for node size and link distribution do not require contact tracing data. A predictive model was developed from data collected early in the monkeypox outbreak and tested against subsequent surveillance records.

Keywords: monkeypox, network model, hierarchical model, surveillance data, susceptible exposed infectious resistant model, underreporting, disease dynamics, maximum likelihood

1. INTRODUCTION

1.1 Purpose

A generalized maximum-likelihood method for estimating infective disease dynamics parameters in metapopulations, where subpopulations exist in partial spatial isolation, surveillance data are not systematically sampled, and cases are underreported is presented. The author proposes that network parameters for a host population may be implied from surveillance data and do not require contact tracing data. The basic reproductive number for an infectious disease, R_0 , may then be used with network parameters to estimate outbreak trajectory, and make predictions of epidemic growth.

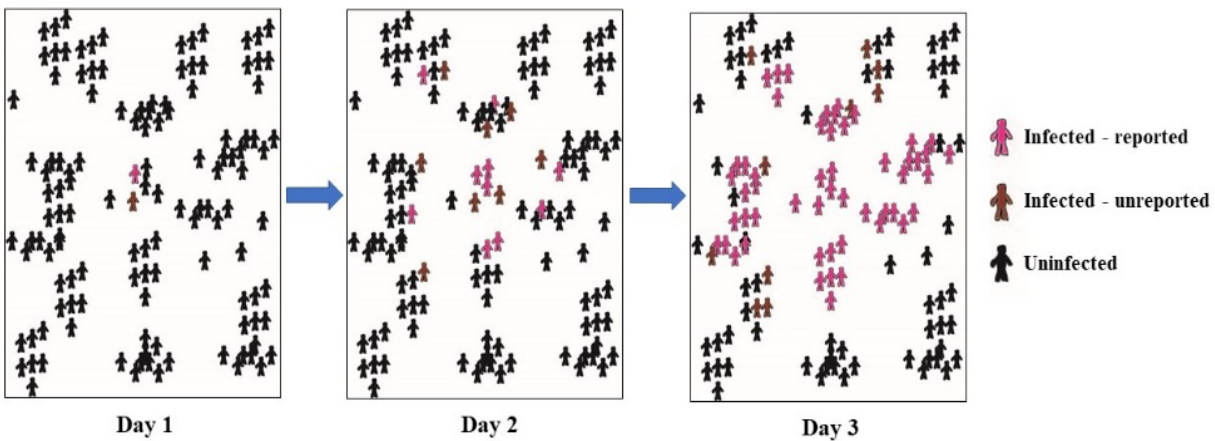


Figure 1. Spatial spread of a hypothetical disease through a network of unevenly connected hosts.

Models of disease dynamics are usually based on an assumption that the host population is well-mixed; that is, that all hosts in the population have an equal chance of contact with an infective host.¹ However, natural populations are not typically well-mixed. Contacts with infective hosts are uneven, due clustering within the population (Figure 1). Within each population, there exists a subpopulation, smaller than the total population size, that is in contact with infective hosts. This subpopulation will be called the susceptible class (*S*). Disease transmission models that relax the well-mixed assumption are called network models.²

Furthermore, reporting of disease may be spatially auto-correlated, resulting in uneven underreporting (Figure 1, brown symbols). That is, reporting rates may be higher at some locations. Hierarchical models can be formulated to accommodate uneven underreporting,³ and incorporated into network models such as in Estimators for Disease Dynamics with Imperfect Surveillance (EDDIS).⁴ EDDIS can then be used to parameterize a system of differential equations which can then predict changes in epidemic trajectory.

1.2 Background

A set of categories useful for describing the state of infection within hosts includes Susceptible (*S*): individuals that are available to become hosts to the disease, Exposed (*E*): recently exposed individuals that have not yet developed transmissible disease, Infective (*I*): individuals that have acquired the disease and are able to spread it to others, and Recovered (*R*): individuals that have acquired immunity so can no longer become hosts or transmit the disease to others. Models containing these categories are called SEIR models.^{1,5} Because natural populations are not well-mixed, the number of hosts within the *S* class responds to spatial movement of hosts as well as disease dynamics.⁴ Therefore, the size of class *S* must be estimated separately from the total population size. A method for estimating *S* from surveillance data is presented by Ingersoll,⁴ and is extended below.

$$\frac{dS}{dt} = \nu - (\beta I + \mu)S \tag{1}$$

$$\frac{dE}{dt} = \beta SI - (\mu + \sigma)E \tag{2}$$

$$\frac{dI}{dt} = \sigma E - (\mu + \gamma)I \tag{3}$$

$$\frac{dR}{dt} = \gamma I - \mu R \tag{4}$$

S, E, I, R are the count of hosts in each of the compartmental model classes, as given above (Figure 2). The birth rate is ν . β is the epidemic growth rate. The rate of transition from exposed to infective is σ . The death rate is μ . The recovery rate is γ .

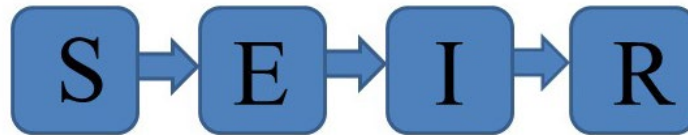


Figure 2. Susceptible, Exposed, Infective, and Recovered (SEIR) compartmental model of disease dynamics.

The cumulative case count is the sum of *I* and *R*, and can frequently be found in surveillance reports. β is a function of R_0 . While R_0 can be estimated using EDDIS, reliable estimates of monkeypox are presented in literature.⁶

Methods using hierarchical models are well-established for correcting underreporting, and have been extended to not require an assumption, common to capture/recapture methods, of even underreporting.³ These methods are particularly relevant for cumulative case counts, where underreporting rates typically change as the outbreak progresses and surveillance resources are deployed. Adjustment for underreporting uses the probability of detection, as given below (Equation 5).

A method for estimating detection probability using predicted values from dynamic models, and count data from surveillance is found using Isaac Newton’s Binomial Theorem (Equation 5).

$$P = \binom{n}{k} (p)^k (1 - p)^{n-k} \tag{5}$$

For our purposes, *n* is the day’s cumulative case count from the dynamic model (*I+R*), *k* is the day’s case count from the surveillance data, *p* is the detection probability, and *P* is the probability of the parameters *n* and *p*, given the datum

k. The product of P across all the data is the model likelihood. The result is a maximum likelihood method for estimating the detection probability p , in turn, correcting underreporting expected to be present in the surveillance data. Newton’s Theorem can be used to adjust observed imperfect counts to estimates of the true number of cases in the population, a number which often cannot be directly observed. The theorem also provides a vehicle to adjust the parameters for the dynamic model, also via maximum likelihood, which produce the value n . The result is data assimilation, where data are used to adjust a statistical model for detection, and terms of the dynamic model.

1.3 Data sources

Cumulative case counts for the 2022 monkeypox outbreak were reported by the World Health Organization and are available in open source.⁷ Data are available for the United States and globally. Monkeypox is a zoonosis, with alternative human and animal hosts.⁶ Data for the United States were chosen because the data were uncomplicated by contacts with potential infected wildlife hosts, which would require a more complicated compartmental model.⁹ Data started with the first reported United States cases on 3 June 2022, and continued until preparation of this report on 28 September 2022, for a period of 118 days. A total of 79 case counts were reported, with records missing for the remainder of the period. EDDIS computer codes were extended as part of the ongoing generalization effort to accommodate these missing records.

2. METHODS

2.1 Methods development

Models were based on SEIR models developed for the 2003 SARS infection.¹⁰ These models were executed in the computational language R,¹¹ using the R library of differential equation solvers deSolve.¹² Hierarchical methods in EDDIS were used to estimate and model detection probability, adjust parameters for the differential equations, and estimate network characteristics. New functions written and archived by the author execute EDDIS in a forward stepwise iterative process for each 5-day period, beginning with an initial 15-day seed period, and providing estimates for overlapping 15-day periods. EDDIS was extended to update parameter estimates, including heterogeneous detection, for each period in the series. This resulted in 19 iterations to produce an analytical model covering 115 days. Parameters were estimated using maximum likelihood methods contained in EDDIS.⁴ EDDIS and its current extensions are now mostly contained in 2 compact functions written by the author in the computational language R,¹¹ and only requiring 140 lines of code.

Every 5 days the estimate of S was updated, to simulate the movement of susceptible hosts into contact with infective hosts. The analytic model (Figure 3) produced output for epidemic dynamic parameters, and estimate of S , an estimate of the true case count with adjustment for underreporting, and the detection probability.

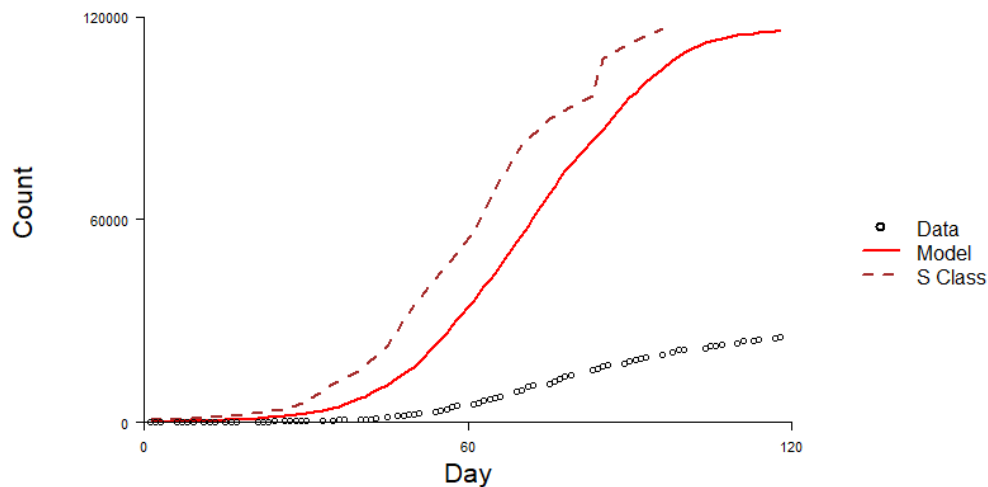


Figure 3. Analytic model for underreported disease data. The true case count estimate (red trace) is approximately five times the observed data due to underreporting. The estimated affected population size (brown trace) is the susceptible (S) class from the compartmental model.

2.2 The predictive model

A predictive model was formulated using the first 75 days of data (Figure 4). This model was then used to predict the observed counts for the remainder of a 110-day period. Correlation between the predicted and observed counts across each time-lag from 75 through 110 days was calculated and visualized in a cross-correlogram (Figure 5).

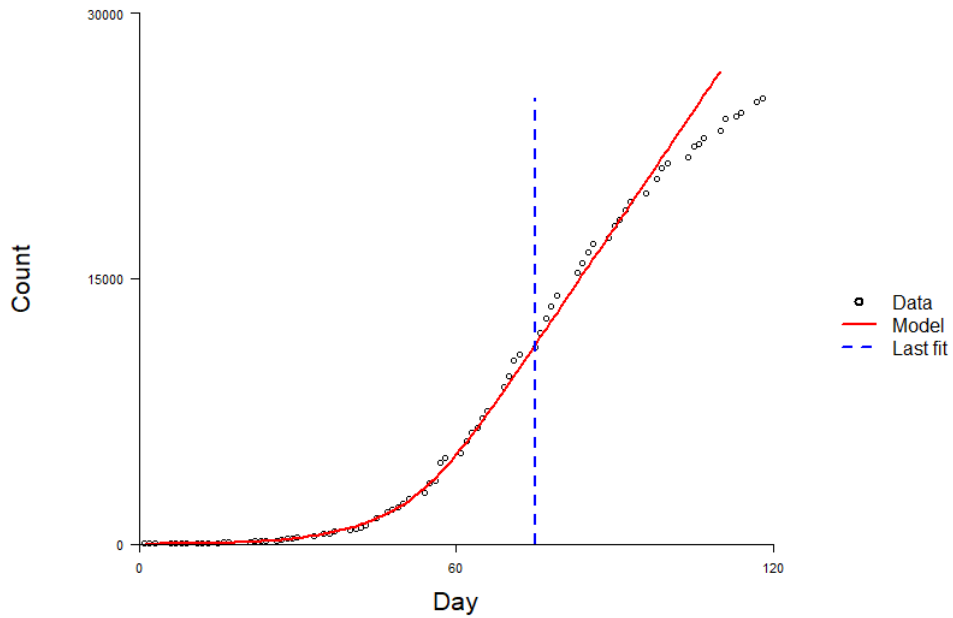


Figure 4. Predictive model for US Monkeypox data (black circles). The model (red trace) parameters were fit until day 75 (blue trace) and interpolated to day 110 for comparison to the subsequent trajectory of data.

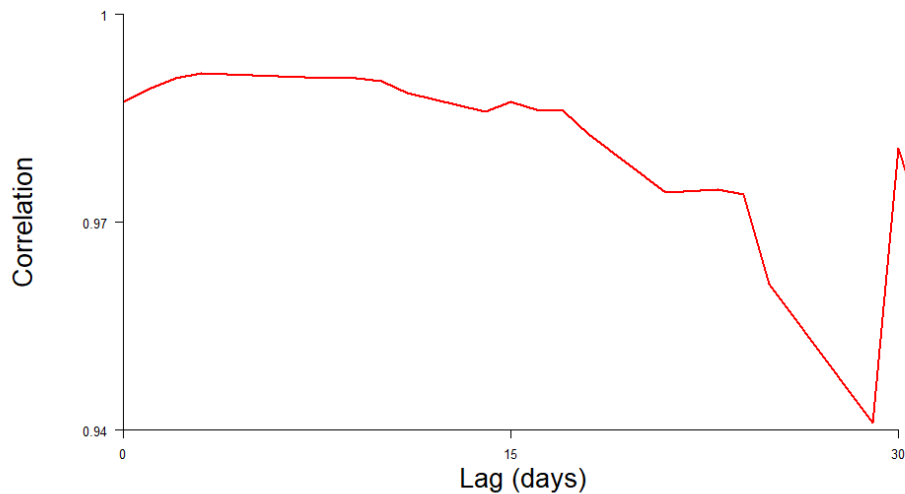


Figure 5. Correlation between model predictions and observed case counts subsequent to the last fit to data. Model predictions remained 95 % reliable for four weeks.

3. RESULTS AND DISCUSSION

3.1 The analytic model and the trajectory of the United States outbreak

According to the selected model (Figure 3), monkeypox was first reported from a node of 625 susceptible individuals. Detection probability (p) was consistently low, remaining at 0.2 for all but the initial seed period where it was 0.3. This suggests that only about 1 out of 5 monkeypox cases were reported. It was estimated that 105,000 cases of monkeypox were present in the US by September 6, 2022, with only 19,851 of these cases reported in data. This has consequences for the planned subsequent deployment of only 90,000 doses of vaccine.

3.2 Predictive modeling

The data provided an exceptionally good fit to the predictive model for observations across the 75-day fitting period. This can be attributed to a low level of random error in the data, resulting in a relatively smooth curve. A long delay (days 1:40) preceding exponential growth is characteristic of network dynamics, where host populations are not well-mixed.⁴ Predicted values following day 75 (red trace) follow the data until they begin to diverge around day 100, likely due to a decrease in daily incidence following deployment of vaccines.

The predictive model demonstrated a very high level of reliability for 28 days following the last day of model fitting. This suggests that this model might be useful for outbreak management and mitigation, such as planning the number of vaccine doses required for outbreak suppression. However, processes introduced by events outside the model fitting period will cause the model trajectory to diverge from the observed counts.

3.3 Success of the demonstration

It was successfully demonstrated that EDDIS, a tool for estimating infective disease-dynamics parameters when contact rates are uneven, surveillance data are not systematically sampled, and cases are underreported, could be extended to diseases other than special cases such as Coronavirus disease 2019. EDDIS proved to perform well on monkeypox data and to provide reliable predictions for a reasonable period. New developments for EDDIS include a forward-stepping iterative fitting process, and the accommodation of missing records. Continued development of EDDIS could include further validation for more generalized cases, development of plausible confidence intervals, and further automation to allow estimation of a broader suite of network parameters, such as link intensity. Application to link intensity might best be studied by applying EDDIS to data from the 2014 West-African ebolavirus disease outbreak. Additionally, increased automation will facilitate further validation and generalization. EDDIS is developing into an effective tool that can inform mitigation, control strategies, and decision-making.

ACKNOWLEDGMENTS

Funding was provided by the Director, Combat Capabilities Development Command Chemical Biological Center under the authorities and provisions of Section 2363 of the FY 2022 NDAA to develop new technologies, engineer innovations, and introduce game-changing capabilities.

REFERENCES

- [1] Anderson, R.; May, R. *Infectious Diseases of Humans, Dynamics and Control*; Oxford University Press, **1991**.
- [2] Keeling, M.J.; Eames, K.T.D. Networks and epidemic models. *J. R. Soc., Interface*. **2005**, *2* (4), pp 295–307.
- [3] Royle, J.A., Dorazio, R.M. *Hierarchical Modeling and Inference in Ecology*; Elsevier, **2008**.
- [4] Ingersoll, T. E., Estimators for Disease Dynamics with Imperfect Surveillance. DEVCOM CBC-TR1747. **2021**.
- [5] Keeling, M.J.; Rohani, P. *Modeling infectious diseases in humans and animals*; Princeton University Press, **2008**.
- [6] Kaler, J.; Hussain, A.; Flores, G.; Kheiri, S.; Desrosiers, D. Monkeypox: A comprehensive review of transmission, pathogenesis, and manifestation. *Cureus*. **2022**, *14* (7), pp e26531.
- [7] Global.health. *Monkeypox 2022 repository*. <https://github.com/globaldothealth/monkeypox> (accessed on 2022-09-28).
- [8] Kline, M. *History of mathematical thought*; Oxford University Press, **1972**.

- [9] Reynolds, H.T., Ingersoll, T.E.; Barton, H.A. Modeling the environmental growth of *Pseudogymnoascus destructans* and its impact on the white-nose syndrome epidemic. *J. Wildl. Dis.* **2015**, *51* (2), pp 318–331.
- [10] Riley, S., Fraser, C.; Donnelly, C.A.; Ghani, A.C.; Abu-Raddad, L.J.; Hedley, A.J.; Leung, G.M.; Ho, L.M.; Lam, T.H.; Thatch, T.Q.; Chau, P.; Chan, K-P.; Leung, P- Y.; Tsang, T.; Ho, W.; Lee, K-H.; Lau, E.M.C.; Ferguson, N.M.; Anderson, R.M. Transmission dynamics of the etiological agent of SARS in Hong Kong: Impact of Public Health Interventions. *Science.* **2003**, *300* (5627), pp 1961–1966.
- [11] R Core Team. *R: A language and environment for statistical computing*. R Foundation for Statistical Computing: Vienna, Austria, **2019**; <https://www.R-project.org/>.
- [12] Soetaert, K.; Petzoldt, T.; Woodrow, R. Solving Differential Equations in R: Package deSolve. *J. Stat. Softw.* **2010**, *33* (9), pp 1–25.

A modified nucleotide mass spectrometry library for epitranscriptome and epigenomic analysis

Conor C. Jenkins^{a*}, Gabrielle Rizzo^a, Allison E. Melka^b, Daniel J. Angelini^a

^aU.S. Army Combat Capabilities Development Command Chemical Biological Center, Research & Operations Directorate, 8198 Blackhawk Rd., Aberdeen Proving Ground, MD 21010

^bExcet Inc., 6225 Brandon Ave., Suite 360, Springfield, VA 22150

ABSTRACT

Modifications at the genomic and transcriptomic level affect a staggering variety of biochemical processes. DNA methylation has been shown to regulate gene expression and act as an indicator of environmental and physiological stimuli. Deleterious modifications can cause mismatched base pairing leading to a variety of detrimental effects in the host cell. Post-transcriptional modifications at the RNA level have been shown to impact mRNA function, metabolism, translation, and decay. Hundreds of these nucleic acid modifications have been observed, with over 100 of these related to human disease (e.g., Huntington's Disease). Unfortunately, investigating these modifications has been extremely difficult, requiring both specialized sample preparation and next-generation sequencing methods. Mass spectrometry-based epigenomic and epitranscriptomic methods set out to solve this by enabling a researcher to observe global modifications for every type of RNA and DNA in a single streamlined methodology. However, the data analysis pipeline remains a challenge due to the required extensive manual investigation of spectra. We seek to begin building a mass spectrometry library of modified nucleotides to simplify the data analysis and enable the center to investigate epitranscriptomic and epigenomic events when exposed to chemical threat agents.

Keywords: post-transcriptional modifications, mass spectrometry, exposomics, epitranscriptome, epigenome

1. INTRODUCTION

To mitigate the risk of the Warfighter's exposure to deleterious environmental factors and chemical warfare agents, extensive multiomic characterization has been performed to unveil the underlying mechanisms of action of these chemicals in the human body. While observing changes in the transcriptome, proteome, and metabolome can give great insight into potential therapeutics and direct effects of exposure, epigenomics and epitranscriptomics, two severely under-investigated "omics" fields, may reveal the long-term detrimental side-effects of exposure and provide supplemental evidence to the multiomic stories that still have missing pieces.

The goal of epigenomic and epitranscriptomic research is to investigate changes that do not alter the nucleotide sequence but instead chemically modify the nucleotides. Over 300 modified nucleotides have been identified and this number is increasing every year.¹ These modifications continue to emerge as key factors leading to effects on transcription, translation, and higher order structure, thus must be studied to provide the mechanistic basis to understand the biological effects of various classes of environmental exposures. Over 175 modifications have been linked to different detrimental health outcomes. One such observation is the case of increased nucleotide methylation events have been observed in samples that have been exposed to herbicides such as Agent Orange and sulfur mustard chemical warfare agents.²⁻⁴

More specific examples of detrimental nucleotide modifications exist. N-nitrosodimethylamine (NDMA) is a known carcinogen that has been utilized as a poison and found in drinking water near rocket launch sites.⁵ This compound increases the occurrence of the nucleotide 7-methylguanine, which is associated with hypoxic pulmonary hypertension and the development of other human disease.⁶ Another modified nucleotide of interest is 5-methyluridine, which is implicated in the development of several diseases and stress response; these could be used as a marker for soldier performance and a potential early indicator of chemical exposure.^{7,8} Tissue-specific gene expression patterns in humans are also influenced by 5-methylcytosine, another nucleotide modification. Levels of 5-methylcytosine are maintained in equilibrium by α -ketoglutarate which has been shown to be affected by exposure to the chemical warfare agent VX, showing a promising avenue for study.⁹ Traditionally, modified nucleotides across the genome and transcriptome have been analyzed through DNA and RNA sequencing technologies with enrichment techniques such

as miCLIP-seq or FICC-seq, but these methods are expensive both in time and cost and their specificity have come into question.^{10,11} Another issue is that these methods can only investigate one species of modification at a time, thus dramatically decreasing throughput of global modification profiling. Mass spectrometry-based methods have been deployed to address these issues by enabling an individual to observe global profiling of many different modifications in a single sample.^{12,13}

In this study, we seek to build out an easily portable mass spectrometry (MS) library of 20 modified nucleotides that contains optimal fragmentation parameters for investigating the global levels of nucleotide modifications in a single sample in a high throughput and reproducible manner. We then seek out to test the method on samples exposed to chlorpyrifos, an organophosphate insecticide which potentially causes perturbations of modified nucleotides.¹⁴

2. METHODOLOGY

2.1 Standards for mass spectrometry library generation

N6-methyladenosine (Cayman Chemical), 2'-O-methyladenosine (Cayman Chemical), 5,6-dihydrouridine (Cayman Chemical), N6-(Δ^2 -isopentenyl)adenosine (Cayman Chemical), 2'-O-methylguanosine (Cayman Chemical), Nucleosides Test Mix (MilliporeSigma), and adenosine (MilliporeSigma) were utilized to obtain optimal spectra for library creation. Single standards were diluted to a concentration of 5 $\mu\text{g}/\mu\text{L}$ in mass spectrometry grade water with 0.1% formic acid (Fischer Scientific). The Nucleosides Test Mix contained nucleotides in the following concentrations: cytidine 50 $\mu\text{g}/\text{mL}$, guanosine 25 $\mu\text{g}/\text{mL}$, inosine 25 $\mu\text{g}/\text{mL}$, 1-methyladenosine 25 $\mu\text{g}/\text{mL}$, 5-methylcytidine 100 $\mu\text{g}/\text{mL}$, 2'-O-Mmethylcytidine 20 $\mu\text{g}/\text{mL}$, 3-methylcytidine methosulfate 100 $\mu\text{g}/\text{mL}$.

2.2 Mass spectrometry acquisition

Sample data was collected on a Thermo Q Exactive™ Plus Orbitrap Mass Spectrometer coupled to a Thermo Vanquish™ HPLC system. Samples were separated by reverse phase chromatography on a Cortecs T3 column (120 Å, 2.7 μm , 2.1 mm x 150 mm) with gradient elution utilizing mobile phase A consisting of 5 mM ammonium acetate (pH 5.6) and mobile phase B as 60/40 mobile phase A/acetonitrile. Gradient elution was performed using a flow rate of 350 $\mu\text{L}/\text{min}$ under the following steps: 0–3 min; 0 %B, 3–4.5 min; 0–5 %B, 4.5–5.5 min; 5–7 %B, 5.5–16 min; 7–15 %B, 16–17.5 min; 15–40 %B, 17.5–20 min; 40–50 %B, 20–23 min; 50–75 %B, 23–26.5 min; 75–100 %B, 26.5–30; 100 %B, 30–36.000; 0 %B. A positive mode Data-Dependent MS2 acquisition strategy was deployed utilizing a top 20 method. MS1 resolution was at 70,000 scanning between 110–600 m/z. A normalized stepped collision energy fragmentation strategy was used at energies 60, 75, and 90. MS2 resolution was set at 17,500 with a 4.0 m/z isolation window excluding changes > 3 with a 10.0 s Dynamic exclusion window.

2.3 Human cell culture and viability assays

The human microvascular endothelial cell line HMEC-1 (ATCC CRL-3243) was obtained from ATCC® (Manassas, VA) and cultured in MCDB131 culture media (ATCC®) supplemented with 10 ng/mL epidermal growth factor, 1 $\mu\text{g}/\text{mL}$ hydrocortisone, 10 mM L-glutamine, 1 % penicillin-streptomycin, and 10 % fetal bovine serum (all supplements from ThermoFisher Scientific™; Waltham, MA). HMEC-1 cells have been shown to express all the typical endothelial cell markers, have endothelial cell morphology, and form consistent endothelial cell barriers.¹⁵ HMEC-1 cells were plated in 96-well tissue culture plates at a density of 5×10^3 cells/well and allowed to attach for 72 hours. The cells were then treated for 24 hours with increasing concentrations of chlorpyrifos (0.1–1000 μM ; Sigma-Aldrich; St. Louis, MO), equivalent amounts of vehicle control (EtOH), or media alone. Following each 24 hour exposure, an MTT Assay (Abcam; Waltham, MA) was performed according to the manufacturer's instructions. Results were read on a SpectraMax plate reader (Molecular Devices; Sunnyvale, CA) and expressed as percentage of relative viability.

2.4 Sample preparation and mass spectrometry analysis of RNA

For the collection of RNA, 1×10^5 HMEC-1 were plated on 60-mm cell culture dishes and allowed to grow for 72 h (37 °C/5 % CO₂). The cells were then exposed to either chlorpyrifos (50 μM) or media alone for 3 hours or 24 hours in six biological replicates for each state. At the conclusion of the exposure period, the media was removed, 1 mL TRIzol™ Reagent (ThermoFisher) was added to each dish, and then the lysates collected. The resultant samples were then stored at -80 °C for further analysis. Samples were prepared for MS as previously described.¹² Briefly, samples

were removed from -80 °C storage, thawed, and 100 µL aliquots were made of each sample. Following the thawing step, 6 µL 0.365 M ammonium acetate (Fisher Chemical) was added to each aliquot, followed by the addition of 2.09 µL enzyme mixture (0.99 U alkaline phosphatase [Worthington Biochemical], 0.1 U phosphodiesterase I [Worthington Biochemical], and 25 U benzonase [Sigma]). Next, 10 µL of bovine serum albumin (Sigma) was added to each sample, followed by addition of 4.95 µL of a 0.1 µg/µL solution of pentostatin (Sigma). Samples were then incubated for 3 hours at 37 °C and transferred to autosampler vials for MS analysis. Data analysis was performed in Compound Discoverer ver 2.2.

3. DATA

3.1 Mass spectrometry library generation

The standards analyzed by mass spectrometry yielded 19 identified nucleotides. As an example, 5,6-dihydrouridine (Figure 1A) had 19 peaks corresponding to theoretical peaks generated by Thermo Fischer Scientific's Fragment Ion Search tool (FISH). This tool generates theoretical fragment ions of an input structure and then compares the experimentally obtained spectra the theoretical fragments with a corresponding FISH coverage score based on the percentage of ions matching. An accepted baseline number of peaks for small molecule identifications is often much fewer (4-6 peaks for a high confident match).¹⁶ The majority of assigned spectra to each nucleotide was able to achieve a FISH coverage of >40% corresponding to >10 MS2 peaks (Table 1).

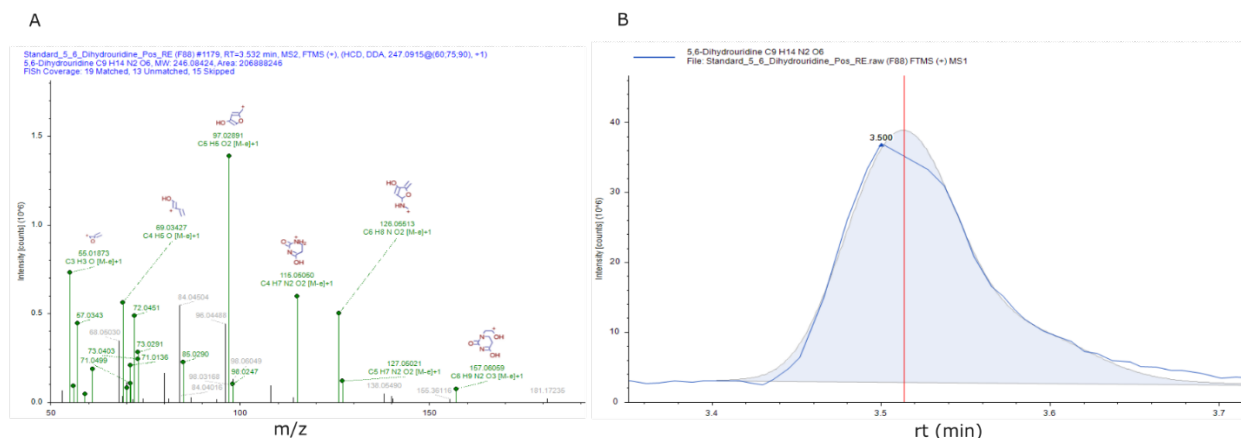


Figure 1: (A) The 5,6-dihydrouridine fragmentation spectrum shows 19 matched peaks (in green) to the FISH fragmentation prediction along with the predicted fragment portions and their m/z. (B) The chromatographic peak of 5,6-dihydrouridine centered at 3.51 minutes (red line).

The reverse phase chromatography provided good separation on the different species across the run and Gaussian-shaped peaks. Again using 5,6-dihydrouridine as an example, the peak eluted over ~12 seconds and shows an ideal elution profile (Figure 1B). The compounds eluting at the initial isocratic part of the gradient (cytidine, 5-methylcytidine, 3-methylcytidine) would not be able to be separated on a standard C18 column due to its inability to run at 100% aqueous solution but can be separated on the Cortex T3 column utilized in this study. N6-Δ-2-isopentyladenosine (iPA) has a long hydrophobic modification which retains on column much longer than the other species (19.571 min). Since the separation method in its current form takes place over 36 minutes, this provides an area where optimization could decrease the total acquisition time necessary to separate all the compounds, increasing the throughput of this method by reducing separation to 20 minutes per sample

Table 1. A list of modified nucleotides added to the in-house library with their monoisotopic mass, the deviation in the observed mass, the FISH coverage, and the retention time of the nucleotide.

NUCLEOTIDE	MONOISOTOPIC MASS	ΔPPM	FISH COVERAGE (%)	RT (MIN)
CYTIDINE	243.0855	-3.61	66.67	1.764
5-METHYLCYTIDINE	257.1012	-3.75	66.67	2.948
3-METHYLCYTIDINE	257.1012	-3.28	68.42	2.948
B-PSEUDOURIDINE	244.0695	-3.69	40.00	3.254
URIDINE	244.0695	-3.69	48.57	3.254
2'-O-METHYLADENOSINE	281.1124	-2.79	76.36	3.885
5,6-DIHYDROURIDINE	246.0852	-3.02	59.38	3.562
2-THIOCYTIDINE	259.0627	-3.17	59.22	4.054
7-METHYLGUANOSINE	298.1151	-3.28	16.67	5.115
ADENOSINE	267.0968	-2.61	77.78	5.198
2'-O-METHYLCYTIDINE	257.1012	-4.57	67.80	5.356
INOSINE	268.0808	-3.77	50.00	6.764
GUANOSINE	283.0917	-3.93	56.72	6.795
5-METHYLURIDINE	258.0852	-2.93	46.34	7.021
2'-O-METHYLGUANOSINE	297.1073	-3.60	54.41	7.715
N6-METHYLADENOSINE	281.1124	-3.66	75.63	7.988
1-METHYLADENOSINE	281.1124	-3.23	70.00	8.772
N6-DIMETHYLADENOSINE	295.1281	-3.16	56.30	13.369
N6-Δ-2-ISOPENTYLADENOSINE	203.1171	-3.22	21.84	19.571

3.2 Effect of chlorpyrifos on HMEC-1 viability

To establish an appropriate dosage of chlorpyrifos, a HMEC-1 viability assay was performed over a range of 0.1 μM to 1000 μM chlorpyrifos. After 24 hours of exposure, chlorpyrifos induced a dose-dependent decrease in cell viability at concentrations greater than 300 μM (Figure 2). Based on these data, 50 μM was selected as an effective experimental chlorpyrifos concentration for RNA collection.

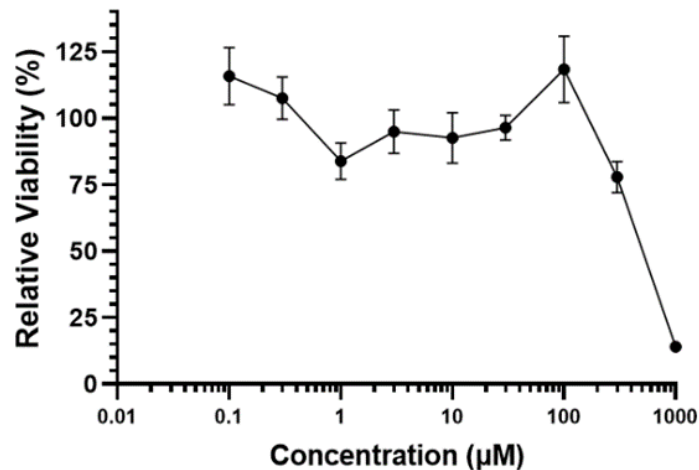


Figure 2: HMEC-1 viability assay showing that at concentrations of chlorpyrifos >100 μM, cell viability is negatively impacted; thus, a 50 μM concentration was chosen for exposure.

3.3 Effect of chlorpyrifos on HMEC-1 viability

iPA is a modified nucleoside with an isopentenyl modification at the N6 location of adenosine that is generated by the mevalonate pathway which is fundamental for cholesterol synthesis.^{17,18} It has been shown to also affect cytokine response and mitogen-activated protein kinase signaling intermediates downstream of interleukin-2 receptor directly, two major aspects of cellular defense.⁵ Chlorpyrifos is an organophosphate pesticide that has been shown to cause

disorders of lipid metabolism and have a direct effect on cholesterol levels.^{19,20} We observe a significant ($p < 0.05$, student's t-test) decrease ($\log_2FC -2.31$) in levels of iPA (Figure 3). This indicated that iPA could potentially be an early indicator of chlorpyrifos exposure.

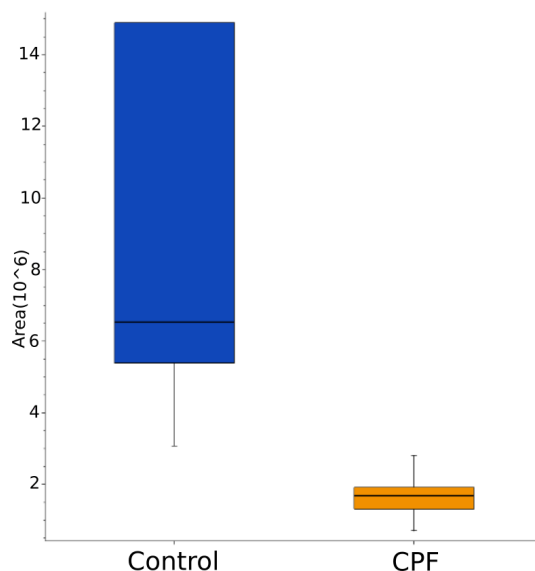


Figure 3: iPA levels in the control (blue) and the chlorpyrifos exposed samples (orange).

4. CONCLUSIONS

In this study, we generated a mass spectrometry-based library containing 19 modified nucleotides. This library facilitates the rapid and high confidence identification of these nucleotides to monitor the epitranscriptome and epigenome at a faster rate and lower cost when compared to next generation sequencing platforms. Further optimization of the chromatography will allow for an even greater throughput of samples. With the chromatography optimized, we can continue to add additional modified nucleotides to the panel. One of interest would be 5-hydroxymethylcytosine (5-hmC). Humans have a distinct balance between 5-methylcytosine and 5-hmC which plays an integral role in development and baseline physiology. 5-methylcytosine can be oxidized to 5-hmC by enzymes which use α -ketoglutarate as substrates. α -ketoglutarate has been shown to be drastically affected by VX, an organophosphate nerve agent exposure.²¹ To date, no study investigating the 5-hmC/5-methylcytosine homeostasis and how VX can perturb it has been performed. The methodology in this paper opens investigation of chemical warfare agent mechanism of action that has yet to be studied.

ACKNOWLEDGMENTS

Funding was provided by the Director, Combat Capabilities Development Command Chemical Biological Center under the authorities and provisions of Section 2363 of the FY 2018 NDAA to develop new technologies, engineer innovations, and introduce game-changing capabilities.

REFERENCES

- [1] Boccaletto, P.; Stefaniak, F.; Ray, A.; Cappannini, A.; Mukherjee, S.; Purta, E.; Kurkowska, M.; Shirvanizadeh, N.; Destefanis, E.; Groza, P.; Avşar, G.; Romitelli, A.; Pir, P.; Dassi, E.; Conticello, S.G.; Aguiló, F.; Bujnicki, J.M. MODOMICS: a database of RNA modification pathways. 2021 update. *Nucleic Acids Res.* **2021**, *50* (D1), pp D231–D235.

- [2] Korkmaz, A.; Yaren, H.; Kunak, Z.I.; Uysal, B.; Kurt, B.; Topal, T.; Kenar, L.; Ucar, E.; Oter, S. Epigenetic perturbations in the pathogenesis of mustard toxicity; hypothesis and preliminary results. *Interdiscip. Toxicol.* **2010**, *1* (3-4), pp 236–241.
- [3] Rytel, M.R.; Butler, R.; Eliot, M.; Braun, J.M.; Houseman, E.A.; Kelsey, K.T. DNA methylation in the adipose tissue and whole blood of Agent Orange-exposed Operation Ranch Hand veterans: a pilot study. *Environ. Health.* **2021**, *20* (1), p 43.
- [4] Simons, T.; Steinritz, D.; Bölcck, B.; Schmidt, A.; Popp, T.; Thiermann, H.; Gudermann, T.; Bloch, W.; Kehe, K. Sulfur mustard-induced epigenetic modifications over time – a pilot study. *Toxicol. Lett.* **2018**, *293*, pp 45–50.
- [5] Mitch, W.A.; Sharp, J.O.; Trussell, R.R.; Valentine, R.L.; Alvarez-Cohen, L.; Sedlak, D.L. N-Nitrosodimethylamine (NDMA) as a Drinking Water Contaminant: A Review. *Environ. Eng. Sci.* **2003**, *20* (5), pp 389–404.
- [6] Wang, H.; Chen, R.B.; Zhang, S.N.; Zhang, R.F. N7-methylguanosine modification of lncRNAs in a rat model of hypoxic pulmonary hypertension: a comprehensive analysis. *BMC Genomics.* **2022**, *23* (1), p 33.
- [7] Jonkhout, N.; Tran, J.; Smith, M.A.; Schonrock, N.; Mattick, J.S.; Novoa, E.M. The RNA modification landscape in human disease. *RNA.* **2017**, *23* (12), pp 1754–1769.
- [8] Guo, G.; Wang, H.; Shi, X.; Ye, L.; Yan, K.; Chen, Z.; Zhang, H.; Jin, Z.; Xue, X. Disease Activity-Associated Alteration of mRNA m⁵C Methylation in CD4⁺ T Cells of Systemic Lupus Erythematosus. *Front. Cell Dev. Biol.* **2020**, *8*, p 430.
- [9] Glaros, T.; Dhummakupt, E.S.; Rizzo, G.M.; McBride, E.; Carmany, D.O.; Wright, L.K.M.; Forster, J.S.; Renner, J.A.; Moretz, R.W.; Dorsey, R.; Marten, M.R.; Huso, W.; Doan, A.; Dorsey, C.D.; Phillips, C.; Benton, B.; Mach, P.M. Discovery of treatment for nerve agents targeting a new metabolic pathway. *Arch. Toxicol.* **2020**, *94* (9), pp 3249–3264.
- [10] Carter, J.-M.; Emmett, W.; Mozos, I.R.; Kotter, A.; Helm, M.; Ule, J.; Hussain, S. FICC-Seq: a method for enzyme-specified profiling of methyl-5-uridine in cellular RNA. *Nucleic Acids Res.* **2019**, *47* (19), pp e113.
- [11] Jiang, J.; Song, B.; Tang, Y.; Chen, K.; Wei, Z.; Meng, J. m5UPred: A Web Server for the Prediction of RNA 5-Methyluridine Sites from Sequences. *Mol. Ther. Nucleic Acids.* **2020**, *22*, pp 742–747.
- [12] Clark, K.D.; Rubakhin, S.S.; Sweedler, J.V. Single-Neuron RNA Modification Analysis by Mass Spectrometry: Characterizing RNA Modification Patterns and Dynamics with Single-Cell Resolution. *Anal. Chem.* **2021**, *93* (43), pp 14537–14544.
- [13] Clark, K.D.; Rubakhin, S.S.; Sweedler, J.V. Characterizing RNA Modifications in Single Neurons using Mass Spectrometry. *J. Visualized Exp.* **2022**, 182.
- [14] Burke, R.D.; Todd, S.W.; Lumsden, E.; Mullins, R.J.; Mameczarz, J.; Fawcett, W.P.; Gullapalli, R.P.; Randall, W.R.; Pereira, E.F.R.; Albuquerque, E.X. Developmental neurotoxicity of the organophosphorus insecticide chlorpyrifos: from clinical findings to preclinical models and potential mechanisms. *J. Neurochem.* **2017**, *142* (Suppl 2), pp 162–177.
- [15] Ades, E.W.; Candal, F.J.; Swerlick, R.A.; George, V.G.; Summers, S.; Bosse, D.C.; Lawley, T.J. HMEC-1: establishment of an immortalized human microvascular endothelial cell line. *J. Invest. Dermatol.* **1992**, *99* (6), pp 683–690.
- [16] Xiao, J.F.; Zhou, B.; Ransom, H.W. Metabolite identification and quantitation in LC-MS/MS-based metabolomics. *Trends Anal. Chem.* **2012**, *32*, pp 1–14.
- [17] Ciaglia, E.; Pisanti, S.; Picardi, P.; Laezza, C.; Malfitano, A.M.; D'Alessandro, A.; Gazzero, P.; Vitale, M.; Carbone, E.; Bifulco, M. N6-isopentenyladenosine, an endogenous isoprenoid end product, directly affects cytotoxic and regulatory functions of human NK cells through FDPS modulation. *J. Leukocyte Biol.* **2013**, *94* (6), pp 1207–1219.
- [18] Tricarico, P.M.; Crovella, S.; Celsi, F. Mevalonate Pathway Blockade, Mitochondrial Dysfunction and Autophagy: A Possible Link. *Int. J. Mol. Sci.* **2015**, *16* (7), pp 16067–16084.
- [19] Leonel Javeres, M.N.; Habib, R.; Judith Laure, N.; Abbas Shah, S.T.; Valis, M.; Kuca, K.; Muhammad Nurulain, S., Chronic Exposure to Organophosphates Pesticides and Risk of Metabolic Disorder in Cohort from Pakistan and Cameroon. *Int. J. Environ. Res. Public Health.* **2021**, *18* (5), pp 2310.
- [20] Li, J.; Ren, F.; Li, Y.; Luo, J.; Pang, G. Chlorpyrifos Induces Metabolic Disruption by Altering Levels of Reproductive Hormones. *J. Agric. Food Chem.* **2019**, *67* (38), pp 10553–10562.
- [21] Glaros, T.; Dhummakupt, E.S.; Rizzo, G.M.; McBride, E.; Carmany, D.O.; Wright, L.K.M.; Forster, J.S.; Renner, J.A.; Moretz, R.W.; Dorsey, R.; Marten, M.R.; Huso, W.; Doan, A.; Dorsey, C.D.; Phillips, C.; Benton, B.; Mach, P.M. Discovery of treatment for nerve agents targeting a new metabolic pathway. *Arch. Toxicol.* **2020**, *94*, pp 3249–3264.

Elucidating the mechanism of organophosphate nerve agent simulant reaction with thioether rhodium(II) complexes

Neal D. Kline^{a*}, Desiree Moore^b, Eric Fussell^b, Ampofo Darko^b

^aU.S. Army Combat Capabilities Development Command Chemical Biological Center, Research & Operations Directorate, 8198 Blackhawk Rd., Aberdeen Proving Ground, MD 21010

^bUniversity of Tennessee, Department of Chemistry 552 Buehler Hall, 1420 Circle Dr., Knoxville, TN 37996

ABSTRACT

This study aims to synthesize rhodium(II) complexes containing a thioether or guanidine ligand, which both selectively attack phosphate esters, a functional group present in organophosphate nerve agents. Upon nucleophilic attack, the organophosphate nerve agent will degrade and the rhodium(II) complex will bind the leaving group resulting in a color change and specific identification based on the leaving group identity. In this study, we selected a nerve agent simulant, diethyl chlorophosphate, to investigate the reaction mechanism with three thioether rhodium(II) complexes using Raman and Fourier transform infrared spectroscopy. The anticipated products formed from exposing the rhodium(II) complexes with the nerve agent simulant were observed as key changes to the vibrational spectra.

Keywords: infrared spectroscopy, Raman spectroscopy, organophosphate nerve agent simulant, thioether rhodium complex, diethyl chlorophosphate

1. INTRODUCTION

The extreme toxicity and potency of organophosphate nerve agents (OPNAs) is linked to the rapid reactivity of the phosphorous center with electron-rich species in biological systems, such as water, thiols, or alcohols. Although the Geneva Convention prohibits the use of chemical warfare agents (CWAs) in combat, the use of OPNAs prevails in recent history, including during the Syrian Civil War in 2013, in a 2017 assassination in Malaysia, and in a 2018 murder attempt in the UK.¹⁻³ The devastating impacts of OPNAs may be reduced with fast, sensitive detection methods for these agents.

While several strategies exist for OPNA detection and degradation, the most inexpensive and convenient method is chromogenic detection via M8 and M9 paper. M8 paper contains three sensitive dyes selected to indicate the presence of liquid G and V nerve agents and H blister agents based on a change of color within 30 seconds of exposure. Selective detection of each CWA is achieved by incorporating a pH-sensitive dye that undergoes a distinct color change based on the acidity of the agent. Despite both M8 and M9 paper sharing similar detection mechanisms, M9 paper only contains one indicator dye and does not necessarily differentiate among the agent types. One advantage for using M9 paper, however, is that it may be purchased as a single roll of paper with an adhesive backing that allows it to be attached to clothing or equipment. Although these paper-based chromogenic systems offer rapid detection of CWAs, M8 and M9 paper are susceptible to false positives due to the nature of the pH indicator dyes. Additionally, there is a significant opportunity for developing a reliable chromogenic detection method that achieves high selectivity among competing analytes, sensitivity towards OPNAs, and an immediate response.

Cleavage of phosphate ester bonds plays a fundamental role in the degradation of OPNA compounds and may be exploited for chromogenic detection technology.^{4,5} Guanidine and thioether ligands are selective towards phosphate esters for nucleophilic attack and Rhodium (II) (Rh(II)) centers have a high affinity for binding a variety of neutral and anionic ligands at its electrophilic active site, which causes a colorimetric change that can be used for detection.⁶⁻¹⁰ The exchange of a thioether ligand around the Rh(II) center, initiated with an OPNA, is hypothesized to enable chromogenic detection through the modulation of the electronic properties of the metal complex. Initial work exposing a solution of the Rh(II) complex to an OPNA simulant, diethyl chlorophosphate (DCP), a color change was observed with UV-vis spectroscopy. Following this preliminary experiment, additional characterization is required to confirm the proposed mechanism. Here we report the Fourier transform infrared (FTIR) and Raman spectra of three Rh(II) thioether complexes before and after exposure with DCP.

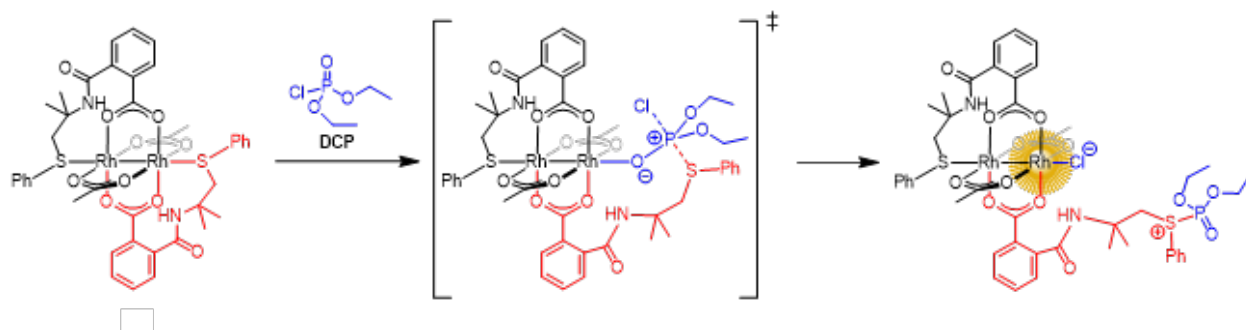


Figure 1. Proposed mechanism of Rh(II) complex with thioether ligand degrading simulant DCP. When the chlorine atom binds to the Rh(II) center replacing the sulfur atom that was there previously, a color change will be observed.

2. METHODS

2.1 Preparation of solutions and samples for spectroscopy measurements

Rh(II) complexes were synthesized at the University of Tennessee, differing in the substituent group attached to the sulfur in the molecular system (Figure 2). They were obtained as a powder and stock solutions of the Rh(II) complexes were prepared (2 mM) in dichloroethane. Thin films for Raman analysis were prepared by placing a stock solution (10 μL) onto a glass slide and then placing the glass slides into a fume hood to allow the dichloroethane to evaporate leaving behind the thin film. Thin films for Fourier transform infrared (FTIR) analysis were prepared by placing aliquots of stock solution (0.3–0.5 μL) directly onto a platinum diamond crystal attenuated total reflectance (ATR) accessory, allowing dichloroethane to evaporate in between placement of the droplets. DCP Raman samples were prepared by pipetting DCP (10 μL) onto a glass slide and analyzing the neat DCP liquid, DCP FTIR samples were prepared by pipetting the neat liquid (15 μL) onto the ATR crystal for analysis.

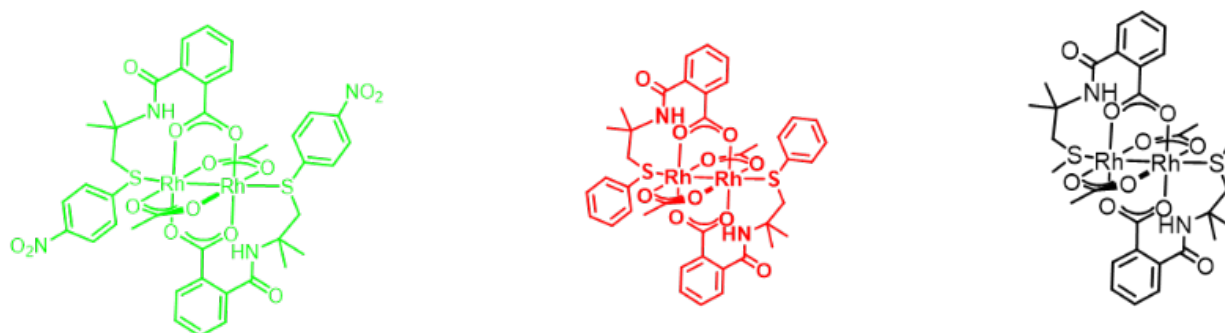


Figure 2. Structures of Rh(II) complexes under investigation: $\text{Rh}_2(\text{OAc})_2(p\text{-NO}_2\text{ArTCB})_2$ (left, green), $\text{Rh}_2(\text{OAc})_2(\text{PhTCB})_2$ (middle, red), and $\text{Rh}_2(\text{OAc})_2(\text{MeTCB})_2$ (right, black).

Post-exposure product solutions were made by pipetting the Rh(II) complex stock solution (200.0 μL) into custom glass dish with volume 700 μL and pipetting neat DCP (6 μL , 100 equivalents) into the Rh(II) complex solution and briefly mixing using the pipette tip (1–5 s). Solutions sat until a color change was observed (5–10 min). Post-exposure samples for Raman analysis were prepared by pipetting the post-exposure solution (10 μL) onto a glass slide and placing it into a vacuum oven set at 25 $^\circ\text{C}$ until all dichloroethane and excess DCP had evaporated from slide leaving a thin film. Post-exposure samples for FTIR analysis were prepared by taking remainder of the product solution in glass dish and placing into vacuum oven at 25 $^\circ\text{C}$ until dichloroethane and DCP had evaporated leaving thin film in the reactor dish. The post-exposure film was re-dissolved in dichloroethane and aliquots of the solution (0.3–0.5 μL) were deposited directly onto ATR crystal for analysis.

2.2 Raman Measurements

Raman spectra of the Rh(II) complex thin film and neat DCP were collected with an Alpha 300R confocal Raman imaging microscope (WITec, Ulm Germany) using a 532 nm excitation laser with 100X microscope objective and 10X objective for thin film and neat DCP analysis, respectively. A UHTS200S_VIS spectrometer (WITec, Ulm

Germany) with a 600 lines mm⁻¹ diffraction grating was used for the Raman measurements. Each spectrum of the pre- and post-exposure Rh(II) complexes was acquired with a 15 second integration time and 0.6 mW laser output in “continuous mode”, in which a 10 x 10 μm spot size was chosen on the thin film preparation and was rastered over by the excitation laser. Spectra were collected throughout the experiment measuring 10 points per line on the image and 10 lines per image for a total of 100 spectra collected. Neat DCP data was collected using an integration time of 15 seconds with five co-added spectra and a laser power of 6 mW. All spectra were averaged with baseline removal and cosmic ray removal performed with the built-in functions in the WITec Project 5.2 version software.

2.3 ATR-FTIR Measurements

ATR-FTIR measurements of the Rh(II) complex thin film and neat DCP were performed using a Bruker Invenio-X FTIR (Bruker, Billerica, MA, USA), with INTEGRAL interferometer and platinum diamond crystal ATR accessory. The spectrometer was continuously purged with ultra-high purity argon during measurements. Spectra were recorded in the mid-infrared (IR) (7500–370 cm⁻¹) and far-IR (680–30 cm⁻¹) ranges averaging 48 scans and 96 scans, respectively, per spectrum acquired with a DTGS detector and a resolution of 2 cm⁻¹. Zinc selenide windows were used for mid-IR measurements while polyethylene windows were used for far-IR measurements. A background spectrum of the clean sampling stage was taken at the beginning of each day and background features were subtracted from the sample spectra automatically during measurements using OPUS 8.7 software (Bruker Optics).

3. RESULTS AND DISCUSSION

Table 1 contains key vibrational assignments for the pre-exposure Rh(II) complexes. The Raman spectra contain low, frequency Rh–O stretching bands present in all three systems in addition to a very intense, sharp band around 310 cm⁻¹ representing Rh – Rh stretch of the complexes (Figure 3). From 500 cm⁻¹ to 900 cm⁻¹ the complexes share features attributable to the acetate, amide, and sulfide moieties present in the structures. The Rh₂(OAc)₂(PhTCB)₂ and Rh₂(OAc)₂(*p*-NO₂ArTCB)₂ derivatives can be differentiated based on the unique bands arising from the phenyl and *p*-NO₂ phenyl moieties. All the systems contain carbonyl stretching and C–H stretching in the 1570 cm⁻¹ and 3000 cm⁻¹ regions, respectively. As seen in the Raman spectra, the three Rh(II) complexes feature similar band structures in the FTIR spectra but feature unique bands due to the presence of the additional phenyl ring and the *p*-NO₂ substitution of the additional ring. The 500 cm⁻¹–1000 cm⁻¹ regions of all spectra contain bands attributed to the acetate functionality, deformation of a phenyl ring, and phenyl C–H wagging. Above 1000 cm⁻¹, the Rh₂(OAc)₂(MeTCB)₂ and Rh₂(OAc)₂(MeTCB)₂ exhibit similar vibrational structure while the main differences arise from very strong NO₂ features in the Rh₂(OAc)₂(*p*-NO₂ArTCB)₂ complex. In the 3000 cm⁻¹–3500 cm⁻¹ regions, there are –H and N–H stretching bands observed in all the complexes.

Table 1. Raman and IR assignments for pre-exposure Rh(II) complexes. Abbreviations used in this table: vs, very strong; s, strong; m, medium; w, weak; vw, very weak; sh, sharp; br, broad; γ, out-of-plane distortion; δ, in-plane distortion; δ_s, scissor; τ, torsion; υ, stretching; ω, wag; ρ, rock; σ, symmetric; and as, antisymmetric.

Rh ₂ (OAc) ₂ (<i>p</i> -NO ₂ ArTCB) ₂				Rh ₂ (OAc) ₂ (PhTCB) ₂				Rh ₂ (OAc) ₂ (MeTCB) ₂			
Raman (cm ⁻¹)	Assignment	IR (cm ⁻¹)	Assignment	Raman (cm ⁻¹)	Assignment	IR (cm ⁻¹)	Assignment	Raman (cm ⁻¹)	Assignment	IR (cm ⁻¹)	Assignment
1575 vs,sh	ν _{as} (NO ₂), ν(C=C, phenyl)	3400 vw,br	ν(N-H)	1596 m	ν(C=C, phenyl)	3415 vw,br	ν(N-H)	1593 m	ν(C=C, phenyl)	3290 m,br	ν(N-H)
1334 vs,sh	ν ₂ (NO ₂)	3300 vw,br	ν(N-H)	1578 s	ν(C=C, phenyl)	3310 vw,br	ν(N-H)	1575 m	ν(C=C, phenyl)	1653 s	ν(C=O)
1109 s	ν(C-NO ₂), phenyl breathing	1651 m	ν(C=O)	1157 vw	ν(C=O)	1661 m	ν(C=O)	1156 w	ρ(CH ₃), ρ(C-H, phenyl)	1639 s	ν(C=O)
1087 s	ν(C-H, phenyl)	1603 w	ν(C=O)	1080 m,sh	ρ(C-H, phenyl)	1605 m,sh	ν _{as} (OCO)	1038 m	ν(C-C)	1604 m,sh	ν _{as} (OCO)
1038 vw	ρ(C-H, phenyl)	1589 s,sh	ν _{as} (OCO)	1036 m	ρ(C-H, phenyl)	1590 s,sh	ν _{as} (OCO)	941 w	ν(C-C)	1589 s,sh	ν _{as} (OCO)
942 w	ν(C-C)	1576 s,sh	ν _{as} (OCO)	1023 m	ρ(C-H, phenyl)	1574 m,sh	ν _{as} (OCO)	850 m	δ _s (OCO)	1576 m,sh	ν _{as} (OCO)
854 m	δ ₂ (ONO), δ ₂ (OCO)	1515 s	ν _{as} (NO ₂), ν(C=C, phenyl)	997 s,sh	δ(C-C-C trigonal, phenyl)	1439 m	ν ₂ (OCO), δ _{as} (CH ₃)	361 w	ν(Rh-O)	1440 m	ν ₂ (OCO), δ _{as} (CH ₃)
723 m	ω(ONO), ν(C-S)	1440 m	ν ₂ (OCO), δ _{as} (CH ₃)	310 vs,sh	ν(Rh-Rh)	1403 vs	δ _{as} (CH ₃)	310 vs,sh	ν(Rh-Rh)	1406 vs,sh	δ _{as} (CH ₃)
402 w	ρ(NO ₂)	1402 vs	δ _{as} (CH ₃)	264 vw	ν(Rh-O)	804 w	ω(C-H, phenyl), ω(N-H)	1200 m	ρ(CH ₃)-S	790 w	ω(C-H, phenyl), ω(N-H)
311 vs,sh	ν(Rh-Rh)	1339 vs,sh	ν ₂ (NO ₂)			788 w	ω(C-H, phenyl), ω(N-H)	751 m	ω(C-H, phenyl)	751 m	ω(C-H, phenyl)
263 vw	ν(Rh-O)	1089 m	ρ(C-H, phenyl)			750 m	ω(C-H, phenyl)	699 s	δ ₂ (OCO)	699 s	δ ₂ (OCO)
		853 s,sh	δ ₂ (NO ₂)			698 s	δ ₂ (OCO)				
		743 m	ω(C-H, phenyl)								
		698 s	δ ₂ (OCO)								

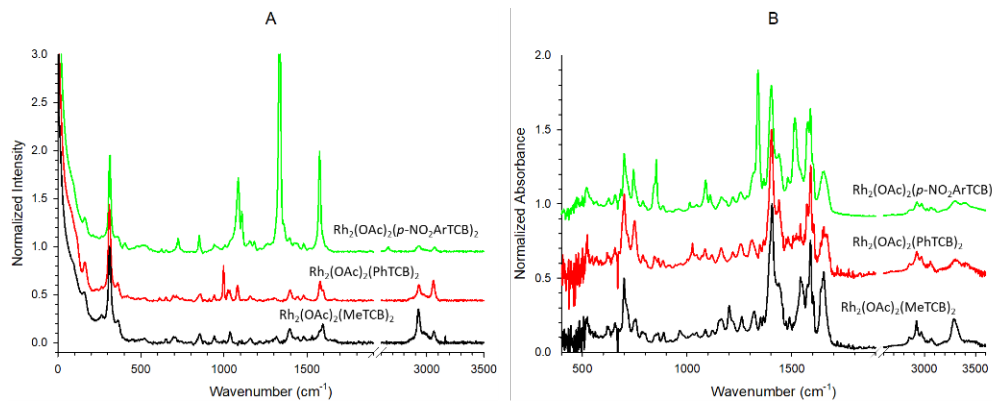


Figure 3. A) Raman and B) ATR-FTIR spectra of the pristine Rh(II) complexes.

Prior to exposure experiments, the structure of DCP was similarly studied with Raman and ATR-FTIR spectroscopy (Figure 4) with vibrational assignments in Table 2. The Raman and ATR-FTIR spectra contain bands associated with P-Cl stretching (~550 cm⁻¹) and symmetric P-OC₂H₅ stretching (~750 cm⁻¹). The antisymmetric P-OC₂H₅ stretch (~1000 cm⁻¹) is the strongest band in the ATR-FTIR spectrum, while it is only weakly observed in the Raman spectrum. In the region above 1000 cm⁻¹, the Raman and IR spectra exhibit features mainly arising from alkyl vibrations and a P=O stretch between 1200 cm⁻¹ and 1300 cm⁻¹.

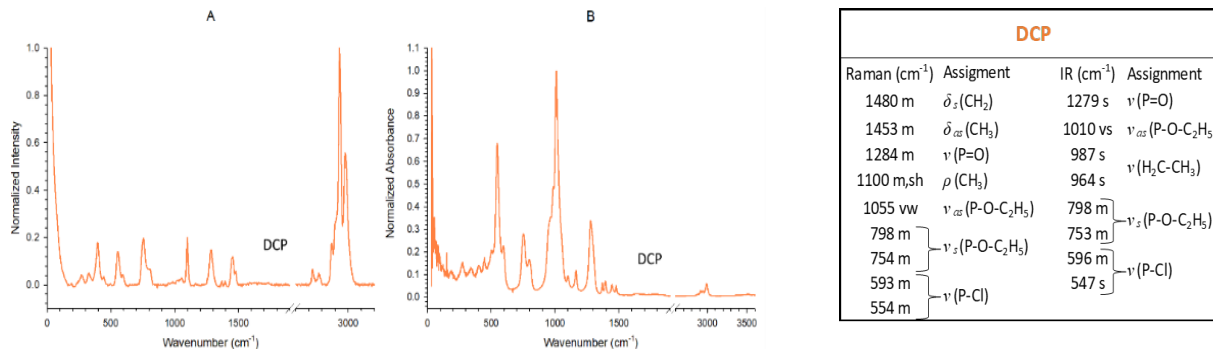


Figure 4. A) Raman, B) ATR-FTIR spectra of DCP, and C) Raman and ATR-FTIR assignments for DCP. Abbreviations are listed in Table 1.

To further probe the proposed mechanism, solutions of the Rh(II) complexes were exposed to DCP (100 equivalents); a distinct color change was observed after 5 to 10 min. The resulting materials were characterized with Raman and ATR-FTIR spectroscopy, Figure 5. The post exposure data clearly contain spectral signatures from DCP and the Rh(II) complexes. In the post-exposure Raman spectra, the C-H stretching from DCP is easily identified. The region between 1000 cm⁻¹ and 1700 cm⁻¹ remained unchanged and contained distinct bands from DCP and the Rh(II) complexes.

Table 3: Raman and IR assignments for post-exposure Rh(II) complexes. Abbreviations are listed in Table 1.

Rh ₂ (Oac) ₂ (ρ-NO ₂ ArTCB) ₂ Post-Exposure Product				Rh ₂ (Oac) ₂ (PhTCB) ₂ Post-Exposure Product				Rh ₂ (Oac) ₂ (MeTCB) ₂ Post-Exposure Product			
Raman (cm ⁻¹)	Assignment	IR (cm ⁻¹)	Assignment	Raman (cm ⁻¹)	Assignment	IR (cm ⁻¹)	Assignment	Raman (cm ⁻¹)	Assignment	IR (cm ⁻¹)	Assignment
1575 vs,sh	ν _{as} (NO ₂), ν(C=O)	3404 vw,br	ν(N-H)	1596 m	ν(C=O)	3415 vw,br	ν(N-H)	1596 m	ν(C=O)	3283 vw,br	ν(N-H)
1453 m		3286 vw,br		1579 s,sh		3310 vw,br		1578 m		1723 w	
1395 w	δ _{as} (CH ₂)	1720 vw	ν(C=O)	1452 m	δ _{as} (CH ₂)	1720 vw	ν(C=O)	1478 m	δ _z (CH ₂)	1657 m	ν(C=O)
1338 vs,sh		1651 w		1287 m		1657 m		1452 s		δ _{as} (CH ₂)	
1287 m	ν(P=O)	1603 vw	ν _{as} (OCO)	1095 m	ρ(CH ₃)	1605 m	ν _{as} (OCO)	1287 m	ν(P=O)	1590 m	ν _{as} (OCO)
1102 s,sh	ρ(CH ₃), ν(C=C, phenyl)	1590 m		1077 s,sh		1591 s		ν _{as} (OCO)		1160 w	
1081 vs,sh	ν(C=C, phenyl)	1576 m	ν(C=C phenyl)	1039 m,sh	ν(C=C phenyl)	1574 m	ν _z (OCO), δ _{as} (CH ₂)	1096 s,sh	ρ(CH ₃)	1443 m	ν _z (OCO), δ _{as} (CH ₂)
1038 w		1516 m		1022 m,sh		1441 m		1403 s		δ _{as} (CH ₂)	
997 w	δ _z (OCO)	1401 s	δ _{as} (CH ₂)	996 s,sh	ν _z (P-O-C ₂ H ₅)	1403 s	δ _{as} (CH ₂)	1038 m	ν _z (P-O-C ₂ H ₅)	1396 s	ν(P=O)
850 m,sh		1339 s,sh		801 m		1277 s,br		753 w		ν(P=O)	
802 m	ν _z (P-O-C ₂ H ₅)	1260 s,br	ν(P=O)	753 w	ν _{as} (P-O-C ₂ H ₅)	1030 vs	ν _{as} (P-O-C ₂ H ₅)	341 vs,br	ν(Rh-Rh)	1029 vs	ν _{as} (P-O-C ₂ H ₅)
753 vw		1025 vs		330 vs,br		981 vs		297 vs,br		977 vs	
723 m	ν(C-S)	976 vs	ν(H ₂ C-CH ₃)	293 vs,br	ν(Rh-Rh)	943 vs	ν(H ₂ C-CH ₃)	943 vs	ν(H ₂ C-CH ₃)	943 vs	ν(H ₂ C-CH ₃)
401 vw	ν(NO ₂)	942 vs		804 m		804 m		818 m			
333 vs,br	ν(Rh-Rh)	802 m	ω(C-H Phenyl), ω(N-H)	789 m	ω(C-H Phenyl), ω(N-H)	789 m	ω(C-H Phenyl), ω(N-H)	801 m	ν _z (P-O-C ₂ H ₅)	801 m	ν _z (P-O-C ₂ H ₅)
294 vs,br		744 m		744 m		751 m		754 m			
		698 m	δ _z (OCO)			698 s	δ _z (OCO)			699 m	δ _z (OCO)

Exposure to DCP created several noticeable changes to the Raman bands of the Rh(II) complexes and DCP below 1500 cm^{-1} . First, the Rh–Rh band shifted from approximately 310 cm^{-1} to 295 cm^{-1} and appears to have broadened. This red-shift is consistent with the resulting Rh(II) complex being bound to a more electronegative atom, such as chlorine. The broadening of the Rh–Rh band may indicate a range of Rh–Rh bond lengths, which could be linked to a loss of crystallinity after exposure, as opposed to the pre-exposure Rh–Rh band shape which was very sharp indicating a well-defined bond length that may have been supported by the long-range structure and order of the crystalline Rh(II) complexes. Second, the P–Cl stretch (550 cm^{-1}) of DCP disappeared indicating the chlorine atom acted as a leaving group and there is no longer a P–Cl bond present in the system. Third, the P=O stretch (1284 cm^{-1}) also changed significantly by broadening and there appears to be a new band near 690 cm^{-1} that occurs in each post-exposure Raman spectra. The $\text{Rh}_2(\text{OAc})_2(\text{PhTCB})_2$ and $\text{Rh}_2(\text{OAc})_2(p\text{-NO}_2\text{ArTCB})_2$ post-exposure complexes also have additional new features at 422 cm^{-1} and 620 $\text{cm}^{-1}/514 \text{ cm}^{-1}$, respectively. These additional features could indicate P–O or P–S stretching, more data are needed to confidently assign these bands.

While structural changes to DCP and the Rh(II) complexes after the reaction were observed in both the ATR-FTIR and Raman spectra, there were additional alterations to IR bands. The P=O (1279 cm^{-1}) and N–H (3300 cm^{-1}) stretching bands showed a slight red shift to $\sim 1265 \text{ cm}^{-1}$ and $\sim 3280 \text{ cm}^{-1}$, respectively, and broadening compared to the pre-exposure presentation. This suggests that intramolecular hydrogen bonding may be occurring between the P=O group of DCP and the N–H group of the Rh(II) complexes. There were drastic changes to the bands between 950 cm^{-1} and 1050 cm^{-1} , which are ascribed to $\text{H}_2\text{C}-\text{CH}_3$ stretching and $\text{P}-\text{OC}_2\text{H}_5$ antisymmetric stretching bands, respectively. A blue shift in the $\text{P}-\text{OC}_2\text{H}_5$ antisymmetric stretching band of DCP (1010 cm^{-1} to 1030 cm^{-1}) suggests the phosphorous center bonded with an atom less electronegative than chlorine, such as sulfur, which would shift more electron density to the P–O bond. Computational modeling of the reaction products may be required to identify the molecular origins of the red shift in the $\text{H}_2\text{C}-\text{CH}_3$ stretching bands as seen in the Raman spectra, the P–Cl stretching band of DCP disappears in the post-exposure ATR-FTIR spectra, further confirming the presence of the intended reaction products.

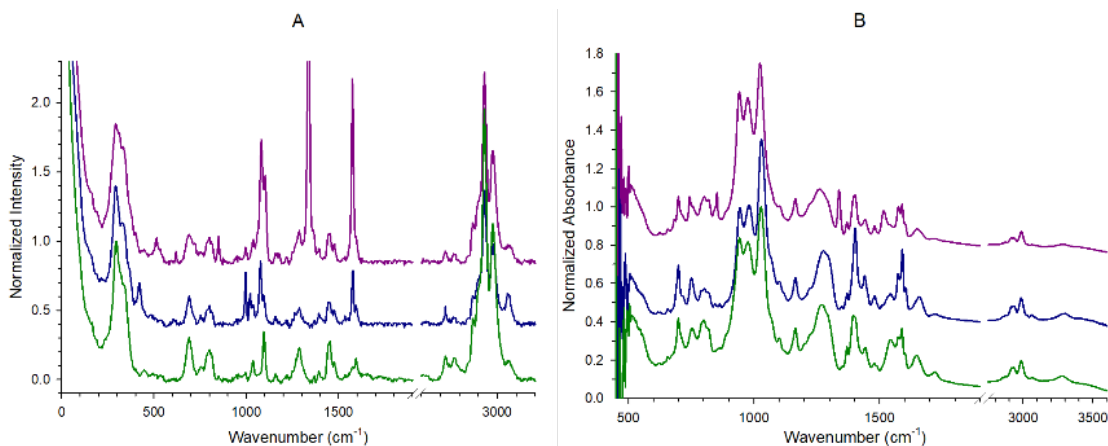


Figure 5. A) Raman and B) ATR-FTIR spectra of the post-exposure Rh(II) complexes.

4. CONCLUSIONS

This work describes progress towards a novel chromogenic detection system for organophosphate nerve agents using thioether-functionalized Rh(II) complexes. Previous results under this objective confirmed a distinct color change of the Rh(II) complex within minutes after exposure to a simulant, diethyl chlorophosphate (DCP). Efforts discussed here aimed to elucidate key structural motifs of the metal complex after exposure to the simulant using Raman and FTIR spectroscopic techniques. Several distinct changes in the vibrational band structure of the Rh(II) complexes and DCP following exposure supported the proposed mechanism, which serves as the basis for the chromogenic detection mechanism. This evidence includes the distortion of the Rh–Rh stretching bands in Raman, the distortion of the P–OCH₃ stretching bands of DCP in FTIR, and disappearance of the P–Cl bond present in DCP seen with Raman and ATR-FTIR. Future experimentation seeks to study the chemistry of the phosphorous atom using ³¹P-NMR spectroscopy, expand capabilities to identify Rh–Cl stretching behavior in the far-IR region, assess crystallinity throughout the reaction with powder X-ray diffraction, and investigating the impact of substituting the sulfur atom of the Rh(II) complex with selenium.

ACKNOWLEDGMENTS

Funding was provided by the Director, Combat Capabilities Development Command Chemical Biological Center under the authorities and provisions of Section 2363 of the FY 2018 NDAA to develop new technologies, engineer innovations, and introduce game-changing capabilities.

REFERENCES

- [1] Nepovimova, E.; Kuca, K. The History of Poisoning: From Ancient Times Until Modern Era. *Arch. Toxicol.* **2019**, *93*, pp 11–24.
- [2] Pitschmann, V. Overall View of Chemical and Biochemical Weapons. *Toxins.* **2014**, *6*, pp 1761–1784.
- [3] Franca, T.; Kitagawa, D.; Cavalcante, S.; da Silva, J.; Nepovimova, E.; Kuca, K. Novichoks: The Dangerous Fourth Generation of Chemical Weapons. *Int. J. Mol. Sci.* **2019**, *20*, p 1222.
- [4] Emsley, J.; Hall, D. *The Chemistry of Phosphorus*, Harper & Row, London, **1976**.
- [5] Moon, S.; Liu, Y.; Hupp, J. T.; and Farha, O. K. *Angew. Chem. Int. Ed.* **2015**, *54*, pp 6795–6799.
- [6] Menegon, G.; Loos, M.; Chaimovich, H. Ab Initio Study of the Thiolytic of Trimethyl Phosphate Ester in the Gas Phase. *J. Phys. Chem. A.* **2002**, *106*, pp 9078–9084.
- [7] Fu, X.; Tan, C. Mechanistic Considerations of Guanidine Catalyzed Reactions. *Chem. Commun.* **2011**, *47*, pp 8210–8222.
- [8] Arantes, G.; Chaimovich, H. Thiolytic and Alcoholysis of Phosphate Tri- and Monoesters with Alkyl and Aryl Leaving Groups. An ab Initio Study in the Gas Phase. *J. Phys. Chem. A.* **2005**, *109*, pp 5625–5635.
- [9] Anderson, B.G.; Cressy, D.; Patel, J.J.; Harris, C.F.; Yap, G.; Berry, J.F.; Darko, A. *Inorg. Chem.* **2019**, *58*, pp 1728–1732.
- [10] Ying, W.; Kim, S.; Lee, M.; Go, N.; Jung, H.; Ryu, S.; Lee, B.; Lee, K. Toward a Detoxification Fabric Against Nerve Gas Agents: Guanidine-Functionalized poly[2-(3-butenyl)-2-oxazoline]/Nylon-6,6 Nanofibers. *RSC Adv.* **2017**, *7*, pp 15246–15254.
- [11] Esteban, J.; Ros-Luis, J.; Martinez-Manez, R.; Marcos, M.; Moragues, M.; Soto, J.; Sancenon, F. Sensitive and Selective Chromogenic Sensing of Carbon Monoxide by Using Binuclear Rhodium Complexes. *Angew. Chem. Int. Ed.* **2010**, *49*, pp 4934–4937.
- [12] Hirva, P.; Esteban, J.; Lloret, J.; Lahuerta, P.; Perez-Prieto, J. Determination of Equilibrium Constants and Computational Interaction Energies for Adducts of $[\text{Rh}_2(\text{RCO}_2)_{4-n}(\text{PC})_n]$ ($n=0-2$) with Lewis Bases. *Inorg. Chem.* **2007**, *46*, pp 2619–2626.
- [13] Berry, J. F. The Role of Three-Center/Four-Electron Bonds in Superelectrophilic Dirhodium Carbene and Nitrene Catalytic Intermediates. *Dalton Trans.* **2012**, *41*, pp 700–713.
- [14] Socrates, G. *Infrared and Raman Characteristic Group Frequencies: Tables and Charts*; John Wiley & Sons, LTD: West Sussex, **2001**.
- [15] Lin-Vien, D.; Colthup, N. B.; Fateley, W. G. and Grasselli, J. G. *The Handbook of Infrared and Raman Characteristic Frequencies of Organic Molecules*; Academic Press Inc: San Diego, **1991**.
- [16] Clark, R.J.H.; Hempleman, A.J. Infrared and Raman Spectroscopy of the Dirhodium Tereacetate Complexes $\text{Rh}_2(\text{O}_2\text{CCH}_3)_4$, $\text{Rh}_2(^{18}\text{O}_2\text{CCH}_3)_4$, $\text{Rh}_2(\text{O}_2\text{CCD}_3)_4$, and $\text{Rh}_2(\text{O}_2\text{CCH}_3)(\text{H}_2\text{O})_2$. *Croat. Chem. Acta.* **1988**, *61*, pp 313–329.

Utilizing bioprinting technology to develop a 3D *in vitro* liver model

Priscilla E. Lee^{a*}, Dylan H. Fudge^b, Bradley R. Ruprecht^a, James D. Severtsen^a

^aU.S. Army Combat Capabilities Development Command Chemical Biological Center, Research & Operations Directorate, 8198 Blackhawk Rd., Aberdeen Proving Ground, MD 21010

^bDefense Threat Reduction Agency, 8725 John J Kingman Rd. #6201, Fort Belvoir, VA 22060

ABSTRACT

The field of bioprinting holds great potential for developing in-house, customizable organ models that would contribute to U.S. Army Development Command Chemical Biological Center's predictive toxicology effort. Bioprinting technology combines traditional additive manufacturing techniques with living cells to create physiologically relevant structures. This project used an Allevi 1 bioprinter housed in the Makerspace laboratory that had not been utilized for any prior projects. As a proof of concept, a liver model was developed using the Allevi 1 system and a human liver cell line. The bioprinter parameters were troubleshot and optimized for liver cells and biosupport materials. HepG2 cells and Pluronic F-127 were combined to serve as the bioink for the three-dimensional *in vitro* model. To ensure liver cell viability and functionality after printing, a live/dead assay was utilized. Confocal microscopy was used to confirm the bioprinted liver cells were metabolically active and maintained their structure after printing. This project was the first bioprinting effort at U.S. Army Development Command Chemical Biological Center and yielded successful results with a vast potential for future research harnessing this technology.

Keywords: Bioprinting, *in vitro* model, liver, Pluronic F-127, HepG2

1. INTRODUCTION

1.1 Bioprinting technology

Bioprinting technology combines traditional three-dimensional (3D) techniques with living cells to create physiologically relevant models.¹ Rather than using inorganic materials, bioprinters construct structures by printing one layer of cells at a time while maintaining both cell viability and functionality.² By combining additive manufacturing methods with the biological aspect, bioprinting holds a great potential for developing customizable *in vitro* organ models. The Makerspace laboratory houses an Allevi 1 bioprinter that had not been utilized prior to this project. This bioprinter features one CORE™ extruder that controls the printing of the cells with a platform that can hold various bases, such as a petri dish or 6-well plate. The Allevi 1 is controlled by Bioprint Essential software (Allevi), which importantly allows a wireless connection to the bioprinter's network. This allows control of the bioprinter from outside the biosafety cabinet.

1.2 Pluronic F-127

Pluronic F-127 (pf127) is a nonionic copolymer that exhibits unique biomaterial properties for bioprinting applications.³ The material itself has low toxicity, reverse thermal gelation properties, and is biologically inert for a variety of cells.⁴ The material is in a liquid aqueous phase at colder temperatures and a solid phase at warmer temperatures, ideally suiting this biomaterial for bioprinting technologies. Past studies have found that pf127 forms an adequate gel around 20–30 °C during printing and can maintain its printed structure at 37 °C.⁶ The proportions (weight/volume) of pf127 have also been well studied in the literature for tissue engineering applications.⁵ Typically, pf127 is used in concentrations from 10 % to 40 % (w/v) for bioprinting purposes.⁴ Due to its availability and ease of use, pf127 was selected for developing the bioprinted liver model.

2. METHODOLOGY

2.1 Computer aided design of the models

SOLIDWORKS® computer aided design (CAD) software was used for the design of the various bioprinted models. As a base model, a 7 x 7 x 2 mm³ cube was developed to initiate bioprinting efforts. The total volume of this cube design is ~100 mm³ for a standard measurement, which also equates to 100 microliters. This model was also scaled up by a factor of 10, yielding ~1000 mm³ or 1 mL volume cube. When bioprinting the designs, the infill is another parameter that can be altered depending on the size and design of the print.

2.2 Bioprinting with pf127

Prior to this project, the settings and functions of the bioprinter had not yet been explored. The printer extruder controls both the temperature and pressure of the material being dispersed, which also is impacted by the needle attached on the extruder (smaller or larger gauge needs will alter pressures and affect shear force on cells). The software also lets the user select features such as layer height, print speed, infill distance, and direction. All of these settings must be characterized for each type of biomaterial used for printing and cell types being used. Prior to incorporating cells, the parameters for the pf127 had to be optimized and validated. The pf127 available was 40 % weight/volume (w/v) in deionized water and purchased from Allevi.

2.3 Cell culture

Cells from the HepG2 human liver cell line (ATCC) were thawed and expanded in tissue culture flasks. Eagle’s Minimum Essential Medium (EMEM, ATCC) was supplemented with 10 % Fetal Bovine Serum (FBS, ATCC) for cell maintenance. Cells were passaged on a weekly basis once confluence reached 70 % and fresh medium was exchanged every 2-3 days. For the bioprinting, HepG2 cells were passaged and reconstituted to the desired concentration in cell medium.

2.4 Bioprinting HepG2 cells with Pluronic F-127

There have been no previous studies focused on bioprinting models with HepG2 cells with pf127. Thus, the first step was to find the optimal ratio of HepG2 cells and media to F157 for functional bioprinting. The ratios of cells to pf127 were tested at 1:2, 1:4, 1:6, and 1:8 for printability. Approximately 5 x 10⁵ HepG2 cells/mL were prepared with each ratio of pluronic and mixed on ice. Once the mixture had become fully aqueous, it was transferred into a 10 mL syringe with a 30-gauge plastic needle tip. The bioprinter settings shown in Table 1 were used for testing the printing various ratios. It was discovered that the 1:6 ratio was optimal for bioprinting HepG2 cells and pf127 (40% w/v). The lower ratios (1:2 and 1:4) were too liquid to print and the higher ratio (1:8) was too densely solid to extrude material.

Table 1. Bioprinting settings for pf127.

Feature	Setting
Layer Height	0.2 mm
Print Speed	6 mm/s
Infill Type	Grid
Infill Distance	1 mm
Direction	0 degrees
Temperature	4 °C
Pressure	40 psi
Needle Type	¼ inch and 30 gauge
Build Plate	100 mm ³ Petri Dish

2.5 Live/dead assay

To determine cell viability after printing, LIVE/DEAD® Viability/Cytotoxicity Kit assays (Invitrogen, Carlsbad, CA, USA) were used. Using a modified protocol from Forsythe et al.,⁵ prior to printing, the cells were spun down into a pellet. The cell pellet was washed with phosphate buffered saline (PBS) and spun at 1200 g for 5 minutes. This was repeated three times. The pellet was then mixed with 2 mL of PBS and two dyes were added: 2.0 μM calcein AM (emission wavelength at 520 nm), and 4 μM ethidium homodimer (emission wavelength at 603 nm). The solution was allowed to incubate for 30 minutes at room temperature.⁵ After incubation, the cells were washed and spun down under the same conditions as the initial wash for a total of three times. Following staining, the cells were bioprinted into structures for imaging by microscopy. The ethidium bromide (EB) fluoresces in the red spectrum, representing the dead cells and the calcein AM green staining represents the metabolically live cells.⁵ EB indicates cell death as it is not able to diffuse unless the cell membrane is damaged or compromised. Calcein AM is a widely used live cell stain as nonfluorescent calcein AM converts to a green, fluorescent calcein through acetoxymethyl ester hydrolysis; dead cells lack esterase activity which makes calcein AM a useful live cell stain. The images were taken with the Keyence BZ-X Fluorescence Microscope which encompasses brightfield and fluorescent imaging settings (confocal microscope).

2.6 Maintenance of the bioprinted structure

The bioprinted model was kept in a sterile petri dish and maintained in a cell culture incubator at 37 °C, 5 % CO₂, and 90 % relative humidity. These conditions served a dual purpose to simulate the conditions the biostructures will be exposed to for storage and to prevent evaporation and contraction of the pluronic structures due to drying out. When printing with cells, these conditions are required to maintain living metabolically active cells. Media changes were attempted every 2–3 days, but there were issues with the bioprinted structure integrity after adding fresh media. This could be further investigated in a future follow up study.

3. RESULTS

3.1 Bioprinted models

Once the settings were optimized, the models were able to be printed and visualized. Prior to analyzing the models on the microscope, images of the physical models were taken, shown in Figure 1. The two models had approximately a ten-fold difference in volume.



Figure 1. Bioprinted liver models: 100 mm³ (left) and 1000 mm³ (right).

We investigated if the customizable bioprinted models would hold structural integrity with using pf127 over time. Brightfield images were taken of the bioprinted model for 35 days using the Keyence microscope at 4X magnification. As shown in Figure 2, the model retained its structural integrity while under cell culture conditions.

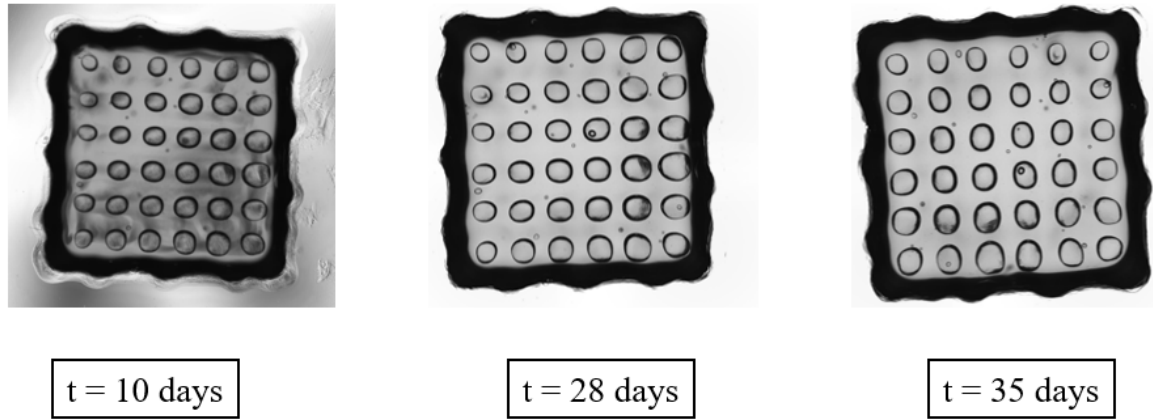


Figure 2. Images (4X magnification) of the 100 mm³ bioprinted liver model at three different time points spanning 35 days.

3.2 Live/dead assay

As described in the methods section 2.5, the cells were stained to ascertain cell viability prior to mixing with pf127 and to printing. Prior to bioprinting, the cells were imaged for live/dead staining and images were taken at 4X magnification using the Keyence microscope (Figure 3).

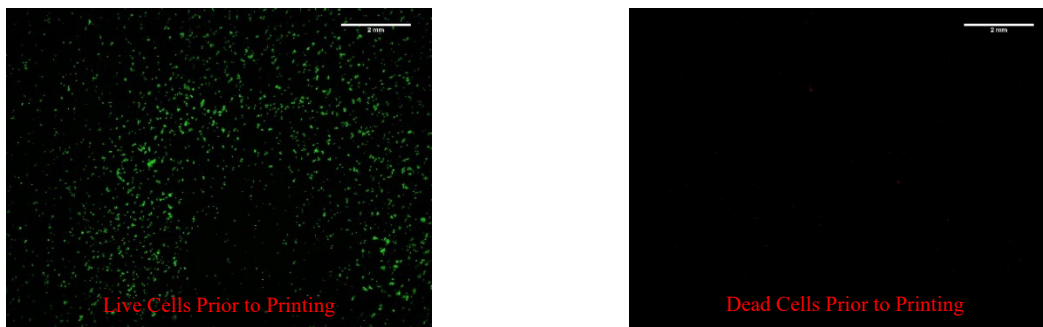
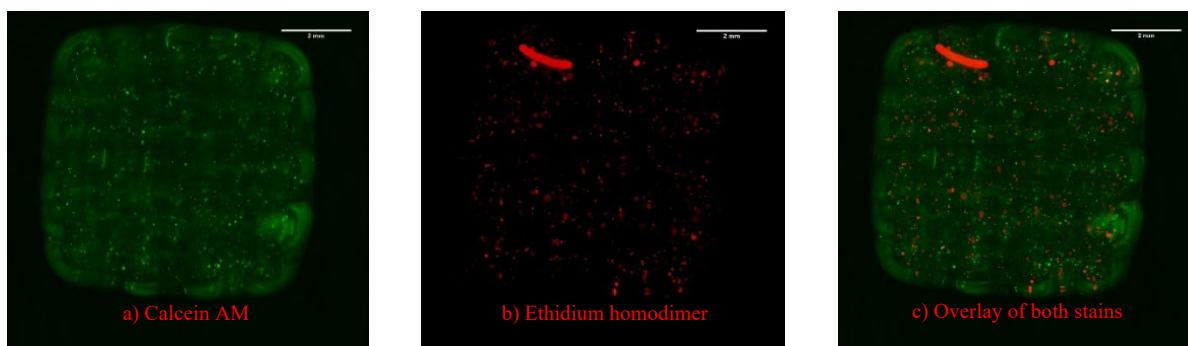


Figure 3. Stained HepG2 cells prior to bioprinting at 4X magnification. Calcein AM staining was used to represent live cells (a) and ethidium homodimer was used to represent dead cells (b). The scale bars represent a length of 2 mm.

These cells were qualitatively evaluated and showed ~95 % viability before being prepared for bioprinting. Immediately after printing, the models were imaged on the Keyence microscope (Figure 4) and then placed in a cell culture incubator. The pf127 material is slightly auto fluorescent; however, the signal from the calcein AM stain is clearly present, indicating the presence of live cells throughout the bioprinted structure (Figure 4a). The ethidium homodimer staining (Figure 4b) is indicative of dead cells which are present. Although by comparing the live cells and the dead cells using an overlaid image (Figure 4c) of the two fluorescent channels shows there are more live cells than dead following bioprinting. Fluorescent microscopy quantitative analysis showed ~70 % cell viability after the printing process. In a future study, a quantitative method such as running an LDH based assay with cells prior to plating and then after dissolving the bioprinted structure could be implemented for cell viability comparison. Cell death was expected as the cells underwent mechanical stress from being extruded from the printer and dramatic temperature shifts when mixing the cells with the pluronic. As a result, a bioprinted liver model has been produced through this work and validated to contain viable liver cells immediately after printing.

Figure 4. The 100 mm³ liver model imaged with calcein AM (a), ethidium homodimer (b), and both stains overlaying (c).



Scale bar represents 2 mm.

3.3 Customizing the liver model

A unique and extremely beneficial feature of bioprinting is the customizability of each model. Since the models have their own structural support, it is easy for the user to scale their models. To show this, we designed a cube that is 1000 mm³, or 1 mL in volume, a ten-fold increase compared to the original 100 mm³ model. To achieve this volume, the CAD file was designed to be 10 mm x 10 mm x 10 mm. This larger model was printed with the same conditions as in Table 1. Figure 5 shows a bright field image in 4X magnification of the structure for the larger model and the corresponding calcein AM staining, showing live cells.



Figure 5. The upscaled 1000 mm³ liver model, shown by (a) brightfield microscopy and (b) fluorescence microscopy with calcein AM staining in green with 4X magnification. Scale bar represents 5 mm.

4. CONCLUSION

In this study, we have initiated the first bioprinting efforts at U.S. Army Development Command Chemical Biological Center by developing a bioprinted liver cell line model. HepG2 cell survival after printing has been proven with our optimized bioprinting protocol and has provided a foundation to use the Allevi 1 bioprinter. A follow-up study would include characterizing the functionality of the model. There are many future applications that could be developed as a result from this project, including bioprinting a more complex multicellular liver model or expanding into using different cell types such as primary cells for a more physiologically accurate model. DEVCOM CBC currently houses several microphysiological systems where bioprinting would be extraordinarily beneficial. Specifically, adding bioprinted organ models as a tool for ongoing predictive toxicology studies for compounds of interest. Lastly, bioprinting allows the user to customize the model to their own standards rather than relying on industry settings.

ACKNOWLEDGMENTS

Funding was provided by the Director, Combat Capabilities Development Command Chemical Biological Center under the authorities and provisions of Section 2363 of the FY 2018 NDAA to develop new technologies, engineer innovations, and introduce game-changing capabilities. Additional acknowledgements go to the Makerspace laboratory and the Advanced Design Manufacturing team for their assistance and guidance throughout this project.

REFERENCES

- [1] Panda, S.; Hajra, S.; Mistewicz, K.; Nowacki, B.; In-na, P.; Krushynska, A.; Mishra, Y.K.; Kim, H.J. A focused review on three-dimensional bioprinting technology for artificial organ fabrication. *Biomater. Sci.* **2022**, *10*, pp 5054–5080.
- [2] Murphy, S.V.; Atala, A. 3D bioprinting of tissues and organs. *Nat. Biotechnol.* **2014**, *32*, pp 773–785.
- [3] National Center for Biotechnology Information. PubChem Compound Summary for CID 10154203, Pluronic F-127, **2022**. <https://pubchem.ncbi.nlm.nih.gov/compound/Pluronic-F-127> (accessed August 31, 2022).
- [4] Gioffredi, E.; Boffito, M.; Calzone, S.; Giannitelli, S.M.; Rainer, A.; Trombetta, M.; Mozetic, P.; Chiono, V. Pluronic F127 hydrogel characterization and biofabrication in cellularized constructs for tissue engineering applications. *Procedia CIRP.* **2016**, *49*, pp 125–132.
- [5] Forsythe, S.D.; Devarasetty, M.; Shupe, T.; Bishop, C.; Atala, A.; Soker, S.; Skardal, A. Environmental toxin screening using human-derived 3D bioengineered liver and cardiac organoids. *Front. Public Health.* **2018**, *6*, pp 103.
- [6] Cunha-Filho, M.S.S.; Alvarez-Lorenzo, C.; Martínez-Pacheco, R.; Landin, M. Temperature-sensitive gels for intratumoral delivery of β -lapachone: effect of cyclodextrins and ethanol. *Sci. World J.* **2012**, *2012*, pp 126723.

Activated surfaces through aerosolized particle deposition

Monica McEntee*, Gregory Peterson, Christopher Karwacki
U.S. Army Combat Capabilities Development Command Chemical Biological Center, Research
& Operations Directorate, 8198 Blackhawk Rd., Aberdeen Proving Ground, MD 21010

ABSTRACT

In this report, activated textile surfaces were generated by aerosolizing and depositing particles of metal-organic frameworks (MOFs) particles onto unreactive swatches of cellulose/polyester. The capability of these MOF-doped swatches to absorb and decompose chemical warfare agents was probed with two simulants, 2-chloroethyl ethyl sulfide and dimethyl methylphosphonate. Our hypothesis was that aerosolizing and depositing MOF particles onto substrates would create active surfaces that interact with chemical warfare agent simulants and behave similarly to the powdered MOF. Following deposition of the MOF using a simple spray nozzle, the surface and particle morphologies were analyzed using scanning electron microscopy. Textile swatches with deposited MOF particles were then exposed to chemical warfare agent simulants for 1 h, after which the residual species were extracted and characterized with gas chromatography-mass spectrometry. The concentration of reaction products was too low to be detected; however, the MOF-doped swatches did absorb a significant portion of the chemical warfare agent simulants as seen by the decrease in simulant signal by 15–40 % compared to the blank swatches.

Keywords: active, aerosols, surfaces, simulants, metal-organic frameworks

1. INTRODUCTION

Over the past 5 years, our research group set out to develop next-generation materials that could be worn by the warfighter to protect them against toxic industrial chemicals (TICs) and chemical warfare agents (CWAs). These advanced materials are developed in two stages: i) synthesizing the powder material and characterizing its reactivity and ii) incorporating the powder material into the fabric of the uniform or suit that the warfighter would wear on the battlefield.

Our approach focused on generating active surfaces by aerosolizing and depositing reactive, advanced materials onto unreactive surfaces and measuring the reactivity of these activated surfaces towards decomposing or removing CWA simulants. Our hypothesis is that deposited particles will create surfaces that exhibit favorable reactivity toward CWA simulants and act similarly to the powdered form of the base materials. Metal-organic frameworks (MOFs) were chosen as the initial material for this study as they are well researched and characterized. In particular, HKUST-1, NU-1000, and UiO-66 MOFs were chosen as test materials because HKUST-1 has large pores and has proven to be active towards mustard; NU-1000 also has large pores and has been proven to be active against the nerve agent simulant methyl paraoxon; and lastly, UiO-66 has a high surface area. After depositing the particles using a simple spray nozzle, the surface and particle morphologies were analyzed using scanning electron microscopy (SEM). Dose-extraction experiments of CWA simulants, 2-chloroethyl ethyl sulfide (CEES) and dimethyl methylphosphonate (DMMP), was then conducted. The remaining fraction of simulant and any resulting reaction products were identified using gas chromatography-mass spectrometry (GC-MS).

2. EXPERIMENTAL PROCEDURE

2.1 Suspension formation

Each MOF suspension was generated by simply adding solid MOF to methanol in a spray bottle. Each MOF suspension had an approximate concentration of 6 mg/mL.

2.2 SEM imaging

Each MOF suspension was sprayed onto separate pieces of carbon tape situated on gold slides and sprayed 5 times in 15-minute intervals for a total of 1 hour and allowed to dry for several hours (Figure 1). For each aerosolized material, SEM images were taken using a Nanoscience Instruments Phenom Pro SEM at high (8–30 μm) and low (80–100 μm) resolutions.

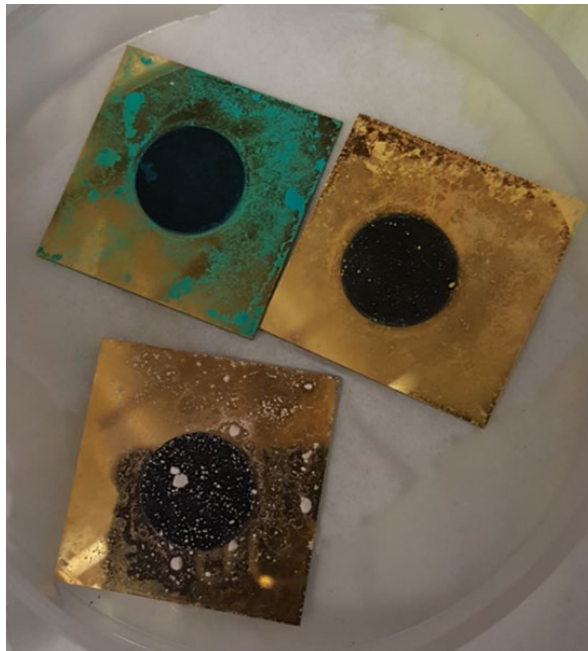


Figure 1. Macroscopic aerosol deposition onto carbon tape. hKUST-1 MOF (top left), NU-1000 MOF (top right), UiO-66 (bottom)³

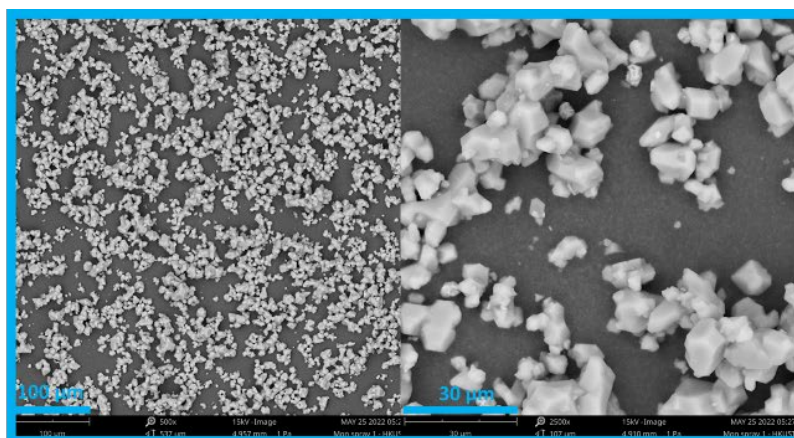
2.3 Dose-extraction

The MOF suspensions were sprayed onto square cellulose/polyester swatches until a visible coverage could be seen visibly and the samples were then allowed to dry for several hours. Additionally, two versions of blank swatches with no MOF doping were studied: the first version contained no MOF but was sprayed with methanol and allowed to dry for several hours; the second version was just a blank swatch with no methanol or MOF added. The neat simulant was dosed onto each swatch (1 μL), including the blank swatches, and allowed to react (1 h), before extracting with acetonitrile. The area under the curve of the largest simulant peak in the GC is recorded as 100% before reaction, and 60 minutes later, the % remaining percentage is recorded. Extracted compounds were analyzed via GC-MS using an Agilent Technologies 5977B MSD detector coupled to a 7890B GC.

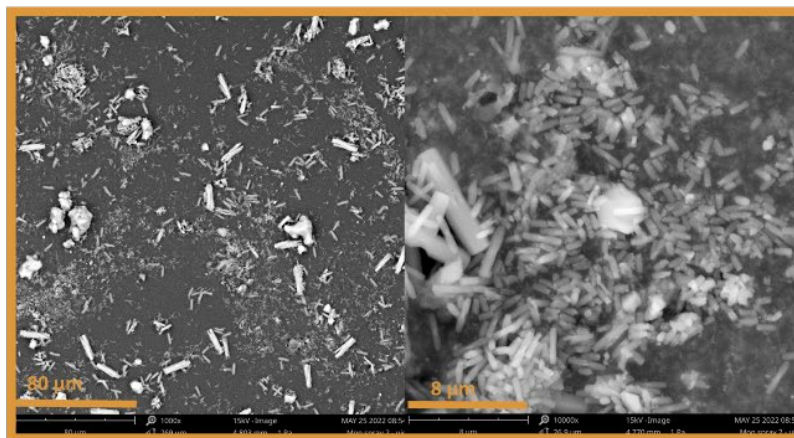
3. CONCEPT & DESIGN

Previous studies from both DEVCOM CBC and external groups reported decontamination sprays composed of $\text{Zr}(\text{OH})_4$ dispersed in aqueous and organic solvents that can be sprayed onto large equipment and effectively degrade simulants. Here we invoked a similar concept to activate surfaces by depositing a MOF suspension, that would retain the capture and degradation capabilities of the powder MOF. Once deposited, we could then dose those MOFs with CWA simulants and then perform dose-extraction on the deposited surfaces to see if any reaction or sorption occurred. We opted to use CWA simulants but intend to test the analogous agents with positive results from these initial proof-of-concept experiments. The selected CWA simulants are CEES and DMMP, which share structural similarities to blister agents and nerve agents, respectively. These simulants provide close physical and chemical properties to their respective CWA counterparts.³

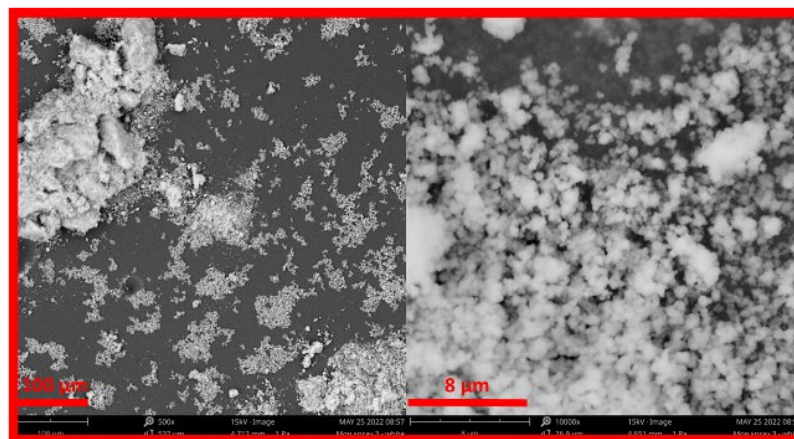
4. RESULTS



HKUST-1

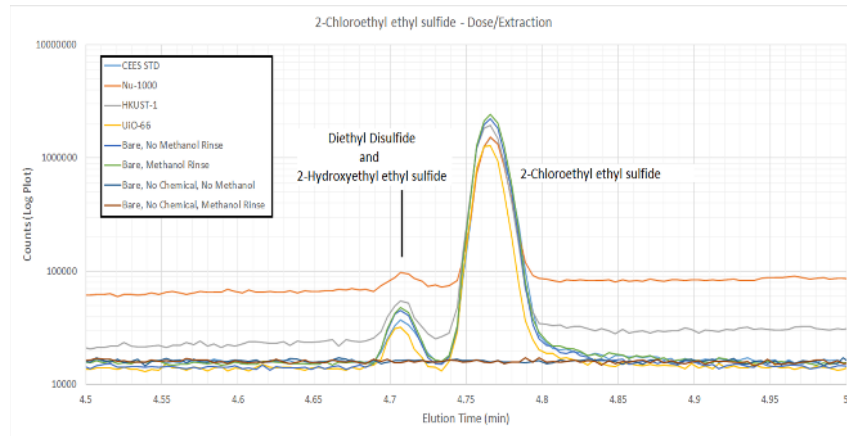


NU-1000

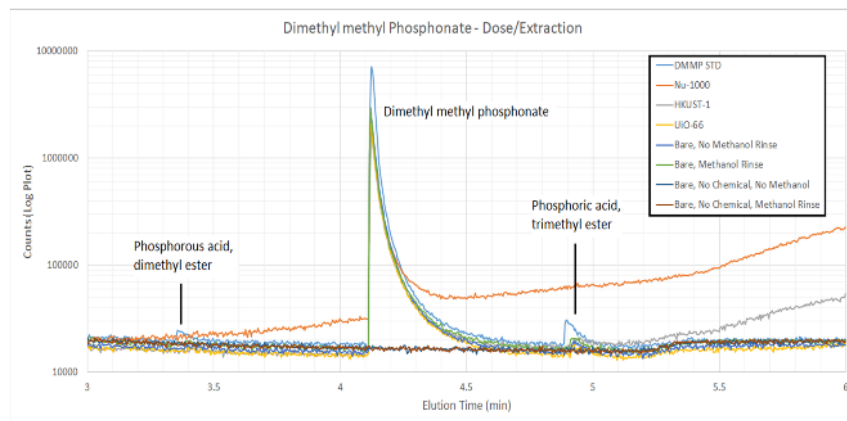


UiO-66

Figure 2. SEM images of Au slide-deposited aerosolized particles. (TOP) HKUST-1 MOF at 1000 μm (top left) and 30 μm (top right) (MIDDLE) NU-1000 MOF at 80 μm (middle left) and 8 μm (middle right) (BOTTOM) UiO-66 at 100 μm (bottom left) and 8 μm (bottom right).



2-Chloroethyl ethyl sulfide Results			
MOF	Integration	% Remaining	% Removed
NU-1000	17028430	61.8	38.2
HKUST-1	23235088	84.4	15.6
UiO-66	14868862	54	46
Bare/No MeOH	26166227	100	0
Bare/MeOH	28919000	100	0



Dimethyl methyl phosphonate Results			
MOF	Integration	% Remaining	% Removed
Nu	35192378	76.3	23.7
HKUST-1	32110526	69.6	30.4
UiO-66	38042283	82.5	17.5
Bare/No MeOH	46604643	100	0
Bare/MeOH	45632878	100	0

Figure 3. GC-MS dose-extraction results for CEES and DMMP on MOFs.

5. DISCUSSION AND CONCLUSIONS

5.1 Aerosol deposition and SEM imaging

The MOFs dispersed relatively easily in methanol and generated good macro-dispersion. Generally, the smaller particles dispersed more effectively. Each MOF showed good micro-dispersion (Figure 2). However, some

clustering/clumping occurred but that was not enough to block visibility of the surfaces. Solvent choice will play an important role when scaling this method up in the future; water or other environmentally friendly solvent should be considered and tested. Additionally, finer MOF particles should be used to generate higher dispersion and reduced aggregation of particulates.

5.2 Dose-extraction

No reaction products were recovered for CEES or DMMP reactions of the treated surfaces; however, loss of both compounds was seen for all MOF covered surfaces (Figure 3). These results suggest these surfaces are useful for, at the very least, sequestration of the investigated CWA simulants. It is interesting to note that no phosphorous acid dimethyl ester or phosphoric acid trimethyl ester for Nu-1000, impurities found in DMMP, could be detected. The lack of impurities indicates Nu-1000 has an affinity for these compounds.

6. FUTURE DIRECTIONS

Although these results are promising, more studies are required that focus on both material type and loading. Other reactive materials, such as metal oxides, are strong candidates for our purposes. Further investigation should be conducted to determine physisorption or chemisorption. Based on this preliminary work, we aim to write a proposal that focuses on other reactive materials and aerosol characterization.

ACKNOWLEDGEMENTS

Funding was provided by the Director, Combat Capabilities Development Command Chemical Biological Center under the authorities and provisions of Section 2363 of the FY 2022 NDAA to develop new technologies, engineer innovations, and introduce game-changing capabilities.

REFERENCES

- [1] Lohmann, U.; Feichter, J. Global indirect aerosol effects: a review. *Atmos. Chem. Phys.* **2005**, *5* (3), pp 715–737.
- [2] McMurry, P.H. A review of atmospheric aerosol measurements. *Atmos. Environ.* **2000**, *34* (12-14), pp 1959–1999.
- [3] DeCoste, J.B.; Peterson, G.W. Metal–organic frameworks for air purification of toxic chemicals. *Chem. Rev.* **2014**, *114* (11), pp 5695–5727.

This page intentionally left blank

DNA extraction on a nano-organosilane coated polymer sheet: a novel, low size, weight, and power idea for field forward biological weapon agent sample prep

Jennifer W. Sekowski* and Daniel Angelini

U.S. Army Combat Capabilities Development Command Chemical Biological Center, Research
& Operations Directorate, 8198 Blackhawk Rd., Aberdeen Proving Ground, MD 21010

ABSTRACT

Extracting nucleic acids with a minimal amount of manipulation from a biological sample is a major gap for field forward biodetection. Current field sample preparation requires multiple reagents, steps, and tubes, complicating the use of these assays in austere or resource-poor environments. Here, we explored a novel use of an organosilane nanoparticle-based printed surface on a flexible polymer tape with the hypothesis that the printed organosilane nanoparticles would serve to puncture microbial cell walls, and the electrochemical interactions within the cell nucleus would release usable nucleic acid. To test this feasibility, we used several approaches to test the bacterial binding and lysing ability of the tape ahead of further tests to extract and amplify DNA directly from nanoparticle chemistry-coated thin, flexible paper or polymer sheet (vs. uncoated polymers) upon which bacteria are applied. Our initial results indicate that the organosilane nanoparticle printed surface of the tape does not bind or lyse *Bacillus anthracis* vegetative cells (attenuated, delta Stern strain) to a significant degree different than the uncoated control polymer tape. Further work is needed to determine whether there is a possibility to extract bacterial DNA from coated and/or standard polymer tape surfaces using standard DNA extraction materials.

Keywords: antimicrobial, tape, DNA, sample preparation, trace collection, forensic collection

1. INTRODUCTION

Activities that depend on critical point detection or forensic evidence collection are dependent upon tools and methods that can provide successful collection and extraction of biological materials, including bacteria and viruses. Collecting bacteria from surfaces and extracting biomolecules that aid in the specific identification of the bacteria, such as DNA, can be a challenging task in austere and remote field forward conditions. Collection of biological materials from surfaces typically involves a wetted cotton, or other polymer, tipped swab and a collection tube filled with a liquid collection medium that aids in the preservation of the DNA ahead of other molecular procedures to extract the DNA. All of those materials and methods are associated with a weight, time and overall logistics burden to the Warfighter that could potentially be alleviated by materials and methods using less water, requiring fewer steps, and that employ multifunctional materials that can combine collection and extraction into one tool, for example.

The goal of this Seedling work is to address this Warfighter need by assessing the potential of a commercial off the shelf (COTS) antimicrobial polymer tape to bind, lyse, and release DNA from the lysed bacteria (Figure 1). The product, “SaferTouch™” (Touch Point Science, Inc.) is not originally designed for this purpose, but is used as a means to keep high touch surfaces (i.e., touch screens, door handles, elevator buttons, etc.) safer by rendering them “clean” by binding and destroying the bacteria and viruses that come into contact with them (Figure 2).

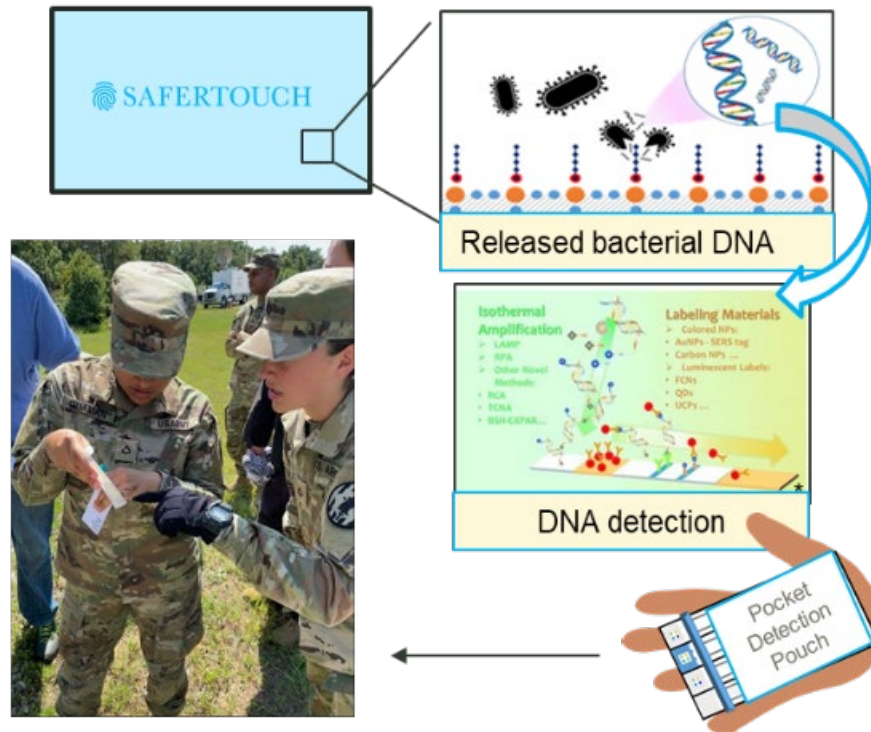


Figure 1. Schematic work using SaferTouch™ coated tape to bind and lyse bacteria, then release DNA for use in downstream, low size, weight, and power (SWAP) applications such as paper-based DNA detection assays in the Pocket Detection Pouch.

Materials such as counter tops, small handles, fabric or concrete require special care to collect a sufficient sample. The majority of research to date for both DNA collection from surfaces has focused on types and methods of swab-based¹⁻³ or tape-based methods.⁴

The work described here investigated a non-adhesive but organo-nanosilane coated tape that is used to prevent transmission of bacteria and viruses from person to person. The bacteria used is a surrogate for a more pathogenic version and is of general interest to the Department of Defense community. *Bacillus anthracis*, sporulation deficient, delta Sterne, lacks the genes necessary for both sporulation and production of the lethal factor that grants the bacteria its high pathogenicity and ability to enter is highly persistent spore state. Fortunately, its cell wall and other cellular properties are much the same as the original. Together, these properties made it an ideal candidate for us to use as a test bacterium in our BSL2 laboratory.

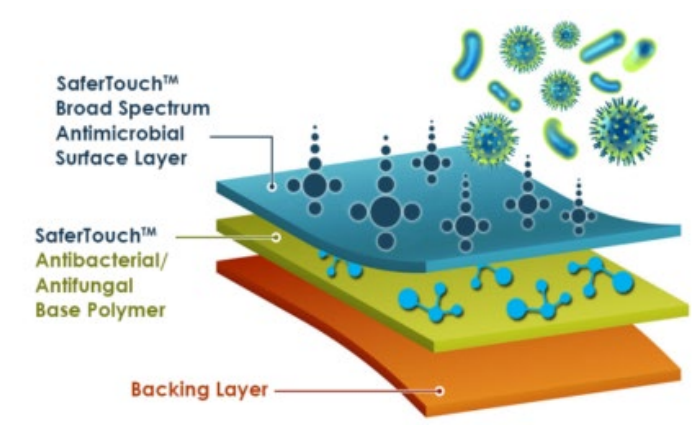


Figure 2. Schematic of SaferTouch™ coated polymer layers.

2. METHODOLOGY

2.1 Preparation of SaferTouch™ tape test sections

Test sections of the Nano-organosilane coated SaferTouch™ tape (ST) and uncoated Control Tape (CT) (Touch Point Science) were cut into 2" by ½" sections and arrayed on a sterile aluminum foil surface inside of a Biosafety Cabinet (Type II) and labeled on the foil only. The adhesive side of the tape was left covered by the paper backing. To prevent any conflation of the two types of similar appearing tape samples, the CT paper backing was marked with a pencil.

2.2 *B. anthracis* sample preparation and application

A colony from a growth Luria Bertani (LB) agar plate containing vegetative *B. anthracis* (delta Sterne spo -/-), was mixed with 10 mL of fresh media, and grown in a filter-capped 50 mL conical tube at 37 °C in a shaker incubator overnight. Once proper growth was confirmed, by checking optical density (OD) at 600 nm, a 1:10 dilution series was created with LB media. 100 µL of each dilution that was equivalent to 10⁵–10⁸ bacteria/mL was carefully arrayed in 10 x 10 µL spots evenly across the top surface of each type of tape in triplicate. LB media was also spotted on test tape sections as a negative control. Tape test sections were allowed to dry completely in the biological safety cabinet for between 1–1.5 hours.

2.3 Determination of the concentration of the *B. anthracis* (delta Sterne spo -/-), culture

Accurate concentration and range finding controls were performed for each of three (3) full experiments. Briefly, 100 µl of each bacterial culture dilution was spread on sterile LB agar Petri dishes in duplicate. Dishes were then incubated at 37 °C in a standard bacterial incubator overnight. Colonies were counted visually, and calculated to reveal the colony number per mL of media present in the samples spotted on the tape test sections.

2.4 Washing of the adhered bacteria on tape test sections

Dried tape test sections from above were added to 1 mL phosphate buffered saline at room temperature in 15 ml conical tubes, and vortexed for 2 minutes at full speed. The liquid, also termed washate, was collected for testing for the presence of bacteria and for DNA. The test tape section was retained in tubes for up to 1 hour before testing for the presence of viable bacteria on LB agar Petri dishes.

2.5 Assessing quantity of recovered DNA from washed surfaces

To determine concentration of any DNA washed off the tapes, liquid from above the above washing method was tested for the presence of released DNA. Briefly, a high sensitivity QUBIT HS (high sensitivity) (Thermo Scientific) DNA quantification kit with a range from 10 pg/µL to 100 ng/µL was used following manufacturer instructions. Following initial negative results (compared to positive control DNA at the low end of the kit sensitivity range), concentration columns and extraction buffer from a DNeasy Mini Kit (Qiagen) was used to concentrate the entire washate from both duplicates. This resulted in concentrating the combined duplicate samples to slightly less than 2 mL of sample to 35 µL samples, a factor of approximately 57x concentration. This was done for each concentration and each type of tape. After the concentration steps, the QUBIT HS DNA quantification kit, was used again to quantify any DNA present in the concentrated washate.

2.6 Assessing quantity of recovered bacteria from washed surfaces

To determine quantity of any bacteria washed off the tapes, paper backings, or stainless-steel plate, liquid from above washing method was tested for the presence of released bacteria. Briefly, the entire 1 mL washate from each surface sample was spotted on an LB agar Petri dish and incubated at 37 °C in a standard bacterial incubator overnight. Growth was visually inspected.

2.7 Assessing viability of remaining bacteria on tape test sections

To determine the viability of any remaining bacteria adhering to the washed tape test sections or paper backings, each washed surface was placed "face down" on a sterile LB agar Petri dish and incubated at 37 °C in a standard bacterial incubator overnight. Growth was visually inspected.

3. RESULTS

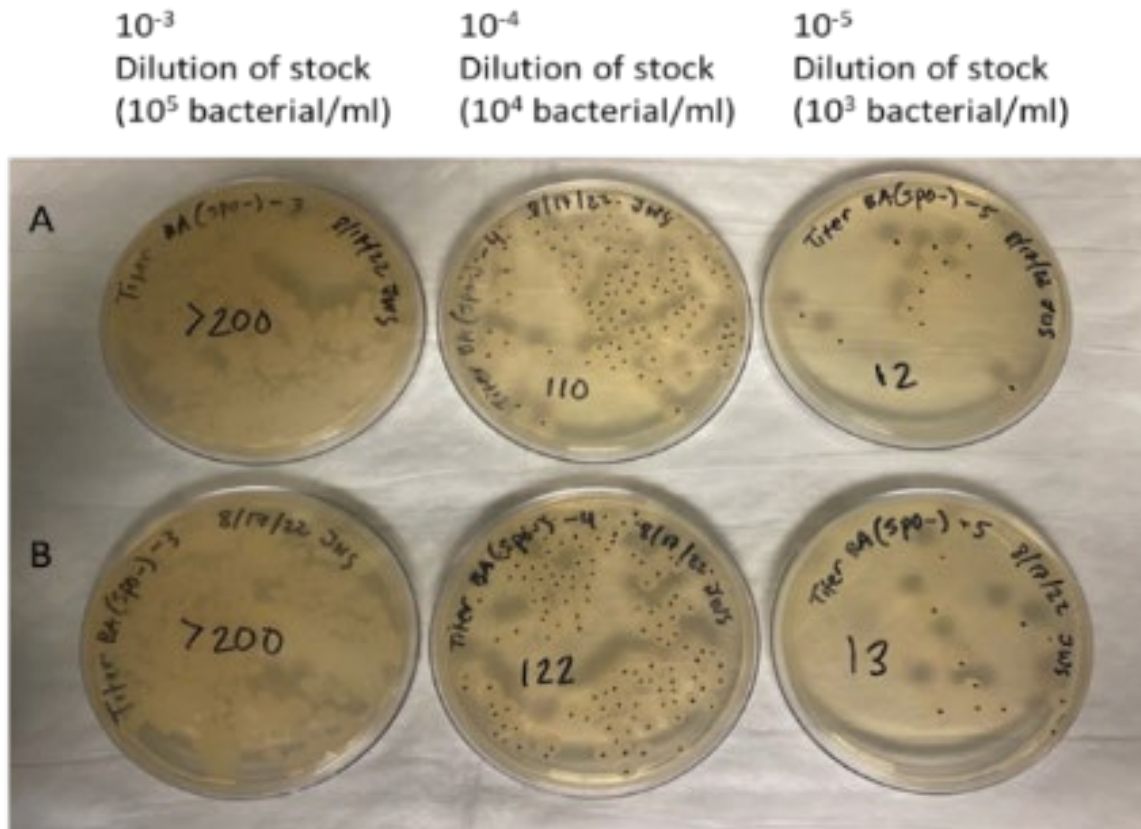


Figure 3. Representative titer plates (in duplicate) from 100 μ L diluted bacterial culture. Colonies counted were used to determine starting concentration of *B. anthracis* (delta Sterne spo^{-/-}) applied to Test tape sections.

3.1 Titers for determination of *B. anthracis* test concentrations

For each of experiment, one colony from an LB agar plate containing vegetative *B. anthracis* (delta Sterne spo^{-/-}) colonies were collected and grown overnight in LB media as described in the Methodology section. After proper growth was confirmed, a 1:10 dilution series was plated on sterile LB agar Petri dishes in duplicate as titers. After plates were incubated overnight, colonies were counted by hand, and calculated to estimate the cell number per milliliter media present in the samples spotted on the tape test sections. Figure 3 shows images of a representative set of titer plates with colonies written on lids.

3.2 Assessment of the release of bacteria from SaferTouch™ Tape post drying

To determine what bacteria could be washed off from the bacteria-exposed, dried tape test sections, tape test sections were exposed and dried as described in the Methodology section. Concentrations used for the tape exposures ranged from 10⁷ to 10⁵ bacteria per mL, and the amount applied to each test section was 100 μ L. Thus, between 10⁶ and 10⁴ bacteria were applied to each active tape surface. After drying, the sections were washed in PBS and the washate liquid tested for the presence of viable bacteria. As shown in Figure 4, almost no measurable viable bacteria were recovered from either of the ST or CT test sections. A few colonies are visible, but there is no significant difference between the ST and control tapes.

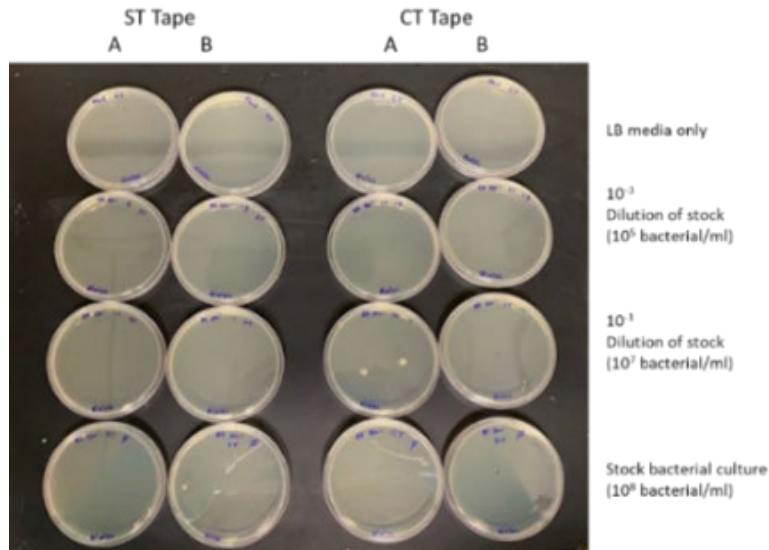


Figure 4. Representative plates (in duplicate) after overnight incubation of 1 ml washate from experiments with ST and CT tape sections using (top to bottom): 0, 10^5 , 10^7 , and 10^8 bacteria/mL.

3.3 Assessment of release of DNA from SaferTouch™ Tape

To determine if any DNA could be recovered from the exposed test sections, tape test sections were treated as described in the Methodology, and the washate tested for the presence of DNA. As described for the bacterial release experiments, concentrations used for DNA release experiments also ranged between 10^6 to 10^4 bacteria applied to each tape surface. After drying, the sections were washed, and the washate liquid was tested for the presence of DNA using the high sensitivity (HS) QUBIT kit for DNA. Given the concentration exposed to the active ST surface, we expected to see some DNA released due to the predicted lysing activity of the ST tape. Unfortunately, none was able to be measured. To make sure the concentration was not just diluted below the limit of detection, an additional step was added to concentrate the entire remaining washate (1800 μ L for each combined sample) using a Qiagen DNAeasy kit column, extracting each into 35 μ L DNase-free water. However, as shown in Table 1, still no measurable DNA was observed above the limit of detection for the QUBIT HS Kit (10 pg/ μ L).

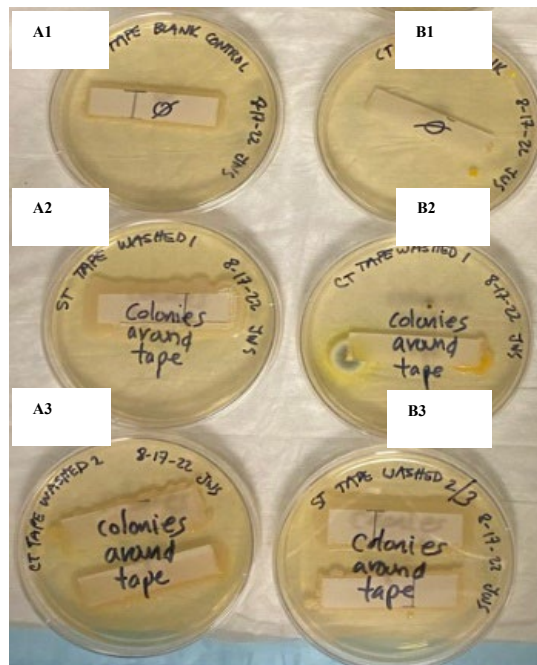


Figure 5. ST and CT tape sections. A1) Control ST tape, A2-A3) Washed ST tape strips, B1) Control CT, B2-B3) Washed CT tape strips.

Table 1. Presence of DNA in tape washates.

Conditions applied to Test Tape Sections	SaferTouch™ Tape Washate	Control Tape Washate
	Combined and concentrated duplicates	Combined and concentrated duplicates
LB Media Control	<10 pg/μL	<10 pg/μL
10 ⁵ bacteria	<10 pg/μL	<10 pg/μL
10 ⁶ bacteria	<10 pg/μL	<10 pg/μL
10 ⁷ bacteria	<10 pg/μL	<10 pg/μL

3.4 Assessment of the SaferTouch™ bactericidal effect

To determine the viability of any remaining bacteria adhering to the washed tape test sections, 10⁷ *B. anthracis* (*spo*-) cells (or blank media), was applied. Each washed tape section was placed “face down” on a sterile LB agar Petri dish and incubated at 37 °C in a standard bacterial incubator for 48 hours. As shown in Figure 5, there was robust growth from both the ST and the CT tape sections. While aseptic technique was followed in the biological safety cabinet during the experiment, the tapes are not sterile. The growth on the control tape sections for both the ST and CT experiments is attributed to background bacteria present on the tape before washing, and the incubation time used in this experiment.

3.5. Determination of control surfaces’ bacterial binding activity

To determine if the bacterial binding effect we observed with the two types of test tapes was due to the tape itself, two other surfaces were tested: paper (from the backing of the test tapes) and stainless-steel test surfaces. As shown in Figure 6A, bacteria were readily washed off the paper when treated in the identical manner as the tape test strips. In fact, so many bacteria washed off, Figure 6 shows only the lower concentrations, since complete lawns developed on the plates with higher concentrations after overnight incubation. There were also viable bacteria observed on the paper after washing, as shown in Figure 6B, with a magnified section for clarity. Following exposure to stainless steel test plates, the bacteria was washed in the same manner. Figure 7 show the results from washate from those exposed stainless-steel plates. The bacteria remaining on the steel test plate could be tested in the same way as the paper; however, the steel could not be adhered to the agar plate to allow correct growth conditions.



Figure 6. *B. anthracis* (*spo*-) bacteria present on and from paper test strips exposed to culture equivalents 10³–10⁵ bacteria. A) Culture plates (in duplicate) with washate from paper test strips, B) Washed paper test strips from the same tests. Plates 1-3: Triplicate paper test strips (10⁵ test), Plate 4: Media, Plate 5: Control plate (10⁵ bacteria).

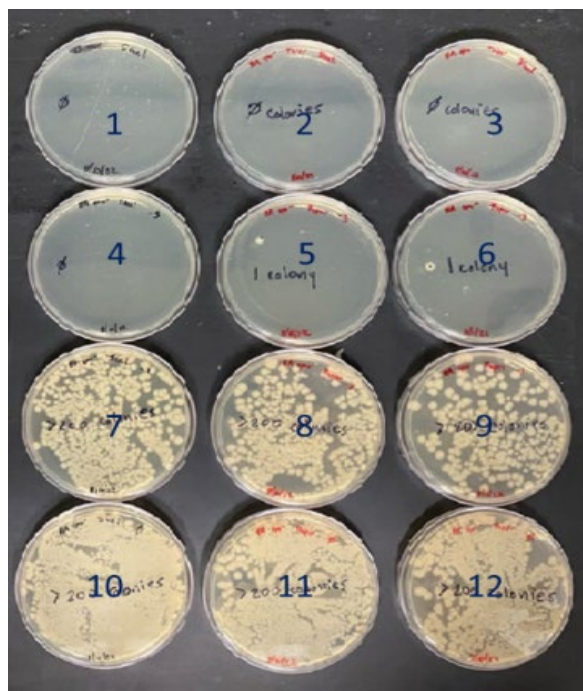


Figure 7. *B. anthracis* (spo^{-/-}) bacteria present in steel washate. A) Plates 1–3: Triplicate blank controls on steel test plates, Plates 4–6: Triplicate tests from 10² bacteria, Plates 7–9: Triplicate tests from 10³ bacteria, Plates 10–12: Triplicates from 10⁴ bacteria.

4. CONCLUSIONS

Experiments carried out in this project demonstrated clearly that both the coated and uncoated tapes adhered the test bacteria *B. anthracis* (delta Sterne spo^{-/-}), to the surface. There was not significant killing of bacteria on the surfaces. Furthermore, either no DNA was far below the limit of detection. Regardless, neither tape appeared to carry anticipated lysing or DNA release. In experiments with other surfaces, neither the paper, the steel, nor the simple effect of drying induced significant bacterial binding or killing. While some bacteria were retained and viable on the control paper strips after washing, they also released a large portion of viable bacteria, indicated by both plated paper and washate experiments indicated. The steel also released many viable bacteria after drying in the parallel experiments. While the growth of any bacteria remaining on the steel was not specifically tested, it is likely that those bacteria remained viable as well.

While the initial hypothesis for this work, the ability to lyse bacteria and release DNA directly on the ST tape, appears to have been rejected by these data there are a few possibilities left to explore. While we have expended resources allocated to this work, if additional resources were available, next steps would include: 1) image control and coated tapes in both clean and bacterial-exposed conditions by scanning electron microscopy, 2) repeat the work using a common skin bacterium, and 3) explore the efficiency of the tape solely as a bacterial or viral collection medium, and 4) extract the DNA directly from bacteria adhered to the tape. Overall, we greatly appreciated the opportunity to explore this hypothesis. Perhaps a future opportunity will allow further exploration of low size, weight, and power biodetection-related advantages the SaferTouch™ Tape may offer the Warfighter's biodetection mission.

ACKNOWLEDGMENTS

Funding for this Seedling Project was provided by the Director, Combat Capabilities Development Command Chemical Biological Center under the authorities and provisions of Section 2363 of the FY 2018 NDAA to develop new technologies. The authors would like to thank Ms. Capacine Brunson for her administrative support, and Dr. Kelly Nobles for her supervisory support of this work.

REFERENCES

- [1] Pang, B.C.; Cheung, B.K. Double swab technique for collecting touched evidence. *Leg. Med.* **2007**, *9* (4), pp 181–184.
- [2] Mawlood, S.K.; Alrowaithi, M.; Watson, N. Advantage of ForensiX Swabs in Retrieving and Preserving Biological Fluids. *J. Forensic Sci.* **2015**, *60* (3), pp 686–689.
- [3] Angelini, D.J.; Harris, J.V.; Burton, L.L.; Rastogi, P.R.; Smith, L.S.; Rastogi, V.K. Evaluation of Commercial-off-the-Shelf Materials for the Preservation of *Bacillus anthracis* Vegetative Cells for Forensic Analysis. *J. Forensic Sci.* **2018**, *63* (2), pp 412–419.
- [4] Barash, M.; Reshef, A.; Brauner, P. The use of adhesive tape for recovery of DNA from crime scene items. *J. Forensic Sci.* **2010**, *55* (4), pp 1058–1064.

Protective ratio of claramine against the toxic effects of melittin in mice

Nicole M. Vincelli^{a*}, Ryan Limbocker^b, Michael S. Horsmon^a, Theodore S. Moran^a

^aU.S. Army Combat Capabilities Development Command Chemical Biological Center, Research & Operations Directorate, 8198 Blackhawk Rd., Aberdeen Proving Ground, MD 21010

^bDepartment of Chemistry and Life Sciences, United States Military Academy, 646 Swift Rd., West Point, NY, 10996

ABSTRACT

The development of novel approaches to safeguard against known biological threat agents, as well as presently unknown toxins that are under development by our adversaries, represents a key area of fundamental research necessary to protect the Warfighter. Previous studies have indicated the chemical compound claramine may neutralize the toxic effects of the toxic polypeptide melittin in neuroblastoma cells. A pilot study was conducted with mice to potentially validate these findings in a living system. An LD₅₀ for melittin was estimated to be 7.69 mg/kg when administered intraperitoneally and a protective ratio of 1.13 both when claramine was administered 10 minutes prophylactically and when co-administered with melittin.

Keywords: Claramine, melittin, aminosterol, biotoxin neutralization, biothreat

1. INTRODUCTION

The development of novel approaches to safeguard against known biological threat agents, as well as presently unknown toxins that are under development by our adversaries, represents a key area of fundamental research with the potential to protect the Warfighter. The molecular composition of the plasma membrane plays a key role in mediating the susceptibility of cells to perturbations induced by toxic molecules. Therefore, the pharmacological regulation of the cell membrane has the potential to enhance cellular resilience to a wide variety of chemical and biological compounds. The aminosterol family of molecules have been previously studied for their unique ability to protect cell membranes from the toxic effects of protein aggregation in Alzheimer's and Parkinson's diseases when administered prior to or concurrent with exposure of cells to toxins.¹⁻³ Similarly, it was recently demonstrated that aminosterols can neutralize the toxicity of model biological threat agents in cells.⁴ Specifically, they found claramine, a blood-brain-barrier permeable small aminosterol molecule, neutralizes the toxicity of acute biological threat agents by blocking interactions with cell membranes. To date, claramine has been shown to specifically inhibit melittin from honeybee venom and α -hemolysin from *Staphylococcus aureus*.⁴ While these findings establish a framework by which medical countermeasures can safeguard cells from toxins, more information is needed to assess the utility of aminosterols in protecting cells from biological threat agents in living systems and subsequently facilitate a collaborative National Institutes of Health/Defense Threat Reduction Agency-level grant. A pilot study was conducted at U.S. Army Combat Capabilities Development Command Chemical Biological Center (DEVCOM CBC) with mice to potentially validate these findings in a living system.

2. METHODOLOGY

Twenty-nine adult male CD1 mice (Charles River Laboratories, Wilmington, MA) were delivered to DEVCOM CBC for use on study. All mice were allowed a minimum of 7 days of acclimation prior to use in the study and were group housed. Mice were provided certified lab feed, water ad libitum, and were maintained in a 12-hour light and 12-hour dark cycle with a monitored and controlled room temperature and humidity. All animal study work was conducted under an animal use protocol that was approved by the DEVCOM CBC Institutional Animal Care and Use Committee. On the day of the study, each mouse was body weighed and assigned a study number.

Melittin from honeybee venom ($\geq 85\%$ purity, Sigma Aldrich, St. Louis, MO) and Claramine (trifluoroacetate salt, $\geq 98\%$ purity, Sigma Aldrich, St. Louis, MO) was stored at $-80\text{ }^{\circ}\text{C}$ and $4\text{ }^{\circ}\text{C}$, respectively. On the day of the study, both reagents were brought to room temperature prior to being prepared for administration. Both materials were purchased from the same vendor with the same purity specifications to duplicate the work that was previously conducted at the United States Military Academy (USMA). All solutions were prepared for injection in sterile normal 0.9% saline. The study was broken into a total of four groups: 5 mg/kg claramine (study control group), melittin only (to determine the LD_{50}), melittin co-administrated with 5 mg/kg claramine, and 5 mg/kg claramine administered 10 minutes prior to melittin injection. When determining the protective ratio for this study, only the concentration of melittin was modified.

To determine the lethal dose 50 (LD_{50}) (median lethal dose to 50% of a population) a modified “up and down” method was used.⁵ A previously published LD_{50} for melittin in mice of 4.98 mg/kg was used to start.⁶ For the co-administration group, appropriate volumes of both melittin and claramine were drawn into a single syringe per individual and allowed to incubate for 30 minutes at $37\text{ }^{\circ}\text{C}$ prior to administration. Protective ratio was determined by dividing the calculated LD_{50} for each dosing group (co-administered and prophylactic) by the calculated LD_{50} for melittin alone. All mice were dosed with all compounds via intraperitoneal (IP) injection in the lower right quadrant after brief manual restraint. All animals were continuously observed following compound administration for overt clinical signs. The endpoint for this study was 24 hours following exposure, assuming death did not occur before then. A terminal blood sample was collected for blood chemistry analysis specifically to look for any changes to liver and kidney enzymes samples were analyzed immediately after collection. At the time of necropsy, animals were perfused with cold buffer solution and tissues were collected (lung, liver, kidneys, and brain) and fixed in 4% paraformaldehyde solution. These samples will be analyzed by USMA for histopathological changes.

3. DATA AND RESULTS

All five animals in the claramine 5 mg/kg control group showed no overt clinical response to receiving the compound aside from grooming the injection site. Tissue samples will be analyzed to ensure that no cellular effects are being caused by claramine as a therapeutic compound.

All animals receiving any of the dosages of melittin had immediate responses, within 1–2 minutes of injection. Immediately following melittin administration, all mice held their back ends lower to the cage and went through periods of activity followed by inactivity with abnormal posture. Within a few minutes, they would display additional signs of pain including orbital tightening, piloerection, hitched breathing, and a lack of activity, appetite, and output (urine/feces). Animals that were moribund displayed a darkening of the vasculature and skin on their tails. The animals at the lowest dose of melittin, 4.98 mg/kg , displayed signs of pain following exposure for multiple hours but were displaying normal behaviors again by the morning. The animals in the next highest melittin group, 7.92 mg/kg , that also received claramine, either by pre-treatment or co-administration, were alive the following morning but not all were life sustaining (lack of activity and no interest in eating or drinking). Animals receiving the highest dose of melittin, at 12.5 mg/kg , all died within 24 hours. One individual, mouse number 9, was believed to have an issue with dose administration as this animal did not progress through the typical pain response as compared to the other animals and did not succumb. Another animal was exposed at this dose concentration and died as would have been expected. LD_{50} values were estimated to include and exclude mouse number 9 below in Table 1. Each dosing group is detailed below in Tables 2-4.

Table 1. Summary of LD_{50} for melittin and protective ratio of claramine against melittin in mice.

Condition	LD_{50} (mg/kg)	Protective Ratio
Melittin Only	7.69	N/A
Melittin Only (without #9)	7.47	1
Co-Administration	8.41	1.13
Pre-Treatment	8.41	1.13

Table 2. Summary of LD₅₀ for melittin data. X-died, O-lived.

Animal #	Melittin (mg/kg)	Claramine (mg/kg)	24hr Lethality
6	5.0	N/A	O
9	12.5	N/A	O
12	12.5	N/A	X
13	7.92	N/A	X
16	5.0	N/A	O
17	7.92	N/A	X
20	5.0	N/A	O
21	7.92	N/A	O
22	7.92	N/A	X
23	7.92	N/A	X

Table 3. Summary of claramine and melittin co-administered data. X-died, O-lived.

Animal #	Melittin (mg/kg)	Claramine (mg/kg)	24hr Lethality
7	4.98	5	O
10	12.5	5	X
14	7.92	5	O
18	7.92	5	O
24	7.92	5	O
25	7.92	5	X
26	7.92	5	O

Table 4: Summary of claramine and melittin pre-treatment data. X-died, O-lived.

Animal #	Melittin (mg/kg)	Claramine (mg/kg)	24hr Lethality
8	4.98	5	O
11	12.5	5	X
15	7.92	5	O
19	7.92	5	O
27	7.92	5	O
28	7.92	5	X
29	7.92	5	O

4. CONCLUSIONS

The clinical signs following the exposure to melittin include typical displays of pain in mice, which is not surprising as melittin is the primary component of honeybee venom that causes pain.⁷ The length of time that the animals displayed signs of pain following exposure to melittin, however, was surprising. Previously published research with rats exposed to melittin subcutaneously indicated a pain response for about an hour following injection.⁷ The difference in the duration of pain could be due to difference in the injection location as the rat study utilized subcutaneous injections into the paw which could cause a more localized pain and inflammation response compared to the IP injections utilized in the current study. Melittin exposure in the abdomen would allow for a much larger surface area for inflammatory reactions and a faster introduction into systemic circulation, potentially resulting in a more widespread reaction to the toxin. Additionally, the nociceptive activation could be more pronounced following IP exposure leading to a much longer pain response time.

This pilot study showed claramine has a marginal effect of protection against lethality from melittin exposure in mice. While the results from this pilot study seem marginal, the small study numbers play a role in that outcome. Further investigation would be needed to properly evaluate the full potential of claramine, or aminosterol compounds as a class, as a suitable medical countermeasure against melittin. Claramine was able to protect against lethality at a single therapeutic dose, but additional research would be needed to optimize this dose. A pharmacokinetic study would

provide the half-life for the compound and allow a better understanding of how much would be needed and when the best time to administer it therapeutically. This pilot study did not look at whether claramine could offer the same neutralization when given after exposure to melittin which is an important follow-on question. Further, it would be beneficial to screen claramine against additional biological threats. Cellular effects are pending histopathological analysis at USMA but the ability of claramine to protect against lethality offers some promise.

ACKNOWLEDGMENTS

Funding for this work was provided by the Director, Combat Capabilities Development Command Chemical Biological Center under the authorities and provisions of Section 2363 of the FY 2022 NDAA to develop new technologies, engineer innovations, and introduce game-changing capabilities. The authors also wish to acknowledge Dr. Ryan Limbocker for the collaborative efforts of the USMA Chemistry and Life Sciences Department for both the concept behind the study and histopathology analysis of study samples and intellectual discussions, Dr. Stanley Hulet for General Supervision of the research project, intellectual discussions, and technical editing, and Mr. Michael S. Horsmon and Mr. Theodore S. Moran for their direct technical assistance of the study and intellectual discussions.

REFERENCES

- [1] Limbocker, R.; Chia, S.; Ruggeri, F.S.; Perni, M.; Cascella, R.; Heller, G.T.; Meisl, G.; Mannini, B.; Habchi, J.; Michaels, T.C.T.; Challa, P.K.; Ahn, M.; Casford, S.T.; Fernando, N.; Xu, C.K.; Kloss, N.D.; Cohen, S.I.A.; Kumita, J.R.; Cecchi, C.; Zasloff, M.; Linse, S.; Knowles, T.P.J.; Chiti, F.; Vendruscolo, M.; Dobson, C.M. Trodusquemine enhances A β ₄₂ aggregation but suppresses its toxicity by displacing oligomers from cell membranes. *Nat Commun.* **2019**, *10* (225), pp 1–13.
- [2] Limbocker, R.; Staats, R.; Chia, S.; Ruggeri, F.S.; Mannini, B.; Xu, C.K.; Perni, M.; Cascella, R.; Bigi, A.; Sasser, L.R.; Block, N.R.; Wright, A.K.; Kreiser, R.P.; Custy, E.T.; Meisl, G.; Errico, S.; Habchi, J.; Flagmeier, P.; Kartanas, T.; Hollows, J.E.; Nguyen, L.T.; LeForte, K.; Barbut, D.; Kumita, J.R.; Cecchi, C.; Zasloff, M.; Knowles, T.P.J.; Dobson, C.M.; Chiti, F.; Vendruscolo, M. Squalamine and Its Derivatives Modulate the Aggregation of Amyloid- β and α -Synuclein and Suppress the Toxicity of Their Oligomers. *Front Neurosci.* **2021**, *15*:680026/fnins.2021.680026.
- [3] Limbocker, R.; Errico, S.; Barbut, D.; Knowles, T.P.J.; Vendruscolo, M.; Chiti, F.; Zasloff, M. Squalamine and trodusquemine: two natural products for neurodegenerative diseases, from physical chemistry to the clinic. *Nat. Prod. Rep.* **2022**, *39*, pp 742–753.
- [4] Kreiser, R.P.; Wright, A.K.; Sasser, L.R.; Rinauro, D.J.; Gabriel, J.M.; Hsu, C.M.; Hurtado, J.A.; McKenzie, T.L.; Errico, S.; Albright, J.A.; Richardson, L.; Jaffett, V.A.; Riegner, D.E.; Nguyen, L.T.; LeForte, K.; Zasloff, M.; Hollows, J.E.; Chiti, F.; Vendruscolo, M.; Limbocker, R. A Brain-Permeable Aminosterol Regulates Cell Membranes to Mitigate the Toxicity of Diverse Pore-Forming Agents. *ACS Chem Neurosci.* **2022**, *13* (8), pp 1219–1231.
- [5] Rispin, A.; Farrar, D.; Margosches, E.; Gupta, K.; Stitzel, K.; Carr, G.; Greene, M.; Meyer, W.; McCall, D. Alternative methods for the median lethal dose (LD₅₀) test: the up-and-down procedure for acute oral toxicity. *ILAR Journal.* **2002**, *43* (4), pp 233–243.
- [6] Askari, P.; Namaei, M.H.; Ghazvini, K.; Hosseini, M. *In vitro* and *in vivo* toxicity and antibacterial efficacy of melittin against clinical extensively drug-resistant bacteria. *BMC Pharmacol Toxicol.* **2021**, *22* (1), pp 1–12.
- [7] Chen, J.; Guan, S.M.; Sun, W.; Fu, H. Melittin, the Major Pain-Producing Substance of Bee Venom. *Neurosci Bull.* **2016**, *32* (3), pp 265–272.